

Proceedings of the Second
Workshop

Coastal and Marine Applications of SAR

8 - 12 September 2003
Svalbard, Norway

ESA SP-565

June 2004

Proceedings of the Second Workshop

Coastal and Marine Applications of SAR

8 – 12 September 2003
Svalbard, Norway

Sponsored by:



**European Space Agency
Agence spatiale européenne**

Organizing Committee

Yves-Louis Desnos (ESA-ESRIN)
 Johnny A. Johannessen (NERSC)
 Chuck Luther (ONR)
 William Pichel (NOAA)
 Robert Shuchman (Altarum)
 Per Erik Skrøvseth (Norwegian Space Centre)
 Ann-Lisbeth Ruud (Norwegian Space Centre)

Scientific Committee

Bertrand Chapron (Ifremer)
 Pablo Clemente-Colon (NOAA)
 Jose Da Silva (University of Lisboa),
 Mark Drinkwater (ESA)
 Jochen Horstmann (GKSS)
 Johnny A. Johannessen (NERSC)
 Harald Johnsen (NORUT-IT)
 Ian Robinson (SOC)
 Donald Thompson (JHU-APL)
 Paris Vachon (CCRS)
 Christopher Wackerman (VERIDIAN)

<i>Publication</i>	Proceedings of the Second Workshop on Coastal and Marine Applications of SAR, 8 – 12 September 2003, Svalbard, Norway (ESA SP-565, June 2004)
<i>Editor:</i>	H. Lacoste
<i>Published and distributed by:</i>	ESA Publications Division ESTEC Postbus 299 2200 AG Noordwijk The Netherlands
<i>Printed in:</i>	The Netherlands
<i>Price:</i>	€ 30
<i>ISBN No:</i>	92-9092-876-X
<i>ISSN No:</i>	1609-042X
<i>Copyright:</i>	© 2004 European Space Agency

CONTENTS

Overview

Operational Monitoring of Coastal and Marine Environment with Spaceborne SAR Systems: Where Are We Now and Where Are We Going <i>C.C. Wackerman & J. Johannessen</i>	3
--	---

Wind Session

Chairs: F. Monaldo & V. Kerbaol

The SAR Measurement of Ocean Surface Winds: An Overview <i>F. Monaldo, V. Kerbaol, & the SAR Wind Team</i>	15
Using Satellite SAR in Offshore Wind Resource Assessment <i>B.R. Furevik, C.B. Hasager, M. Nielsen, T. Hamre, B.H. Jørgensen, O. Rathmann, & O.M. Johannessen</i>	33
The Correction of Surface Layer Wind Speeds for Atmospheric Stratification and Height <i>R.C. Foster, T.D. Sikora & G.S. Young</i>	39
Estimation of Small-Scale Wind Fields from Synthetic Aperture Radar Data <i>D.R. Lyzenga</i>	49
A Projection Method for Automatic Estimation of Wind Vectors with RADARSAT SAR Imagery <i>C. Wackerman, W.G. Pichel & P. Clemente-Colón</i>	55
High Resolution Ocean Surface Wind Fields Retrieved from Spaceborne Synthetic Aperture Radars Operating at C-Band <i>J. Horstmann & W. Koch</i>	61
SAR Wind Fields for Offshore Wind Farming <i>T. Schneiderhan, J. Schulz-Stellenfleth, S. Lehner & J. Horstmann</i>	69

Wave Session

Chairs: S. Lehner & F.J. Ocampo-Torres

The SAE Measurement of Ocean Waves: Wave Session Whitepaper <i>S. Lehner & F. J. Ocampo-Torres</i>	77
Estimation of Two-Dimensional Ocean Wave Spectra from Envisat ASAR Wave Mode Data Using a Maximum a posteriori Approach <i>J. Schultz-Stellenfleth & S. Lehner</i>	89
Validation of the ASAR Wave Mode Level 2 Product Using WAM and Buoy Spectra <i>H. Johnsen, G. Engen & B. Chapron</i>	95

Current Feature Session

Chairs: R. Romeiser & S. Ufermann

Status Report on the Remote Sensing of Current Features by Spaceborne Synthetic Aperture Radar <i>R. Romeiser, S. Ufermann, & S. Kern</i>	105
Hot-spots of Internal Wave Activity Off Iberia Revealed by Multisensor Remote Sensing Satellite Observations – SPOTIWAVE <i>A. Azevedo, S. Correia, J.C.B. da Silva & A.L. New</i>	125
Satellite Synthetic Aperture Radar Sea Surface Doppler Measurements <i>B. Chapron, F. Collard & V. Kerbaol</i>	133
On Radar Imaging of Ocean Phenomena <i>V. Kudryavtsev, D. Akimov, J.A. Johannessen, O.M. Johannessen & B. Chapron</i>	141

ICE SESSION

Chairs: R. Shuchman & S. Sandven

SAR Measurement of Sea Ice parameters: Sea Ice Session Overview Paper <i>R.A. Shuchman & D.G. Flett</i>	151
Sea Ice Mapping Using Envisat ASAR Wideswath Images <i>S. Sandven, K. Kloster, H. Tangen, T. S-Andreassen, H. Goodwing & K. Partington</i>	161
Automated Location of Ice Regions in RADARSAT SAR Imagery <i>C. Wackerman, W.G. Pichel & P. Clement-Colón</i>	169
Routine Production of SAR-Derived Ice and Ocean Products in the United States <i>W.G. Pichel, P. Clemente-Colón, C. Bertoia, M. Van Woert, C.C. Wackerman, F. Monaldo, D.R. Thompson, K.S. Friedman & X. Li</i>	175
Operational Use of SAR at the Canadian Ice Service: Present Operations and a Look to the Future <i>D.G. Flett</i>	183

Sea Ice Geophysical Measurements from SEASAT to the Present, with an Emphasis on Ice Motion: A Brief Review and a Look Ahead <i>B. Holt & R. Kwok</i>	199
---	-----

VALIDATION

Validation of SAR Ocean Data Products and Verification of Process Models Used for SAR Interpretation <i>I. Robinson & S. Ufermann</i>	211
--	-----

USER SURVEY

User Requirements for SAR Data in the Coastal and Marine Environment <i>C. O'Mahony, V. Cummins, N. Dwyer & J.A. Johannessen</i>	219
---	-----

FUTURE SPACEBORNE SAR SYSTEM

The TerraSAR-L System and Mission Objectives <i>M. Zink</i>	227
TerraSAR-X for Oceanography – Mission Overview <i>S. Lehner, J. Horstmann, J. Schulz-Stellenfleth, A. Roth & M. Eineder</i>	233
A Brief Overview of the Advanced Land Observing Satellite (ALOS) and its Potential for Marine Applications <i>A. Rosenqvist, D. Ichitsubo, Y. Osawa, A. Matsumoto, N. Ito & T. Hamazaki</i>	239
SAOCOM – 1 Argentina L-Band SAR Mission Overview <i>A.E. Giraldez</i>	245

List of Participants	252
-----------------------------	-----

Overview

**This page intentionally
left blank (pagination)**

OPERATIONAL MONITORING OF COASTAL AND MARINE ENVIRONMENT WITH SPACEBORNE SAR SYSTEMS: WHERE ARE WE NOW AND WHERE ARE WE GOING

Christopher Wackerman¹ and Johnny Johannessen²

¹General Dynamics Advanced Information Systems, P.O. Box 134008, Ann Arbor Michigan, 48113-4008 USA

chris.wackerman@gd-ais.com

²Nansen Environmental and Remote Sensing Center, Edvard Griegsvei 3a, 5059 Bergen, Norway

Johnny.johannessen@nersc.no

ABSTRACT

The 2nd workshop on Coastal and Marine Applications of Synthetic Aperture Radar was held in Svalbard Norway on 8-12 September 2003. This conference was focused on providing an overview of the tools now available within the international community for utilizing synthetic aperture radar (SAR) systems to characterize the marine environment. Applications were specifically focused on wind, waves, sea ice, and currents. This paper provides an overview of the discussions from that workshop and proposes the next steps along the road of achieving true operational usage of SAR sensors for monitoring the marine environment.

1. INTRODUCTION

With the coming of simultaneous flight operations of three calibrated spaceborne Synthetic Aperture Radar (SAR) systems (ENVISAT, RADARSAT-2 and ALOS) employing wide swath (~500km), multi-frequency and multi-polarization technology, SAR application will be on the threshold of a new era. Add to this the more focused satellite systems being planned by individual countries (ESA's TerraSAR-L, Germany's TerraSAR-X, Italy's Cosmo-Skymed, and Argentina's SAOCOM) and we find that we are entering a period where the availability, coverage, and diversity of SAR data will be unprecedented throughout the world.

After ten years of research into estimation of environmental information from spaceborne imaging SAR, now is the time to demonstrate the operational capability of such systems to monitor the marine environment. As will be clear from this summary and the papers in this volume, many of the tools are in place and much of the research and applications are mature, and as is clear above, data availability has never been better. If we do not successfully demonstrate operational capabilities within the next few years, the opportunity to build a sustainable international user base in support of imaging SAR systems for marine monitoring will be lost.

To do this will require international collaboration to facilitate data access and to allow the development and harmonization of uniform systems operating simultaneously at different regions around the world. Such uniformity will be essential to build an international user base that is familiar with a standard set of SAR-derived marine environmental products, is familiar with standard methods to access the products, and routinely uses the products in operational systems. Such standardization is required to make imaging SAR truly an asset for operational marine monitoring.

The first step along this path is to get a snapshot of the current state of the art in operational marine monitoring with spaceborne SAR systems. Four years ago the 1st Workshop on Coastal and Marine Applications of Wide Swath SAR was held at the Applied Physics Laboratory in Laurel MD where researchers from facilities around the world presented a summary of the then emerging technologies for utilizing wide-swath SAR imaging systems for coastal and marine applications (Beal & Pichel 2000). The 2nd Workshop on Coastal and Marine Applications of Synthetic Aperture Radar was held in Svalbard Norway on 8-12 September 2003. The second workshop was specifically focused on providing an overview of the operational tools now available within the international community, the new methods and applications that researchers were pursuing, and the future directions that marine applications may go. This proceedings provide that state of the art summary from the 2nd coastal and marine SAR applications workshop.

This second workshop focused on answering three questions: (1) What progress has been made since the first workshop on operational SAR marine applications; (2) What are the currently available tools for deriving marine environmental products and what validation results have been performed; and (3) What are the future directions for marine monitoring. Instead of the traditional approach of allowing individual researchers to present summaries of their work, it was decided that to facilitate answering these questions the workshop would be divided into four applications areas: Winds, Waves, Sea Ice, and Currents & Features. For each application community and workshop participants prepared a single summary

presentation of the state of the art in that application area, addressed these questions, and in the process came to a consensus as to the answers. In this proceedings are four summary papers from each application which resulted from these presentations and were contributed to by all the researchers attending the workshop. Following the summary papers are shorter technical papers submitted by individual researchers discussing their particular application or technique in more detail.

There are of course other applications areas where SAR imaging plays a role, three of particular interest being ship monitoring, oil spill detection, and shallow water bathymetry. The former two areas are currently being addressed in two European programs, the OCEANIDES project and the Detection, Classification and Identification of Marine Traffic from Space (DECLIMS) project. Both of these projects will shortly provide state of the art reports on these applications, and so it was decided not to duplicate their efforts in these proceedings.

Sections 2 and 3 of this paper provide an overall summary of the workshop answers to the questions posed above. These answers are drawn from results generated by all the researchers working internationally in these applications areas, and as such they are all co-authors to this summary. The four summary papers as well as the detailed technical papers that are in these proceedings provide the background, references, and details to support the conclusions we state here. We refer the reader to the other papers in these proceedings and to the summary papers in particular. Section 4 provides the author's view of the next steps toward operational SAR usage, and Section 5 presents a summary and discussion.

2. WHAT PROGRESS HAVE WE MADE OVER THE LAST FOUR YEARS

An important question addressed in this second workshop was to summarize what progress has been made in operational use of SAR since the first workshop. That first workshop focused on emerging technologies and initial demonstrations of utilizing SAR images to manually derive information. Out of the second workshop it became clear that a large body of work has been ongoing to make a number of these applications operational, to incorporate SAR imagery routinely in some operations, and to continue to develop new approaches for estimating marine environmental information.

In the estimation of winds, the accuracy of the extracted wind speeds and directions has been documented over the last years by comparison to *in situ*

buoy observations, winds derived from satellite-based scatterometer sensors, and model winds by a wide range of researchers [Vachon & Dobson (1996), Wackerman et al. (1996), Fetterer et al. (1998), Horstmann et al. (1998), Kerbaol et al. (1998), Korsbakken & Furevik (1998), Korsbakken et al. (1998), Lehner et al. (1998), Mastenbroek (1998), Vandemark et al. (1998), Furevik & Korsbakken (2000), Horstmann et al. (2000a), Horstmann et al. (2000b), Lehner et al. (2000), Monaldo et al. (2001), Thompson et al. (2001), Furevik et al. (2002), Wackerman et al. (2003)]. These new results support that wind speeds can be derived operationally from SAR imagery with errors (in the sense of a root-mean-squared-error, RMSE) of less than 2 m/s and with spatial resolutions of a few kilometers. This is whether wind directions are derived from the SAR image itself or are taken from scatterometer or model data. Wind directions can be derived from SAR imagery directly with RMSEs of 25 degrees over spatial resolutions of 10 to 25 km [Wackerman et al. (1996), Fetterer et al. (1998), Korbakken and Furevik (1998), Vachon and Dobson (2000), Horstmann et al. (2002), Du et al. (2002), Fichaux and Rachin (2002)]. Over the past two years, operational delivery of wind fields (as well as ship location maps) from SAR imagery in under 3 hours has been routinely demonstrated as part of the NOAA/NESDIS Alaska SAR Demonstration Project (Pichel & Clemente-Colon, 2000), getting the system significantly closer to delivery times that weather forecasters require (often within 2 hours). Fig. 1 shows an example wind field product that is automatically generated as part of this project and that combines results from two different algorithms. In addition, the wind fields being derived in the Alaska SAR Demonstration are being used to determine ferry routes around Alaska, and have been used in NATO exercises. Finally new techniques for wind estimation from SAR continue to be developed; utilizing the smearing effects in SAR to estimate wind speed and the cross-spectrum to derive wind vectors [Egen et al. (1998), Kerbaol et al. (1998), Lehner et al. (2000)].

In wave estimation, the use of SAR images (mostly imagerettes; 5 km X 10 km SAR images acquired every 100 to 200 km along the satellite orbit) to estimate wave spectra is now running operationally at a number of meteorological offices (The Met Office UK, Meteo France, Norwegian Met Office, and the European Centre for Medium-range Weather Forecast (ECMWF)) (Loti et al. 2003) using tools based on transfer functions between SAR image modulations and wave height modulations [Hasselmann & Hasselmann (1991), Krogstad et al. (1994), Egen & Johnson (1995)]. Fig. 2 shows an example of such a spectrum that was derived by DLR from ERS-2 imagery processed to simulate ENVISAT data and

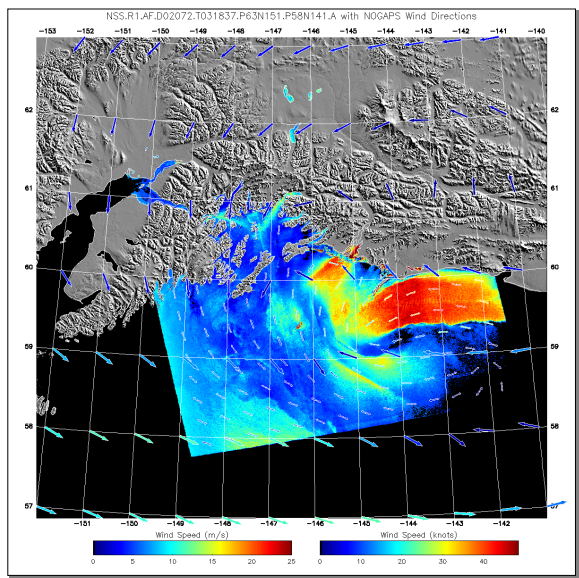


Fig. 1: Example of a wind field product. The wind speed values in color are from the JHU/APL algorithm using model wind directions shown as the large arrows located at the grid line intersections. The smaller arrows embedded in the wind image are from the General Dynamics algorithm. For both, color represents the estimated wind speed.

compared to what was available previously, the ERS UWA Spectrum. The new approaches can estimate wave direction (via the spectrum of the imaginary part) whereas the previous approaches had a 180 degree ambiguity. Over the past years a number of programs have been performed to compare SAR derived spectral parameters to those generated from global wave models (mainly WAM) [Bruning et al. (1994), Heimbach et al. (1998), Lehner et al. (2000)]. RMSE in significant wave height of 0.4 to 0.6 m, in wave period of 1.2 s, and in wave direction of about 20 degrees have been established in a range of experiments. Finally, new techniques for deriving wave spectra from SAR imagery continue to be developed, and in particular techniques that utilize a more accurate non-linear transfer function are currently being tested, as are the possibility to derive individual wave and wave group parameters [Matstenbroek & Falk (2000), Schulz-Stellenfleth & Lehner (2001), Schulz-Stellenfleth & Lehner (2003a), Schulz-Stellenfleth & Lehner (2003b), Dankert et al. (2003)].

ASAR wave mode

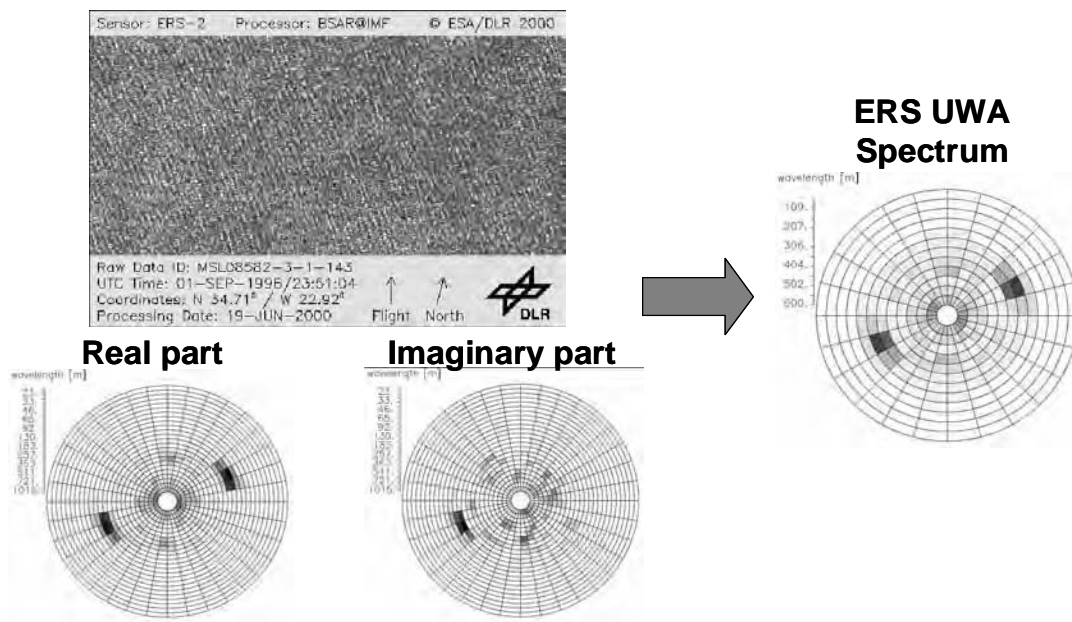
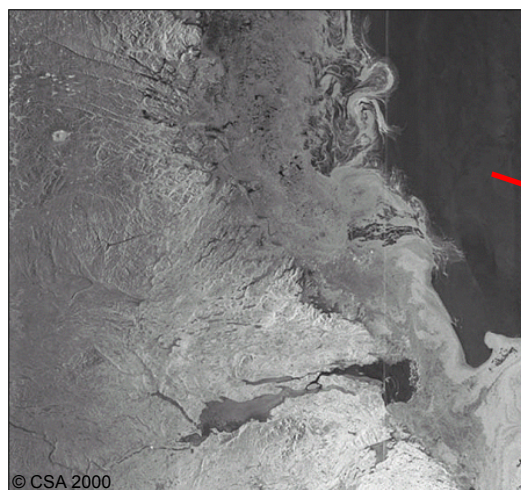
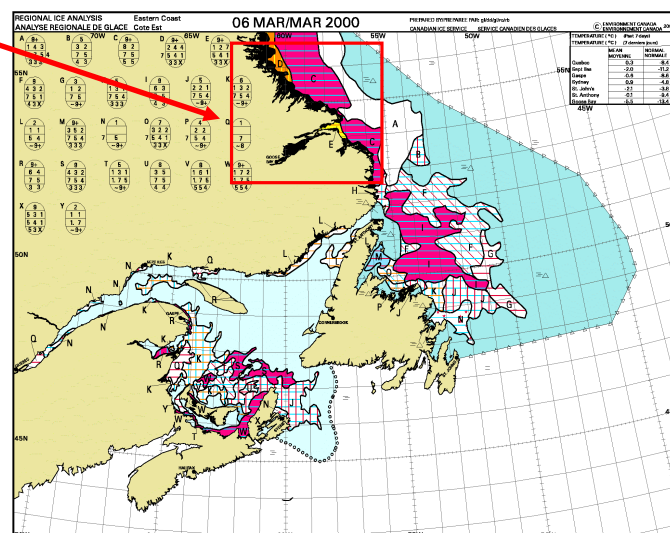


Fig. 2: Example wave spectrum product generated by DLR (bottom left) that comes from the complex-valued imagerettes compared to a product using previous methods (right). The image (upper left) comes from the ERS-2 sensor and was processed to simulate what ENVISAT produces. Note that the old methods did not indicate wave direction whereas the complex-valued imagerettes can generate wave direction via the spectrum of the imaginary part. Figure courtesy of Susanne Lehner, DLR.



Labrador coast - ScanSAR Wide, March 6, 2000



East Coast ice chart - March 6, 2000

Fig. 3: An ice chart for the east coast of Canada (right) that was generated in part using information from the RADARSAT-1 SAR image shown on the left to derive ice edge information. Figure courtesy of Dean Flett, Canadian Ice Service.

In sea ice monitoring, over the past years operational use of SAR imagery to manually derive sea ice type has grown from two centers in 1999 to a number which now include centers in the United States, Canada, Denmark, Finland, Germany, Sweden and Norway [Wohl (1995), Vainio et al., (2000), Bertoia et al., (1999)]. SAR imagery is now fully integrated into operational data analysis and product generation at these ice centers is being used routinely to validate ice edge information derived from QuickScat scatterometers and SSM/I radiometers and to help determine ice type. As an example, Fig. 3 shows a RADARSAT SAR image that was utilized to help develop the ice edge information shown in the attached Canadian East Coast ice chart. Techniques for using SAR imagery to track drifting ice and to estimate ice deformation have recently been utilized by the ice centers as experimental products [Kwok et al (1990), McConnell et al. (1991), Williams et al. (1999)]. New techniques in this field are also being developed, including the use of polarimetric SAR data for ice classification and ice edge locations. However, automated tools for deriving ice information from SAR imagery were identified in the workshop as an important area for ongoing research in the sea ice community [Havercamp et al. (1995), Havercamp & Tsatsoulis (1999), Soh & Tsatsoulis (1999), Weber et al. (2003), Soh et al. (2004)].

Estimating currents from SAR imagery, as well as exploiting other oceanic features, is perhaps the most research-dominated application area addressed by the workshop. Most of the work over the last years has been in development of improved forward models to predict the SAR signatures of regions with changing oceanic currents [Romeiser et al. (1997), Romeiser & Alpers (1997), Johanessen et al. (1996), Jansen et al. (1998), Chubb et al. (1999), Romeiser & Ufermann (2001), Vogelzang (2001), Kudryavtsev et al. (2003a), Kudryavtsev et al. (2003b)]. Fig. 4 shows an example output from one such model, comparing actual radar cross section perturbations across a current front to simulated values. However, operational manual image analysis has become incorporated recently for a number of users, including the Norwegian Navy for locating fronts and tracking oil, the UK Hydrology Office for locating current fronts and internal waves, and the Brazilian oil company Petrobras for tracking oil spills and locating oil seeps. In addition, new techniques for estimating currents based on the Doppler shift in complex-valued SAR imagery are being pursued, as well as the use of along-track interferometric SAR systems for direct observations of surface currents.

Overall, the workshop successfully focused attention on a large amount of work that has been ongoing recently to make SAR marine monitoring more operational. Perhaps more importantly, it also identified a wide range of applications that now routinely utilize SAR imagery in generating products both automatically and manually.

3. WHAT TOOLS ARE CURRENTLY AVAILABLE

A second focus of the workshop was to identify what tools are currently available for extracting marine environmental products from SAR imagery. Clearly, for SAR systems to be operational in marine monitoring, a standardized set of tools for deriving information will need to be established and made available to the community. In fact, as discussed below, demonstrating such a uniform set of tools will be the next step in the path to achieve fully operational utility. For details concerning all of these tools, please see the accompanying summary and detail papers.

In wind vector estimation, a wide range of tools are now available with various degrees of user interaction required, including codes from the German GKSS Research Center, the Canadian Center for Remote Sensing (CCRS), the Norwegian KSAT, the Norwegian Nansen Environmental and Remote Sensing Center (NERSC), the French Boost Technologies, General Dynamics in the U.S., the John Hopkins University Applied Physics Lab in the U.S., the German Aerospace Center (DLR), and the European Space Agency (ESA) [Wackerman et al. (1996), Kerbaol et al. (1998), Korsbakken et al. (1998), Mastenbroek (1998), Horstmann et al. (2000a), Lehner et al. (2000), Monaldo et al. (2001), Vachon and Dobson (2000), Horstmann et al. (2002), Du et al. (2002), Fichaux and Rachin (2002)]. Some of these tools estimate wind speed and direction, some estimate just wind speed.

In wave estimation, a number of institutions have automated tools to generate wave spectra from SAR image spectra. The Max Planck Institute algorithms (MPI-1 and MPI-2) are the ones currently running at the meteorological centers (ECMWF, Meteo France, The Met Office UK) [Hasselmann & Hasselmann (1991), Krogstad et al. (1994)]. In addition there are a range of tools requiring differing forms of inputs (e.g. some require an *a priori* wave spectrum and some do not); a European Space Agency (ESA) algorithm developed by NORUT and IFREMER (usually referred to as the ESA algorithm) (Egen and Johnsen (1995)), an algorithm from ARGOSS called the Semi-Parametric Retrieval Algorithm (SPRA) (Mastenbroek & Falk (2000)), two algorithms from DLR called the

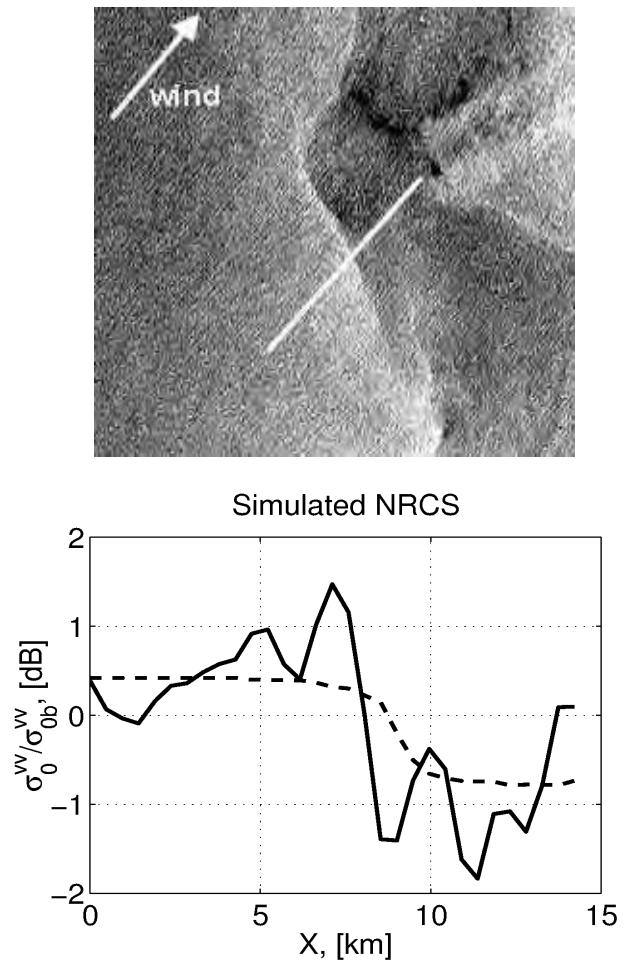


Fig. 4: Example of the accuracies of the forward models for predicting radar cross section signatures of current fronts. The SAR image is shown on the top, with the white line indicating where a cut through the image was taken. The plot on the bottom shows the actual radar cross section values (solid line) versus the simulated values (dashed line). Figure courtesy of (Kudryavtsev et al. 2003b).

Partitioning Rescale and Shift Algorithm (PARSA) and one referred to as LISE (Schulz-Stellenfleth & Lehner (2003)), and an algorithm from General Dynamics (Lyzenga (2002)). All of them have been compared against combinations of WAM predictions and *in situ* observations to varying degrees and have reproduced significant wave heights with RMSEs of 0.4 to 0.6 m, dominant wave periods with RMSE of 1.2 s, and dominant wave directions with RMSEs of 20 degrees.

In sea ice monitoring, most of the tool development to date has been on user interactive tools for helping the ice analysts provide sea ice maps operationally, and these are utilized at all of the international ice centers currently [Wohl (1995), Vainio et al., (2000), Bertoia

et al., (1999)]. The exceptions to these are tools developed by Jet Propulsion Laboratory (JPL) to automatically determine ice deformation over time in the Arctic and automatically track floe motion (both part of the Radarsat Geophysical Processing Station (RGPS) running at the Alaska SAR facility) [Kwok et al., (1990)]. None of the automated tools have yet been validated in the sense of generating RMSEs for specific environmental quantities, although as was noted above a major thrust for the sea ice community is the automation of more monitoring tools [McConnell et al. (1991), Haverkamp et al. (1995), Haverkamp & Tsatsoulis (1999), Soh & Tsatsoulis (1999), Williams et al. (1999), Weber et al. (2003), Soh et al. (2004)].

In estimation of currents and other oceanic features, multiple models are being developed to generate SAR signatures from descriptions of the underlying environmental parameters with four models having reached a level of maturity: the ERIM Ocean Model developed by what is now General Dynamics [Lyzenga and Bennett (1988)], the model developed by the University of Hamburg [Romeiser et al., (1997), Romeiser & Alpers, (1997)], the Radar Imaging Model (RIM) model developed by Nansen International Environmental and Remote Sensing Center (NIERSC) [Krudryavtsev et al. (2003a), Krudryavtsev et al. (2003b)], and the ARGOSS model [Vogelzang (2001)]. All of these are still research codes that contain different physical assumptions to explain SAR signatures observed in various experiments. Automated algorithms have also been developed recently to help users interpret image features, including the Bathymetry Assessment System (BAS) by ARGOSS [Calkoen et al. (2001)] as well as algorithms for automatically locating oceanic features in SAR imagery using wavelet analysis [Rodenas & Garelo (1998), Wu & Liu, (2003)]. Tools to locate and characterize ocean features have also been developed and or refined under the MARS AIS project [Johannessen et al. (2001)]. Tools which require some user interaction are estimations of currents using the Doppler centroid shift in complex-valued SAR imagery (developed by Boost Technologies) and estimation of internal wave parameters by the University of Hamburg.

In summary, the range of tools available for estimating coastal environmental parameters has significantly increased over the last few years. A number of the tools are automated (including estimation of wind vectors, wave spectra, ice deformation, near-shore bathymetry, location of current features and ship detection) whereas a number of the tools still require some level of user interaction (including other wind vector tools, ice type classification, current gradients and radial currents, and oil spill detection). Perhaps

more importantly for operational use, the environmental products are starting to be validated (i.e. generating RMSE values) against *in situ* observations and/or models. The most heavily validated to date with *in situ* observations are the wind vector tools. The wave spectra tools have been validated against some *in situ* observations but mostly compared against model results. However a number of validation campaigns with *in situ* observations are either on-going or being planned. The remaining tools are less mature in their development cycle and thus have not yet been validated to the level of the winds and waves tools, but a number of them, estimation of currents in particular, are just coming into validation studies. Overall, the tools that exist right now already span a large range of the coastal environmental parameters desired by users.

4. WHERE DO WE GO FROM HERE

The 2nd Workshop on Coastal and Marine Applications of SAR has successfully provided a snapshot of the current state of the art in coastal monitoring from SAR systems. Although not specifically addressed in the conference, it is important to also understand where the community could go from here to continue the growth of operational usage of SAR sensors. The authors of this overview paper propose that the next step on the path to achieving operational capability is to provide an international demonstration of environmental products generated from SAR sensors at a range of locations. This demonstration must show uniformity in product generation from all sites, and post all products on the internet for interchange between partners. The tools would be run operationally at each location to demonstrate the timeliness and performance of the products to local users, based on the models of the ongoing NOAA/NESDIS Alaska SAR Demonstration Project which automatically posts wind vectors and ship locations usually within 3 hours of data acquisition, and the Norwegian quasi-operational system for oil spill detection, ship locations and wave retrieval. We envision that the tools would be drawn and integrated from a range of international partners and taken from the set of tools described above, using the most robust approach for each product. Such a demonstration would verify the capability of SAR sensors to provide uniform, world-wide, coastal products, determine the timeliness of the product generation, and validate the performance of the products.

We envision the demonstration lasting for one year, from mid-2004 to mid-2005. The tools that would be used to generate products would fall into two types; automated and user-interaction. It is clear that the automated tools currently available would include: (1)

wind fields; (2) wave spectra (include parameters derived from the spectra); (3) ship locations; and (4) ice deformation. The user-interaction tools would include locating current fronts and generating ice type maps. The products from each tool would be standardized, so that all locations would generate the same format for wind fields, wave spectra, etc. Since NOAA/NESDIS in the U.S. and Nansen Environmental and Remote Sensing Center in Norway are running demonstrations off the coasts of Alaska and Norway, respectively, we envision at least starting with these locations, with the possible early additions of locations off the coasts of Florida, Great Britain, and France, since all of these locations have some form of image download capability and are generating some form of products now from SAR imagery. Over the course of the demonstration, other sites could be added.

Operational access to SAR imagery will be an issue for such a demonstration, even though the number of satellites flying could be unprecedented. Under existing cost structures such a demonstration may not be able to afford running for a full year, so it may require special arrangements for access to, and sharing of, SAR imagery among the sites. In addition, although a number of satellites may be available, it is not clear what the duty cycle for each will be, and most importantly how much of that cycle could be devoted to coastal applications. It would be ironic indeed to have more satellites than ever before with less marine collections than ever before.

With the results from such a demonstration in hand however, it would be time to connect to the user community, which often requires proof of operational capability before committing to use a product. Although many, if not all, of the marine environmental products currently being generated were motivated by user needs (and in fact many products are being utilized right now by users operationally), it will be essential to actually show that these products can be used. Perhaps more importantly, it will be important to show that these products are useful, and help users get their jobs done better than they would without the SAR products. If we can demonstrate operational product generation, and demonstrate user need and use of the products, we will be well on the way to building the sustainable international user base in support of SAR imaging systems.

5. SUMMARY AND DISCUSSION

We believe that this summary paper and these proceedings validate the claim that the 2nd Workshop on Coastal and Marine Applications of SAR successfully captured a snapshot of the current state of the art on coastal monitoring with SAR systems.

Furthermore, we believe that the snapshot shows examples of capabilities that are well on their way to operational levels in winds, waves, sea ice and currents, and that are starting to be validated against *in situ* observations of the environmental parameters. Finally, we believe that the snapshot also contains a large range of users who right now are utilizing SAR-derived products operationally; including weather services, ferry operators, meteorological centers, sea ice centers, military organizations, hydrographic offices, and industry. In addition, we expect to see a growing need and use of SAR derived products in the context of Global Monitoring for Environment and Security (GMES); the joint ESA-EU initiative that is currently under development with the goal to be implemented for operational use by 2008. However, much progress still needs to be done before we can claim a sustainable international user base for imaging SAR sensors, and we have attempted to outline a path to that goal with milestones along the way.

As the SAR community moves toward operational coastal monitoring, the issue of the re-visit time that any set of imaging radar sensors would be able to attain needs to be considered. Clearly, the number of satellites required for near-real time radar image acquisition over the globe will never be affordable. Rather, it is incumbent on the application providers to differentiate between real-time operations which may never be supportable by imaging satellites (or which will only be supported in certain locations), versus longer-time statistical descriptions of scenes that a few imaging satellites could readily provide globally. This does not kill the idea of an operational SAR monitoring system, but rather constrains the community to pursue users that can be realistically supported by such systems.

The future of marine monitoring from SAR is clearly bright from the researcher point of view, and is clearly being embraced from a subset of users right now. The challenge for the future is to focus the research community to provide uniform, consistent products, and educate the user community how best to utilize these products. Then the argument for sustainable imaging SAR-like sensors can be realistically made.

Finally, plans are underway for the dedicated 3rd Workshop (of what we hope is an on-going series every two years) sometime in 2005. We would anticipate this workshop focusing on user needs and on making the connection between the demonstrated capabilities and helping the users get their jobs performed effectively. Whereas demonstrated operational product generation will be a goal after this 2nd workshop, validating usage of the products would be the goal after the 3rd workshop.

6. REFERENCES

- Beal R.C., Pichel W.G., eds., 2000, Coastal and Marine Applications Of Wide Swath SAR, *John Hopkins APL Tech. Digest*, **21**.
- Bertoia C., Gineris D., Partington K., Soh L., 1999, Transition from research to operations: ARKTOS – a knowledge-based sea ice classification system, *Proc. International Geoscience and Remote Sensing Symposium (IGARSS 99)*, 1573-1575.
- Bruning C., Hasselmann S., Hasselmann K., Lehner S., Gerling T. 1994., A first evaluation of ERS-1 synthetic aperture radar wave mode data, *Global Atmos. And Ocean System*, **2**, 61-98
- Calkoen C.J., hesselmans G.H.F.W., Wensink G.J., Vogelzang J., 2001, The Bathymetry Assessment System: efficient depth mapping in shallow seas using radar images, *Int. J. Remote Sens.*, **22**, 2973-2998.
- Chubb S.R., Cooper A.L., Jansen R.W., Fusina R.A., Lee J.S., Askari F., 1999, Radar backscatter from breaking waves in Gulf Stream current convergence fronts, *IEEE Trans. Geosci. Remote Sens.*, **37**, 1951-1966.
- Dankert H., Horstmann, J., Lehner, S., Rosenthal W., 2003, Detection of wave groups in SAR images and radar-image sequences, *IEEE Trans. Geosci. Remote Sens.*, **41**
- Du, Y., P. Vachon, J. Wolf, 2002: Wind direction estimation from SAR images of the ocean using wavelet analysis, *Can. J. Remote Sens.*, **28**, 498-509
- Engen, G. and H. Johnsen, 1995, SAR-ocean wave inversion using image cross spectra, *IEEE Trans. Geosci. Remote Sensing*, **33**, 1047-1056.
- Engen G., Hoegda K.A., Johnsen H., 1998, A new method for wind field retrieval from SAR data, *In proc. CEOS SAR Workshop*, **WWP-138**, 43-51.
- Fetterer, F., D. Gineris, C. Wackerman, 1998: Validating a scatterometer wind algorithm for ERS-1 SAR. *IEEE Trans. Geosc. Remote Sens.*, **36**, 479-492
- Fichaux, N., T. Rachin, 2002: Combined extraction of high spatial resolution wind speed and direction from SAR images: a new approach using wavelet transform, *Can. J. Remote Sens.*, **28**, 510-516
- Furevik, B.R., Korsbakken, E. 2000: Comparison of derived wind speed from synthetic aperture radar and scatterometer during the ERS tandem phase, *IEEE Trans. Geosci. Remote Sens.*, **38**, pp.1113
- Furevik B.R., Johannessen, O.M., Sandvik A.D. 2002: SAR-derived wind in polar regions – Comparison with in situ and atmospheric model output, *IEEE Trans. Geosci. Remote Sens.*, **40**, 1720-1732
- Hasselmann K., Hasselmann S., 1991, On the nonlinear mapping of an ocean wave spectrum into a synthetic aperture radar image spectrum, *J. Geophy. Res.*, 10713-10729.
- Hasselmann S., Bruning C., Hasselmann K., Heimbach P., 1996, An improved algorithm for the retrieval of ocean wave spectra from synthetic aperture radar image spectra, *J. Geophys. Res.*, **101**, 16615-16629.
- Havercamp D., leen K., Tsatsoulis C., 1995, A comprehensive, automated approach to determining sea ice thickness from SAR data, *IEEE Trans. Geosci. Remote Sens.*, **33**, 46-57.
- Havercamp D., Tsatsoulis C., 1999, Information fusion for estimation of summer MIZ ice concentration from SAR imagery, *IEEE Trans. Geosci. Remote Sens.*, **37**, 1278-1291.
- Heimbach P., Hasselmann S., Hasselmann K., 1998, Statistical analysis and intercomparison with WAM model data of three years of global ERS-1 SAR wave mode spectral retrievals, *J. Geophys. Res.*, **103**, 7931-7977.
- Horstmann, J. Koch, W., Lehner, S., Rosenthal, W. 1998, Ocean wind fields and their variability derived from SAR, *Earth Observ. Quart.*, **59**, 8-12.
- Horstmann, J., W. Koch, S. Lehner, R. Tonboe, 2000a: Wind retrieval over the ocean using synthetic aperture radar with C-band HH polarization. . *IEEE Trans. Geosc. Remote Sens.*, **38**, 2122-2131
- Horstmann, J., S. Lehner, W. Koch, R. Tonboe, 2000b: Computation of wind vectors over the ocean using spaceborne synthetic aperture radar, *The John Hopkins Univ. Tech. Dig.*, **21**, 100-107.
- Horstmann, J., W. Koch, S. Lehner, R. Toeboe, 2002: Ocean winds from RADARSAT-1 ScanSAR, *Can. J. Remote Sens.*, **28**, 524-533
- Jansen, R.W., Shen C.Y., Chubb S.R., Cooper A.L., Evans T.E., 1998, Subsurface, surface and radar modeling of a Gulf Stream current convergence, *J. Geophys. Res.*, **103**, 18723-18743.

- Johannessen, J.A., Shuchman R.A., Digranes G., Lyzenga D.R., Wackerman C., Johannessen O.M., Vachon P., 1996, Coastal ocean fronts and eddies images with ERS-1 synthetic aperture radar, *J. Geophys. Res.*, **101**, 6651-6667.
- Johannessen, J.A., Garello R., Chapron B., Romeiser, R., Pavlakis P., Robinson I., Connolly N., Nittis K., Hamre T., Ufermann S., Alpers W., Espedal H., Furevik B., Cummins V., Tarchi D., 2001, Marine SAR analysis and interpretation system – MARS AIS, *Ann. Telecommun.*, **56**, 655-660.
- Kerbaol, V., Chapron, B., Queffelec, P., 1998, Analysis of the wind field during the Vendée Globe race: A kinematic SAR wind speed algorithm, *Earth Observ. Quart.*, **59**, pp.16
- Korbakken, E., Johannessen, J.A., Johannessen, O.M., 1998, Coastal wind retrievals from ERS synthetic aperture radar, *J. Geophys. Res.*, **103**, 7857-7874
- Korbakken, E., Furevik, B., 1998, Wind field retrieval from SAR compared with scatterometer wind field during the ERS tandem mission, *Earth Observ. Quart.*, **59**, p. 23
- Krogstad, H., O. Samset, and P. Vachon, 1994, Generalizations of the nonlinear ocean-SAR transform and a simplified SAR inversion algorithm, *Atmos. Ocean*, **32**, 61-82.
- Krudryavtsev, V., Hauser D., Caudal C., Chapron B., 2003a, A semi-empirical model of the normalized radar cross-section of the sea surface. Part 1: The background model, *J. Geophys. Res.*, **108**
- Krudryavtsev, V., Hauser D., Caudal C., Chapron B., 2003b A semi-empirical model of the normalized radar cross-section of the sea surface. Part 2: radar modulation transfer function, *J. Geophys. Res.*, **108**
- Kwok R., Curlander J., McConnell R., Pang S., 1990, An ice-motion tracking systems at the Alaska SAR Facility, *IEEE J. Oceanic Eng.*, **15**, 44-54.
- Lehner, S., J. Horstmann, W. Koch, W. Rosenthal, 1998: Mesoscale wind measurements using recalibrated ERS SAR images, *J. Geophys. Res.*, **103**, 7847-7856
- Lehner, S., J. Schulz-Stellenfleth, B. Schattler, H. Breit, J. Horstmann, 2000: Wind and wave measurements using complex ERS-2 SAR wave mode data, *IEEE Trans. Geosci. Remote Sens.*, **38**, 2246-2257
- Lotfi A., Lefevre J.M., Hauser D., 2003, Optimization of the assimilation scheme of directional wave spectra in wave model WAM: Application to real ASAR-ENVISAT wave spectra, *Proc. Thirteenth International Offshore and Polar Engineering Conference, Honolulu, Hawaii*
- Lyzenga D., Bennett J., 1988, Full-spectrum modeling of synthetic aperture radar internal wave signatures, *J. Geophys. Res.*, **93**, 12345-12354.
- Lyzenga, D.R., 2002, Unconstrained inversion of waveheight spectra from SAR images, *IEEE Trans. Geosci. Remote Sens.*, **40**, 261-270.
- Mastenbroek, K., 1998, High resolution wind fields from ERS SAR, *Earth Observ. Quart.*, **59**, pp. 20
- Mastenbroek, C., Falk C.F., 2000, A semi-parametric algorithm to retrieve ocean wave spectra from synthetic aperture radar, *J. Geophys. Res.*, **105**, 3497-3516.
- McConnell, R., Kwok R., Curlander J., Kober W., Pang S., 1991, psi-s correlation and dynamic time warping: two methods for tracking ice floes in SAR images, *IEEE Trans. Geosci. Remote Sens.*, **29**, 1004-1012.
- Monaldo, F., D.R. Thompson, R.C. Beal, W.G. Pichel, P. Clemente-Colon, 2001: Comparison of SAR-derived wind speed with model predictions and ocean buoy measurements, *IEEE Trans. Geosci. Remote Sens.*, **39**, 2587-2600
- Pichel, W., Clemente-Colón, P., 2000, NOAA Coastwatch SAR Applications and Demonstration, *John Hopkins APL Tech. Dig.*, **21**, 49-57.
- Rodenas J.A., Garello R., 1998, Internal wave detection and location in SAR images using wavelet transform, *IEEE Trans. Geosci. Remote Sens.*, **36**, 1494-1507.
- Romeiser, R., Alpers W., Wismann V., 1997, An improved composite surface model for radar backscattering cross section of the ocean surface: 1. Theory of the model and optimization/validation by scatterometer data, *J. Geophys. Res.*, **102**, 25237-25250.
- Romeiser R., Alpers W., 1997, An improved composite surface model for the radar backscattering cross section of the ocean surface: 2. Model response to surface roughness variations and radar imaging of underwater bottom topography, *J. Geophys. Res.*, **102**, 25251-25267.

Romeiser, R., Ufermann S., Alpers W., 2001, Remote sensing of oceanic current features by synthetic aperture radar – achievements and perspectives, *Ann. Telecommun.*, **56**, 661-671.

Schulz-Stellenfleth J., Lehner S., 2001, Ocean wave imaging using an airborne single pass cross track interferometric synthetic aperture radar, *IEEE Trans. Geosci. Remote Sens.*, **39**, 38-44.

Schulz-Stellenfleth, J., Lehner S., 2003a, Measurement of two-dimensional sea surface elevation fields using complex synthetic aperture radar data, submitted to *IEEE Trans. Geosci. Remote Sens.*

Schulz-Stellenfleth, J., Lehner S., 2003b A parametric scheme for ocean wave spectra retrieval from complex synthetic aperture radar data using prior information, under submission to *J. Geophys. Res.*

Thompson, D.R., R.C. Beal, 2000: Mapping high-resolution wind fields using synthetic aperture radar, *The John Hopkins Univ. Tech. Dig.*, **21**, 58-67

Soh L., Tsatoulis C., 1999, Unsupervised segmentation of ERS and RADARSAT sea ice images using multiresolution peak detection and aggregated population equalization, *Int. J. Remote Sens.*, **20**, 3087-3109.

Soh L., Tsatsoulis C., Gineris D., Bertoia C., 2004, ARKTOS: An intelligent system for SAR sea ice image classification, *IEEE Trans. Geosci. Remote Sens.*, **42**, 229-248.

Thompson, D.R., Monaldo, F.M., Winstead N.S., Pichl W.G., Clemente-Colon P., 2001, Combined estimates improve high-resolution coastal wind mapping, *EOS*, **82**, 368-374

Vachon, P., F.W. Dobson, 1996: Validation of wind vector retrieval from ERS-1 SAR images over the ocean, *Global Atmos. Ocean Syst.*, 177-187

Vachon, P., F.W. Dobson, 2000: Wind retrieval from RADARSAT SAR images: selection of a suitable C-band HH polarization wind retrieval model, *Can. J. Remote Sens.*, **26**, 306-313

Vainio J., Simila M., Gronvall H., 2000, Operational use of RADARSAT SAR data as aid to winter navigation in the Baltic sea, *Can. J. Remote Sens.*, **26**, 314-317.

Vandermark, D., P.W. Vachon, B. Chapron, 1998, Assessment of ERS-1 SAR wind speed estimates using an airborne altimeter, *Earth Observ. Quart.*, **59**, 5-8.

Vogelzang, J., 2001, A model comparison study to the imaging of submarine reefs with synthetic aperture radar, *International Journal of Remote Sensing*, **22**, 2509-2536.

Wackerman, C., C.L. Rufenach, R.A. Shuchman, J.A. Johannessen, K.L. Davidson, 1996: Wind vector retrieval using ERS-1 synthetic aperture radar imagery, *IEEE Trans. Geosci. Remote Sens.*, **34**, 1343-1352

Wackerman, C., Pichel, W.G., Clemente-Colon, P., 2003, Automated estimation of wind vectors from SAR, *Proc. 12th Annual Conference on Satellite Meteorology at the 83rd Annual Meteorological Association Meeting, Long Beach CA.*

Weber F., Nixon D., Hurley J., 2003, Semi-automatic classification of river ice types on the peace River using RADARSAT-1 synthetic aperture radar (SAR) imagery, *Can. J. Civil Eng.*, **30**, 11-27.

Williams R., Rees W., Young N., 1999, Technique for identification and analysis of icebergs in synthetic aperture radar images of Antarctica, *Int. J. Remote Sens.*, **20**, 3183-3199

Wohl, G., 1995, Operational sea ice classification from synthetic aperture radar imagery, *Photogramm. Eng. & Remote Sens.*, **61**, 1455-1462.

Wu S.Y., Liu A.K., 2003, An automated ocean feature detection, extraction and classification algorithm for SAR imagery, *Int. J. Remote Sens.*, **24**, 935-951.

Wind Session

Chairs: F. Monaldo & V. Kerbaol

**This page intentionally
left blank (pagination)**

THE SAR MEASUREMENT OF OCEAN SURFACE WINDS: AN OVERVIEW

Frank Monaldo¹, Vincent Kerbaol² and the SAR Wind Team

¹*Johns Hopkins University, Applied Physics Laboratory, Laurel, MD 20723-6099 USA, Frank.Monaldo@jhuapl.edu*

²*BOOST Technologies, 135 rue Claude Chappe, 29280 Plouzané, France, Vincent.Kerbaol@boost-technologies.com*

ABSTRACT

This paper represents a consensus on the state-of-the-art in wind field retrievals using synthetic aperture radar (SAR) as it emerged during the 2nd Workshop on Coastal and Marine Applications of SAR in Longyearbyen, Spitsbergen, Norway, held on 8–12 September 2003. This work is the result of the efforts of many co-authors. The length of the author list compels us to include it as a footnote,¹ but the contributions of these co-authors represent far more than a footnote to this paper. These contributions were critical to completeness and accuracy of this paper.

This paper documents the substantial progress that has been accomplished in SAR wind speed retrieval. The consensus is that SARs can estimate wind speed to better than 2 m/s and wind direction to 25° with clear evidence that these values can be improved upon.

1. INTRODUCTION

The ability to retrieve wind fields from synthetic aperture radar images, with the high resolution (sub-kilometer) and wide coverage (500 km) represents an important improvement for applications where knowledge of the wind field at fine spatial scales is crucial. SAR wind fields have made conspicuous marine atmospheric phenomena that were known to exist, but were previously difficult to measure and monitor. For example, we can identify the location of synoptic scale and mesoscale fronts and vortices, including hurricanes and polar and mesoscale cyclones. Moreover, we can observe a host of additional mesoscale and microscale phenomena such as cellular convection, roll vortices, gravity waves, gap flows, barrier jets, and von Kármán vortices.

Figure 1 is an example of the sort of high-resolution wind field available from SAR imagery. Wind speed in this image is computed from RADARSAT-1 SAR imagery over the Aleutian Islands. Note the vortices and gap flows generated by wind flow over the islands visible only in high resolution imagery.

From a practical perspective, the high-resolution wind fields from SAR imagery offer the prospect of making important contributions to many applications:

Weather analysis and prediction: When available on a timely basis, SAR wind fields can aid local forecasters. Moreover, the understanding of wind field dynamics possible from the routine production of SAR wind field retrievals in coastal areas will allow meteorologists to extend and improve coupled atmospheric-ocean numerical models allowing enhanced high-resolution wind predictions even when SAR data are not available (Young 2000).

Climate Research: An improved understanding of wind field dynamics in general and in coastal areas in particular will aid in the climate prediction modeling. It is in coastal areas that potential climate change will have its largest impact on humans.

Risk Management: Statistical analysis of SAR high-resolution wind retrievals will aid in the assessment of risks relevant to marine engineering, environment pollution, security, search and rescue, and defense.

Commercial Consequences: High-resolution winds can be used to aid energy production (the placement of wind turbine farms), improve ship routing, and provide data useful to naval architects designing ships to operate in the coastal environment.

Other SAR Applications: SAR-derived wind fields can contribute to the usefulness of other SAR applications. For example, SAR winds can aid wave field retrieval by providing a first guess wind-wave spectrum. Algorithms for automated detection of oil spills and ships as well as ice identification can be improved with knowledge of the local wind field.

The recent availability of calibrated wide-swath SAR imagery from RADARSAT-1 has inched us closer to

¹Pablo Clemente-Colón, Birgitte Furevik, Jochen Horstmann, Johnny Johannessen, Xiaofeng Li, William Pichel, Todd Sikora, Donald Thompson, and Christopher Wackerman.

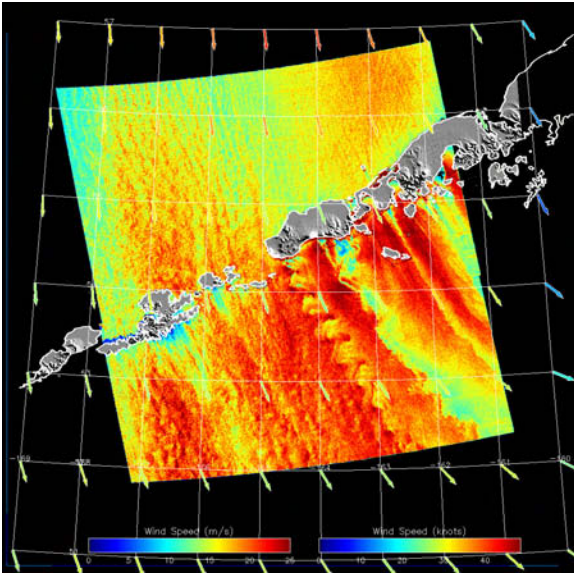


Figure 1. Sample RADARSAT-1 SAR wind speed image crossing the Aleutian Islands with wind speed displayed in pseudo color. Note the von Kármán vortices in the lee of a volcano and gap flows caused by land topography.

the realization of operational measurement of high-resolution winds. Although such wind retrievals had been made with SAR imagery from the ERS-1/2 imagery, RADARSAT-1 and now ENVISAT, wide-swath imagery, some of it available in near real time, offer the tantalizing prospect of operational wind products.

To address some of the challenges of wide-swath SAR imagery the Coastal and Marine Applications of Wide Swath SAR Symposium was held at the Johns Hopkins University Applied Physics Laboratory (JHU/APL) in Laurel, Maryland, 23–25 March 1991.² Since then, the community has enjoyed the availability of near real time data from RADARSAT-1 and has had time to evaluate SAR wind speed retrievals against more conventional techniques. Now that wide-swath ENVISAT data are available, it is incumbent on the SAR scientific community to assess the state-of-the-art in wind vector retrievals from SAR and consider how such data can be deployed in an operational context. This overview paper represents such a consensus on wind vector retrieval as it has emerged from the 2nd Workshop on Coastal and Marine Applications of SAR in Longyearbyen, Spitsbergen, Norway, held on 8–12 September 2003.

One important goal of this workshop was to identify the progress made since the last workshop in 1999. In this paper, we will describe in greater detail the following important advances since the last workshop.

1. The accuracy of a “scatterometry” approach to wind field retrievals has been documented. Wind speed retrievals using such an approach achieves root-mean-square (RMS) errors smaller than 2 m/s in wind speed for the 2 to 20 m/s wind speed range,

²An online version of the proceedings can be found at: <http://www.jhuapl.edu/techdigest/td2101/index.htm>.

down to a resolution of a few kilometers when compared to other measurements. Corresponding wind directions have been retrieved to an RMS accuracy of 25° at a spatial resolution of 25 km.

2. Quasi-operational delivery of SAR winds speeds has been demonstrated with delivery times on the order of 3 hours from time of data acquisition at the satellite.

After we explain the approaches to SAR wind field retrieval, we will describe the steps that have been taken toward creating operational products, and finally discuss some important applications and uses of SAR wind fields. This paper is followed by a series of more specific, detailed papers on methods for and application of wind field retrievals from SAR.

2. WIND VECTOR RETRIEVAL TECHNIQUES

We group wind retrieval techniques into three categories: the scatterometer approach, the “kinematic” approach, and emerging approaches. These approaches should be thought of as complimentary in that we anticipate that by applying all techniques possible for a single image, the final retrieval will improve.

2.1. Scatterometry-based approach

From wind vector to radar cross section: The fundamental idea behind the scatterometry-based approach to the measurement of ocean surface wind from SAR is straightforward. As the wind blows across the surface, it generates surface roughness generally aligned with the wind. Consequently the radar backscatter from this roughened surface is related to the wind speed and direction. All active spaceborne wind measurement techniques rely on this relationship and use various approaches to infer the wind vector from backscatter measurements. Much of the scatterometry-based research in wind measurement from space consists of understanding and describing important details in the wind-vector-to-radar-cross-section relationship and how the combination of such active measurements can be used to retrieve wind speed and sometimes the wind vector.

For medium range incident angles (20° to 60°), the canonical relationship between the wind vector and the normalized radar cross section takes the form of:

$$\sigma^0(U, \phi, \theta) = A(\theta)U^\gamma(\theta) [1 + B(U, \theta) \cos \phi + C(U, \theta) \cos 2\phi] \quad (1)$$

where represents σ^0 normalized radar cross section (NRCS), U is statically neutral wind speed normalized to 10 m height, ϕ represents the angle between the radar look direction and the wind direction, θ is the incident angle, and A , B , C , and γ are parameters describing the “geophysical model function” (GMF). The details of this model function can vary depending on the investigator.

Some investigators have added a $\cos 3\phi$ term (Shimada et al. 2003), while others include an exponent modifying the term in the square brackets. However, these modifications represent details that, though important, do not require us to deviate from the general form in Equation 1 for our discussion here.

The dominant mechanism for microwave backscattering for moderate incident angles is Bragg scattering, i.e., the dominant return is proportional to the roughness of the ocean surface on the scale of the radar wavelength. For spaceborne microwave measurements this wavelength can range from decimeters (L-Band) to centimeters (C and Ku-band).³ In general, as wind speed increases surface roughness increases and hence NRCS increases. However, for certain radar wavelengths, it is possible for this roughness to saturate at some wind speed. At a given wind speed and incident angle, the primary maximum NRCS occurs when the wind is blowing directly toward the radar, with a secondary maximum for wind blowing away from the radar. NRCS is a minimum when the wind blows perpendicular to the radar look direction.

The salient feature of the GMF is that given a wind speed and direction, it is possible to predict the corresponding NRCS. However, we cannot infer a unique wind speed and direction from a single NRCS measurement. Such a NRCS may correspond to any number of wind speed and direction pairs. Therein lies the important challenge in retrieving the wind vector from radar measurements.

History: The age of microwave measurement of wind from space can be said to have begun in 1974 when a combination radiometer and radar scatterometer flew on Skylab (Moore 1974). Partially based on the favorable results of that experiment, Seasat was conceived and ultimately launched in 1978. On Seasat, the primary wind-measuring instrument was the SASS (Seasat-A Satellite Scatterometer). This four-stick, dual-polarization scatterometer measured NRCS at different aspect angles and polarizations at Ku-band (Boggs 1982). Using multiple NRCS measurements, the SASS scatterometer was able to retrieve a four-fold ambiguous wind vector. Usually, error statistics and considerations of wind field continuity permitted the retrieval of the wind vector. Typically, the Seasat scatterometer achieved a wind speed accuracy of 1.6 m/s with respect to buoy measurements [Brown (1983), Hawkins & Black (1983), Pierson (1983), Wentz et al. (1986)]. Since then, scatterometers have flown on ERS-1/2, Adeos-1, QuikSCAT, and Adeos-2. QuikSCAT and Adeos-2 use rotating pencil beams as opposed to stick antenna to measure the ocean NRCS from multiple aspect angles. In all these cases, the general principle of operation is similar: measure the NRCS of a particular point on the ocean surface from different incident and/or aspect angles, and reduce the number of possible wind speed and direction pairs to a manageable number, so that unambiguous wind vector retrieval is possible. The random error in modern scatterometer measurements is 1.3 m/s in

speed and 17° in direction with respect to buoy measurements (Freilich & Dunbar 1999).

The original purpose of the L-band SAR on Seasat was not the measurement of wind speed, but rather the measurement of ocean surface wave spectra. Prior to launch, aircraft SAR measurements suggested that long ocean surface waves (> 50 m) modulated the surface radar cross section. Spectral analysis of SAR imagery offered the prospect of measuring the ocean surface wave spectrum.

Even the earliest SAR images, however, showed patterns of NRCS consistent with variations in the wind field. Fu and Holt (1982) showed Seasat SAR images with clear impressions of hurricane and meteorological circulation patterns. Perhaps most importantly for SAR wind retrieval, Fu & Holt (1982) noted the presence of “wind rows” or roll vortices, linear meteorological features generally aligned with wind direction [Brown (1980), Brown (1986), Clemente-Colón et al. (1998), Foster & Levy (1998)].

Early comparisons [Weissman et al. (1979), Beal (1980), Jones et al. (1981)] demonstrated a correspondence between the L-band Seasat SAR image intensity and Seasat scatterometer wind speed. However, the Seasat SAR was not sufficiently well calibrated for consistent and reliable wind retrievals.

Gerling (1986) made practical application of the observation that roll vortices aligned with the wind were visible in SAR imagery and the general correspondence of increasing NRCS with increasing wind speed. He divided Seasat SAR imagery into 25 km frames. Using Fourier transform techniques, he determined the direction the roll vortices were aligned. Since the Seasat SAR was not calibrated, he then empirically estimated a relationship between SAR image intensity value and wind speed. At the same time, Seasat’s SASS scatterometer was making wind vector measurements. Figure 2 from Gerling (1986) shows the correspondence between SAR estimates of the wind direction from the wind row alignment (the proper 180° ambiguity selected) and the SASS wind direction. Figure 3 shows a similar correspondence in the wind speed retrieval.

After initial efforts to extract the wind field from Seasat SAR data and even after the launch of ERS-1 in 1991, little attention was paid to SAR-derived winds. Like Seasat, the SAR on ERS-1 was thought of primarily as a wave spectra measuring device. This lack of interest in SAR winds started to reverse itself later in the 1990s as investigators again began to observe the signatures of meteorological phenomena in SAR and real aperture imagery [Sikora & Young (1993), Atlas (1994), Alpers & Brümmer (1994), Alpers (1994), Alpers et al. (1995), Mourad & Walter (1996), Sikora et al. (1997), Johannessen et al. (1997), Alpers et al. (1998), Zecchetto et al. (1998), Korsbakken et al. (1998), Mourad et al. (2000), Quilfen et al. (1998), Sandvik & Furevik (2002), Vachon et al. (1994a), Vachon et al. (1995), Winstead & Mourad (2000), Winstead & young (2000), Winstead et al. (2001), Sikora et al. (2002)].

These observations were followed by efforts to quanti-

³Frequency band designations have their own, sorted history. For our purposes here, we employ the designations of the American Society for Photogrammetry and Remote Sensing. L-band spans the frequencies 1–2 GHz and 30–15 cm in wavelength, C-band spans 4–8 GHz and 7.5–3.75 cm, and Ku-band 12.5–18 GHz and 2.4–1.67 cm.

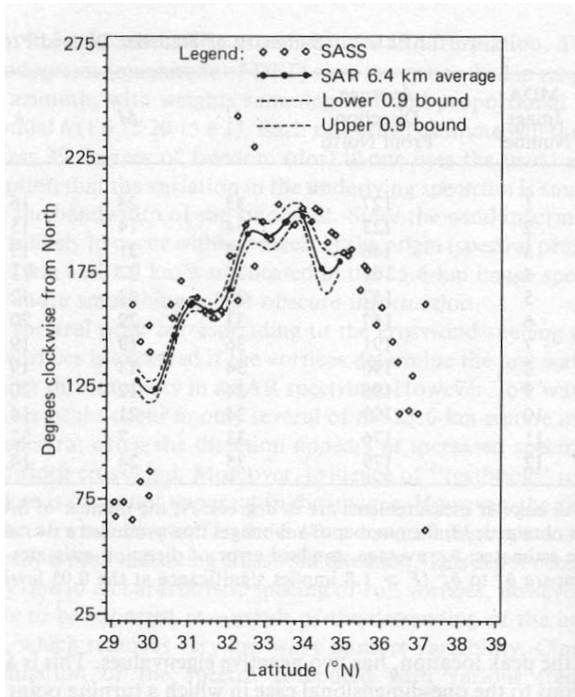


Figure 2. Seasat SAR estimated wind directions versus scatterometer directions from pass 1339 (Gerling 1986).

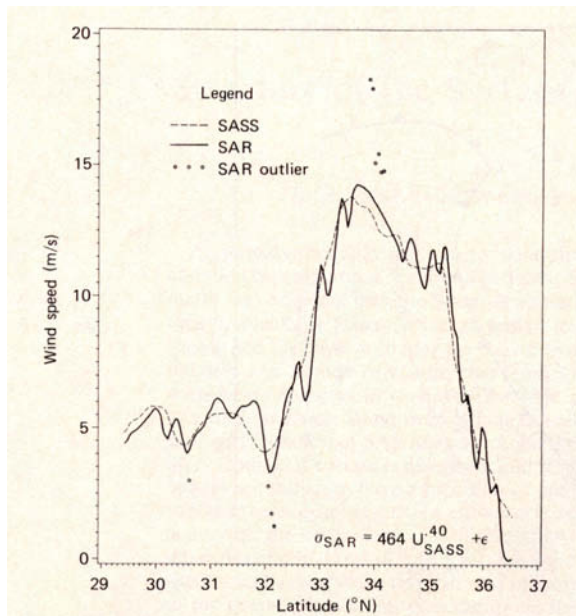


Figure 3. Seasat SAR estimated wind speeds versus scatterometer speeds from pass 1339 (Gerling 1986).

tatively estimate wind speed and direction. Vachon & Dobson (1996), Wackerman et al. (1996), Fetterer et al. (1998) and Lehner et al. (1998) extended the approach of Gerling to ERS-1 SAR imagery. Since ERS-1 produced calibrated NRCS imagery [Offiler (1994), Quilfen & Bentamy (1994), Scoon et al. (1996), Meadows & Wright (1994), Meadows et al. (1998), Stoffelen & Anderson (1999), Laur et al. (1996)] to about 0.5 dB in spite of a severe ADC saturation effect on SAR products, it was then possible to use the SAR NRCS in conjunction with the directions to estimate wind speed.

The SAR on ERS-1 represented one mode of operation for the C-band VV-polarization Active Microwave Instrument (AMI). An alternative configuration was the scatterometer mode. Its primary purpose was the measurement of the ocean surface wind vector. Hence, significant resources were deployed to develop and validate the wind vector to C-band, VV polarization GMF. The modeling of the relationship between the wind vector and ocean surface roughness and electromagnetic scattering from such a surface also progressed substantially [Romeiser et al. (1997), Elfouhaily et al. (1999), Babin & Thompson (2000)], but wind retrievals are still most accurate using empirical geophysical model functions.

Empirical work comparing NRCS with measured wind vectors and numerical model predictions of the wind vector resulted in the development of the CMOD4 model function [Attema (1986); Stoffelen & Anderson (1993), Stoffelen & Anderson (1997a), Stoffelen & Anderson (1997b)]. In parallel, an analogous CMOD-IFR2 was developed at the *Institut Français de Recherche et d'Exploitation de la Mer* [IFREMER (1996), Bentamy et al. (1994)]. More recently, Hersbach (2003) proposed an upgrade of CMOD4 (conveniently named CMOD5) to address certain wind speed biases in the CMOD4 model function. Whether this new model function will improve retrievals is still an area of investigation.

The availability of a validated GMF and calibrated SAR imagery provided the necessary ingredients to explore SAR wind vector retrieval. Over the next several years a large number of investigators used ERS-1 and ERS-2 (launched in 1995) SAR data from both the imaging and wave modes (usually used for wave spectra retrieval) to evaluate the potential of SAR to measure high-resolution winds, comparing retrievals to numerical forecast models, buoys, and scatterometer and altimeter data [Scoon et al. (1996), Vachon & Dobson (1996), Wackerman et al. (1996) Horstmann (1997), Horstmann et al. (1998), Kerbaol et al. (1998a), Kerbaol et al. (1998b), Korsbakken & Furevik (1998), Korsbakken et al. (1998), Lehner et al. (1998), Mastenbroek (1998), Vandemark et al. (1998), Furevik & Korsbakken (2000), Horstmann et al. (2000a), Horstmann et al. (2000b), Lehner et al. (2000), Furevik et al. (2002)].

In 1995, the Japanese launched J-ERS-1 with an L-band SAR. Unfortunately, the signal-to-noise ratio for ocean scenes was quite low, limiting the usefulness of such data for wind speed retrieval. Nonetheless, Shimada et al. (2003) have recently developed a wind speed GMF for L-band, which may prove valuable for future L-band SAR data from ALOS (Advanced Land Observing Satellite)

scheduled for launch in 2004.

The initial successes of these efforts were heartening in that they showed positive results. However, they were frustrating since available swaths (100 km) from ERS-1/2 did not provide sufficient coverage to capture dynamic coastal areas except in the most limited sense. The launch of RADARSAT-1 in 1995 with its wide-swath (500 km) mode offered a potential remedy that was further extended with the launch of ENVISAT ASAR (Advanced SAR) in April 2002. The application of RADARSAT-1 data to wind retrieval has been limited by two major constraints: calibration and the lack of an appropriate GMF.

Radiometric calibration of wide-swath imagery is more difficult than SAR imagery in its conventional 100 km swaths. Calibrated RADARSAT-1 wide-swath SAR imagery was not available for years after launch and it may still fairly be said that the calibration is not as good as for standard mode data. Indeed, the burst (i.e., the transmission of pulses in groups) mode of wide-swath products makes the SAR processing very sensitive to the correction for the two-way antenna pattern both in elevation and azimuth. As a result, along-track stripes featuring the different beams antenna pattern in elevation as well as scalloping effect resulting from incorrect radiometric compensation for the azimuth antenna pattern are frequently visible on both ENVISAT and RADARSAT-1 products. We should note here that these seams are less conspicuous in ENVISAT than in RADARSAT-1 imagery.

Geophysical model functions issues: RADARSAT-1 operates at HH polarization, while ERS-1/2 operated at VV polarization. The elaborate campaigns and analysis responsible for defining a wind speed to NRCS GMF were not available for RADARSAT-1, and the GMF's developed for VV polarization were not directly applicable.

This latter challenge has been dealt with by attempting to define a polarization ratio function that will map the CMOD4-predicted NRCS at VV polarization into a corresponding NRCS for HH polarization. One simple characterization of the polarization ratio relating the NRCS at VV polarization to NRCS at HH polarization is given in Equation 2 as

$$\sigma_H^0 = \frac{(1 + \alpha \tan^2 \theta)^2}{(1 + 2 \tan^2 \theta)^2} \sigma_{V,CMOD4}^0 \quad (2)$$

where α is a parameter relating to the type of surface scattering (Thompson et al. 1999). For $\alpha = 0$ the results correspond to Bragg scattering. For $\alpha = 1$, the HH polarization NRCS corresponds to that predicted by the Kirchhoff geometric optics approximation (Elfouhaily et al. 1999). Note that Equation 2 is referenced to the empirical CMOD4 GMF.

Equation 2 is a first-order result and is probably a function of the angle between the wind direction and the radar look direction, making Equation 2 an incomplete representation. Nonetheless, Equation 2 has provided a framework within which to begin retrievals with HH polarization imagery [Horstmann et al. (2000a), Thompson & Beal (2000), Vachon & Dobson (2000), Wackerman (2000), Horstmann et al. (in press, 2003), Horstmann

et al. (2003b), Horstmann et al. (2003a)]. Results from Unal et al. (1991) and Thompson et al. (1999) initially suggested that $\alpha = 0.6$ but others have suggested values as high as 1.0. Wackerman et al. (2002) have proposed a two-scale model suitable for retrieving the wind field at both VV and HH polarizations.

The GMF may also be dependent upon other factors besides wind speed. Atmospheric stability, the air-sea temperature difference, can effect how much wind speed at a height above the ocean surface roughens that surface [Clemente-Colón (1998), Weissman et al. (1980)].

The GMFs are becoming sufficiently mature that an assessment of their adequacy is approaching the limits possible given the accuracy of SAR NRCS measurements. As future SARs are launched, the comparison of the SAR wind speed distribution using nominal GMFs may prove to be a sensitive way to assess the accuracy of the NRCS measurement. Given this limitation, we may have to resolve ourselves to using the commissioning phase of any SAR satellite to compare NRCS against nominal wind retrievals to jointly tune the GMF to the sensor and perhaps adjust the sensor to make NRCS measurements of improved accuracy.

The primary remaining limitation of the GMF may be at the higher wind speeds (greater than 20 m/s) where there exists a dearth of independent measurements against which to compare SAR NRCS measurements. The development of CMOD5 attempted to address this issue via systematic comparisons of SAR NRCS with numerical model estimates from the European Centre for Medium Range Weather Forecasting (ECMWF). However, the inherent limitation of such an approach is the assumption that models, on average, produces the correct distribution of high wind speeds. For wind speeds less than 20 m/s all CMOD model functions (CMOD4, CMOD5, and CMOD-IFR2) are very close. Which GMF is most appropriate is still an open question.

Wind direction retrieval for the scatterometry approach: The use of model data provides the easiest and most direct method to obtain a reasonable *a priori* estimate of wind direction to use for wind speed inversion. The Alaska SAR Demonstration Project (See section 3.2.) has been using Naval Operational Global Atmospheric Prediction System (NOGAPS) model data provided by the Master Environmental Library supported by the Defense Modeling and Simulation Office for wind speed inversion [Monaldo & Beal (1998); Monaldo (2000)]. This approach has been generally successful yielding retrieved wind speeds with standard deviations of 1.8 m/s when compare to buoys and other independent wind speed measurements [Monaldo et al. (2001), Monaldo et al. (2003), Monaldo (2003), Thompson et al. (2001)].

Unfortunately, numerical forecast models usually have coarse sampling (NOGAPS data are provided on a $1^\circ \times 1^\circ$ longitude latitude grid). High spatial frequency fronts can be missed or displaced in such models. Some of these problems have been alleviated by the application of high-resolution atmospheric models like MM5 (Horstmann et al. 2003a).

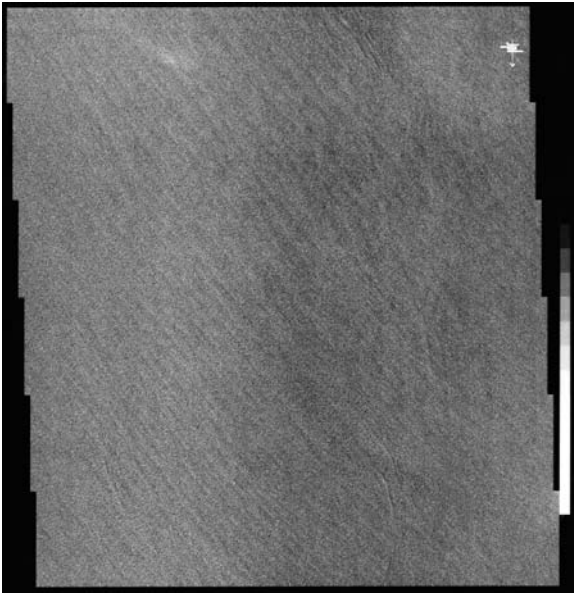


Figure 4. Roll vortices in a Seasat SAR image (Fu & Holt 1982).

Despite the empirical success of using model directions for the SAR wind speed inversion, this approach unnecessarily ignores wind direction information in the SAR image itself. The fundamental phenomenology underpinning wind direction measurement is the detection of linear features aligned with the wind direction. Winds produce complementary pairs of clockwise and counter-clockwise flows aligned with the wind [Brown (1970), Brown (1980), Brown (2000), Müller et al. (1999), Sikora et al. (1995)]. These phenomena are referred to as atmospheric roll vortices. At the surface, this circulation pattern induces lines of increased and decreased near surface winds, which, in turn, produce lines of increased surface roughness and hence SAR NRCS. Figure 4 is the first example of SAR observed roll vortices from Seasat (Fu & Holt 1982). In addition, linear features aligned with the wind direction can be the consequence of elongated convective cells, wind-driven Langmuir cells, or the distribution of surfactants by the wind [Leibovich (1983), Vachon & Dobson (1996), Fetterer et al. (1998), Babin et al. (2003), Dankert et al. (in press, 2003), Wackerman et al. (2003b)].

We point out here that not all linear meteorological signatures found in SAR imagery, for example atmospheric gravity waves, align with wind direction. Fortunately, these tend to occur on spatial scales longer than roll vortices. However, roll vortices themselves can align several tens of degrees off the near-surface wind direction depending on atmospheric stability and baroclinicity (Sikora & Young 2002). As a practical matter, wind directions retrieved from SAR generally exhibit little bias and agree with independent estimates to within 25°. Foster and Sikora discuss this topic in this issue.

Gerling (1986) first exploited the presence of roll vortices computing the Fourier spectrum of SAR images. In the low frequency range of the spectra, 600 m to about 2 km, roll vortices create more spectra energy in the direction

perpendicular to the wind. Gerling fit the low frequency end of the spectra to low-order polynomial. The short-axis of this polynomial was asserted to be the wind direction.

Similar techniques have been applied to ERS-1/2 data [Vachon & Dobson (1996), Wackerman et al. (1996), Horstmann (1997), Horstmann et al. (1998), Fetterer et al. (1998), Kerbaol et al. (1998b), Korsbakken & Furevik (1998), Korsbakken et al. (1998), Lehner et al. (1998), Mastenbroek (1998), Vandemark et al. (1998), Furevik et al. (2002), Horstmann et al. (2000a), Horstmann et al. (2000b), Lehner et al. (2000)] and to RADARSAT-1 data [Campbell & Vachon (1997), Vachon et al. (1998), Vachon et al. (2000a), Vachon et al. (2000b), Wackerman (2000)].

Others have retrieved the direction of linear features using alternative approaches such as estimating spatial gradients on different spatial scales (Horstmann et al. 2000b) and wavelet analysis [Du et al. (2002), Fichaux & Rachin (2002)]. These alternate techniques seek to circumvent the Nyquist limits on estimating low frequency spatial variations and thereby improve the resolution of SAR direction retrieval to better than 10 km. Recently, Wackerman et al. (2003a) has demonstrated the correspondence between using variance as a measure of the wind direction of linear features and the gradient approach. In this new variance approach, the image is averaged along one direction and the variance of the resulting line of data computed. The image is then rotated again, averaged along the corresponding direction, and a new variance computed. The rotation that yields the largest variance is associated with the wind direction.

Wind direction retrievals directions from linear features show an agreement (accounting for an inherent 180° ambiguity) ranging from 15° to 40° when compared to independent measurements (Wackerman et al. 2003b).

The key advantage to using SAR imagery for the wind retrieval is that high spatial frequency variations in wind direction missed by a model and conventional scatterometry may be caught in the imagery itself. In addition, there is no timing or spatial mismatch as might be the case with model directions. Some of the limitations of using linear features for wind direction retrieval are that such features are not always visible, other features on the same spatial scales can contaminate the measurement arising either from physical process or processing artifacts (e.g., scalloping effect signature visible on wide swath products), and they are encumbered by a 180° ambiguity.

SARs are by no means the only instruments that can measure wind direction. Although scatterometers, like the ones currently flying aboard QuikSCAT and Adeos-2, cannot match the sub-kilometer resolution obtainable by SARs, they do produce validated wind speed and directions at a 25 km resolution (Freilich & Dunbar 1999). When these data are available, it is incumbent to use them as part of the wind speed retrieval process. Horstmann et al. (2000a), Thompson et al. (2001) and Monaldo et al. (2003) have demonstrated that using QuikSCAT wind directions for wind retrievals from the RADARSAT-1 SAR, a wind speed with a standard deviation of 1.24 m/s with

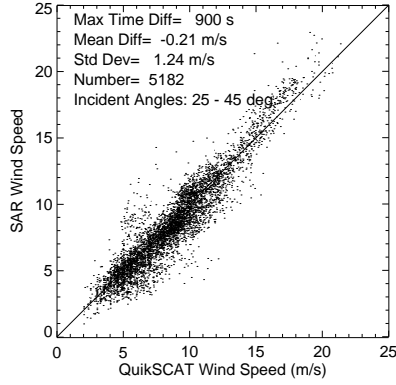


Figure 5. RADARSAT-1 SAR wind speed retrievals using QuikSCAT directions to initialize the retrievals versus the QuikSCAT wind speeds. The GMF was tuned to minimize residuals. QuikSCAT data flagged as rain contaminated were not included in this comparison.

little bias with respect to the QuikSCAT wind speed can be obtained. Figure 5 is a comparison of RADARSAT-1 SAR retrieved wind speeds using QuikSCAT directions versus the associated QuikSCAT wind speeds. Similarly, Furevik & Korsbakken (2000) have successfully used ERS-1 scatterometer directions to initialize wind retrievals from ERS-2 SAR imagery.

The launch of WindSat, which promises to use polarimetric radiometry to measure wind speed and direction at a resolution and accuracy comparable to active scatterometry, is an alternative source of wind directions. If proven successful, such wind directions could also be used for SAR wind speed retrieval.

Of course, the use of alternative sources of direction is limited to those cases when such data are available.

2.2. A kinematic-based approach

Description: Another source of information can be exploited to complement the SAR scatterometry approach for wind field retrieval. A SAR uses Doppler information to achieve fine-scale azimuth (along-track) resolution. Corruption of this Doppler information by ocean surface motion smears the SAR image in the azimuth direction, but also provides information about the distribution of the motion of surface scatterers. This motion, in turn, is related to the near surface wind field. Analysis of the observed smearing of SAR imagery in the azimuth direction, often referred to as spectral azimuth cut-off, can thus provide wind speed information.

According to theory, azimuth smearing is proportional to the RMS line-of-sight wave orbital velocity field. At near nadir incident angles, this radial component is dominated by the ocean surface vertical velocity variance, which is mainly caused by the shortest waves. By contrast, longer waves are the major contributors to wave height variance (Jackson & Peng 1985). For typical environmental conditions, the portion of the spectrum associated with the

short waves represents the wind sea part of the spectrum. For such a situation, using measurable SAR azimuth resolution degradation to infer wind speed is a very valuable complement to the scatterometer approach. Indeed, convincing comparisons between these cut-off parameters with simultaneous co-located scatterometer wind speeds estimates first highlighted the preponderant role of the wind generated wave random motions in SAR azimuth resolution losses, and thus the ability to derive a simple wind speed algorithm [Kerbaol et al. (1998b), Lehner et al. (2000)].

This kinematic approach requires a robust estimation method for the SAR azimuth cutoff parameter. Since, the azimuth cutoff estimation issue is crucial in retrieving the two-dimensional wave spectrum from the SAR image spectrum, several methods have been proposed. These methods include estimating the azimuth cutoff in the spectral domain [Vachon et al. (1994b), Hasselmann et al. (1996)] and fitting the SAR image azimuthal autocorrelation function with a Gaussian function (Kerbaol et al. 1998b).

An empirical wind speed algorithm using a kinematic approach: To first order, the SAR image power spectrum may be written as:

$$P_S = \exp(-k_{az}^2 \rho^2) P_{lin}(k) \quad (3)$$

where $P_{lin}(k)$ represents the power spectrum of the linear transform of the ocean spectrum and ρ^2 is the total variance of azimuthal displacement within the SAR integration time and is equal to:

$$\rho^2 = \int |T_{vb}(k)|^2 S(k) dk \quad (4)$$

Here $T_{vb}(k)$ is the velocity-bunching modulation transfer function, $S(k)$ the sea surface elevation-variance spectrum, and k is ocean surface wavenumber. At low incident angles ($\sim 20^\circ$), the ρ^2 parameter has the interesting property that it depends primarily upon the vertical component of the orbital velocities (i.e., we may neglect the wave directions. Hence, we may write:

$$\rho^2 = \left(\frac{R}{V}\right) \int \omega^2 S(k) dk \quad (5)$$

Taking advantage of the unique ERS-1/2 C-band VV polarization Advanced Microwave Instrument (AMI) to obtain interlaced scatterometer data and SAR Wave Mode imagerettes, a global comparison was performed between SAR azimuth cutoff values estimated on ERS imagerettes and collocated wind speed estimates inferred from scatterometer measurements at CERSAT (*Centre ERS d'Archivage et de Traitement*), located at IFREMER Kerbaol et al. (1998b).

Fitting the Azimuthal Correlation Function (ACF) with a Gaussian function:

$$C(x) \sim \exp\left(-\frac{\pi^2 x^2}{\lambda^2}\right) \quad (6)$$

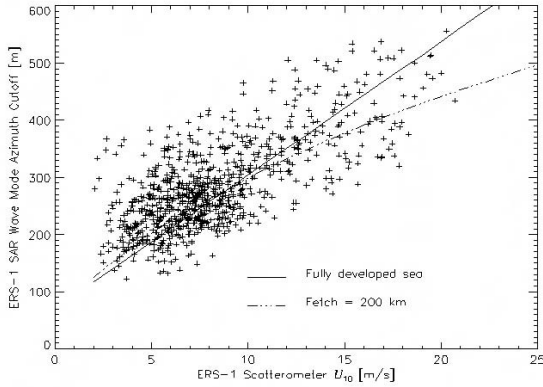


Figure 6. ERS-1 SAR azimuth cutoff versus co-located 10-m wind speed inferred from the ERS-1 scatterometer.

an empirical linear relationship between SAR azimuth cutoff parameter and scatterometer-derived wind speed ($\lambda \approx 25U$) was obtained from a collocated ERS data set. See Figure 6.

Algorithm properties: The main advantage of this approach is that no information is required on the wind direction at low incident angles. Such a method may then provide a valuable first guess wind speed estimate. Practical application of such a linear relationship has been demonstrated by Korsbakken (1996) and Korsbakken et al. (1998).

For wide-swath products, this algorithm is obviously not expected to contribute, except for smaller incident angles (25°). However, for the wide-swath near range, it might be possible to use this method to confirm the wind direction used in the more conventional scatterometer approach to SAR wind field retrieval.

As explained, the relationship only holds for C-band, VV polarization and at low incident angles. This empirical linear coefficient is expected to decrease at lower radar frequency because of the change of the integration limits in the theoretical expression of the parameter. For HH polarization, additional contribution such as strong accelerations of specular breaking events may also contribute to increasing the smearing effect.

Finally, one must be cautious since the SAR cut-off parameter estimates also include long wave orbital motion contributions that may contaminate the results. The azimuth cut-off parameter is entirely associated with the random wave motions, which are not associated with wind-generated waves. In particular, for the case of fetch-limited or relaxation conditions, as well as in the presence of large swell systems, this may affect the relation between cut-off wavelength and wind speed.

2.3. Emerging approaches

The Doppler centroid analysis: SAR image interpretation for wind speed has generally focused on backscatter signal analysis, while the complementary information

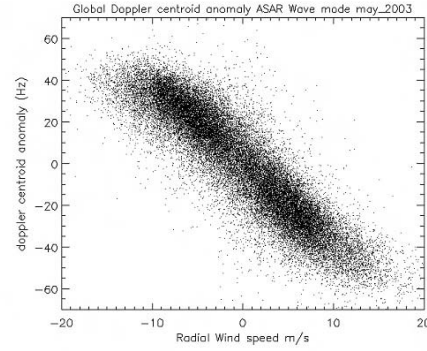


Figure 7. Global Doppler centroid anomaly of ENVISAT SAR Wave Mode data versus co-located ECMWF wind speed radial component.

carried in the phase of the received signals has been neglected.

Moving targets produce Doppler frequency shifts proportional to their relative velocities toward the receiving antenna. Over moving ocean scenes, these frequency shifts along the radial direction are randomly distributed. One can make use of the expected statistical sea surface homogeneity to measure the first-order moment of the Doppler distribution, the so-called “Doppler centroid.” To first order, this mean shift is proportional to radar line-of-sight mean velocity from those scatterers at the Bragg wavelength. These decimeter to centimeter scale waves are predominantly influenced by the wind speed and direction and any surface current.

Recently, a data set of Doppler centroid estimates from ENVISAT SAR complex imageries were compared with over 500,000 wind vectors from ECMWF. After correctly taking into account local platform orbital geometry and kinematics, the measured mean Doppler shifts were highly correlated with local ocean surface motion effects. As shown Figure 7, the ENVISAT ASAR data clearly reveal the potential to monitor line-of-sight sea surface detected motions. As already emphasized, application of this technique requires very precise orbit knowledge from a highly stable platform.

The Doppler anomalies are generally of opposite sign for descending and ascending tracks primarily due to the presence of predominantly stable basin-scale wind and wave fields systems (i.e. the Antarctic Circumpolar Current, equatorial trade winds, monsoons, etc.). Since these Doppler anomalies are highly correlated to line-of-sight wind wave induced motions, this information might be used to better resolve the conventional 180° wind direction ambiguity inherent in obtaining directions from linear features in a SAR image.

SAR cross-spectrum analysis: Another approach for estimating wind direction exploits the inter-look correlation technique used for resolving wave directions in SAR wave spectra. A SAR ocean image spectrum is the sum of a wind dependent contribution (from waves smaller

than the SAR resolution) and a longer wave contribution. The idea is to use the information contained in the wind dependent spectral domain. This is done by analyzing the cross-spectrum phase-plane tilt (Engen et al. 1998). Indeed, the non-linear redistribution of energy in the SAR mapping is wind-direction dependent. If sufficiently well sampled (depending upon the number of along-track points), this technique seems very reliable for high wind conditions.

Furthermore, a differential azimuth cut-off estimator can also be defined by simply using the ratio of the azimuth cross-spectrum profiles obtained for two different look separation time. The idea is to make use of the extremely short lifetime of the wind-generated ripples that impact the overall smearing of the SAR scene. This extended analysis of the inter-look methodology is thus related to the measure of the SAR scene coherence time, which is also closely related to the local wind stress (breaking characteristics).

2.4. Synthesis

Table 1 represents a summary of different approaches that have been used to infer wind parameters (speed, direction) from SAR images. Each approach has its advantages and drawbacks. However, given these alternative approaches, there ought to be ways to assimilate the wind directions from these different methods to produce a best estimate of the wind direction field. For example, one could use the model data to help de-alias the wind directions derived from linear features. Another approach might be to use the directions from the linear features or from the alternative sources to adjust the model directions in time and space to achieve greater consistency between the approaches. This adjusted model field could then be interpolated down to the SAR image pixel and used to compute wind speed from the NRCS measurements.

Though offering the potential of improved wind directions, this combined approach is still in its infancy. Modest efforts attempted as part of the Alaska SAR Demonstration use NOGAPS model directions to de-alias wind directions computed using General Dynamics software for SAR wind direction retrieval.

Alternatively, the Portabella et al. (2002) approach is likely to provide higher degree of flexibility when the coarse resolution of numerical models fails to describe the high spatial variability of the wind field. The idea is to use the medium to high-resolution wind field predicted by a numerical model, for example MM5 or the High-Resolution Limited Area Model (HIRLAM), as *a priori* information in a Bayesian estimation method of the SAR-derived wind field.

3. THE MOVE TO OPERATIONAL PRODUCTS

3.1. COASTWATCH and MARSAIS

An implementation of a system to use ERS-1/2 SAR imagery to monitor the Norwegian coast began as part of COASTWATCH [Johannessen et al. (1994), Johannessen (2000)]. Although wind fields were a component of the project, SAR imagery was also used for oil spill detection, current monitoring and the examination of shallow water bathymetry. Johannessen et al. (2001) began addressing the more general issue of applying SAR data in a coastal environment in an operational context. The assimilation of numerical weather predictions and various sources of remotely sensed data was emphasized.

More recently, the integration and application of SAR data is being prototyped as part of the Marine SAR Analysis and Interpretation System (MARSAIS) as a joint project led by the Nansen Environmental and Remote Sensing Center.⁴ The goal is to produce products and tools to permit the more effective utilization of SAR data in coastal areas. The availability of ENVISAT SAR imagery capable of wide swaths and multiple polarizations provides an ideal test bed for application of SAR imagery in the coastal environment.

3.2. Alaska SAR Demonstration

It is one thing to process SAR imagery to wind retrievals in a research mode, a few images at a time. To assess the potential impact of SAR wind retrievals requires making retrievals in a quasi-operational environment. Toward this end, the National Oceanic and Atmospheric Administration (NOAA) in conjunction with the JHU/APL and General Dynamics⁵ embarked on StormWatch [Beal & Pichel (1998), Beal (2000)]. Since then, the project has continued under the auspices of the Alaska SAR Demonstration.

As RADARSAT-1 passed within the station mask of the Alaska Satellite Facility (ASF), SAR data from the Alaska region were transmitted down. These data were “quick look” processed into calibrated SAR imagery, transmitted to NOAA’s National Environmental Satellite, Data, and Information Service (NESDIS) in Suitland, Maryland, processed into wind speed retrievals, and the results posted on the World Wide Web [Pichel & Clemente-Colón (2000), Monaldo & Beal (1998), Monaldo (2000)]. At the beginning of the Alaska SAR Demonstration, the interval from data acquisition at ASF and posting on the web was 5 to 6 hours. Since then, the addition of computing resources has reduced this latency to 3 to 4 hours. This could be reduced to the 2-hour range with modest additions of computing resources or by moving the wind retrieval processed to the ground station reception station.

⁴<http://marsais.ucc.ie/index.htm>

⁵The software was initially developed by the Environmental Research Institute of Michigan (ERIM), which became Veridian International. Veridian International was recently acquired by General Dynamics.

The Alaska SAR Demonstration relied on two approaches for wind retrievals. The first approach, led by JHU/APL relied on wind direction data from the NOGAPS model. These directions were provided on a $1^\circ \times 1^\circ$ longitude-latitude grid and interpolated down to each SAR image pixel to perform the wind speed retrieval. After inversion, the high-resolution wind speed images were posted on the web (Monaldo 2000). Figure 1 is a sample wind speed image created as part of the Alaska SAR Demonstration. The image covers part of the Aleutian Islands. The large arrows represent the wind vectors from NOGAPS model. These directions were used in the wind speed retrieval. This image is particularly interesting in that it shows just a small fraction of the meteorological phenomena revealed in high-resolution wind imagery. Note the von Kármán vortices in the lee of a volcano in the island chain (Li et al. 2000). The effect of topography and shadowing are often evident in SAR imagery tens to hundreds of kilometers down wind from shore.

The second approach, led by General Dynamics, broke the SAR images into 25 km \times 25 km sub-images. Various numerical techniques were then applied to estimate the wind direction from linear features in the SAR image. This wind direction plus the image NRCS is used to estimate wind speed (Wackerman 2000).

The Alaska SAR Demonstration Project has thus far accumulated over 10,000 images which has created a statistically significant data base to evaluate SAR wind speed retrieval. When compared to either buoy data or QuikSCAT scatterometer data, both approaches used in the Alaska SAR Demonstration yield standard deviations when compared to other instruments ranging from 1.24 to 1.8 m/s. Directions retrieved using the Veridian direction retrieval approach agreed with buoy data to 32° .

It is clear that SAR wind retrievals have reached the point where they can be provided in an operational time frame and are valuable especially in coastal areas.

4. APPLICATIONS

We divide SAR wind speed applications into two categories: near-real-time applications that require rapid availability of SAR products in order to be useful and long-term applications which can effectively use SAR data on a non-time-critical basis.

4.1. Near Real Time

Coastal wind field measurement: Perhaps the most advanced wind application for SAR has been its use to monitor the wind field in coastal areas [Beal & Pichel (1998), Beal (2000), Monaldo & Beal (1998), Monaldo (2000), Wackerman (2000), Wackerman et al. (2003b), Friedman et al. (2001)]. SAR wind fields from the Alaska SAR Demonstration were provided in near real time to the Alaska Weather Service so that they might evaluate its

usefulness in forecasts. The delay of 3 to 6 hours inhibited the operational use of the information, but individual forecasters have indicated that the wind maps complemented their intuitions about the very local wind field effects under given synoptic conditions. Recently, the Alaska SAR Demonstration has demonstrated the ability to achieve 3 hour data latency. We recommend that the community continue to encourage more timely distribution of SAR winds.

Sometimes SAR data have proven uniquely valuable. For example, in 2001, Coast Guard cutters unsuccessfully searched for 14 missing crewman from the fishing boat *Arctic Rose* lost near 174°W and 60°N , approximately 200 miles northwest of Saint Paul Island. The wind speed imagery from the RADARSAT-1 SAR proved to be one of the few sources of wind data available in the region. Although there is no way to determine if more timely and high-resolution wind vector information would have saved crew of the *Arctic Rose*, this incident does serve to highlight the potential importance of remotely sensed winds to critical issues of marine safety.

Ship Navigation: In coastal areas, the wind speed field often exhibits sharp gradients, changing by over 10 m/s in over a few kilometers. Unexpected shifts of this kind can impact safety, particularly of small craft, as well as having an impact on ship travel times (Winstead 2001). NOAA reports the use of Alaska SAR Demonstration SAR wind imagery posted on the World Wide Web by a ship captain for use in ship routing. Of course, timeliness of such data is important for this application.

Spill Detection: Oil spill detection by SAR results from the dampening effect caused by surfactant on capillary surface wave. As a result, polluted areas will appear as dark regions on the image. Under low wind conditions, the precise knowledge of the local wind vector is likely to resolve some ambiguities over areas where low backscatter will not necessarily be caused by oil surfactants. However, ancillary data may further be required (sea surface temperature, ocean color) to avoid misinterpreting the signature of natural films or upwelling. Not only is it important to detect the illegal dumping of oil and other surfactants, but tracking the dispersion of oil in emergence situations can aid in the mitigation of resulting ecological and environmental damage.

Ship Detection: Usually ships appear as bright spots in SAR imagery, but this signature can be masked in high wind conditions. Knowing the wind conditions from the SAR data itself could aid in separating high backscatter returns from ships and those caused by wind and wave conditions.

The enforcement of limits on commercial exploitation in exclusive economic zones can be aided by satellite monitoring of ship location. The Alaska SAR Demonstration showed that it is possible to locate ships in near real time using RADARSAT-1 data. The high 25-m resolution SAR images were most effective at locating ships, but their 100-kilometer swath width provided less coverage than the 50 to 100-m resolution wide-swath data having a 500 km wide swath.

Table 1. Summary of approaches to obtaining the wind field.

Approach	Pros	Cons
<i>Scatterometry</i> using model directions.	Always available. Reasonable fields. Validated.	Low resolution. Space/time mismatch.
<i>Scatterometry</i> using linear features in SAR image (Fourier techniques, gradient methods, wavelet analysis).	Space/time sampling exact. High spatial frequency features	Not always available. Contaminated by other features, 180° ambiguity. Johannessen et al. (1994)
<i>Scatterometry</i> using alternative measurements.	Independently validated directions. Validated.	Infrequent coincidences with SAR and alternative measurements ambiguity. Low resolution.
<i>Kinematics</i> using azimuth cutoff analysis.	Independent from wind direction (at low incidence).	Overestimation at low wind speed. Fetch dependent. Limited to low incidence. Validation pending.
<i>Kinematics</i> using Doppler analysis.	Indication of up/down wind direction.	One-dimensional wind component. Requires single-look complex data. Low resolution. Validation pending.

Currents: Ocean surface currents affect the relative speed between the surface and the air and can affect the surface roughness. This in turn can make current fronts visible in SAR imagery. Current fronts, moreover, are usually associated with water masses of different temperature. This can affect the air-sea temperature difference and consequently the surface stress. The difference in surface stress changes the short wave structure causing changes in NRCS. Strong current boundaries are often visible in SAR imagery. Knowledge of the local wind conditions can help in interpretation of current features. Moreover, use of Doppler shifts in the return SAR signal for current measurement must be partitioned into the component associated with currents and the part associated with wind and waves. Knowledge of wind speed and direction can aid in this partitioning.

Ice Edge: Changes in the NRCS from the open ocean to sea ice help locate the ice edge. Discrimination between ice and open ocean returns can be aided with SAR wind speed information.

Waves: As discussed previously, the traditional application of SAR imagery is to estimate ocean wave spectra. The azimuth, or along SAR ground track, resolution is often degraded by ocean surface motion, which is dependent on the wind-sea portion of the wave spectrum. Direct measurement of the local wind speed can help estimate the level of this degradation and potentially aid in the wave spectrum retrieval. Additionally, knowledge of the wind speed is also useful to estimate the wind vector dependent tilt modulation transfer function (Kerbaol et al. 1998b). As operationally implemented on the wave retrieval scheme to produce ENVISAT Level 2 Wave Mode products, this information leads to a better estimation of the significant wave height.

4.2. Long-term

Understanding coastal dynamics: The unique capability of a spaceborne SAR to measure the wind field at sub-kilometer resolution makes observation of rapid spatial

variations in the wind field possible. While these observations are valuable when available, these conditions vary rapidly and at present there are not sufficient number of SARs available for continuous coastal wind field monitoring.

However, SAR wind fields can be used to validate and constrain very high-resolution coastal models [Lehner et al. (1998), Horstmann et al. (2000a), Portabella et al. (2002), Furevik et al. (2002)]. If such models can be made to agree with SAR wind field estimates when available, we can gain confidence in the predictive skill of the models when there is no observation available. Recently, favorable comparisons of the Regional Atmospheric Modeling System (RAMS) predictions in Prince William Sound Alaska with coincident RADARSAT-1 SAR wind speed images have been demonstrated.⁶

Monitoring and study of meteorological phenomena: SAR imagery has proved useful in monitoring hurricanes and other large-scale features [Friedman & Li (2000), Sikora et al. (2000a)]. SAR imagery has revealed indications of strong convective cells associated with rain cells and rain bands. Secondary circulations have been observed in SAR images of hurricanes. Katsaros et al. (2000) suggest that such imagery can be usefully employed to understand storm dynamics.

SAR imagery have also been used to study and help understand other phenomena such as atmospheric lee waves atmospheric internal waves, von Kármán vortices and the statistics of turbulence in the planetary boundary layer [(Vachon et al. 1994b), Vachon et al. (1995), Alpers & Stilke (1996), Li et al. (2000), Horstmann et al. (2000b), Sikora et al. (2000b), Young & Sikora (1998), Young et al. (2000)].

Clearly, considerable effort has already been focused into describing and understanding how SAR imagery can be employed to examine marine meteorological phenomena of varying scales. Mourad (1999) provides an early review of this topic. Apel (in press, 2003) and Sikora et al.

⁶<http://koyukuk.at.uaa.alaska.edu/AEFF/rams/SAR1.html>

(in press, 2004) provide more contemporary discussions on this topic. The continual availability of SAR wind imagery will complement the research outlined in those reviews and can be expected to yield more substantive findings in the future.

Wind Turbine Site Location: Significant progress has been made in the application of SAR wind imagery for offshore wind energy exploitation. Wind energy is expected to play a major role as the European Union seeks to increase significantly the share of energy production from renewable resources (Furevik et al. in press 2003).

The unique offshore wind environment can be monitored with SAR imagery. Offshore placement of wind turbines offers several advantages: the wind speeds are usually higher offshore and the turbulence is lower, reducing fatigue loads. Nonetheless, wind speeds are inevitably less well characterized offshore than onshore and accurate estimates of wind speed are required to establish generation costs. The optimal placement of such turbines depends on the very local climatology.

The unique contribution of SAR to the measurement wind climatology for placement of wind generators is that SAR wind imagery provides high-resolution spatial information (as opposed to time series delivered for at least one year by tall offshore mast with anemometers and temperature sensors in different heights) and actual observational data (as opposed to numerical model estimates). SAR wind speed imagery offers the highest resolution possible from a spaceborne wind speed measurement sensor. A representative sample of SAR imagery can be used to guide such placement decisions [Johannessen & Korsbakken (1998), Lehner & Horstmann (2001), Furevik & Espedal (2002), Hasager et al. (2002)].

However, wind fields inferred from SAR images could benefit from higher accuracy and more frequent coverage. Revisit times are expected to significantly decrease in the coming years with the planned wide-swath SAR missions.

Risk and Cost Assessment: Routine measurement of high winds makes possible the development of high-resolution wind climatologies for specific geographical areas. These climatologies can serve for local planning purposes. Cold Bay, Alaska was considering whether to use ferries or ground transportation to travel from one part of the bay to the other. Ferries can safely operate in a range of wind speeds, but wind speed was measured at only a few places near the Bay. SAR climatology permitted a computation of the likelihood that wind speed would exceed a safety level at various parts of the bay given a certain measurement of wind speed at fixed locations (Winstead 2001).

5. TOOLS

There are two software tools available that are suitable for the automatic, operational processing of calibrated SAR imagery into wind field measurements. One is available from JHU/APL and one from General Dynamics.

The tool from JHU/APL uses model wind directions plus SAR NRCS to produce high-resolution wind speed images. Though operationally the JHU/APL tool depends on model directions, other sources of direction can be used. The General Dynamics tool uses SAR NRCS to estimate both wind speed and direction. Both tools are running operationally as part of the NOAA's Alaska SAR Demonstrations.

There are a number of primarily research tools for estimating SAR wind fields. These are summarized in Table 2.

6. THE FUTURE

6.1. Sensors

At present there are three operating spaceborne civilian SARs: RADARSAT-1 and ERS-2, ENVISAT ASAR, all operating at C-band, though the ERS-2 satellite is nearing the end of its lifetime. RADARSAT-1 operates at HH-polarization while ENVISAT ASAR operates at with HH or VV in its wide-swath mode. Since the VV-polarization GMF is best understood and since VV-polarization NRCS values are higher and less subject to system noise, C-band VV-polarization is the preferred mode of operation for wind speed retrieval.

This C-band preference is the consequence of experience rather than a systematic evaluation of the best frequency/polarization combination. A modest amount of work has been done with the L-band JERS-1 SAR, but the GMF is not well understood. It is likely that L-band response would be poorer than C-band at low wind speeds, but the possibility remains that such L-band may exhibit less saturation in NRCS at higher winds speeds. We know that X-band radars are responsive to wind speed, but the GMF has not been as well defined.

6.2. Improvements

In terms of future efforts towards operational use of near surface wind fields derived from SAR, we recommend the following steps be pursued:

1. Operational timeliness in inexpensive and useful quantities: The availability of RADARSAT-1 SAR imagery and its subsequent wind field estimates in near real time has demonstrated the operational utility of such information. We recommend that all future SAR systems develop and exploit the ability to deliver wind imagery in near real time. Moreover, such data must be provided in sufficient quantities (hundreds even thousands of image frames per year) at low cost so that a systematic and statistically significant evaluation of performance can be made.
2. Optimum wind direction estimation: There are a number of methods to estimate wind direction for

Table 2. Manual SAR wind speed tools. All methods estimate wind speed, but differ significantly in wind direction inputs used.

Name/Source	Features
GKSS	Uses gradient method to determine wind direction.
Ocean Monitoring Workstation (OMW)	Uses directions from SAR imagery but can ingest external sources of directions.
Canadian Centre for Remote Sensing (CCRS)	Uses directions from SAR imagery but can ingest external sources of directions.
KSPT	Uses directions from SAR imagery but can ingest external sources of directions.
NERSC	Uses directions from SAR imagery but can ingest external sources of directions.
ESA (Norut, IFREMER, BOOST)	Uses cross spectrum analysis
SARTool (BOOST Technologies)	Uses directions from SAR imagery but can ingest external sources of directions.

SAR wind field retrieval including model wind directions, wind direction estimates from the SAR, and direction estimates from other remote sensors. A rational way to assimilate all these data into a self-consistent wind direction field would not only improve wind direction retrievals, but wind speed retrievals as well.

3. GMF for high wind speeds: Most current GMFs are tuned for best results in the 2 to 20 m/s wind speed regime. However, some of the most interesting imagery may be in the vicinity of storms where winds speeds could be higher. Current work to adapt GMF's for higher wind speeds should continue and undergo sufficient validation.
4. GMF for L and X-band: The GMF for C-band is well-developed. Since some future SAR's will likely operate at L and X-bands, there is a need for improved GMF at these frequencies.
5. Multi-channel utilization: Presently, ENVISAT ASAR operates at HH and VV polarization. In its narrow swath mode, it can operate at both polarizations simultaneously. With both polarizations, we anticipate the possibility of improved wind retrievals.
6. Masking: While it is possible to create precision land masks to separate water from ocean, a robust technique for masking to separate sea ice from open water conditions would extend confidence in wind retrievals to the ice edge. In addition, current features and oil spill features can be mistakenly identified as variations in wind speeds. Flagging of these features would prevent miss interpretation of SAR wind fields.
7. Training tools for users. There is no dedicated tool for helping users understand the principles underpinning SAR wind retrieval. While there are a number of presentations available that provide some background information, there is no comprehensive interactive tool
8. An understanding of user needs: The production of wind speed products can not be effectively used un-

less there is an understanding of what products and in what form various users would prefer the data. A more through understanding of user needs is required to advance the application of SAR winds.

7. CONCLUSIONS

Five years ago it could fairly concluded that the SAR measurement of the ocean wind field was an experimental technique still under evaluation for operational use. In the intervening years, is it has become clear that conventional and wide-swath SARs can measure wind speed at sub-kilometer scales. Validation of such winds over a few kilometers shows agreement with buoy measurements to better than 2 m/s in the 2 to 20 m/s wind speed range. If divided into 25 km on-a-side sub-frames, directions can be estimate from the imagery at better than 25°, albeit with a 180° ambiguity. These results represent conservative estimates. Comparison of SAR wind speeds with respect to spaceborne scatterometer measurement suggests that the random error in SAR wind speeds could be as low as 1.3 m/s and wind direction errors in some studies are as low as 15°. Continued debates about the best GMF's or the best methods to extract wind direction from SAR imagery represent arguments about details. Indeed, the merging of different approaches offers the prospect of maximum exploitation of the data. Nonetheless, these efforts at continued improvement in approaches to extract the wind field from SAR imagery should not obscure the present positive consensus on the ability to retrieve SAR winds.

In this paper, we have outlined a number of directions for improved exploitation of SAR data. However, perhaps the most important recommendation is that large numbers of image frames must be provided in near real time at low cost. Although SAR wind fields can be used retrospectively to understand wind dynamics in coastal regions, improve coastal environmental models, help in the location of wind generation structures, and aid in risk assessments; the full value of high resolution winds will not be realized until such data can also be provided in a robust way and an operationally useful time frame. Presently,

the Alaska SAR Demonstration provides a model for such a system. RADARSAT-1 SAR imagery is processed into wind speed estimates in near real time; about three hours from satellite acquisition to posting on the web. ENVISAT SAR data appear to have less image artifacts than RADARSAT-1 data, but ENVISAT SAR data are generally not provided in an operational time frame. We recommended that near real time access to ENVISAT data be explored. Moreover, thousands of image frames per year are required not only provide statistically useful amounts of data for continued evaluation of SAR wind retrieval performance, but to cover the coastal regions on a timely basis.

REFERENCES

- Alpers W., 1994, Measurement of mesoscale oceanic and atmospheric phenomena by ERS-1 SAR, *Radio Sci. Bull.*, vol. 275, pp. 14–22.
- Alpers W., Brümmer B., Jun. 1994, Atmospheric boundary layer rolls observed by the synthetic aperture radar aboard the ERS-1 satellite, *J. Geophys. Res.*, vol. 99, no. C6, pp. 12613–12621.
- Alpers W., Stilke G., 1996, Observation of a nonlinear wave disturbance in the marine atmosphere by the synthetic aperture radar aboard the ERS-1 satellite, *J. Geophys. Res.*, vol. 101, pp. 6513–6525.
- Alpers W., Gade M., Melsheimer C., et al., Jul. 1995, The imaging of different ocean and atmospheric phenomena by SIR-C/X-SAR, In: *Proc. 1995 International Geoscience and Remote Sensing Symposium*, pp. 219–224, Florence, Italy.
- Alpers W., Phal U., Gross G., Apr. 1998, Katabatic wind field in coastal areas studied by ERS-1 synthetic aperture radar imagery and numerical modeling, *J. Geophys. Res.*, vol. 103, no. C4, pp. 7875–7886.
- Apel J., in press, 2003, SAR Users Manual, National Oceanic and Atmospheric Administration.
- Atlas D., 1994, Footprint of storms on the seas: A view from spaceborne synthetic aperture radar, *J. Geophys. Res.*, vol. 99, pp. 7961–7969.
- Attema E.P.W., 1986, An experimental campaign for the determination of the radar signature of the ocean at C-band, In: *Proc. Third International Colloquium on Spectral Signatures of Objects in Remote Sensing*, ESA SP-247, pp. 791–799, LesArcs, France.
- Babin S.M., Thompson D.R., 2000, Effects of atmospheric boundary-layer moisture on friction velocity with implications for SAR imagery, *IEEE Trans. Geosci. and Remote Sensing*, vol. 38, pp. 618–612.
- Babin S.M., Sikora T.D., Winstead N.S., 2003, A case study of satellite synthetic aperture radar signatures of spatially evolving atmospheric convection over the Western Atlantic Ocean, *Bound.-Layer Meteorol.*, vol. 106, pp. 527–546.
- Beal R.C., Sep. 1980, The Seasat SAR wind and ocean wave monitoring capabilities: A case study for pass 1339M, *Tech. Rep. S1R 79U-019*, Johns Hopkins APL.
- Beal R.C., Jan. 2000, Toward an International StormWatch using wide-swath SAR, *The Johns Hopkins Univ. Tech. Dig.*, vol. 21, no. 1, pp. 12–20.
- Beal R.C., Pichel W.G., Jul. 1998, StormWatch 1997–98 and beyond: application of SAR as a high-resolution scatterometer in coastal regions, In: *Proc. International Geoscience and Remote Sensing Symposium*, pp. 1195–1200, Seattle, WA.
- Bentamy A., Quilfen Y., Queffelec P., Cavanié A., 1994, Calibration of the ERS-1 scatterometer C-Band model, *Tech. Rep. DRO-OS/OS-94-01*, Inst. Fr. de Rech. pour l'Exploit. de la Mer, Brest, France.
- Boggs D.H., 1982, Seasat Scatterometer Geophysical Data Record (GDR) Users Handbook, *Tech. Rep. D-129*, Jet Propulsion Laboratory, California Institute of Technology, Pasadena, CA.
- Brown G.S., 1970, A secondary flow model for the planetary boundary layer, *J. Atmos. Sci.*, vol. 27, pp. 742–757.
- Brown R.A., 1980, Longitudinal instabilities and secondary flows in the planetary boundary layer: A review, *Rev. Geophys.*, vol. 18, pp. 683–697.
- Brown R.A., 1983, On satellite scatterometer capabilities in air-sea interactions, *J. Geophys. Res.*, vol. 88, pp. 1663–1673.
- Brown R.A., 1986, On a satellite scatterometer as an anemometer, *J. Geophys. Res.*, vol. 91, pp. 2221–2232.
- Brown R.A., 2000, Serendipity in the use of satellite scatterometer, SAR, and other sensor data, *The Johns Hopkins Univ. Tech. Dig.*, vol. 21, pp. 100–107.
- Campbell J.W.M., Vachon P.W., 1997, Extracting ocean wind vectors from satellite imagery, *Backscatter*, vol. 8, pp. 16–21.
- Clemente-Colón P., 1998, Coastal Oceanography Applications of Spaceborne Synthetic Aperture Radar (SAR) in the Middle Atlantic Bight (MAB), Ph.D. thesis, College of Marine Studies, University of Delaware, Newark, DE.
- Clemente-Colón P., Foster R.C., Levy G., 1998, The contribution of organized roll vortices to the surface wind vector in baroclinic conditions, *J. Atmos. Sci.*
- Dankert H., Horstmann J., Rosenthal W., in press, 2003, Ocean wind fields retrieved from radar-image sequences, *J. Geophys. Res.*
- Du Y., Vachon P.W., Wolf J., 2002, Wind direction estimation from SAR images of the ocean using wavelet analysis, *Canadian J. Remote Sens.*, vol. 28, pp. 498–509.
- Elfouhaily T., Thompson D.R., Vandemark D., Chapron B., 1999, A new bistatic model for electromagnetic scattering from perfectly conducting random surfaces, *Waves in Random Media*, vol. 9, pp. 281–294.
- Engen G., Hoegda K.A., Johnsen H., 1998, A new method for wind field retrieval from SAR data, In: *Proc. CEOS SAR Workshop*, vol. WPP-138, pp. 43–51.
- Fetterer F., Gineris D., Wackerman C.C., 1998, Validating a Scatterometer Wind Algorithm for ERS-1 SAR, *IEEE Trans. Geosci. and Remote Sensing*, vol. 36, no. 1, pp. 479–492.

- Fichaux N., Rachin T., 2002, Combined extraction of high spatial resolution wind speed and direction from SAR images: A new approach using wavelet transform, *Canadian J. Remote Sens.*, vol. 28, pp. 510–516.
- Foster R.C., Levy G., 1998, The contribution of organized roll vortices to the surface wind vector in baroclinic conditions, *J. Atmos. Sci.*, vol. 58.
- Freilich M.H., Dunbar R.S., 1999, The accuracy of the NSCAT-1 vector winds: comparisons with National Data Buoy Center buoys, *J. Geophys. Res.*, vol. 104, no. C5, pp. 11,231–11,246.
- Friedman K.S., Li X., 2000, Monitoring hurricanes over the ocean with wide-swath SAR, *The Johns Hopkins Univ. Tech. Dig.*, vol. 21, pp. 80–85.
- Friedman K.S., Sikora T.D., Pichel W.G., Clemente-Colón P.C., Hufford G., 2001, Using spaceborne synthetic aperture radar to improve marine surface analyses, *Weather Forecast.*, vol. 16, pp. 270–276.
- Fu L.L., Holt B., 1982, Seasat views oceans and seas with synthetic aperture radar, *Tech. Rep. JPL Publ. 81–102*, Jet Propulsion Laboratory, California Institute of Technology, Pasadena, CA.
- Furevik B.R., Espedal H.A., 2002, Wind energy mapping using synthetic aperture radar, *Canadian J. Remote Sens.*, vol. 28, pp. 196–204.
- Furevik B.R., Korsbakken E., 2000, Comparison of derived wind speed from synthetic aperture radar and scatterometer during the ERS tandem phase, *IEEE Trans. Geosci. and Remote Sensing*, vol. 38, pp. 1113.
- Furevik B.R., Johannessen O.M., Sandvik A.D., 2002, SAR-retrieved wind in polar regions — Comparison with in situ and atmospheric model output, *IEEE Trans. Geosci. and Remote Sensing*, vol. 40, pp. 1720–1732.
- Furevik B.R., Espedal H.A., Hamre T., et al., in press 2003, Satellite-based wind maps as guidance for siting offshore wind farms, *Wind Engr.*
- Gerling T.W., 1986, Structure of the Surface Wind Field from the Seasat SAR, *J. Geophys. Res.*, vol. 91, no. C2, pp. 2308–2320.
- Hasager C.B., Frank H., Furevik B.R., 2002, On offshore wind energy mapping using satellite SAR, *Canadian J. Remote Sens.*, vol. 28, pp. 80–89.
- Hasselmann S., Brüning C., Hasselmann K., Heimbach P., Jul. 1996, An improved algorithm for the retrieval of ocean wave spectra from synthetic aperture radar image spectra, *J. Geophys. Res.*, vol. 101, pp. 16,615–16,629.
- Hawkins J.D., Black P.G., 1983, Seasat scatterometer detection of gale force winds near tropical cyclones, *J. Geophys. Res.*, vol. 88, pp. 1674–1682.
- Hersbach H., Jan. 2003, An improved geophysical model function for ERS C-band scatterometry, *Tech. Rep. ECMWF 395*, ECMWF, Reading, UK.
- Horstmann J., 1997, Investigation of wind speed retrieval with synthetic aperture radar aboard the ERS-1/2 satellites, *Tech. Rep. GKSS 97/E/55*, GKSS.
- Horstmann J., Koch W., Lehner S., Rosenthal W., 1998, Ocean wind fields and their variability derived from SAR, *Earth Observ. Quart.*, vol. 59, no. 5, pp. 8–12.
- Horstmann J., Kock W., Lehner S., Tonboe R., 2000a, Wind Retrieval over the Ocean using Synthetic Aperture Radar with C-band HH Polarization, *IEEE Trans. Geosci. and Remote Sensing*, vol. 38, no. 5, pp. 2122–2131.
- Horstmann J., Lehner S., Kock W., Tonboe R., Jan. 2000b, Computation of wind vectors over the ocean using spaceborne synthetic aperture radar, *The Johns Hopkins Univ. Tech. Dig.*, vol. 21, no. 1, pp. 100–107.
- Horstmann J., Koch W., N. S. W., F. M. Monaldo P.C.C., Pichel W.G., Jul. 2003a, Comparison of RADARSAT-1 SAR retrieved ocean wind fields to QuikSCAT and numerical models, In: *Proc. International Geoscience and Remote Sensing Symposium*, Toulouse, France.
- Horstmann J., W. Koch S.L., Tonboe R., 2003b, Comparison of RADARSAT-1 SAR retrieved ocean wind fields to QuikSCAT and numerical models, *Canadian J. Remote Sens.*, vol. 28, pp. 524–533.
- Horstmann J., Schiller H., Schulz-Stellenfleth J., Lehner S., in press, 2003, Ocean winds from RADARSAT-1 ScanSAR, *IEEE Trans. Geosci. and Remote Sensing*.
- IFREMER, Mar. 1996, Off-line wind scatterometer ERS products — User Manual : version 2.0, IFREMER, c2-MUT-W-01-IF.
- Jackson F.C., Peng C.Y., Jul. 1985, Comment on “Imaging radar observations of directional properties of ocean waves” by W. McLeish and D. B. Ross, *J. Geophys. Res.*, vol. 90, no. C4, pp. 7367–7370.
- Johannessen J., 2000, Coastal observing systems: The role of synthetic aperture radar, *The Johns Hopkins Univ. Tech. Dig.*, vol. 21, pp. 41–48.
- Johannessen J.A., Vachon P.W., Johannessen O.M., 1997, ERS-1 SAR imaging of marine boundary layer process, *Earth Observ. Remote Sensing*, vol. 14, pp. 449–461–5.
- Johannessen J.A., Garello R., Chapron B., et al., 2001, Marine SAR analysis and interpretation system — MARS AIS, *Annales de Telecommunications*, vol. 56, pp. 655–660.
- Johannessen O.M., Korsbakken E., 1998, Determination of wind energy from SAR images for siting windmill locations, *Earth Observ. Quart.*, vol. 59, pp. 2–4.
- Johannessen O.M., Espedal H., Furevik B., Akimov D., Jenkins A., 1994, COASTWATCH: Integrating satellite SAR in an operational system for monitoring coastal currents, wind, surfactants and oil spills, *Earth Observ. Quart.*, vol. 46, pp. 1–5.
- Jones W.L., Delnore V.E., Bracalente E.M., 1981, Spaceborne Synthetic Aperture Radar for Oceanography, chap. The study of mesoscale winds, pp. 87–94, *The Johns Hopkins University Press*, Baltimore, MD.
- Katsaros K.B., Vachon P.W., Black P.G., Dodge P.P., Uhlhorn E.W., 2000, Wind fields from SAR: Could they improve our understanding of storm dynamics?, *The Johns Hopkins Univ. Tech. Dig.*, vol. 21, pp. 86–93.
- Kerbaol V., Chapron B., Queffeuilou P., 1998a, Analysis of the wind field during the Vendée Globe race: A kinematic SAR wind speed algorithm, *Earth Observ. Quart.*, vol. 59, pp. 16.

- Kerbaol V., Chapron B., Vachon P.W., 1998b, Analysis of ERS-1/2 synthetic aperture radar wave mode images, *J. Geophys. Res.*, vol. 103, pp. 7833–7846.
- Korsbakken E., 1996, Quantitative Wind Field retrievals from ERS SAR Images, Tech. rep., ESA.
- Korsbakken E., Furevik B., 1998, Wind field retrieval from SAR compared with scatterometer wind field during ERS tandem phase, *Earth Observ. Quart.*, vol. 59, pp. 23.
- Korsbakken E., Johannessen J.A., Johannessen O.M., 1998, Coastal wind retrievals from ERS synthetic aperture radar, *J. Geophys. Res.*, vol. 103, pp. 7857–7874.
- Laur H., Bally P., Meadows P., et al., Jun. 1996, ERS SAR Calibration – Derivation of Backscattering coefficient in ESA ERS SAR PRI Products, Tech. Rep. ES-TN-RS-PM-HL09, Eur. Space Agency - Eur. Space Res. Inst., Frascati, Italy.
- Lehner S., Horstmann J., Dec. 2001, High resolution wind fields retrieved from spaceborne synthetic aperture radar and numerical models, In: *Offshore Windenergy Conference*, Brussels, Belgium.
- Lehner S., Horstmann J., Koch W., Rosenthal W., 1998, Mesoscale wind measurements using recalibrated ERS SAR images, *J. Geophys. Res.*, vol. 103, pp. 7847–7856.
- Lehner S., Schulz-Stellenfleth J., Schattler B., Breit H., Horstmann J., 2000, Wind and wave measurements using complex ERS-2 SAR wave mode data, *IEEE Trans. Geosci. and Remote Sensing*, vol. 38, pp. 2246–2257.
- Leibovich S., 1983, The form and dynamics of Langmuir circulations, *Annu. Rev. Fluid Mech.*, vol. 79, pp. 715–743.
- Li X., Clemente-Colón P., Pichel W.G., Vachon P.W., 2000, Atmospheric vortex streets on a RADARSAT SAR image, *Geophys. Res. Lett.*, vol. 27, pp. 1655–1658.
- Mastenbroek K., 1998, High-resolution wind fields from ERS SAR, *Earth Observ. Quart.*, vol. 59, pp. 20.
- Meadows P., Wright P.A., Sep. 1994, ERS-1 SAR analogue to digital converter saturation, In: *Proc. CEOS SAR Calibration and Validation Workshop*, pp. 24–27, Ann Arbor, MI.
- Meadows P., Laur H., Sanchez J.I., Schattler B., 1998, ERS-1 SAR analogue to digital converter saturation, In: *Proc. CEOS SAR Workshop*, pp. 223–232, Noordwijk, The Netherlands.
- Monaldo F.M., Jan. 2000, The Alaska SAR Demonstration and near real-time synthetic aperture radar winds, *The Johns Hopkins Univ. Tech. Dig.*, vol. 21, no. 1, pp. 75–84.
- Monaldo F.M., Feb. 2003, Comparison of high-resolution SAR Images with QuikSCAT wind measurements, In: *Proc. 12th Annual Conference on Satellite Meteorology at the 83rd Annual Meteorological Association Meeting*, Long Beach, CA.
- Monaldo F.M., Beal R.C., Jul. 1998, Toward real-time processing, blending, and dissemination of operational wind products from the RADARSAT SAR, In: *Proc. 1998 International Geoscience and Remote Sensing Symposium*, pp. 959–961, Seattle, WA.
- Monaldo F.M., Thompson D.R., Beal R.C., Pichel W.G., Clemente-Colón P., Dec. 2001, Comparison of SAR-derived wind speed with model predictions and buoy comparisons, *IEEE Trans. Geosci. and Remote Sensing*, vol. 39, no. 12, pp. 2587–2600.
- Monaldo F.M., Thompson D.R., Pichel W.G., Clemente-Colón P., In Press 2003, A Systematic Comparison of QuikSCAT and SAR Ocean Surface Wind Speeds, *IEEE Trans. Geosci. and Remote Sensing*.
- Moore R.K., 1974, Simultaneous active and passive microwave response of the Earth: The Skylab RADSCAT experiment, In: *Proc. Ninth International Symposium on Remote Sensing of the Environment*, vol. I, pp. 189–217, University of Michigan.
- Mourad P.D., 1999, *Air-Sea Exchange: Physics, Chemistry, and Dynamics*, chap. Footprints of atmospheric phenomena in synthetic aperture radar image of the ocean surface: A review, Kluwer Academic Publishers, Boston, MA.
- Mourad P.D., Walter B.A., 1996, Viewing a cold air outbreak using satellite-based synthetic aperture radar and Advanced Very High Resolution Radiometer imagery, *J. Geophys. Res.*, vol. 101, pp. 16,391–16,400.
- Mourad P.D., Thompson D.R., Vandemark D.C., Jan. 2000, Extracting fine-scale wind fields from synthetic aperture radar images of the ocean surface, *The Johns Hopkins Univ. Tech. Dig.*, vol. 21, no. 1, pp. 108–115.
- Müller G., Brümmer B., Alpers W., 1999, Roll convection with an Arctic cold-air outbreak: Interpretation of in situ aircraft measurements and spacecraft SAR imagery by a three-dimensional atmospheric model, *Monthly Wea. Rev.*, vol. 127, pp. 363–380.
- Offiler D., 1994, The calibration of ERS-1 satellite scatterometer winds, *J. Atmos. Oceanic Technol.*, vol. 11, pp. 1002–1017.
- Pichel W.G., Clemente-Colón P., Jan. 2000, NOAA CoastWatch SAR Applications and Demonstration, *The Johns Hopkins Univ. Tech. Dig.*, vol. 21, no. 1, pp. 49–57.
- Pierson W.J., 1983, The measurement of synoptic scale wind over the ocean, *J. Geophys. Res.*, vol. 88, pp. 1683–1708.
- Portabella M., Stofflen A., Johannessen J.A., 2002, Toward an optimal inversion method for synthetic aperture radar wind retrieval, *J. Geophys. Res.*, vol. 107.
- Quilfen Y., Betamy A., Aug. 1994, Calibration/validation of ERS-1 scatterometer and precision products, In: *Proc. 1994 International Geoscience and Remote Sensing Symposium*, pp. 945–947, Pasadena, CA.
- Quilfen Y.B., Chapron B., Elfouhaily T., Katsaros K., Tournadre J., 1998, Observation of tropical cyclones by high-resolution scatterometry, *J. Geophys. Res.*, vol. 103, pp. 7767–7786.
- Romeiser R., Alpers W., Wissmann V., May 1997, An improved composite model for the radar backscattering cross section of the ocean surface; 1. Theory and model validation/optimization by scatterometer data, *J. Geophys. Res.*, vol. 102, no. C5, pp. 25,237–25,250.
- Sandvik A.D., Furevik B.R., 2002, Case study of a coastal jet at Spitzbergen — comparison of SAR and

- model estimated wind, *Mon. Wea. Rev.*, vol. 19, pp. 1040–1051.
- Scoon A., Robinson I.S., Meadows P.J., 1996, Demonstration of an improved calibration scheme for ERS-1 SAR imagery using a scatterometer wind model, *Int. J. Remote Sens.*, vol. 17, no. 2, pp. 413–418.
- Shimada T., T., Kawamra H., Shimada M., 2003, An L-band geophysical mode function for SAR wind retrieval using JERS-1 SAR, *IEEE Trans. Geosci. and Remote Sensing*, vol. 41, pp. 518–531.
- Sikora T.D., Young G.S., 1993, Observations of planview flux patterns with convective structures of the marine atmospheric surface layer, *Bound.-Layer Meteorol.*, vol. 65, pp. 271–288.
- Sikora T.D., Young G.S., Jun. 2002, Wind-direction dependence of quasi-2D SAR signature, In: *Proc. International Geoscience and Remote Sensing Symposium*, pp. 1887–1889, Toronto, CA.
- Sikora T.D., Young G.S., Beal R.C., Edson J.B., 1995, Use of spaceborne synthetic aperture radar imagery of the sea surface in detecting the presence and structure of the convective marine atmospheric boundary layer, *Mon. Wea. Rev.*, vol. 123, pp. 3623–3632.
- Sikora T.D., Young G.S., Shirer H.N., Chapman R.D., 1997, Observations of planview flux patterns with convective structures of the marine atmospheric surface layer, *J. Appl. Meteorol.*, vol. 36, pp. 833–845.
- Sikora T.D., Friedman K.S., Pichel W.G., Clemente-Colón P., 2000a, Synthetic aperture radar as a tool for investigating polar mesoscale cyclones, *Weather Forecast.*, vol. 15, pp. 745–758.
- Sikora T.D., Thompson D.R., Bleidorn J.C., 2000b, Testing the diagnosis of marine atmospheric boundary-layer structure from synthetic aperture radar, *The Johns Hopkins Univ. Tech. Dig.*, vol. 21, pp. 94–99.
- Sikora T.D., Thompson D.R., Mourad P.D., 2002, Direct influence of gravity waves on surface-layer stress during a cold air outbreak as shown by synthetic aperture radar, *Mon. Wea. Rev.*, vol. 130, pp. 2764–2776.
- Sikora T.D., Young G.S., Vachon R.C.B.P.W., Winstead N.S., in press, 2004, *Atmosphere Ocean Interactions*, vol. 2, chap. Applications of synthetic aperture radar in marine meteorology, WIT Press.
- Stoffelen A.C.M., Anderson D.L.T., 1993, ERS-1 scatterometer data characteristics and wind retrieval skill, *Adv. Space Res.*, vol. 13, pp. 553–560.
- Stoffelen A.C.M., Anderson D.L.T., 1997a, Scatterometer data interpretation: Measurement and inversion, *J. Atmos. Oceanic Technol.*, vol. 14, pp. 1298–1313.
- Stoffelen A.C.M., Anderson D.L.T., 1997b, ERS-1 scatterometer data characteristics and validation of the transfer function: CMOD4, *J. Geophys. Res.*, vol. 102, pp. 5767–5780.
- Stoffelen A.C.M., Anderson D.L.T., 1999, A simple method for calibration of a scatterometer over the ocean, *J. Atmos. Oceanic Technol.*, vol. 16, pp. 275–282.
- Thompson D.R., Beal R.C., Jan. 2000, Mapping high-resolution wind fields using synthetic aperture radar, *The Johns Hopkins Univ. Tech. Dig.*, vol. 21, no. 1, pp. 58–67.
- Thompson D.R., Elfouhaily T.M., Chapron B., Jul. 1999, Polarization ratio for microwave backscattering from the ocean surface at low to moderate incidence angles, In: *Proc. 1999 International Geoscience and Remote Sensing Symposium*, pp. 1671–1673.
- Thompson D.R., Monaldo F.M., Winstead N.S., Pichel W.G., Clemente-Colón P., Oct. 2001, Combined estimates improve high-resolution coastal wind mapping, *Eos*, vol. 82, pp. 368–374.
- Unal C.M.H., Snooji P., Swart P.J.F., 1991, The polarization-dependent relation between radar backscatter from the ocean surface and wind vectors at frequencies between 1 and 18 GHz, *IEEE Trans. Geosci. and Remote Sensing*, vol. 29, pp. 621–626.
- Vachon P.W., Dobson F.W., 1996, Validation of Wind Vector Retrieval from ERS-1 SAR Images over the Ocean, *Global Atmos. Ocean Syst.*, vol. 5, pp. 177–187.
- Vachon P.W., Dobson F.W., Aug. 2000, Wind Retrieval from RADARSAT SAR Images: Selection of a Suitable C-Band HH Polarization Wind Retrieval Model, *Canadian J. Remote Sens.*, vol. 26, no. 4, pp. 306–313.
- Vachon P.W., Johannessen O.M., Johannessen J.A., Nov. 1994a, An ERS-1 synthetic aperture radar image of atmospheric Lee waves, *J. Geophys. Res.*, vol. 99, no. C11, pp. 22,483–22,490.
- Vachon P.W., Krogstad H.E., Patterson J.S., Mar. 1994b, Airborne and Spaceborne Synthetic Aperture Radar Observations of Ocean Waves, *Atmos. Ocean*, vol. 32, no. 1, pp. 83–112.
- Vachon P.W., Johannessen J.A., Browne D.P., Jul. 1995, ERS-1 SAR images of atmospheric gravity waves, *IEEE Trans. Geosci. and Remote Sensing*, vol. 33, no. 4, pp. 1014–1025.
- Vachon P.W., Chunchuzov I., Dobson F.W., 1998, Wind field structure and speed from RADARSAT SAR images, *Earth Observ. Quart.*, vol. 59, pp. 12.
- Vachon P.W., Dobson F.W., 2000a, Wind retrieval from RADARSAT SAR images: Selection of a suitable C-band HH polarization wind retrieval model, *Canadian J. Remote Sens.*, vol. 26, pp. 306–313.
- Vachon P.W., Adlakha P., Edek H., et al., Jan. 2000b, Canadian Progress Toward Marine and Coastal Applications of Synthetic Aperture Radar, *The Johns Hopkins Univ. Tech. Dig.*, vol. 21, no. 1, pp. 33–40.
- Vandemark D., Vachon P.W., Chapron B., 1998, Assessment of ERS-1 SAR wind speed estimates using an airborne altimeter, *Earth Observ. Quart.*, vol. 59, pp. 5–8.
- Wackerman C.C., 2000, Estimating wind vectors from RADARSAT synthetic aperture radar imagery, *Tech. Rep. 10032100-1-T*, Veridian ERIM International, P.O. Box 134008, Ann Arbor, MI 48113-4008.
- Wackerman C.C., Rufenach R., Johannessen J., Davison K., 1996, Wind vector retrieval using ERS-1 synthetic aperture radar imagery, *IEEE Trans. Geosci. and Remote Sensing*, vol. 34, pp. 1343–1352.
- Wackerman C.C., Clemente-Colón P., Pichel W.G., Li X., 2002, A two-scale model to predict C-band VV and HH normalized radar cross section values over the ocean, *Canadian J. Remote Sens.*, vol. 28, pp. 367–384.

- Wackerman C.C., Horstmann J., Koch W., Jul. 2003a, Operational estimation of coastal wind vectors from RADARSAT SAR imagery, In: Proc. International Geoscience and Remote Sensing Symposium, Toulouse, France.
- Wackerman C.C., Pichel W.G., Clemente-Colón P., Feb. 2003b, Automated estimation of wind vectors from SAR, In: Proc. 83rd AMS Annual Meeting, Long Beach, CA.
- Weissman D.E., King D., Thompson T.W., 1979, Relationship between hurricanes surface winds and L-band radar backscatter from the sea surface, *J. Applied Meteorol.*, pp. 1023–1034.
- Weissman D.E., Thompson T.W., Legeckis R., 1980, Modulation of seas surface radar cross section by surface stress: Wind speed and temperature affects across the Gulf Stream, *J. Geophys. Res.*, pp. 5032–5042.
- Wentz F.J., Mattox L.A., Peteherych S., 1986, New algorithms for microwave measurements of ocean winds, Applications to Seasat and the Special Sensor Microwave Imager, *J. Geophys. Res.*, pp. 2289–2307.
- Winstead N.S., May 2001, Characteristics of the wind speed distribution over Cold Bay and Leonard Harbor Alaska, Tech. Rep. SRO-01-09, Johns Hopkins APL Tech. Rep., Laurel, MD.
- Winstead N.S., Mourad P.D., 2000, Shallow Great Lake scale atmospheric thermal circulation imaged by synthetic aperture radar, *Mon. Wea. Rev.*, vol. 128, pp. 2654–3663.
- Winstead N.S., young G.S., 2000, Analysis of drainage flow exit jets over the Chesapeake Bay, *J. Applied Meteorol.*, vol. 39, pp. 1269–1281.
- Winstead N.S., Schaaf R.M., Mourad P.D., 2001, Synthetic aperture radar observations of the surface signatures of cold-season bands over the Great Lakes, *Weather Forecast.*, vol. 16, pp. 315–328.
- Young G.S., 2000, SAR signatures of the marine atmospheric boundary layer: Implications for numerical weather forecasting, *The Johns Hopkins Univ. Tech. Dig.*, vol. 21, pp. 27–32.
- Young G.S., Sikora T.D., 1998, Distinguishing boundary layer signatures from mesoscale and ocean clutter in SAR imagery, In: Proc. International Geoscience and Remote Sensing Symposium, pp. 1385–1387, Seattle, WA.
- Young G.S., Sikora T.D., Winstead N.S., 2000, Inferring marine atmospheric boundary layer properties from spectral characteristics of satellite-borne SAR imagery, *Mon. Wea. Rev.*, vol. 128, pp. 1506–1520.
- Zecchetto S., Trivero P., Fiscella B., Pavese P., 1998, Wind stress structure in the unstable marine surface layer detected by SAR, *Boundary-Layer Meteorol.*, vol. 86, pp. 1–28.

USING SATELLITE SAR IN OFFSHORE WIND RESOURCE ASSESSMENT

B. R. Furevik⁽¹⁾, C. B. Hasager⁽²⁾, M. Nielsen⁽²⁾, T. Hamre⁽¹⁾, B. H. Jørgensen⁽²⁾, O. Rathmann⁽²⁾, and O. M. Johannessen^(1,3)

(1) Nansen Environmental and Remote Sensing Center, Edv. Griegsvei 3A, N-5059 Bergen, Norway, email:

Birgitte.Furevik@nersc.no

(2) Risø National Laboratory, Wind Energy Department, Frederiksborgvej 399, DK-4000 Roskilde, Denmark, email:

charlotte.hasager@risoe.dk

(3) also at the Geophysical Institute, University of Bergen, Norway.

ABSTRACT

Offshore wind farms are a growing business worldwide. The energy output of a wind farm can be predicted by knowing the local wind climate. Usually, the wind climatology is based on at least one year of accurate wind measurements. Before such data are available at a site, satellite-based wind mapping can be a helpful tool in giving the first estimates of the wind conditions. In the Wind Energy Mapping using Synthetic Aperture Radar (WEMSAR) project wind fields from SAR, in situ measurements and model output from three test-sites have been analysed. Subsequently, a tool for retrieving wind maps from SAR images and utilising them in the Wind Atlas analysis and application Programme (WAsP) has been developed.

1 - INTRODUCTION

Usually the prediction of the energy production of a wind farm is based on a combination of historical data from the region and one year of accurate *in situ* measurements from a mast on the specific site. Measurements are carried out in three different heights with the aim of predicting the mean wind speed within $\pm 5\%$. The wind conditions at a nearby location at a certain hub height is traditionally estimated by using micro-siting models such as the Wind Atlas analysis and application Programme (WAsP¹) developed at Risø National Laboratory, Denmark [1]. In some areas of the world where no observations are available, satellite Synthetic Aperture Radar (SAR) and other remote sensing wind measurements can aid in giving the first estimate of the 10 m wind conditions at a site.

The previous work done on the topic reveals a few different approaches. The first approach using 1-5 SAR images from a site [2] is not useful for estimating the wind climate. But choosing the images during periods of typical local wind conditions it can be a quick way to get an idea of some wind phenomena in the area, in particular when the coast is mountainous and thus local wind is more unpredictable and spatially inhomogeneous.

The other extreme is to aim at ordering and analysing enough SAR scenes from the site of interest so as to represent a time series. This approach is necessary in trying to estimate the Weibull parameters of the wind speed distribution from the data. These parameters can then be input to the WAsP programme [3]; [4]. According to [5] and [6] 60-70 SAR scenes are needed to give a reliable estimate of the mean wind speed and the Weibull scale parameter, while about 250 scenes are needed in order to fit the Weibull parameters. With the present cost and coverage of SAR data, it would be optimistic to believe we could acquire this much data over any coastal site on the Earth. In addition, the SAR wind vectors are of limited accuracy and the acquisition not random. The accuracy of the data is generally agreed to be around 2 m/s in speed and 2-20 degrees in wind direction [7]. The acquisition of satellite SAR scenes is dependent on the needs of the SAR community and may therefore be strongly biased from the purpose of the original order (interest in wind, oil slick, natural film, current shear etc.). Additional bias occurs due to the satellites passing the site at the same time of the day.

A compromise of the two approaches is to utilise for instance scatterometer winds to give the temporal coverage while ordering as many SAR scenes as possible for the spatial variability [8]. The main limitation of the scatterometer data is, of course, the coarse resolution and the lack of wind vectors near the coast. The area of interest for wind farm projects is related to the water depth that should not exceed 20-30 m. Using micro-siting models such as WAsP to move the offshore scatterometer observations closer to the coast may solve this problem.

2 - APPROACH

The second approach is used in the WEMSAR project. SAR PRI (SAR precision image) products from the ERS-1 and ERS-2 satellites are calibrated² to obtain the normalised radar cross section (NRCS) [9]. The images are averaged down to a pixel size of 400 m x 400 m in

¹ <http://www.wasp.dk/>

² using software from <http://earth.esa.int/services/best/>

order to reduce noise, while still allowing detailed mapping of the wind. The wind directions are estimated from the peaks in the FFT-derived image spectra in areas of 12.5 km x 12.5 km over the SAR scene as described in [2] and [10]. This wind direction field is interpolated to the whole image and used as input to the CMOD-IFR2 algorithm [11] to obtain the wind speed at 10 m above sea level.

In addition to SAR wind maps, results are shown from Karlsruhe Atmospheric Mesoscale Model (KAMM2), a non-hydrostatic atmospheric model forced with NCEP/NCAR data. Output from the model runs has been compared to SAR wind maps and the Wind Atlas analysis and application Programme (WAsP) has been used to correct the wind speed observations from the mast at 33 m above sea level (a.s.l.) down to 10 m a.s.l. to be easier comparable to the wind estimates from SAR data. WAsP is a siting tool for the wind farm industry based on a mathematical flow model. WAsP and KAMM2 have been run on 7 of the 49 days with SAR coverage at the Norwegian west coast [12], [13].

3 - RESULTS

The *in situ* data at the Norwegian west coast are obtained by the Norwegian Meteorological Institute (met.no) at the island Hellisøy. The weather station on Hellisøy is situated on top of a 10 m high mast mounted beside a house, and surrounded by several other masts and buildings. Such obstacles, the topography and the very rough terrain affect the wind climate. The anemometer is situated 33 m above sea level and records the average wind speed over ten minutes every hour. The speed-up effect caused by the terrain varies for the different wind directions and may be considerable under certain conditions [14].

Previously a comparison between offshore SAR wind speed and the mast observations was made [2]. In this paper, WAsP was used to calculate the wind speed down from the mast level (33 m a.s.l.) to the level of the SAR wind speed estimations at 10 m a.s.l. by correcting for topography and roughness. The WAsP results are valid until about 10 km from the mast at Hellisøy. SAR wind speeds are compared with the model results of KAMM2 and WAsP within an area of 5.5 km x 5.5 km offshore from Hellisøy/Fedje (Fig. 3 ii)).

The comparison for the 7 cases of model runs and SAR coverage is shown in Fig. 1. For only one situation the SAR retrieved wind speed (12.3 m/s) does not agree with either WAsP or KAMM2 wind speeds (9.0 m/s and 5.8 m/s respectively). For the rest of the cases SAR wind speed agrees within ± 2 m/s with at least one of the models. The wind directions used in the CMOD-IFR2 are from SAR in 5 of the 7 cases from Fig. 1, these are

presented against KAMM2 directions and *in situ*/WAsP directions in Fig. 2.

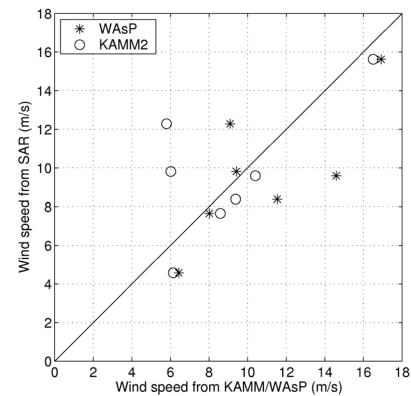


Fig. 1: Wind speed from SAR using CMOD-IFR2 plotted against model wind speed from WAsP * and KAMM2 ° over the area outside the Norwegian west coast shown in Figure 2 (Previously published in Wind Engineering, vol. 27, issue 5 (2003) by Multi-Science Publishers, UK) [3].

The two cases where SAR significantly underestimates the wind speed compared to WAsP are related to unstationary weather conditions, since the wind speed is changing at the time of the SAR acquisition. As southern Norway lies in the zone of the westerlies, unstationary wind conditions are the rule rather than the exception due to the frequently incoming atmospheric lows.

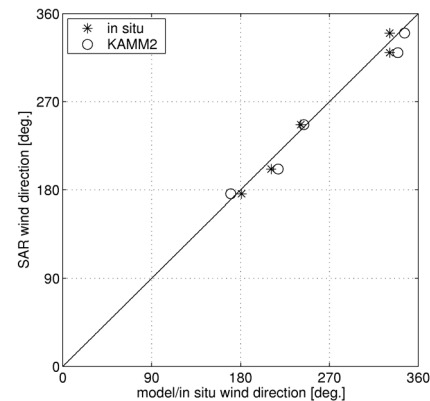


Fig. 2: Wind directions from SAR for 5 cases compared to KAMM2 and in situ directions outside Hellisøy.

Fig. 3 shows a comparison between WAsP output and the SAR retrieved wind from February 14 1996 at 21:35 UTC during on-shore wind conditions. The SAR wind speed steadily increases towards the coast from 6 m/s offshore to 10 m/s near to the coast. Clear linear features in the SAR image (Fig. 3 i)) indicate a southwesterly wind direction. At 2100 UTC, the anemometer at 33 m asl on Hellisøy recorded southwesterly wind 18.1 m/s 199°. From the time

series of anemometer data shown in Fig. 3, note that wind speed was steadily increasing during the day and decreasing after satellite passage which may be the reason for this variable SAR wind field. A profile through the three data sets (SAR, WAsP and KAMM2) in the along wind direction from the coast across Fedje

to the sea is indicated in all three plots and shown in Fig. 3 (iv). Based on the 18.1 m/s recording at Hellisøy, WAsP predicts an offshore wind speed of 14.5 m/s. KAMM2 and CMOD-IFR2 agree on a somewhat lower wind of 10 m/s offshore. Leeward of Fedje all three capture a drop of 1-2 m/s in wind speed.

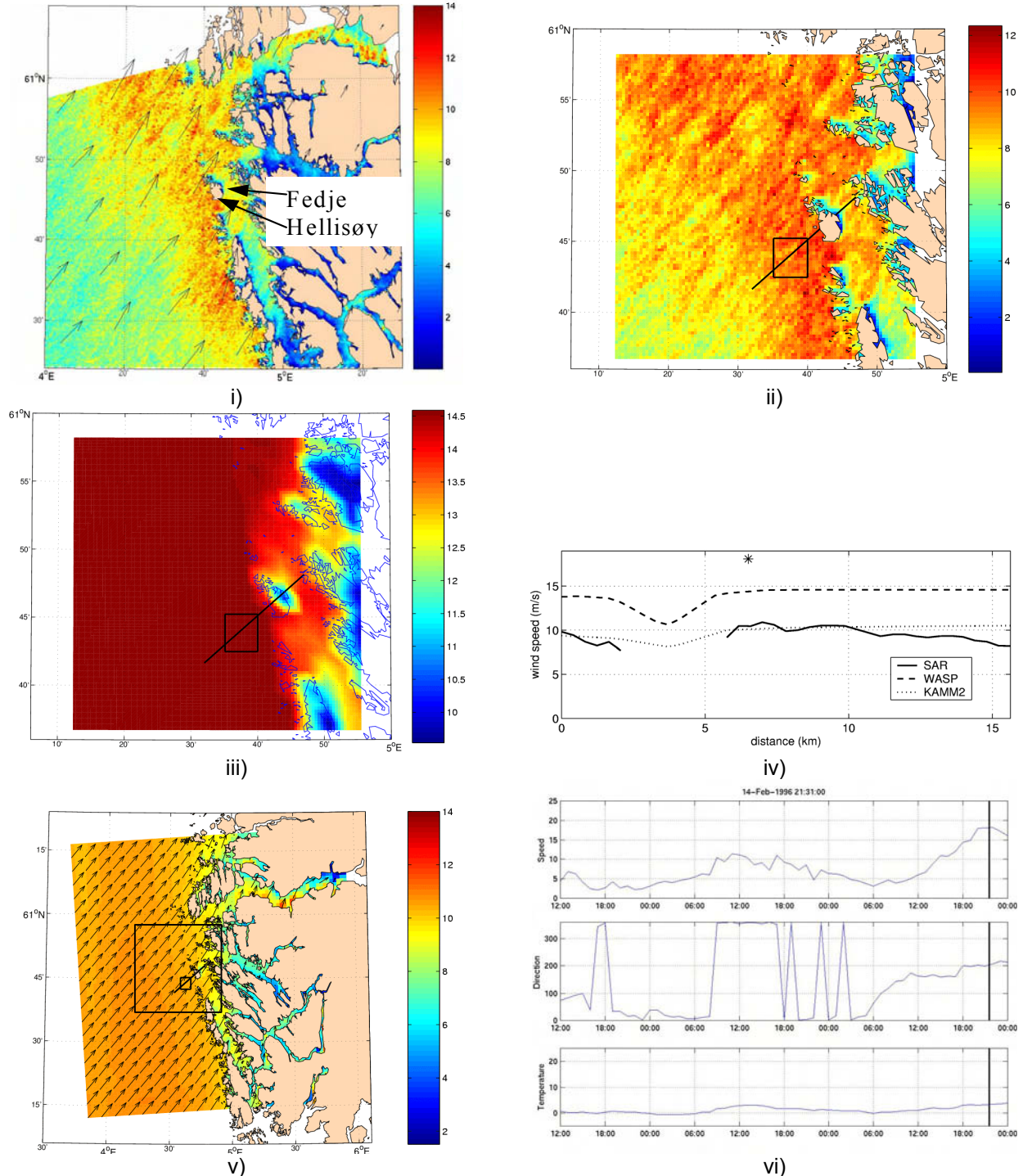


Fig. 3: (i) ERS SAR wind field over the Norwegian west coast, February 14 1996. (ii) SAR retrieved wind speeds (interpolated to the WAsP grid) with the box for comparison in Figure 1 and profile line indicated. (iii) Model output from WAsP at 10 m a.s.l. with box for comparison in Figure 1 and profile line indicated (v) Model output from

KAMM2 with WAsP area, box for comparison in Figure 1 and profile line indicated. (iv) Profiles along the line oriented from land across the island Fedje and to the open sea in the SAR wind speed map, WAsP and KAMM2 output from the same hour. * is the observation at Hellisøy. (vi) Plots of wind speed, wind direction and temperature at the Hellisøy weather station. The vertical bar indicates the time of the SAR passage. All wind speeds are in m/s, please note that the WAsP results are only valid out to a distance of about 10 km from the Hellisøy weather station. (Previously published in Wind Engineering, vol. 27, issue 5 (2003) by Multi-Science Publishers, UK) [3].

At the Norwegian west coast 49 ERS SAR images were analysed. This is not quite enough for a definitive statistical analysis. In particular, the scenes obtained contain a fairly large number of low wind situations. However, in order to collect the information all the available wind maps have been geocoded to the same grid and averaged. The resulting mean wind speed map is seen in Fig. 4 i) and the SAR wind speed data in an area offshore from Hellisøy shown in histogram in Fig. 4 iii). The corresponding histogram for the same days but using data from Hellisøy weather mast is also shown. The number of scenes used for the mean wind map is shown in Fig. 4 ii) and the Weibull distribution and histogram based on two years of data from the weather station is shown as a reference (Fig. 4 iv)). The probability density function of the wind speed U for the Weibull distribution is given by

$$f(U) = \frac{k}{A} \left(\frac{U}{A} \right)^{k-1} \exp \left\{ - \left(\frac{U}{A} \right)^k \right\} \quad (1)$$

where A is called the scale parameter and k is the shape parameter³. The shape parameter k is expected to lie at a value around 2.

The mean wind speed map (Fig. 4 i)) suffers from too few scenes and the line pattern of the coverage map clearly shows. But within the area covered by the largest number of scenes (40) the map starts to give some information of the relative wind distribution (even if the mean wind speed is too low). The SAR wind speed histogram clearly shows that more SAR data are needed to be able to estimate the wind statistics with SAR.

During the WEMSAR project, a first version of a tool has been developed for retrieving wind fields from ERS SAR images and integrating these data into the WAsP programme [15]. The tool consists of the two parts; wind retrieval and statistical analysis. The first part of the tool is the wind retrieval from ERS SAR images. This module reads calibrated image files and the associated header files, retrieving wind speed and wind direction, which are then read by the statistical

module. In this module all the satellite wind fields are treated together to provide input to WAsP.

The WEMSAR statistical module has been developed as add-on software to the WAsP programme [4]. The basic functionality is to area-average the relevant footprint area of the SAR wind map into a wind speed and wind direction and use it for calculating observed climatology from the series of wind maps. The relatively low sample number might compromise the accuracy of the statistical model for the wind speed distribution. Therefore the RWT program first fit a Weibull distribution to the entire dataset independent of wind direction and applies the shape parameter of this for all directions. The Weibull scale parameters representative for different wind direction sectors is determined by individual average wind speeds. The observed wind climate file, needed as input to the WAsP program, is generated from the estimated Weibull distributions. A selection of Weibull fitting methods were implemented, and tested by wind speed measurements from buoys. The error of using few measurements was evaluated by comparison of fits to random selections and a fit to the long-term data set. A theory for the error was derived and found in agreement with this analysis [6]. The accuracy depends on sample size and Weibull shape parameter, and it is comparable for most of the evaluated methods. The Weibull shape parameters quoted herein are estimated by the maximum likelihood method [16].

4 - CONCLUSIONS

The aim of the study is to utilise the advantages of remote sensing in offshore wind resource assessment. Wind fields from the Norwegian coastal zone calculated from the KAMM2 mesoscale model and the WAsP wind farm siting program was compared to SAR wind maps. The comparison of spatial features shows a fair agreement for the example shown, and all three methods (SAR, WAsP and KAMM2) capture a decrease in wind speed of 1-2 m/s in the lee of Fedje and Hellisøy islands.

³ This nomenclature is widely used in the wind energy community, however in other parts of the literature the parameters $a=A^{-k}$ and $b=k$ can be found.

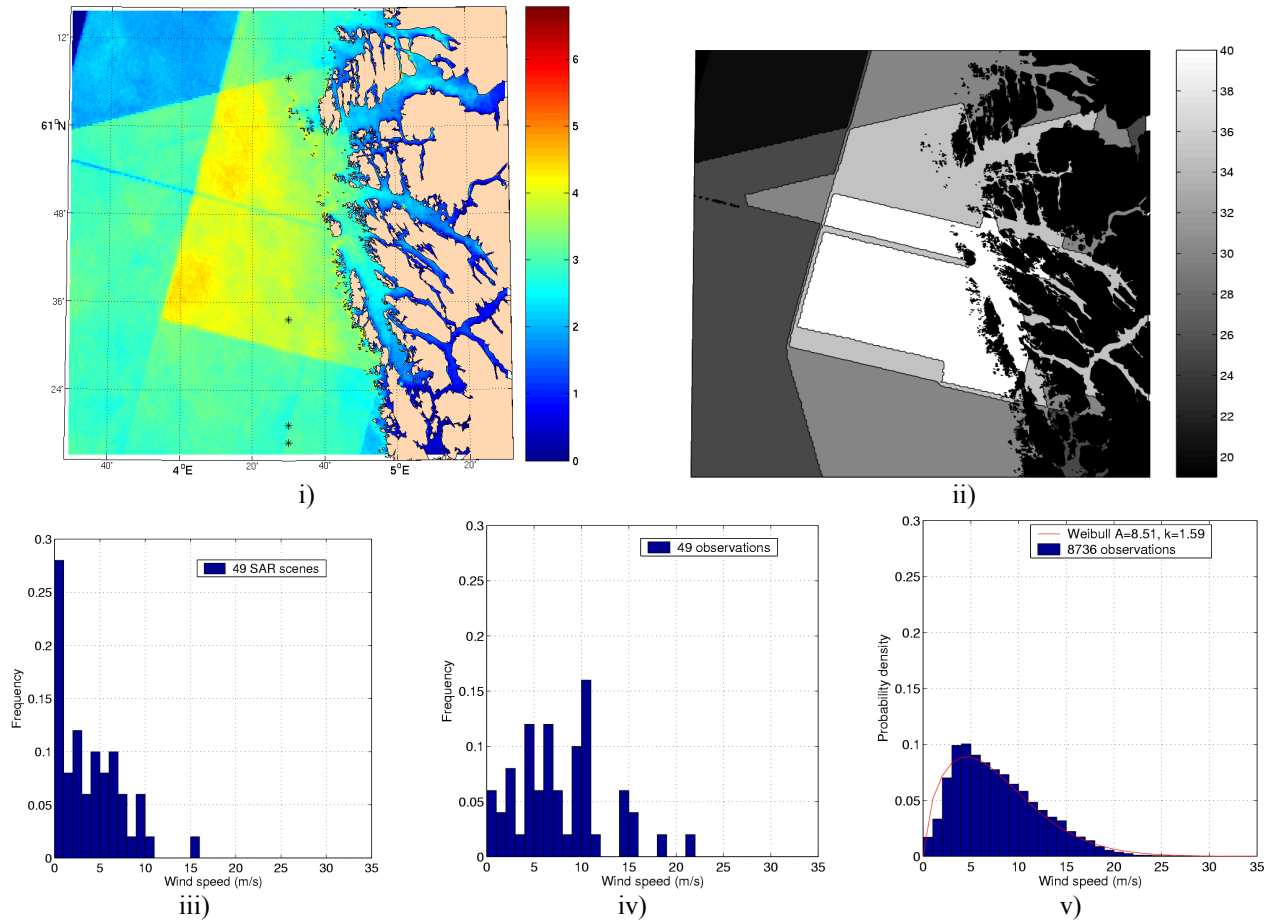


Fig. 4: i) Mean wind speed from a total of 49 ERS SAR scenes at the Norwegian west coast and ii) the number of scenes used (between 19 and 40 over the area). The wind speed distribution from iii) SAR data, iv) Hellisøy data on the days with SAR passage and v) two years of hourly measurements from Hellisøy weather station. The distributions are normalised with the length of the time series.

Comparing SAR surface wind speeds with wind speed from WAsP runs based on the Hellisøy observations normalised to 10 m a.s.l. was in fairly good agreement i.e. to within ± 2 m/s for four cases. The reason for the disagreement (SAR underestimating in two cases and overestimating in one case) for the last three cases seems to be due to un-stationary weather situations or oceanic influence on the images. On the other hand, in two of these cases the SAR wind speeds estimates agree well with the KAMM2 wind speeds. This may indicate that WAsP runs may not deal with special conditions over the ocean (with respect to atmospheric boundary layer, sea surface roughness) as well as an atmospheric model. The fact that the SAR winds agree with one model or the other in six of the seven cases suggests that the surface measurements carried out using the SAR may add useful information. At present, the strength of SAR wind maps lies in the added spatial information, as the relative accuracy within each image is good. Comparing SAR wind speed with measurements from an offshore mast about 13 km from

the coast (not shown) gives a good agreement, which also is encouraging for the future work [17].

A prototype software, the so-called WEMSAR Tool, has been developed for utilising SAR retrieved wind measurements in WAsP. The major advantage of the software is that it can handle a large number of SAR scenes to give the first wind estimations in offshore areas where no suitable in-situ wind observations are available. Although SAR has not yet made a difference in the decision process of wind farm projects, the potential will be greatly improved when including Radarsat and Envisat data and combining with high temporal resolution scatterometer data.

Acknowledgements

The study was carried out during the EC project 'Wind energy mapping using Synthetic Aperture Radar (WEMSAR)', project number ERK6-CT99-00017, and with funding from the Norwegian Research Council

(project no. 151424/432). Figure 1 and 3 was reproduced with permission from the editor of *Wind Engineering*. Thanks are due to L. C. Christensen, NEG Micon A/S, for valuable comments. ERS SAR data are provided by the European Space Agency, through AO3-281, AO3-153 and EO-1356, Helligsø lighthouse data was provided by met.no.

References

1. Mortensen, N. G., D. N. Heathfield, L. Landberg, O. Rathmann, I. Troen, and E. L. Petersen, Wind atlas analysis and application program: WAsP 7.0 Help facility, User's guide, Risø National Laboratory, Frederiksborgvej 399, Roskilde, Denmark, ISBN 87-5502667-2, 2000.
2. Furevik, B. R., and H. A. Espedal, Wind energy mapping using Synthetic Aperture Radar, *Canadian Journal of Remote Sensing*, Vol 28, no. 2, pp. 196-204, 2002.
3. Furevik, B. R., H. A. Espedal, T. Hamre, C. B. Hasager, O. M. Johannessen, B. H. Jørgensen and O. Rathmann, "Satellite-based wind maps as guidance for siting offshore wind farms", *Wind Engineering*, Vol. 27, no. 5, 2003.
4. Hasager, C. B., Rathmann, O., Nielsen, M., Barthelmie, R., Pryor, S. C., Dellwik, E., and B.R. Furevik, Offshore wind resource assessment based on satellite wind field maps. *Proceedings from 2003 EWEC - European Wind Energy Conference*. 16-19 June 2003, Madrid, Spain, CD-ROM, 11 p, 2003.
5. Barthelmie, R.J. and S. C. Pryor, Can satellite sampling of offshore wind speeds realistically represent wind speed distributions? *Journal of Applied Meteorology*, 42(1), p 83-94, 2003.
6. Pryor, S., M. Nielsen, R. Barthelmie and J. Mann, Can satellite sampling of offshore wind speeds realistically represent wind speed distributions? Part II Quantifying uncertainties associated with sampling strategy and distribution fitting methods. *J. Appl. Meteorol.* In Press, 2004.
7. Monaldo, F. and V. Kerbaol, The SAR measurement of ocean surface winds: An overview for the 2nd workshop on coastal and marine applications of SAR, *this publication*, 2004.
8. Fichaux, N. and T. Ranchin, "Evaluating offshore wind energy resources by space-borne radar sensors: A multi-source approach" In Proceedings of the European Wind energy conference: Wind energy for the new millennium, Copenhagen, Denmark 2-6 July 2001, pp. 864-867, 2001.
9. Laur, H., P. Bally, P. Meadows, P. J. Sanchez, B. Schaettler and E. Lopinto, Derivation of the backscattering coefficient σ_0 in ESA ERS SAR PRI products, *Doc. ES-TN-RS-PM-HL09*, issue 2, rev. 2, Eur. Space Res. Inst., Frascati, Italy, June 28, 1996.
10. Furevik, B., O. M. Johannessen and A. D. Sandvik, SAR-retrieved wind in polar regions – comparison with in situ data and atmospheric model output, *IEEE Trans., of Geosc. Rem. Sens.*, Vol. 40, no. 8, 2002.
11. Quilfen, Y., B. Chapron, T. Elfouhaily, K. Katsaros, J. Tournadre, Observation of tropical cyclones by high-resolution scatterometry. *Journal of Geophysical Research*, Vol. 103, No. C4, pp. 7767-7786, 1998.
12. Jørgensen, B. H., B. Furevik, C. B. Hasager, P. Astrup, O. Rathmann, R. Barthelmie, S. Pryor, Developments in mesoscale modelling and SAR imaging of Off-shore wind maps, Global Wind Power, EWEA Conference, Paris, France, 2002.
13. Hasager, C.B., P. Astrup, R. J. Barthelmie, E. Dellwik, B. H. Jørgensen, N. G. Mortensen, M. Nielsen, S. Pryor, O. Rathmann, Validation of satellite SAR offshore wind speed maps to in-situ data, microscale and mesoscale model results. *Technical report*. Risø-R-1298(EN), p. 271, 2002.
14. Jackson, P. S., and J. C. R. Hunt, Turbulent wind flow over a low hill, *Quarterly Journal of the Royal Meteorological Society*, Vol. 101, pp. 929-955, 1975.
15. WEMSAR Consortium, WEMSAR Final Report, *NERSC Technical Report*, no. 237, Nansen Environmental and Remote Sensing Center, Edv. Griegsvei 3a, N-5059 Bergen, Norway, March 2003.
16. Ghosh, A., A FORTRAN program for fitting Weibull distribution and generating samples, *Computers and Geosciences*, vol. 25, 729-738, 1999.
17. Hasager, C. B., E. Dellwik, M. Nielsen, B. R. Furevik, Validation of ERS-2 SAR offshore wind-speed maps in the North Sea, Accepted in *International Journal of Remote Sensing*, January 2004.

THE CORRECTION OF SURFACE LAYER WIND SPEEDS FOR ATMOSPHERIC STRATIFICATION AND HEIGHT

Ralph C. Foster⁽¹⁾, Todd D. Sikora⁽²⁾ and George S. Young⁽³⁾

⁽¹⁾*Applied Physics Laboratory, University of Washington, 1013 NE 40th St., Seattle, WA, 98105-6698, USA,
ralph@apl.washington.edu*

⁽²⁾*Department of Oceanography, U.S. Naval Academy, Nimitz Library, 589 McNair Road, Annapolis, MD 21402, USA,
sikora@usna.edu*

⁽³⁾*Department of Meteorology, Pennsylvania State University, 503 Walker Bldg, University Park, PA 16802, USA,
young@ems.psu.edu*

ABSTRACT

The comparison of SAR-derived wind speeds from scatterometer-based transfer functions and *in situ* or model wind speeds requires that both data sets represent the presence of equivalent atmospheric stratification and measurement height. We discuss the atmospheric surface layer dynamics underlying corrections to equivalent atmospheric stratification and measurement height. In addition, we review available methods for carrying out the corrections focusing on bulk flux algorithms available in the literature.

1. INTRODUCTION

Recently, there has been much effort put into extracting kilometer and sub-kilometer scale wind speed estimates from synthetic aperture radar (SAR) imagery using scatterometer-based transfer functions (see [1], this issue). These transfer functions are designed to retrieve the 10 m neutral equivalent wind speed, U_{10}^N , from active microwave measurements of the small-scale wave state (i.e. the Bragg wave state) that is in equilibrium with the sea surface stress (τ) [2]. U_{10}^N is the virtual wind speed at 10 m that, in neutral stratification, would produce the same τ as the actual wind. It is useful because it can be directly converted into surface stress without requiring independent information about atmospheric stratification.

Comparing SAR-derived wind speeds from scatterometer-based transfer functions and *in situ* or model wind speeds requires that all data sets be corrected to equivalent atmospheric stratification and measurement height. Under standard conditions, the stratification correction at 10 m is small, on the order of a few percent. Under light winds, the correction can be tens of percent [2], but it must be noted that scatterometer and SAR wind retrievals are suspect at low winds. The correction for typical measurement height adjustments is comparable. For the common application of moving a buoy wind at 5 m to 10 m, the correction is about 7% at neutral stratification.

Numerical weather forecast model surface winds are frequently compared to remotely sensed winds.

Regional mesoscale model winds are usually used when available because their spatial resolution is generally finer than large-scale or global models. Because SAR winds can be retrieved very near to the coastline, local mesoscale features such as gap winds can play a major role in establishing the local wind field. The relatively high resolution of mesoscale models allows them to resolve such orographically-induced features. However, since these models generally do not generate U_{10}^N as a standard output, stratification and height corrections must be applied. A very commonly used mesoscale model is the PSU/NCAR mesoscale model, version 5 (MM5).

Here, we discuss the atmospheric surface layer dynamics that necessitate the stratification and measurement height corrections, focusing on Monin-Obukhov (M-O) similarity theory. For a more complete review of these topics, the reader is encouraged to consult [3], [4], [5], [6], [7].

In addition, we review available methods for carrying out the corrections, focusing on the commonly available bulk flux algorithms since they are the standard tool for making height and stratification corrections. Bulk flux models are parameterizations of M-O similarity combined with parameterizations of the basic air-sea transfer processes.

In the following discussion, we adopt the notation that uppercase variables or overbars denote mean quantities and zero-mean perturbations from that mean are in lower case. To simplify the following discussion, we will assume a horizontal coordinate system (x) aligned with the mean wind (U), horizontally homogeneity, and barotropic conditions. The mean flow in the atmospheric surface layer has, to an excellent approximation, no directional shear in the vertical direction, z . The latter two assumptions will, at times be inappropriate. For example, these conditions may be violated near coastlines and near sea surface temperature or atmospheric frontal zones.

2. COMPONENTS OF STRESS ABOVE THE SEA

Stress is the transport of momentum per unit area and per unit time. The vertical transport of horizontal momentum to or from the sea surface is the dominant term. There are three components of this stress above the sea (molecular stress, pressure drag stress, and turbulent stress). Each mechanism contributes to the production of τ and the wave state. Thus, each mechanism is an element upon which scatterometer-based transfer functions depend.

2.1 Molecular Stress

The mean current-relative wind speed must equal zero at the air-sea interface because the air-water interface presents a no-slip boundary condition. This results in an atmospheric momentum transfer at the air-sea interface due to molecular diffusion, also known as the molecular stress (τ_m), where:

$$\tau_m = \rho \nu \frac{\partial U}{\partial z} \quad (1)$$

Here, ν is the kinematic molecular viscosity coefficient of air (approximately $1.5 \times 10^{-5} \text{ m}^2 \text{ s}^{-1}$) and ρ is air density. Momentum is transferred molecule-to-molecule from the air to the sea for a positive wind shear ($\partial U / \partial z$). Conversely, momentum is transferred molecule-to-molecule from the sea to the air for a negative wind shear. Thus, the momentum transfer is down the gradient of mean momentum and occurs within the molecular sub-layer at the air-sea interface. The larger the magnitude of wind shear and molecular viscosity within the molecular sub-layer, the larger the transport of momentum due to molecular diffusion, and, hence, the larger the molecular stress.

Note however that the thickness of the layer where molecular stress is significant is only millimeters thick. Pressure fluctuations can transfer momentum from the turbulent layer across this thin viscous layer very efficiently and are not significantly affected by the low viscosity of air. However, in stark contrast to this efficiency for momentum, transport of scalar quantities such as heat and water vapor between the ocean and atmosphere are strongly inhibited by this thin viscous layer since they are transferred by viscous diffusion.

2.2 Pressure Drag Stress

Pressure drag stress (τ_p) is the form of momentum transfer between the atmosphere and ocean that results from the dynamic pressure differential between the upwind and downwind faces of a wave. This form of momentum transfer exists unless the wave phase speed (c) matches the surface layer wind speed in the direction of wave propagation. This criterion is more often

expressed as a ratio of c to friction velocity (u_*), where $u_* = \sqrt{\tau / \rho}$. A value of approximately 16 yields zero pressure drag [8] and thus an equilibrium or mature sea. For growing seas, the pressure drag stress is a sink of momentum for the atmosphere, and decreases with height, becoming comparable to the turbulent component at a height of about 1/6 the dominant wave's length and fading to negligibility at several times that height (i.e. the top of the wave boundary layer) [8]. For decaying seas, a similar height dependence holds, but the pressure drag stress is a source of momentum for the atmosphere instead of a sink.

2.3 Turbulent Stress

The turbulent stress (τ_t) arises from the quadratic nonlinear advection contribution to the mean momentum budget when the full flow is decomposed into the mean and the zero-mean perturbations from that mean. The turbulent stress describing the vertical transport of horizontal momentum is proportional to the covariance of the horizontal and vertical components of the wind vector, $-\overline{\rho u w}$. The net transfer of momentum is downward ($\tau > 0$) so the instantaneous fluctuations that contribute positively to τ are of opposite sign. Turbulent eddies that contribute positively to the stress transport have downward-moving horizontal gusts ($u > 0, w < 0$) and upward-moving horizontal lulls ($u < 0, w > 0$). Contributions from same-sign fluctuations are also present but the overall average generally results in a positive turbulent stress and a down-gradient transport of momentum.

To a good approximation the turbulent stress in the near surface layer can be calculated from the mean wind shear analogously to the molecular stress:

$$\tau_t = \rho K_m \frac{\partial U}{\partial z} \quad (2)$$

Here, K_m is the eddy viscosity coefficient, rather than the molecular viscosity coefficient found in Eq. 1. For neutral stratification, a typical value for K_m at $z = 10 \text{ m}$ is $1 \text{ m}^2 \text{ s}^{-1}$. This is about 5 orders of magnitude larger than the kinematic molecular viscosity of air. Thus, while turbulent stresses may be neglected in the viscous sublayer, viscous stresses may be neglected in the turbulent layer. This parameterization implies that the momentum transfer is down gradient. The larger the magnitude of wind shear and eddy viscosity, the larger the transport of momentum due to turbulence, and, hence, the larger the turbulent stress.

3. SUM OF STRESS ABOVE THE SEA

The atmospheric surface layer is commonly defined as that portion of the lower atmosphere where turbulent fluxes are nearly constant with height. The practical definition only requires that the fluxes vary by less than 10 % from their surface values [7]. The M-O theory we discuss below is based on the assumption that the fluxes are constant with height in the surface layer. Thus, we assume that the turbulent transfer of momentum within the surface layer is constant. An increasing fraction of this momentum is transferred by pressure drag as one moves down into the wave boundary layer. Momentum which is not transferred by pressure drag before reaching the top of the molecular sub-layer is transferred to the ocean surface by molecular diffusion. The ratio of these three momentum transfer mechanisms thus changes with height although their sum remains nearly constant from the top of the atmospheric surface layer to the air-sea interface.

Because we assume that the sum is nearly constant with height, one can assess the net stress on the sea surface by examining the turbulent stress at some point in the surface layer, above the wave induced pressure perturbations. In essence, we are stating that $\tau = \tau_i$ in the surface layer. For a given τ_i , different values of surface layer wind shear can be expected for different stratification conditions. These effects are quantified in surface layer (M-O) similarity theory.

4. MONIN-OBUKHOV SIMILARITY THEORY

M-O similarity theory is a cornerstone of our understanding of atmospheric surface layer dynamics. We note, however, that the theory becomes questionable in highly statically stable or unstable conditions (e.g., see [5], Chapter 3). The presence of certain sea states, such as rapidly growing or decaying seas, also affects the applicability of M-O similarity theory [9]. In any of these cases, SAR wind retrievals may themselves be less certain. Thus, care must be exercised to ensure that it is reasonable to either employ M-O similarity theory to correct for stratification and height, or to employ scatterometer-based SAR wind retrievals.

The basic premise of M-O similarity is that the surface layer mean flow may be characterized by length, velocity, temperature and humidity scales based on the surface fluxes and the height above the surface. The scales are z , $u_* = \sqrt{uw}$, $\theta_* = -\overline{w\theta}/u_*$ and $q_* = -\overline{wq}/u_*$ respectively in which $H_0 = \overline{w\theta}$ and $Q_0 = \overline{wq}$ are the kinematic surface fluxes of sensible heat and water vapor, and u , w , θ and q are the perturbation horizontal and vertical velocities, potential temperature and specific humidity respectively. A second length scale,

called the Obukhov length, may be formed from the fluxes, $L = -u_*^3 / \left[k \frac{g}{\Theta_v} (\overline{w\theta_v}) \right]$ in which the kinematic buoyancy flux is $\overline{w\theta_v} = H_0 + 0.61TQ_0$, g/Θ_v is the buoyancy parameter and $k = 0.4$ is called von Karmen's constant. In most conditions the buoyancy flux is primarily due to the sensible heat flux with a smaller contribution from evaporation that is usually positive over the ocean. In the tropics the sensible heat flux contribution in some cases may be slightly negative but the evaporation contribution is sufficient to maintain an upward buoyancy flux. Over cold waters, such as portions of the California current, the buoyancy flux may be negative.

Under conditions where M-O similarity holds we find that profiles of mean quantities are "universal" functions of the only surviving nondimensional parameter, z/L , which may be interpreted as a surface layer stratification parameter. In particular, we have the following:

$$\frac{kz}{u_*} \frac{\partial U}{\partial z} = \phi_m \left(\frac{z}{L} \right) \quad (3)$$

$$\frac{kz}{\theta_*} \frac{\partial \Theta}{\partial z} = \phi_\theta \left(\frac{z}{L} \right) \quad (4)$$

$$\frac{kz}{q_*} \frac{\partial q}{\partial z} = \phi_q \left(\frac{z}{L} \right) \quad (5)$$

A primary goal of surface layer studies is to determine the empirical forms for the ϕ functions (e.g., [10]).

When the surface buoyancy flux is zero, the surface layer is neutrally stratified and the ϕ functions equal one. This yields, for example, the classic surface layer logarithmic wind profile:

$$\frac{U(z) - U_0}{u_*} = \frac{1}{k} \ln \frac{z}{z_0} \quad (6)$$

in which the "0" subscript denotes a surface value and z_0 is the roughness length, the height where the velocity difference goes to zero. For non-zero buoyancy fluxes the universal profiles include corrections to the logarithmic profiles:

$$\frac{U(z) - U_0}{u_*} = \frac{1}{k} \left(\ln \frac{z}{z_0} - \psi_m \left(\frac{z}{L} \right) \right) \quad (7)$$

$$\frac{\Theta(z) - \Theta_0}{\theta_*} = \frac{1}{k} \left(\ln \frac{z}{z_0} - \psi_\theta \left(\frac{z}{L} \right) \right) \quad (8)$$

$$\frac{q(z) - q_0}{q_*} = \frac{1}{k} \left(\ln \frac{z}{z_q} - \psi_q \left(\frac{z}{L} \right) \right) \quad (9)$$

Here, z_T and z_q are the roughness lengths for temperature and specific humidity. The stratification corrections (ψ) are integrals of the ϕ functions:

$$\psi_i \left(\frac{z}{L} \right) = \int_{z_0/L}^{z/L} \frac{1 - \phi_i(\xi)}{\xi} d\xi \quad (10)$$

in which the lower integration limit is nearly always set to zero. Fig. 1 shows typical M-O stratification

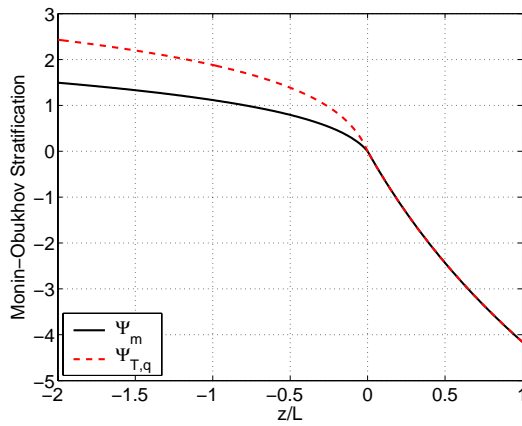


Fig. 1. Parameterization of M-O stratification functions Ψ_m and $\Psi_{T,q}$ used in most bulk flux models.

functions [11] used in most surface layer codes.

4.1 Net Effect of Stratification

In neutral stratification turbulence is produced by the interaction between the turbulent eddies and the mean shear. Momentum is transferred down the gradient of momentum by shear-driven eddies. The resulting wind shear profile is defined by Eq. 6.

In unstable stratification, turbulence is also produced through conversion of potential energy of the mean stratification. Although the shear production is reduced in this case, the total turbulence production over the depth of the surface layer is increased which enhances the turbulent vertical transports of momentum, heat and water vapor compared to neutral stratification. The resulting wind shear profile is defined by Eq. 7 which implies that ψ_m should be positive in unstable stratification. For a particular U_{10} , the net result is to impose a higher stress on the sea surface in unstable stratification compared to what the same wind would produce in neutral stratification.

Turbulence is suppressed by stable stratification resulting in a less efficient downward transfer of horizontal momentum. Thus, for a given U_{10} , the sea surface stress is reduced compared to what this wind could induce in neutral stratification. From Eq. 7, we see that ψ_m must be negative in stable stratification.

4.2 Bulk Flux Method

A common problem is to estimate τ , H_0 and Q_0 given measurements of the mean wind, temperature and humidity at the surface and at some height or heights in the surface layer. If we knew the three roughness lengths for momentum, heat and water vapor and the M-O ψ functions, we could iterate Eqs. 7-9 to solve for these surface fluxes. This is why parameterizing the roughness lengths and M-O functions for use in bulk flux models is one of the main goals of air-sea interaction experiments. The flux models can also be used to correct mean measurements for height and or stratification because given the surface fluxes (hence L) along with $\psi_{m,T,q}$, and $z_{0,T,q}$, we can calculate the mean wind, temperature and humidity profiles in the surface layer.

The correction is simple. The mean measurements (along with the corresponding measurement heights) are fed into the bulk flux model, which iterates to find estimates of the surface fluxes and roughness lengths. These values can then be used to calculate the desired wind speed (neutral or actual) at the desired z . Usually there is no information on surface currents so the surface wind speed is set to zero. This can lead to significant errors when currents are strong such as in the Equatorial Pacific and western boundary currents such as the Gulf Stream. In most cases the error is trivial.

The most commonly used bulk flux model is called the COARE algorithm [12]. It was developed during the Tropical Ocean - Global Atmosphere Coupled-Ocean Atmosphere Response Experiment (TOGA-COARE) although it has been periodically updated as new information and experimental data become available. The most recent version (and older ones) of the COARE algorithm can be downloaded from <http://ftp.etl.noaa.gov/et7/users/cfairall/bulkalg/>. It currently includes many enhancements such as SST skin temperature corrections and fluxes due to rain. However, we will discuss just the elementary air-sea interaction parameterizations since these are all that are needed to make the height and stratification corrections.

The bulk flux formulas (at their standard 10 m reference levels) are:

$$\tau = \rho u_*^2 = \rho C_D U_{10}^2 \quad (11)$$

$$H_0 = -\rho c_p u_* T_* = -\rho c_p C_T U_{10} (\Theta_{10} - \Theta_0) \quad (12)$$

$$Q_0 = -\rho L_v u_* q_* = -\rho L_v C_E U_{10} (q_{10} - q_0) \quad (13)$$

in which the “10” subscript refers to the 10 m level, $c_p = 1004 \text{ J kg}^{-1} \text{ K}^{-1}$ is the specific heat of dry air and $L_v = 2.5 \times 10^6 \text{ J kg}^{-1}$ is the latent heat of vaporization for water. The bulk transfer coefficients are:

$$C_D = \frac{k^2}{\left(\ln \frac{z_{10}}{z_0} - \psi_M \left(\frac{z_{10}}{L} \right) \right)^2} \quad (14)$$

$$C_T = \frac{k^2}{\left(\ln \frac{z_{10}}{z_0} - \psi_M \left(\frac{z_{10}}{L} \right) \right) \left(\ln \frac{z_{10}}{z_0} - \ln \frac{z_0}{z_T} - \psi_T \left(\frac{z_{10}}{L} \right) \right)} \quad (15)$$

$$C_E = \frac{k^2}{\left(\ln \frac{z_{10}}{z_0} - \psi_M \left(\frac{z_{10}}{L} \right) \right) \left(\ln \frac{z_{10}}{z_0} - \ln \frac{z_0}{z_q} - \psi_q \left(\frac{z_{10}}{L} \right) \right)} \quad (16)$$

in which we have used the identity $\log \left(\frac{z}{z_{T,q}} \right) = \log \left(\frac{z}{z_0} \right) + \log \left(\frac{z_0}{z_{T,q}} \right)$ to define the viscous sub-layer (VSL) effect on the scalar fluxes as $\log \frac{z_0}{z_{T,q}}$.

The neutral drag coefficient is:

$$C_D^N = \left(\frac{u_*}{U_{10}^N} \right)^2 = k^2 \left(\ln \frac{z_{10}}{z_0} \right)^{-2} \quad (17)$$

which shows the relationship between U_{10}^N , surface stress and z_0 .

Most sea surface roughness parameterizations are of the form $z_0 = z_0(u_*)$. Fig. 2 shows a set of common ocean surface roughness length parameterizations plotted as functions of U_{10}^N using (17). Above about 3 m s^{-1} ($u_* \sim 0.1 \text{ m s}^{-1}$) all parameterizations increase with increasing U_{10}^N . At low winds z_0 increases again in most parameterizations. Note that there is a fairly significant spread between the parameterizations which imply a quite different stress estimate for a given wind speed.

As mentioned above, molecular diffusion across the thin viscous sublayer at the sea surface can be a more restrictive barrier to air-sea exchange of heat and water

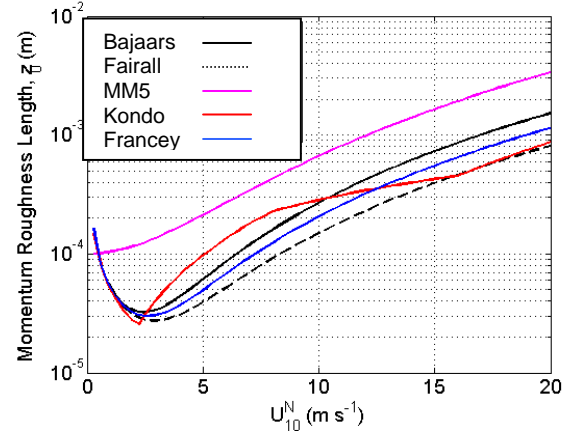


Fig. 2. Typical sea-surface momentum roughness length parameterizations, including that of [13], [14], [15], and [16].

vapor than for momentum. This effect is parameterized by having $z_{T,q} < z_0$ for higher winds. Most parameterizations are of the form $z_{T,q} = f(R_r)$ in which $R_r = \frac{u_* z_0}{\nu}$ is the roughness Reynolds number.

Various VSL parameterizations are plotted in Fig. 3 as

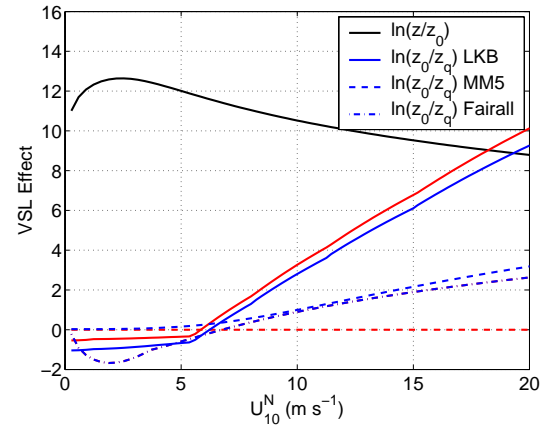


Fig. 3. Typical sea-surface scalar roughness lengths used in M-O temperature and humidity profiles. Red curves are for temperature and blue for humidity. Solid: LKB; dash-dot: [12]; dashed: MM5. The black curve shows $\ln(10/z_0)$ for the [13] momentum roughness length for comparison.

$\log \frac{z_0}{z_{T,q}}$ vs. U_{10}^N . On this plot z_T is red and z_q is blue with different line types for the different parameterizations. For reference the black curve shows $\log \frac{10}{z_0}$ from the [13] parameterization and $z_{T,q}$ were

calculated from this roughness length. Analogous behavior can be expected for the other roughness length parameterizations. The most commonly used VSL parameterization is from [17] and is usually called the LKB parameterization. LKB was used in the COARE flux algorithms up to version 2.59. Later versions are closer to the [12] model. Comparing the plot with Eqs. 15 and 16 shows that near 10 m s^{-1} the VSL effect represents about a 30% reduction in surface fluxes in LKB, which is comparable to the M-O stratification effect, but about 10% in [12]. C_E is currently thought to be nearly constant with U_{10}^N which is reflected in the [12] parameterization. Interestingly, the standard MM5 VSL parameterization for heat is zero while for humidity it is similar to that proposed by [12]. Note also that the MM5 z_0 parameterization (Fig. 2) is much higher than the others. This implies that both the buoyancy flux and surface stress are likely too strong in MM5. It turns out that the net effect on L is very small hence MM5 estimates of U_{10}^N are very close to those from COARE, even though the individual MM5 fluxes will likely have large biases.

A common need is to convert buoy winds to U_{10}^N in order to compare *in situ* winds with SAR-derived winds. As an example we convert a month (December, 2002) of winds from NOAA NDBC buoy 44008 to U_{10}^N . This buoy has a Nomad hull with wind sensors at 5 m and temperature and dew point sensors at 4 m above the surface. We use the [13] z_0 roughness and the [12] $z_{T,q}$ VSL parameterizations. The results are shown in Fig. 4 plotted in terms of $U_{10}^N/U(5m)$ vs. z_{10}/L . The

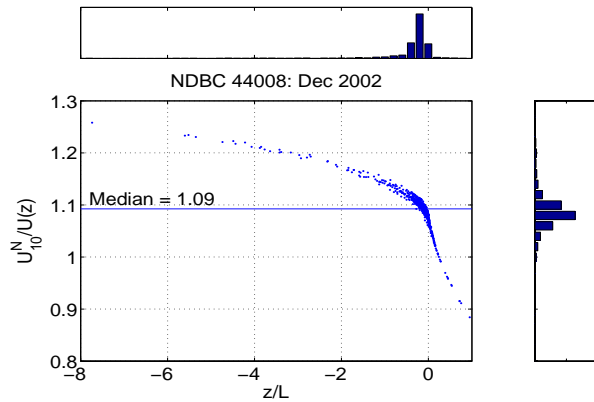


Fig. 4. Calculation of U_{10}^N correction for December, 2002 of hourly wind data from NDBC buoy 44008. The scatter plot shows the ratio of U_{10}^N to the buoy wind as a function of $10/L$. The histogram above the scatter plot shows the distribution of $10/L$ and the histogram to the right shows the distribution of U_{10}^N/U_5 .

distribution of z_{10}/L shows that the most common stratification condition was near-neutral but slightly unstable, which is typical. The median total correction (height plus stratification) is about 9% but many points have much larger or smaller corrections so a constant correction factor would be inappropriate. We also note that calculations using the LKB parameterization produce a distribution very close to the one plotted in Fig. 4 but individual corrections may be slightly different.

To see the relationship between the wind correction and the buoy variables we show a typical 7-day segment of the buoy record in Fig. 5. The primary indicator of the

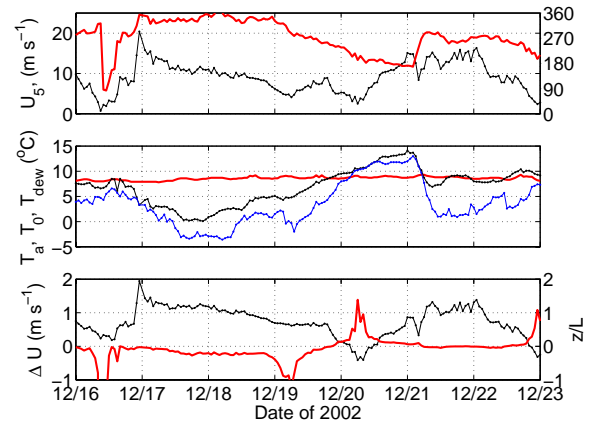


Fig. 5. Hourly meteorological data from buoy 44008 16-23 December, 2002. A: Wind speed (black) and direction (red, right axis) at 5 m. B: black: Air temperature, blue: Dew point both at 4 m, and red: Sea surface temperature. C: black: $U_{10}^N - U_5$; red (right axis): $10/L$.

surface layer static stability is the difference between the air and water temperatures and the primary indicator of the near-surface shear is the 5 m wind speed. The product of the temperature difference and the wind speed is proportional to the sensible heat flux, which is the main contributor to the buoyancy flux in this case. The contribution of the evaporation to the buoyancy flux is higher during periods when the dew point is depressed from temperature (drier conditions) and tends towards zero when the air is closer to saturation. The surface layer stratification is proportional to the ratio of the temperature difference to the wind speed squared. This explains the large excursions in z/L when the wind speed drops and why the changes in z/L are different depending on the magnitude and/or sign of the temperature difference.

The mean flow is northerly for the first three days of the record implying cold advection and generally more unstable stratification. Note that the wind direction is quite variable when the surface wind speed is low. For both of these reasons SAR wind retrievals would be suspect in this period. From the 19th to the 21st the wind gradually shifts to a southerly direction, implying warm advection, and the local stratification becomes stable. An atmospheric front appears to pass over the buoy early on the 21st and the flow shifts sharply westerly bringing in colder, drier air and nearly neutral stratification. Note that the wind speed correction is positive nearly all the time, going negative only for brief periods in light winds and stable stratification. Both the SAR winds and buoy estimated U_{10}^N could be suspect in these cases.

To help partition between the height and stratification corrections, we repeated the calculation assuming that the buoy measurements were all acquired at 10 m. The result is shown in Fig. 6. Now the median correction is

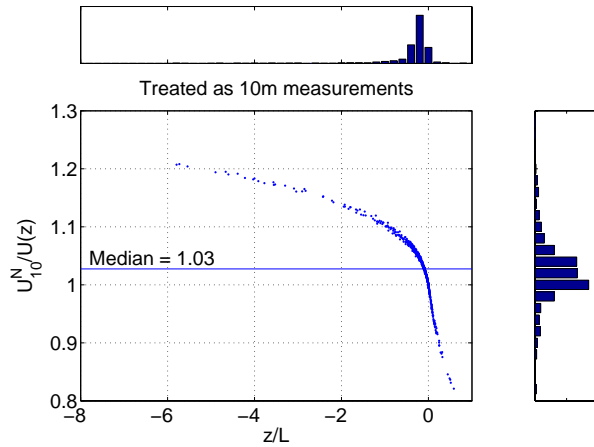


Fig 6. As in Fig. 4, except the buoy measurements heights were assumed to all be acquired at 10 m.

about 3%, again with a fairly wide spread. This shows that for the standard NDBC buoys the height correction is generally larger than the stratification correction. Since the shear decreases with height, we note that the total correction from 15 m down to 10 m is overall smaller than from 5 m to 10 m.

A note of caution on using bulk flux models as black boxes. As stated earlier, M-O similarity breaks down in either very stable or very unstable stratification. Thus calculations in such conditions should be flagged and checked for reasonableness.

Many bulk flux models include a “convective velocity” fix in order to estimate fluxes in very unstable stratification (e.g. [12]). In very unstable stratification, typified by light winds and large negative air-sea

temperature differences, the boundary layer turbulence is characterized by large convective eddies that directly connect the surface with the top of the boundary layer. If the mean wind is zero, the standard bulk flux models (Eqs. 11-13) would predict zero surface fluxes. However, the near-surface inflow feeding the convective eddies would be expected to induce fluxes. The convective velocity fix is intended to parameterize this effect.

In the presence of large convective eddies and near-zero mean wind, u_* and z are no longer characteristic surface layer velocity and length scales. A more relevant length scale is the boundary layer depth, z_i . In unstable stratification the buoyancy flux and z_i may be combined to define a convective velocity as

$$w_* = \left(\frac{g}{\Theta_v} \overline{w\theta_v} z_i \right)^{1/3}.$$

Many bulk flux models in unstable stratification conditions adjust the mean surface wind according to the formula $U_{eff} = \sqrt{U^2 + cw_*^2}$ where c is a constant near one. This can affect estimates of U_{10}^N since it removes the direct relationship between U_{10}^N and u_* thus the convective velocity correction should be omitted in U_{10}^N calculations. Setting $z_i = 0$ in the input to the bulk flux code will usually work. Note that a commonly used stratification parameter in unstable stratification is $\frac{z_i}{L} = -\frac{kw_*^3}{u_*^3}$.

5. OTHER POTENTIAL METHODS FOR THE STRATIFICATION CORRECTION

Recent research has examined the possibility of stratification-correcting SAR-derived neutral wind speeds directly from information contained within the SAR-derived wind speed data. These two SAR-only methods apply M-O and mixed layer similarity theory and have, at present, been developed only for unstable stratification [18]. Both methods are still being tested and should thus be considered experimental. A recent test of the variance method described below highlights the dependence of output accuracy on image quality. Reference [19] demonstrates that, in cases with image problems, estimates of z/L produced by application of the variance algorithm to RADARSAT-1 ScanSAR imagery from the Alaska SAR Facility do not compare well with those produced by bulk flux models from buoy data.

5.1 SAR Variance Method

The first SAR-only method, described in [18], uses the variance of the SAR-derived wind speed imagery (σ_s^2) for the stratification correction. The assumption is that this variance is a direct result of the atmospheric turbulence discussed in Sections 3 and 4. The variance of wind speed is then converted to the variance of the stream-wise component of wind speed (σ_u^2), combined with SAR-derived estimate of atmospheric boundary layer depth (z_i) [20], and a SAR-derived estimate of u_* (via the wind imagery), to yield an Obukhov length via:

$$L = -z_i / (((\sigma_u / u_*)^2 - 4) / 0.6)^{3/2} \quad (18)$$

L is in then used to calculate a stratification-corrected drag coefficient (c_d) via Eq. 14 which is in turn combined with u_* to produce a stratification-corrected wind speed image:

$$U = \sqrt{\frac{u_*^2}{C_D}} \quad (19)$$

The family of equations is solved by iteration, with refined values of L resulting in refined values of the stratification-corrected wind speed. Two simplifications from the [18] method may be used. In the surface layer we find that $\sigma_u / S = \sigma_s / S + 0.5 \sigma_s^2 / S^2$, where S is the surface wind speed, is a good parameterization and that for nearly all the images we examined $\sigma_u / S \approx \sigma_s / S$. A common and simpler parameterization than Eq. 18 for the velocity variance shows that the Obukhov length may be parameterized as $L = z_i \left(24 - 2(\sigma_u / u_*)^3 \right)^{-1}$.

5.2 SAR Spectral Method

The second SAR-only method, also described in [18], uses the small-scale (inertial subrange) part of the SAR-derived wind speed spectrum rather than the variance (i.e. the integral under the entire spectrum). The spectral power on these sub-kilometer scales can be combined with z_i to yield the convective velocity (w_*) via the mixed-layer similarity form of the Kolmogoroff inertial subrange spectrum:

$$w_*^3 = \left[\frac{\left(\frac{2\pi z_i}{\lambda} \right) k S(k)}{\frac{4}{3} \alpha_1 \Psi^{2/3}} \right]^{1/2} \quad (20)$$

where $S(k)$ is the spectral power density at wave number k , α_1 is the Kolmogoroff inertial subrange spectral constant for wind speed (~ 0.55), and Ψ is the nondimensional turbulence kinetic energy dissipation

rate (~ 0.6). The Obukhov length can be found from the convective velocity scale by:

$$L = \frac{z_i u_*^3}{k w_*^3} \quad (21)$$

The Obukhov length is then used to stratification-correct the SAR-derived wind speed as described in Section 4.

6. SUMMARY

As described in [1] (this issue), estimates of wind speed from SAR imagery of the sea surface hold much promise. To advance this research, we provide background and guidance on the stratification and measurement height correction of wind speeds. Such corrections may be necessary because the SAR-derived wind speeds are 10 m neutral equivalent winds. The comparison of SAR-derived wind speeds and *in situ* or model wind speeds requires that all data sets represent equivalent atmospheric stratification and measurement height. Thus, in non-neutral stratification and *in situ* measurement heights other than 10 m, there is a need to correct the data such that each represents equivalent atmospheric stratification and measurement height.

Similarity theory as implemented in standard bulk flux models provides a fundamental means of estimating stratification and height corrections. Two newer methods that exploit the high spatial resolution of SAR have been proposed as possible means of stratification correcting SAR winds without the need for external sources of stratification data. They are the SAR variance and spectral methods described in [18]. However, neither of these methods has been subjected to a careful verification and the variance method has proved sensitive to data quality issues.

Acknowledgements: This work was supported in part by grant ATM-0240869 from the National Science Foundation. RCF acknowledges support from NASA through grants NAG5-10114 and NAG5-13128.

7. REFERENCES

1. Monaldo, F. M., et al., The SAR Measurement of Ocean Surface Winds: A White Paper for the 2nd Workshop on Coastal and Marine Applications of SAR, 2004.
2. Liu, W. T., and Tang, W., Equivalent Neutral Wind, JPL Publication 96-17, 1996.
3. Geernaert, G. L., Bulk Parameterizations for the Wind Stress and Heat Fluxes, in *Surface Waves and Fluxes*, edited by G. L. Geernaert and W. J. Plant, Kluwer Academic Publishers, 1990.

4. Kraus, E. B. and Businger, J. A., *Atmosphere-Ocean Interaction*, Oxford University Press, 1994.
5. Garrett, J. R., *The Atmospheric Boundary Layer*, Cambridge University Press, 1992.
6. Panofsky, H. A. and Dutton, J. A., *Atmospheric Turbulence: Models and Methods for Engineering Applications*, Wiley-Interscience, 1984.
7. Stull, R. B., *An Introduction to Boundary Layer Meteorology*, Kluwer Academic Publishers, 1988.
8. McWilliams, J. C. and Sullivan P. P., Turbulent Fluxes and Coherent Structures in Marine Boundary Layers: Investigation by Large-Eddy Simulation, in *Air-Sea Exchange: Physics, Chemistry and Dynamics*, edited by G. L. Geernaert, Kluwer Academic Publishers, 1999.
9. Donelan, M. A., et al., The Air-Sea Momentum Flux in Conditions of Wind Sea and Swell, *J. Phys. Oceanog.*, Vol. 27, 2087-2099, 1997.
10. Businger, J. A., et al., Flux Profile Relationships in the Atmospheric Surface Layer. *J. Atmos. Sci.*, Vol. 28, 181-189, 1971.
11. Dyer, A. J., Review of Flux-Profile Relationships, *Boundary-Layer Meteorol.*, Vol. 7, 363-372, 1974.
12. Fairall, C. W., et al., Bulk Parameterization of Air-Sea Fluxes: Updates and Verification for the COARE Algorithm, *J. Climate*, Vol. 16, 571-591, 2003.
13. Beljaars, A. C. M., The Parameterization of Surface Fluxes in Large-Scale Models Under Free Convection, *Quart. J. Roy. Meteor. Soc.*, Vol. 121, 255-270, 1995.
14. Fairall, C. W., et al., Bulk Parameterization of Air-Sea Fluxes for Tropical Ocean-Global Atmosphere Coupled-Ocean Atmosphere Response Experiment, *J. Geophys. Res.*, Vol. 101, 3747-3764, 1996.
15. Kondo, J., Air-Sea Transfer Coefficients in Diabatic Conditions, *Boundary-Layer Meteorol.*, Vol. 9, 91-112, 1975.
16. Francey, R. J. and Garrett, J. R., Interpretation of Flux-Profile Observations at ITCE (1976), *J. Appl. Meteor.*, Vol. 20, 603-618, 1981.
17. Liu, W. T., et al., Bulk Parameterization of Air-Sea Exchange of Heat and Water Vapor Including the Molecular Constraints at the Interface, *J. Atmos. Sci.*, Vol. 36, 1722-1735, 1979.
18. Young, G. S., et al., Inferring Marine Atmospheric Boundary Layer Properties from Spectral Characteristics of Satellite-Borne SAR Imagery, *Mon. Wea. Rev.*, Vol. 128, 1506-1520, 2000.
19. Foster, R. C., et al., Critical Examination of a Method for Estimating the Buoyancy Flux from SAR Imagery, *12th Conference on Interactions of the Sea and Atmosphere*, American Meteorological Society, 2003.
20. Sikora, T. D., et al., Estimating Convective Atmospheric Boundary Layer Depth from Microwave Radar Imagery of the Sea Surface, *J. Appl. Meteorol.*, Vol. 36, 833-845, 1997.

**This page intentionally
left blank (pagination)**

ESTIMATION OF SMALL-SCALE WIND FIELDS FROM SYNTHETIC APERTURE RADAR DATA

David R. Lyzenga

*General Dynamics Advanced Information Systems
Ann Arbor, MI 48113-4008 USA
Email: David.Lyzenga@gd-ais.com*

ABSTRACT

This paper explores the possibility of estimating small-scale vector wind fields from SAR data by applying certain dynamical constraints to the wind field. The method is illustrated for the case of a diverging surface flow field that is intended to represent a precipitation-induced downdraft. A simulated radar cross section map generated from this flow field is used to reconstruct the wind field by choosing the wind direction at each point so as to minimize the vorticity. The method works well for this case because the input wind field was chosen to be irrotational. For cases in which the vorticity is not zero, it may be possible to generalize the method by applying other dynamical constraints.

1. INTRODUCTION

The surface wind vector over the ocean can be estimated from radar cross section measurements taken from two or more look directions. If the radar cross section is measured from a single look direction, as is typical for synthetic aperture radar images, there is an inherent ambiguity in the estimated winds because of the fact that the radar cross section is determined by both the wind speed and direction. Previous investigators have solved this problem by using independent estimates of the wind direction from models [1] or from spatial patterns in the imagery [2-4]. However, these methods are not applicable for small-scale wind fields such as those due to convection cells or downdrafts.

Some examples of such features are shown in Fig. 1. This figure shows a Radarsat-1 image collected over the Gulf of Alaska on May 10, 1998, with a wind front extending diagonally across the image and a number of circular features to the left of the front. The front was moving eastward at 30 km/hr, as inferred from a sequence of SSM/I images collected on May 9-10, 1998. Although the wind front itself was clearly visible on the SSM/I imagery, the smaller features behind it are not resolved by this sensor. The passage of the front is also evident in the wind measurements made by NOAA Buoy 46001 which is located about 250 km west of the image. The circular features appear to be precipitation-induced downdraft cells similar to those reported in [5].

This interpretation is supported by the NOAA buoy measurements, which show variations in the wind speed and direction behind the front as would be expected due to the passage of downdraft cells over the buoy. The mean wind speed indicated by the buoy in this region was 7-8 m/s from 230 °T. The winds within a downdraft cell as envisioned by Atlas [5] are shown in Fig. 2.

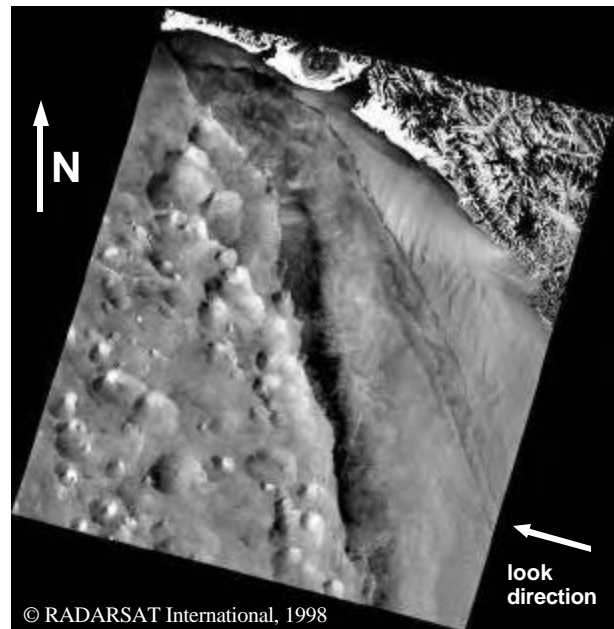


Fig. 1. Gulf of Alaska Radarsat image, extending from approximately 55° to 60° N and 136° to 144° W.

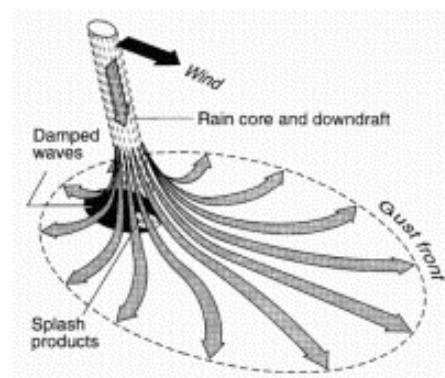


Fig. 2. Diagram depicting winds in a precipitation-induced downdraft (from [5]).

2. RCS MODEL FUNCTION

Any attempt to extract information about the winds from SAR images must begin with a model for the relationship between the winds and the radar cross section. We will neglect for the present the question of whether fetch and/or duration effects are important in these cases, and assume that there is a unique relationship between the wind speed and direction and the radar cross section as viewed from a particular perspective. Such a relationship has been well developed in the form of the CMOD4 model function for VV polarization Gband measurements [6, 7]. To extend this relationship to HH polarization (as in Radarsat data) we have developed a model for the wave spectrum that reproduces the CMOD4 values when used with a conventional two-scale scattering model [8]. Some cuts through this spectrum are shown in Fig. 3, and a comparison of the two-scale and CMOD4 radar cross sections is shown in Fig. 4. This spectrum was then used with the two-scale model to predict the radar cross section for HH polarization.

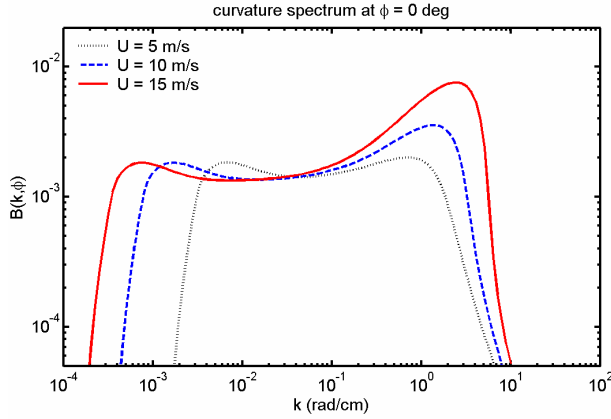


Fig. 3. Wave curvature spectrum inferred from CMOD4 model function (from [8]).

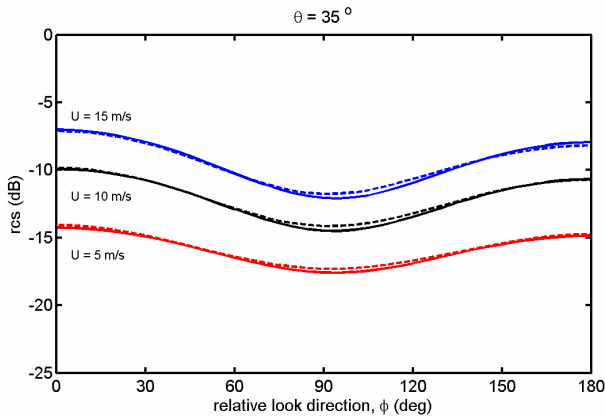


Fig. 4. Comparison of CMOD4 radar cross sections (solid curves) with model predictions (dashed curves) for three wind speeds at $\theta=35^\circ$.

The resulting model function for C-band, HH polarization, at 35 degrees incidence was then inverted to obtain an expression for the wind speed in terms of the radar cross section and look direction. The expression for the wind speed is

$$\log U = b_0 + b_1 \cos(\mathbf{f}_\ell - \mathbf{f}) + b_2 \cos[2(\mathbf{f}_\ell - \mathbf{f})] \quad (1)$$

where \mathbf{f}_ℓ is the look direction, \mathbf{f} is the wind direction, and b_0 , b_1 , and b_2 are functions of the radar cross section as shown in Fig. 5. This model allows the wind speed to be calculated for a specified radar cross section, if the wind direction is known. The problem of determining the wind direction is discussed in the following section.

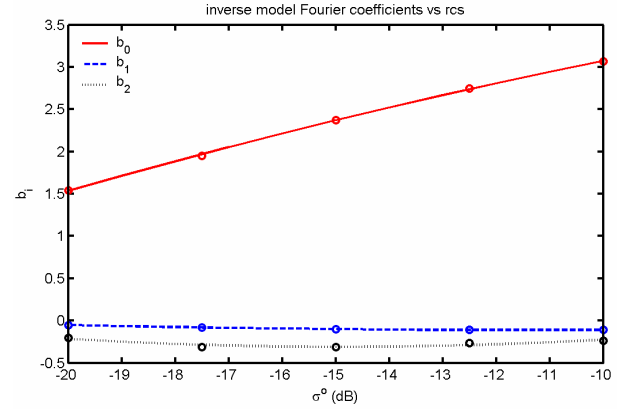


Fig. 5. Fourier coefficients for the wind speed as a function of the radar cross section at HH polarization and 35° incidence.

3. VORTICITY MINIMIZATION

Given a radar cross section map (or SAR image), there are infinitely many combinations of the wind speed and direction at each sample location that are consistent with the data. For a given choice of the wind direction $\mathbf{f}(x, y)$, the wind speed $U(x, y)$ can be calculated from Eq. 1 (other model functions could also be used, with appropriate modifications to Eq. 5-7 and 13-14 below). The resulting wind field has a divergence \mathbf{d} and vorticity \mathbf{z} given by

$$\mathbf{d} = \frac{\partial u}{\partial x} + \frac{\partial v}{\partial y} \quad \text{and} \quad \mathbf{z} = \frac{\partial v}{\partial x} - \frac{\partial u}{\partial y} \quad (2)$$

where $u = U \cos \mathbf{f}$ and $v = U \sin \mathbf{f}$. The problem we consider here is how to choose $\mathbf{f}(x, y)$ so as to minimize the vorticity, under the assumption that the true wind field is irrotational. A similar procedure could be used to minimize the divergence or other properties of the wind field. To do this, we assume a rectangular grid with M grid points spaced by Δx in the x -direction and N grid points spaced by Δy in the y -direction. Using a

centered difference to approximate the derivatives, the mean-squared vorticity is given by

$$V = \frac{1}{MN} \sum_{i=2}^{M-1} \sum_{j=2}^{N-1} V^2(i, j) \quad (3)$$

where

$$V(i, j) = \frac{v(i+1, j) - v(i-1, j)}{2\Delta x} - \frac{u(i, j+1) - u(i, j-1)}{2\Delta y}. \quad (4)$$

Changing the wind direction at grid point (m, n) by the amount $\Delta \mathbf{f}(m, n)$ produces a change in the magnitude of the wind speed $U(m, n)$ of

$$\Delta U = [b_1 \sin(\mathbf{f}_\ell - \mathbf{f}) + 2b_2 \sin 2(\mathbf{f}_\ell - \mathbf{f})] U \Delta \mathbf{f} \quad (5)$$

and a change in the components of the wind speed

$$\begin{aligned} \Delta u &= \Delta U \cos \mathbf{f} - U \sin \mathbf{f} \Delta \mathbf{f} \\ &= [b_1 u \sin(\mathbf{f}_\ell - \mathbf{f}) + 2b_2 u \sin 2(\mathbf{f}_\ell - \mathbf{f}) - v] \Delta \mathbf{f} \end{aligned} \quad (6)$$

and

$$\begin{aligned} \Delta v &= \Delta U \sin \mathbf{f} + U \cos \mathbf{f} \Delta \mathbf{f} \\ &= [b_1 v \sin(\mathbf{f}_\ell - \mathbf{f}) + 2b_2 v \sin 2(\mathbf{f}_\ell - \mathbf{f}) + u] \Delta \mathbf{f}. \end{aligned} \quad (7)$$

This produces a change in the mean-squared vorticity of

$$\begin{aligned} \Delta V &= [V(m-1, n) - V(m+1, n)] \frac{\Delta v(m, n)}{MN \Delta x} \\ &\quad - [V(m, n-1) - V(m, n+1)] \frac{\Delta u(m, n)}{MN \Delta y} \end{aligned} \quad (8)$$

where $V(i, j) = 0$ if $i = 1$ or $i = M$ or $j = 1$ or $j = N$. Combining these equations, the gradient of V with respect to \mathbf{f} is

$$\nabla V(m, n) = \frac{\Delta V}{\Delta \mathbf{f}(m, n)} \quad (9)$$

$$\begin{aligned} &= \frac{V(m-1, n) - V(m+1, n)}{MN \Delta x} [2b_2 v(m, n) \sin 2(\mathbf{f}_\ell - \mathbf{f}) + u(m, n)] \\ &\quad - \frac{V(m, n-1) - V(m, n+1)}{MN \Delta y} [2b_2 u(m, n) \sin 2(\mathbf{f}_\ell - \mathbf{f}) - v(m, n)] \end{aligned}$$

The change in the wind direction required to decrease V in the direction of steepest descent is therefore $\Delta \mathbf{f}(m, n) = -\mathbf{e} \nabla V(m, n)$ where \mathbf{e} is the same positive number for all (m, n) .

To estimate the step size parameter \mathbf{e} , we assume that the mean-squared vorticity can be approximated by the quadratic cost function

$$J(\mathbf{e}) = \frac{1}{MN} \sum_{i=1}^M \sum_{j=1}^N [V_0(i, j) + V_1(i, j) \mathbf{e}]^2 \quad (10)$$

where

$$V_0(i, j) = \frac{v(i+1, j) - v(i-1, j)}{2\Delta x} - \frac{u(i, j+1) - u(i, j-1)}{2\Delta y}, \quad (11)$$

$$V_1(i, j) = \frac{\tilde{v}(i+1, j) - \tilde{v}(i-1, j)}{2\Delta x} - \frac{\tilde{u}(i, j+1) - \tilde{u}(i, j-1)}{2\Delta y}, \quad (12)$$

$$\tilde{u}(i, j) = -[2b_2 u(i, j) \sin 2(\mathbf{f}_\ell - \mathbf{f}) - v(i, j)] \nabla V(i, j) \quad (13)$$

and

$$\tilde{v}(i, j) = -[2b_2 v(i, j) \sin 2(\mathbf{f}_\ell - \mathbf{f}) + u(i, j)] \nabla V(i, j). \quad (14)$$

The minimum value of this function occurs at $\mathbf{e}_o = -J'(0) / J''(0)$ where

$$J'(0) = \frac{2}{MN} \sum_{i=1}^M \sum_{j=1}^N V_0(i, j) V_1(i, j) \quad (15)$$

and

$$J''(0) = \frac{2}{MN} \sum_{i=1}^M \sum_{j=1}^N V_1^2(i, j). \quad (16)$$

The minimum can be located more exactly, if necessary, by evaluating the cost function at three location near $\mathbf{e} = \mathbf{e}_o$ and fitting a quadratic function to these values. After completing this line minimization, the cost function gradient is recomputed at the new minimum and the process is repeated until some convergence criterion is met.

The iteration can be made to converge faster by using the conjugate gradient method, according to which the change in the wind direction during the i^{th} iteration is $\Delta \mathbf{f}(m, n) = -\mathbf{e} h_i(m, n)$ where $h_i(m, n) = g_i(m, n)$ for $i=1$ and $h_i(m, n) = g_i(m, n) + \mathbf{g} \cdot h_{i-1}(m, n)$ for $i>1$. Here $g_i(m, n)$ is the actual cost function for the i^{th} iteration and $\mathbf{g} = g_i \cdot (g_i - g_{i-1}) / (g_{i-1} \cdot g_{i-1})$ where the dot product is defined as $g_i \cdot g_j = \sum_m \sum_n g_i(m, n) g_j(m, n)$.

4. SIMULATION TESTS

The procedure described in the previous section was tested by assuming an irrotational wind field of the form

$$u(x, y) = 2.6 u_m (x/a) \left[1 + (r/a)^2 \right]^{-3/2} + u_b \quad (17)$$

and

$$v(x, y) = 2.6 u_m (y/a) \left[1 + (r/a)^2 \right]^{-3/2} + v_b \quad (18)$$

where $r^2 = x^2 + y^2$ and u_m is the maximum radial velocity. The radar cross section was calculated using the forward model described in section 2, and is shown in Fig. 6 for the case $u_m = 4$ m/s, $a = 5$ km, $u_b = 8$ m/s and $v_b = 0$, with the radar look direction along the x -axis. The procedure described above was applied by setting $\mathbf{f}(x, y) = 0$ for the first estimate and iterating 40 times. The rms values of the vorticity and divergence for the estimated wind field are shown versus the number of iterations in Fig. 7. After 40 iterations the vorticity is reduced to virtually zero and the divergence approaches the actual value for the assumed wind field.

The estimated and actual wind velocity components along the x and y axes are shown in Figs. 8 and 9.

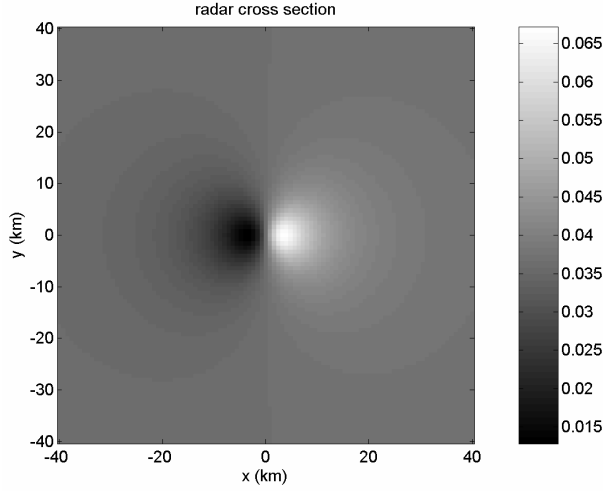


Fig. 6. Simulated radar cross section map.

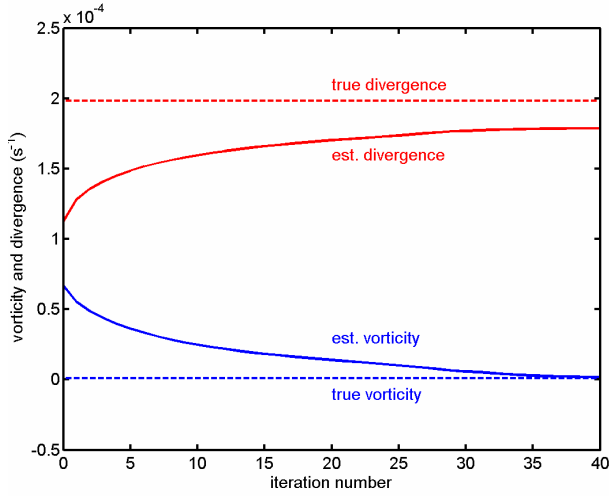


Fig. 7. Vorticity and divergence of wind field.

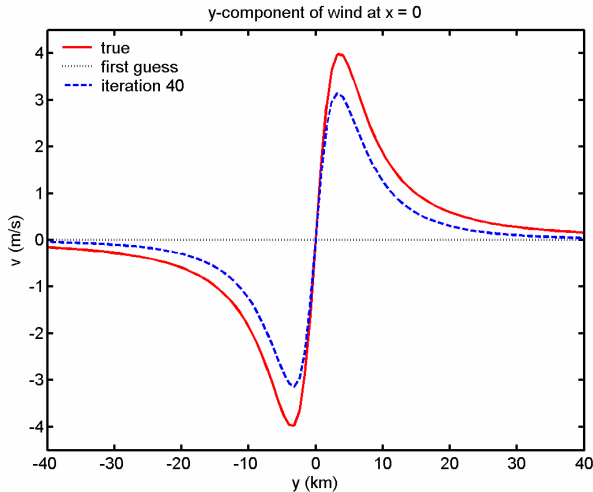


Fig. 8. Transverse component of wind along y -axis.

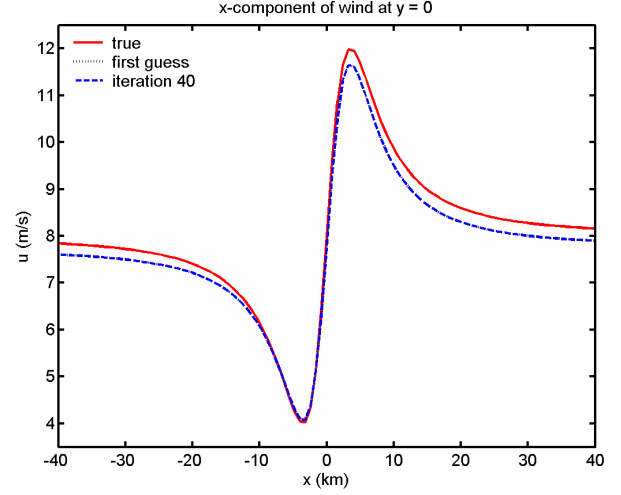


Fig. 9. Longitudinal component of wind along x -axis.

5. DISCUSSION

The method outlined in this paper shows promise for estimating small-scale vector wind fields using radar backscatter measurements taken from a single look direction. We have demonstrated this potential using a simulated radar cross section map generated from an assumed wind field, intended to mimic the winds in a precipitation-induced downdraft. The use of simulations separates the question of the efficacy of the inversion procedure from the question of the accuracy of the rcs model function (or the calibration of the data). It is also very difficult to validate such small scale wind field retrieval with real data because detailed, coincident two-dimensional wind observations very rarely exist. Nevertheless, the next logical step would be to test the procedure with real data to see if at least reasonable results are obtained. Of course, the actual wind field may not be irrotational in all cases, and so the inversion procedure may need to be modified to account for this possibility. In reality, the wind field may have a correlated vorticity and divergence (or convergence) due to Coriolis effects. Perhaps a linear combination of the vorticity and divergence should be minimized, or some other dynamical constraint could be applied to produce better estimates of the wind field.

References:

1. Monaldo, F.M., D.R. Thompson, R.C. Beal, W. Pichel, and P. Clemente-Colon, Comparison of SAR-derived wind speed with model predictions and ocean buoy measurements, *IEEE Trans. Geoscience and Remote Sensing* 39, 2587-2600, 2001.

2. Wackerman, C.C., C.L. Rufenach, R.A. Shuchman, J.A. Johannessen, and K.L. Davidson, Wind vector retrieval using ERS-1 synthetic aperture radar imagery, *IEEE Trans. Geoscience and Remote Sensing* 34, 1343-1352, 1996.
3. Fetterer, F., D. Gineris and C.C. Wackerman, Validating a scatterometer wind algorithm for ERS-1 SAR, *IEEE Trans. Geoscience and Remote Sensing* 36, 479-492, 1998.
4. Horstmann, J., W. Kock, S. Lehner, and R. Tonboe, Wind retrieval over the ocean using synthetic aperture radar with C-band HH polarization, *IEEE Trans. Geoscience and Remote Sensing* 38, 2122-2131, 2000.
5. Atlas, D., Origin of storm footprints on the sea seen by synthetic aperture radar, *Science* 266, 1364-1366, 1994.
6. Stoffelen, A. and D. Anderson, Scatterometer data interpretation: Estimation and validation of the transfer function CMOD4, *J. Geophys. Res.* 102, 5767-5780, 1997.
7. Stoffelen, A. and D. Anderson, Scatterometer data interpretation: measurement space and inversion, *J. Atmos. And Ocean. Tech.* 14, 1298-1313, 1997.
8. Lyzenga, D.R., Ocean wave spectrum and growth rate inferred from CMOD4 model function, submitted to *J. Geophys. Res.*, Dec 2003.

**This page intentionally
left blank (pagination)**

A PROJECTION METHOD FOR AUTOMATIC ESTIMATION OF WIND VECTORS WITH RADARSAT SAR IMAGERY

Christopher Wackerman⁽¹⁾, William G. Pichel⁽²⁾, Pablo Clement-Colón⁽²⁾

⁽¹⁾General Dynamics Advanced Information Systems, P.O. Box 134008 Ann Arbor Michigan 48113-4008 USA

chris.wackerman@gd-ais.com

⁽²⁾NOAA/NESDIS, WWBG E/RA3, Room 102 5200 Auth Rd. Camp Springs MD 20746-4304 USA

William.G.Pichel@noaa.gov

ABSTRACT

A new approach for automatically estimating wind vectors for SAR imagery is presented, which relies on a projection operation to generate wind direction estimates. A threshold can be applied to the projection results in order to eliminate estimation of wind directions in regions where the SAR image contains no visible features. The process also allows multiple possible directions to be generated at a given location using the image features, which are then resolved to a single direction based on uniformity across local regions of the image. The algorithm has been validated using 137 comparisons to in situ buoy observations, giving a direction RMSE of 39° (mean error of 10° , error standard deviation of 38°) and a wind speed RMSE of 2.2 m/s (mean error = -1.4 m/s, standard deviation of the error = 1.7 m/s). The largest errors come from automatically utilizing strong features in the image that are not aligned with the local wind, such as atmospheric lee waves are current fronts. If we manually eliminate these from the comparisons, then the direction RMSE is 31° (mean error of 20° , error standard deviation of 20°) and the wind speed RMSE is 2.1 m/s (mean error = -1.2 m/s, standard deviation of the error = 1.7 m/s).

1. INTRODUCTION

As part of the NOAA/NESDIS Alaska SAR Demonstration Project [1], a multi-year demonstration of the production and use of RADARSAT SAR HH polarization imagery to generate products in a pre-operational environment, a wind product is created that automatically generates wind vectors over the coastal ocean. Two methods are used. One uses wind directions from atmospheric models that are run over the same region and close in time to the SAR image collection. These directions are then combined with the radar cross section from the SAR imagery to generate wind speed using an empirically derived correction to a VV model to generate the HH relationship between radar cross section and wind speed [2]. The second method estimates the wind direction from the SAR imagery itself using large-scale features that are aligned with the local wind, such as wind rows, elongated convective cells, or surfactant

streaks, then combines this direction with the radar cross section of the imagery to generate wind speed. The currently implemented algorithm for estimating wind direction from the SAR imagery is based on a spectral approach that uses the Fourier transform of image subsets to automatically determine directions of maximal spectral energy, then assumes that these directions correspond to 90° from the wind direction [3,4]. This direction is then combined with the image radar cross section to generate wind speed using a semi-analytical two-scale model to derive the HH relationship between radar cross section and wind speed [5]. The directions estimated from the SAR imagery have an inherent 180° ambiguity, since from a static image one can at most estimate the line along which the wind is blowing, but not the direction along that line.

One significant problem with estimating wind directions from SAR imagery is that there may not always be features in the image that the algorithm can use to estimate directions. Convective cells, wind rows, and surfactant streaks depend on there being other processes going on (such as turbulence or very little mixing of the near-surface ocean layer) rather than simply the existence of a wind field. The spectral approach that is currently implemented has no means of determining when a wind direction is able to be estimated from a region of the SAR image, and thus will often generate erroneous directions over featureless regions of the ocean surface. Therefore a study was initiated to develop a new approach for estimating wind directions, referred to here as the projection method, that would be able to recognize when no robust estimate of direction was able to be extracted from the imagery.

2. PROJECTION METHOD FOR WIND DIRECTION ESTIMATION

The user determines a window size that will be moved through the image, and for each placement of the window one wind vector will be estimated. The window size should be driven by the scales of the features that are going to be used to estimate wind direction. For wind rows, these are typical from 3 to 10 km, so usually the window should not be much

smaller than 10 km. For the results in this paper, a 24 km window was used and the window was shifted every 16 km to generate a new wind vector estimate, thus there is some overlap of image samples used to create successive wind vectors. For a given window placement, the projection of the image samples within the window along a direction are generated for directions from -90° to $+90^\circ$. That is, for each direction a one-dimensional function is generated by stepping through the middle of the window in the specific direction, and at each image sample along that direction averaging all of the image samples that are in the orthogonal direction. For the results in this paper a projection was calculated every 1° , however in the results below (particularly Fig. 2) it can be seen that one could use a coarser angular sampling of the projections as long as the peaks of the feature contrasts (as defined below) can be resolved. This projection is then flattened to remove linear trends in the function.

Fig. 1 shows an example where the top image displays the SAR image values within a local window, and the bottom image displays the resulting projections for the full range of angles, with a different projection at each line. For each flattened projection, the contrast (standard deviation divided by the mean) is calculated and a plot of contrast versus direction (i.e. the direction of the projection that generated the contrast value) is created. Fig. 2 shows the resulting contrast plot generated from the projections shown in Fig. 1. All of the local peaks that have a contrast above some threshold are found, and 90° from these directions are considered as candidate wind directions for this window. For the results in this paper, the contrast threshold was set to 0.03 based on manual analysis of the obvious visual features in the imagery. Note however that although this metric is invariant to scale factors, it may depend on the processor used since the contrast of a feature will change whether the image was saved as 8 bits, 16 bits, in log values, etc. For the plot shown in Fig. 2, local peaks would have been found around -25° , $+25^\circ$, and $+50^\circ$. For each possible wind direction, the radar cross section of the image (calculated over the local window) is used to generate a wind speed via the model describe in Ref. 5.

Once the local window has been moved through the SAR image, there will in general be multiple possible wind directions (or no wind direction if no contrast value was above the threshold) for any image location. To determine which wind direction to use, we first choose the direction at each location that generated the maximum contrast. Then we iteratively move through the image as follows. At each location, we calculate the norm of the vector difference between each possible wind vector (direction and speed) at that location and all the other wind vectors that we are

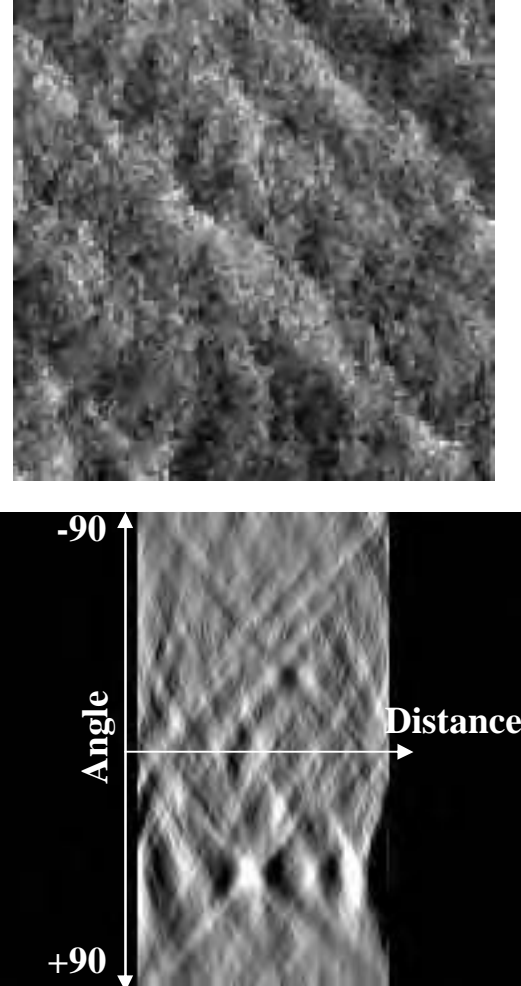


Fig. 1 Top image shows a subset of a SAR image. Bottom image shows the resulting projections from the image subset at various angles.

assuming are correct at the other locations, where we weight the vector sums by a Gaussian fall-off function whose width represents the spatial scales over which we assume that the wind vectors would be correlated. For all the results in this paper, we set the Gaussian width to four window lengths which represents 96 km. We then replace the wind vector at this location with the vector that generated the minimum vector norm (note that it might be the same vector as we started with). This is done at each location as we move through the image, using the new vectors at previous locations and the old vectors at future locations. This iterative process is repeated until the image converges to a solution; i.e. until the process does not change any wind vectors at any location.

Thresholding the contrast of the projection allows the algorithm to not generate a wind direction for image

Finding the Angle with Maximum Contrast

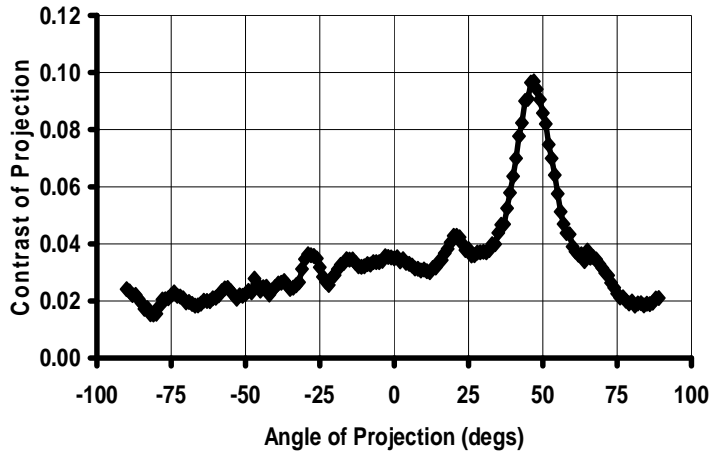


Fig. 2 A plot of contrast versus projection angle for the projections shown in Fig. 1. Local maxima at angles of approximately -25, +25 and +50 degrees are candidate wind directions.

regions where there are no features with sufficient modulation to be used for wind direction estimation.

Fig. 3 shows the results of varying the contrast threshold for a SAR image. The top image shows direction results (indicated as blue lines on the image) when no threshold is applied. The middle and bottom images show results for thresholds of 0.03 and 0.06 respectively. Note that as the threshold increases, we filter out all but the highest contrast features to use, and automatically eliminate the low contrast regions which were generating erroneous directions under the spectral approaches.

The final step in estimating wind vectors is to apply a median-like operation to the wind vectors to eliminate outliers. This is done by replacing the wind vector in the middle of a local box by the vector within the box that minimizes the norm of the difference between that vector and all of the others. Note that this approach has the advantage of only using wind vectors that have been estimated from the image (i.e. we do not average vectors such that a resulting vector was never seen anywhere in the image), and of preserving wind fronts in the final wind vector map. Also note that this final step is the spatial equivalent of the approach we use to determine a unique vector at each location. Instead of choosing the vector from a list of possible vectors at a given location, we chose the vector from the list of neighboring vectors. The size of the median filter window then plays the equivalent role of the width of the Gaussian fall-off weighting. For the results in this paper we used a median filter size of three local window lengths (72 km) and repeated the process over the entire image two times.

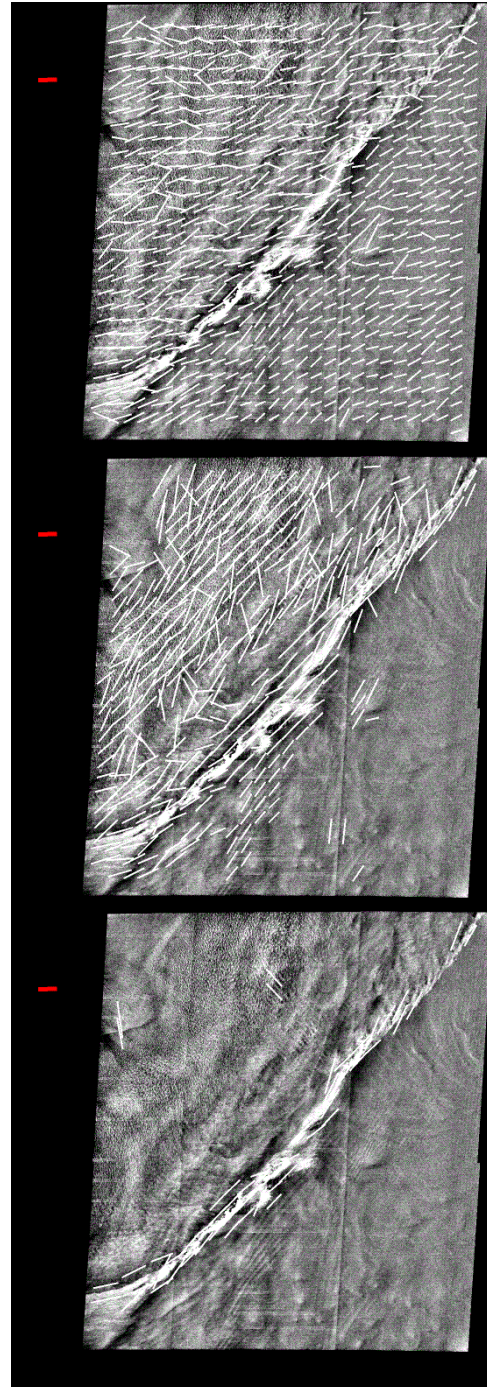


Fig.3: Examples of using the threshold on projection contrast to remove image regions with no strong features. Top image shows estimated wind directions (white lines) with no threshold, middle images has a threshold of 0.03 and the bottom image 0.06. Note that as the threshold increases, we eliminate all but the highest contrast features. The red line at the left shows the buoy derived wind direction. Image was collected March 29 2000 at 10:51:14. ©Canadian Space Agency 2000.

3. PROJECTION ALGORITHM PERFORMANCE

To determine how well the projection approach estimated the actual wind direction we used a series of RADARSAT SAR images collected off the east coast of the United States for which there was buoy wind information generated approximately simultaneously with the image acquisition and located spatially within the SAR image. The SAR imagery was processed at the Alaska Satellite Facility and represented 100 m resolution imagery with 50 m sample spacing. The buoy winds were converted to 10 m winds to make them consistent with the radar cross section models being used to estimate wind speed. The buoy information was compared to wind vectors estimated from the SAR image derived close to where the buoy was located. We eliminated any comparisons that occurred at incidence angles less than 25° due to possible calibration errors in the processed image, any comparisons for which the SAR-derived vector was more than 24 km away from the buoy location, and any comparisons for which the buoy wind speed values were less than 5 m/s, since for these locations there may be no significant radar cross section response from the ocean surface. Note that although 24 km is somewhat far from the *in situ* observations for comparison, it was used since that was the size of our local image window, and putting a more severe constraint (e.g. half the window size) resulting in too few comparisons.

These constraints resulted in a total of 137 comparisons between buoy observations and wind vectors estimated from the SAR imagery. A plot of SAR-derived wind direction vs. buoy wind direction is shown in Fig. 4. Due to the 180° ambiguity in the SAR-derived directions, a value of 180 was added or subtracted from the SAR-derived direction to get it within $\pm 90^\circ$ from the buoy direction. In Fig. 4 the solid black line represents a perfect answer, i.e. the SAR-derived direction equals the buoy direction, and the dashed lines are $\pm 90^\circ$ from the solid line which represents the region of possible SAR-derived values. The final root-mean-squared error (RMSE) is 39° (mean error of 10° , error standard deviation of 38°). Note that if we were to randomly assign a direction uniformly in the range of $[-90^\circ, +90^\circ]$ we would expect a RMSE of 52° , which looks like we are only slight better than a random guess. However, an examination of the errors in Fig. 4 shows that they are not uniformly distributed, but rather tend to cluster around the “perfect” line. This is shown quantitatively in Fig. 5, where a histogram of the absolute value of the direction error is plotted. The x-axis of Fig. 5 is the top value of the error bin for the histogram. Thus the first point

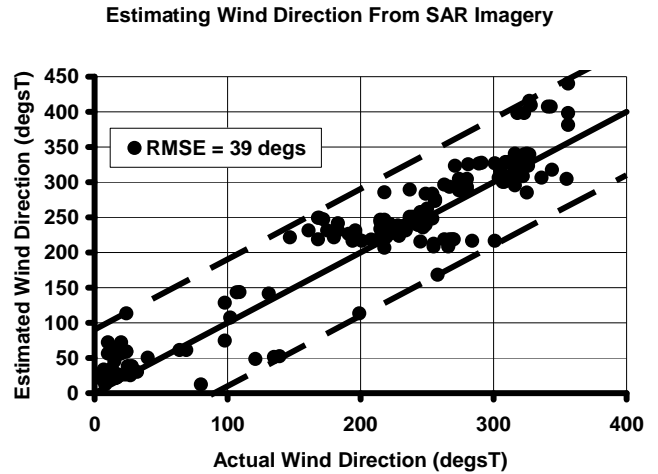


Fig. 4: Scatter plot of actual wind direction from buoy observations vs. SAR-derived wind directions. The total RMSE is 39 degs.

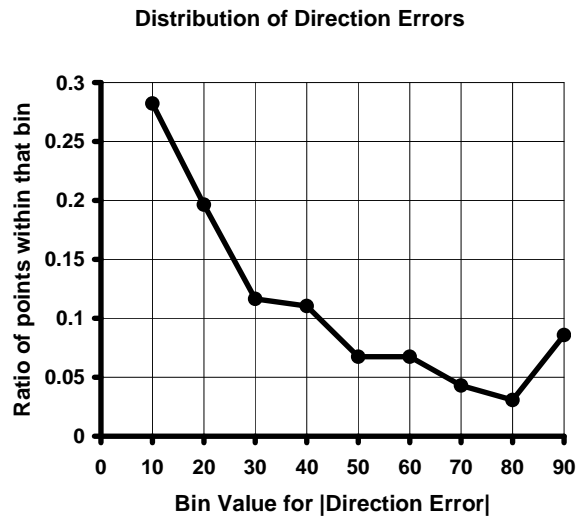


Fig. 5: Histogram of the absolute value of the direction error. X-axis is the bin values for the error, y-axis is the ratio of points that fall into that bin. Note that 60% of the samples have errors less than 30 degrees

represents errors of 10° or less, the second points represents errors between 20° and 10° , etc. Fig. 5 indicates that 60% of all of samples have an absolute direction error that is less than 30° . Note that if we were uniformly guessing a direction, the histogram in Fig. 5 would be a flat line around 0.1. The results in Figs. 4 and 5 were generated automatically; the algorithm was run with no user interaction or modification of the resulting directions.

Fig. 4 shows that there are a number of comparisons for which the estimated wind direction is as worse as it can get; i.e. 90° from the true direction. In fact, Fig. 4 shows a number of isolated points that are almost right

on the $\pm 90^\circ$ dashed lines, particularly for the lower dashed line. From manually examining these images we have found that typically these are caused by there being a feature in the image that has high contrast but is not aligned with the local wind. Figs. 6 and 7 show examples of such situations where the blue lines are the SAR-derived wind vectors and the red lines are the buoy wind vectors. In Fig. 6, convective cells can be seen that are due to downdrafts of wind and that appear as “holes” or “hills” in the image. The algorithm keys on the portion of the convective cell that has the higher contrast, which for the middle portion of the image tend to be the edge of the cell oriented vertically. The wind however is blowing right through the middle of the cell horizontally, as is indicated from the buoy observation. In Fig. 7 the algorithm is keying on a current front that is running along the coast, yet the wind is actually blowing orthogonal to the coast and thus orthogonal to the current fronts. Note that in Fig. 7 the algorithm is keying on a feature that is not even physically connected to the wind.

These results indicate that one of the significant remaining problem with automated extraction of wind directions from SAR is being able to automatically classify the image features (i.e. into convective cell, current front, wind row, wind front, surfactants, etc.) so that we can eliminate those high contrast features that

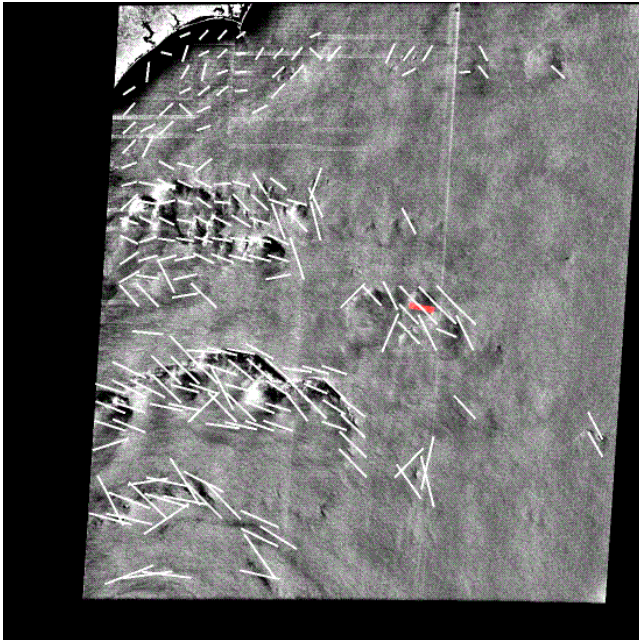


Fig. 6: Example of a feature for which the direction of maximum contrast does not align with the local wind. White lines indicate SAR-derived direction, red lines indicate buoy directions. For the convective cells, the maximum contrast direction is 90 degrees from the actual wind direction. Image was collected August 29 1999 at 11:04:55. ©Canadian Space Agency 1999.

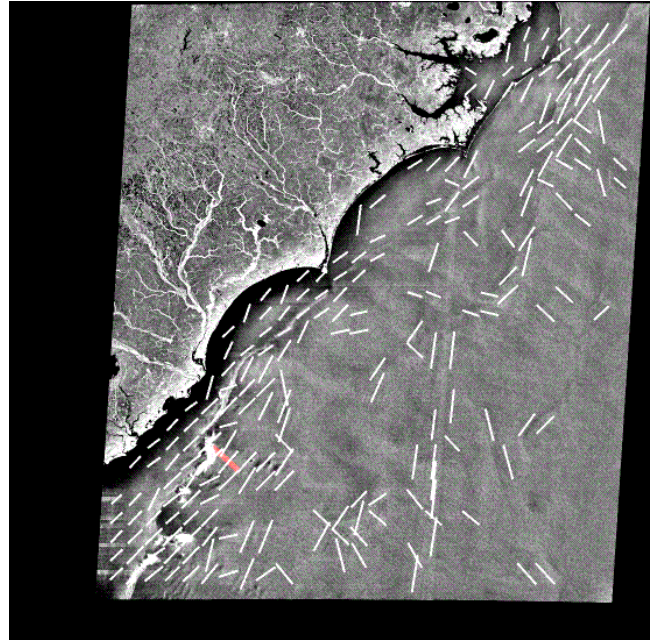


Fig. 7: Example of a feature not aligned with the local window. In this case the algorithm is keying on a current front along the coast (white lines) whereas the actual wind is blowing orthogonal to the coast (red lines). Image was collected January 20 2000 at 11:12:51. ©Canadian Space Agency 2000.

are not connected with the local wind (such as current fronts) or which need to be treated differently then just aligning with the direction of highest contrast (such as convective cells). In fact, by manually examining the imagery, we have found that almost all of the wind direction errors that are in the $[80^\circ, 90^\circ]$ bin of Fig. 5 are caused by this problem. Note that the histogram in Fig. 5 has a significant increase in the number of errors in this bin versus the general fall-off within the other bins. If we eliminate these comparisons, the RMSE for wind direction drops to 31° .

Fig. 8 shows a comparison of estimated wind speed versus buoy wind speed for this data set. The black dots used the wind direction as derived from the SAR image and the radar cross section model in Ref. 5. The RMSE is 2.2 m/s (mean error = -1.4 m/s, standard deviation of the error = 1.7 m/s). The red dots used the buoy wind directions and the same radar cross section model; the RMSE is 2.0 m/s (mean error = -0.7 m/s, standard deviation of the error = 1.9 m/s). Note that there is not much difference in the RMSE or standard deviation of the error between using the SAR-derived directions or the true direction (as observed by the buoy). However there is a significant change in the mean error; it is a factor of 2 worse using the SAR-derived directions. If we remove all the comparisons

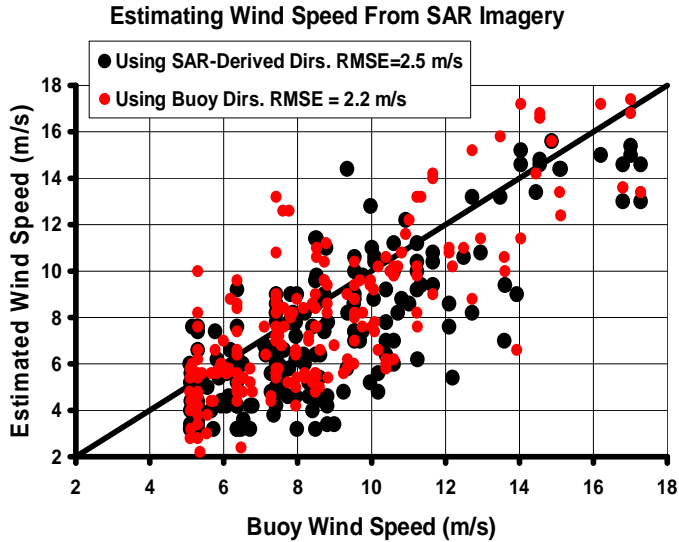


Fig. 8: Estimated wind speed from the SAR imagery vs. buoy wind speeds. Black dots are using SAR-derived directions and have an RMSE of 2.5 m/s, red dots are using buoy directions (i.e. truth) and have an RMSE of 2.2 m/s.

for which the SAR-derived wind direction has an absolute error greater than 80° (as discussed above these points are assumed to be dominated by image features not aligned with the local wind), then the wind speed RMSE drops to 2.1 m/s, with a mean error of -1.2 m/s and a standard deviation of the error of 1.7 m/s. Note that removing these points does not change the error standard deviation at all; the decrease in RMSE comes strictly from the improvement in the mean error.

The bias in wind speed estimation, even using buoy wind directions, is an issue. It may be indicative of a problem with the radar cross section model used [5], calibration with the imagery, or it may come from the fact that we are comparing estimates of the local wind averaged over 24 km to buoy point measurements. Future work will attempt to address these issues.

4. SUMMARY

As part of the NOAA/NESDIS Alaska SAR Demonstration Project, we have developed an automated algorithm for estimating wind vectors from SAR imagery that will not generate wind information over regions of the image that do not contain features. The algorithm is based on projections of the image subsets and uses a projection direction of high contrast to estimate the wind direction. When compared to 137 buoy observations, the direction RMSE is 39° , with 60% of the estimates having an absolute value of the error less than 30° . A significant remaining problem is finding an approach that can automatically determine the nature of the image feature, and remove those that

are unconnected to the local wind (such as current fronts) and modify others for which the wind is not necessarily aligned with the high contrast features (such as convective cells). If we manually remove these, the RMSE drops to 31° . The RMSE for wind speed estimation is 2.2 m/s using this approach, with a large bias of -1.4 m/s. Manually removing those comparisons that are using features not aligned with the local wind, the wind speed RMSE drops to 2.1 m/s with a bias of -1.2 m/s. If we use buoy wind directions instead of those derived from the SAR image, the wind speed RMSE is 2.0 m/s with a bias of -0.7 m/s. The cause of the large negative bias in wind speed is under investigation.

5. ACKNOWLEDGEMENTS

This study was supported and monitored by the Office of Research and Applications of the National Oceanic and Atmospheric Administration (NOAA) under ONR Contract N00014-00-D-0114.

The views, opinions, and findings contained in this report are those of the authors and should not be construed as an official National Oceanic and Atmospheric Administration of U.S. Government position, policy or decision.

6. REFERENCES

1. Pichel, W., Clemente-Colón, P. NOAA Coastwatch SAR Applications and Demonstration, *John Hopkins APL Tech. Dig.*, vol. 21(1), 49-57, 2000.
2. Monaldo, F.M., Thompson, D.R., Beal, R.C., Pichel, W.G., Clemente-Colón, P. Comparison of SAR-Derived Wind Speed With Model Predictions and Buoy Measurements, *IEEE Trans. Geosc. Remote Sens.*, vol. 39, 2587-2599, 2001.
3. Wackerman, C.C., Rufenach, C.L., Shuchman, R.A., Johannessen, J.A., Davidson, K.L. Wind Vector Retrieval Using ERS-1 Synthetic Aperture Radar Imagery, *IEEE Trans. Geosc. Remote Sens.*, vol. 34, 1343-1352, 1996.
4. Fetterer, F., Gineris, D., Wackerman, C., Validating a Scatterometer Wind Algorithm For ERS-1, *IEEE Trans. Geosc. Remote Sens.*, vol. 36, 479-492, 1998.
5. Wackerman, C.C., Clemente-Colón, P., Pichel, W.G., Li, X. A Two-Scale Model To Predict C-Band VV and HH Normalized Radar Cross Section Values Over the Ocean, *Can. J. Remote Sensing*, vol. 28, 367-384, 2002.

HIGH RESOLUTION OCEAN SURFACE WIND FIELDS RETRIEVED FROM SPACEBORNE SYNTHETIC APERTURE RADARS OPERATING AT C-BAND

Jochen Horstmann and Wolfgang Koch

Institute for Coastal Research, GKSS Research Center, 21502 Geesthacht, Germany

ABSTRACT

This paper introduces algorithms designed to retrieve high-resolution ocean surface wind fields from satellite borne synthetic aperture radars (SARs) operating in C-band at either vertical (VV) or horizontal (HH) polarization in transmit and receive. Wind directions are extracted from wind induced streaks that are visible in SAR images at scales above 200 m and that are approximately in line with the mean surface wind direction. To extract the orientation of these streaks two algorithms are introduced, which are applied either in the spatial or spectral domain. Wind speeds are derived from the normalized radar cross section (NRCS) and image geometry of the calibrated SAR images, together with the local SAR-retrieved wind direction. Therefore several C-band models (CMOD4, CMOD_LFR2, and CMOD5) are available which were developed for VV polarization and have been extended for HH polarization. To compare the different algorithms and C-band models and demonstrate their applicability, SAR retrieved wind fields are compared to numerical model results considering SAR data from the European satellite ERS-2 and ENVISAT.

Key words: ocean surface, wind speed, wind direction, wind field, synthetic aperture radar, C-band, polarization.

1. INTRODUCTION

Nowadays, several scatterometers (SCATs) are in orbit, which enable to measure wind fields with a resolution of up to 25 km on a global and operational basis independent on daylight and cloudiness. All these SCATs were originally not designed to measure high resolution wind fields and therefore make it difficult to measure the highly spatially variable winds, which are especially important in coastal areas. However, satellite borne synthetic aperture radar (SAR) instruments enable to image the ocean surface with a very high resolution, typically below 100 m. Since the launch of the European remote sensing satellites ERS-1, ERS-2 and ENVISAT as well as the Canadian satellite RADARSAT-1, SAR images have been acquired over the oceans on a continuous basis over the last 12 years. Their high resolution and large spatial coverage make them a valuable tool for measuring geophysical parameters such as ocean surface

winds, waves, and sea ice. All the above mentioned SARs operate at C-band (5.3 GHz) with either vertical (VV) or horizontal (HH) polarization in transmit and receive and at moderate incidence angles between 15° and 50° . For this electromagnetic wavelength and range of incidence angles the backscatter of the ocean surface is primarily caused by the small-scale surface roughness (in the range of 5 to 10 cm), which is strongly influenced by the local wind field and therefore allows the backscatter to be empirically related to the wind.

In this paper algorithms for wind field retrieval from satellite borne SARs operating at C-band with either VV- or HH-polarization are introduced. The algorithms are applied to retrieve wind fields from the SAR systems aboard the satellites ERS-2 and ENVISAT. To compare the different algorithms and C-band models and demonstrate their applicability, SAR retrieved wind fields are compared to results of numerical atmospheric models and the SCAT aboard ERS-2.

2. UTILIZED SAR DATA

For the following investigations SAR data acquired by the European remote sensing satellites ERS-1, ERS-2 and ENVISAT are used. All these platforms operate in a Sun-synchronous polar orbit in a height of ~ 800 km with an orbital period of 100 min and a repeat cycle of 35 days. For this study the ENVISAT advanced SAR (ASAR) data were acquired in the ScanSAR wide swath mode. The ScanSAR images are generated by scanning the incidence angle and sequentially synthesizing images for different sub-swaths at incidence angles between 15° and 45° . The ScanSAR wide swath mode enables to image a swath of up to ~ 450 km width with a spatial resolution of ~ 100 m. The ENVISAT ScanSAR data were acquired at C-band (5.34 GHz) with either HH- or VV-polarization. The utilized ERS-1 and ERS-2 SAR data were also acquired at C-band in the SAR image- or wave mode at VV-polarization. In the image mode $100 \text{ km} \times 100 \text{ km}$ SAR images are acquired with a resolution similar to 30 m and at incidence angles between 20° and 26° . In the wave mode ERS-1 and 2 acquire $10 \text{ km} \times 5 \text{ km}$ SAR imagerettes every 200 km along the orbit on a continuous and global basis with a resolution of ~ 30 m at a fixed incidence angle of 23° .

3. WIND DIRECTION RETRIEVAL

The most popular methods for SAR wind direction retrieval are based on the imaging of linear features at scales above 400 m, which are visible in SAR images. Most of these features are associated to wind streaks (Drobinski & Foster 2003) and marine atmospheric boundary layer rolls (Alpers & Brümmer 1994). In Fig. 1 a RAR image of the ocean surface is shown, which was integrated in time over 60 s to remove the effect of ocean gravity waves. Wind induced streaks can be seen in the image at different scales. Studies of Dankert et al. (in press 2003) utilizing high resolution real aperture radar (RAR) imagery have shown that wind induced streaks at scales between 50 to 1500 m are very well aligned with the mean surface wind. Their comparison of 3272 radar image sequences, acquired over a six month period, to *in situ* wind measurements showed that the streaks are very well aligned with the surface wind directions (root mean square error of 14.2° and bias of 0.6°). Therefore, in the following the linear features visible in the SAR images are assumed to be aligned with the mean surface wind direction. Furthermore, the results of Dankert et al. (in press 2003) encourage to focus on the smallest possible scales, which can be utilized from space borne SAR.

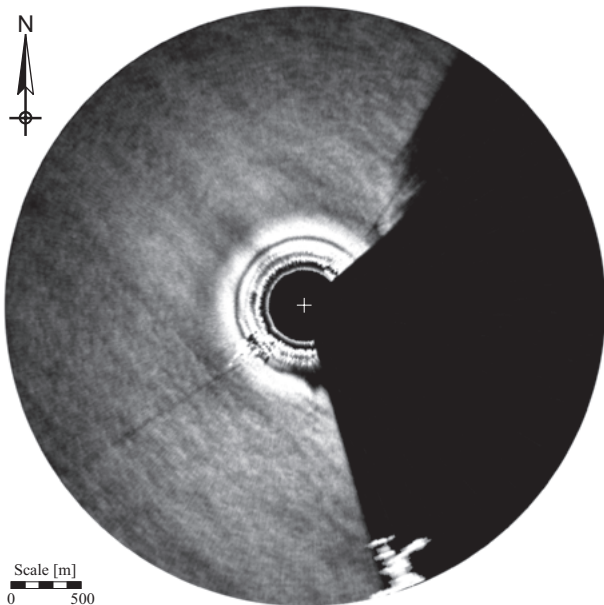


Figure 1. High resolution real aperture image of the ocean surface, acquired at X-band with horizontal (HH) polarization in transmit and receive at grazing incidence. The image results of an image sequence of 32 images acquired within a time interval of 60 s. Wind induced streaks are clearly visible at scales below 500 m.

3.1. Local Gradient Method

In the spatial domain the orientation of the streaks is derived by retrieving the local gradient at different scales. In the following this method is referred as the Local Gradient Method (LG-Method). In the LG-Method the wind direction is defined as normal

to the direction of the local gradient derived from smoothed amplitude images (Horstmann et al. 2002; Koch in press 2003). In a first step the SAR images are smoothed and reduced to a pixel size of 100, 200 and 400 m, representing scales above 200 m. From these pixels the local directions, defined by the normal to the local gradient, are computed with a 180° ambiguity. In a next step all pixels that are effected by non wind induced features, e.g. land, surface slicks, sea ice etc. are masked. Therefore, land masks and SAR image filters, which are described by Koch (in press 2003), are applied. Finally, from all of the resulting directions only the most frequent directions in a predefined grid cell are selected. The wind directions resulting from the 100, 200 and 400 m pixel sizes vary typically only by a few degrees, except for cases where additional features are present in the SAR image, e.g. scalloping. The 180° directional ambiguity can be removed if wind shadowing is present, which is often visible in the lee of coastlines. If such features are not present in the image other sources, e.g., atmospheric models or *in situ* measurements, have to be considered.

In Fig. 2 an ERS-1 SAR image is depicted, which was acquired at the marginal ice zone off the coast of Spitzbergen. In Fig. 2 A) the mask resulting from the filtering is superimposed to the SAR image. It is clearly visible that most pixels effected by sea ice are included in the masked area. In Fig. 2 B) the wind direction retrieved via the LG-Method are plotted with (red arrows) and without (blue arrows) the filter. It can be seen that the wind directions significantly improve utilizing the filter.

3.2. Fast Fourier Transformation Method

The most popular method for extraction of the wind direction from SAR imagery searches for the dominant wind streak direction in the spectral domain and is referred to as the Fast Fourier Transformation Method (FFT-Method). This method was first introduced by Gerling (1986) and later modified by several other groups (e.g. Vachon & Dobson 1996; Wackerman et al. 1996; Lehner et al. 1998).

In a first step all pixels in the SAR image that are affected by non wind induced features, e.g. land, surface slicks, sea ice etc. are masked. Therefore a land mask and the filters, already used in the LG-Method, are applied to the image. In the next step the SAR image is split up into subimages, which represent the wind direction resolution that is typically set to $10 \text{ km} \times 10 \text{ km}$. Then all masked pixels in each subimage are replaced by the mean intensity value of the selected subimage, this enables to use the FFT-Method also close to the shore or at the marginal ice zone (Fig. 2 C). In the last step a regression is estimated, weighted with the energy densities for wavelengths between 500 and 1800 m. The threshold of 500 m is set to exclude ocean surface waves, while the threshold of 1800 m is set to exclude larger scale features e.g. inflection point instabilities and Lee waves. The main spectral energy is located perpendicular to the orientation of the streaks, giving the wind direction

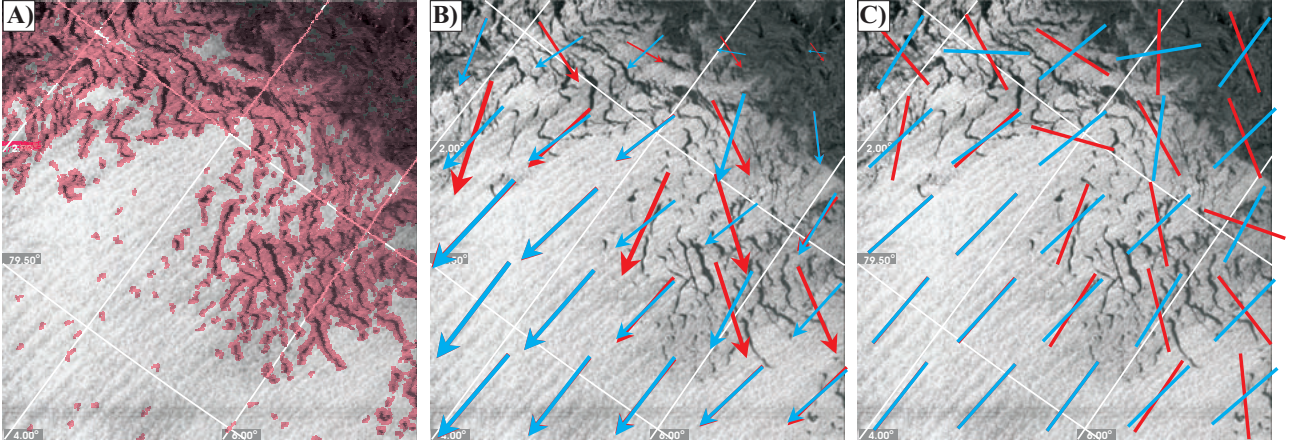


Figure 2. ERS-1 SAR image acquired at the marginal ice zone off the coast of Spitzbergen. A) shows the mask superimposed to the SAR image, which results from the filtering. B) gives the wind directions resulting from the Local Gradient Method (LG-Method) with (blue arrows) and without (red arrows) consideration of the filter. C) shows the wind directions resulting from the Fast Fourier Transformation Method (FFT-Method) with (blue bars) and without (red bars) utilizing the filter.

with a 180° directional ambiguity. The 180° ambiguity can be removed if wind shadowing, e.g. in the Lee of the coast, or additional data e.g. wind forecasts are available.

In Fig. 2 C) the wind direction are plotted as retrieved via the FFT-Method with (red bars) and without (blue bars) the filter. It can be seen that, similar to the LG-Method results, the wind directions significantly improve utilizing the filter.

4. WIND SPEED RETRIEVAL

For the wind speed retrieval a model function relating the NRCS of the ocean surface to the local near-surface wind speed, wind direction versus antenna look direction and incidence angle is utilized. This function is dependent on radar frequency and polarization. In case of the ERS-1 SCAT operating at C-band with VV polarization several empirical functions have been developed, of which the CMOD4 (Stoffelen & Anderson 1997) and CMOD.IFR2 (Quilfen et al. 1998) are the most commonly used and the CMOD5 (Hersbach 2003) is the most recently developed. It has been shown that these functions are applicable for wind speed retrieval from VV polarized SAR images (e.g. Vachon & Dobson 1996; Lehner et al. 1998; Horstmann et al. 2003). For wind speed retrieval from C-band HH polarized SAR images no similar well developed model exists so that a hybrid model function is applied that consists of the prior mentioned models, e.g. CMOD4, and a C-band polarization ratio (PR) (Horstmann et al. 2000; Thompson & Beal 2000; Vachon & Dobson 2000), defined as,

$$PR = \frac{\sigma_0^{HH}}{\sigma_0^{VV}} \quad (1)$$

where σ_0^{HH} and σ_0^{VV} are the HH and VV polarized NRCS, respectively. So far the PR is not well known and several different PR's are suggested in literature (e.g. Elfouhaily 1997; Thompson et al. 1998).

The PR proposed by Thompson et al. (1998) neglects wind speed and wind direction dependency and is given by:

$$PR = \frac{(1 + \alpha \tan^2 \theta)^2}{(1 + 2 \tan^2 \theta)^2} \quad (2)$$

where α is a constant and set to 0.6, fitting the measurements of Unal et al. (1991). This form is closely related to theoretical forms of the PR, where $\alpha = 0$ gives the theoretical PR for Bragg scattering and $\alpha = 2$ results in Kirchhoff scattering. Several different values for α have been suggested in the past considering RADARSAT-1 SAR data, they vary between 0.4 and 1.2 (Horstmann et al. 2000; Vachon & Dobson 2000; Monaldo et al. 2002). Comparisons of RADARSAT-1 SAR data of different SAR processing facilities showed that the different findings of α are most likely due to the different calibrations of RADARSAT-1 SAR data.

5. COMPARISON OF SAR RETRIEVED WIND FIELDS TO NUMERICAL MODELS AND SCATTEROMETER RESULTS

5.1. Comparison of SAR retrieved wind fields in the coastal zone

To compare the different algorithms and C-band models and demonstrate their applicability for SAR wind field retrieval in the coastal zone 12 ENVISAT ScanSAR images of the North Sea were considered. From the 12 ENVISAT ScanSAR images 6 were acquired at VV polarization and 6 at HH polarization respectively. For the comparison in the North Sea wind fields from the model of the German Weather Service (DWD) were utilized, which represent 6 hour analyzed wind fields that were additionally interpolated to the SAR acquisition time. The SAR wind fields were retrieved from the area corresponding to the grid cell in the DWD model output, resulting in an average grid cell size of approximately $45 \text{ km} \times 75 \text{ km}$. The directional ambiguities of the SAR-retrieved wind directions were removed by considering wind shadowing as well as weather charts. The

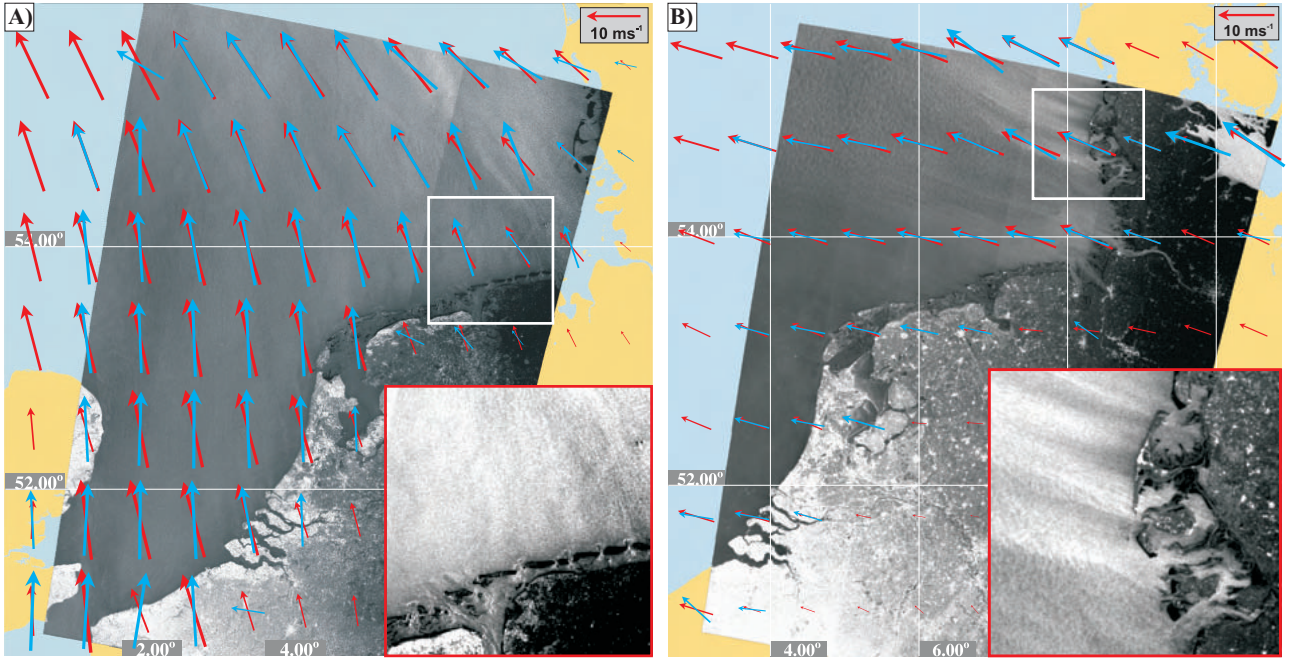


Figure 3. ENVISAT ASAR images of the southern North Sea acquired on 1. December, 2002 with VV polarization (A)) and on 14. December, 2002 with HH polarization (B)). Superimposed to the images are the wind vectors resulting from the SAR data using the LG-Method and the CMOD4 (blue arrows) and from the model of the German weather service (red arrows). The contrast enhanced cutouts (lower right of A) and B)) shows the wind shadowing due to the coast, which is used to remove the directional ambiguity.

resulting wind direction, mean NRCS, and mean incidence angle of each grid cell is taken as input to the wind speed retrieval algorithm for VV or HH polarization respectively.

Fig. 3 A) shows an ENVISAT ASAR image of the Southern North Sea and the Street of Dover acquired on December 1, 2002 at 10:02 UTC in the ScanSAR mode with VV polarization. Superimposed to the image are the wind vectors as retrieved from the SAR image considering the LG-Method and the CMOD4 (blue arrows) and resulting from the DWD model (red arrows). The wind direction ambiguities could be removed due to the wind shadowing, which is especially visible at the north coast of Germany. The contrast enhanced cutout (lower right of Fig. 3 A)) shows the coastal wind shadowing in more detail. In most parts of the image the SAR retrieved winds agree very well to the DWD model results both in magnitude and direction. Fig. 3 B) shows an ENVISAT ASAR image of the southern North Sea acquired on December 14, 2002, at 09:53 UTC. In this case the image was acquired in HH polarization. Again the wind fields resulting from the SAR image and the DWD model agree very well.

The comparison considering all 12 ENVISAT ScanSAR images is shown in Fig. 4 and Fig. 5. Concerning the comparison of wind directions resulting from the DWD model to those retrieved from the ENVISAT ASAR images the LG-Method (Fig. 4 A)) showed significantly better results than the FFT-method (Fig. 4 B)). However, the FFT-Method is strongly affected by scalloping, which is visible in most of the utilized ENVISAT ASAR images. Scalloping processing problem, which turns out as lin-

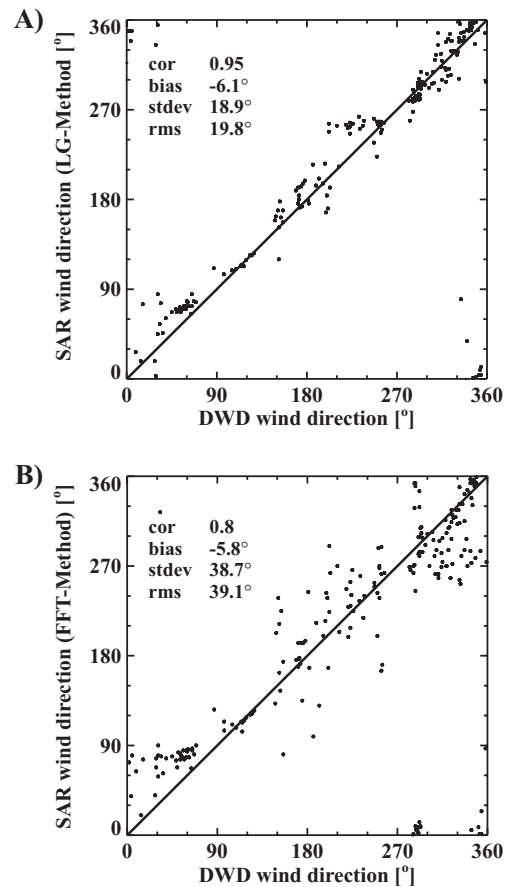


Figure 4. Comparison of DWD model wind directions to ENVISAT ASAR retrieved wind directions. In A) wind directions were retrieved with the LG-Method and in B) with the FFT-method.

Wind directions		
	LG-Method	FFT-Method
cor	0.95	0.8
bias	-6.1 °	-5.8°
stdev	18.9 °	38.7°
rms	19.8 °	39.1°

Wind speeds			
	CMOD4	CMOD_IFR2	CMOD5
cor	0.87	0.81	0.85
bias	0.11 ms ⁻¹	0.51 ms ⁻¹	0.76 ms ⁻¹
stdev	2.54 ms ⁻¹	2.73 ms ⁻¹	2.78 ms ⁻¹
rms	2.54 ms ⁻¹	2.78 ms ⁻¹	2.88 ms ⁻¹

Table 1. Main statistical parameters concerning the comparison of ENVISAT ASAR retrieved wind fields to results of the DWD model.

ear features that are aligned in range direction with a spacing within the scales evaluated by the FFT-Method and can therefore lead to a misinterpretation of wind directions. The effect of scalloping can be detected in Fig. 4 B), where SAR wind directions of similar to 90° and 270° occur quite often, which are approximately in range direction of the ASAR scenes. In case of the LG-Method scalloping only affects the reduced pixel sizes below 400 m, which enables the algorithm to overcome this handicap.

In the following all SAR retrieved wind speeds were derived using as input to the C-band model the wind directions resulting from the LG-Method. Fig. 5 A), shows the scatterplot of wind speeds resulting from the DWD model and from the ENVISAT ASAR data using the CMOD4 model. The resulting correlation is 0.87 with a bias of 0.1 ms⁻¹ and a root mean square error of 2.5 ms⁻¹. Comparison of CMOD4 retrieved wind speeds to CMOD_IFR2 retrieved wind speeds (Fig. 5 B)) shows that CMOD_IFR2 predicts in average slightly higher wind speeds (bias = 0.4 ms⁻¹) only for wind speeds below ~ 4 ms⁻¹ CMOD4 gives higher wind speeds. Comparison of SAR wind speeds retrieved using CMOD_IFR2 and CMOD5 respectively (Fig. 5 C)) show that CMOD5 gives higher wind speeds at low (< 4 ms⁻¹) and high wind speeds (> 17 ms⁻¹). Concerning the statistics resulting of the comparison of DWD wind speeds to SAR wind speeds retrieved by each of the C-band models (Table 1), CMOD4 gives the best results. However, especially at high wind speeds CMOD4 underestimates the wind speeds significantly. CMOD_IFR2 and CMOD5 give better results at high wind speeds but still underestimate the wind speed. Overall, a much larger data set has to be investigated to conclude on which C-band model is the best to use.

Considering the wind direction retrieval using the LG-Method the results look very promising especially if compared to the wind direction error of 15° achieved by the SCAT aboard ERS (Quilfen et al. 1998). The comparison of SAR retrieved wind speeds to the model results do not show a good consistency, which is most likely due to the scarce resolution of the atmospheric models, which is too coarse for resolving wind shadowing as well as other small scale

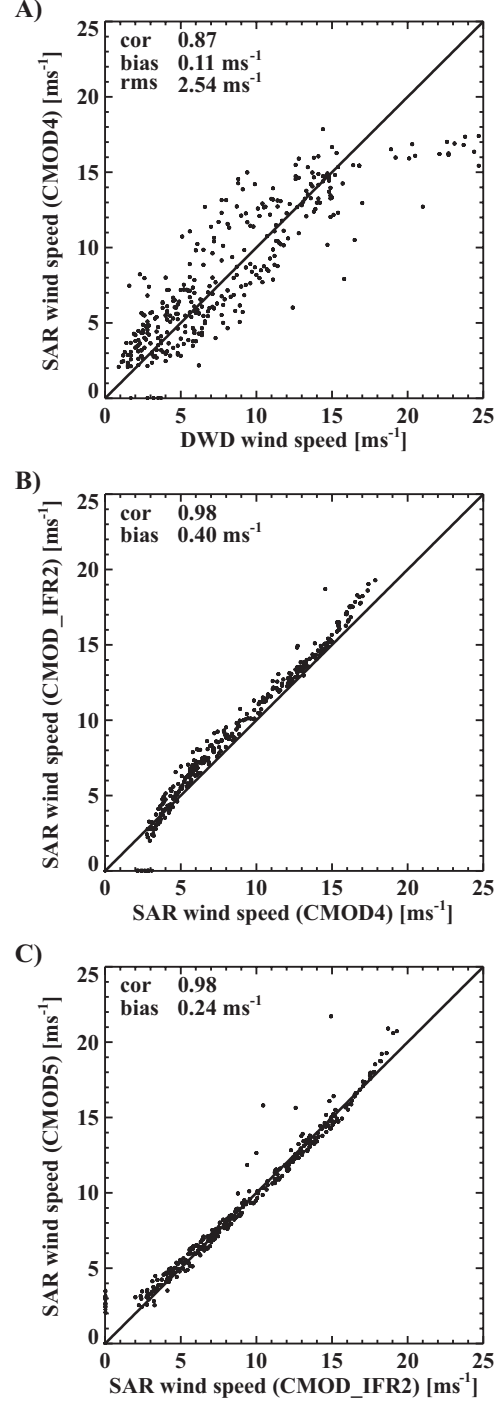


Figure 5. Scatterplots of: A) wind speeds resulting from the DWD model versus results from ENVISAT ASAR using the CMOD4 model. B) SAR wind speeds retrieved via CMOD4 and CMOD_IFR2. C) SAR wind speeds retrieved via CMOD_IFR2 and CMOD5.

features that occur especially near to the coasts. Similar results were obtained by Horstmann et al. (2002), when comparing RADARSAT-1 ScanSAR retrieved wind fields to numerical model results at the coasts of Greenland. Their comparison resulted in a correlation of 0.92 with a bias of -3.5° and a root mean square error of 21.6° for wind directions retrieved via the LG-Method and a correlation of 0.71 with a bias of -0.9 ms⁻¹ and a root mean square error of 3.47 ms⁻¹ for wind speeds using CMOD4.

5.2. Comparison of SAR Retrieved Wind Speeds on a Global Basis

To investigate the cause of the large wind speed errors observed in the regional comparisons, wind speeds were retrieved from SAR imagettes on a global basis (Horstmann et al. 2003). SAR imagettes are typically acquired off the coasts and therefore the wind field is not effected by land, e.g., wind shadowing. The SAR imagette retrieved wind speeds were compared to co-located model results of the European Center for Medium-range Weather Forecast (ECMWF) and measurements from the ERS-2 SCAT. Therefore, three weeks of ERS-2 SAR wave mode data, representing a total of 34 000 SAR imagettes, were utilized. Prior to wind speed retrieval all SAR imagettes, which show surface features not due to the local winds, were excluded from the data set following the procedure introduced by Horstmann et al. (2003). For applications of the C-band models the wind direction are needed as input, which were taken for this comparison from the ECMWF model or the ERS-2 SCAT measurements, respectively. The resulting scatterplots of the comparison are shown in Fig. 6.

Overall the agreement to both ECMWF and ERS-2 SCAT results is excellent (Horstmann et al. 2003) and agrees well to the error of 1.3 ms^{-1} reported for ERS-2 SCAT wind speeds.

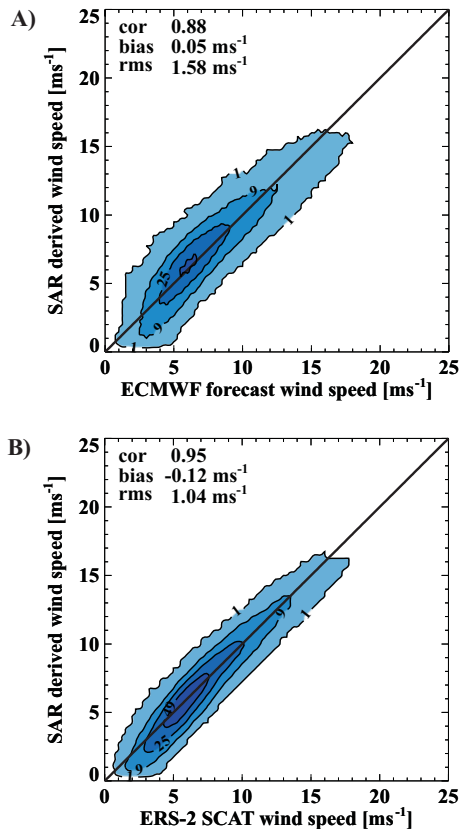


Figure 6. Scatterplots of wind speeds resulting from the ECMWF (A)) and ERS-2 SCAT (B)) versus CMOD₄ retrieved SAR results, which considered the wind directions from ECMWF (A)) and ERS-2 SCAT (B)), respectively.

6. CONCLUSIONS

Two methods the LG- and FFT-Method for retrieving wind directions from wind induced streaks have been introduced. The LG-Method retrieves the orientation of the wind streaks in the spatial domain considering the local gradients at a grid cell size of 100, 200 and 400 m. The FFT-Method extracts the wind direction in the spectral domain searching for the dominant spectral peak at wave lengths between 500 and 1800 m. Both methods work significantly better if the filters proposed by Koch (in press 2003) are considered, these are especially important when retrieving wind fields in the marginal ice zone. Comparison of SAR retrieved wind directions, using both methods, to the DWD model analysis resulted in a standard deviation of 18.9° with a bias of -6.1° for the LG-Method and a standard deviation of 38.7° with a bias of -5.8° for the FFT-Method respectively. The LG-Method shows significantly better results than the FFT-Method but needs significantly larger computer resources as well as longer computation time. Unfortunately the ENVISAT ASAR images utilized were affected by scalloping, which lead to a increase of error when using the FFT-Method.

For wind speed retrieval the C-band models CMOD4, CMOD_{IFR2} and CMOD5, which were developed for the VV polarized C-band scatterometers aboard ERS, are used. In case of HH polarization these C-band models are extended by an incidence angle dependent PR. As input to these models the NRCS, incidence angle and wind direction is needed, which can be retrieved from the SAR image. Comparison of SAR retrieved wind speeds to DWD model analysis resulted in a standard deviation of 2.5 ms^{-1} and a bias of 0.1 ms^{-1} using CMOD4. Both, CMOD_{IFR2} and CMOD5 show slightly larger errors. Comparison of wind speeds retrieved from the ERS-2 SAR wave mode data utilizing CMOD4 to wind speeds from the ERS-2 SCAT and ECMWF model resulted in a root mean square error of 1.04 ms^{-1} and 1.58 ms^{-1} respectively. In contrast to the ENVISAT ASAR ScanSAR images the ERS-2 wave mode data were acquired well off the coast. It is very likely that the scarce resolution of the DWD model is too coarse to resolve small scale features such, e.g., wind shadowing, which occur especially near to the coasts.

The good agreement of SAR retrieved wind directions and wind speeds to numerical model and ERS-2 SCAT results shows the applicability of C-band SAR for wind field retrieval. The obtained SAR wind retrieval errors are in the same magnitude as the results achieved by satellite borne SCATs.

Future investigations will have to concentrate on the validity of the C-band models, especially concerning high wind speeds and polarization, but also effects due to fetch limitations. Concerning the wind direction retrieval from wind induced streaks, it has to be investigated which scales are the most appropriate to infer on the near surface wind direction.

ACKNOWLEDGMENTS

The authors were supported by the German Bundesministerium für Bildung und Forschung in the framework of the ENVOC project. The ERS-2 SAR and ENVISAT ASAR data were kindly provided by the European Space Agency within the projects COMPLEX and BIGPASO.

REFERENCES

- Alpers W., Brümmer B., 1994, Atmospheric boundary layer rolls observed by the synthetic aperture radar aboard the ERS-1 satellite, *J. Geophys. Res.*, vol. 99, pp. 12 613–12 621.
- Dankert H., Horstmann J., Rosenthal W., in press 2003, Ocean Winds Fields Retrieved from Radar-Image Sequences, *J. Geophys. Res.*
- Drobinski P., Foster R., 2003, On the Origin of Near-Surface Streaks in the Neutrally-Stratified Planetary Boundary Layer, *Bound.-Layer Meteorol.*, vol. 108, no. 2, pp. 247–256.
- Elfouhaily T., 1997, Physical modeling of electromagnetic backscatter from the ocean surface; Application to retrieval of wind fields and wind stress by remote sensing of the marine atmospheric boundary layer, Ph.D. thesis, Travail de recherche effectué au sein Département d'Océanographie Spatiale de l'Institut Français de Recherche pour l'Exploitation de la Mer (IFREMER), Brest, France.
- Gerling T., 1986, Structure of the surface wind field from Seasat SAR, *J. Geophys. Res.*, vol. 91, pp. 2 308–2 320.
- Hersbach H., 2003, CMOD5 an improved geophysical model function for ERS C-band scatterometry, Internal report, European Centre for Medium-Range Weather Forecast.
- Horstmann J., Koch W., Lehner S., Tonboe R., 2000, Wind retrieval over the ocean using synthetic aperture radar with C-band HH polarization, *IEEE Trans. Geosci. Remote Sens.*, vol. 38, no. 5, pp. 2 122–2 131.
- Horstmann J., Koch W., Lehner S., Tonboe R., 2002, Ocean winds from RADARSAT-1 ScanSAR, *Can. J. Remote Sens.*, vol. 28, no. 3, pp. 524–533.
- Horstmann J., Schiller H., Schulz-Stellenfleth J., Lehner S., 2003, Global Wind Speed Retrieval from SAR, *IEEE Trans. Geosci. Remote Sens.*, vol. 41, no. 10, pp. 2277–2286.
- Koch W., in press 2003, Directional analysis of SAR images aiming at wind direction, *IEEE Trans. Geosci. Remote Sens.*
- Lehner S., Horstmann J., Koch W., Rosenthal W., 1998, Mesoscale wind measurements using recalibrated ERS SAR images, *J. Geophys. Res.*, vol. 103, pp. 7 847–7 856.
- Monaldo F., Thompson D., Beal R., Pichel W., Clemente-Colon P., 2002, Comparison of SAR-derived wind speed with model predictions and ocean buoy measurements, *IEEE Trans. Geosci. Remote Sens.*, vol. 39, no. 12, pp. 2587–2600.
- Quilfen Y., Chapron B., Elfouhaily T., Katsaros K., Tournadre J., 1998, Observation of tropical cyclones by high-resolution scatterometry, *J. Geophys. Res.*, vol. 103, pp. 7 767–7 786.
- Stoffelen A., Anderson D., 1997, Scatterometer data interpretation: Estimation and validation of the transfer function CMOD4, *J. Geophys. Res.*, vol. 102, pp. 5 767–5 780.
- Thompson D., Beal R., 2000, Mapping of mesoscale and submesoscale wind fields using synthetic aperture radar, *John Hopkins APL Tech. Dig.*, vol. 21, no. 1, pp. 58–67.
- Thompson D., Elfouhaily T., Chapron B., 1998, Polarization ratio for microwave backscattering from the ocean surface at low to moderate incidence angles, In: *Proc. Int. Geosci. Remote Sens. Symp.* 1998, Seattle, USA.
- Unal C., Snoeij P., Swart P., 1991, The polarization-dependent relation between radar backscatter from the ocean surface and surface wind vectors at frequencies between 1 and 18 GHz, *IEEE Trans. Geosci. Remote Sens.*, vol. 29, pp. 621–626.
- Vachon P., Dobson F., 2000, Wind retrieval from RADARSAT SAR images: Selection of a suitable C-band HH polarization wind retrieval model, *Can. J. Remote Sens.*, vol. 26, no. 4, pp. 306–313.
- Vachon P.W., Dobson F., 1996, Validation of wind vector retrieval from ERS-1 SAR images over the ocean, *Global Atmos. Ocean Syst.*, vol. 5, pp. 177–187.
- Wackerman C., Rufenach C., Schuchman R., Johannessen J., Davidson K., 1996, Wind vector retrieval using ERS-1 synthetic aperture radar imagery, *J. Geophys. Res.*, vol. 34, pp. 1 343–1 352.

**This page intentionally
left blank (pagination)**

SAR WIND FIELDS FOR OFFSHORE WIND FARMING

Tobias Schneiderhan⁽¹⁾, Johannes Schulz-Stellenfleth⁽¹⁾, Susanne Lehner⁽¹⁾, Jochen Horstmann⁽²⁾

⁽¹⁾DLR, Oberpfaffenhofen, 82230 Wessling, Email: Tobias.Schneiderhan@dlr.de

⁽²⁾GKSS Research Center, Max-Planck Strasse, 21502 Geesthacht

1. INTRODUCTION

Active microwave radar satellites transmit and receive radar signals with wavelengths in the range of centimetres to one meter thus measuring the roughness of the sea surface, which enables the retrieval of wind and ocean wave fields. Synthetic Aperture Radars (SARs) are capable of imaging synoptic wind fields with a coverage of up to 500 km x 500 km and a resolution of down to 100 m. As the radar signals penetrate clouds, these sensors have all weather capability and can acquire data as well during nighttime. Therefore, they are especially suited for sea surface observations in coastal regions and in severe weather conditions (Lehner *et al.*, 2001a).

In this paper an overview is given of the technique to measure wind fields with SAR and their relevance for offshore wind farming.

2. OFFSHORE WIND FARMING IN EUROPE

In Europe wind farming is developing expeditiously (Fig. 1). Because of the shortage of suitable onshore sites this development is now moving offshore. During the past 10 years several wind parks have been constructed all over Europe. Within the last few years a fast extension of wind energy production has taken place with more than 23000 MW installed in Europe by the end of the year 2002 and nearly 32000 MW worldwide. Wind energy is about to replace hydropower as the most important commercial source of clean, renewable energy. Up to now about 280 MW offshore power is installed all in the North and Baltic Sea. In near future many wind farms with over 100 single wind turbines with an output of more than 5000 MW covering areas of more than 200 km² are planned and already under construction.

For example, the first planned and approved German offshore wind park Borkum West will have more than 200 wind turbines with a total power yield of up to 1000 MW and will cover an area of nearly 200 km². The largest wind park that is already in operation is Horns Rev (Fig. 3), which is situated in the North Sea at the west coast of Denmark. Fig. 3 shows a SAR image of the wind park Horns Rev while still under.



Fig. 1. Development of wind power installations [MW] in Europe (courtesy of IWR).

construction. Today 80 wind energy converters are running at this offshore site producing 160 MW

Globally the development of the wind energy shows an increase of more than 25 percent per year with Europe as the main market and leading operator. In Table 1 the development of the offshore wind energy is displayed. Although the figures are from February 2002, the tendency to offshore wind parks of tremendous sizes can be seen. In the last years the estimates of the increase in installations were all corrected to higher prognoses because of the fast development of the installation activities in Europe.

Table 1. Marine wind energy in Europe (Source: BWE-Windenergie 2002, Bundesverband WindEnergie e.V. (BWE), February 2002).

	Installed power (MW) (total)	Installed power (MW) (offshore)	Plans (MW) (offshore)	Potential (TWh) (offshore)
BEL	30	0	300	24
DK	2750	49.95	4000	550
GER	8750	0	60000	237
GB	475	4	1500	986
IRE	125	0	1000	-
NL	483	13.4	350	136
N	20	0	-	-
ESP	3.350	0	-	-
SWE	300	22,75	1.000	-

In Europe the basic conditions are advantageous for offshore turbine installations. Large parts of the North and Baltic Sea show shallow waters and high mean wind speed promising a vast potential for wind park installations. The European plans of 5000 MW installed offshore in 2010 and more than 50000 MW in 2020 seem to be more than realistic.

Several mainly ecological short- and long-term effects of these parks on the environment are under investigation. One important parameter that can be observed with space borne SARs is the high-resolution wind field in the vicinity of the wind farms. SAR enables to investigate changes of the wind field due to the wind turbines, e.g. turbulent wakes and blockage effects in front of the wind farm, which are of great interest not only for the construction of wind farms but also for the environment.

3. SAR WIND MEASUREMENTS

SAR wind field retrieval is a two-step process. In the first step wind directions are retrieved, which are a necessary input into the second step to retrieve wind speeds from the intensity values. Wind directions are retrieved from wind-induced phenomena aligned in wind direction, which are visible in most investigated SAR images. Their imaging by SAR is caused by phenomena such as boundary layer rolls, Langmuir cells and wind shadowing. The orientation of these streak-like features is approximately in direction of the mean surface wind. The method used hereafter, defines the wind direction as normal to the local gradients derived from smoothed amplitude images. Therefore the SAR images are smoothed and reduced to an appropriate pixel size, e.g., 100 m, 200 m, and 400 m. From these pixels the local directions, defined by the normal to the local gradient is computed leaving a 180° ambiguity (Koch, 2003; Horstmann and Koch, this issue). From the resulting directions the most frequent and most probable local direction is selected using additional assumptions about the wind flux pattern. The 180° ambiguity can be removed if wind shadowing is present, which is often visible in the lee of coastlines and large objects such as offshore structures.

For retrieving wind speeds from SAR data a model function relating the Normalized Radar Cross Section (NRCS) of the ocean surface σ_0 to the local near-surface wind speed u , wind direction versus antenna look direction Φ , and incidence angle θ ,

$$\sigma_0^{pol} = a(\theta)u^{\gamma(\theta)}[1 + b(\theta)\cos\Phi + c(\theta)2\cos\Phi] \quad (1)$$

is applied. Here a , b , c and γ are coefficients that in general depend on radar frequency and polarization pol . These coefficients were determined empirically in

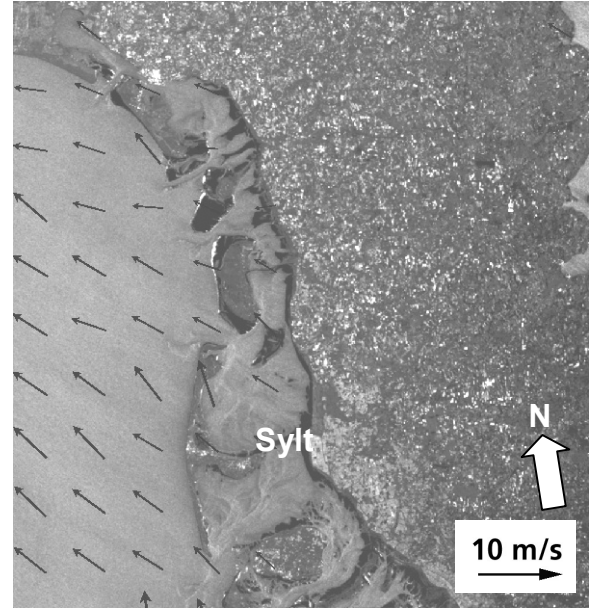


Fig. 2. ERS-2 SAR image mode scene with derived wind field (10 km resolution), acquired on November 28, 2002, 10:23 UTC.

the case of the model functions CMOD4 by evaluation of scatterometer data of the European satellite ERS-1 and wind fields from the ECMWF (Stoffelen and Andersen, 1997). CMOD4 has been applied successfully for wind speed retrieval from C-band vertical polarized (VV) ERS-1 and ERS-2 SAR images (Lehner *et al.*, 1998; Horstmann *et al.*, 2002, 2003) in which the accuracy of the algorithm was shown to be about 1 ms⁻¹ in wind speed and about 22° in wind direction. The CMOD4 was extended to horizontal polarization (HH) (Horstmann *et al.*, 2000b), which enables to extract wind fields also from HH-polarized SAR imagery as acquired by the Canadian satellite RADARSAT-1 and on demand can also be acquired by the European satellite ENVISAT.

Beside the wind, hail, strong rain as well as surface slicks change the roughness of the surface and thus the image intensity, which influences the wind velocity derivation. But also the wind directions can change as for instance within an atmospheric front. In addition areas with ocean current shear can show a pattern in the scale of wind streaks that can be misinterpreted as the wind direction. To avoid influences of features not due to the local wind, e.g. atmospheric fronts or current shear, that occur in some of the analysed SAR scenes, complementary wind measurements have to be considered.

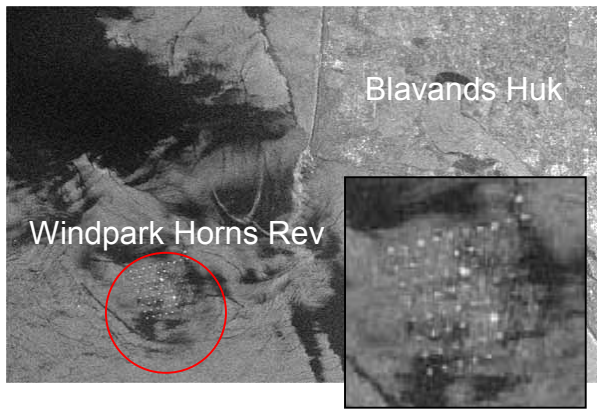


Fig. 3. Cut-out of a SAR image mode scene with zoom (8 x 8 km) of the wind park Horns Rev, acquired on July 30, 2002, 10:25 UTC.



Fig. 4. Utgrunden wind park from air and from space (ERS SAR image mode scene, 5 x 5 km zoom).

4. UTILIZED SAR DATA

Since the launch of the European remote sensing satellites ERS-1 and ERS-2 in 1991 and 1995 and ENVISAT in 2002, SAR images have been acquired over the oceans on a continuous basis.

The ERS SAR operates at C-band with vertical polarization in transmit and receive. The resolution is about 30 m in range (across flight direction) and 10 m in azimuth (along flight direction).

The European remote sensing satellites ERS-1, ERS-2, and ENVISAT as well as the Canadian satellite RADARSAT-1 are positioned in a near-circular, polar and sun-synchronous orbit at an altitude of ~790 km. ERS provides in the image mode calibrated high-resolution images of the earth's surface in a range of incidence angles, between 20° and 26° perpendicular to the flight direction, corresponding to a coverage of 100 km x 100 km.

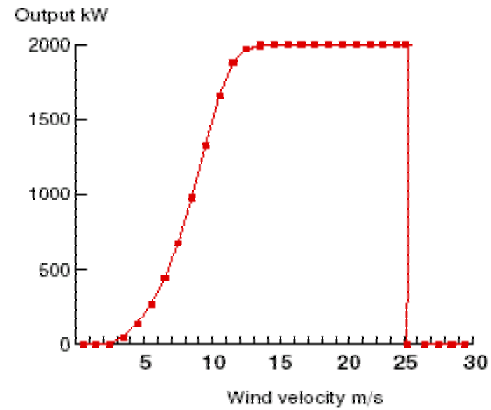


Fig. 5. Energy output of a 2 MW wind turbine for wind speeds from 0 to 30 ms^{-1} (courtesy of ELSAM).

Table 2. Average revisit cycle per 35-day orbit (descending path only).

Incidence Angle	Latitude			
	0°	45°	60°	70°
No Constraints	5	7	11	16
'+/- 5°	3	4	6	9
'+/- 2°	1	1.4	2	3
Exact Repeat	1	1	1	1

RADARSAT-1 ScanSAR and ENVISAT ASAR ScanSAR mode provides an additional wide swath mode with incidence angles between 15° and 50° covering thus a swath width of up to 500 km.

This mode gives the opportunity to get a synoptic overview of large areas, e.g. nearly the entire North Sea. The alternative image mode shows higher resolution and guarantees the continuity of the standards of the ERS SAR data. That way, comparisons with historic scenes are possible and statistics over more than 12 years of wind field data can be undertaken. The revisit time of the ERS satellites was about 11 days caused by the coverage of 100 km x 100 km. With ENVISAT the revisit time in the wide swath mode (450 km x 450 km) is reduced to about 3 days at mid latitudes (Table 2).

5. WIND POWER

Local wind speed is the key parameter for estimating the generating power of a wind farm. The power output is in a first approximation proportional to the cube of wind speed. For an idealized wind turbine with blade diameter D the power yield is given by

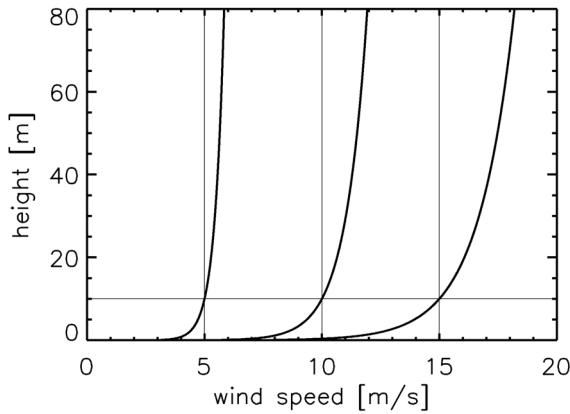


Fig. 6. Vertical wind profiles for U_{10} of 5, 10 and 15 ms^{-1} .

$$\text{power} = \frac{\pi}{8} \rho \cdot D^2 \cdot U^3, \quad (2)$$

where U is the wind speed at hub height and ρ is the air density ($\approx 1 \text{ kg m}^{-3}$). In practice wind converters are limited to a certain range of wind speeds. Typically, wind turbines are operating at wind speeds between 4 and 25 ms^{-1} (see also Fig. 5, output of a 2 MW class turbine). The maximum energy output is reached with wind speeds of more than 13 ms^{-1} . When the wind speed reaches 25 ms^{-1} the wind converters have to be switched off, because of possible damages.

Therefore, special interest is given to the increasing part of the power curve between 4 and 13 ms^{-1} . In this range even small uncertainties in wind speed result in big differences in the estimated energy output.

To estimate the power output of the wind turbines the U_{10} wind speed is extrapolated to the needed hub height. Fig. 6 shows respective wind profiles together with a horizontal line at U_{10} , the height to which the SAR measurements are calibrated. Profiles are given for $U_{10}=5, 10$, and 15 ms^{-1} .

6. SUPPORT FOR OFFSHORE WIND FARMS

The short- and long-term effects of these parks on the environment are not yet well understood. One important parameter that can be observed with space borne SAR is the high-resolution wind field in the vicinity of the wind parks. The SAR enables to investigate changes of the high-resolution wind field due to the wind turbines, e.g. turbulent wakes, as well as ocean surface wave fields.

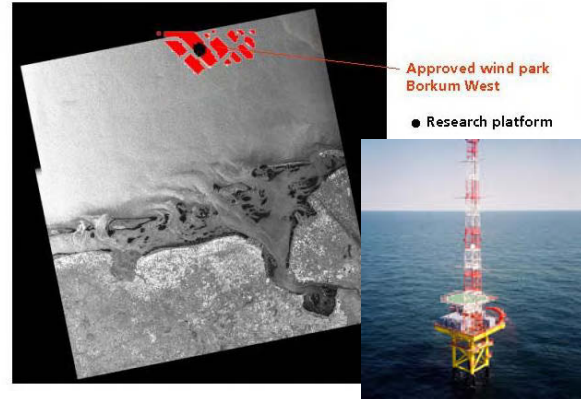


Fig. 7. FINO-platform at offshore wind park site Borkum West (*Forschungsplattformen in Nord- und Ostsee*).

A summary of the state of the art of SAR wave measurements is given in Lehner et al. (this issue). In the near future the first approved German wind park “Borkum West” will be built about 35 km north of Borkum island. In a first step 12 turbines of the 3,5 to 5 MW class will be erected. At this site the research platform *Forschungsplattformen in Nord- und Ostsee* (FINO-I) was installed for logging numerous different parameters like wind speed and wind directions at different heights (Fig. 7). Time series in different frequency scales are logged that support SAR wind measurements and turbulence investigations. This enables small-scale analysis of possible effects on the local wind field like turbulent wakes or wind shadowing (Ainslie, 1988). But also data about air pressure, air temperature, humidity or e.g. rainfall is taken at this station to improve weather forecast that can be used for validating short-term forecasts by SAR. The research platform FINO-I at Borkum West is comparable to the platform at Horns Rev logging data since 1999.

During the planning stage of wind farms SAR retrieved wind fields will help to solve the following issues

- Optimal siting of the wind farm as a whole
- Optimal positioning of wind turbines within the wind farm

For the first point it is helpful to have a long record of historic data, which provide information on the wind and wave parameters relevant for wind farms. Up to now ERS data are available since 1991. Relevant geophysical parameters are

- Mean wind speed and direction – it is clear that a certain minimum of average wind speed is required for economic operation of the wind farm
- Wind variability
- Turbulences induced by the wind turbines and the whole wind park

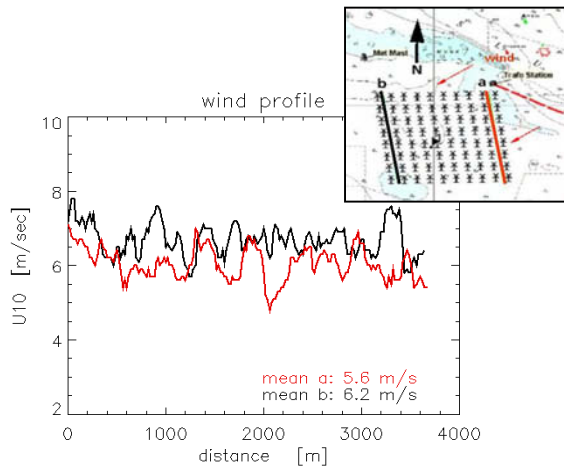


Fig. 8. Profile plot at the wind park Horns Rev. Red line shows first line of the wind park and the black line the last row

Using satellite borne SAR data will offer following opportunities:

- Get synoptic overviews of the wind field.
- Use the possibilities of in situ measurement to improve the wind field algorithms.
- Improve mesoscale models used for short term power forecast.
- Increase the awareness of wind farmers to use remote sensing data in their planning.
- Estimate the effects offshore wind farms have on the environment.

For the offshore wind farming special high resolution regional operational forecasting of metocean conditions is needed (Barthelmie et al, 1996). Additionally, large wind farms will themselves influence the wind field and related parameters, something which has to be incorporated into the operational models.

Strategic siting requires detailed knowledge on the impact of turbines (Mengelkamp, 1999) on the local wind field to

- Optimise the output
- Minimise the impact on environmental conditions

While many studies are on the way, concerned either with improving the technology of wind turbines, e.g., constructing larger and more powerful ones for offshore use, or with environmental issues like the effect on birds and fishery, no joint studies have been undertaken on how this new technology can be assisted by operational forecasting. Similar experience exists in respect to offshore oil industry. Another research aspect is to investigate how these large wind farms alter the wind field and the related processes themselves. With SAR wind measurement high-resolution wind fields can be derived that gives the

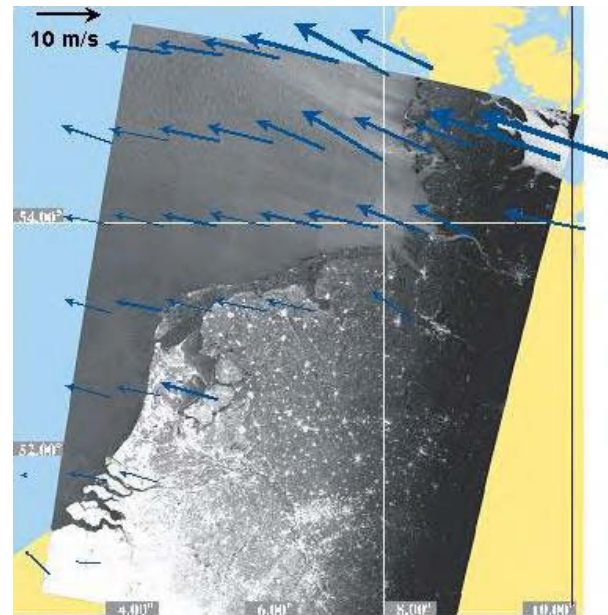


Fig. 9. ASAR wide swath scene with imprinted wind field.

opportunity to look into wind parks to investigate small-scale features like turbulences or shadowing effects. In Fig. 8 two wind speed profiles at the wind farm Horns Rev are shown.

The red line represents the wind speed behind the first row of turbines of the wind park and the black line the last one seen from wind direction. The values are smoothed to 300 m resolution to reduce the influence of speckle of SAR images. The higher wind speed behind the turbines is due to turbulences that increase the near surface wind velocity.

This example shows the possibilities given by the high-resolution SAR wind fields.

7. OUTLOOK AND CONCLUSIONS

For future applications ENVISAT data are available in the same format as ERS. An additional wide swath mode with up to 450 km swath width and 150 m spatial resolution extends the application of this tool to an area covering nearly the whole North Sea in one scene (an example for an ASAR wide swath scene is given in Fig. 9). This gives new opportunities to compare more offshore wind farm sites and validate the results with *in situ* stations located in the images yielding a synoptic overview. Furthermore, due to the larger area covered the repetition rate of the acquisitions is increased to nearly daily measurements. Future missions such as the German TerraSAR-X will guarantee the ongoing of high-resolution radar oceanography after 2005.

8. ACKNOWLEDGEMENTS

A special thanks goes to ELSAM for the permission to use the figure 5. The SAR data were kindly provided by ESA in the frame of an ERS AO.

9. REFERENCES

1. Ainslie J.F. (1988), Calculating the flow field in the wake of the wind turbines. *Journal of the Wind Engineering and Industrial Aerodynamics*, Vol. 27, pp 213-224.
2. Barthelmie R.J., Courtney M.S., Hostrup J and Larsen S.E. (1996) Meteorological aspects of offshore wind energy: Observations from the Vindeby wind farm. *Journal of Wind Engineering and Industrial Aerodynamics*, Vol. 62, pp 191-211.
3. Horstmann J., S. Lehner, W. Koch, and R. Tonboe (2000a), Computation of wind vectors over the ocean using spaceborne synthetic aperture radar, *John Hopkins APL Tech. Dig.*, Vol. 21(1), pp. 100-107.
4. Horstmann J., Koch W., Lehner S. and Tonboe R.. (2000b), Wind retrieval over the ocean using synthetic aperture radar with C-Band HH polarization, *IEEE Trans. Geosci. Remote Sens.*, Vol. 38(5), pp 2122-2133.
5. Horstmann J., Koch W., Lehner S. and Tonboe R (2002), Ocean Winds from RADARSAT-1 ScanSAR, *Canadian Journal of remote Sensing*, Vol. 28, No 3,, pp. 524-533.
6. Horstmann J., H. Schiller, J. Schulz-Stellenfleth, and S. Lehner (2003), Global Wind Speed Retrieval from SAR, *IEEE Trans. Geosci. Remote Sens.*, Vol 41(No. 10), 2277-2286.
7. Horstmann J. and Koch W., High Resolution Ocean Surface Wind Fields Retrieved from Spaceborne Synthetic Aperture Radars Operating at C-Band, this issue
8. Koch W. (2003), Directional analysis of SAR images aiming at wind direction, *IEEE Trans. Geosci. Remote Sens.*, accepted.
9. Lange B., Hostrup J., Larsen S.E. and Barthelmie R.J. (2001). A fetch dependent model of sea surface roughness for offshore wind power utilisation. *Proc. of the Europ. Wind Energy Conf.*, Copenhagen, Denmark, pp, 830-833.
10. Lehner S., Horstmann J., Koch W. and Rosenthal W. (1998), Mesoscale wind measurements using recalibrated ERS SAR images, *J. Geophys. Res.*, vol. 103, pp. 7847-7856.
11. Lehner S. and Ocampo-Torres S.J., Radar Measurement of Ocean Waves, this issue
12. Lehner S., Schulz-Stellenfleth J., Schättler B., Breit H. and Horstmann H. (2000), Wind and Wave measurements using complex ERS-2 wave mode data, *IEEE Trans. Geosci. Remote Sens.*, Vol. 38(5), pp 2246-2257.
13. Lehner S., Schulz-Stellenfleth J., Horstmann J. (2001a), Marine parameters from radar satellite data, *Archive of Hydro-Engineering and Environmental Mechanics*, Vol. 48, no 2, pp 17-29.
14. Lehner S., and J. Horstmann (2001b), High Resolution wind fields retrieved from spaceborne synthetic aperture radar and numerical models, *Proc. of Offshore Windenergy Conference*, Brussels, Belgium.
15. Mengelkamp T. (1999), Wind climate simulation over complex terrain and wind turbine energy output estimation, *Theoretical and Applied Climatology*, Vol. 63.
16. Stoffelen A. and Anderson D. (1997), Scatterometer data interpretation: Estimation and validation of the transfer function CMOD4, *J. Geophys. Res.*, Vol. 102, pp. 5767-5780.
17. Wackermann C.C., Rufenach C.L., Shuchman R.A., Johannessen J.A. and Davidson K.L. (1996), Wind vector retrieval using ERS-1 synthetic aperture radar imagery, *IEEE Transactions on Geoscience and Remote Sensing*, 34, pp. 1343-1352

Wave Session

Chairs: S. Lehner & F.J. Ocampo-Torres

**This page intentionally
left blank (pagination)**

THE SAR MEASUREMENT OF OCEAN WAVES: WAVE SESSION WHITEPAPER

S. Lehner⁽¹⁾ and F. J. Ocampo-Torres⁽²⁾

⁽¹⁾*DLR, Oberpfaffenhofen, D 82230 Wessling, Email: Susanne.Lehner@dlr.de*

⁽²⁾*CICESE, Ensenada, BC 22860, México, Email: ocampo@cicese.mx*

ABSTRACT

Remote sensing techniques enable the measurement of ocean wave fields with both high resolution and large coverage. As the acquisition of active radar data is independent of daylight and cloud conditions, these data are therefore believed to be most suited for operational use at weather centers and governmental agencies, as well as for many ongoing scientific investigations. In the present overview paper the determination of sea state parameters from radar images together with some results from the operational use at weather centers are given.

Synthetic aperture radar (SAR) yields high resolution two dimensional images of the radar backscatter properties of the sea surface and can thus be used to measure wind fields and sea state from space.

The determination of ocean wave spectra from SAR

image spectra is sensitive to various imaging effects due to sea surface features, spatial variation of wind speed, rain, current and motion of the sea surface. Thus, measuring ocean wave parameters is related to most of the other measurements of marine parameters described in this volume.

In this paper an overview of the SAR satellite missions is given, as well as a description of the basic techniques to measure ocean waves by SAR and validation against wave model results and other space borne and in situ measurements.

The full two dimensional SAR image spectrum provides information on the directional ocean wave spectrum. This can be used to determine expectation values of, e.g., significant wave height, mean wavelength and direction in order to improve the wave model prediction. In addition information can be gathered from the radar images directly such as individual wave height, crest length and groupiness of the ocean waves. Thus, the distribution of maximum wave height can be investigated globally, or wave refraction and diffraction in coastal areas can be studied in detail.

In the following an overview of ocean wave measurements from space are given, the papers presented in the wave session are put into the general context and applications for weather prediction, ship routing, oil and shipbuilding industry and ship classifying societies are discussed.

A general overview on theory and measurement of directional wave spectra, including a special chapter on remote sensing of directional ocean wave spectra together with an extensive literature list is given in the COST Book (2004).

1. INTRODUCTION – MISSION OVERVIEW

In this section mainly the SEASAT, ERS and ENVISAT missions are discussed. Although data analysis of the shuttle missions and several aircraft experiments yielded new results on the spatial

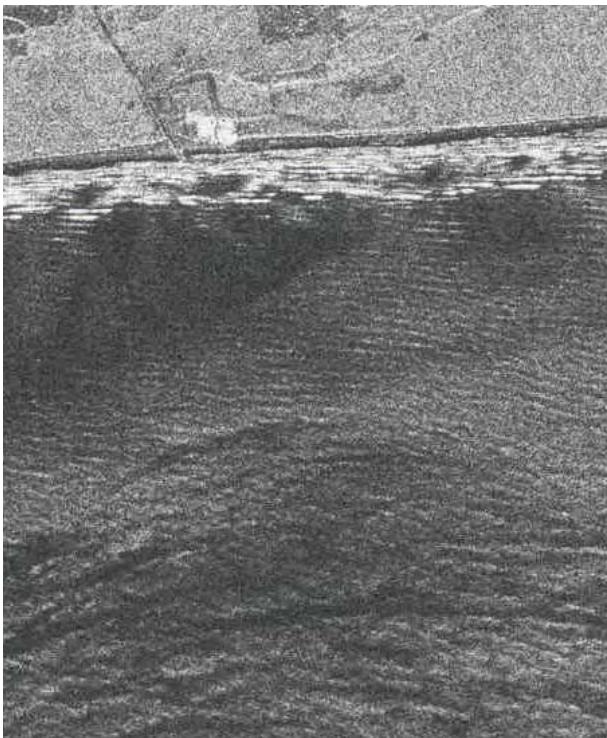


Fig. 1: 10 x 15 km cutout from a SEASAT SAR image acquired on 20 Aug 1978 at the Portuguese coast showing swell refraction, wave breaking and internal waves.

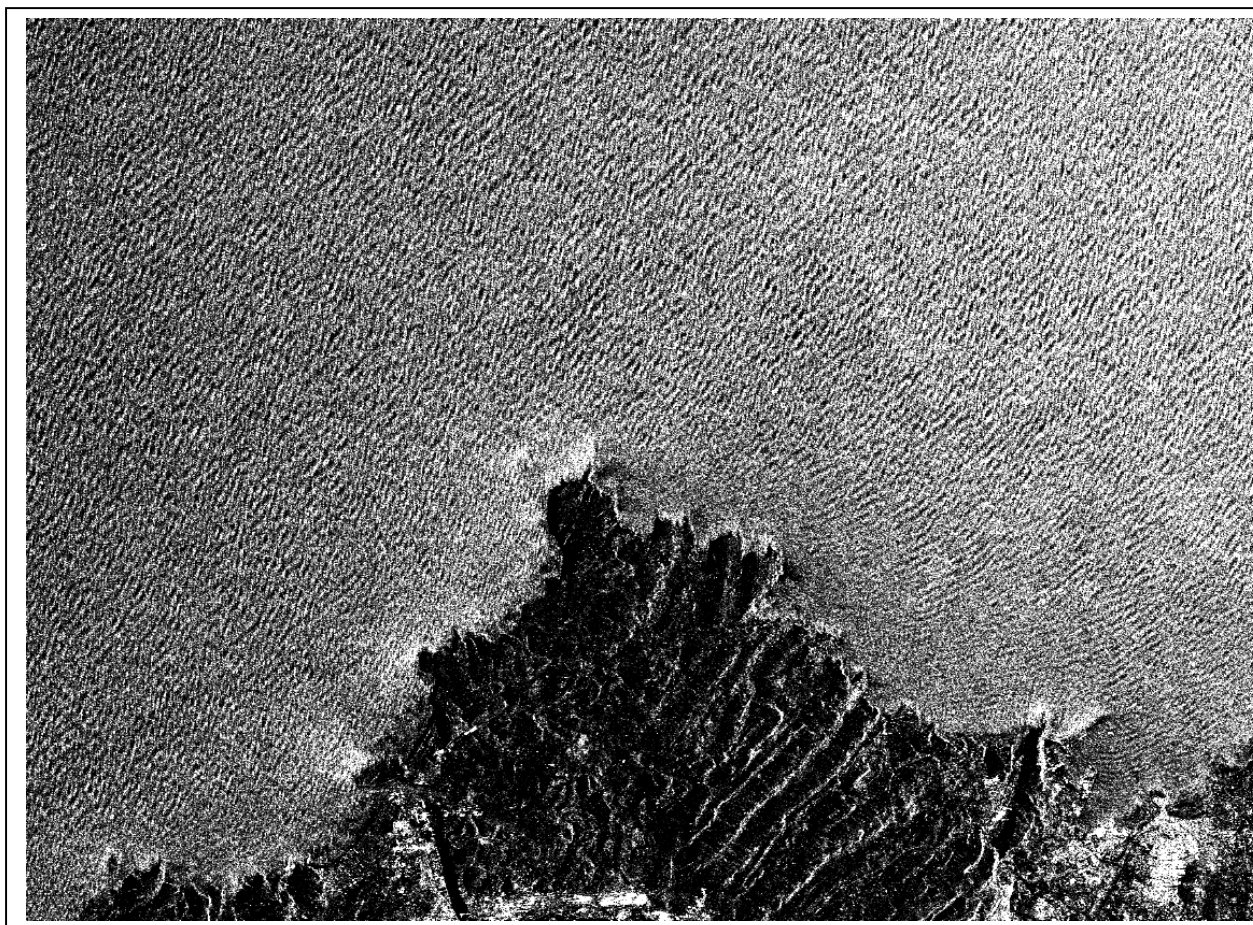


Fig. 2: 30x20 km² cutout of an ERS SAR image taken in the vicinity of Cabo de Peñas (Northern Spain).

behaviour of ocean waves and new radar sea state measurement algorithms, these missions can mainly be regarded as preparation for satellite missions and their operational applications.

1.1 THE SEASAT MISSION

Before the first oceanographic radar satellite SEASAT which operated in L Band in the 30 cm wavelength range, was launched in 1978, many scientists (amongst them radar experts) doubted, that its images would show ocean waves. Radar processing was still done optically, e.g. at ERIM, using conical lenses on long strips of film. It was considered a new quality of sea state measurement capabilities, when the SEASAT films not only showed ocean wave like structures, but by using a series of digitised images along the film it could be shown, that these waves by their direction and wavelength could be traced back to storm centers, that had generated them (Lehner, 1981).

The first digitally processed 30 x 30 km SEASAT SAR images, that still needed 8 hours processing time each,

gave the opportunity to develop and validate first SAR imaging algorithms and study individual ocean wave refraction patterns. Fig. 1 is a 10 x 15 km subimage of a digitally processed SEASAT image from the Portuguese Coast, acquired on August 20th, 1978, showing swell refraction, breaking waves and internal wave patterns. Generally, the SEASAT L-Band data show very distinct features of ocean waves, internal waves and bathymetry. Results were, e.g. published by Beal (1983), Kasischke (1983).

1.2 THE ERS-1/2 MISSIONS

After the rather short lived SEASAT mission, data from the next continuous spaceborne mission were only available 13 years after SEASAT with the launch of the European Remote Sensing Satellite ERS-1 in 1991.

In between data from several aircraft and shuttle missions, e.g. SIR B in 1984 and SIRC/X SAR in 1994 were used for further development of ocean wave measurements by spaceborne SAR, see e.g. Gerling

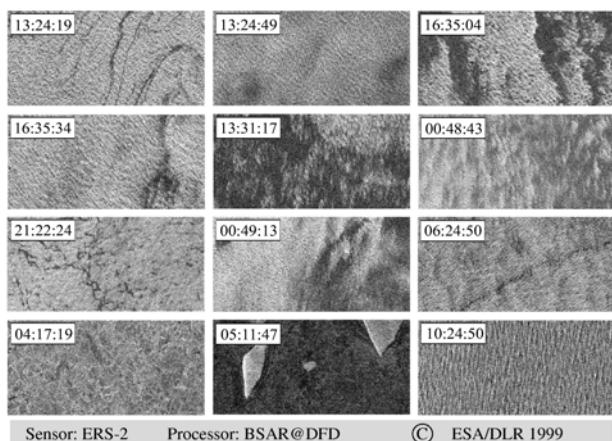


Fig.3: ERS-2 Wave Mode Images showing sea surface features.

and Beal, (1992), Beal et al. (1986), Monaldo and Beal, (1988) and Melsheimer et al., 1998.

The ERS-1, C-Band mission yielded SAR images of ocean waves longer than about 100 m wavelength, depending on propagation direction, with certain restrictions when imaging ocean waves in flight (azimuth direction) due to tilt and motion effects. ERS-1 was followed by the almost identical satellite ERS-2 launched in 1995, which is still operational today. Together the ERS SAR data now cover global ocean wave measurements for over 13 years, which can now be analysed for decadal variations.

ERS SAR images of 100 x 100 km size are available in the so called ERS SAR image mode, at a high resolution of 30 m. This mode can only be acquired, when the satellite is in line of sight of a receiving antenna station, due to onboard storage capability. Fig. 2 shows a 30 by 20 km sub-image of the Spanish North Coast near the harbour of Gijon showing wave refraction and wave reflection at the mountainous coast. This SAR image mode has been very successfully used in many coastal applications like offshore wind farming, coast line detection, sediment transport, current feature determination and ship and harbor security.

For global ocean wave measurements additionally, the so called wave mode was defined, that yields global measurements of two dimensional SAR image spectra.

The ERS wave mode consists of 5 x 10 km SAR images at the same high (30 m) resolution as in image mode, but is acquired only every 200 km along the satellite track. The data are stored onboard, and are transmitted when in line of sight of an antenna station (Kiruna, MasPalomas). They thus yield the first global coverage of the oceans with radar images. For the use

at weather centers only the rather coarsely girded image spectra (UWA spectra) were sent in real time to the centers, to improve ocean wave prediction. One of the main applications of ERS SAR data was considered to be the improvement of spectral wave models like, e.g., the WAM model (the WAMDI group, 1988). WAM is running operationally at ECMWF, where assimilation of satellite SAR spectra is used.

Due to data handling capacity limits, the small wave mode images are not kept as an official ESA product and only the raw data are stored in a permanent archive. In new studies these radar raw data sets are being reprocessed and analysed for image information like sea surface features, sea ice, storm tracks and individual ocean wave features (Lehner et al., 2000; Horstmann et al., 2003). In Figure 3 a number of such reprocessed ERS wave mode images on which surface features were detected by an automatic inhomogeneity test are shown. These features are caused by low wind speed below 3 m/sec, i.e. the breakdown of the short Bragg waves, sea ice (frazil and pancake) or icebergs. The homogeneous image in the lower right corner is given for comparison.

Data from the RADARSAT mission, launched in 1995, were mainly used for investigations in coastal areas (Vachon et al, 1995, Ocampo-Torres, 2001). One of the main applications of the RADARSAT mission is on the Scan SAR mode, which is more geared towards ship, oil slick and sea ice detection and wind field determination (see Monaldo and Kerbaol this issue).

1.3 ENVISAT ASAR

In March 2002 the ENVISAT satellite was launched, which carries as sensors the ASAR, the spectrometer MERIS, the altimeter RA and the passive microwave instrument AATSR, that represent the main fields of ocean remote sensing and thus a new synergistic use of wind field and ocean wave measurements together with geo-biological parameters derived from MERIS is possible for the first time.

Furthermore an improved wave mode has been installed for the ENVISAT ASAR. The wave mode images themselves, acquired in the ENVISAT mission every 100 km along the satellite track are now available as a standard ESA data product, yielding up to 2500 radar snapshots of the oceans globally every day.

In addition the ASAR on ENVISAT can acquire data in a Scan-SAR mode, which gives the possibility to monitor the sea surface on a larger, 400 x 400 km scale. This yields new insight into the mesoscale wind field used as input for wave models. Due to the much

coarser resolution though, Scan SAR mode does not give the possibility to study wind fields with the high resolution needed for impact studies in offshore wind farming, ocean wave measurements or coastal studies. Some new research interest is directed into processing SLC Scan SAR images with high resolution in range direction, which then allows to study the development of ocean waves over a fetch of 500 km in range direction.

2. SAR IMAGING OF OCEAN WAVES

In order to make optimal use of the SAR image information several algorithms were developed relating sea surface height to SAR image intensity.

Common SAR imaging forward models, relating the modulation I_m of a SAR image I to the sea surface elevation η consist of the following parts :

- Determination of radar cross section from backscatter of a rough ocean surface, e.g., by specular reflection and Bragg scattering,
- A real aperture radar (RAR) modulation model, which explains the modulation of the radar cross section by ocean waves.
- A velocity bunching model, which explains the impact of sea surface motion on the SAR image formation process.

An overview of the backscattering mechanisms is given in Valenzuela, (1978), Plant and Keller (1983), Plant (1990), Elfouhaily (2001) and Kudryatsev et al., 2003.

RAR modulation is a combination of many different effects. In its simplest form it is described by a two scale model of the ocean surface, the backscattering short ocean waves which are in the range of the radar wavelength and the modulating long ocean waves.

A first imaging algorithm explaining the modulation by tilt effects due to long ocean waves and hydrodynamic interaction of short and long waves was developed by Schieler (1977), Rufenach (1979), Alpers and Rufenach (1981) and Hasselmann et al. (1985). The model is valid for the case of a linear superposition of a Gaussian wave field and RAR function and thus valid mainly for low to moderate sea states.

Validation of the RAR part of the forward function took place, e.g. on the North Sea platform (Hara and Plant, 1984; Feindt et al., 1986; Caudal and Hauser, 1996 and Schmidt et al., 1995). Data from these experiments showed strong scatter of intensity and phase of the RAR modulation function. Most recent

results from wave tank experiments are given in Plant et al., 1999.

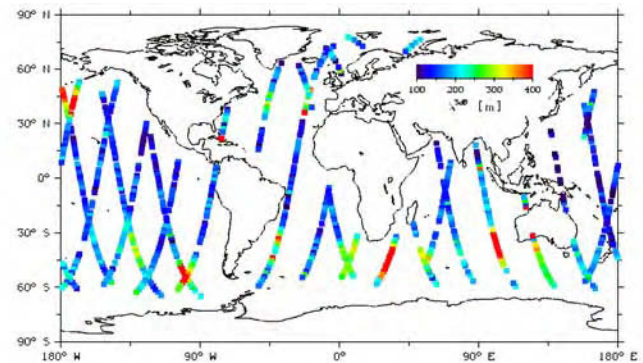


Fig. 4: Cutoff Wavelength derived from ERS wavemode data for October, 12th, 1996.

Conventional ship radars can be used as an ocean wave measuring device. Recently X-band (real aperture) marine radar has been used to investigate radar backscatter of ocean waves (Dankert and Rosenthal, 2004). In particular this technique allows to study the real aperture radar backscatter of the sea surface on a sequence of radar images.

SAR imaging of a stationary surface is discussed in Bamler et al. (1991). As the high resolution of a SAR is achieved by recording intensity as well as phase and by taking the Doppler shift of the backscattered signal into account, motions of the sea surface lead to radar imaging effects. The main characteristics of the mapping relation is a low pass filtering of the SAR image spectrum in the azimuth direction. This so called azimuthal cut-off leads to information loss on shorter waves traveling in flight direction. A global map of the cutoff wavelength derived from ERS wavemode data for October 12th, 1996 is shown in figure 4.

This effect was explained by Alpers and Rufenach (1979) and Hasselmann et al. (1985) as velocity bunching and acceleration smearing due the orbital motion of the long ocean waves affecting the SAR image spectrum. Further SAR imaging models were presented by, e.g., Romeiser (1994) extending the model to three scales, and Lyzenga (1986) adding edge scattering. Kudryatsev et al. (2003) give a general overview of the existing theory on backscattering, adding breaking and parasitic capillaries as additional processes contributing to the backscatter.

Further developments of a SAR forward model are based on non Gaussian sea surface models, e.g. Gerstner waves (Fouquet et Krogstad, 2003). Due to the many effects contributing to the radar backscatter, research is ongoing.

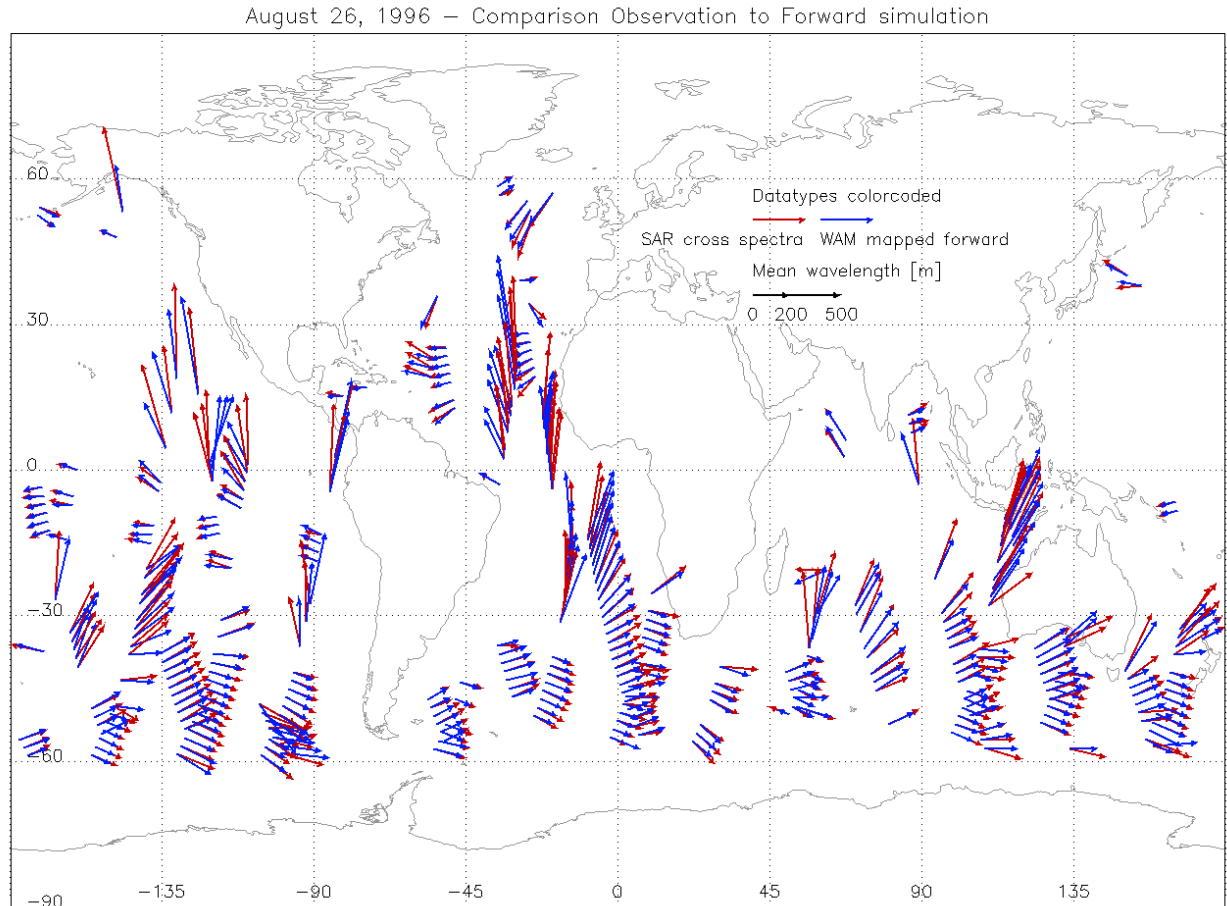


Fig. 5.: Mean wave length derived by forward mapping of WAM spectra (blue) into simulated SAR spectra (red) for a global wave mode data set.

In order to identify areas or weather situations in which the SAR observation differs from an ocean wave model like WAM and thus to identify areas in which the model consistently does yield different results to observations, the forward mapping of the WAM model spectra into SAR image spectra was analysed on a statistical basis. This forward mapping (FOMAP) is usually the first step of an inversion procedure, followed by an optimisation. Instead of comparing the two spectra in the space of the ocean wave spectrum, in FOMAP the comparison is done in the SAR observation space, making this a straightforward technique to identify inconsistencies between SAR measurements and numerical model results. A first systematic analysis of this approach (FOMAP) was presented in Hoja et al., (2002).

Fig. 5 shows a comparison of mean wave length derived from the SAR image variance spectrum (red) and the WAM spectrum mapped forward into a simulated SAR observation (blue) for one day of wave mode measurements, August, 26th, 1996. The arrows

are plotted in mean direction. Agreement in mean wavelength and direction as observed in the SAR measurement is very good, not a large additional input can be expected from the SAR measurements. That is these mean parameters like mean wavelength and direction are well captured in WAM. In Hoja et al., 2002 statistics for a three week dataset during southern winter are given. The SAR cross spectra observations show consistently a slightly longer mean wavelength than the WAM spectra. The variation in cross spectra shows larger deviations between WAM and SAR of both signs, especially in severe weather situations.

3. INVERSION ALGORITHMS

In the previous section the mapping of sea surface height into SAR images is discussed. For applications at weather centers an algorithm to derive two dimensional ocean wave spectra from the UWA SAR image spectra that works in real time is needed.

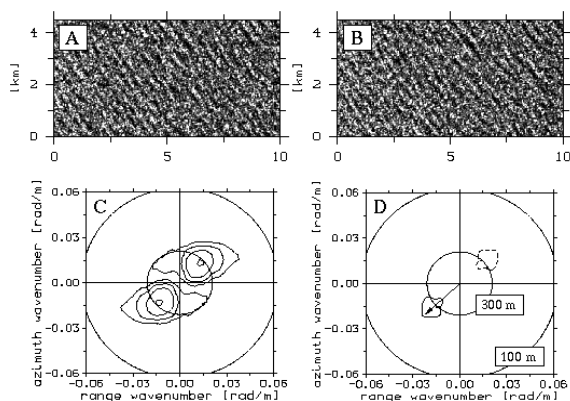


Fig. 6 Multilooking technique shown for ENVISAT ASAR wave mode data together with the cross spectrum.

The first algorithm derived, taking nonlinear imaging effects into account, is the so called ‘first guess inversion’ MPI-1 algorithm, that was developed by Hasselmann and Hasselmann in 1991 and redescribed by characteristic functions by Krogstad (1992). In adapted forms (MPI-2) the algorithm is still in use at the ECMWF for the inversion of ENVISAT ASAR data.

To derive information on ocean waves shorter than the cutoff wavelength, a first guess from a wave model is used together with the SAR information in order to obtain the complete two dimensional ocean wave spectrum.

Global applications of the algorithm was demonstrated by Brüning et al. (1994), Hasselmann et al (1994), Krogstad et al (1994) and Heimbach et al (1998). The inverted wave model data are used for validation of daily forecasts, e.g. at the UK and French Met Offices (Lotfi and Lefevre, 2003), for assimilation at ECMWF (ECMWF Report, 2002), as well as for various applications, e.g. ship routing purposes (Lehner and Hasselmann, 1995).

With the inversion procedures as described above, the possibility of using SAR imagery to measure ocean wave spectra is thus restricted to the limited number of institutions, that have a sophisticated wave model available as first guess. For general use and coastal applications it is desirable to be able to deduce sea state parameters from SAR images without having to use a first guess from a wave model.

Mastenbroek and de Valk (2000) developed a spectral inversion algorithm, the so called SPRA scheme, that would use only the SAR image spectra as input. Instead of taking a model wave spectrum as a first guess the missing information on the wind sea is derived from the scatterometer wind vector

measurement, that is available simultaneously on the ERS satellites. The main advantage of the method is, that wave measurements could be performed independent from a sophisticated wave model providing a first guess and global input wind fields as only available at weather centers.

Thus in the SPRA algorithm instead WAM spectra being used as a first guess, the inherent simple wave model consists of deriving a parametric JONSWAP type wind sea spectrum in which wave age is fitted from the available scatterometer wind vector. The performance of the SPRA algorithm therefore depends on the quality of the SCAT wind vector and the validity of the assumption of a fully developed sea.

The SPRA paper presented as well a first comparison to buoys, showing some difficulty of the MPI-1 algorithm to retrieve significant wave height accurately. The reason was later detected to be due to problems with the spectral calibration routine, which in turn led to an improvement in the MPI-2 algorithm at the weather centers. Numerical results from SAR inversion algorithms in articles published before 2000 thus have to be considered with care.

4. CROSS SPECTRA ALGORITHMS

From the complex images cross spectra can be derived, by multilooking technique. Standard multilooking basically yields two SAR images of coarser resolution images instead of one that are separated by a short time interval (order of one second). The cross spectrum of the two looks contains in the imaginary part information on the propagation direction of the ocean waves (Engen and Johnson, 1995).

Figure 6 shows an example of the derivation of an image cross spectrum. These cross spectra are as well the basis for a new inversion algorithms (Johnson, 2003, and this issue) and are the only ESA level 2 (i.e. geophysical) product for ENVISAT. In the ESA algorithm for derivation of ocean wave spectra from ENVISAT image spectra only the local wind speed vector is used as additional input, similar as in the SPRA algorithm. As ENVISAT does not have a

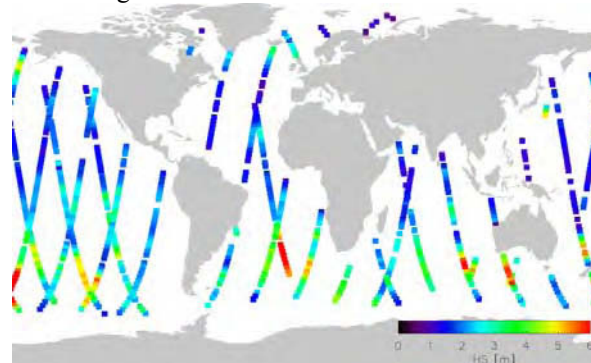


Figure 7. Significant wave heights estimated from a global data set of complex ERS-2 imageries ($10 \times 5 \text{ km}^2$) acquired on September 5, 1996 using the PARSA retrieval scheme.

scatterometer on board, the wind vector is usually taken from a wind field derived again at a weather center. Validation of the algorithm is ongoing.

Another algorithm making use of the cross spectra information is the PARSA algorithm developed by Schulz-Stellenfleth and Lehner (2003). Partitioning of the different wave systems and subsequent inversion is used in order to improve the wave model spectra. PARSA is described in a separate article in this issue (Schulz-Stellenfleth and Lehner). Figure 7 shows a map of significant wave heights derived from the PARSA algorithm applied to the ERS-1 SAR image wave mode data acquired on September 5, 1996. Validation of the ESA and PARSA algorithms are ongoing.

During the last decade, performance of ocean wave models has been improved at weather centers, due to information on sea state from satellite altimeter data, and an improved input wind field, which especially in the southern hemisphere has become much more accurate, due to scatterometer measurements. Standard mean parameters as derived from SAR spectra like significant wave height or mean direction and wavelength are usually well predicted by the WAM model for ocean waves longer than 100 m in time intervals of several hours (6h). In severe weather situations though, differences up to several meters in significant wave height can occur.

A rigorous inter-comparison of the different spectral algorithms and inter-comparison to buoy and other remote sensing data still needs to be undertaken. For this purpose a new buoy collocation dataset of more than 300 000 points has been made available on the IFREMER web site.

5. COASTAL STUDIES AND VALIDATION EXPERIMENTS

A number of SAR aircraft campaigns have been undertaken in order to assess the performance of the satellite sensors or to design new missions. Several papers dealing with the MARSEN experiment, which took place near the island of Sylt in the German Bight in 1979 were already discussed in the SAR imaging section. Here, only the most recent experiments will be discussed. New developments are the investigation of multipolarisation images and the use of several receiving antennas in the interferometric mode. Experiments are the SINEWAVE experiment (Schulz-Stellenfleth and Lehner, 2001) in the North Sea, near Heligoland, the Gijon and VALPARESO experiment. Further details on interferometry are given in the white paper of the current section (Romeiser and Ufermann, this issue).

In 2002 the VALPARESO ENVISAT ASAR validation experiment an airborne polarimetric radar was flown near the coast of Brittany during ENVISAT overflights (Hauser et al., 2003). One purpose was to validate the polarimetric image mode of the ASAR sensor.

Ocean wave behaviour in coastal areas is more difficult to predict than in the open ocean. With the development of new high resolution wave models like, e.g. the K-model (Günther et al 2002), further new applications for SAR measurements are supposed to be validation of wave models in coastal areas. Furthermore information on rather variable input fields like wind fields, topography and currents can be retrieved from the SAR images.

Several nearshore applications are based on measurements at the North Sea oil platforms, where many in situ measurements are available. SAR images yield the opportunity to measure the variability of the ocean wave field in respect to significant wave height, wave groupiness and individual wave height around the oil platform and, e.g., investigate the 'near misses' of particularly high ocean waves.

At the sea ice boundary ERS SAR images were e.g. used to analyze the damping of short ocean waves by sea ice (Schulz-Stellenfleth and Lehner, 2001) and thus derive information on the sea ice thickness.

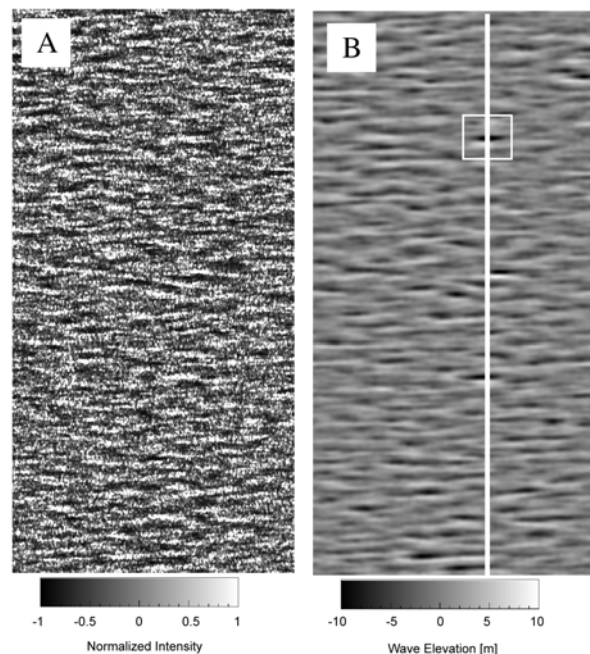


Fig. 8: ERS-2 wave mode image (left) and corresponding sea surface elevation field (right) computed with the LISE inversion scheme.

Further validation of ERS SAR two dimensional ocean wave measurements using HF radar (Lehner, 2003) and marine radar (Dankert, Nieto, 2004) in coastal areas is in progress.

6. INDIVIDUAL WAVE HEIGHT

In the past 10 years more than 200 large ships have been lost the reason is believed to be encounter of high individual waves (Lotfi et al, 2003). In the MAXWAVE project (Rosenthal and Lehner, 2004) the global distribution of extreme sea states and related ship accidents were investigated. While some accidents are known to happen in areas of strong currents due to steepening and focussing the waves, others were related to extended storms, crossing seas or moving fetch conditions.

Many of these accidents happen in areas where no other, but satellite measurements are available. Analysis of the SAR image information is thus used to gain insight into the distribution of individual wave height and to derive information on single ocean wave parameters (Rosenthal et al., 2003). Due to the availability of the global SAR wave mode images from ENVISAT and recent image analysis methods a new focus in SAR ocean wave research is on these individual ocean wave properties like individual wave height (Schulz-Stellenfleth and Lehner, 2004), crest length (Monaldo, 2000) and grouping of waves (Dankert et Rosenthal, 2003, Nieto Borge et al., 2004).

The inversion technique to derive the sea surface from SAR images takes the transfer functions described above in order to obtain wave elevation maps. The inverted radar images or radar-image sequences are then used for the investigation of the behaviour of single wave, extreme waves and wave groups.

Fig. 8 shows an example of a wave elevation map derived from the inversion scheme of an ERS-2 SAR imagette using the LISE method (Schulz-Stellenfleth et Lehner, 2004). The square in the right part of the figure (the wave elevation map) locates the highest wave within the imagette area.

SAR derived sea surfaces can, e.g. be used as input for the simulations in numerical wave tanks, for which information on realistic and two dimensional sea surfaces is lacking (Wouter and Bittner Gregersen, 2003). Up to now only information from a buoy is used to reconstruct the sea surface.

Global statistics of individual wave height as well as of mean spectral parameters are needed in wave ship design and classification.

7. GROUPING OF OCEAN WAVES

Wave groups play an important role for the design and risk assessment for offshore-platforms, breakwaters or ships, because successive large single wave crests or deep troughs can cause severe damages due to their impact, or they can excite the resonant frequencies of the structures. For ships, an encounter with wave groups can sometimes cause capsizes or severe damage. An extreme wave can develop from a large wave group due to interference of its harmonic components.

Using wavelet analysis of individual transects extracted

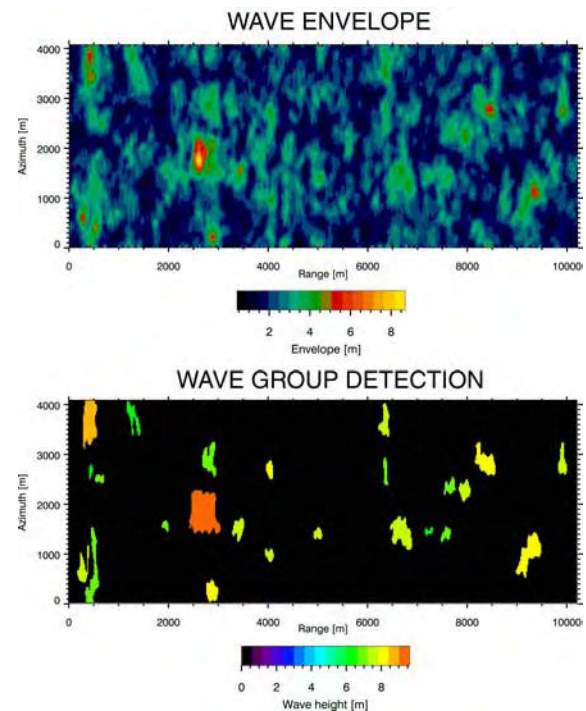


Fig. 9: Wave groups derived from envelope determination by Hilbert transform

from SAR images of the coastal region the grouping of the ocean wave field has been detected (Ocampo-Torres 2001).

For the derivation of groupiness from SAR images in two dimensions two different algorithms have been developed. One is based on using Hilbert methods to determine the ocean wave envelope (Dankert et al 2003, Nieto Borge et al., 2004), the other one is based on a wavelet decomposition technique to detect the borders between areas of different intensity within the SAR image, thus detecting and grouping wave crests (Niedermeier et al., 2004).

In the upper part of Figure 9 a wave envelope of SAR derived sea surface elevation is shown, in the lower part the corresponding wave groups are detected.

8. INTERFEROMETRIC MEASUREMENTS

Interferometric SAR (InSAR) measurements are based on the combined use of complex images acquired by different SAR antennas. Information about sea surface elevation, orbital velocity and currents are derived

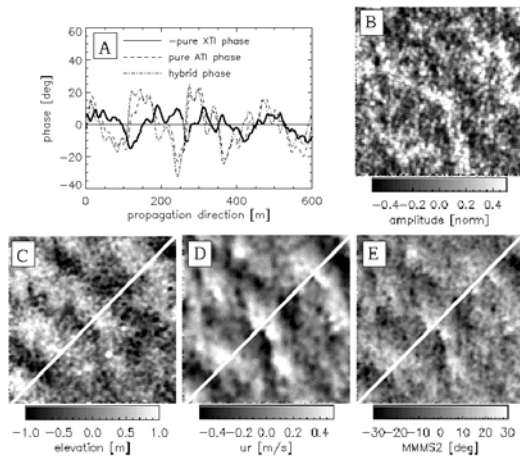


Fig. 10: Interferometric data acquired by a three antenna airborne InSAR system during the Gijon experiment.

from the corresponding interferograms. For measurements of the sea surface topography single pass interferometry, for which the antennas are mounted on the same platform, has to be used, since the correlation time of the sea surface is about 50 ms. The SAR antennas are arranged either in flight direction, along track (ATI) or on both sides, i.e. across track (XTI) configuration.

In the along track InSAR configuration the images are acquired with a time offset (depending on the speed of the aircraft and the interferogram thus contains information on the orbital velocity and currents. The ocean imaging capability of such a system has been investigated, e.g., in Ainsworth (1995). For further details on ATI current measurements see the overview paper on currents (Romeiser), this issue.

The two main conclusions in respect to the ocean wave imaging from interferometric studies as given in Schulz-Stellenfleth and Lehner are:

- Like in conventional SAR imaging interferometric data are affected by a cutoff in the flight direction.
- Interferometric data are much less dependent on the RAR modulation mechanism than conventional SAR imagery. As only rough estimates exist for the RAR MTF, this is an advantage of InSAR data.

When acquired under realistic conditions, interferograms in most cases contain a mixture of along and across track components (hybrid interferograms). To decouple the different contributions one can e.g. fly perpendicular tracks with a dual antenna system. This is a method to measure currents as described for a North Sea experiment in Siegmund et al., 2004. Another option is to use a three antenna system to measure ocean waves. This method was first demonstrated in the Gijon experiment (Lehner et al., 2004). In Fig. 12 a result of such a three antenna system is shown, the images show the intensity, the across and the along track component from the phase images. Thus the relation between backscatter, elevation and current can be investigated, yielding, e.g., information on the phase of the Real aperture radar modulation.

9. OUTLOOK AND CONCLUSIONS

The spaceborne SAR missions ERS1/2 and ENVISAT have been imaging the oceans on a global and continuous basis, collecting a dataset of 1500 to 2000 images of the oceans of 5 x 10 km size every day for since 1991. It is intended to use this large dataset in studies looking at decadal change of wind fields, sea state and sea ice parameters.

These images show ocean waves from about 100 m wavelength, dependent on travel direction.

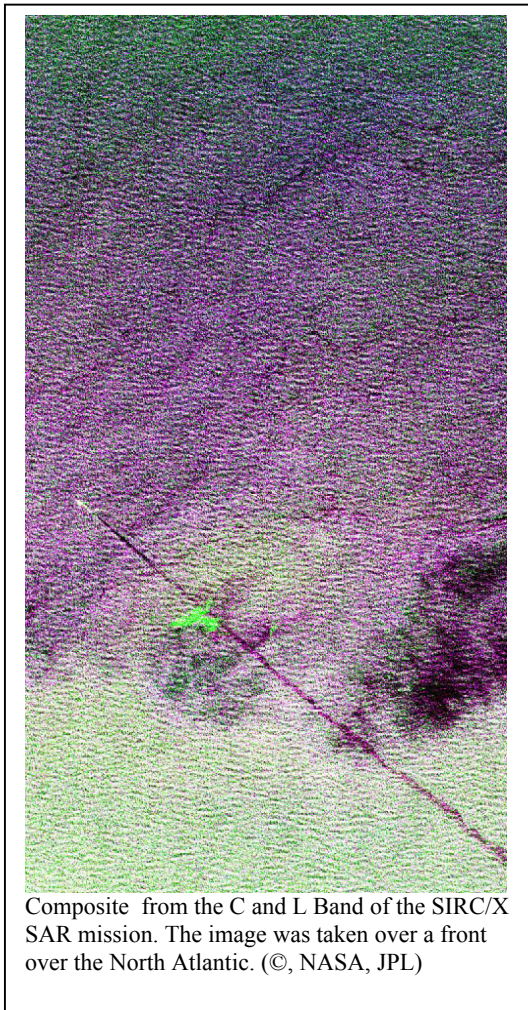
While derivation of mean ocean wave parameters from SAR image spectra is already an operational issue at weather centers, SAR measurements of individual ocean waves is still a fast developing and debated field.

From the ERS missions only rather coarsely grided image spectra were available from ESA, from the ASAR on ENVISAT full image information and image cross spectra are available. Several algorithms were developed to derive ocean wave spectra from this information. At ECMWF results from the MPI inversion algorithm are assimilated into the WAM model. The official ESA level 2 products are still being validated, improvement of the algorithm is under validation. Detailed results from the ESA algorithm and the PARSA algorithm are discussed in this issue (Johnson et al., Schulz-Stellenfleth et al).

An intercomparison of these new cross spectra algorithms using collocated buoy dataset is planned.

Up to now mainly two dimensional spectra were derived from SAR images. The analysis of SAR images in the spatial domain is of new interest due to the availability of global wave mode image information from ENVISAT.

Polarimetric images of the sea surface are analysed, this yields new information on, e.g., breaking waves. Using several SAR antennas information on currents and orbital velocity can be gained using along track interferometry (ATI) and on individual wave height using across track interferometry (XTI). Investigations are based on aircraft experiments, which are preparing for future missions. Results on the relation between sea surface height and movement are to be expected from such datasets.



TerraSAR-X is a follow up high resolution SAR mission, to be launched 2006, see Lehner and al., this issue. This mission yields a resolution up to 1 meter in SPOT light mode and has a full polarisation mode. TerraSAR-L is in the planning phase (Drinkwater, this issue). Several studies (e.g. Schmidt et al. 1995) indicated that L-Band is particularly well suited to measure ocean waves.

New algorithms to derive wind field and sea state parameters described in this paper are based on C-Band

radar imagery. For these new missions the wind and wave algorithms have to be transferred from C-Band to X- and L- band. For this task the existing SEASAT L and SIR-C/X-SAR data can be re-evaluated, using the advanced algorithms that are available today.

The high resolution needed for ocean wave imaging is usually not met in Scan SAR mode. For ocean wave measurements the SAT image mode is preferred in near coastal areas and SAR wave mode on the oceans. For Scan SAR images, which are acquired due to other requests such as oil spill monitoring a new Scan SAR product with high range resolution is under investigation. These images will at least contain information on range travelling waves.

Thus SAR image data yield insight into the two dimensional behaviour of ocean wave field in the spatial domain. These data are available in extreme weather events in areas, where they could not be observed before, like the ocean around Antarctica. SAR images from this area helped to derive new concepts of the sea surface, the development of high crests and breaking and grouping of waves. For practical purposes at operational weather centers, SAR image spectra can be inverted to ocean wave spectra and used to validate and improve model output. Many users like government agencies, ship classifying societies, ship builders and owners and transport industry are still not familiar with remote sensing data and need in a first step just some simple tools to visualize the daily stream of data like 2000 ENVISAT images a day.

10. REFERENCES

1. Ainsworth, T., S.Chubb, R.Fusina, R. Goldstein, R. Jansen, J.-S. Lee and G. Valenzuela, "INSAR Imagery of Surface Currents, Wave Fields and Fronts, IEEE, TGARS, vol 33, n 5, pp. 1117—1123, 1995
2. Alpers, W. R., Rufenach, C.L., The effect of orbital motions on synthetic aperture radar imagery of ocean waves, IEEE Trans. Antennas Propag., Vol 27, pp. 685-690, 1979
3. Alpers, W. R., Ross, D.B., Rufenach, C.L., On the detectability of ocean waves by real and synthetic aperture radar, J. of Geophys. Res., Vol 86, pp. 6481-6498, 1981
4. Beal, R.C., Monaldo, F.M., Tilley, D.G., Irvine, D.E., Walsh, E.J., Jackson, F.C., Hancock III, D.W., Hines, D.E., Swift, R.N., Gonzalez, F.I., Lyzenga, D.R., Zambreski, L.F., A comparison of SIR-B directional ocean wave spectra with aircraft scanning radar spectra, Science, 1986, vol.232, pp. 1531-1535

5. Beal, R.C., Tilley, D.G., Monaldo, F.M., Large and small scale spatial evolution of digitally processed ocean wave spectra from SEASAT synthetic aperture radar, *J. Geophys. Res.*, Vol 88, pp. 1761-1778, Vol. 88, 1983.
6. Brüning, C., S. Hasselmann, K. Hasselmann, S. Lehner, T. Gerling, A first evaluation of ERS-1 synthetic aperture radar wave mode data, *The Glob. Atmos. And Ocean System*, vol 2, pp 61-98, 1994
7. Caudal, G. and Hauser, D., Directional spreading function of the sea wave spectrum at short scale, inferred from multifrequency radar observations, 1996, *J. Geophys. Res.*, Vol. 101, No. C7, pp. 16601-16613
8. The COST 714 Book, Directional Wave spectra Part I, 2004, Tech. Editor H. Krogstad
9. Dankert H., J. Horstmann, S. Lehner and W. Rosenthal, 2003, Detection of Wave Groups in SAR images and Radar-Image Sequences, *IEEE Trans. Geosci. Remote Sens.*, Vol. 41, No. 6., 1437-1445
10. Dankert H., and W. Rosenthal, 2004, *Ocean Surface Determination from X-Band Radar-Image Sequences*. *IEEE Trans. Geosc.* in print 2004
11. Engen, G. and H. Johnson, 1995, SAR ocean wave inversion using image cross spectra, *IEEE TGARS*, Vol. 33, No. 4, pp. 1047-1995
12. Fouques S., Krogstad, H., A numerical study of the nonlinear ocean-SAR spectral transform, *Proc. of the IGARSS 2003 conference in Toulouse*, 2003
13. Dysthe K.B., Refraction of gravity wave by weak current gradients, 2001, *J. Fluid. Mech.*, Vol. 442, pp. 157-159.
14. Feindt, F., Schröter, J., Alpers, W., 1986, Measurements of the Ocean Wave-Radar Modulation transfer function at 35 GHz from a sea based platform in the North Sea, *J. Geophys. Res.*, vol.91, No C8, , pp. 9701-9708
15. Hasselmann K., R.K.Raney, W.J.Plant, W.Alpers, R.A. Shuchman, R.A.Lyzenga, C.L. Rufenach, and M.J. Tucker, Theory of SAR ocean wave imaging: A MARSEN view, *J. Geophys. Res.*, vol.90, pp.4659-4686, 1985
16. Hasselmann, K., and Hasselmann, S., On the nonlinear mapping of an ocean wave spectrum into a synthetic aperture radar image spectrum and its inversion, *J. Geophys. Res.*, vol 96, pp. 10713-10729, 1991.
17. Hasselmann, S., Brüning, Hasselmann, K., Heimbach, P. An improved algorithm for the retrieval of ocean wave spectra from synthetic aperture radar image spectra, *J. Geophys. Res.*, Vol. 101, pp. 16615-16629, 1996.
18. Hara, T. and Plant, W. J., Hydrodynamic modulation of short wind wave spectra by long waves and its measurement using microwave backscatter, *J. of Geophys. Res.*, Vol 99, pp. 9767-9784, 1994
19. Heimbach, P., Hasselmann, S., Hasselmann, K., Statistical Analysis and intercomparison with WAM model data of three years of global ERS-1 SAR wave mode spectral retrievals, *J. Geophys. Res.*, Vol. 103, pp. 7931-7977, 1998.
20. Hoja, D., Schulz-Stellenfleth, J., Lehner, S., and König, T., 2002, Global Analysis Of Ocean Wave Systems From SAR Wave Mode Data, 3 Pages. IGARSS. Toronto, June 24rd-28th 2002, WEE, New York.
21. Horstmann, J., Schiller, H., Schulz-Stellenfleth, J., and Lehner, S., 2003, Global Wind Retrieval from SAR, Submitted to *IEEE Trans. Geosci. Remote Sensing*.
22. Kasischke, E.S., Shuchman, D.R., Lyzenga, D.R., Meadows, G.A., *Detection of bottom features on SEASAT Synthetic Aperture Radar Imagery*, *Photogram. Eng. Remote Sens.*, 49, pp. 1341-1353, 1983.
23. Krogstad, HEK, 1992, A simple derivative of Hasselmann's nonlinear ocean-synthetic aperture radar transform, *J. Geophys. Res.*, Vol 33, No. 4, pp. 1047-1056
24. Krogstad, H.E., O.Samset, and P.Vachon, Generalization of the nonlinear ocean-SAR transformation and simplified SAR inversion algorithm, *Atmos. Ocean*, vol. 105, 2000, pp. 3497-3516
25. Krogstad, H.E., K. B. Dysthe, H. Socquet-Juglard, J. Liu, K. Trulsen, Spatial Extreme Value Analysis Of Nonlinear Simulations Of Random Surface Waves, *Proc. OMAE 2004*, Vancouver, 2004
26. Kudriatsev, V., D. Hauser, G. Caudal, B. Chapron, A semiempirical model of the normalized radar cross-section of the sea surface, 2003, Part 1: The background model, Part 2: Radar Modulation transfer function, *J. Geophys. Res.*, Vol. 108, No C3, 8054
27. Johnson, H., Engen G., Chapron B., Validation of ASAR wave mode level 2 product, *Proc. of the IGARSS 2003 conference in Toulouse*, 2003
28. Lehner, S., Schulz-Stellenfleth, Schättler, J.B. H. Breit, H., Horstmann, J., 2000, Wind And Wave Measurements Using Complex ERS-2 Wave Mode Data, *IEEE GRS*, Vol.3 8, No. 5, Pp. 2246-2257.
29. Lehner, S., Schulz-Stellenfleth, J., Horstmann, 2001, *Marine Parameters From Radar Satellite Data*, *Archives Of Hydro-Engineering And Environmental Mechanics*, Vol. 48, No. 2, Pp. 17-29.
30. Lehner, S., J. Schulz-Stellenfleth, A. Niedermeier, J. Horstmann, W. Rosenthal, Extreme Waves detected by satellite borne Synthetic Aperture Radar, In *Proc of OMAE 2002*, Oslo, June, 2002

31. Lehner, S. Schulz-Stellenfleth, J., Niedermeier, A., Horstmann, J., Rosenthal, W., 2002, Detection Of Extreme Waves Using Synthetic Aperture Radar Images, 3 Pages. IGARSS 2002, Toronto, June 24rd-28th 2002, WEE, New York.
32. Longuet-Higgins M.S., 1986, Wave group statistics, E.C. Monahan and G. Mac Niocell (eds.), Oceanic Whitecaps, pp. 15-35.
33. Lyzenga, D. R. , Numerical simulation of synthetic aperture radar image spectra for ocean waves, IEEE Trans. Geosci. And Rem. Sens., Vol 24, pp. 863-872. , 1986.
34. Mastenbroek, C., Falk, C. F., A semi-parametric Algorithm to retrieve ocean wave spectra from synthetic aperture radar, J. Geophys. Res., Vol 105, pp. 3497-3516, 2000.
35. Melsheimer, C., M.Bao and W.Alpers, Imaging of ocean waves on both sides of an atmospheric front by the SIRC/X-SAR multifrequency SAR, JGR, Vol 103, pp 18839—18849, 1998
36. Monaldo, F., *Measurement of wave coherence properties using spaceborne synthetic aperture radar*, Marine Structures, Elsevier, 2000, pp. 349-366
37. Niedermeier, A., Schulz-Stellenfleth, J., Lehner, S., Dankert, H., 2002, *Ocean Wave Groupiness From ERS-1/2 And ENVISAT Images*, 3IGARSS 2002, Toronto, June 24rd-28th 2002, WEE, New York.
38. Nieto-Borge, J.C., Rodriguez, G., Hessner, K., Izquierdo, P., 2004, Inversion Of Nautical Radar Images For Surface Wave Analysis, in print Journal Of Atmospheric And Oceanic Technology.
39. Nieto-Borge, J.C., Schulz-Stellenfleth, J., Niedermeier, A., Lehner, S., Determination of Ocean Wave Groupiness from Spaceborne Synthetic Aperture Radar, submitted to JGR, 2004
40. Ocampo-Torres, F. J., On the Homogeneity of the Wave Field in Coastal Regions as Determined from RADARSAT Synthetic Aperture Radar Images of the Ocean Surface, *Scientia Marina*, Vol. 65, No. 1, 215-228, 2001.
41. Ocampo-Torres, F. J., and I. S. Robinson, 1990, Wind Wave Directionality Effects on the Radar Imaging of Ocean Swell. *J. Geophys. Res.* Vol. 95, No. C11, 20347-20362, 1990.
42. Plant, W.J., and L.M. Zurk, Dominant wave directions and significant wave heights from synthetic aperture radar imagery of the ocean, JGR, 1998
43. Romeiser, R., A three scale composite surface model for the ocean wave-radar modulation transfer function, J. Geophys. Res., Vol 99, pp. 9785-9801, 1994.
44. Rosenthal, W. and S. Lehner, Results from the MAXWAVE Project, Proc. OMAE 2004, Vancouver, 2004
45. Schieler, M., Interactions in a two-scale model of the sea as a contribution to the remote sensing problem and the energy balance of the short waves of the sea, *Hamburger Geophys. Einzelschriften*, Wittenborn Söhne, Hamburg, 1977
46. Schulz-Stellenfleth, J., Lehner, S., Spaceborne Synthetic Aperture radar observations of ocean waves travelling into sea ice, J. Geophys. Res., Vol. 107, pp. 1029 –1039, 2002
47. Schulz-Stellenfleth, J., Lehner, S., Ocean Wave Imaging using an airborne single pass cross track interferometric synthetic aperture radar, IEEE TGARS, Vol 39, pp. 38-44, 2001
48. Schulz-Stellenfleth, J., Lehner, S., 2004, Measurement Of Two-Dimensional Sea Surface Elevation fields Using Complex Synthetic Aperture Radar Data, IEEE TGARS, in print.
49. Schulz-Stellenfleth, J., Lehner, S. 2003, A Parametric Scheme For Ocean Wave Spectra Retrieval From Complex Synthetic Aperture Radar Data Using Prior Information. under submission to J. Geophys. Res.
50. Rosenthal, W., S.Lehner, A. Niedermeier, J.-C Nieto Borge, J. Schulz-Stellenfleth, H. Dankert and J. Horstmann, Analysis of two dimensional sea surface elevation fields using space borne and ground based remote sensing techniques, Proc. ISOPE, Hawaii, 2003
51. Siegmund, R., Bao, M., Lehner, S., Mayerle, R., First Demonstration of surface currents imaged by hybrid along / across track Interferometric synthetic Aperture radar, Accepted by IEEE TGRASS, in Press, 2003
52. Toffoli A., J.M. Lefevre, J. Monbaliu, H. Savina, E. Bitner-Gregersen, Freak Waves: Clues for Prediction in Ship Accidents?, Proc of the ISOPE 2003, Hawaii, 2003
53. Vachon, P.W., Dobson, F.W., Wind Retrieval from RADARSAT SAR images: selection of suitable C-Band HH polarization wind retrieval model, Canadian Journal of Remote Sensing, Vol. 26, No. 4, pp. 306-313, 2000.
54. Wackermann, Individual wave height from airborne radar, Proc, IGARSS 2002, Toronto, 2002
55. The WAMDI Group, WAM, The WAM model-a third generation wave prediction model, Journal of Physical Oceanography, 18, pp 1775-1810, 1988

ESTIMATION OF TWO-DIMENSIONAL OCEAN WAVE SPECTRA FROM ENVISAT ASAR WAVE MODE DATA USING A MAXIMUM A POSTERIORI APPROACH

J. Schulz-Stellenfleth, S. Lehner

DLR, Oberpfaffenhofen, 82230 Wessling, Germany, Email: Johannes.Schulz-Stellenfleth@dlr.de

ABSTRACT

Two-dimensional ocean wave spectra are measured from ENVISAT ASAR wave mode cross spectra on a global scale. The measurement is performed using a parametric retrieval scheme, which makes use of prior information taken from numerical wave models.

The Partition Rescale and Shift algorithm (**PARSA**) is based on a partitioning technique, which splits an a priori wave spectrum into its wave system components. Integral parameters of these systems, such as mean direction, mean wavelength, waveheight, and directional spreading are then adjusted iteratively to improve the consistency with the SAR observation. The method takes into account the full nonlinear SAR imaging process and uses a maximum a posteriori approach, which is based on statistical model quantifying the errors of the SAR imaging model, the SAR measurement, and the prior wave spectra.

The method is applied to a global data set of ENVISAT ASAR data acquired during the CAL/VAL phase. The benefit of cross spectra compared to conventional symmetric image spectra is demonstrated.

1. INTRODUCTION

Spaceborne synthetic aperture radar (SAR) is still the only instrument providing directional ocean wave information on a global and continuous basis. Different retrieval schemes for derivation of two-dimensional ocean wave spectra F_k from SAR data have been developed (Krogstad, 1994; Hasselmann et al., 1996; Mastenbroek, 2000; Dowd, 2001; Johnson et al., 2003).

More recent schemes are based on SAR cross spectra, which allow to resolve the directional wave propagation ambiguity present in conventional SAR image variance spectra (Engen, 1995; Johnson et al., this issue). The cross spectra technique is based on a special processing technique, where two SAR images (looks), which are separated by about half a second (Engen, 1995) are generated. By calculating the cross spectrum Φ_k of the two looks information can be obtained about the wave propagation direction.

A difficult problem in SAR wave retrieval schemes is the fact that SAR data contain information mainly about longer waves, whereas shorter waves in particular those propagating in the flight direction

(azimuth) are strongly distorted or completely filtered out in many cases. In order to obtain a complete two-dimensional wave spectrum a retrieval scheme therefore has to blend SAR information and prior information in some consistent way. The **Partition Rescaling and Shift Algorithm (PARSA)** scheme is able to deal with this problem and has several additional features compared to the scheme described in Hasselmann (1996):

- The scheme has the directional spreading of the different wave systems as an additional parameter.
- The algorithm is based on explicit models for the measurement error, errors in the forward model, and uncertainties in the prior wave spectrum.
- The scheme is based on a maximum a posteriori approach. The second iteration loop used in Hasselmann (1996), where the prior wave spectrum is adjusted and fed back into the optimal estimation problem is avoided. This approach has two advantages:
 - The sensitive cross assignment procedure used in Hasselmann (1996) is not required;
 - Based on the rigorous formulation as an optimal estimation problem it is possible to estimate the error covariance of the retrieved parameters.
- The scheme makes use of the phase information contained in cross spectra to resolve ambiguities in wave propagation direction.
- The side condition $F_k > 0$ is treated in a rigorous way.

The **PARSA** scheme is designed for the needs of global wave model assimilation, which is regarded as the primary application.

2. RETRIEVAL APPROACH

The **PARSA** scheme is based on a maximum a posteriori approach where the conditional probability of the retrieved wave spectrum given the SAR measurement and the prior information is maximised.

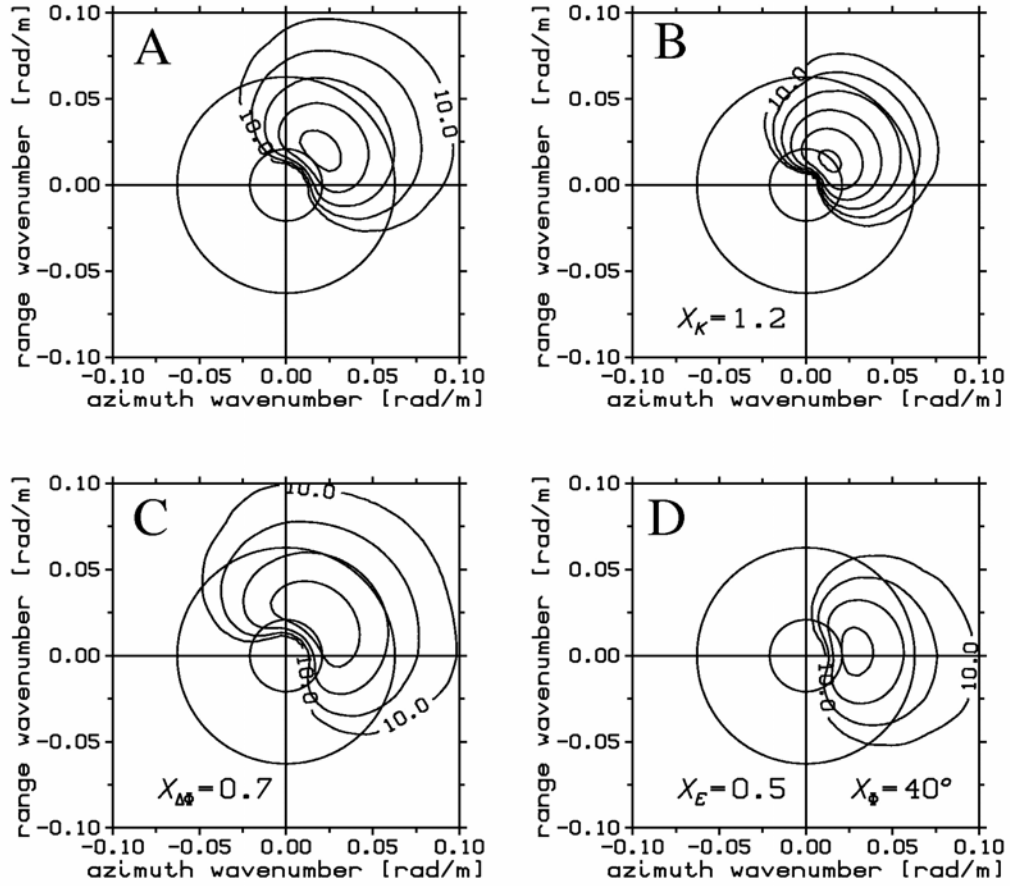


Figure 1: Transformations of wave systems used in the PARSA retrieval scheme. (A) Prior wave system with 250 m peak wavelength. (B-D) Transformed wave spectra with wavenumber rescaled (B), directional spreading changed (C) and simultaneous rotation and energy rescaling (D).

Using the Bayes theorem this probability can be written as

$$pdf(F_k, \alpha | \Phi_k) = \frac{pdf(\Phi_k | F_k, \alpha) pdf(F_k) pdf(\alpha)}{pdf(\Phi_k)} \quad (1)$$

where the different factors have the following meanings:

$pdf(\Phi_k | F_k, \alpha)$ is the conditional distribution of the measured cross spectrum Φ_k given an ocean wave spectrum F_k and a forward model, which contains a stochastic parameter vector α .

$pdf(\alpha)$ is the prior distribution of parameters in the forward model;

$pdf(F_k)$ is the prior distribution of the ocean wave spectrum F_k ;

$pdf(\Phi_k)$ is the (irrelevant) prior distribution of the cross spectrum.

Taking the logarithm of eq. 2 leads to a cost function minimisation problem, the exact form of which is determined by the error models described in the next section.

σ_{a1}	σ_{a2}	σ_{vRF}	σ_{vIF}
0.2	250 m ²	0.1	0.1

Table 1: Parameters describing uncertainties in the SAR imaging model

3. ERROR MODELS

3.1 Model for prior knowledge

The error model for the prior wave spectrum F_p^k is based on a partitioning scheme. For each subsystem B^i , $i=1, \dots, n_p$ of F_p^k the confidence in the mean direction, the mean wavelength, the energy, and the directional spreading is quantified by defining respective stochastic models. With the partitions given on a polar grid (k, Φ) , the corresponding processes B^i can be written as (compare Fig. 2):

20020709082431

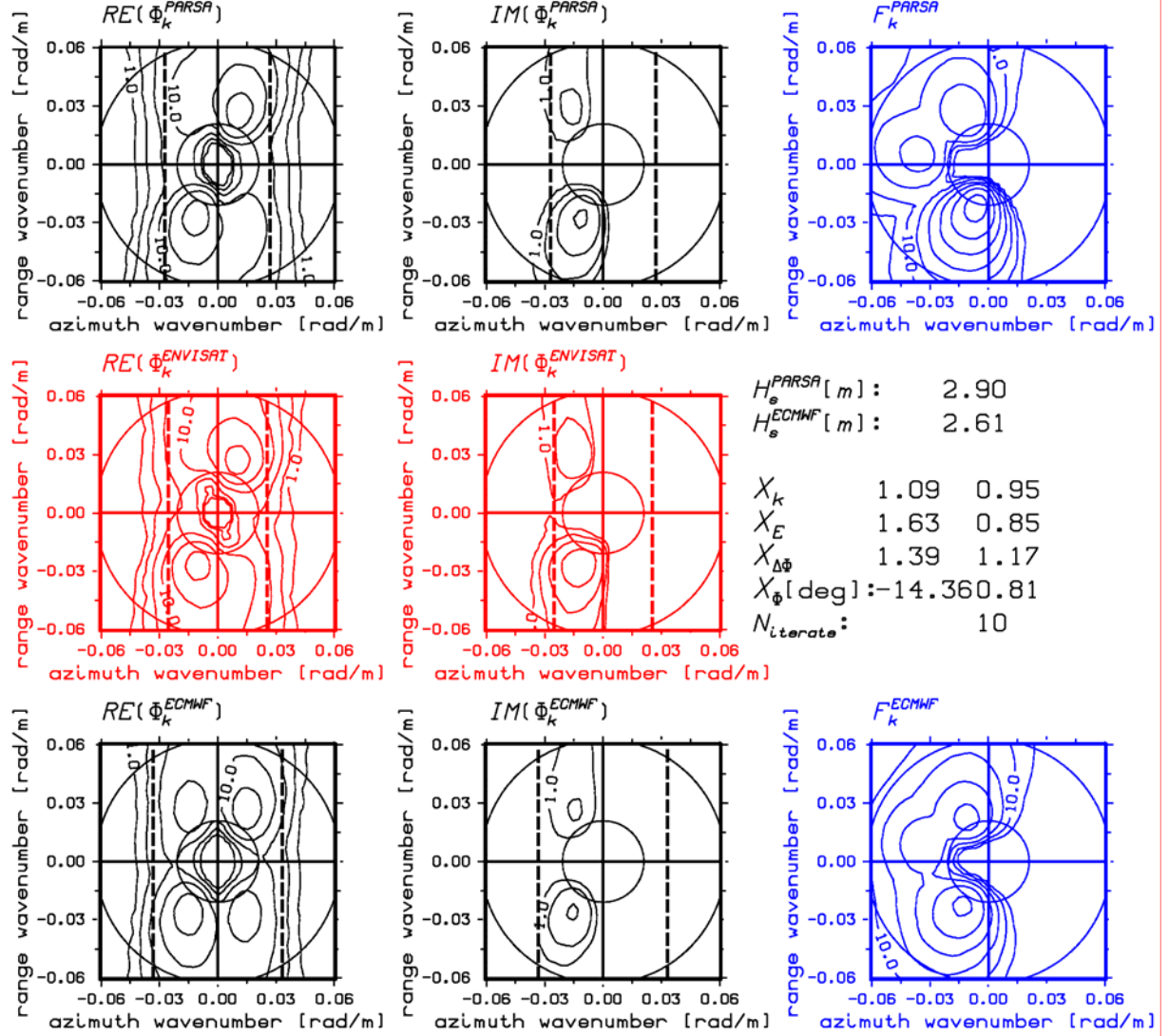


Fig. 2: **PARSA** retrieval for an ENVISAT cross spectrum acquired in the Indian Ocean at -64.81°N 130.7°W on Jul 9, 2002, 8:24 UTC. The satellite heading is 337.2° . The dashed vertical lines indicate the azimuthal cut-off

α_E	α_k	σ_Φ	$\sigma_{\Delta\Phi}$
0.1	0.1	20°	0.1

Table 2: Parameters describing uncertainties in the prior wave spectrum

$$\tilde{B}^i(\phi, k) = X_E^i X_{\Delta\phi}^i X_k^i \cdot B^i(\Phi_0^i + (\Phi - X_\Phi^i - \Phi_0^i) X_{\Delta\Phi}^i, X_k^i k) \quad (2)$$

for $i=1, \dots, n_p$. The stochastic vector $(X_E^i, X_k^i, X_\Phi^i, X_{\Delta\Phi}^i)$ is assumed to be Gaussian with mean $(1, 1, 0, 1)$ and standard deviations as given in the lower right table 2.

3.2 Model Measurement Errors

The following model is used for deviations between the simulated and the observed cross spectrum Φ_k^{sim} due to errors in the SAR imaging model:

$$\bar{\Phi}_k = \alpha_1 \exp[-k_x^2 \alpha_2] \Phi_k^{\text{sim}} + \varepsilon_k^F$$

Here, k_x is the azimuth component of the wavenumber vector and α_1 , α_2 and ε_k^F have the following meanings:

- α_1 is a Gaussian distributed variable with unit mean and standard deviation σ_{α_1} , which describes errors in the overall energy level of the spectrum;

- α_2 is a Gaussian distributed variable with zero mean and standard deviation σ_{α_2} , which describes uncertainties in the cut-off wavelength of the forward model;
- ε^F is additive white Gaussian noise with independent real and imaginary part and zero mean. It is supposed to take into account errors in the fine scale structure of the spectrum.

The standard deviations used here are given in table 1, where $\sigma_{\mu RF}$, $\sigma_{\mu IF}$ denote the relative errors of the real and imaginary part of ε^F .

4. NUMERICAL INVERSION PROCEDURE

From the mathematical point of view the **PARSA** method solves a minimisation problem with 4 n_p unknown parameters. The optimisation problem is solved on a polar grid using a Levenberg-Marquard (LM) (Rodgers, 1998) method, with an iteration scheme of the following form:

$$X^{n+1} = X^a + (C_X^{-1} + \lambda^n I_N)^{-1} D_n^T S_\varepsilon^{-1} (\phi^{obs} - \phi^{sim} + D_n (X^n - X^a) + \lambda^n (X^n - X^a))$$

Here, X^a , X^n are the prior and nth iterate parameter vectors, C_X is the covariance matrix

$$C_X = (D_n^T S_\varepsilon^{-1} D_n + S_a^{-1})^{-1}$$

of X^a , D_n is the Jacobian matrix of the SAR imaging model, S_ε is the errors covariance matrix of the measured cross spectrum, I_N is the identity matrix, and λ^n is the relaxation parameter of the LM method. The relaxation parameter is adjusted iteratively depending on whether or not the cost function was reduced in the last iteration step.

$$\lambda^{n+1} = \begin{cases} 0.5 \lambda^n & \text{if } J^{n+1} < J^n \\ 2 \lambda^n & \text{if } J^{n+1} \geq J^n \end{cases}$$

5. PARSA INVERSION OF ENVISAT ASAR DATA

Fig. 2 shows a **PARSA** inversion of an ENVISAT wave mode cross spectrum. The prior wave spectrum provided by the European centre for Medium-Range Weather Forecast (ECMWF) on the lower right contains three wave systems propagating in different directions. The observed real part of the cross spectrum in the centre (red) only shows the dominant wave system propagating to the lower left. The imaginary

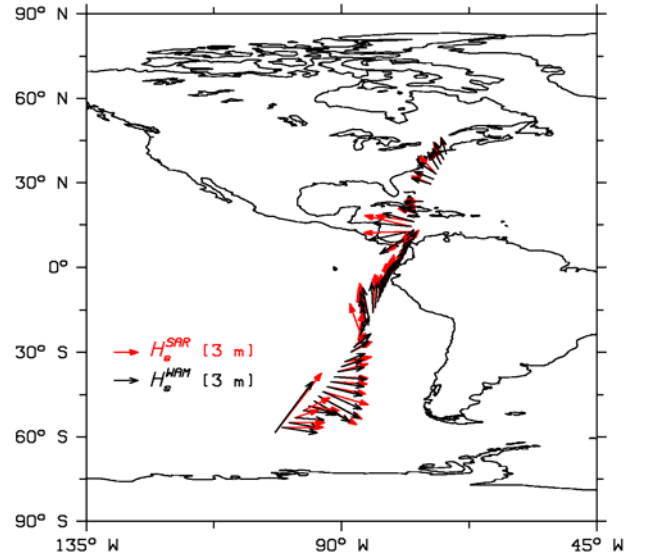


Figure 3: Mean wave direction and significant waveheight derived from ENVISAT ASAR wave mode data using the **PARSA** scheme (read arrows) and respective colocated ECMWF model spectra (black arrows) for one (descending) track acquired on July 9, 2002.

part (centre right) shows the second system propagating to the upper left in addition. As can be seen in the inverted spectrum on the upper right the **PARSA** scheme uses this information to slightly change both wavelength and propagation direction of the two wave systems. Comparing the first simulated cross spectrum with the cross spectrum simulated from the retrieved spectrum, shows that the scheme in fact leads to an improved agreement with the observation. In particular the cut-off wavelength indicated by the dashed lines is improved. The scheme needed 10 iterations to compute the solution of the minimisation problem.

The example is interesting as it shows that the **PARSA** scheme is able to extract the new information given by the imaginary part of the observed ENVISAT cross spectra. This means in particular that the symmetric SAR image spectra provided as standard product from the ERS-1/2 SAR lack a lot of valuable wave information.

Fig. 3 shows a map with mean wave directions and significant wave heights derived from ENVISAT ASAR wave mode data (read arrows) and colocated ECMWF model spectra (black arrows) for one track in the Pacific acquired on July 9, 2002. One can see that the corrections applied by the **PARSA** scheme are

smooth and consistent. The deviations in mean propagation directions are in most cases due to redistribution of energy among different subsystems (up to three occurred for this track), rather than rotations of single wave systems.

6. CONCLUSION AND OUTLOOK

An inversion scheme was presented which estimates two-dimensional wave spectra from look cross spectra using prior information. The scheme is able to blend SAR information and wave model output in a consistent way based on rigorous errors models for the SAR measurement and the prior information, and is therefore ideally suited for wave model assimilation.

The scheme is currently validated in close cooperation with UK Met office and the French Met office. The validation is performed in the framework of the ENVISAT Cal/Val activities in which a large data set of buoy co-locations is generated.

It is expected that the method will give valuable contributions to the improvement of numerical wave models in particular concerning swell dissipation.

It is furthermore planned to extend the scheme for use with ENVISAT dual polarisation data, which will help to reduce a couple of uncertainties in the current SAR imaging model.

REFERENCES

1. Dowd, M., Vachon, P.W., *Ocean Wave extraction from RADARSAT Synthetic Aperture Radar Inter-Look Image Cross Spectra*, IEEE TGARS, Vol 39, pp. 21-37, 2001
2. Engen, G., Johnson, H., *SAR ocean wave inversion using image cross spectra*, IEEE Trans. Geosci. Rem. Sens., Vol. 33, pp. 1047-1056, 1995.
3. Hasselmann, K., and Hasselmann, S., *On the nonlinear mapping of an ocean wave spectrum into a synthetic aperture radar image spectrum*, J. Geophys. Res., pp. 10713-10729, 1991.
4. Hasselmann, S., Brüning, Hasselmann, K., Heimbach, P. *An improved algorithm for the retrieval of ocean wave spectra from synthetic aperture radar image spectra*, J. Geophys. Res., Vol. 101, pp. 16615--16629, 1996.
5. Hoja, D., Schulz-Stellenfleth, J., Lehner, S., and König, T., 2002, *Global Analysis Of Ocean Wave Systems From SAR Wave Mode Data*, 3 Pages. IGARSS. Toronto, June 24rd-28th 2002, WEE, New York
6. Horstmann, J., Schiller, H., Schulz-Stellenfleth, J., and Lehner, S., *Global Wind Retrieval from SAR*, Submitted to IEEE Trans. Geosci. Remote Sensing, 2003
7. Johnson, H., Engen G., Chapron B., Validation of ASAR wave mode level 2 product, Proc. of the IGARSS 2003 conference in Toulouse, 2003
8. Johnson, H., G. Engen, B. Chapron, Validation of ASAR wave mode Level 2 products using WAM and buoy spectra, this issue
9. Krogstad, H., Samset, O., Vachon, P.W., Generalization o the nonlinear ocean-SAR transformation and a simplified SAR inversion algorithm, Amos. Ocean, Vol. 32, pp. 61-82, 1994
10. Lehner, S., Schulz-Stellenfleth, Schättler, J.B. H. Breit, H., Horstmann, J., 2000, *Wind And Wave Measurements Using Complex ERS-2 Wave Mode Data*, IEEE GRS, Vol.3 8, No. 5, Pp. 2246-2257.
11. Lehner, S., Schulz-Stellenfleth, J., Horstmann, 2001, *Marine Parameters From Radar Satellite Data*, Archives Of Hydro-Engineering And Environmental Mechanics, Vol. 48, No. 2, Pp. 17-29.
12. Lyzenga, D., *Unconstrained Inversion of Waveheight Spectra from SAR Images*, IEEE TGARS, Vol 40, pp. 261-270, 2002.
13. Schulz-Stellenfleth, J., S. Lehner, SAR observations of ocean waves travelling into sea ice, Journal of Geophysical Research, 107, 2002
14. Schulz-Stellenfleth, J., S. Lehner, Measurement of two dimensional sea surface elevation fields from complex synthetic aperture radar data, Accepted by IEEE TGARS, 2004.

**This page intentionally
left blank (pagination)**

VALIDATION OF THE ASAR WAVE MODE LEVEL 2 PRODUCT USING WAM AND BUOY SPECTRA

Harald Johnsen⁽¹⁾, Geir Engen⁽¹⁾, Bertrand Chapron⁽²⁾

⁽¹⁾Norut Informasjonsteknologi AS, PP 6463 Forskningsparken, N-9294 Tromsø, Email:harald.johnsen@itek.norut.no

⁽²⁾IFREMER, PP 70, 29280 Plouzane, France, Email:bchapron@ifremer.fr

ABSTRACT

More than 70 thousands of ASAR Wave Mode Level 2 products are validated globally using co-located ECMWF WAM spectra and wind speed data. A large number of co-located ASAR, WAM and buoy spectra are also used in the validation. The data used in the validation covers all ASAR Wave Mode acquisitions in the period April and March 2003. Globally, the geophysical validation of wind and wave parameters show reasonably agreement for the mean wave period, significant waveheight and mean wave direction, especially for the long wavelength part of the spectra. However, for certain coastal and sheltered areas larger deviations are observed, probably due to fetch limitations and/or impact of other coastal surface features on the SAR signature. On average the ASAR tends to measure a slightly longer mean swell period ($\approx 0.8s$) than predicted by WAM. Comparing ASAR, WAM and buoy spectra, examples are shown where ASAR consistently adds information on the swell systems beyond what is predicted by WAM. For the ASAR Level2 significant waveheight, saturation effects at high sea-states are observed, increasing with increasing wind speed. Less saturation is observed for the long wavelength part of the spectrum. The saturation is mostly due to the well-known effect of azimuth cut-off, which increases with increasing sea state. At low wind speed an overestimation of waveheight is observed compared to WAM. This is caused by the use of CMOD-IF2 based MTF [5] which underestimates the backscatter modulation at low wind speed as compared to SAR due to the high spatial variability of SAR cross section at low wind speeds. Statistics and global maps comparison are also presented, showing the capabilities of ASAR Wave Mode to provide global coverage of wave spectral parameters.

1. VALIDATION APPROACH

Following the approach of validation of ASAR Wave Mode given in [1], more than two months of global coverage of ASAR wave mode data is validated against co-located ECMWF model data, and where available also locally against buoy data from the NDBC and MEDS networks. Statistics of ASAR-WAM deviations are presented together with global coverage comparison.

The ASAR Wave Mode Level 2 spectra are given on log-polar grid in wavenumber and direction domain, $F(k, \varphi)$ [4]. Note that the ASAR spectrum is in general not the total ocean wave spectrum, but only the wave spectrum within the SAR imaging domain [3]. The size of this domain is again dependent on the sea state. The frequency-, $F(f)$ and directional spectra, $\psi(\varphi)$ are then derived from the Level 2 spectra, $F(k, \varphi)$ according to the formulas:

$$(1) \quad F(f) = \int F(k, \varphi) k \cdot dk d\varphi \cdot d\varphi$$

$$(2) \quad \psi(\varphi) = \int F(k, \varphi) dk$$

$$(3) \quad \phi(f) = \tan^{-1} \left(\frac{\int F(k, \varphi) \sin \varphi d\varphi}{\int F(k, \varphi) \cos \varphi d\varphi} \right)$$

where $dkdf = 4\pi\sqrt{k/g}$. The significant waveheights, H_s, H_s^{12} mean periods, T_p, T_p^{12} , and mean wave direction, Φ are then computed as:

$$(4) \quad H_s = 4 \sqrt{\int_{f_{\min}}^{f_{\max}} F(f) df}, \quad H_s^{12} = 4 \sqrt{\int_{f_{\min}}^{f_{\max}} F(f) df^{1/12}}$$

$$(5) \quad T_p = \frac{\int_{f_{\min}}^{f_{\max}} F(f) f^{-1} df}{\int_{f_{\min}}^{f_{\max}} F(f) df}, \quad T_p^{12} = \frac{\int_{f_{\min}}^{f_{\max}} F(f) f^{-1} df^{1/12}}{\int_{f_{\min}}^{f_{\max}} F(f) df}$$

$$(6) \quad \Phi = \tan^{-1} \left(\frac{\int_{f_{\min}}^{f_{\max}} F(f) \sin(\phi(f)) df}{\int_{f_{\min}}^{f_{\max}} F(f) \cos(\phi(f)) df} \right)$$

where f_{\min}, f_{\max} are the lowest and highest frequencies in the spectrum to be computed over. Similar parameters can be derived from the co-located WAM and buoy spectra. Spectral peak period, T_{peak} and direction, Φ_{peak} are also extracted from the spectra and compared. The wave directions are always clock-wise from north towards the direction the waves propagate.

2. VALIDATION RESULTS

In the following, results from the geophysical validation of wave spectra parameters, wind field and radar cross section are shown and discussed.

2.1 Wave Spectra Parameters

Validation of wave parameters is performed globally against ECMWF WAM spectra and locally against buoy data from the network of buoys outside US, Canada and Hawaii. The locations of the buoys used are shown in Fig. 1. The data used in the validation covers all ASAR Wave Mode acquisitions in the period April and March 2003.

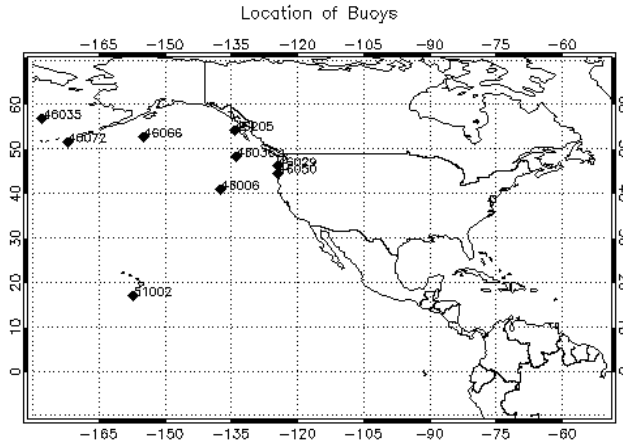


Fig. 1. Map showing the location of buoys used in validation of ASAR WM Level2 wave spectra.

The co-location of the data is done at IFREMER/Cersat. A typical output of the co-location is shown in Fig. 2. The spatial distance between ASAR, buoy and WAM should be taken into account when interpreting the plots in Fig. 3. The WAM and ASAR are always well co-located spatially, while the ASAR and buoy are seldom co-located better than 50km. In the comparison between WAM and ASAR parameters, we should also keep in mind that the

spatial scales are very different (ASAR $\approx 5 \times 10 \text{ km}^2$, WAM $50 \times 50 \text{ km}^2$).

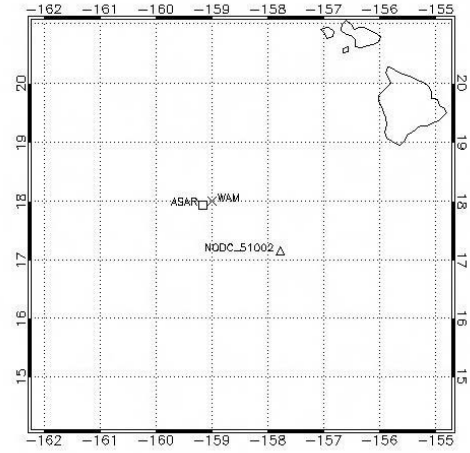
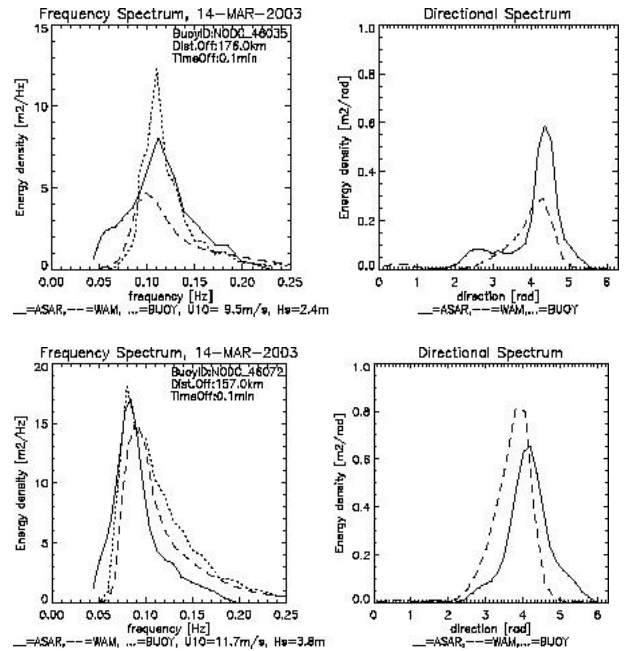


Fig. 2. Example of triple co-location of ASAR, WAM and buoy outside Hawaii.

In the validation process we have restricted the ASAR data set to those with normalized image variance between $\sigma^2/\mu^2 \in [1.0, 1.4]$. This is done in order to avoid data corrupted by slicks, currents and other coastal surface features. Fig. 3 shows $F(f)$ and $\phi(f)$ spectra from ASAR, ECMWF WAM, and buoy computed according to equations (1) and (2). Note that only $F(f)$ spectra are available from buoys, except for buoy 46029.



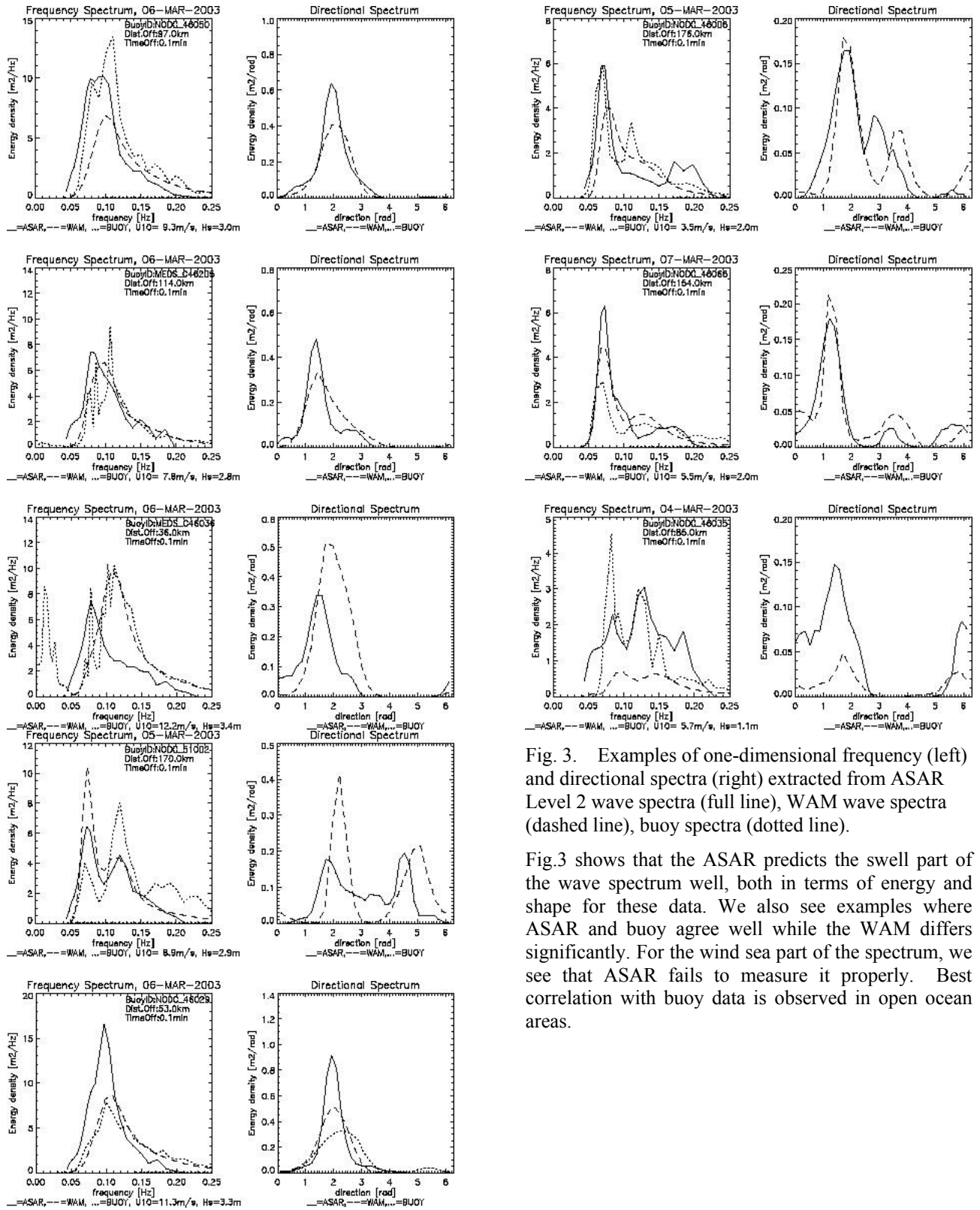


Fig. 3. Examples of one-dimensional frequency (left) and directional spectra (right) extracted from ASAR Level 2 wave spectra (full line), WAM wave spectra (dashed line), buoy spectra (dotted line).

Fig.3 shows that the ASAR predicts the swell part of the wave spectrum well, both in terms of energy and shape for these data. We also see examples where ASAR and buoy agree well while the WAM differs significantly. For the wind sea part of the spectrum, we see that ASAR fails to measure it properly. Best correlation with buoy data is observed in open ocean areas.

Global statistics of the comparison of significant waveheight, mean and peak wave period, and mean and peak wave direction from ASAR and WAM are shown in Fig. 4 to Fig. 7. Fig. 4 and Fig. 5 show the results for the significant waveheight.

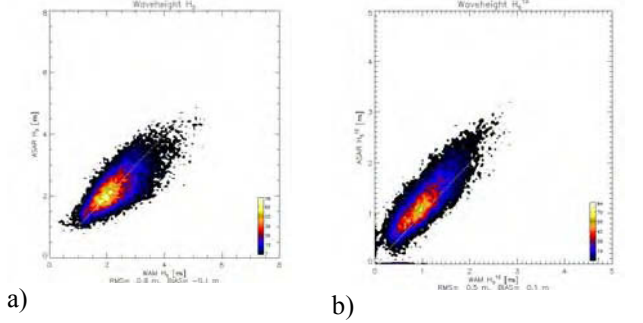


Fig. 4. Scatter plot of significant waveheight derived from co-located WAM and ASAR Wave Mode spectra globally, a) : H_s , b) : H_s^{12} .

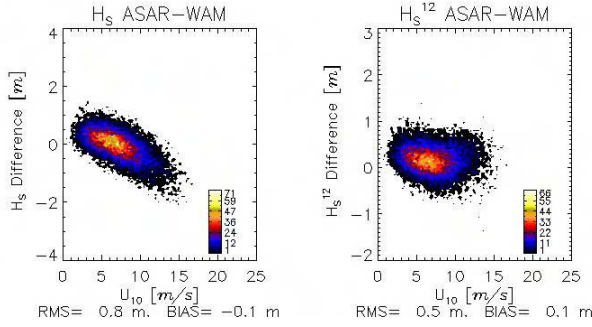


Fig. 5. Waveheight difference between ASAR and WAM as function of wind speed (left plot : ΔH_s , right plot: ΔH_s^{12}).

Fig.4 and Fig.5 show that ASAR Level 2 products predict the significant waveheight well, especially at wind speeds between 5 m/s and 10 m/s. At higher wind speeds the azimuth cut-off will highly affect the ASAR spectrum by filtering out the contribution from the wind sea part of the spectrum. At lower wind speed the SAR tends to overestimate the waveheight. The latter is most likely due to the use of scatterometer based CMOD-IF2 in the SAR wave retrieval. The low-resolution CMOD-IF2 derived backscatter tends to be biased high for low wind speed when compared to high-resolution SAR backscatter (see Fig. 10a). This will affect not only the wind speed retrieval but also the wave retrieval since the RAR MTF used is based on the CMOD-IF2 properties [5].

Fig.6 shows the comparison between ASAR and WAM mean and peak wave period, and Fig. 7 shows the same for the wave direction.

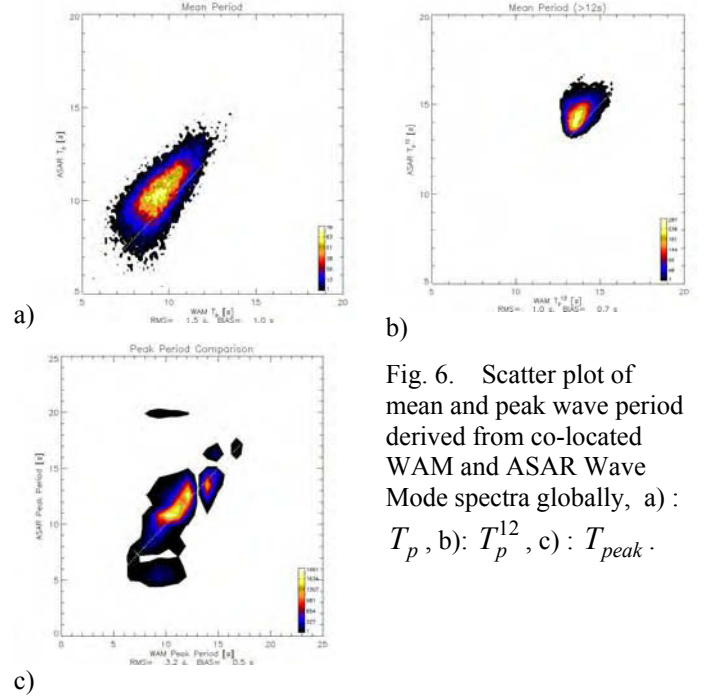


Fig. 6. Scatter plot of mean and peak wave period derived from co-located WAM and ASAR Wave Mode spectra globally, a) : T_p , b) : T_p^{12} , c) : T_{peak} .

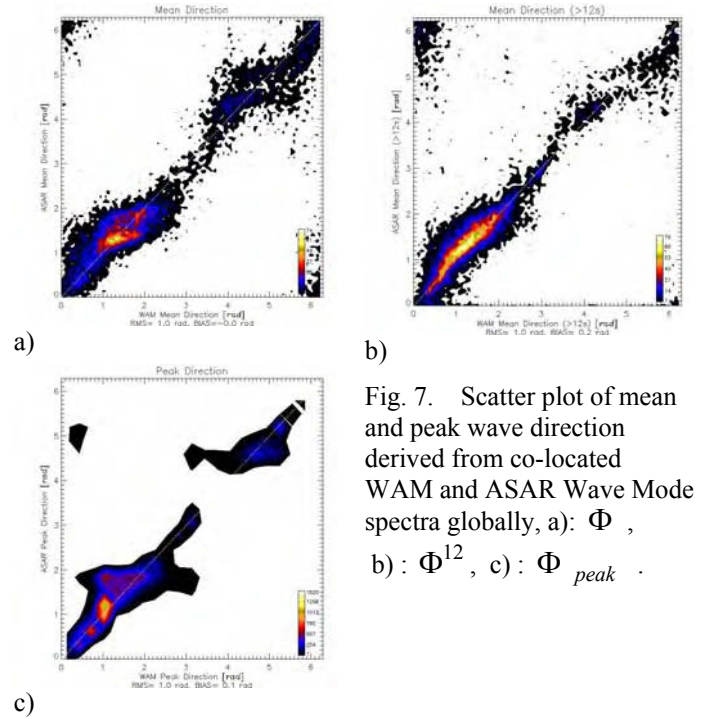


Fig. 7. Scatter plot of mean and peak wave direction derived from co-located WAM and ASAR Wave Mode spectra globally, a) : Φ , b) : Φ^{12} , c) : Φ_{peak} .

Fig.6 shows that the SAR slightly measures a larger value than the WAM for both the mean and the peak period, which for some cases can be explained by the

azimuth smearing effect. However, comparison with buoys (see Fig. 3) show that WAM sometimes underestimates the swell. If we restrict the computation of the mean period to waves with period larger than 12 s, both the bias and the RMS error are reduced, but the bias is still significant (0.8s). From the global plots shown in Fig. 9, we will see that the overestimation of mean wave period dominates at certain coastal and sheltered areas.

For the wave direction we see from Fig.7 that the ASAR and WAM mean wave direction agrees well taken into account that part of the ASAR spectra may be rotated towards range due to the azimuth cut-off effect [2]. The standard deviation is around 57° while the bias is between 0° and 17° .

In the next figures are shown global maps of waveheight, mean wave period, and wind speed for one month of data (March 2003). We see the same global features in both the ASAR and WAM maps for all the parameters considered here.

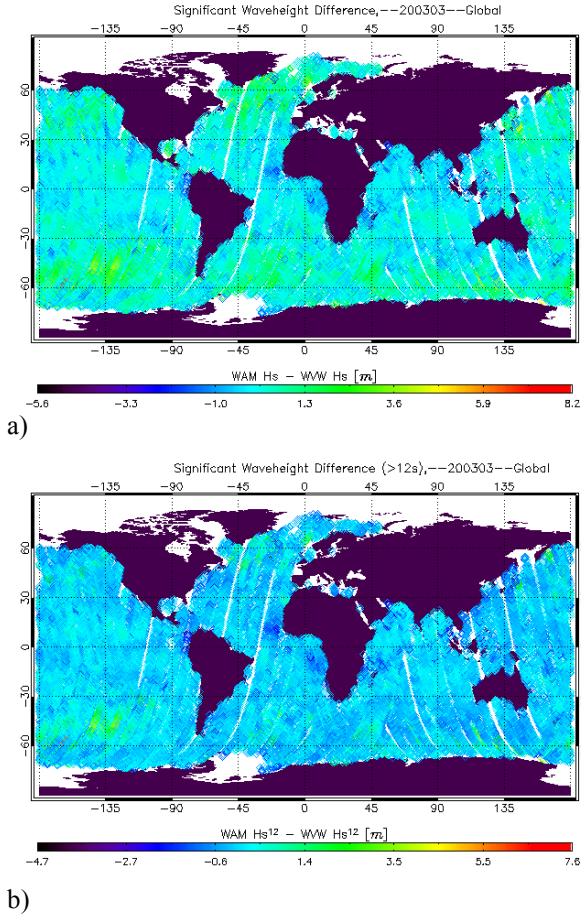


Fig. 8. Global map of one month (March 2003) average difference between ASAR WVV and WAM significant waveheight, a) for ΔH_s , b) for ΔH_s^{12} .

The global waveheight difference maps of Fig.8 show that the largest deviation between ASAR and WAM occurs in the low pressure regions. This is the area with highest wind speed (wind sea) as seen from Fig.12 causing severe azimuth cut-off problems in the ASAR wave spectra as shown in Fig.12. In the low wind areas around Equator, better agreement in waveheight is observed. We also see from Fig. 8b that considering only waves with periods larger than 12 s, reduces the deviations between WAM and ASAR WVV, especially in the wind sea areas.

In Fig.9 is shown the global maps of the ASAR and WAM difference in mean wave period.

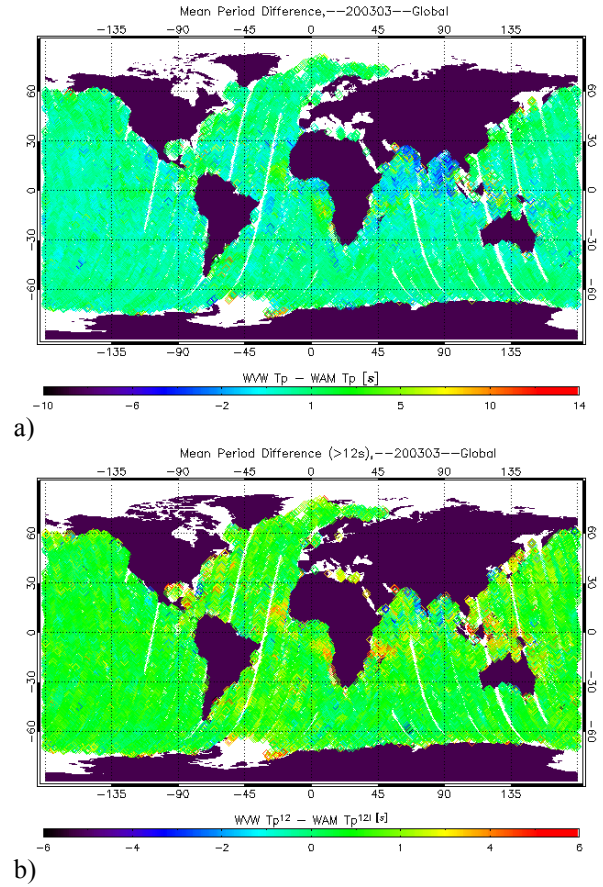


Fig. 9. Global map of one month (March 2003) difference between ASAR WVV and WAM mean wave period, a) for ΔT_p , b) for ΔT_p^{12} .

For the mean wave period shown in Fig.9 we see a very good agreement globally. However, for certain areas around coast of Africa and some sheltered regions at East Coast of US and between Australia and Asia, we see that ASAR tends to measure a longer mean wave period than WAM for the swell part of the spectrum. For the sheltered areas this can be due to effects from fetch-limitation and/or surface features interpreted as long wavelength systems in the ASAR

WVW product. These regional effects are reproduced also in the April 2003 data. Of particular interest is the localized deviations observed outside coast of West-Africa. These areas are known as swell pools [6], and will be investigated in more detail when the corresponding WVI products become available.

2.2 Wind Speed and Radar Cross Section

In the following a validation of backscatter and wind speed is done using CMOD-IF2 backscatter model and the co-located wind field from ECMWF. Backscatter comparison is shown in Fig. 10.

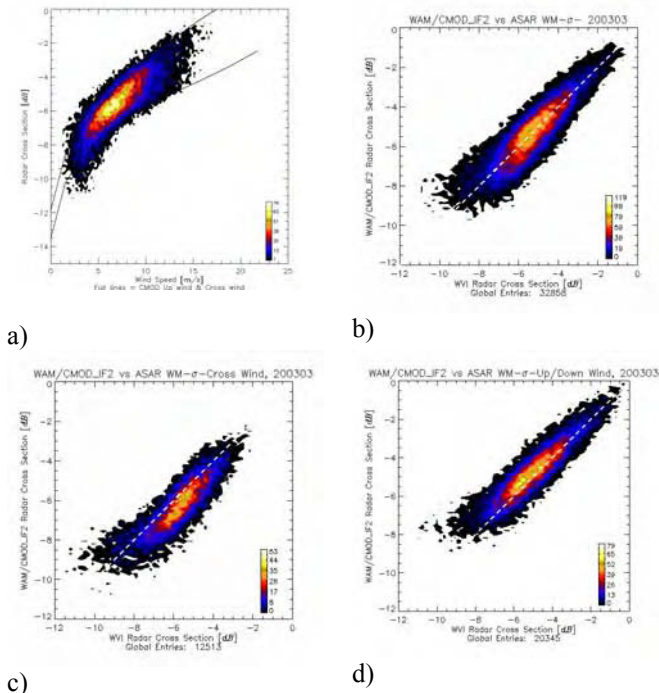


Fig. 10. a) ASAR measured radar cross-section versus ECMWF wind speed. Full lines show the dynamic range of CMOD-IF2 predicted cross section. b) CMOD-IF2 radar cross section versus ASAR WM cross-section – all wind directions c) CMOD-IF2 radar cross section versus ASAR WM cross-section – cross wind directions. d) CMOD-IF2 radar cross section versus ASAR WM cross-section – up/down wind directions.

From Fig. 10a we see that at low wind speed the SAR tends to measure higher radar cross-section than predicted by CMOD-IF2. This is most likely to cause the overestimation of waveheight at low wind speeds shown in Fig. 5. Another observation (Fig 10 c and d) is the difference in predicted and observed radar cross section for cross wind versus up/down wind. The up/down wind data seems to fit better to CMOD-IF2 model than the cross wind data. No difference was observed between up and down wind data.

The wind speed retrieval in the ASAR WM Level 2 product is based on using CMOD-IF2 with a fixed wind direction of 45° relative to range, and calibration constant derived from co-located WAM and ASAR data from the Commissioning Phase. The results are shown in Fig. 11.

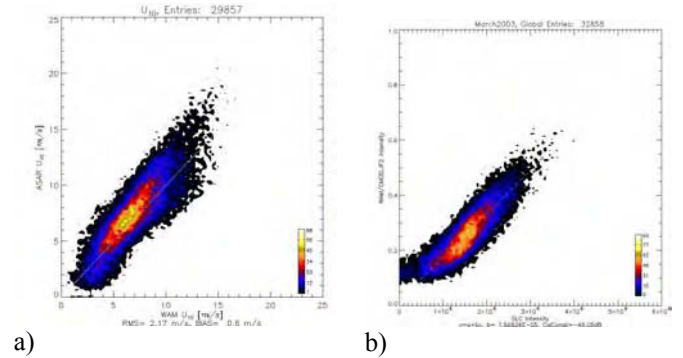
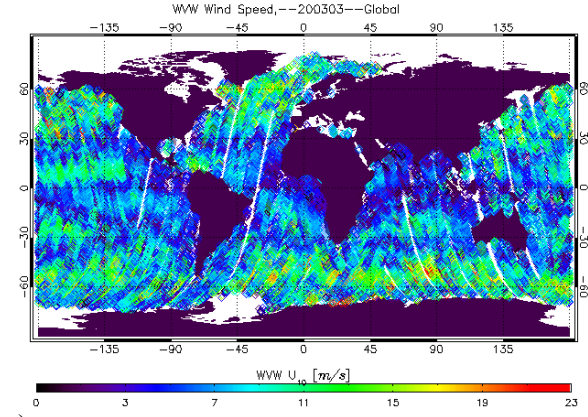


Fig. 11. a) Scatter plot of wind speed derived from co-located ECWMF atmospheric model and ASAR Wave Mode Level 2 product. b) Scatter plot of CMOD-IF2 intensity versus ASAR WM Level 1b image intensity.

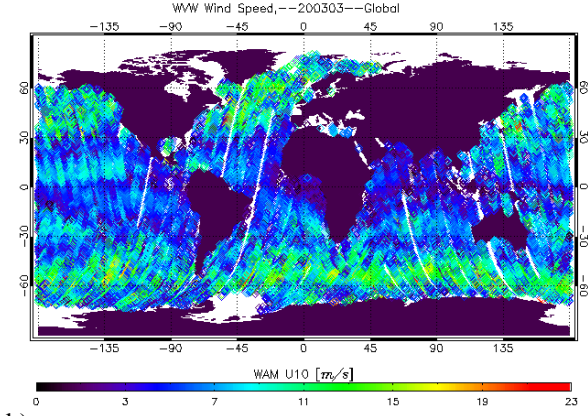
The standard deviation for the wind speed comparison is around 2.2 m/s with a bias of 0.5 m/s. The effect of spatial variability at low wind speeds is again observed to increase the deviation between ASAR and WAM. The absolute calibration constant achieved is 48.05dB, which is around 0.5dB higher than what was achieved from transponders.

Fig.12 shows the global maps of ASAR and WAM wind speed from March 2003. The same global features are observed, but the ASAR has larger variability than the WAM, which is expected due to the different spatial scales.

Fig.13 shows the azimuth cut-off wavelength of the ASAR wave spectra for March 2003. Comparing the plot with Fig.12 we see, as expected, a strong correlation between the wind speed and the azimuth cut-off.



a)



b)

Fig. 12. Global map of ASAR WWV (a) and ECMWF (b) wind speed from March 2003.

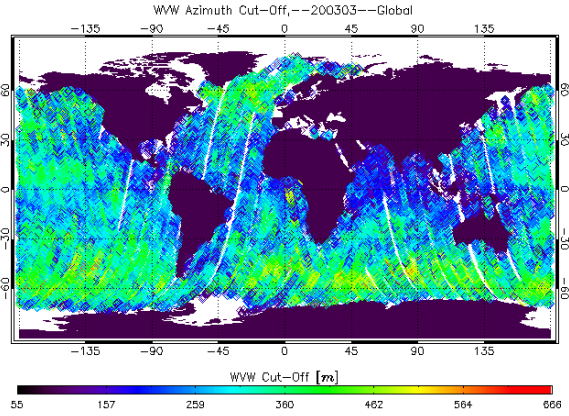


Fig. 13. Global map of ASAR WWV azimuth cut-off wavelength from March 2003.

3. SUMMARY

Validation of ASAR Wave Mode shows that the Level 2 product performs well in terms of providing a 2-d ambiguity free wave spectra within the SAR imaging

domain. Cross comparison of data from WAM, ASAR and buoys shows examples where ASAR consistently adds information on ocean swell beyond what WAM predicts. Significant bias is observed for the wave period while for the waveheight deviation increases with wind speed. An overestimation of waveheight is observed at low wind speeds which can be due to the effect of using low-resolution scatterometer based CMOD-IF2 in the wave retrieval. The deviation at higher wind speeds is due to the azimuth cut-off increasing with increasing wind speed/sea state. Global comparison shows that the bias in wave period is largest in certain coastal and sheltered areas, while the deviation in waveheight is largest in the low pressure (high wind) areas.

In the table below a summary of differences between WAM and ASAR Level 2 product is shown for some key wave and wind parameters.

$H_s, H_s^{12} [m]$		$T_p, T_p^{12} [s]$		$T_{peak} [s]$	
RMS	Bias	RMS	Bias	RMS	Bias
0.8	-0.1	1.7	1.2	3.1	0.5
0.6	0.2	1.1	0.8		
$\Phi, \Phi^{12} [rad]$		$\Phi_{peak} [rad]$		$U_{10} [m/s]$	
RMS	Bias			RMS	Bias
1.0	0.0	1.0	0.1	2.2	0.5
1.0	0.3				

Table 1: Performance of key ASAR Level 2 parameters as compared with ECMWF WAM data.

ACKNOWLEDGEMENT:

The work was co-funded by the Research DG of the European Commission under contract EVG1-CT-2001-00051, “EnviWave”, and by ESA under the AO-799 project, and the ESRIN/Contract No. 17376/03/I-OL.

REFERENCES

1. Johnsen H., Engen G., Chapron B., Walker N., and Closa J., *Validation of ASAR Wave Mode Level 2 Product*, Proc. of Envisat Cal/Val Workshop, ESA SP-531, <http://envisat.esa.int/workshops/>.
2. Rufenach C., Johnsen H., Høgda K.A., *An approximative analytical method for correcting distortion in Synthetic Aperture Radar ocean wave spectral peaks*, IEEE Trans. Rem. Sens., Vol. 33, No.2, pp.504-509, 1995.
3. Engen G., Johnsen H., Høgda K.A., Chapron B., *Envisat ASAR Level 2 Wave Mode Product Algorithm Specification – Software Requirement Document*, NORUT IT Doc. No.: 650/1-01,v2.2.5, Oct., 2001.
4. Envisat Data Product Handbook, <http://envisat.esa.int/dataproducts/asar/>.

5. Johnsen H., Engen G., Chapron B., Envisat ASAR Wind&Wave Measurements from Level1 product – wind and wave retrieval methodologies”, Norut IT report No. IT650/2-01, Version 1.2, 2001.
6. Chen G., Chapron B., Ezraty R., Vandemark D., “A Global View of Swell and Wind Sea Climate in the Ocean by Satellite Altimeter and Scatterometer”, J. of Atm. & Ocean Techn., Vol. 19, pp. 1849-1859, 2002

Current Feature Session

Chairs: R. Romeiser & S. Ufermann

**This page intentionally
left blank (pagination)**

STATUS REPORT ON THE REMOTE SENSING OF CURRENT FEATURES BY SPACEBORNE SYNTHETIC APERTURE RADAR

Roland Romeiser⁽¹⁾, Susanne Ufermann⁽²⁾, and Stefan Kern⁽¹⁾

⁽¹⁾ *Institute of Oceanography, University of Hamburg, Bundesstraße 53,
20146 Hamburg, Germany, E-Mail: romeiser@ifm.uni-hamburg.de / kern@ifm.uni-hamburg.de*

⁽²⁾ *School of Ocean and Earth Science, Southampton Oceanography Centre, European Way,
Southampton SO14 3ZH, United Kingdom, E-Mail: ufermann@soton.ac.uk*

ABSTRACT

Spatial variations in ocean surface currents can become visible in synthetic aperture radar (SAR) images via hydrodynamic modulation of the surface roughness. The interpretation of such SAR signatures is a challenging problem, since the imaging mechanism is quite complex and nonlinear and cannot be inverted easily. Furthermore, the distinction between SAR signatures of current features and other phenomena can be difficult. However, SAR is the only existing technique for the observation of current variations on spatial scales of tens of meters from satellites. There is a vital demand for such information, particularly in coastal regions. A variety of algorithms have been developed for the retrieval of information on current features from SAR images for different purposes. We give an overview of the state of the art, existing and potential applications, and future perspectives and requirements.

1. INTRODUCTION

Compared to the retrieval of wind vectors or wave spectra from synthetic aperture radar (SAR) images of the ocean, the interpretation of SAR signatures of current features is a more complex and diverse problem: Depending on the nature, the dimensions, and the strength of a current feature as well as on the wind speed vector and the imaging geometry, the modulation of the SAR image intensity can be dominated by different highly nonlinear mechanisms, and SAR signatures of similar features can look quite different under different conditions. Furthermore, completely different phenomena such as current features, variations in the wind field, rain, surfactants, or sea ice, can give rise to very similar signatures, which are often superimposed upon each other. This can lead to a complete misinterpretation. Finally, one must be aware of the fact that only current gradients, not absolute current values, can be retrieved directly from SAR intensity images.

Due to the complexity of the problem, it is practically impossible to develop a universal tool for an automatic interpretation of SAR signatures of current features: The highly nonlinear, multi-stage SAR imaging mechanism

cannot be inverted easily; simplifications by linearization or the use of empirical model components are not adequate for wide parameter ranges. Furthermore, one cannot expect to obtain a unique and exact solution for a retrieved current field without additional information or a priori assumptions about its nature.

Despite these difficulties and limitations, SAR images of current features are being used successfully by a number of users for several specific applications. In this paper we give an overview of the state of the art and of future perspectives in this field. In the following section we discuss the SAR imaging mechanism of current features, basic strategies for the retrieval of information on current features from their SAR signatures, typical users of SAR images of current features and their specific applications and requirements, and existing alternatives to the observation of current features by SAR. In section 3 we present examples of existing algorithms for various purposes and typical results. Section 4 gives an outlook to expected and desirable improvements in the near future, including a direct retrieval of absolute currents from Doppler centroid processing of conventional SAR data and high resolution current measurements by along-track interferometry. We discuss requirements and recommendations for a better monitoring of current features by future spaceborne SARs. Finally, our main conclusions are discussed in section 5.

2. BACKGROUND

The fact that current gradients in the ocean can become visible in microwave radar images has been known since the 1970s. First spaceborne SAR images of the ocean with impressive signatures of oceanic features were acquired during the SEASAT mission in 1978 [1]. First theoretical models of the radar imaging mechanism were developed in the 1980s. With the launch of the scientific satellites ERS-1 and ERS-2 in 1991 and 1995, respectively [2], and of the commercial RADARSAT-1 in 1995 [3], the systematic use of spaceborne SAR for the remote sensing of current features began.

Today, recent and upcoming wide swath SARs such as ENVISAT ASAR [4] and RADARSAT-2 SAR [5] pro-

vide continuity and improved coverage at C band, and future systems at different frequencies, such as the German TerraSAR-X (X band) [6][7], will extend the variety of available data. The following subsections give a brief overview of basic principles, users and user requirements, and alternatives to spaceborne SAR.

2.1. SAR Imaging Theory of Current Features

A first quantitative, analytical theory of the SAR imaging of the spatially varying currents over underwater sandwaves was presented in 1984 [8]. Another group of authors published results of numerical simulations on the basis of the same fundamental ideas and equations in 1985 [9].

According to these theories, variations in the radar image intensity result from the straining of the short Bragg waves at the water surface, which are in resonance with the microwaves, by the spatially varying currents. After some simplifying assumptions in [8], the modulation of the image intensity was found to be proportional to the surface current convergence in radar look direction and to the reciprocal value of the so-called relaxation rate of the Bragg waves. The relaxation rate is a measure of the tendency of surface wave intensities to return to an equilibrium value after a distortion. It increases with the wind speed and with the wavenumber. Accordingly, the expression derived in [8] predicts that the strongest signatures of surface current gradients should be observed at low radar frequencies and that the maximum of the modulation should occur at the location of the strongest current convergence in look direction.

This first model was valuable for a basic understanding of the imaging mechanism, and it could be inverted easily, but it was found to underestimate most observed radar signatures, to overestimate the frequency dependence of the image intensity modulation, and to miss some other observed effects such as phase shifts between current gradients and radar signatures. Better results are obtained with so-called composite surface models which account for contributions of the entire two-dimensional ocean wave spectrum to radar signatures, such as the models described in [10] and in [11], [12]. The latest versions of these models account for effects of SAR imaging artifacts and of additional modulation mechanisms such as wave breaking. Nevertheless, the quantitative explanation of some observed signatures, such as very bright narrow lines at oceanic convergent fronts, is still a challenging problem for which no universal, generally accepted solution exists. Due to the complexity of the models and a lack of suitable reference data from experiments, the inclusion, tuning, and – in particular – the validation of new model components is usually difficult and time consuming or – in some cases – not possible at all.

2.2. Current Retrieval Strategy

Since SAR image intensities are sensitive to current gradients and not to the currents themselves, only variations in the surface current field, but not absolute currents, can be retrieved from observed SAR signatures if no additional information is available. As described in [13], the inversion of the imaging mechanism can theoretically be performed in an iterative approach, where a first-guess current field is modified until best agreement between simulated and observed SAR signatures is obtained. However, the resulting best estimate of the current field is not necessarily independent of the choice of the first-guess current field and the optimization strategy, thus these elements of the model inversion scheme must be selected with great care. Further problems can arise from the facts that the existing SAR imaging models are not perfect, that some model parameters are usually not well known, and that SAR signatures of wind variations can be very similar to the ones of current variations and occur at the same locations. Due to these limitations and difficulties, the full model inversion from a SAR image to a two-dimensional surface current field is not a very promising approach. For most existing applications, very specific algorithms have been developed, which exploit characteristic properties of the current feature of interest for major simplifications.

2.3. Users and Applications

Despite the limitations of the method and the difficulties in the data interpretation, spaceborne SAR is a valuable tool for a number of applications, since it is the only available instrument which can provide information on current features in areas of many square kilometers with a spatial resolution on the order of meters on a regular basis. Such information is particularly important in coastal areas, making the potential output attractive to a wide end user community. International collaborations such as the Global Ocean Observing System (GOOS) and its European branch EuroGOOS were specifically set up to increase the operational exploitation of marine data and identify the requirements of existing and potential end users [14]. In a more SAR-specific context, a similar analysis of end-user requirements has been carried out within the European project MARS AIS (Marine SAR Analysis and Interpretation System) [15].

Results of these studies suggest that typical users come from a variety of research-oriented and industry backgrounds, all of which are strongly related to or dependent on coastal dynamics. These include environmental protection and preservation agencies, coastal authorities, fisheries, oil and offshore industries, oceanographic research institutions, and users from a military background. Since quantitative information on ocean currents is difficult to retrieve with currently available al-

gorithms and usually requires a high degree of user interaction and expertise, most existing applications focus on feature detection and statistical image analysis. Current features that are currently monitored by SAR at operational or pre-operational levels include fronts, eddies, and internal waves. Additionally, the Bathymetry Assessment System developed by the Dutch company Argoss for the monitoring of bathymetric changes in coastal waters [16] provides, to our knowledge, the only commercially available service based on current retrieval from SAR imagery (see section 3.5).

The main factors hindering the operational use of SAR imagery by a wider user community fall into two categories. First, there is a lack of maturity of existing algorithms. Potential end users request methods that offer a certain ease of use, robustness and reliability. Also, the lack of distribution of algorithms outside specialist circles makes it difficult for end users to find out about existing tools. The second group of factors is inherent to the nature of SAR data. Inappropriate timing of available data, unsuitable spatial and temporal coverage and pricing of existing data can make SAR data quite unattractive for applications which require a fast response time and continuous monitoring on shorter time scales. Especially in coastal areas, this shortfall poses a significant problem that is only partly resolved by an improved coverage from wide-swath SARs.

Although the general problem of extracting currents from SAR data is far from being solved, it is possible to estimate some parameters of interest for specific applications. For example, the current field at an oceanic front can be parameterized by the width of the front and the difference between the currents at both sides of the front, thus the current retrieval can be reduced to the optimization of two or three parameters. The current field over oceanic internal waves is closely related to the internal waves' wavelength and phase velocity, which can be determined from the SAR image independently. Also in this case the current retrieval reduces to an optimization of a few parameters within limited ranges. In fact, not the surface current field, but the corresponding interior ocean parameters are the main parameters of interest. Also the currents over underwater bathymetry are only an interim model output in the retrieval of water depths from SAR signatures.

2.4. Alternatives to SAR

SAR is the only existing technique for the observation of surface current variations on spatial scales of tens of meters from spaceborne platforms. To understand its potential for particular applications, one should be aware of alternative methods and instruments for current measurements and their characteristic advantages and disadvantages. These are listed in the following.

Airborne SAR: SAR images very similar to the ones from satellites can be acquired from airborne platforms as well. The imaging mechanism and the data processing and interpretation techniques are the same. Advantages: Radar parameters, imaging geometry, and flight times can be optimized for the particular application. Disadvantages: The coverage in space and time is quite limited compared to a spaceborne SAR, and logistical efforts and operation costs may be more expensive than the use of standard data products from a satellite.

Multi-temporal image analysis / feature tracking: Instead of looking for signatures of current gradients in a single SAR image, one can try to identify features floating on the sea surface, such as oil films, in two images separated by some minutes to hours and compute the surface currents from the displacement of these features. This method is being used successfully for monitoring sea ice motions. Advantages: Absolute two-dimensional velocity vectors are obtained (mean velocities for the time period between the two images). Disadvantages: There are no suitable features in most SAR images of the open ocean; the time lag between spaceborne SAR images of the same area from the same sensor is usually too long; the spatial resolution of this current retrieval method is quite limited; the observed velocities of features are not necessarily surface current velocities. The method may be useful, however, for studies of the dynamics of larger current features, such as mesoscale eddies and meandering fronts (Gulf Stream). Also data from other spaceborne imaging sensors, such as ocean color or sea surface temperature images, are suitable for this kind of analysis.

Microwave Doppler radar: Like a police radar, a Doppler radar measures Doppler shifts of the frequency of the backscattered radar signal, which are proportional to line-of-sight (radial) target velocities. Conventional SAR images do not contain Doppler information, since the Doppler history of the backscattered signal is used for obtaining a high resolution in azimuth direction (flight direction) by creating a long synthetic aperture. However, some Doppler information can be preserved and used for current retrieval at lower resolutions, as described in section 4.3. Advantages: Absolute currents can be detected; the imaging mechanism is much more direct than the SAR intensity imaging mechanism of current features. Disadvantage: Limited spatial resolution. Doppler measurements at full SAR resolution can be obtained from an along-track InSAR with two antennas; see section 4.4. There are also ground-based microwave Doppler radars for current measurements. They can be used, for example, for current measurements in rivers or tidal channels, but the spatial resolution and coverage is quite limited. Two-dimensional current measurements can be obtained by looking at a test area from two different directions.

HF radar: The HF radar (high frequency radar) is a Doppler radar using wavelengths in the meter range. HF radar systems can be used for current measurements from the shore or from ships. State-of-the-art HF radar systems, such as WERA [17], have a maximum range on the order of 60 km and a spatial resolution of 300 m or worse. Two-dimensional current measurements are obtained by looking at a test area from two different directions. Advantages: Continuous current measurements with a temporal resolution of a few minutes can be obtained over long periods, which is important, for example, for the monitoring of shipping routes with strong tidal currents. Disadvantages: Limited spatial coverage and resolution; access to test areas and logistic requirements may be a problem; HF radar is not well suited for open ocean applications.

Optical imaging: Roughness variations at the sea surface, which result from wave-current interaction and which modulate the image intensity of SAR images, can also become visible in optical imagery of areas where specularly reflected sunlight is available. The imaging theory is discussed, for example, in [18]. In principle, this may be an alternative to SAR, but the imaging geometry is quite complex, and only areas which reflect direct sunlight towards the sensor can be probed. The method will not work at night or if clouds are present over an area of interest. Furthermore, some spaceborne optical sensors, such as SeaWiFS [19], have specific tilting mechanisms to avoid sunglint in the images, thus they cannot be used at all for this application.

Radar altimetry: Radar altimetry is a well established technique for the observation of geostrophic currents in the open ocean by measuring sea surface heights from satellites [20]. Latest instrument designs or mission concepts promise height measurements with a fine along-track resolution on the order of a few 100 meters [21] as well as measurements of cross-track surface slopes [22][23], permitting to retrieve two-dimensional current variations on scales of a few kilometers. Advantages: Depth-integrated currents are detected; the data satisfy the requirements of many open-ocean applications. Disadvantages: Only phenomena which affect the sea surface elevation are detected; the resolution is low compared to the resolution of a SAR; the measuring principle is not suited for coastal applications. Radar altimeters and SARs complement each other rather than competing with each other.

In-situ measurements from moorings, buoys, or ships: Of course one can measure currents in situ, which is usually done by mechanical instruments or by acoustical instruments, such as acoustic Doppler current profilers (ADCPs). Advantages: The techniques are well established and respected and can be used without major efforts; measurements can be performed at the depths of

interest; continuous measurements over a long period are possible. Disadvantages: Only point measurements are obtained; near-real-time data access from moorings and buoys is difficult; ice in the water, animals, ships, etc. can destroy the instruments.

Drifters / tracers: Instead of measuring currents at fixed locations (Eulerian approach), one can monitor the locations of drifters or chemical tracers which are floating freely within the moving water masses (Lagrangian approach). Advantage: One obtains information on actual paths of individual elements of the water body, integrated over relatively long times. Disadvantages: The coverage in space and time and the spatial and temporal resolution are very limited. This method is mainly used for observations of large scale circulation phenomena over long periods.

Hence, direct surface current measurements at spatial resolutions comparable with SAR images are extremely difficult. This limits the availability of validation data.

3. EXISTING ALGORITHMS

A variety of algorithms for the retrieval of information on current features from SAR imagery has been developed for a variety of purposes. We cannot discuss all existing algorithms and their specific qualities and potential applications in the context of this paper. However, we give an overview of some important classes of algorithms and particular examples which are representative of the state of the art in this field. For each algorithm class we describe the problem it is trying to solve, typical users and applications and their requirements, the technical concept of the algorithms, and the present status of the algorithm development and utilization.

3.1. Feature Detection

A correct detection and / or classification of SAR signatures of current features is a fundamental requirement for any further interpretation. While the detection of ships or oil spills has been performed in operational environments for a while, most existing algorithms for signatures of current features are less mature for various reasons: Signatures of current features are more complex than signatures of ships or oil spills; they can be similar to signatures of atmospheric or other features; and requirements of different users and applications are much more diverse than the well-focused requirements in the fields of ship and oil detection.

The problem: While SAR signatures of ships are always brighter and signatures of oil spills are always darker than the ambient image intensity and both kinds of features have clear other characteristic properties such as

typical shapes and sizes, surface current features can give rise to bright and dark signatures with wide ranges of modulation depths, sizes, and shapes. Furthermore, there can be very similar signatures of other features such as variations in the wind field. While specialists may be able to identify signatures of features of their interest and select appropriate algorithms for their further interpretation, this can be difficult for inexperienced users or just not reasonable in operational environments which require an automatic, ideally unsupervised, analysis of many SAR images. In addition to the general detection problem, SAR signatures of current features are often superimposed by signatures of atmospheric features which can be very similar. In such cases, a reliable classification algorithm is required to identify and separate signatures of oceanic and atmospheric origin and to avoid misinterpretation. An example of an ERS SAR image with signatures of oceanic internal waves as well as signatures of surface films and various atmospheric phenomena is shown in Fig. 1.



Fig. 1. ERS-1 SAR image of the Strait of Messina, Mediterranean Sea (8 September 1992), showing signatures of various atmospheric features and surface films and of two oceanic internal wave packets propagating southwest along the coast of Sicily (© ESA).

Applications and users: Feature detection and classification algorithms are useful for almost all applications dealing with SAR imagery of ocean scenes. They facilitate the interpretation of images with many different signatures, such as the one shown in Fig. 1. They are a basic requirement for an automatic analysis of large numbers of SAR images. Very likely, the availability of reliable feature detection algorithms would attract many new users of SAR imagery, who are interested in information on particular features that can be retrieved from SAR signatures, but who lack the knowledge or capacity to perform the feature detection or specific algorithm developments on their own. A reliable classification of SAR signatures of oceanic and atmospheric origin would improve the exploitation of both kinds of signatures, since information on wind variations on spatial scales on the order of some hundreds of meters within areas of many square kilometers can be quite valuable for meteorologists and can hardly be obtained from other spaceborne sensors.

Algorithm concept: An algorithm for the detection of signatures of (oceanic) internal waves was presented in [24]. It is based on a wavelet transform. It can analyze SAR images for the presence of internal waves signatures and show the location of such signatures. A more general wavelet-based algorithm, which can detect and classify signatures of features like fronts, internal waves, and eddies as well as ice edges and oil spills, was presented in [25]. A flow chart of this algorithm, which nicely visualizes the different steps of feature detection and classification, is shown in Fig. 2. For the detection of line features, a Radon transform [26] may be more appropriate than a wavelet transform.

If dual-polarization images, such as ASAR Alternating Polarization Mode data from ENVISAT [4], are available, one can exploit characteristic differences in the dependence of signatures of current and wind variations on the polarization. Very drastic differences of this kind were found in airborne real aperture radar data from the JUSREX experiment off the U.S. east coast in 1992: Pairs of images of the same scene at HH and VV polarization, acquired at a frequency of 13.3 GHz (Ku band) and a near-grazing incidence angle of 80° , exhibit pronounced signatures of oceanic internal waves at HH and of atmospheric convection cells at VV polarization – the two images look completely different [27].

A first theoretical explanation for the observed effect was given in [28]: Wave-current interaction usually has the strongest effect on wave intensities in the wavelength range of decimeters to meters, while wind variations on relatively short spatial scales will mainly modulate the shorter ripple waves which are directly generated by the wind. Since the relative contribution of waves which are long compared to the Bragg waves to

the backscattered power is larger at HH than at VV polarization, signatures of oceanic phenomena are stronger at HH. However, the model discussed in [28] cannot explain why radar signatures of wind variations should be stronger at VV than at HH polarization, since the relative contributions of short waves to the backscatter at both polarization should be the same.

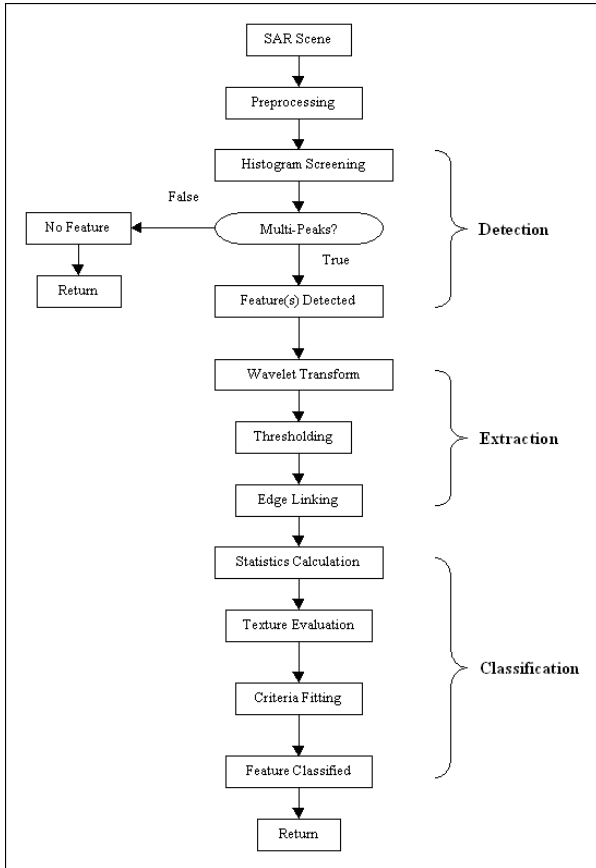


Fig. 2. Flow chart of the feature detection and classification scheme described in [25] (provided by A. Liu).

Characteristic polarization dependencies of SAR signatures of oceanic and atmospheric features have also been found in SAR data acquired from spaceborne platforms and at steeper incidence angles: Fig. 3 shows a pair of C band SAR images of a scene in the Atlantic Ocean which were acquired from the Space Shuttle Endeavour during the SIR-C / X-SAR mission in April 1994. The incidence angle is 31° . Both images exhibit strong signatures of two different features: A large signature consisting of multiple lines, extending from the lower left to the upper right, and a smaller signature consisting of a single bright line in the lower left, oriented almost perpendicular to the large signature. While the modulation depth of the large signature is almost the same in both images, the small signature is clearly stronger at HH than at VV polarization. Very likely, the feature causing the large signature is an atmospheric

internal wave, while the small feature must be an oceanic feature. This is a matter of ongoing research. Unfortunately, high-resolution in-situ data from the test area are not available.

Present status: To our knowledge, none of the described feature detection / classification algorithms has been implemented in such a way that it is being used operationally, although successful tests and performance analyses have been performed. The lack of mature feature detection and classification tools may be one of the main reasons for the relatively poor utilization and exploitation of SAR images of current features at present.

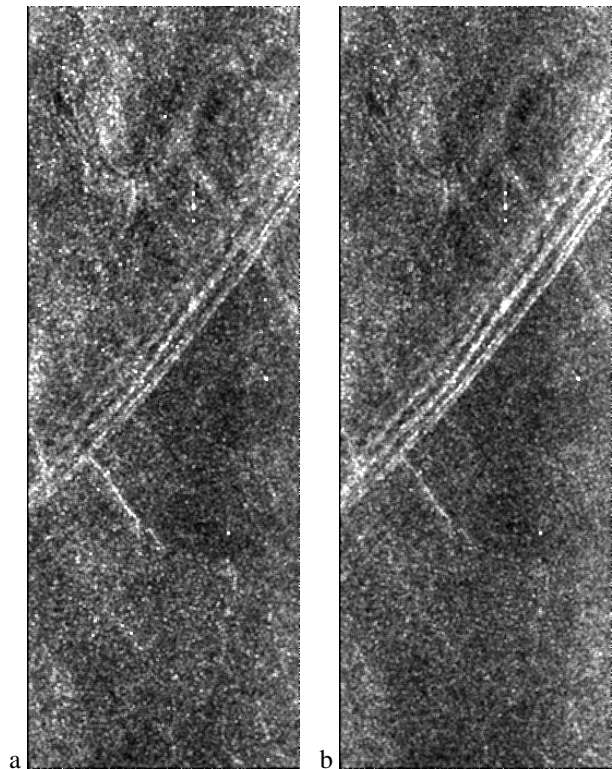


Fig. 3. Pair of C band SAR images (smoothed) of a scene in the Atlantic Ocean (14 April 1994) acquired from the Space Shuttle Endeavour during the SIR-C / X-SAR mission (from R. Romeiser and S. Ufermann). Incidence angle: 31° ; polarization: (a) HH, (b) VV; swath width: Approx. 31 km.

3.2. Feature Tracking

Feature tracking has already been listed in section 2.4 as an alternative to the retrieval of current gradients from SAR image intensity variations. We would like to mention it once more under "existing algorithms", since it is a method for the retrieval of absolute currents from multitemporal SAR images which can be quite useful where such images are available and where the knowledge of absolute currents is important. It can also com-

plement the analysis of signatures of surface current gradients, since information on mean currents can be valuable for the generation of a first-guess current field for further iterative optimization.

The problem: Conventional SAR intensity images do not contain information on absolute currents. If two or more SAR images of the same scene are available with a time lag that is short compared to the decorrelation time of visible surface feature patterns, one can try to identify features which are moving with the surface current and determine current vectors from the locations of these features in the different images.

Applications and users: Absolute current measurements are useful for a variety of applications. Since the spatial resolution and coverage of the currents that can be determined from multi-temporal images is quite limited (depending on the visible features and on the resolution and temporal separation of the SAR images, resolutions on the order of hundreds of meters to kilometers are realistic), one cannot use this technique to obtain information on current gradients at oceanic fronts (see section 3.3) or spatial variations of the currents over oceanic internal waves (section 3.4) or underwater bathymetry in coastal waters (section 3.5). However, low-resolution information on absolute surface current vectors can be valuable for oceanographic studies on larger-scale features such as the Gulf Stream or eddies. Furthermore, low-resolution currents from multi-temporal image analysis can provide valuable information on mean currents for a further retrieval of current variations at a higher resolution from SAR intensity signatures of features like oceanic fronts or underwater bathymetry.

Algorithm concept: Feature tracking requires the availability of two or more SAR images of the same scene with some time lag. Distinct features must be visible in both images (or pairs of adjacent images), which can be identified unambiguously. For example, patterns in surface films can be used. The feature tracking algorithm itself can be an extended feature detection algorithm or an algorithm analyzing the cross correlation function of the two images for individual sub-areas. For a correct calibration of the results, the rectification and collocation of the SAR images must be carried out with care.

An example of a feature tracking exercise with airborne SAR data was presented in [29]: In this case, two images of surface film patterns near the Gulf Stream edge with a temporal separation of 20 minutes were analyzed. Reasonable agreement of the SAR-derived currents with ADCP data was found; remaining differences are at least partly due to wind drift effects. The two SAR images and retrieved current vectors as well as a diagram showing a comparison of SAR-derived and ADCP-derived currents are shown in Fig. 4.

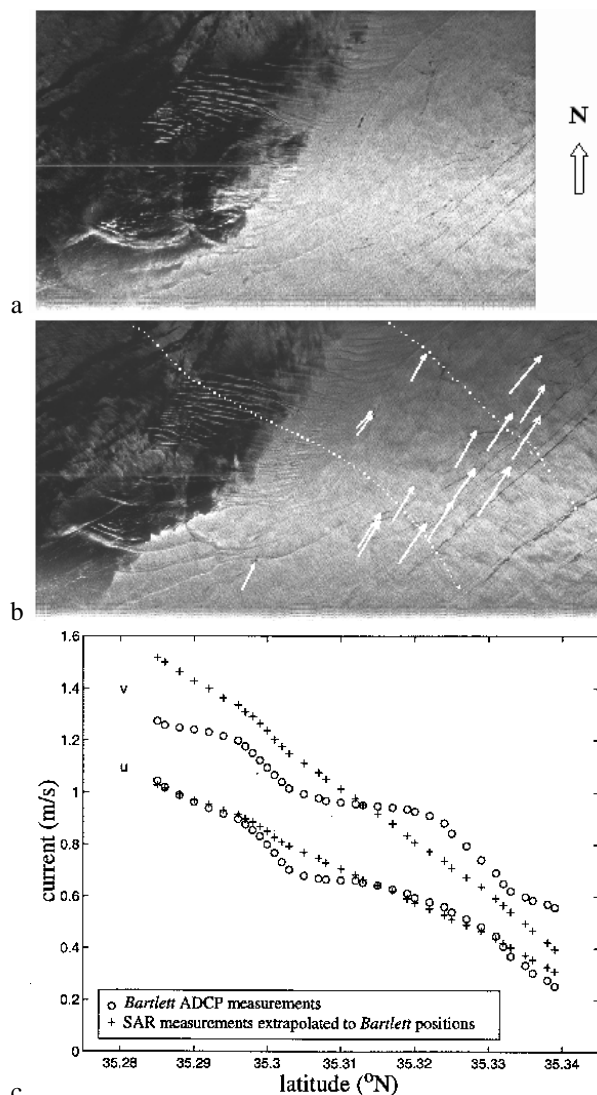


Fig. 4. Airborne L band SAR images of the Atlantic Ocean off Cape Hatteras, NC, USA, and surface currents retrieved by feature tracking; (a) first image, acquired on 16 September 1991, 16:30 UTC; (b) second image, acquired 20 minutes later; superimposed are retrieved surface current vectors and dotted lines indicating two ship tracks; (c) comparison of SAR-derived (+) and ADCP-derived currents (o) along the two ship tracks (from [29]; provided by D. Lyzenga).

To some extent, even slick patterns in single SAR images can be used as indicators of surface flow patterns [30][31][32][33]. However, as shown in [29] (cf. Fig. 4b), the slicks do not necessarily line up with the currents: The slick orientations are governed by the current gradients rather than the mean currents.

Present status: Feature tracking algorithms have been developed and used successfully for many technical applications, using images of a variety of objects from a variety of sources. The main problem in their applica-

tion to spaceborne SAR imagery of the ocean is the fact that suitable data are hardly available: To track surface features like surface films with spatial scales of tens to hundreds of meters, which can move at velocities on the order of decimeters to meters per second and change their shapes on time scales of minutes to hours, one needs images with a temporal separation on the order of minutes. Such data are not available from a single spaceborne SAR. However, tandem missions with two satellites on the same orbit, following each other within several minutes, can provide suitable data. Such missions are under consideration for topographic mapping purposes. In the framework of a tandem mission with a considerable duration of several months, the implementation and use of feature tracking algorithms for oceanographic studies may be useful.

3.3. Current Gradient Retrieval at Ocean Fronts

SAR signatures of oceanic current fronts, which can be very narrow bright lines, have attracted the interest of oceanographers as well as remote sensing scientists for quite a while, since they provide valuable information on circulation and mixing processes on the one hand, and they can cause enormous difficulties for modelers of SAR signatures of current features on the other hand, since most imaging models underestimate the observed strong signatures significantly. Thus SAR images with signatures of current fronts are popular test cases for SAR imaging models and interpretation algorithms. An example of an ERS SAR image of oceanic fronts off the south coast of Mexico is shown in Fig. 5.

The problem: The detection of signatures of fronts in SAR images is relatively easy, since fronts will usually become visible as distinct lines which are clearly brighter or darker than the ambient regions or which separate regions of different mean image intensities. However, the further interpretation of the signatures is difficult since the convergent currents at ocean fronts can give rise to a variety of effects which have an impact on the backscattered radar signal, such as hydrodynamic wave-current interaction, wave breaking, or wave damping by accumulated surface films. Furthermore, different temperatures of the water masses at both sides of an oceanic front can affect the atmospheric stratification and thus give rise to wind stress variations. The parameterization and / or modeling of these phenomena is quite difficult. Furthermore, high-resolution reference data from in-situ measurements for a calibration and validation of imaging models and current retrieval algorithms for ocean fronts are very rare.

Applications and users: Information on ocean fronts is useful to fishing industries and resource planners as well as oceanographers interested in circulation and mixing phenomena, transport of pollutants, nutrients, etc.



Fig. 5. ERS-2 SAR image of coastal waters off the Pacific coast of Mexico (3 April 1996, 16:50 UTC), showing signatures of several current fronts (from <http://www.ifm.uni-hamburg.de/ers-sar>, © ESA).

Algorithm concept: Until now, research in this field has mainly focused on dedicated experiments and case studies for a better understanding of fundamental hydrodynamic processes at current fronts. The analysis of radar signatures of current fronts has usually been complemented by in-situ measurements and analytical or numerical model calculations, such as in [34], [35], [36], [37], [38], [39], [40], [41]. The temporal evolution of current fronts is analyzed in [42]. Radar imaging models of ocean fronts have been discussed, for example, in [43], [44], [45]. A radar imaging model performance analysis was presented in [46]. The relative effect of current shear vs. convergence on SAR signatures of ocean fronts has been assessed in [35], [37]. The exploitation of information from multi-frequency / multi-polarization SAR images for an independent iterative optimization of current and wind variations at the Gulf

Stream front is demonstrated in [47]. A prototype of an interactive tool for an automatic analysis and interpretation of SAR signatures of current fronts on the basis of numerical simulations has been developed and demonstrated within MARS AIS [15]. Nevertheless, all existing models and algorithms for SAR signatures of ocean fronts are still pre-operational. For more information on latest developments in this field see [48] in this issue.

Present status: The existing models and algorithms for the analysis of SAR signatures of ocean fronts are in a pre-operational stage and cannot be given to inexperienced users. For the development and validation of robust models and algorithms, further dedicated experiments and theoretical studies need to be performed.

3.4. Analysis of Internal Waves Signatures

In a stratified ocean the interaction of the tidal flow with topographic features can generate internal solitary waves (ISWs), for instance at sills [49][50] and at continental shelf breaks and slopes [51][52][53]. The ISWs are gravity waves and usually develop as a single soliton which disintegrates into a train of ISWs. The associated currents induce regions of convergent and divergent surface currents, which can become visible as bright and dark bands, respectively, in SAR images. A first theory of the radar imaging mechanism of ISWs was presented in 1985 [54]. Since then, numerous investigations of ISW SAR signatures have been carried out, showing that ISWs are ubiquitous in the ocean [55].

The problem: It is difficult to derive oceanic parameters from SAR signatures of ISWs because the relationship between environmental parameters (stratification, bottom topography, ambient current, wind speed and direction) and ISW parameters (characteristic half width, amplitude, propagation speed) is quite complex. However, assuming a two-layer stratified ocean, the mixed-layer depth [51][56] and the temporal and spatial evolution of an ISW [49] can be estimated to some extent from the SAR signatures. The development and demonstration of an inversion scheme for the retrieval of oceanic parameters from SAR signatures of ISWs has been one of the objectives of MARS AIS [15].

Applications and users: In continental shelf regions, shoaling and breaking of ISWs enhances nutrient concentration and mixing [57][58]. This is of interest primarily for studies concerning the nutrient budget and biological activity on continental shelves. Deep water ISWs, such as the ones observed in the Sulu Sea [59], can have peak-to-trough amplitudes of more than 100 m, and propagation speeds exceeding 2 m/s. Current changes caused by the passage of such an ISW may create shear currents that are dangerous for any sort of underwater activity. Moreover, there is evidence that

ocean tides alone are insufficient to account for the loss of rotational energy of the Earth-Moon system [55], and that the energy of ISW dissipation may make a small but significant contribution [60]. Accordingly, parameters of interest for scientists and other users are the presence and frequency of ISWs, their amplitudes, characteristic half widths, propagation speeds, pycnocline / interface depths, and the current variations during the passage of ISWs.

Algorithm concept: Many models have been developed to describe ISWs [55]. Under the assumption of a two-layer stratified ocean, an ISW can be described by a one-dimensional form of the Korteweg-deVries (KdV) equation for shallow water waves [61][62]. The algorithm developed within MARS AIS uses a combination of an analysis of the SAR signatures of ISWs (location, wavelength, modulation depth of the image intensity), analytical calculations, and simulations with the forward SAR imaging model M4S [11][12]. Profiles are extracted from the ISW signatures in a SAR image as shown in Fig. 6. A look-up table relates densities and depths of the two water layers, total water depth, propagation speed, and surface currents according to the KdV equation. Possible realizations of the horizontal surface current profile associated with each individual ISW of the wave train are obtained from the look-up table, depending on the ISW's propagation speed (determined from its distance from the point of generation and the tidal phase), the total water depth, and first-guess values of the densities and depths of the two water layers, using climatological values.

For each current field corresponding to a possible parameter combination, the numerical SAR imaging model M4S is used to compute a theoretical SAR image intensity profile. The model results are then compared with the measured intensity profile. The density and water layer depth values that correspond to the best-fit simulated SAR signature are considered as best estimate of the actual oceanic conditions in the test case. Fig. 7 shows a SAR image intensity profile derived from Fig. 6 together with the corresponding best-fit model result.

Present status: The algorithm developed within MARS AIS is available only to project partners so far. It has been applied to data acquired in the Straits of Gibraltar and Messina, comparing well with in-situ validation data collected at the latter location. However, further work is needed before the algorithm can be applied to a wider range of geographic locations or to extend the algorithm to areas with ISWs for which the shallow-water approximations do not hold [55][63]. Accurate knowledge of wind speed and direction are required as input parameters for the algorithm since they can have a significant effect on the resulting SAR signatures [64], as can natural or anthropogenic surface films [65].

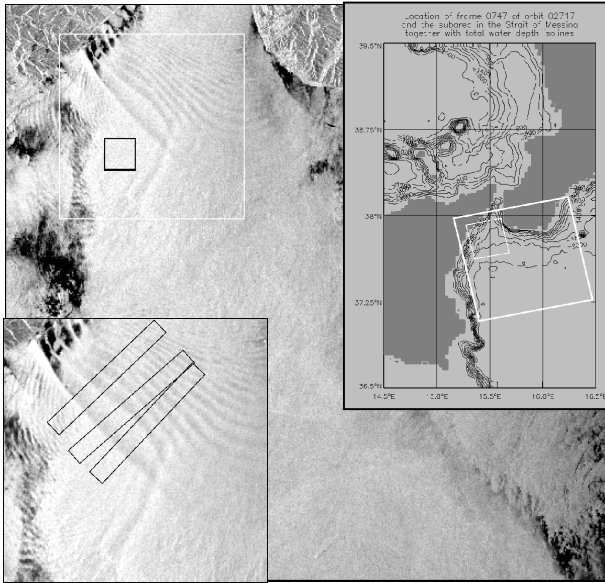


Fig. 6. ERS-2 SAR image of the area south of the Strait of Messina, Mediterranean Sea (27 October, 1995). The map inset shows the location of the frame together with the bathymetry. The inset on the bottom left shows a blowup of the area marked by the white square (31 km \times 31 km). Three black rectangles mark user-defined transects. The small black square in the main image marks the region over which image intensities were averaged for wind speed retrieval (from S. Kern).

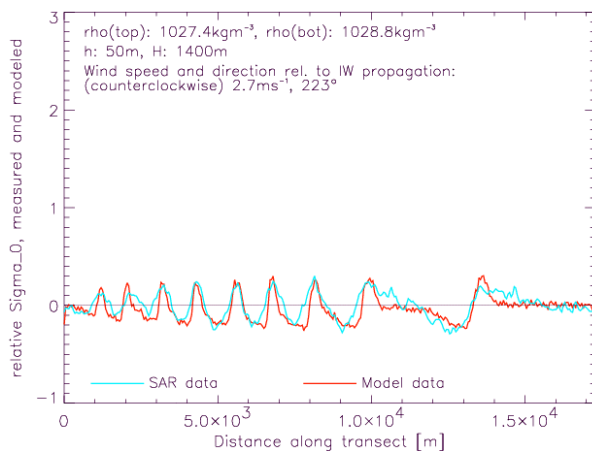


Fig. 7. Profiles of the measured (blue) and modeled (red) relative SAR image intensity for one of the transects shown in Fig. 6; correlation and regression coefficients are 0.797 and 0.983, respectively (from S. Kern).

3.5. Bathymetry Assessment

One of the most mature applications based on SAR imagery of current features is the monitoring of bathymetric changes in coastal waters. In close collaboration with coastal authorities (Rijkswaterstaat), the small company Argoss in the Netherlands has made quite some progress in this field during the last years. A detailed overview of

their "Bathymetry Assessment System" (BAS) with example results is given in [16]. For more literature on the radar imaging of underwater bottom topography see, for example, [8], [9], [18], [66], [12], [67].

The problem: It has been known since the 1970s that underwater bottom topography in coastal waters can become visible in radar images [68][69]. First theoretical models were presented in 1984 and 1985 in [8], [9]. It was realized that the radar signatures, which sometimes appear to show the actual underwater bathymetry (an example is shown in Fig. 8) result from a modulation of tidal currents by the spatially varying water depths. The inversion of SAR images into topographic maps would be quite attractive for various applications, thus several research and development projects in this field have been carried out since the 1980s.

Applications and users: Bathymetric surveys are important for applications such as the monitoring of shipping routes, morphodynamics, coastal protection, and high-resolution circulation modeling. Typical users are coastal authorities, environmental protection agencies, oil and offshore industries, and research institutions. Bathymetric surveys have traditionally been performed by echosoundings from ships, which are time-consuming and expensive, particularly if they have to be carried out frequently in highly dynamic areas. The integration of SAR data in a bathymetric monitoring system makes sense if it helps to reduce costs or to improve the spatial and temporal coverage and sampling.



Fig. 8. ERS-1 SAR image of the east coast of China (8 July 1995, 2:34 UTC), showing clear signatures of underwater bottom topography (from <http://www.ifm.uni-hamburg.de/ers-sar>, © ESA).

Algorithm concept: The BAS uses a combination of echosoundings on a relatively coarse grid and SAR imagery. A model suite consisting of a flow model, a wave-current interaction model, and a radar scattering model, is applied to an initial bottom topography obtained from the echosoundings, and model parameters as well as water depths between the existing data points are optimized iteratively until best agreement between simulated and observed SAR signatures is obtained.

Present status: The BAS has been applied successfully to a variety of test areas and scenarios (mainly off the Dutch coast), including dedicated validation studies as well as quasi-operational applications. It has been shown that the amount of echosoundings can be reduced significantly (compared to a purely traditional approach) without losing accuracy and spatial resolution (see [16]). Argoss is offering bathymetry retrieval as an operational service. As far as we know, the Dutch coastal administration Rijkswaterstaat (RWS) decided in fall 2003 to integrate the Bathymetry Assessment System into its operational coastal monitoring activities.

4. THE FUTURE

As can be seen from the algorithm descriptions in section 3, the exploitation of SAR signatures of most kinds of current features is still in an experimental stage. Reasons for this are manifold: Existing algorithms or numerical imaging models are not available to potential users, have not reached mature levels of development, or are not sufficient to satisfy the requirements of some applications. Also the spatial and temporal coverage of the areas of interest of some potential users and a continuous data availability over longer periods can be serious problems. In the following we discuss these problems and possible solutions as well as the potential of two emerging new techniques for current measurements by SAR, that is, the Doppler centroid analysis and along-track interferometry.

4.1. Improved Exploitation of Available Data

The current feature algorithms that are available today and the corresponding SAR images are not being used by many potential users, even if the results would satisfy their requirements perfectly. Many people, laboratories, or agencies are not aware of the availability of SAR imagery and algorithms and of their potential. Another problem is the fact that many algorithms have not reached a stage of development where they can be used by inexperienced users without major problems or where they have been tested and validated so convincingly that potential users are willing to use them for routine applications. Projects like MARS AIS [15], in which interpretation algorithms for SAR signatures are

implemented with user-friendly interfaces and presented to potential users together with educational material and example results, are hopefully helping to overcome these shortcomings and to improve the awareness and the acceptance of the potential of SAR imagery.

Other users may be reluctant to use SAR images in operational contexts since the continuity of the data supply is not guaranteed: Satellites like ERS-1, ERS-2, and ENVISAT must be considered as research satellites with a limited lifetime, which have been designed to achieve certain mission goals and to test and demonstrate some new technologies and data products, but there has been no guarantee for a continuous availability of the data products over periods longer than the lifetimes of the satellites. This is a significant difference between existing spaceborne SARs (except, perhaps, the RADARSAT program) and other remote sensing instruments or satellites such as the AVHRR program of NOAA or the METEOSAT program of ESA [70].

Further impediments to the use of SAR data and algorithms may arise from the difficulties and costs associated with the ordering and the analysis of SAR images: Inexperienced users may be not willing or not able to figure out what kinds of data products they can order, how this must be done, and how the data must be processed to obtain the desired information. Also the availability of user-friendly algorithms is a problem in this context. Since the current features and the specific applications of different users are quite diverse, space agencies cannot deliver higher-order data products to end users (as it can be done, for example, with SAR-derived wind fields and ocean wave spectra), but they must give the SAR images themselves to the users and hope that the users know how to interpret the data. A free distribution of feature detection algorithms and other useful tools and educational materials to customers of SAR images would probably help to make the handling and interpretation of SAR imagery easier and to attract some of the less ambitious users this way.

4.2. Model and Algorithm Improvements

Not only the availability and ease of use of existing algorithms, but also the quality of the underlying theoretical models for the SAR imaging mechanism of current features is a considerable problem which has been completely neglected in some recent projects with a strong emphasis on the demonstration of the capabilities of SAR to inexperienced potential users. In fact, there are many open questions in the modeling of SAR signatures of oceanic phenomena, and the basic research in this field needs to be continued if the development of more accurate, more reliable, and more general algorithms for the retrieval of information on current features is a serious objective.

A hot topic in this field is the modeling of wave breaking effects. The breaking of ocean waves can reduce the energy in some parts of the wave spectrum and enhance the energy in other parts. Furthermore, steep waves can become highly nonlinear and form higher-order harmonics. The evolution of the waves in spatially varying current fields and their radar backscattering properties under such conditions can be quite different from predictions of small perturbation theories. Several studies on wave breaking processes and their effect on radar signatures have been carried out during the last 10 years or so [71][72][44][45][73], but a completely satisfactory model has not been developed yet, and some more dedicated laboratory and field experiments will probably be required in order to understand all relevant physical processes of wave breaking and to validate various model components (see also [48]). Also other modulation mechanisms, such as the feedback effects between the spatially varying surface roughness and the wind stress [74][75], need to be investigated in more detail.

In this context one should be aware of the fact that there are some mature numerical SAR imaging model suites which are available to interested users and scientists for test calculations and scientific investigations, such as the ERIM Ocean Model (EOM) based on the theory described in [10], the M4S model [11][12][81], and the WHIT model [66][67]. These programs offer various options for model terms and parameters and can be quite valuable for sensitivity analyses of SAR signatures, the development of inversion algorithms, and similar activities. To obtain the model suites (source code or executables), one should contact the authors. Also the model used at the U.S. Naval Research Laboratory [44][45] and the one described in [48] may be available on request.

4.3. Current Retrieval from Doppler Centroids

In the conventional processing of SAR raw data, the Doppler history of the backscattered signal is exploited for the creation of a long synthetic aperture in order to obtain a high resolution in azimuth direction. As an artifact of this processing, the extra Doppler shift associated with the line-of-sight velocity of a moving target is translated into an azimuthal displacement of this target in the image (train-off-the-track effect). Except for this effect, the fully processed SAR image does not contain explicit information on target velocities anymore.

One can, however, preserve some information on mean Doppler shifts (Doppler centroids) by processing the data at a reduced resolution or retrieve Doppler shifts from the phase statistics of complex data. This idea was first proposed in 1979 in [76], but it could not be demonstrated very well with L band SAR data from SEASAT. A successful demonstration with C band data

from ERS SAR was presented in the late 1990s [77]. A crucial element of the technique is the computation of theoretical Doppler centroids of non-moving terrain, which result from the relative motion between satellite and rotating earth, and which need to be subtracted from the measured Doppler centroids to obtain the Doppler shifts associated with sea surface motions. The spatial resolution obtained from the Doppler centroid analysis is on the order of 1 to 2 km, thus comparable to the real aperture radar resolution of a spaceborne SAR.

The Doppler centroid analysis has also been demonstrated with ENVISAT ASAR wave mode data. The qualitative agreement between SAR-derived surface velocities and the known general circulation has been found to be good, but the correction of absolute retrieved radial surface velocities for contributions associated with the local wind vector and ocean wave spectrum is crucial and a matter of ongoing studies [78]. If these problems can be solved, surface current measurements with SAR at spatial resolutions on the order of kilometers can be quite attractive for some applications. Furthermore, a systematic application of the method to historical ERS-1 and ERS-2 SAR raw data (particularly wave mode data covering the global oceans) could result in a quite valuable data base of worldwide surface currents since 1991. Details of the Doppler centroid analysis technique, example results, and potential applications are discussed in another paper in this issue [78].

4.4. Along-Track InSAR

The along-track InSAR (along-track interferometric SAR) technique combines the high resolution of a SAR with Doppler shift measurements. Thus an along-track InSAR can directly detect radial surface currents and current variations on spatial scales of a few meters. The concept was first proposed in 1987 in [79]: Two complex SAR images of a scene (containing amplitude and phase information of the backscattered signal for each pixel) which are acquired with a short time lag on the order of milliseconds exhibit phase differences proportional to the time lag and to the Doppler shift of the signal. To obtain two images with a short time lag, two SAR antennas must be separated by some distance in flight (along-track) direction.

Experiments with airborne along-track InSARs have been performed since 1989 [80]. The data interpretation has turned out to be more complicated than originally expected, since the InSAR-derived velocities have to be corrected for contributions of wave motions. However, the InSAR imaging mechanism of currents is much more linear than the SAR intensity imaging mechanism of current gradients, and the correction of the data is relatively easy and does not require specific assumptions regarding the nature of a current feature of interest

like the interpretation of SAR intensity imagery. Detailed theoretical descriptions of the along-track InSAR imaging mechanism and the inversion problem can be found in [80], [81], [82].

Along-track interferometry from a spaceborne platform was recently demonstrated with data from the Shuttle Radar Topography Mission (SRTM) in early 2000 [83][84]. The interferometric X band SAR on the Space Shuttle Endeavour was mainly designed for the generation of digital elevation maps of land surfaces by cross-track interferometry. The cross-track antenna separation was 60 m. For technical reasons, there was also an along-track separation of 7 m, which could be used for current measurements. Unfortunately, the along-track separation of 7 m and the corresponding time lag of 0.5 ms between the two SAR images are quite short compared to the ideal time lag at X band, which would be on the order of 3 to 5 ms [81], [82]. This results in a relatively low sensitivity for small current variations and relatively high phase noise. However, phase noise can be reduced by averaging over many pixels.

Fig. 9 shows an example of a current field derived from an SRTM phase image of the "Waddenzee" area off the Dutch coast. This current field looks still somewhat noisy, but it exhibits clear signatures of tidal current patterns. A comparison with a simulated current field from the Dutch circulation model KUSTWAD [85] for the same tidal phase revealed an overall correlation of 0.558, which is reasonable in view of the remaining noise in the SRTM result and obvious systematic differences between the SRTM- and KUSTWAD-derived currents in some parts of the test area. Very likely, these differences can be attributed mainly to actual differences between the current field at the time of the SRTM overpass and the simulated current field, not to shortcomings of the SRTM result.

As discussed in [84], results of a more detailed statistical analysis indicate that the agreement of spatial variations in the SRTM- and KUSTWAD-derived current fields on different length scales is constantly good down to scales on the order of 1 km. Autocovariance functions of both current fields show consistently that most of the variations occur at longer length scales. Accordingly, one can conclude that practically all variations in the current field which are relevant to the circulation model are resolved by SRTM. In view of the fact that the parameters of SRTM are quite unfavorable for current measurements, this is an encouraging result.

A simulation with the numerical SAR / InSAR imaging model M4S, using the current field from KUSTWAD as input and all relevant parameters of the SRTM overpass scenario, confirmed that M4S is well suited for the simulation of InSAR data products. Not only the domi-

nant current patterns, but also the noise characteristics of the original SRTM data are reproduced realistically in the simulation. M4S can thus be used well for performance analyses of future InSARs or InSAR concepts.

As a first satellite with along-track InSAR capabilities, the German TerraSAR-X will be launched in late 2005 [6][7]. The phased-array X band SAR antenna of TerraSAR-X with a total length of 4.8 m can be switched to a split antenna mode, in which two halves act as separate receiving antennas with an along-track separation of 2.4 m between the phase centers. The split antenna mode will be implemented mainly for polarimetric measurements over land and ice, but it can be used as well for interferometric current measurements with an effective time lag of 0.17 ms.

At an incidence angle of 40° this translates into a horizontal velocity / phase ratio of about 140 m/s per 2π . That is, the sensitivity is even worse than the one of SRTM in the "Waddenzee" test case by a factor of about 3.6; a current change by 1 m/s corresponds to a phase difference change of only 2.6° . However, the single-look spatial resolution of TerraSAR-X (3 m in the stripmap mode with a swath width of 30 km) is much higher than the one of SRTM (12.5 m); more than 1100 independent samples of the phase difference can be averaged within $100 \text{ m} \times 100 \text{ m}$. Model predictions indicate that this will finally result in current measuring capabilities very similar to the capabilities of SRTM in the "Waddenzee" test case. That is, one can expect current measurements at reasonable quality at a resolution of a few 100 meters from TerraSAR-X.

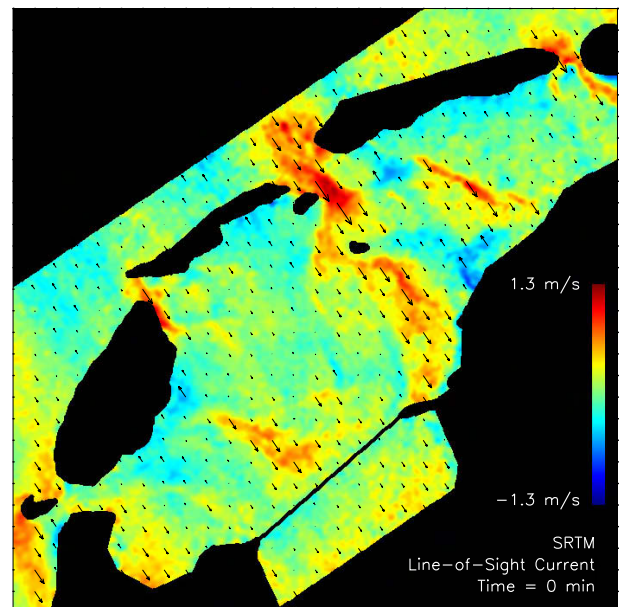


Fig. 9. Line-of-sight current field derived from an SRTM phase image of the Dutch coast; test area size = $70 \text{ km} \times 70 \text{ km}$ (from R. Romeiser).

With a longer antenna separation, much higher resolutions could be obtained, and the InSAR could be used, for example, for measurements of orbital wave motions (see also [86]). Also the limitation to one-dimensional measurements of the line-of-sight current component could be overcome with a dual-beam along-track InSAR, as proposed in [87]. If a successful TerraSAR-X mission triggers a considerable demand for along-track InSAR data, such advanced along-track InSAR systems can be implemented on satellites within about 10 years. In view of the facts that along-track InSAR is clearly superior to conventional SAR for all applications dealing with surface current features and that there is a high demand for current measurements and for information on current features, this is a likely development.

4.5. Future SAR Mission Requirements

As already mentioned, some continuity in the availability of certain types of SAR imagery (say, C band VV data) appears to be desirable, since users will have to analyze signatures of current features on their own and will not want to invest considerable amounts of money in the development and implementation of algorithms and data handling structures which can be used for very limited periods only. For many applications an improved temporal sampling of test areas would be more important than, for example, improvements in the spatial resolution or changes in the available radar frequencies. To some extent, a better temporal sampling can be achieved by using wide swath SARs such as the ones on RADARSAT-1 [3], ENVISAT [4], or RADARSAT-2 [5]. Even better are concepts with multiple satellites, such as the French-Italian COSMO-SkyMed program for an advanced monitoring of the Mediterranean Sea (<http://www.alespazio.it/program/tlr/cosmo/cosmo.htm>).

The frequency requirements for different applications are somewhat diverse, although this is not a critical problem: C band is fine, but because of a more linear relationship between surface current gradients and modulated Bragg wave and SAR image intensities at lower frequencies, L band would be desirable for the retrieval of surface currents or bathymetric maps from SAR imagery. In contrast, the along-track InSAR imaging mechanism is more linear at higher frequencies [81], the two InSAR antennas can be so closely together at X band that they can be installed on a single platform, which is practically impossible at L band (the ideal antenna separation scales with the radar wavelength). Thus X band is preferred for along-track InSARs. An along-track InSAR is quite desirable, since it permits direct current measurements at full SAR resolution.

Regarding the radar polarization, dual-polarization (HH and VV) systems have advantages for the identification of signatures of oceanic and atmospheric phenomena

(see section 3.1). Incidence angle requirements are diverse: The incidence angle should not be too high to avoid signal-to-noise problems (particularly at HH polarization) and complicated scattering effects such as shadowing or multiple scattering, and it should not be too low to avoid strong specular reflection. For current measurements by along-track InSAR or Doppler centroid analysis, incidence angles should be as high as possible to maximize the relative contribution of horizontal velocities to the Doppler shift of the signal by the moving water surface. Altogether, incidence angles of about 30° to 60° appear to be the best compromise.

Finally, we would like to point out that a dual-beam SAR or InSAR system looking forward and backward at, say, 45° from the broadside direction would have several advantages for oceanographic applications: In addition to the possibility to measure two current components at once, a system of this type would permit an analysis of feature contrast variations with look direction, and it would certainly benefit wind measurement applications.

5. DISCUSSION

Since the first Workshop on Coastal and Marine Applications of Wide Swath SAR in 1999 [88], considerable progress has been made in the field of the observation of ocean current features by SAR: Commercial services such as the "Bathymetry Assessment System" have been established, various pre-operational image interpretation algorithms for oceanic internal waves, fronts, and other features have been implemented and demonstrated, and initiatives like EuroGOOS and MARS AIS have investigated user requirements quite comprehensively and tried to disseminate the potential of spaceborne SAR to many potential users. Furthermore, some progress has been made in the forward modeling of processes such as wave breaking or the feedback between the hydrodynamically modulated surface roughness and the wind stress, new data analysis techniques such as the Doppler centroid analysis have been developed, along-track interferometry from space has been demonstrated, and attractive new sensors and sensor modes, such as the Alternating Polarization Mode of ENVISAT ASAR or the split antenna mode of TerraSAR-X have been implemented or will be implemented in the near future.

The implementation of the Doppler centroid analysis, high-resolution current measuring capabilities of upcoming InSARs, and a better temporal sampling by multi-satellite systems will make the use of SAR data products attractive for some applications for which satisfactory data products cannot be derived from the intensity images which are available today, such as a near-real-time monitoring and the assimilation of SAR-derived current fields into circulation models for re-

search, public safety, search and rescue, pollution monitoring and prediction, fisheries, or recreational applications. Based on existing data which would be available immediately, one could generate maps of coastal current features such as fronts, eddies, or internal waves, derive an internal wave climatology, and analyze the data for an improved general understanding of physical and biochemical processes in the oceans. A better dissemination of the potential of SAR for such applications is desirable.

A great potential for a better exploitation of SAR imagery lies also in synergies between data from SAR and other sensors [89], as well as in synergies with numerical models and between different SAR data products: For example, temperature data from radiometers and SAR-derived mean wind speeds can be valuable for the interpretation of a SAR signature of an oceanic front.

Some of the emerging applications are just around the corner, some will need more time. However, we are quite optimistic that the use and exploitation of spaceborne SAR for applications related to current features will keep growing and that the introduction of the new technologies and improved algorithms will be a success. Finally, the retrieval of useful and reliable information on current features from SAR data is a more challenging problem than the retrieval of ocean wave spectra or wind fields, and the development and implementation of mature algorithms has consumed more time, money, and manpower, but in view of the variety of potential applications and the promising results of recent projects, this investment appears to be justified.

ACKNOWLEDGMENTS

This paper has emerged from the session on current features at the Second Workshop on Coastal and Marine Applications of SAR at Svalbard, Norway, in September 2003. It is based on opinions, algorithm descriptions, and example results provided by attendees of the workshop and other specialists working in this field. The authors are particularly grateful to Fabrice Collard, Ben Holt, Johnny Johannessen, Vladimir Kudryavtsev, Antony Liu, David Lyzenga, and Christopher Wacker- man for significant contributions.

REFERENCES

1. Fu L.L. and Holt B., *Seasat Views Oceans and Sea Ice With Synthetic-Aperture Radar*, JPL Publ. 81-120, 200 pp., Jet Propulsion Lab., Pasadena, CA, USA, 1982.
2. Alpers W., Measurement of mesoscale oceanic and atmospheric phenomena by ERS-1 SAR, *URSI Radio Sci. Bulletin*, No. 275, 14-22, 1995.
3. RADARSAT International, *RADARSAT Illuminated, Your Guide to Products and Services*, 113 pp., RADARSAT International, Communications Department, Richmond, BC, Canada, available at http://www.rsi.ca/resources/education/rsiug98_499.pdf, 1999.
4. Attema E. et al., *Envisat ASAR Science and Applications*, ESA SP-1225, 59 pp., ESA, Noordwijk, Netherlands, available at http://earth.esa.int/pub/ESA_DOC/SP_1225.pdf, 1998.
5. Canadian Space Agency, *RADARSAT-2, A New Era in Earth Observation*, Technical brochure, 4 pp., available at http://www.space.gc.ca/asc/eng/csa_sectors/earth/radarsat2/inf_tech.asp#Publication, 2000.
6. Suess M., Riegger S., Pitz W., and Werninghaus R., TerraSAR-X – design and performance, *Proc. EUSAR 2002*, 4 pp., VDE Conferences Office, Frankfurt / Main, Germany, 2002.
7. Mittermayer J., Alberga V., Buckreuf S., and Riegger S., TerraSAR-X: Predicted performance, *Proc. SPIE 9th Int. Symp. Rem. Sens.*, 12 pp., Int. Soc. Optical Eng., Bellingham, WA, USA, 2002.
8. Alpers W. and Hennings I., A theory of the imaging mechanism of underwater bottom topography by real and synthetic aperture radar, *J. Geophys. Res.*, Vol. 89, 10529-10546, 1984.
9. Shuchman R.A., Lyzenga D.R., and Meadows G.A., Synthetic aperture radar imaging of ocean-bottom topography via tidal-current interactions: Theory and observations, *Int. J. Rem. Sens.*, Vol. 6, 1179-1200, 1985.
10. Lyzenga D.R. and Bennett J.R., Full-spectrum modeling of synthetic aperture radar internal wave signatures, *J. Geophys. Res.*, Vol. 93, 12345-12354, 1988.
11. Romeiser R., Alpers W., and Wismann V., An improved composite surface model for the radar backscattering cross section of the ocean surface, 1. Theory of the model and optimization / validation by scatterometer data, *J. Geophys. Res.*, Vol. 102, 25237-25250, 1997.
12. Romeiser R. and Alpers W., An improved composite surface model for the radar backscattering cross section of the ocean surface, 2. Model response to surface roughness variations and the radar imaging of underwater bottom topography, *J. Geophys. Res.*, Vol. 102, 25251-25267, 1997.
13. Romeiser R., Ufermann S., and Alpers W., Remote sensing of oceanic current features by synthetic aperture radar – achievements and perspectives, *Ann. Telecommun.*, Vol. 56, 661-671, 2001.

14. Fischer J. and Flemming N.C., *Operational Oceanography: Data Requirements Survey, EuroGOOS Publication No. 12*, 60 pp., Southampton Oceanography Centre, Southampton, United Kingdom, ISBN 0-904175-36-7, 1999.
15. Johannessen J.A., Garello R., Chapron B., Romeiser R., Pavlakis P., Robinson I., Connolly N., Nittis K., Hamre T., Ufermann S., Alpers W., Espedal H., Furevik B., Cummins V., and Tarchi D., Marine SAR analysis and interpretation system – MARS AIS, *Ann. Telecommun.*, Vol. 56, 655-660, 2001.
16. Calkoen C.J., Hesselmanns G.H.F.M., Wensink G.J., and Vogelzang J., The Bathymetry Assessment System: Efficient depth mapping in shallow seas using radar images, *Int. J. Rem. Sens.*, Vol. 22, 2973-2998, 2001.
17. Essen H.H., Gurgel K.W., and Schlick T., On the accuracy of current measurements by means of HF radar, *IEEE J. Oceanic Eng.*, Vol. 25, 472-480, 2000.
18. Hennings I., Doerffer R., and Alpers W., Comparison of submarine relief features on a radar satellite image and on a Skylab satellite photograph, *Int. J. Rem. Sens.*, Vol. 9, 45-67, 1988.
19. Hooker S.B. and McClain C.R., The calibration and validation of SeaWiFS data, *Progress in Oceanography*, Vol. 45, 427-465, 2000.
20. Wunsch C., and Stammer D., Satellite altimetry, the marine geoid, and the oceanic general circulation, *Ann. Rev. Earth Planet. Sci.*, Vol. 26, 129-253, 1998.
21. Raney R.K., The Delay/Doppler Radar Altimeter, *IEEE Trans. Geosci. and Rem. Sens.*, Vol. 36, 1578-1588, 1998.
22. Raney R.K., Fountain G.H., Gold R.E., Lew A.L., and Porter D.L., WITTEX: A constellation of three small satellite radar altimeters, *Proc. 13th Ann. AIAA / Utah State Univ. Conf. on Small Satellites*, Provo, UT, USA, 1999.
23. Pollard B.D., Rodriguez E., Veilleux L., Akins T., Brown P., Kitiyakara A., Zawadski M., Datthanasant S., and Prata A. Jr., The wide swath ocean altimeter: Radar interferometry for global ocean mapping with centimetric accuracy, *Aerospace Conf. Proc.*, Vol. 2, 1007-1020, IEEE, Piscataway, NJ, USA, 2002.
24. Rodenas J.A. and Garello R., Internal wave detection and location in SAR images using wavelet transform, *IEEE Trans. Geosci. and Rem. Sens.*, Vol. 36, 1494-1507, 1998.
25. Wu S.Y. and Liu A.K., An automated ocean feature detection, extraction and classification algorithm for SAR imagery, *Int. J. Rem. Sens.*, Vol. 24, 935-951, 2003.
26. Copeland A.C., Ravichandran G., and Trivedi M.M., Localized Radon transform-based detection of ship wakes in SAR images, *IEEE Trans. Geosci. and Rem. Sens.*, Vol. 33, 35-45, 1995.
27. Etkin V.S., Trokhimovski Y., Yakovlev V.V., and Gasparovic R.F., Comparison analysis of Ku-band SLAR sea surface images at VV and HH polarizations obtained during the Joint US/Russia Internal Wave Remote Sensing Experiment, *Proc. IGARSS 1994*, 744-746, IEEE, Piscataway, NJ, USA, 1994.
28. Ufermann S. and Romeiser R., Numerical study on signatures of atmospheric convective cells in radar images of the ocean, *J. Geophys. Res.*, Vol. 104, 25707-25720, 1999.
29. Lyzenga D.R. and Marmorino G.O., Measurement of surface currents using sequential synthetic aperture radar images of slick patterns near the edge of the Gulf Stream, *J. Geophys. Res.*, Vol. 103, 18769-18777, 1998.
30. Hayes R.M., Detection of the Gulf Stream, in *Spaceborne Synthetic Aperture Radar for Oceanography*, ed. by Beal R.C., DeLeonibus P.S., and Katz I., *Johns Hopkins Oceanogr. Stud.*, Vol. 7, 146-160, 1981.
31. Ochadlick A.R., Cho P., and Evans-Morgis J., Synthetic aperture radar observations of currents colocated with slicks, *J. Geophys. Res.*, Vol. 97, 5325-5330, 1992.
32. Gower J.F.R., Mapping coastal currents with SAR, using naturally-occurring surface slick patterns, *Proc. Second ERS-1 Symposium, ESA SP-361*, 415-418, ESA, Noordwijk, Netherlands, 1994.
33. Munk W., Armi L., Fischer K., and Zachariasen F., Spirals on the sea, *Proc. R. Soc. Lond. A*, Vol. 456, 1217-1280, 2000.
34. Marmorino G.O., Jansen R.W., Valenzuela G.R., Trump C.L., Lee J.S., and Kaiser J.A.C., Gulf Stream surface convergence images by synthetic aperture radar, *J. Geophys. Res.*, Vol. 99, 18315-18328, 1994.
35. Johannessen J.A., Shuchman R.A., Digranes G., Lyzenga D.R., Wackerman C., Johannessen O.M., and Vachon P.W., Coastal ocean fronts and eddies images with ERS 1 synthetic aperture radar, *J. Geophys. Res.*, Vol. 101, 6651-6667, 1996.

36. Marmorino G.O. and Trump C.L., High-resolution measurements made across a tidal intrusion front, *J. Geophys. Res.*, Vol. 101, 25661-25674, 1996.
37. Lyzenga D.R. and Wackerman C.C., Detection and classification of ocean eddies using ERS-1 and aircraft SAR images, *Proc. Third ERS Symposium on Space at the Service of Our Environment, ESA SP-414*, 1267-1271, ESA, Noordwijk, Netherlands, 1997.
38. Vogelzang J., Ruddick K.G., and Moens J.B., On the signatures of river outflow fronts in radar imagery, *Int. J. Rem. Sens.*, Vol. 18, 3479-3505, 1997.
39. Marmorino G.O., Shen C.Y., Allan N., Askari F., Trizna D.B., Trump C.L., and Shay L.K., An occluded coastal oceanic front, *J. Geophys. Res.*, Vol. 103, 21587-21600, 1998.
40. Sletten M.A., Marmorino G.O., Donato T.F., McLaughlin D.J., and Twarog E., An airborne, real aperture radar study of the Chesapeake Bay outflow plume, *J. Geophys. Res.*, Vol. 104, 1211-1222, 1999.
41. Marmorino G.O. and Trump C.L., Gravity current structure of the Chesapeake Bay outflow plume, *J. Geophys. Res.*, Vol. 105, 28847-28861, 2000.
42. Cooper A.L., Mied R.P., and Lindemann G.J., Evolution of freely propagating, two-dimensional surface gravity current fronts, *J. Geophys. Res.*, Vol. 106, 16887-16901, 2001.
43. Lyzenga D.R., Interaction of short surface and electromagnetic waves with ocean fronts, *J. Geophys. Res.*, Vol. 96, 10765-10772, 1991.
44. Jansen R.W., Shen C.Y., Chubb S.R., Cooper A.L., and Evans T.E., Subsurface, surface, and radar modeling of a Gulf Stream current convergence, *J. Geophys. Res.*, Vol. 103, 18723-18743, 1998.
45. Chubb S.R., Cooper A.L., Jansen R.W., Fusina R.A., Lee J.S., and Askari F., Radar backscatter from breaking waves in Gulf Stream current convergence fronts, *IEEE. Trans. Geosci. and Rem. Sens.*, Vol. 37, 1951-1966, 1999.
46. Jenkins A.D., Johannessen O.M., Sandven S., Korsbakken E.K., Espedal H.A., Romeiser R., Brandt P., Alpers W.R., Rubino A., Wensink H., Calkoen C.J., Mastenbroek K., and Lyzenga D., *Intercomparison and improvement of SAR ocean imaging interaction models*, Final Rep. Contract 11969/96/NL/CN, 120 pp., European Space Agency, Noordwijk, Netherlands, 1998.
47. Ufermann S. and Romeiser R., A new interpretation of multifrequency / multipolarization radar signatures of the Gulf Stream front, *J. Geophys. Res.*, Vol. 104, 25697-25706, 1999.
48. Kudryavtsev V., Akimov D., Johannessen J.A., Johannessen O.M., and Chapron B., On radar imaging of ocean phenomena, *ESA SP-565* (this issue), ESA, Noordwijk, Netherlands, 2004.
49. Brandt P., Alpers W., and Backhaus J.O., Study of the generation and propagation of internal waves in the Strait of Gibraltar using a numerical model and synthetic aperture radar images of the European ERS-1 satellite, *J. Geophys. Res.*, Vol. 101, 14237-14252, 1996.
50. Brandt P., Rubino A., Alpers W., and Backhaus J.O., Internal waves in the Strait of Messina studied by a numerical model and synthetic aperture radar images from the ERS-1/2 satellites, *J. Phys. Oceanogr.*, Vol. 27, 648-663, 1997.
51. Porter D.L. and Thompson D.R., Continental shelf parameters inferred from SAR internal wave observations, *J. Atmos. Ocean. Technol.*, Vol. 16, 475-487, 1999.
52. Holloway P.E., Chatwin P.G., and Craig P., Internal tide observations from the Australian North West shelf in summer 1995, *J. Phys. Oceanogr.*, Vol. 31, 1182-1199, 2001.
53. Small J. and Martin J., The generation of non-linear internal waves in the Gulf of Oman, *Continental Shelf Res.*, Vol. 22, 1153-1182, 2002.
54. Alpers W., Theory of radar imaging of internal waves, *Nature*, Vol. 314, 245-247, 1985.
55. Apel J.R., Ostrovsky L.A., and Stepanyants Y.A., Internal solitons in the ocean, *Technical Report MER-CJRA0695*, 67 pp., Applied Physics Laboratory, Johns Hopkins University, Laurel, MD, USA, 1995.
56. Li X., Clemente-Colon P., and Friedman K.S., Estimating oceanic mixed-layer depth from internal wave evolution observed from RADARSAT-1 SAR, *JHU/APL Technical Digest*, Vol. 21, 130-135, Applied Physics Laboratory, Johns Hopkins University, Laurel, MD, USA, 2000.
57. Pingree R.D., Mardell G.T., and New A.L., Propagation of internal tides from the upper slopes of the Bay of Biscay, *Nature*, Vol. 321, 154-158, 1986.

58. Sandstrom H. and Elliott J.A., Internal tide and solitons on the Scotian Shelf: A nutrient pump at work, *J. Geophys. Res.*, Vol. 89, 6415-6426, 1984.
59. Liu A.K., Holbrook J.R., and Apel J.R., Nonlinear internal wave evolution in the Sulu Sea, *J. Phys. Oceanogr.*, Vol. 15, 1613-1624, 1985.
60. Sandstrom H., and Oakey N.S., Dissipation in internal tides and solitary waves, *J. Phys. Oceanogr.*, Vol. 25, 604-614, 1995.
61. Osborne A.R. and Burch T.L., Internal solitons in the Andaman Sea, *Science*, Vol. 208, No. 4443, 451-460, 1980.
62. Zheng Q., Yuan Y., Klemas V., and Yan X.-H., Theoretical expression for an ocean internal soliton synthetic aperture radar image and determination of the soliton characteristic half width, *J. Geophys. Res.*, Vol. 106, 31415-31423, 2001.
63. Vlasenko V., Brandt P., and Rubino A., Structure of large-amplitude internal solitary waves, *J. Phys. Oceanogr.*, Vol. 30, 2172-2185, 2000.
64. Brandt P., Romeiser R., and Rubino A., On the determination of characteristics of the interior ocean dynamics from radar signatures of internal solitary waves, *J. Geophys. Res.*, Vol. 104, 30039-30045, 1999.
65. da Silva J.C.B., Ermakov S.A., Robinson I.S., Jeans D.R.G., and Kijashko S.V., Role of surface films in ERS SAR signatures of internal waves on the shelf: 1. Short-period internal waves, *J. Geophys. Res.*, Vol. 103, 8009-8031, 1998.
66. Vogelzang J., The mapping of bottom topography with imaging radar: A comparison of the hydrodynamic modulation in some existing models, *Int. J. Rem. Sens.*, Vol. 10, 1503-1518, 1989.
67. Vogelzang J., A model comparison study to the imaging of submarine reefs with synthetic aperture radar, *Int. J. Rem. Sens.*, Vol. 22, 2509-2536, 2001.
68. de Loor G.P. and Brunsveld van Hulten H.W., Microwave measurements over the North Sea, *Boundary Layer Meteorol.*, Vol. 13, 113-131, 1978.
69. de Loor G.P., The observation of tidal patterns, currents, and bathymetry with SLAR imagery of the sea, *IEEE J. Oceanic Eng.*, Vol. OE-6, 124-129, 1981.
70. Kramer H.J., *Observation of the Earth and its Environment – Survey of Missions and Sensors*, 960 pp., Springer Verlag, 1996.
71. Lyzenga D.R., Effects of wave breaking on SAR signatures observed near the edge of the Gulf Stream, *Proc. IGARSS 1996*, 908-910, IEEE, Piscataway, NJ, USA, 1996.
72. Walker D.T., Lyzenga D.R., Ericson E.A., and Lund D.E., Radar backscatter and surface roughness measurements for stationary breaking waves, *Proc. R. Soc. Lond. A*, Vol. 452, 1953-1984, 1996.
73. Ericson E.A., Lyzenga D.R., and Walker D.T., Radar backscatter from stationary breaking waves, *J. Geophys. Res.*, Vol. 104, 29679-29695, 1999.
74. Kudryavtsev V., Mastenbroek K., and Makin V.K., Modulation of wind ripples by long surface waves via the air flow. A feedback mechanism. *Boundary-Layer Meteorology*, Vol. 83, 99-116, 1997.
75. Romeiser R., Ufermann S., and Stolte S., Energy transfer between hydrodynamically modulated long and short ocean waves by interaction with the wind field, *Proc. IGARSS '99*, 965-967, IEEE, Piscataway, NJ, USA, 1999.
76. Shuchman R., The feasibility of measurement of ocean current detection using SAR data, *Proc. 13th Int. Symp. on Rem. Sens. of the Environment*, 93-103, Ann Arbor, MI, USA, 1979.
77. van der Kooij M., Hughes W., and Sato S., Doppler current velocity measurements: A new dimension to spaceborne SAR data, available <http://www.atlantis-scientific.com/eoserv.html>, 2001.
78. Chapron B. and Collard F., Satellite synthetic aperture radar sea surface Doppler measurements, *ESA SP-565* (this issue), ESA, Noordwijk, Netherlands, 2004.
79. Goldstein R.M. and Zebker H.A., Interferometric radar measurement of ocean surface currents, *Nature*, Vol. 328, 707-709, 1987.
80. Thompson D.R. and Jensen J.R., Synthetic aperture radar interferometry applied to ship-generated waves in the 1989 Loch Linnhe experiment, *J. Geophys. Res.*, Vol. 98, 10259-10269, 1993.
81. Romeiser R. and Thompson D.R., Numerical study on the along-track interferometric radar imaging mechanism of oceanic surface currents, *IEEE Trans. Geosci. and Rem. Sens.*, Vol. 38-II, 446-458, 2000.
82. Romeiser R., Schwäbisch M., Schulz-Stellenfleth J., Thompson D.R., Siegmund R., Niedermeier A., Alpers W., and Lehner S., *Study on Concepts for Radar Interferometry from Satellites for Ocean (and Land) Appli-*

cations (*KoRIOLiS*), Final Report, 112 pp., University of Hamburg, Germany, available at <http://www.ifm.uni-hamburg.de/~romeiser/koriolis.htm>, 2002.

83. Keydel W. (ed.), *X-SAR / SRTM Shuttle Radar Topography Mission, Mapping the Earth from Space*, 24 pp., available at www.dlr.de, 1999.

84. Romeiser R., Breit H., Eineder M., Runge H., Flament P., de Jong K., and Vogelzang J., Validation of SRTM-derived surface currents off the Dutch coast by numerical circulation model results, *Proc. IGARSS 2003*, 3 pp., IEEE, Piscataway, NJ, USA, 2003.

85. ten Cate H.H., Hummel S., and Roest M.R.T., An open model system for 2d/3d hydrodynamic simulations, *Proc. Hydroinformatics 2000*, Int. Assoc. of Hydraulic Eng. and Res., Madrid, Spain, 2000.

86. Lehner S. and Ocampo-Torres F.J., Radar measurements of ocean waves, *ESA SP-565* (this issue), ESA, Noordwijk, Netherlands, 2004.

87. Frasier S.J. and Camps A.J., Dual-beam interferometry for ocean surface current vector mapping, *IEEE. Trans. Geosci. and Rem. Sens.*, Vol. 39, 401-414, 2001.

88. Beal R.C. and Pichel W.G. (guest eds.), *Coastal and Marine Applications of Wide Swath SAR, JHU/APL Technical Digest*, Vol. 21, 186 pp., Applied Physics Laboratory, Johns Hopkins University, Laurel, MD, USA, 2000.

89. Ufermann S., Robinson I.S., and da Silva J.C.B., Synergy between synthetic aperture radar and other sensors for the remote sensing of the ocean, *Ann. Telecommun.*, Vol. 56, 672-681, 2001.

**This page intentionally
left blank (pagination)**

HOT-SPOTS OF INTERNAL WAVE ACTIVITY OFF IBERIA REVEALED BY MULTISENSOR REMOTE SENSING SATELLITE OBSERVATIONS - SPOTIWAVE

A. Azevedo⁽¹⁾, S. Correia⁽¹⁾, J.C.B. da Silva⁽¹⁾ and A.L. New⁽²⁾

⁽¹⁾*Instituto de Oceanografia, Rua Ernesto de Vasconcelos, Campo Grande 1749-016 Lisbon, Portugal,
Email: jdasilva@fc.ul.pt*

⁽²⁾*Southampton Oceanography Centre, European Way, Southampton SO14 3ZH, England, UK,
Email: A.New@soc.soton.ac.uk*

ABSTRACT

Some results of a study of the distribution of internal waves (IW) off the Iberian Peninsula based on ERS SAR observations are presented. In particular we show observations of very large amplitude internal solitary waves (ISWs) propagating in the deep ocean West of the Galicia Bank, and explain their generation as resulting from semi-diurnal frequency internal tides emanating from the bottom slopes. We determine possible generation sites of these internal tidal waves and their propagation pathways. The most energetic internal tide generation sites are calculated from the distribution of the internal tidal forcing, adapted from a model proposed by Baines [1]. This method is being used to map the internal wave activity off the Iberian Peninsula, identifying the most energetic IW generation sites assuming that the internal tidal waves are generated by the interaction of the semi-diurnal (barotropic) tide with the bottom topography. In addition we reveal SeaWiFS observations of large internal tides with a clear signature of enhanced levels of near-surface chlorophyll in the Bay of Biscay.

1. INTRODUCTION

The standing question about IW generation has not been what processes could generate them, but rather their relative importance. Even with decades of research on IWs, it is still not possible to quantify their generation sources accurately. One of the objectives of the project SPOTIWAVE was to explore the distribution of IW activity off the Iberian Peninsula, ultimately identifying the most energetic IW generation sites and their likely mechanisms. The capability of Synthetic Aperture Radars (SARs) on satellites to observe on a regular basis ocean IWs is now widely accepted [2, 3]. Over a decade of ERS SAR data is available today, and is being used for detailed studies of IW generation sites and mechanisms.

IWs are considered to be the most significant factor for explaining vertical mixing in the open ocean, to such a large extent that they may be a major factor in ocean circulation [4, 5]. Consequently they are important in

climate studies. They may also be important from a biological point of view, since their impact on the development and transport of plankton is significant [6]. Non-linear IWs produce a net transport of in-water particles (phytoplankton, zooplankton and even small fish), which in the upper surface layer is usually in the same direction as the IW propagation. Typical distances reached by such transport have been modelled by Lamb [7] and are of the order of several km for a train of Internal Solitary Waves (ISWs, nonlinear asymmetric IWs). Some of the early work suggested that IW slicks are correlated with shoreward transport of pelagic larvae [8]. IWs have the ability to turn scattered distributions of fish and zooplankton into structured distributions, causing aggregation of organisms in slicks [9]. We note that very little research has been done in this field, in particular off the coast of Portugal and we hope the results of the present study may stimulate further work.

It is generally accepted that one of the main causes of IWs is the interaction between the barotropic tide and submarine topography [10, 1]. Once sufficiently accurate definitions of stratification, topography and amplitude of the tidal currents are known, one should expect that, on average, the size of predicted and observed internal tides should match quite well. These internal tides may disintegrate, subsequently, into non-linear ISWs, if the local seasonal stratification is appropriate [11]. In this paper we show ERS SAR observations of very large amplitude ISWs propagating in the deep ocean (West of Galicia Bank) and explain their generation based on the distribution of the internal tidal forcing, adapted from a model proposed by Baines [1]. Here we propose a method that could, in the future, be used to refine estimates of the global internal tide budget. The large swath scan mode of ENVISAT ASAR (400km wide) could be used to validate the results of our model.

2. INTERNAL TIDAL FORCING MODEL

In the Northern Bay of Biscay (47-48° N, 6-8° W), internal waves of semi-diurnal tidal period result from

the interaction of the surface tide with the steep shelf slope bottom topography, and can propagate both onto the shelf, and into the deeper ocean. In the upper water column, these internal tides are manifested as long wavelength (30-50 km) depressions and elevations of the thermocline of up to 30 m in amplitude. Pingree & New [12] revealed that these internal tides were also visible in remotely-sensed sunglint imagery as long-crested features extending for several hundreds of kilometers in a direction parallel with the shelf break. More recently da Silva et al. [13] showed that these internal tides are capable of producing a “colour” signature in SeaWiFS chlorophyll data (an issue that will be briefly explained in section 4).

Large amplitude ISWs near the sea surface are thought to be generated by the interaction of a beam of internal tidal energy with the seasonal thermocline [14]. This beam of internal tidal energy follows characteristic pathways and has a slope c to the horizontal given by

$$c = \pm \sqrt{\frac{\sigma^2 - f^2}{N^2 - \sigma^2}} \quad (1)$$

where σ is the frequency (corresponding to semi-diurnal tides), N is the Brünt-Väisälä frequency and f the Coriolis parameter.

We have developed two IDL (Interactive Data Language) programs as auxiliary tools for the interpretation of the generation sites/strength of the internal solitary wave trains observed in a data set of the ERS SAR mission. The primary goal of the first method/program was to determine possible generation sites of internal tidal waves, and their propagation pathways. This program calculates critical slopes where generation may take place at semi-diurnal tidal frequencies. It is also able to calculate the pathways of the “rays” of internal tidal energy and the corresponding intersections with the seasonal thermocline. The bottom slopes were calculated using available global bathymetry [15]. The ocean stratification was calculated based on a series of CTD stations of the study region. CTD profiles were obtained from the WOCE Hydrographic Program.

Assuming that the internal tidal waves are generated by the interaction of the semi-diurnal tide (barotropic) with the bottom topography, a second program was developed to determine the regions where the driving body force of the internal wave motion was strongest.

Following Baines [1], the equations governing the internal tides are those of a rotating stratified inviscid fluid, and linearity can be assumed. Subtracting out the barotropic tidal motion (corresponding to an

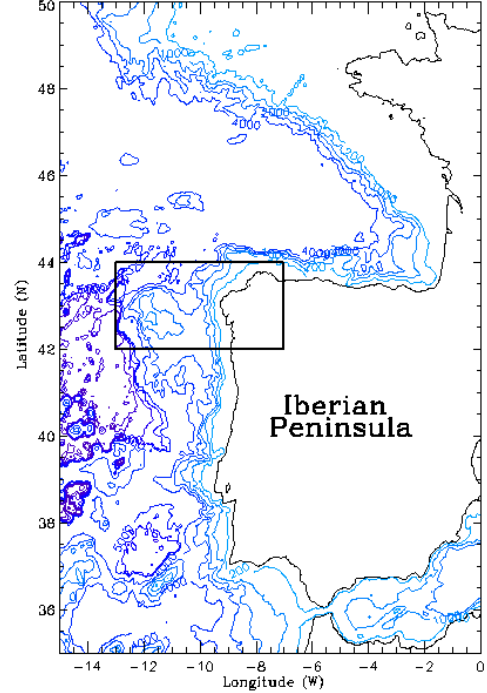


Fig. 1. Map of the study region.

unstratified ocean) from the linearized equations, the internal wave motion is driven by a body force F , that can be found from the following equations:

$$\frac{\partial u_i}{\partial t} + f \times u_i + \frac{1}{\bar{\rho}_0} \nabla p_i + \frac{\bar{\rho} g \hat{z}}{\bar{\rho}_0} = F = -\frac{g \rho_1}{\bar{\rho}_0} \hat{z} \quad (2)$$

where

$$\frac{\partial \rho_1}{\partial t} = -w_1 \frac{d\rho_0}{dz} \quad (3)$$

Variables u_i are the fluid velocity (components of the velocity vector) for the internal wave motion; t the time; f the Coriolis parameter; $\bar{\rho}_0$ the mean density in static equilibrium; p_i the pressure; $\bar{\rho}$ the density for the wave motion; ρ_1 is the density perturbation caused by the barotropic motion; w_1 is the vertical component of the velocity vector of the barotropic motion; g the acceleration due to gravity; \hat{z} the unit vector in the upward vertical direction.

As the barotropic tide is hydrostatic, w_1 can be expressed in terms of a mass flux vector $Q(x,y)$. For the general case $Q_x = u \cdot h$ and $Q_y = v \cdot h$, where u and v are the zonal and meridional components of the velocity vector, respectively and h is the mean depth over $1/2^\circ$ cell. The components of the barotropic velocity vector were obtained by using the tidal model OTIS [16],

from which we can retrieve the tidal current ellipses for each grid point of the study region. Fig. 1. shows the study region (42°-44°N Latitude; 7°-13°W Longitude with $\frac{1}{2}^\circ$ cells) where the model was used. Assuming no phase change for the barotropic tide in the study region, we can define the velocity vector to be equal to the semi-major axis of ellipse at some time ($t=0$), everywhere in the domain. The procedure includes measuring the axis of the tidal ellipses for barotropic currents (U_{max} is the semi-major axis and V_{max} is the semi-minor axis) and the angle α between the semi-major axis and the Eastward direction.

We have computed the components of the mass flux vector (Q_x and Q_y) for a complete tidal cycle. Hence, when Q has been determined for the study region the internal tidal forcing for each level of the water column, F , can be calculated, where,

$$F = -\frac{zN^2(z)}{h^2} \left[\left(\int Q_x dt \right) \frac{\partial h}{\partial x} + \left(\int Q_y dt \right) \frac{\partial h}{\partial y} \right] \quad (4)$$

here z corresponds to depth; h the mean depth over $\frac{1}{2}^\circ$ cell; N the Brunt-Väisälä frequency; Q_x and Q_y the components of the mass flux vector.

The body force shown in Fig. 2 corresponds to F integrated for the water column one quarter through the tidal cycle. This shows the strongest positive body force at any time in the tidal cycle West of Galicia Bank, which is situated at 42.7°N, 11.8°W. The strongest forcing is located on the steep slopes to the West of the Bank.

3. GENERATION OF ISW

Gerkema [11] studied how the characteristics of the thermocline could influence the propagation of internal tidal rays. He showed that depending on the “strength” of the thermocline, internal solitary wave generation can be forced directly by the interfacial internal tide or rather by internal tidal (IT) rays such as those described by equ. (1). In this work we assume that the generation of trains of ISWs in the study region is similar to that of the Bay of Biscay, where the interaction of the IT rays with the seasonal thermocline is believed to be responsible for the short-period IW generation [11, 14].

Fig. 3 presents two SAR frames acquired by ERS-1 on 30 July 1994, showing pronounced surface signatures of short-period IW trains that appear to propagate westwards, as will be discussed later in this section. Fig. 4 shows a bathymetry map of the study region and an interpretation sketch of the two ERS SAR images shown in Fig. 3. Based on the information of the body-force map presented in Fig. 2 we chose to analyze in detail the cross section marked with a dark line in Fig. 4. Fig. 5 shows this cross section and the possible generation zones as well as the corresponding ray pathways. Note also that the cross section presented in Fig. 5 was defined along the direction of propagation of the ISWs observed in the SAR image (see Fig. 6). The geographic coordinates of this section lie in between 42.3°N-13.2°W and 42.5°N-12°W. The rays in Fig. 5 emanate from the points on the topography which are critical in the sense that the bottom slope is equal to the ray slope in equ. (1).

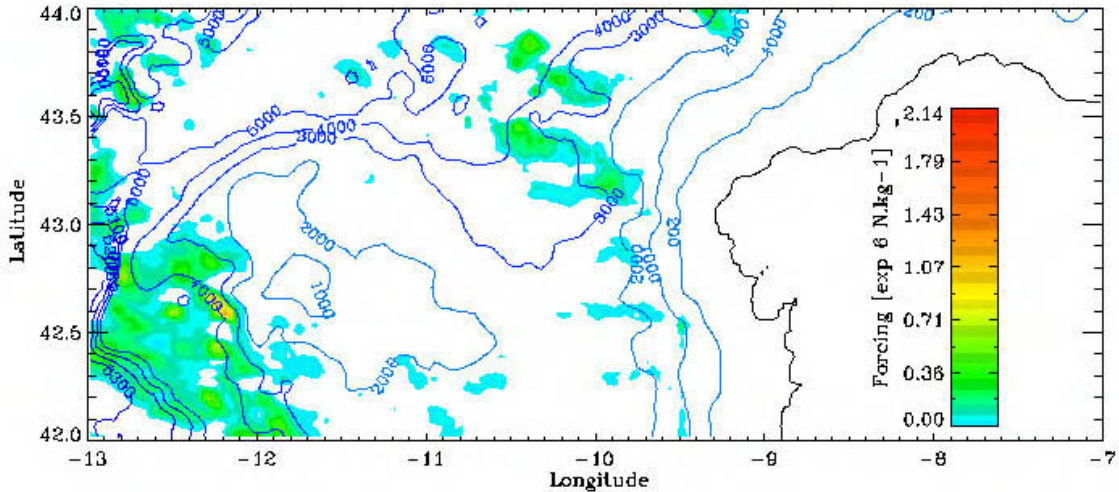


Fig. 2. Map of the forcing due to the barotropic tide M2 for the study region.

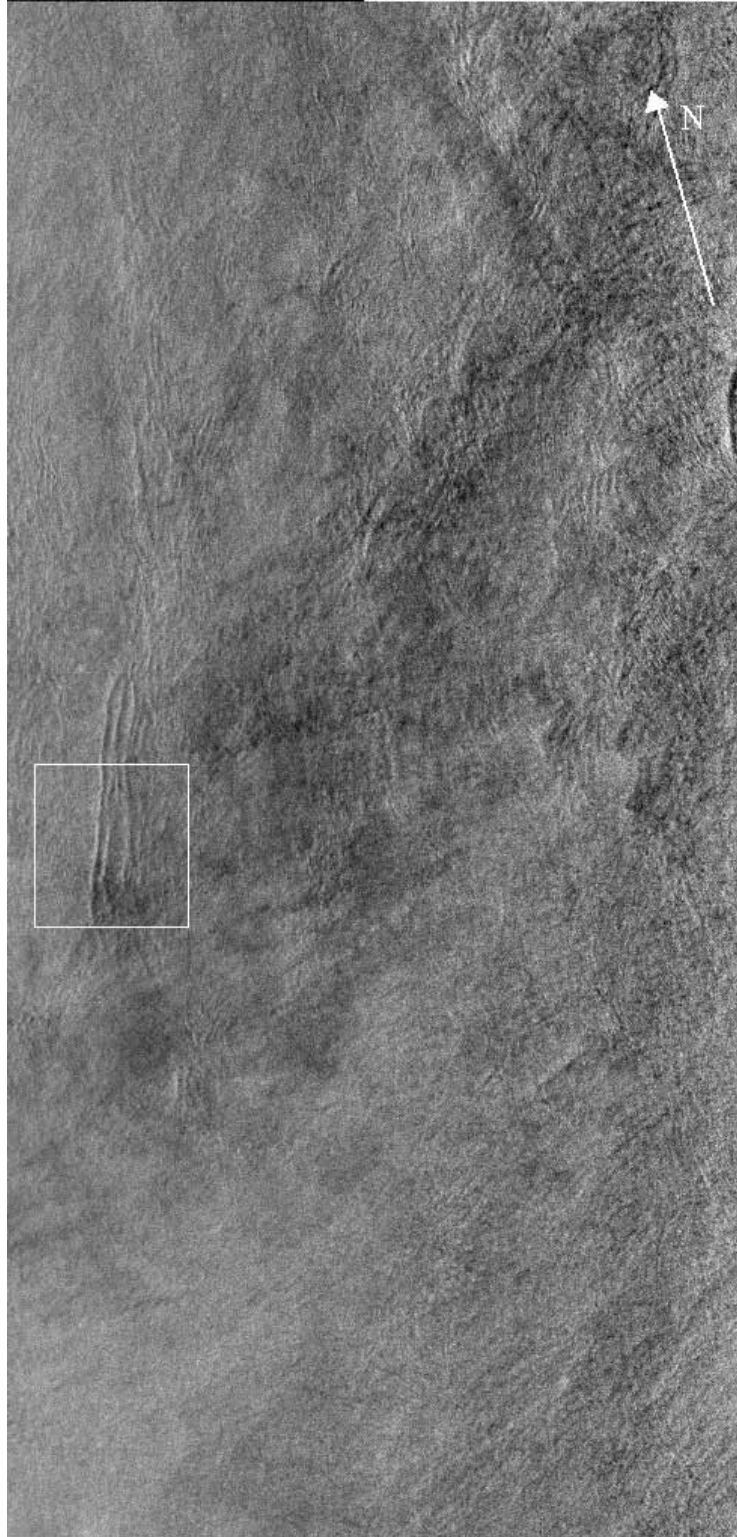


Fig. 3. ERS-1 SAR image (July 30, 1994), acquired at 11:38 (UTC), orbit 15891, frames 2745 and 2763. Several trains of ISWs propagating towards West are observed (North is indicated by the arrow at the top right corner of the figure). The white box represents the image extract shown in Fig. 6 in full resolution, where a profile of the image relative intensity was calculated and presented in Fig. 7.

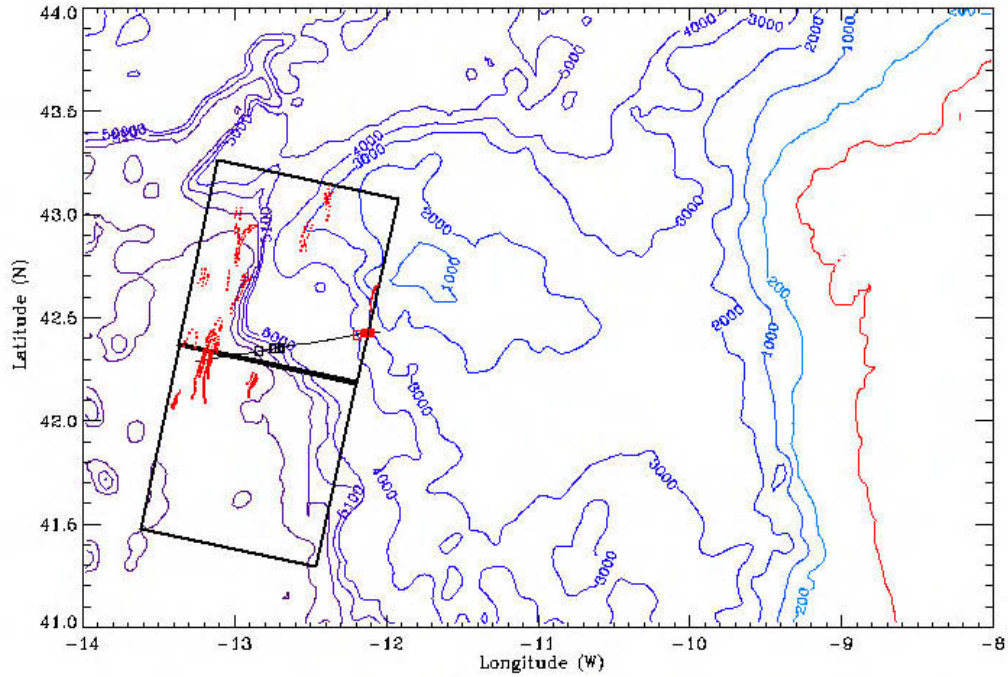


Fig. 4. Map of the study region showing the frames of the ERS SAR images and the ISW packets presented as red lines. Along the section: Red squares represent the deep generation sites; black squares represent the intersections of "rays" with the seasonal thermocline.

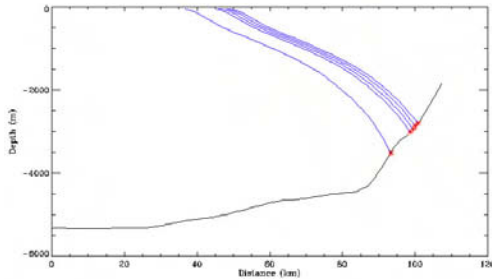


Fig. 5. Section from Fig. 3 showing the internal tidal "rays" along which energy propagates.

The generation sites, according to Baines theory [1] of critical slopes, are identified with red squares in Fig. 4. The positions of the intersection of the internal tidal ray paths with the thermocline (taken to be at 50 metres depth) are also shown and marked with black squares. We note that the critical slopes predicted by the ray-tracing model, which determines both critical slopes and "rays" of internal tidal energy, are consistent with the position of one forcing maximum located at 42.4°N-12.2°W, approximately (see Fig. 2).

Fig. 5 show "ray" trajectories for the section marked in Fig. 4. In Fig. 5, the generation sites are on the Galicia

Bank slope and the beams intersect the thermocline about 50-60 km West from the generation site. These solutions correspond to rays generated at the slope between 2000m and 4000m depth, and which propagate directly upwards.

Despite the fact that the ISWs observed in the SAR images are situated 40 km to the West of the position of the intersection of the internal tidal energy "beam" with the seasonal thermocline, we are convinced (given that the ISWs usually need some tens of kilometers to become well developed [14]) that they were generated by the internal tidal rays originating from the critical slopes shown in Fig. 5, perhaps 11h before (assuming that they propagate with a velocity of 1ms^{-1} , a typical velocity for this type of wave). Given that along the West slopes of the Galicia Bank the general flow direction of the subsurface to deep current is along the topography (with shallow water to the East), the internal tidal rays may interact with the current and the ray paths could reach the surface further to the West, thus increasing the distance from the generation site to the surface location where the IW trains are expected to be generated. Note also that the generation site may include the location of the bottom kink further West in the deeper water (see Fig. 5), depending on local variation of stratification.

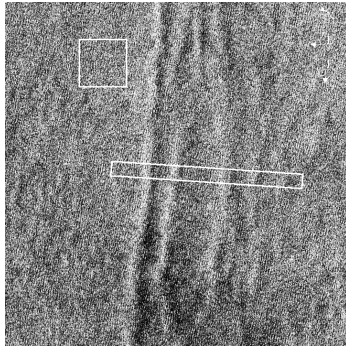


Fig. 6. An extract of ERS SAR image (orbit: 15891, frame 2763) dated 30 July 1994 in full resolution, showing part of the ISW packet.

Fig. 6 exhibits an extract of the full ERS SAR scene presented in Fig. 3. The curvature and the diminishing of the ISWs wavelength, from the front to the rear of the packet, suggests they propagate towards the West, away from the Galicia Bank. We also note that, considering the depth of the ocean in this region, approximately, 5000 m, the ISWs are depression type and present a double sign type of signature. This is easily seen in Fig. 7, which shows a backscatter profile taken from the image in the region identified by the rectangle in Fig. 6, and normalized by the mean backscatter level taken from the region identified by the box.

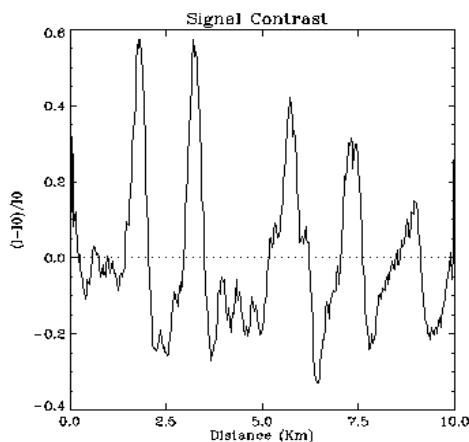


Fig. 7. Internal wave signature retrieved from profile as indicated in Fig. 6 (rectangle), normalized by the background backscatter (square box).

4. OCEAN COLOUR SIGNATURES OF INTERNAL TIDES

Another goal of project SPOTIWAVE was to study a variety of ways in which phytoplankton interact with

internal waves in shelf seas. Optical remote sensing has an advantage over microwave sensors which is the capability to observe in depth, down to several tens of meters in the ocean depending on the water case. In a recent paper, da Silva et al. [13] discussed bands of enhanced levels of near-surface chlorophyll in the central Bay of Biscay in remotely-sensed images from the SeaWiFS ocean colour sensor. They were able to explain the observations as likely to result from the uplifting of a subsurface chlorophyll maximum by the passing internal tides, to such a level as may be “seen” by the satellite sensor. In this section we show one more example of the kind of bands described in [13], supported by ERS SAR observations.

Fig. 8a shows a SeaWiFS image dated 14 August 2002 processed in levels of chlorophyll concentration. Overlaid on the image there is an interpretation sketch

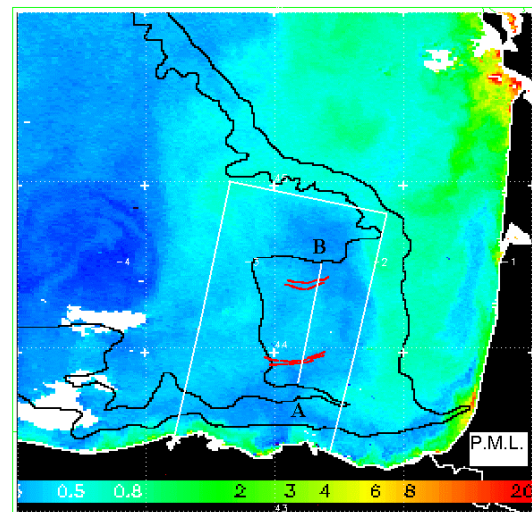


Fig. 8a. SeaWiFS image dated 14 August 2002 processed in levels of chlorophyll concentration. ISW packets are also represented as red lines.

of an ERS-2 SAR image, acquired on the same day, showing strong signatures of trains of internal solitary waves that were found to propagate towards the SE direction (North is up in Fig. 8a). Although the SeaWiFS data is “LAC” (“local area coverage”, with a 1km resolution), it is unable to detect the presence of the ISWs, but the SAR (with a 25 m resolution) is able to image them. It is important to note here that the ISWs that can be readily seen in SAR images are usually co-located with the internal tidal troughs, where the thermocline is usually depressed to more than 100m deep. The ISWs typically have wavelengths between 1-2 km, and periods of 20-40 minutes, and result from the action of nonlinear and dispersive forces on the internal tides themselves [17].

Here, we assume that the ISWs can be considered as marking the positions of the internal tidal troughs. Correspondingly, the internal tidal crests are in between the positions where the ISWs are observed, and there the thermocline rises to about 30 m deep.

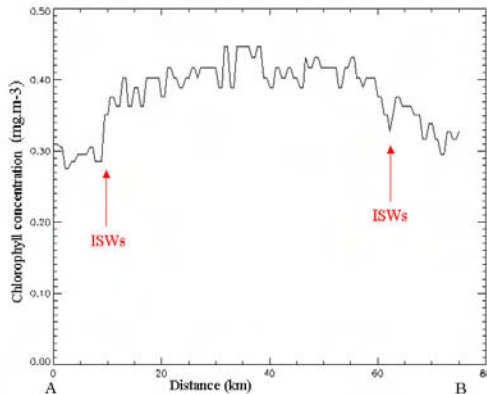


Fig. 8b. Profile of chlorophyll concentration taken perpendicular to internal wave crests (between positions A and B marked in Fig. 8a), showing relative minima of concentration at the positions of the ISW observations.

A Deep Chlorophyll Maximum (DCM) often occurs in the summer when levels of surface nutrients, phytoplankton and chlorophyll have become depleted following the spring bloom, leaving behind a subsurface maximum near the thermocline. This “chlorophyll layer” is typically observed in the northeast Atlantic, centred at the thermocline and reaching thickness of 40 m (A. Poulton, pers. comm.). In these circumstances the top of the DCM would be sufficiently lifted upwards to be within the effective depth of penetration of light, and thus could produce a measurable response to the satellite sensor. This was certainly true in the modelling and similar observations presented by da Silva et al. [13].

The interpretation sketch of the ERS-2 SAR image (acquired at 10:58 UTC), is based on the assumption that the internal wave trains are generated always at the same phase of the semi-diurnal tide, where we phase shifted the ISW trains according to their propagation speeds, predicting their positions at the time of acquisition of the SeaWiFS image (12:15 UTC). Thus, assuming that the phase speed of the solitary wave trains are very close to the internal interfacial tide, and estimating its speed from the inter-packet separation distance in the SAR image (approximately 1m/s), it is reasonable to compare both the SAR and SeaWiFS images after accounting for the IW displacements relative to the image acquisition times.

Analysis of Figs. 8a and 8b indeed show that the bands of enhanced chlorophyll concentration are correlated with the internal tidal crests, that are in between the ISW trains. This is in accordance with the mechanism proposed by da Silva et al. [13], where the uplifting of a DCM by the passage of the internal tidal crests is capable of producing a measurable response to the SeaWiFS sensor.

5. SUMMARY

A method to estimate the spatial distribution of the internal tidal forcing has been successfully applied to explain SAR observations of ISWs, supposed to be generated by the interaction of the semi-diurnal (barotropic) tide with the bottom topography. The most energetic internal tide generation sites are well correlated with the SAR observations of ISWs, demonstrating an important generation process off the Iberian Peninsula. For future work it would be interesting to compare predictions of the seasonal variability of internal wave generation with more SAR observations. It would also be interesting to apply this method to other regions of the world ocean and verify where the generation of ISWs by internal tides is similar.

Correlation between the spatial structure of internal waves and chlorophyll concentration has been presented, taking advantage of sensor synergy, in particular ERS SAR and SeaWiFS image data. In the future we plan to further explore this synergy using ENVISAT ASAR and MERIS data.

ACKNOWLEDGEMENTS:

The project SPOTIWAVE was funded by the Portuguese FCT (proj. code POCTI/CTA/41130/2001). Image data has been provided by ESA in the frame of ENVISAT project AOE-563, and the PI is Prof. Ian Robinson from Southampton Oceanography Centre – Laboratory of Satellite Oceanography. SeaWiFS image data provided by The Remote Sensing Group at Plymouth Marine Laboratory.

6. REFERENCES

1. Baines, P.G., On internal tide generation models, *Deep-Sea Research*, 29, 307-338, 1982.
2. Alpers, W., Theory of radar imaging of internal waves, *Nature*, 314, 245-247, 1985.
3. Thompson, D.R. and Gasparovich, R.F., Intensity modulation in SAR images of internal waves, *Nature*, 320, 345-348, 1986.

4. Munk, W.H. and Wunsch, C., Abyssal Recipes II: energetics of tidal and wind mixing, *Deep Sea Research*, 45, 1977-2010, 1998.
5. Egbert, G.D. and Ray, R.D., Significant dissipation of tidal energy in the deep ocean inferred from satellite altimeter data, *Nature*, 405, 775-778, 2000.
6. Holligan P.M., Pingree, R.D., Mardell, G.T., Oceanic solitons, nutrient pulses and phytoplankton growth, *Nature*, 314, 348-350, 1985.
7. Lamb, K.G., Particle transport by nonbreaking, solitary internal waves, *Journal of Geophysical Research*, 102, C8, 18641-18660, 1997.
8. Shanks, A.L., Surface slicks associated with tidally forced internal waves may transport pelagic larvae of benthic invertebrates and fishes seaward, *Mar. Ecol. Prog. Ser.*, 13, 311-315, 1983.
9. Pineda, J., Circulation and larvae distribution in internal tidal bore warm fronts, *Limnol. Oceanogr.*, 44(6), 1400-1414, 1999.
10. Baines, P.G., The generation of internal tides by flat-bump topography, *Deep-Sea Research*, 20, 179-205, 1973.
11. Gerkema, T., Internal and Interfacial Tides: Beam Scattering and Local Generation of Internal Solitary Waves, *Journal of Marine Research*, 59, 227-255, 2001.
12. Pingree, R.D. and A.L. New, Structure, Seasonal Development and Sunlight Spatial Coherence of Internal Tide on the Celtic and Armorican Shelves and in the Bay of Biscay, *Deep-Sea Research I*, Vol. 42, N° 2, 245-284, 1995.
13. Da Silva, J.C.B., A.L. New, M.A. Srokosz and T.J. Smyth, On the observability of internal tidal waves in remotely-sensed ocean colour data, *Geophys. Research Letters*, Vol. 29 (12), 10.1029/2001GL013888, 2002.
14. New, A.L. and Da Silva, J.C.B., Remote-sensing evidence for the local generation of internal soliton packets in the central Bay of Biscay, *Deep-Sea Research I*, Vol. 49, 915-934, 2002.
15. Smith, W.H.F. and D. T. Sandwell, Global seafloor topography from satellite altimetry and ship depth soundings, *Science*, v. 277, p. 1957-1962, 26 Sept., 1997. http://topex.ucsd.edu/marine_topo/mar_topo.html
16. Egbert, G. and S. Erofeeva, Efficient inverse modeling of barotropic ocean tides, *Journal of Oceanic and Atmospheric Technology*, 19, N2, 183-204, 2002.
17. New, A.L. and R.D. Pingree, An intercomparison of internal solitary waves in the Bay of Biscay and resulting from Korteweg-de Vries type theory, *Progress in Oceanography*, 45, 1-38, 2000.

SATELLITE SYNTHETIC APERTURE RADAR SEA SURFACE DOPPLER MEASUREMENTS

B. Chapron¹, F. Collard², and V. Kerbaol²

¹Laboratoire d'Océanographie Spatiale, IFREMER

²BOOST-Technologies, Plouzané, France

ABSTRACT

For the first time, global line-of-sight synthetic aperture radar (SAR) Doppler measurements over ocean scenes have been systematically extracted and carefully analyzed. This unique opportunity follows the enhanced sampling and processing capabilities offered by the ENVISAT ASAR instrument for the so-called Wave Mode products. Using precise satellite platform orbital and state vector parameters, measurable SAR Doppler frequency shifts can be globally obtained. From a theoretical analysis and co-located atmospheric wind and wave model predictions, these line-of-sight Doppler shifts are shown to carry valuable quantitative information about the expected mean motion between the sea scatters and the satellite platform. To further illustrate the use of these measurements, the analysis is carried out to larger SAR image complex products over coastal regions. Sub-tiling the larger SAR scenes to compute local estimates, the line-of-sight Doppler variations can be connected to local environmental parameter changes (wind, wave, current). Such a capability from standard SAR instruments shall help the developments of new and more consistent SAR retrieval algorithms for scientific and practical application purposes.

Key words: Ocean surface SAR measurements; line-of-sight Doppler frequency shifts; mean sea scatter motions.

1. INTRODUCTION

The circulation of the ocean's surface layer has traditionally received much attention. An important feature of this surface circulation is the motion associated with surface gravity waves and wind drift. In that context, remote sensing and especially Synthetic Aperture Radar (SAR) observations have already been demonstrated to routinely provide information to both detect oil spills and to extract different ocean surface parameters, such as surface wind, swell direction and amplitude. Over ocean scenes, SAR ocean surface remote sensing analysis indeed relies on the very high sensitivity of radar backscatter signal linked to changes on both the local geometry and the spectral density distribution of gravity-capillary ocean wavelets.

Modifications of the short surface waves by the surface layer winds, air/sea temperature variations over water masses, the presence of surface currents, bathymetry features, coastal plumes, and surface slick induced dampings, are common place observations within SAR ocean surface scenes. Challenges still remain to uniquely interpret such a wealth of high resolution identified patterns in terms of physical processes in the upper ocean, e.g. Romeiser et al. (2004). However, understandings and algorithms have evolved, and surface wind and long wave information as well as striking high resolution phenomena are routinely extracted from SAR ocean scenes.

But first, it must be stated that SAR processing technique principles involve the fine analysis of both phase and amplitude of the receiving scattered signals. This is crucial to discriminate returns from different surface areas within the radar illuminated scene according to their different respective Doppler frequencies. While such a key feature is implicitly known, most SAR ocean surface remote sensing studies still mostly focus on the squared magnitude backscatter signal modulation analysis, somehow neglecting the use of the complementary information carried in the phase of the received complex signals. However, time-dependent properties of moving SAR ocean scenes are measurable and exploited to unambiguously retrieve ocean surface swell propagation directions, e.g. Engen et al., 1995, Chapron et al., 2001, Johnsen et al. 2002.

These reliable results, as well as the enhanced processing capabilities offered by the ENVISAT ASAR instruments, such as global complex image (Wave Mode) products, triggered our interest for a more thorough analysis and uses of the direct line-of-sight SAR Doppler measurements, to revisit early concept from Shuchman (1979) and results from Van der Kooij et al. (2001). As foreseen, the goal is to extract an instantaneous apparent local line-of-sight surface velocity to be related with geophysical quantities (wind characteristics, surface current).

Clearly, one-channel radar systems are limited in comparison to multi-channel interferometric SAR, but actual satellite systems can still be used if orbital parameters are precisely known. The basic concept stems from the fact that detected moving targets produce Doppler shifts proportional to their relative velocities toward the receiving radar antenna. Over moving ocean scenes, which can

be represented as a collection of distributed targets, frequency shifts along the cross range will then be randomly distributed with space and time variations. This can limit the SAR imaging abilities, e.g. the velocity bunching phenomenon, but one can also use the expected statistical sea surface homogeneity to reliably infer the first order moment of the illuminated scene Doppler distribution, the so-called Doppler centroid. Accordingly, this shall provide the mean motion between the moving sea scatterers and the SAR platform. If properly demonstrated and interpreted, such a capability from standard satellite SAR instruments may systematically be used in conjunction with backscatter power measurements to help more consistent inversions of the sea surface local environmental characteristics. With the complementary measurements of both geometrical and dynamical properties of the sea surface, complex physical ocean surface processes will be better revealed and analyzed. As already mentioned, interests stem largely to possibly assess wind/wave and current induced surface motions, to be possibly combined with altimeter sea level estimates and/or HF radar measurements. Following, these measurements shall provide independent information to compare with numerical circulation model predictions. This can also further serve our understandings of wave dynamics in large steep seas for marine safety and offshore engineering design, as well as to better characterize air-sea interaction processes.

Our objectives are thus to ensure and demonstrate this potential. To this end, we take full advantages of the enhanced observation capabilities offered by the ENVISAT ASAR instrument to provide global highly sampled Wave Mode complex products with precise orbital parameters. Following the commission period to validate these products, systematic comparisons are made with numerical atmospheric and wave models (ECMWF, WAM). After briefly stating the theoretical background, section 2, the global Wave Mode product line-of-sight Doppler analysis is presented, section 3. The global analysis perfectly illustrates the expected high correlation between line-of-sight sea surface scatter motions and SAR Doppler centroid measurements. In section 4, illustrations and analysis are also given for larger complex image products.

2. THEORETICAL BACKGROUND

For SAR applications, the calculations of the wave scattering problem including the ability to predict quantitatively both the mean radar cross section and mean dynamical quantities, can be based upon an extended two-scale model. This is certainly justified when considering high resolution SAR images to exhibit wave field like patterns. In that sense, a two-scale model somehow introduces a separation between coherently imaged larger scale waves and smaller scale roughness elements controlling the mean backscatter and contrast signals. Under this two-scale description, the larger scales introduce local tilts to modify local incidence angles. This will in turn modify the wavenumber horizontal and vertical projections, the strength and the polarization of the backscatter signals. These larger scales are considered to slowly vary corresponding to the predominant surface

waves, while shorter scales may be described as sporadic or intermittent but statistically stationary in a mean sense. These latter contributions are generally rougher corresponding to steeper surface wave elements. From a statistical view point, these scales have rapidly decaying correlation functions in both time and space. The larger scale waves have instantaneous velocities and accelerations, both contributing to modulate the shorter scales, e.g. hydrodynamical modulations.

To simplify the developments, but to clearly illustrate the fundamental physics of such extended two-scale description, we consider the use of a Kirchhoff-like integral formulation, e.g. Winnebrener and Hasselman (1988), Thompson (1989) or Plant (2002). Over the slowly time varying larger tilting facet, the mean backscatter at a given location and time is then asymptotically approximated as

$$\sigma_{pq}^o(\mathbf{x}, t) = \frac{k_o^2}{\pi \cos^2 \theta'} |g'_{pq}| e^{i\Omega_L t} \times \int_{\mathbf{x}} \langle e^{-2ik_o \cos \theta' (\xi(\mathbf{x}_1, t) - \xi(\mathbf{x}_2, t))} \rangle e^{2ik_o \sin \theta' (\mathbf{x}_1 - \mathbf{x}_2)} d(\mathbf{x}_1 - \mathbf{x}_2) \quad (1)$$

where k_o incident is the impinging wavenumber, ξ the rapidly varying elevation roughness over the larger tilting facet, θ' the local incidence angle according to the larger scale tilt-induced modulation, q and p indicate polarization and g_{pq} is a geometrical polarization function depending upon the dielectric constant and the local incidence angle. The fact that the surface at a given location \mathbf{x} and time t is not frozen is explicitly taken into account with the introduction of a phase term. The Doppler pulsation Ω_L relates to the instantaneous dynamical characteristics, mainly horizontal and vertical velocities v_H and v_V , of the larger tilting facets, as $\Omega_L = -2ik_o [\sin \theta' v_H(\mathbf{x}, t) + \cos \theta' v_V(\mathbf{x}, t)]$.

In Eq. 1, the cross section is evaluated on a plane tilted according to a larger surface slope component. In this expression, the limits of the integration are somehow defining the spatial scale of the larger tilting waves. As discussed by Voronovitch (2002), under the small-slope asymptotic development, this type of solution is robust to scale separation. From numerical investigations and sufficiently short electromagnetic waves, the spatial area that is significant for the calculation of the integral is found to be limited to a small area concentrated around the origin of the surface coherence function $\langle e^{-2ik_o \cos \theta' (\xi(\mathbf{x}_1, t) - \xi(\mathbf{x}_2, t))} \rangle$. To further simplify this illustrative theoretical development, we consider Gaussian statistics, and the latter function simply writes

$$\langle e^{-2ik_o \cos \theta' (\xi(\mathbf{x}_1, t) - \xi(\mathbf{x}_2, t))} \rangle = e^{-4k_o^2 \cos^2 \theta' (\rho(\mathbf{0}) - \rho(\mathbf{x}))} \quad (2)$$

The time dependency is dropped when considering an overall statistical stationarity, i.e. the surface within the larger tilting scales is rougher everywhere the same at any time. Further analytical simplifications also appear when considering the surface to be differentiable. In this case, the correlation function ρ is approximated for short lags by $\rho(\mathbf{x}) = \rho(\mathbf{0}) - m_{ssx} \Delta x^2/2 - m_{ssy} \Delta y^2/2$. This is

obtained for a particular geometry with Δx , Δy chosen to lie along and across the short scale roughness principal axis, i.e. the wind direction. Accordingly, mss_x is the slope variance along the wind direction. Such a simplification leads to an analytical solution for Eq. 1, as

$$\sigma_{pq}^o(\mathbf{x}, t) \simeq \frac{|g'_{pq}|}{2 \cos^4 \theta' \sqrt{mss_x mss_y}} e^{-\frac{\tan^2 \theta'}{2 mss_x mss_y} [mss_x \sin^2 \phi + mss_y \cos^2 \phi]} e^{i[\Omega_L + \Omega_s]t} \quad (3)$$

with ϕ the angle between the wind direction and the line-of-sight plane of incidence. Note that the radar modulation transfer function is then defined as

$$m_{RAR} = \frac{1}{\sigma_{pq}^o} \frac{\partial \sigma_{pq}^o}{\partial \theta'} \quad (4)$$

and will be polarisation and incidence angle dependent, as well as wind induced roughness dependent.

In Eq. 3, Ω_s stands for a Doppler offset associated with the dynamical properties of the more rapidly varying scales within the larger tilting and slowly varying facets. As developed under this simplified framework, this Doppler offset can be associated with an overall local mean velocity, \bar{c} , of the scales contributing the most to the surface coherence function at short spatial lags. At the asymptotic small perturbation electromagnetic solution, \bar{c} would correspond to the resonant Bragg scale phase speed. A coherently imaged facet shall thus exhibit a modified Doppler shift given by $\Omega_s = -2k_o \bar{c} \sin \theta' \cos \phi$. To possibly evaluate this mean velocity \bar{c} , for the Kirchhoff-like solution, the spatio-temporal change of the correlation function around its origin may be considered to yield

$$\Omega_s = -2k_o \bar{c} \sin \theta' \cos \phi \simeq -2k_o \frac{mss_{xt}}{mss_x} \sin \theta' \cos \phi \quad (5)$$

where mss_{xt} is a second order moment term related to the time and spatial derivatives of the correlation function evaluated at the origin. This term, as well as mss_x and mss_y , can be computed as a second order moment of the shorter scale surface roughness spectrum, e.g. Winnebrenner and Hasselman (1988) and Thompson (1989).

Following this development, the local reflectivity has a Doppler shift, proportional to $\Omega_s + \Omega_L$. This instantaneous Doppler shift adds to the nominal expected Doppler shift caused by the local geometry along with the platform velocity. The reflectivity induced extra term is a slow time varying function randomly distributed in space according to the randomness and temporal changes of the tilting larger facet velocities and slopes as probed within the radar illuminated area during the SAR integration time. The Doppler shift, Ω_s , associated with the rapidly varying scales is modulated through local incidence angle changes $\theta'(\mathbf{x}, t)$. Considering the spatial averaging, second order correction related to this effect are expected to be proportional to both the second order moment mss_x of the larger waves and the RAR modulation amplitude. For the contribution of larger waves, correlation between the Doppler shift Ω_L and, mostly tilt induced, modulated local cross section must also be considered. For instance,

wave systems travelling toward the instrument will produce higher cross sections over their forward faces associated with positive vertical velocities. From the definition of a line-of-sight velocity transfer function driven by the larger wave orbital motion, the strength of this effect on the overall mean Doppler will be proportional to both the second order moment $mss_{xt} \simeq \bar{c} mss_x$ of the larger waves and the RAR modulation amplitude, Eq.4.

At this point, it is beyond the scope of the present note to further dwell on this development. Many known possible modulation impacts are not taken into account, e.g. hydrodynamic modulation, tilting larger wave local accelerations, short scale coherence time, ... But to summarize, a mean Doppler shift may be expected and, to first order, directly connected with an overall radar line-of-sight mean velocity, \bar{c} . Following the proposed development which encompasses quasi-specular and composite scattering mechanisms, \bar{c} roughly corresponds to the mean velocity of so-called intermediate scale surface facet slopes.

3. GLOBAL DOPPLER OBSERVATIONS

Using the orbit propagation software developed by ESA, a Doppler centroid can be predicted for any look angle and any orbit time. These calculations include the yaw steering law of the ENVISAT platform and careful estimate of the ASAR antenna boresight. These predicted Doppler centroid estimates are then used as references. Validations have been performed to check that the measured Doppler centroids estimated over land SAR scenes were correctly fitting the predicted Doppler centroid references. Knowing orbit parameters, we thus only need to properly estimate the fractional part of the Doppler centroid. Further, any Doppler ambiguity is removed by comparing measurement and prediction for which deviations of less than 100 hz are solely expected.

During the commission period to evaluate and validate ENVISAT ASAR Wave Mode products, over 300000 products have been analyzed. As part of the effort, ECMWF wind and wave model outputs have been systematically co-located with each ocean ASAR imagette scene. The global dataset thus corresponds to a very wide range of wind and wave conditions. As mentioned above, the expected Doppler centroid frequency is estimated using very accurate pointing angle and attitude information. Thanks to this precise orbital parameter knowledge for the ENVISAT ASAR, nominal Doppler offsets have been computed for each imagette product. These Doppler offsets have then been compared to the Doppler centroid directly computed from the measured complex signals. The analysis then refers to the difference between the expected and measured Doppler shifts.

Illustration of the global observation is given Figure 1. The global observation corresponds to September/October, 2003. As anticipated, the Doppler anomalies are shown to roughly be of opposite sign for descending and ascending tracks. The ASAR instrument is indeed a right-looking antenna, and negative (resp. positive) Doppler anomalies shall correspond to scatters go-

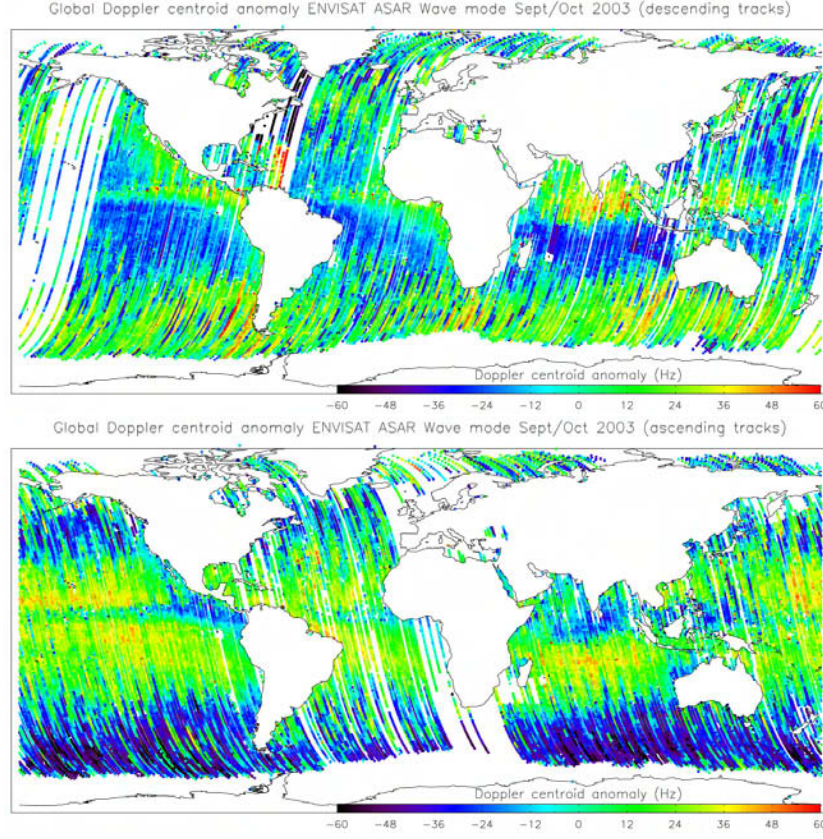


Figure 1. Frequency anomalies observation along ENVISAT ASAR descending (top) and ascending orbits

ing away from (resp. toward) the radar line-of-sight. Consequently and as revealed by this global analysis, trade winds are characterized by negative (resp. positive) frequency shifts for descending (resp. ascending) satellite passes. Clearly, the Doppler anomalies are geophysically pertinent and visually highly correlated to line-of-sight wind wave induced motions.

More quantitatively, the measured frequency shifts range from -50 Hz to 50 Hz. Related to a mean motion by

$$\bar{c} = \frac{\pi}{k_o \sin \theta_o} \Delta f \simeq 0.064 \Delta f \quad (6)$$

a measured anomaly of about 15 Hz translates to a mean motion of about 1 m/s. Using co-located ECMWF wind estimates, a very high correlation between the frequency anomalies and the radial surface wind components is found, Figure 2. The scatter mean motion as detected by the C-band radar at 23° incidence angle may be linearly related to wind speed for moderate wind conditions, 5 m/s to 10 m/s. Over this range, the mean motion \bar{c} is found to lie between one fourth and one fifth of the 10 m surface wind speed, about 6 to 8 times the wind friction velocity. This is one order of magnitude larger than usually reported wind drift and Stokes drift estimates.

These relatively large numbers are consistent with the theoretical approximation presented in section 2. Indeed, considering a standard k^{-4} surface roughness elevation spectra and a linear dispersion relation $c = \sqrt{g/k}$, the mean velocity of the surface slopes may be approached

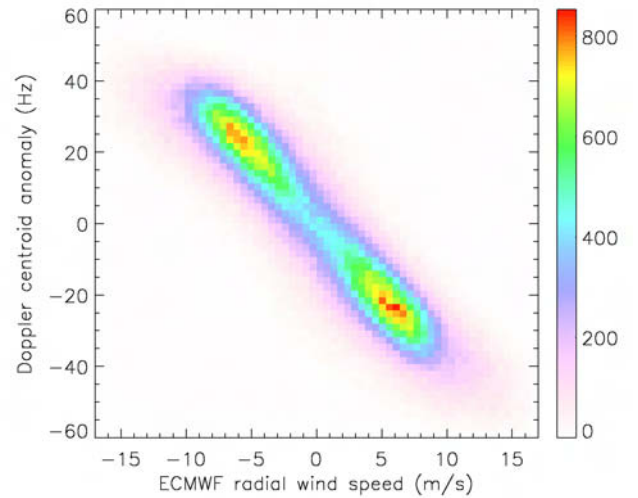


Figure 2. Correlation between the frequency anomalies and the radial surface wind components

as

$$\bar{c} \simeq \alpha c_{max} \left(1 - \frac{c_{min}}{c_{max}}\right) / \log \frac{c_{max}}{c_{min}} \quad (7)$$

For this approximation, the surface waves to be considered are those contributing the most to the surface coherence function, Eq. 2. These scales are mostly associated with the wind sea part of the elevation roughness spectrum. The larger velocity limit may be taken proportional to the wind speed, i.e. $c_{max} \propto c_{peak} \propto U$. The α term is a proportionality constant smaller than 1 related to the definition of the spreading spectral function. For the lower velocity limit, the minimum phase speed c_{min} to be considered may be related to the friction velocity, as shorter waves may not be dispersive. From a composite electromagnetic model point, this lower limit shall correspond to facet sizes larger than 3 to 5 times the radar wavelength, i.e. 15 to 25 cm. To match Doppler anomaly measurements with a semi-empirical algorithm, the global C-band 23° ASAR observations may be approached with Eq.7, setting $c_{max} \simeq 0.8 U$, and $c_{min} \simeq 0.5$ m/s.

4. COASTAL OBSERVATIONS

Considering the above global analysis to successfully prove the fact that line-of-sight C-band detected sea surface scatter motions can be readily extracted from SAR Doppler centroid measurements, it is tempting to further conduct the analysis to SAR images covering a wider area.

To this end, we report the analysis for an ENVISAT ASAR image SLC product taken over the west tip of France, Fig. 3. At the time of acquisition, the scene corresponds to relatively uniform onshore high wind conditions over an area where tidal currents are the dominant surface current contribution. Tidal currents in the area can reach 3.5 m s^{-1} for an average spring tide, with typical velocities of 0.5 m s^{-1} . Finite elements and finite differences 2-D numerical model have been applied to obtain maps of currents at 5 m depth. The tide is generated using well known harmonic constants measured in reference harbours and bottom friction is adjusted to fit observed current ellipses (Le Nestour, 1993). The tidal current at the time of the SAR scene acquisition is computed by interpolation over the one hour resolution output of the model. As observed from local estimates computed over sub-images, Fig. 3, the expected and measured Doppler frequencies are equal to zero over land. The pass is ascending, the wind is onshore, and over the sea, the mean Doppler anomaly is then found mostly negative, i.e. scatterers going away from the antenna.

More interestingly, the Doppler map exhibits local variations, e.g. between Ouessant and Molene islands in the northwestern part of the image, the Doppler anomaly almost changes sign. In this particular area, the measured mean scatter motion is strongly reduced compared to western more open ocean conditions. Figure 4 shows the relative cross section variations over the SAR scene. As revealed, relative increases in backscatter power are generally well connected to these reduced mean scatter

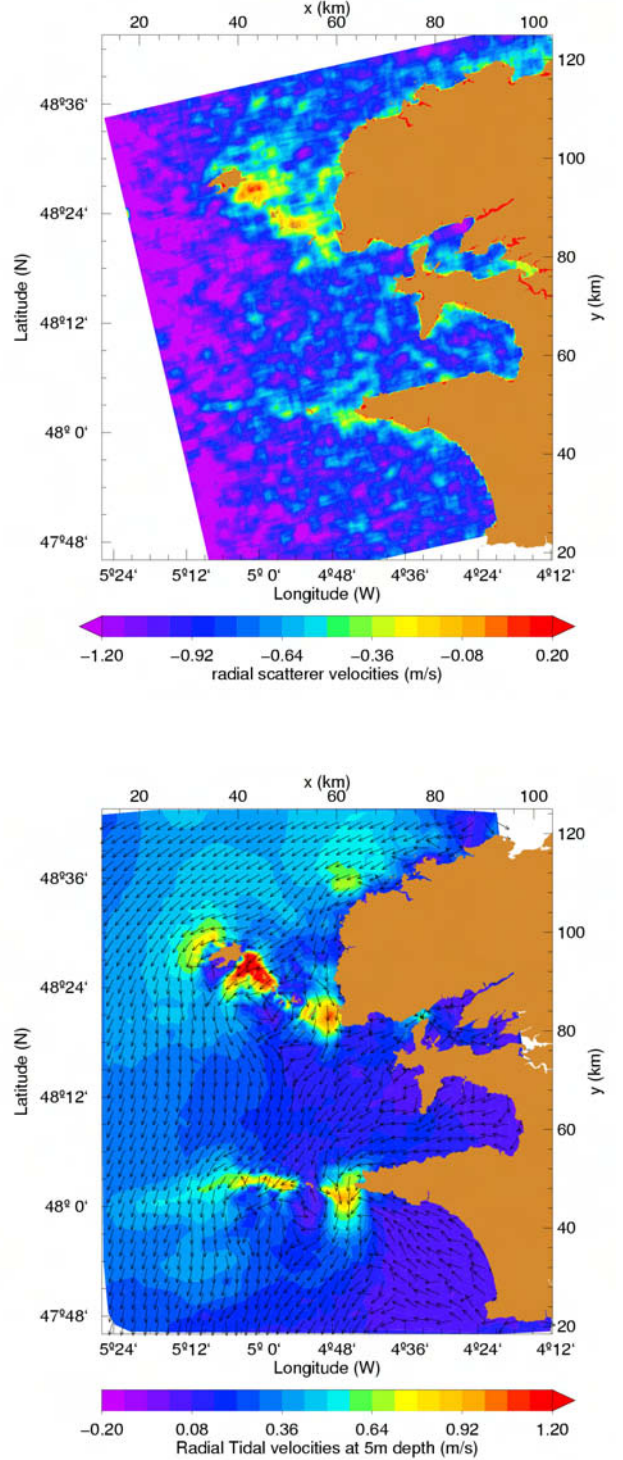


Figure 3. SAR derived horizontal scatterer velocities (top) and Model tide radial velocities

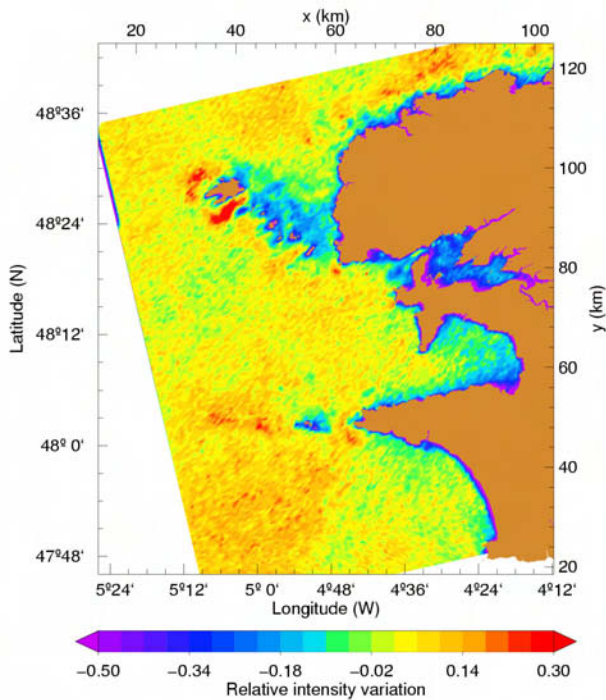


Figure 4. Relative variations of local backscatter intensity

detected motions. In this case, sea surface roughness changes are just well connected to mean surface motion changes, as certainly associated to surface current non-uniformities. The roughness transformations is usually conveniently described according to the wave action conservation, e.g. Kudryavtsev et al. (2004). In particular, adverse surface current will shorten the so-called intermediate ocean surface waves, strongly increasing the mean surface slope variance mss_x , modulating the growth rate at the surface, and thus most likely, the proportion of breaking events. The mean radar cross section will thus strongly increase. As found, estimated Doppler changes can then be ascertained to be effectively related to local environmental conditions.

5. OUTLOOK

Following a theoretical analysis and co-located atmospheric wind and wave model, as well as tide predictions, the line-of-sight Doppler shifts have been successfully shown to carry valuable quantitative information about the expected mean motion between the sea scatterers and the satellite platform. These global ENVISAT ASAR Wave Mode products provide a direct validation of the geophysical nature of the measured Doppler shifts. To first order, it has been theoretically derived that these shifts are dominated by an overall local mean velocity, \bar{c} , related to intermediate scale surface slope. These scales are predominantly wind driven, and in particular, these Doppler shifts have been clearly evidenced to be wind direction dependent. Magnitudes will further be polarization and incidence angle dependent according to the radar

backscatter mechanism and the related tilt and hydrodynamic radar cross section modulation transfer functions.

Changes according to surface current impacts are expected according to wave-current interaction modifications of the wind wave spectrum. As evidenced, such effects are anticipated to be very well observed under local adverse current conditions. As envisaged, combinations of both radar cross section and Doppler measurement variations shall be the key to retrieve underlying surface current characteristics.

Although the resolution may be considered low (about 1 km), the proposed synergy to infer both geometrical and dynamical properties of the sea surface shall be a sufficient independent source of remotely sensed information for most oceanographic applications. Efforts shall certainly be needed to further assess the full potential of these observations. But, such a capability from standard SAR instruments shall certainly help in the near future the development of new and more consistent retrieval algorithms for scientific and practical purposes.

ACKNOWLEDGMENTS

We would like to acknowledge the technical support by the European Space Agency, ESA, in particular, Y.L. Desnos, B. Rosich and B. Duesman. We wish to express our gratitude to J. Closa from Altamira Inc. We further wish to acknowledge D. Hauser and A. Mouche. The coastal case study indeed benefit directly from the VALPARESO experiment to help validation/calibration of the ASAR SAR data taking place over the west tip of France (Brest). We finally thanks F. Arduin from Service Hydrographique de la Marine.

REFERENCES

- Chapron B., H. Johnsen, and R. Garello, Wave and wind retrieval from SAR images of the ocean. *Ann. Telecommun.* 56, 11-12, 682-699, 2001
- Engen, G. and H. Johnsen, SAR-Ocean wave inversion using image cross spectra, *IEEE Trans. Geo. Rem. Sens.*, 33, 4, 1995.
- Johnsen H., Engen G., Chapron B., Walker N., Closa J., Validation of ASAR Wave Mode Level2 Product, *Proc. of Envisat Cal/Val Review, ESA SP-520*, 9-13 September 2002.
- Kudryavtsev, V. K., J. A. Johannessen, D. Akimov, O. M. Johannessen, and B. Chapron, Towards radar imaging of ocean phenomena: model and comparison with observations, *SP-565*, ESA, Noordwijk, 2004.
- R. Le Nestour, "Réalisation de l'atlas de courants de marée de la côte ouest de France, de St-Nazaire à Royan," *Tech. Report. 2*, 1993.
- W.J. Plant, "A stochastic, multiscale model of microwave backscatter from the ocean," *J. Geophys. Res.*, 2002

Romeiser R., S. Hufermann, and S. Kern, Status report on the remote sensing of current features by space-borne synthetic aperture radar, *SP-565*, ESA, Noordwijk, 2004.

Shuchman, R., The feasibility of Measurement of Ocean Current Detection Using SAR data, Proc. of the 13th Int. Symp on Remote Sensing of the Environment, Ann Arbor, pp 93-103, 1979)

Thompson, D. R., Doppler spectra from the ocean surface with a time-dependent composite model, *Radar Scattering from Modulated Wind Waves*, ed. G.J. Komen and W.A. Oos, Kluwer Acad., Norwell Mass., 27-40, 1989

Van der Kooij M., W. Hughes, and S. Sato, Doppler current velocity measurements: A new dimension to space-borne SAR data, available <http://www.atlantisscientific.com/eoserv.html>, 2001

A. Voronovich, "Small-slope approximation for electromagnetic wave scattering at a rough interface of two dielectric half-spaces," *Waves in Random Media*, vol. 4, pp. 337–367, 1994.

A. Voronovitch, "The effect of the modulation of Bragg scattering in small-slope approximation," *Waves in Random Media*, vol. 12, pp. 341–349, 2002.

Winnebrenner, D. P. and K. Hasselmann, Specular contribution to the mean synthetic aperture radar image of the ocean surface, *J. Geophys. Res.*, 93, C8, 9281-9294, 1988

**This page intentionally
left blank (pagination)**

ON RADAR IMAGING OF OCEAN PHENOMENA

V. Kudryavtsev^{1,2)}, D. Akimov³⁾, J.A. Johannessen²⁾,
O.M. Johannessen²⁾ and B. Chapron⁴⁾

¹⁾ Marine Hydrophysical Institute, Sebasopol, Ukraine

²⁾ Nansen Environmental and Remote Sensing Center, Bergen, Norway

³⁾ Nansen International Environmental and Remote Sensing Center, St.Petersburg, Russia

⁴⁾ Institut Français de Recherche pour l'Exploitation de la Mer, Plouzane, France

ABSTRACT

A model of radar imaging of ocean phenomena is proposed. This model is an extension of the background NRCS model [7] in the case of non-uniform medium. Radar scattering component takes into account Bragg and non-Bragg (specular reflections and the impact of wave breaking) scattering mechanisms. Varying surface current, surface temperature (stability effects), and surfactants are the main sources of medium non-uniformities. Transformation of wave spectrum and wave breaking in non-uniform medium is described in the relaxation approximation. Model calculations are compared with field observations. An overall good agreement is obtained. It is shown that wave breaking play important role in the formation of radar signatures of ocean phenomena.

1. INTRODUCTION

Radar signatures of the ocean phenomena (currents features, eddies, temperature fronts, bottom topography, internal waves) have been observed and documented in numerous experiments (e.g. [1, 4, 5, 12]). Experiments showed that radar visibility of ocean phenomena significantly depends on wind conditions, geometry of the radar observations and maybe other poorly studied factors. Wave-current interactions, suppression of waves by surfactants, and influence of atmospheric stratification are the commonly accepted mechanisms responsible for the surface manifestation of the ocean phenomena.

In the present study we propose a radar imaging model which is an extension of the background model [7] in the case of non-uniform medium. In [7] statistical properties of the sea surface results from solution of the energy balance equation. In the extended model the same equations are used to describe evolution of wind waves in a non-uniform medium. This model takes into account radar scattering from breaking waves. Unlike previous studies, the same wave breaking statistics (originally proposed in [10]) is used in both wind waves

and radiowave scattering models. It gives a consistency between the components of the radar imaging model. In [8] the background model was applied for the radar modulation transfer function (MTF). It was shown that inclusion of wave breaking significantly improved agreement between theory and measurements. Here (without any additional tuning) we expand the background model [7] to the problem of radar imaging of ocean phenomena.

2. RADAR SCATTERING FROM SEA SURFACE

Following [7] the sea surface is represented as a “regular” (non-breaking) wavy surface sprinkled with a number of breaking zones. Wave breaking provides a strong radar return forming a spike-like structure of radar images. Though the fraction of the sea surface q covered by breaking waves is small, they may significantly contribute to the normalized radar cross section (NRCS). It is suggested that radar returns from the regular surface (its fraction is $(1 - q)$) is supported by Bragg scattering (σ_{br}^p) and specular reflection (σ_{sp}) from steep surface slopes. Thus the total NRCS is

$$\sigma_0^p = (\sigma_{br}^p + \sigma_{sp})(1 - q) + \sigma_{0wb}q \quad (1)$$

where σ_{0wb} is the NRCS of an individual breaking zone. The quantity q is defined in [7] as a fraction of the sea surface covered by enhanced surface roughness generated by breaking waves, with wavelengths exceeding the radar wavelength by at least a factor of 10. Correspondingly the expression for σ_{0wb} is a consequence of mechanism of specular reflection from breaking zones (see [7], their eq. (55) and (60)). If the impact of breaking waves is ignored, the two first terms in (1) represent composite radar scattering model derived from physical arguments in [14], and later - in [13]. In the composite model spectrum of the sea surface is divided into small scale waves $k > k_d$ (with elevation variance h_s^2) and large scale waves $k < k_d$.

The dividing wavenumber k_d is proportional to radar wavenumber k_r : $k_d = d \cdot k_r$, where d is a constant. In our model dividing parameter is defined as $d = 1/4$, close to the recommendation of [13]. Small-scale waves provide resonant radiowave scattering. In those areas where conditions of specular reflections are fulfilled, short waves reduce the reflection coefficient (by a factor $1 - 4k_r^2 h_s^2$). Large-scale waves (carrying small-scale waves) cause random changes in the local incidence angle (affecting Bragg scattering) and may also provide the conditions for specular reflection.

The real waves are waves of the small slope. As it was argued in [11] tilting of the large-scale surface mainly results in small variations of local incidence angle $\tilde{\theta} \approx \eta_i$ (η_i is the surface slope in the plane of incidence). Neglecting the effect of tilting out of the incidence plane (see also Fig.5 in [7]) the averaged effect of large-scale waves on resonant scattering is

$$\sigma_{br}^p = \int_{\Gamma} \sigma_{obr}^p(\theta - \eta_i) P(\eta_i) d\eta_i \quad (2)$$

where $\sigma_{obr}^p(\theta - \eta_i)$ is the Bragg NRCS (see e.g.[11]), $P(\eta_i)$ is the PDF of the large-scale surface slope in the direction of the incidence plane. In eq.(2) integral range Γ is defined as

$$\Gamma = \{\eta_i \leq \text{tg}(\theta - d/2) \cup \eta_i \geq \text{tg}(\theta + d/2)\}$$

and results from the condition that local Bragg wave number must not exceed k_d . Note that if $\theta > 25^\circ - 30^\circ$ the integral can be evaluated approximately by expansion of σ_{obr}^p in Taylor series up to the second order in the slope of tilting waves (e.g. [12, 7]). However at smaller θ (related to near range of SAR images) such expansion loses its validity.

It is suggested that on some of the large-scale surface patches (where $\eta_i \notin \Gamma$) conditions of the specular reflection can be fulfilled. Then these patches contribute to the NRCS by means of the specular reflection (second term in (1)). Expression for σ_{sp} can be found in e.g. [14, 13].

In [7] spectrum of the sea surface is defined as a composition of the wave spectrum of energy containing waves B_p and equilibrium spectrum B_{eq} :

$$B(\mathbf{k}) = B_p(\mathbf{k}) + B_{eq}(\mathbf{k}) \quad (3)$$

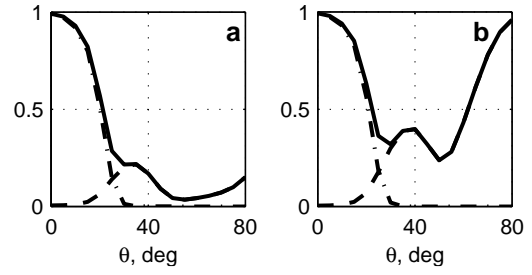


Fig.1. Relative contribution of quasi-specular reflection (dashed-dotted lines), wave breaking (dashed lines) and their sum (solid lines) to the total NRCS for VV (a) and HH (b) polarization at wind speed 10 m/s.

B_p in (3) is defined according to [3], and shape of B_{eq} results from solution of the energy balance equation. In particular, in the equilibrium gravity range the energy balance presumes proportionality between energy input from wind and energy dissipation due to breaking of waves, i.e.

$$\beta \omega E(\mathbf{k}) \propto g^{-1} c^5 \Lambda(\mathbf{k}), \quad (4)$$

where β is the wind growth rate, E is wave energy spectral density; c is phase speed; g is gravity acceleration; $\Lambda(\mathbf{k})$ is the surface density of the total length of breaking fronts of waves in the spectral interval from \mathbf{k} to $\mathbf{k} + d\mathbf{k}$ introduced in [10]. The advantage of this wave breaking statistics is that the same $\Lambda(\mathbf{k})$ -function defines both the energy dissipation (r.h.s. in (4)) and the fraction (q) of the sea surface covered by breaking waves:

$$\begin{aligned} q &\propto \int_{\mathbf{k} < \mathbf{k}_{wb}} k^{-1} \Lambda(\mathbf{k}) d\mathbf{k} \\ &= c_q \int_{\phi} \int_{k < k_{wb}} r_D \beta(\mathbf{k}) B(\mathbf{k}) d\phi d \ln k \end{aligned} \quad (5)$$

where $k_{wb} \approx 10k_r$ is a wavenumber of shortest breaking waves providing radiowave scattering, r_D is the ratio of dissipation to wind input, c_q is a constant. To obtain the second relation in (5), we use (4).

An extensive comparison of the background NRCS model with observations at moderate θ is given in [7]. The most important results relate to polarization ratio, which at moderate θ is always less than the Bragg theory predictions. This fact was mentioned in many studies and clearly indicates that effects of wave breaking on radar scattering are significant. Model calculations done in [7] on total model (1) agree with observations, suggesting that the impact of wave breaking on NRCS is properly taken into account.

The relative contribution of breaking waves, specular reflections and their sum (so called non-Bragg scattering) to the total NRCS for C-band at VV and HH polarization and at wind speed 10 m/s is shown in Figure 1. Since σ_{wb} and σ_{sp} are independent of polarization and $\sigma_{br}^V > \sigma_{br}^H$, the relative contribution of non-Bragg scattering on HH polarization is higher than on VV one. At small incidence angle ($\theta < 20^\circ$) quasi-specular reflections dominate the NRCS both at HH and VV polarization. At HH polarization and moderate θ wave breaking contributes sufficiently to the NRCS while at large θ , it accounts for nearly the entire radar return. At VV polarization the role of wave breaking is quite different; at $\theta > 45^\circ$ its impact is negligible. This Figure can be used to assess the role of different informative parameters in the formation of radar signatures at C-band. At small θ variation in the mean square slope is the determining parameter. The role of Bragg waves and tilting waves is important at moderate θ for both polarizations. At HH polarization, wave breaking becomes important at moderate and dominates at large incidence angles. At VV polarization the role of wave breaking may be noticeable at $\theta \approx 25^\circ \dots 45^\circ$ and is weak at larger incidence angle.

3. TRANSFORMATION OF WIND WAVES

Radar manifestations of oceanographic phenomena can result from modulation of the Bragg wave spectrum, mean square slope variations, and wave breaking in a non-uniform medium. We suggest that the major sources of medium non-uniformity are surface currents, wind field variations, and surfactants.

The characteristic form of the wave action spectral density $N(\mathbf{k})$ equation reads

$$\dot{N}(\mathbf{k}, \mathbf{x}, t) = Q; \quad \dot{\mathbf{k}} = -\Omega_{\mathbf{x}}; \quad \dot{\mathbf{x}} = \Omega_{\mathbf{k}} \quad (6)$$

where dot means total derivative on time, low subscript means partial derivative, Q is the source of wave action spectral density. Also $\Omega = \omega(k) + \mathbf{k} \cdot \mathbf{u}$ is the frequency of waves in the moving medium: \mathbf{u} is the surface current velocity; and ω is the intrinsic frequency. The background spectrum $N_0(\mathbf{k})$ results from solution: $Q(N_0) = 0$. Thus medium non-uniformities disturb the wind wave spectrum relative to its background shape.

3.1 Relaxation approximation

If the source Q is known, (6) with (7) can be solved numerically. However, in our model Q is defined in the equilibrium range only. In the range of energy containing waves, the saturation spectrum B_p is defined empirically. Therefore we analyze eqs. (6) following the relaxation approach developed in [9].

We assume that the energy source in (6) is a difference of wind energy input and a non-linear term: $\beta\omega N - Q_N$. The latter models energy dissipation due to wave breaking (D) and resonant wave-wave interactions (I): $Q_N = D + I$. Eq. (6) for small disturbances \tilde{N} reads:

$$\dot{\tilde{N}} = \tilde{\beta}\omega N_0 - \tilde{N}/\tau \quad (7)$$

$$\tau^{-1} = -\beta\omega + \partial Q_N / \partial N \quad (8)$$

where τ is a relaxation time, which must be consistent with the energy source Q . Following [9] we suggest that eq. (7) must describe spectral variations caused by either currents or wind. Then the definition of τ is:

$$\omega\tau = \frac{m_*}{2\beta} \quad (9)$$

where $m_* = \partial(\ln N_0) / \partial \ln u_*$ is the wind exponent of the wave spectrum. Such a definition of τ does not require any exact form of Q and one needs to know only exponent of the spectrum, which may be known e.g. empirically. For spectrum (3) the wind exponent is

$$m_* = (m_*^p B_p + m_*^{eq} B_e) / B \quad (10)$$

According to [7], the wind exponent in the equilibrium range is $m_*^{eq} = 2/n$, where n is a function of k . It is equal to $n=1$ in capillary-gravity range and $n=5$ in the gravity range. The wind exponent for empirical spectrum B_p [3] at given fetch is $m_*^p = 1$ for developed sea, and $m_*^p \approx 0.7$ for developing one. This indicates that in a developed sea, the dominant role in Q_N comes from resonant wave-wave interactions (which are cubic in the action spectrum) and in the young sea both wave-wave interactions and wave breaking are important. Solution of eqs. (6) and (8) can be simplified for the following two asymptotic regimes. The first is when relaxation time τ is much less than scale L of medium non-uniformity, i.e. τ/L is small (rapid relaxation

regime). The second asymptotic regime is when group velocity c_g is much larger than the current velocity scale \hat{u} , i.e. when c_g / \hat{u} is large (fast wave regime).

We suggest that surface current and wind velocity may be expanded into the Fourier series. Then solution of eq. (6) in terms of amplitude of Fourier harmonic for wave spectrum variations $\hat{B}(\mathbf{k})$ reads

$$T(\mathbf{k}, \mathbf{K}) = m_k^{ij} \hat{u}_{i,j} \frac{l_r}{c_g} \frac{1-i \cdot r}{1+r^2} - m_* \frac{\hat{u}_*}{u_*} \frac{r^2 + ir}{1+r^2} \quad (12)$$

where $m_k^{ij} = k_j \partial \ln N / \partial \ln k_i$ is a tensor of “wavenumber exponent”, $\hat{u}_{i,j}$ and \hat{u}_* are Fourier harmonics for the tensor of current velocity gradient and variation of friction velocity in respect to the local value; $T = \hat{B}(\mathbf{k}) / B_0(\mathbf{k})$ is modulation transfer function, $r = \mathbf{l}_r \cdot \mathbf{K} - \Omega \tau$ is dimensionless relaxation parameter, $\mathbf{l}_r = \mathbf{c}_g \tau$ is the relaxation scale, \mathbf{K} is wavenumber of Fourier harmonic; $\Omega = C / K$; and C is its velocity of advance. Thus the saturation spectrum in physical space is

$$B(\mathbf{k}, t) = B_0(\mathbf{k}, t) \left[1 + \int T(\mathbf{k}, \mathbf{K}) e^{i(\mathbf{K} \cdot \mathbf{x} - \Omega t)} d\mathbf{K} \right] \quad (13)$$

Notice that eq.(12) includes also case of modulation of wind waves by long surface wave considered in [8].

For a given surface wave spectrum, calculations of the mean square slope in non-uniform medium are evident. To obtain relation for wave breaking modulations we suggest that in the energy containing range the exponent of energy dissipation dependence on the spectrum should be the same as in the equilibrium range, i.e. $n+1=6$ (see equation (16) in [7]). Then the harmonic Fourier of q modulation is

$$\hat{q}(\mathbf{K}) = c_q (n+1) \int \int_{k < k_i} r_D \beta B(\mathbf{k}) T(\mathbf{k}, \mathbf{K}) d\varphi d \ln k \quad (14)$$

It can be shown using the relaxation approach that the ratio of energy dissipation to wind input r_D is related to spectral wind exponent by

$$r_D = 2/3 \cdot (m_*^{-1} - 1) \quad (15)$$

In the equilibrium range $m_* = 2/n = 2/5$, thus $r_D = 1$, i.e. wave breaking is a dominating non-linear term. In the energy containing range and a developed sea $r_D = 0$, i.e. wave breaking dissipation is negligible. For

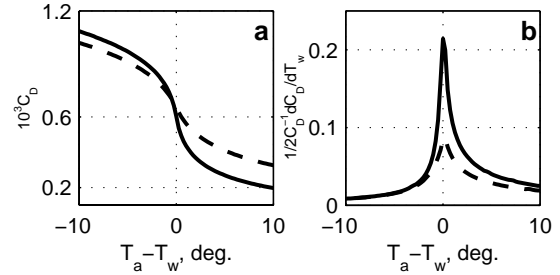


Fig.2. a) Geostrophic drag coefficient as a function of the temperature drop between the sea surface and free atmosphere for geostrophic wind speed 5 m/s (solid lines) and 15 m/s (dashed line). b) Transfer function $1/2 \partial(\ln C_D) / \partial T_w$ describing linear response of air friction velocity on the surface temperature variations.

a young sea ($m_* = 0.7$) the contribution of wave breaking to the energy balance is $r_D \approx 0.3$.

4. IMPACT OF MABL

In many cases ocean phenomena are accompanied with spatial variations of the surface temperature T_w (temperature fronts). Changes in T_w affect stratification of the marine atmospheric boundary layer (MABL) and thus wind surface stress and wind waves. Experimental evidence on correlation of radar return and T_w is given in [1]. To assess effect of MABL we assume that geostrophic wind speed G and temperature of the free atmosphere T_a are horizontally uniform. Then any variations in the surface wind are the result of the planetary MABL transformation over varying T_w . We suggest that wind surface stress may be estimated through the resistance law for the equilibrium planetary MABL, which reads (e.g. [2])

$$\frac{\kappa \mathbf{G}}{\mathbf{u}_*} = \ln(\kappa u_* / f z_0) - B(\mu) - iA(\mu) \quad (16)$$

where $\mu = \kappa u_* / fL$ is the MABL stratification parameter, L is the Monin-Obukhov scale; f is Coriolis parameter, $\mathbf{G} = G \exp(i\varphi_G)$ is complex geostrophic wind velocity; φ_G is its direction; $\mathbf{u}_* = u_* \exp(i\varphi_w)$ is complex friction velocity, φ_w is direction of the near surface wind; z_0 is the sea surface roughness scale. The universal functions $A(\mu)$ and $B(\mu)$ are defined according to [2]. Geostrophic drag coefficient $C_D = u_*^2 / G^2$ as a function of $T_a - T_w$ is shown in panel a of Fig. 2 for $G = 5$ m/s and $G = 15$ m/s. If we suggest that on the upwind side of the front

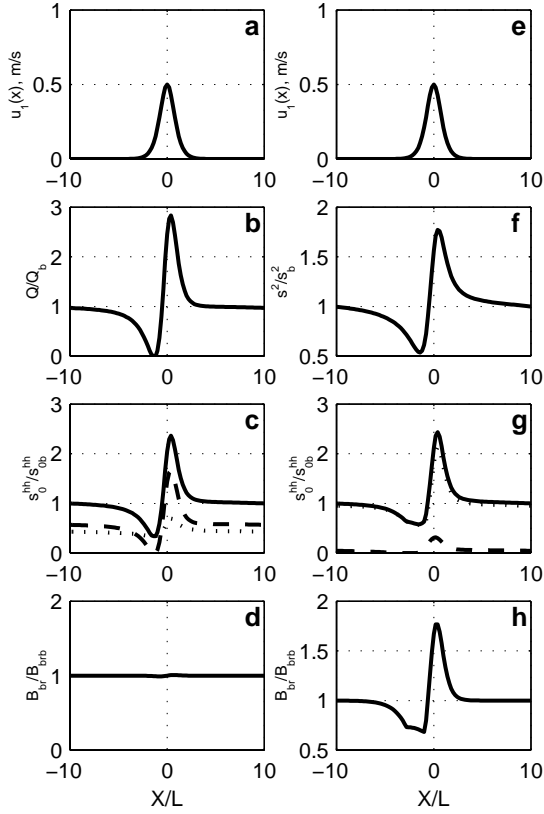


Fig.3. Model calculations of the sea surface manifestation of internal waves traveling upwind.
a,e) Current velocity induced by IW on the sea surface.
b) Modulation of wave breaking.
c) Modulation of the sea surface NRCS at X-band HH polarization: solid line is total NRCS, wave breaking component is dashed line, and Bragg scattering component is dotted line. Contribution of specular component is negligible.
d) Modulation of X-band Bragg waves.
f) Modulation of mean square slope.
g) The same as in c) but for L-band.
h) Modulation of L-band Bragg waves.

MABL stratification is neutral ($T_a - T_w = 0$) and the air flow is running on the warm/cold front with the surface temperature drop $|\Delta T_w| = 5^\circ$, surface wind stress on the downwind side is increased/decreased in 1.7 times. Such enhancement/suppression of wind stress may cause essential variations in wind waves resulting in radar manifestation of a sea front. A linear response of u_* on the surface temperature variations \tilde{T}_w $\tilde{u}_*/u_* = [1/2\partial(\ln C_D)/\partial T_w]\tilde{T}_w$ is shown in panel b of Fig.2. Response of friction velocity is strongest when variations in T_w occur on the background of neutral MABL, and weak if background stratification is either stable or unstable.

5. COMPARISON WITH EXPERIMENTS

5.1 Internal Waves

First we consider radar signatures of internal waves (IW) as the most reliable way to check the model. We chose well-controlled experiment SARSEX [4]. During this experiment trains of soliton-like IW have been observed. Here we model radar signatures of IW packet G. Scale of phase speed of these IW and amplitude of surface velocity were $C=0.7$ m/s and $u_0=0.5$ m/s, correspondingly. Wind speed was 6.0 m/s and its direction in respect to direction of the IW traveling was $\theta_w = -145^\circ$ (i.e. IWs travel approximately opposite to the wind direction). Airborne X- and L-band SAR images on HH polarization of this IW packet can be found in [4]. Radar signature of range travelling IW were observed at incidence angle $\theta = 35^\circ - 45^\circ$.

Results of the model simulation are presented in Fig. 3. As mentioned previously, both wave breaking and mean square slope are significantly disturbed by the IW, with the amplitude of q modulation exceeding the one from s^2 by a factor of two. Enhancement of wave breaking is shifted to the forward face of IW, i.e. toward the region of maximum convergence of the surface current. Peak-over-background ratio for X- and L-band is approximately the same and equal to 2.5 (or 4 dB). These estimates are consistent with radar observations. As it follows from Fig.3 the physics responsible for the enhanced radar return in X- and L-band is different. In X-band peak of radar modulation results from scattering from enhanced breaking waves (65%) and Bragg

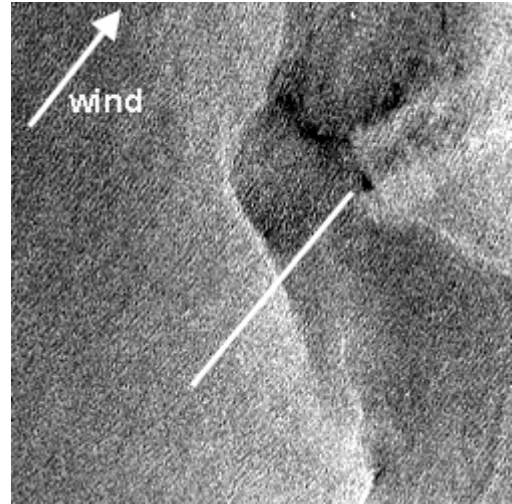


Fig. 4. Extract (30x30 km) of ERS-2 SAR image of Norwegian coastal current obtained at 10:31 on 27 September 1995. Arrow indicates wind direction. White line is the ship route where measurements shown in Fig. 5 were done.

scattering mechanism contributes 35% of return power by means of modulation of mean square slope of tilting waves (in X-band modulation of Bragg waves in negligible). In L-band modulation of Bragg scattering mechanism is a primary source of radar scattering modulations. In this case both modulation of Bragg waves (see plot h) and slope of tilting waves are of the same importance. One may mention that X-band and L-band signatures of the same IW exhibit similar modulation patterns. This experimental fact was mentioned in all studies on radar signatures of IW.

5.2 Sea front: CoastWatch-95 experiment

During the “CoastWatch-95” experiment 56 ERS-1/2 SAR images of the Norwegian coastal zone and *in situ* data (meteorological parameters, surface current velocity, sea temperature and salinity in the upper layer) were collected [6]. In this paper we analyze SAR image obtained at 10:31 on 27.09.1995, when the time gap between the SAR image and *in situ* measurements taken from the ship travelling across the front was minimal, 21 minutes. An extract of the SAR image is shown in Fig. 4. *In situ* measurements along the ship track (indicated on SAR image) are presented in Fig. 5. The drop of T_w across the front is about 4° . In general surface current has a form of a jet-like current running along the front. However in the vicinity of the front it has a perpendicular to the front component. The air-water temperature difference has the opposite sign on the cold and warm sector of the front. This means that the MABL stratification is unstable in the warm sector and stable in the cold one. During the ship measurements, the air flow was steady in direction while its mean wind speed was around 9.5 m/s. Section of the SAR image along ship route shown in Fig. 4 is presented in Fig. 6a. The most remarkable features of

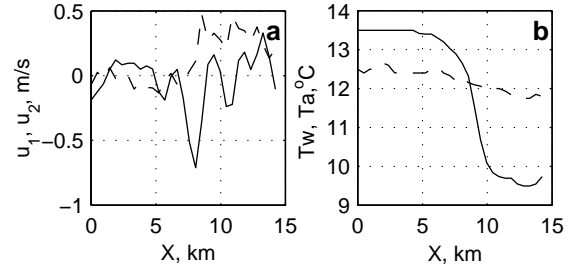


Fig. 5. Measurements taken from the ship crossing the sea front along the line shown in SAR image, Fig. 4.

a) Components of the current velocity parallel (dashed line) and perpendicular (solid line) to the front. b) The sea surface temperature (solid line) and air temperature (dashed line) at $z = 15$ m

the SAR images are easy recognizable. They are: the higher radar scattering from the warm side of the front, and enhanced radar returns in the vicinity of the sea surface temperature front.

Measurements of the sea surface and air temperature, and current velocities shown in Fig. 5 were used to simulate the NRCS of the sea surface. On the first step we have calculated transformation of wind surface stress over the front with use of resistance law (16). Then varying friction velocity and surface currents were used as input for the wind waves transformation equations (12), (13) and (14). These calculations (not shown) indicated that decrease of the wind stress on the cold side of the front causes decrease of the mean square slope and wave breaking. Surface current gives additional contribution to wave transformation. Effect of the current on wave breaking is much stronger than on the mean slope, and wave breaking (as well as MSS) following divergence of the surface current. Effect of the current shear is negligible. Model and observed

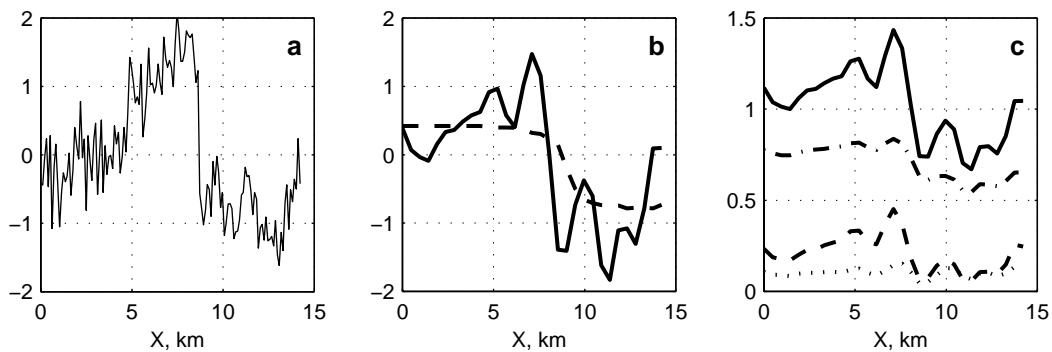


Fig. 6. a) Section of the SAR images (normalized on mean value, in dB) along the line shown in Fig. 4. b) Model NRCS over the front (normalized on mean value in dB), Dashed line demonstrates pure effect of MABL stratification. Solid line is the total NRCS variations caused by current and MABL. c) Relative contribution of different scattering mechanism (normalized on mean NRCS, linear scale): Solid line is total NRCS; dashed-dotted line is contribution of Bragg scattering; dashed line is contribution of wave breaking; dotted line is contribution of specular reflection

radar signatures of the front for the geometry of SAR observations ($\theta = 23^\circ$ and radar look direction in respect to frontal line is $\varphi = 135^\circ$) are shown in Fig. 6. The dashed line in Fig. 6b demonstrates effect of MABL stratification resulting in the stronger radar scattering on the warm side of the front. Solid line shows joint atmospheric and current effect. Fig. 6c demonstrates impact of varying scattering mechanisms on radar return. As it follows from this plot, on the upwind side of the front Bragg scattering is dominating mechanism providing about 80% of the radar return power. However in the vicinity of the front, wave breaking is enhanced. This process causes a significant increase in the radar return. Comparing the contribution of different scattering mechanisms one may conclude that maximum of radar return in the vicinity of the front results from enhanced wave breaking. Effect of the current on radar return mainly follows its divergence. One may conclude that the shapes of observed and model section of the SAR image over the front are quite similar.

6. CONCLUSION

We proposed a radar imaging model of oceanic phenomenon of the arbitrary origin. This model is the extension of semi-empirical model of the sea surface NRCS developed in [7] on the case of the non-uniform medium. It takes into account scattering from “regular” surface (due to Bragg scattering and specular reflections) and scattering from breaking waves. The same wave breaking statistics proposed in [10] is consistently used in the electromagnetic and hydrodynamic component of the radar imaging model.

Wave breaking may significantly contribute to the NRCS at moderate and large incidence angles. At small angles, specular scattering from “regular” (non-breaking) regions of the surface is another important non-Bragg scattering mechanism. Non-Bragg scattering is independent of polarization. Hence its relative role at HH polarization is higher than at VV. At L-band, the impact of non-Bragg scattering is negligible, while at C-band (and at higher radar frequencies) non-Bragg scattering plays an important role.

Transformation of wind waves is described in relaxation approximation. In this model, the relaxation parameter is related to the form of the source term, and hence gives consistency between the background sea state and its transformation in non-uniform media. Surface currents, variable near-surface wind fields (resulting from MABL transformations over surface temperature fronts), and surfactants are considered as the main sources of the medium non-uniformity. Application of the NRCS model to radar MTF is given in [8]. In the

present paper we compared the model with experimental data obtained in SARSEX and CoastWatch95 experiments. A reasonably good agreement between model and observations is obtained.

Acknowledgements:

The authors acknowledge the support of INTAS Association under the Project INTAS-00-598 and the support from the Norwegian Space Center. D. Akimov acknowledges support from INTAS under Young Scientist grant #2002-419.

REFERENCES

1. Beal, R., V. Kudryavtsev, D. Thompson, S. Grodsky, D. Tilley, V. Dulov, and H. Graber, The influence of the marine atmospheric boundary layer on ERS-1 synthetic aperture radar imagery of the Gulf Stream, *J. Geophys. Res.*, 102, C3, 5799-5814, 1997.
2. Brown, R.A., On two-layer models and the similarity functions for the PBL, *Bound. Layer Meteor.*, 24, 451-463, 1982.
3. Donelan, M.A., J. Hamilton, and W.H. Hui, Directional of wind generated waves, *Philos. Trans. R. Soc. London, Ser.A*, 315, 509-562, 1985.
4. Gasparovich R.F., J.A. Apel, and E.S. Kasischke, An overview of the SAR internal wave signature experiment, *J. Geophys. Res.*, 93, C10, 12,304- 12,316, 1988.
5. Johannessen, J., R. Shuchman, G. Digranes, D. Lyzenga, W. Wackerman, O. Johannessen, and P. Vachon, Coastal ocean fronts and eddies imaged with ERS-1 synthetic aperture radar, *J. Geophys. Res.*, 101, 6651-6667, 1996.
6. Johannessen, O.M., E. Korsbakken, P. Samuel, A.D. Jenkins and H. Espedal, COAST WATCH: Using SAR imagery in an operational system for monitoring coastal currents, wind, surfactants and oil spills. In *Operational Oceanography. The Challenge for European Co-operation*. J.H. Stel (editor-in-chief), Elsevier Oceanography Series, 62, 1997.
7. Kudryavtsev, V., D. Hauser, G. Caudal, and B. Chapron, A semi-empirical model of the normalized radar cross-section of the sea surface. Part 1: The background model, *J. Geophys. Res.*, 108, C3, DOI 10.1029/2001JC001003, 2003.
8. Kudryavtsev, V., D. Hauser, G. Caudal, and B. Chapron, A semi-empirical model of the normalized radar cross-section of the sea surface. Part 2: Radar modulation transfer function, *J. Geophys. Res.*, 108, C3, DOI 10.1029/2001JC001004, 2003.
9. Kudryavtsev, V., The coupling of wind and internal waves: modulation and friction mechanism, *J. Fluid Mech.*, 278, 33-62, 1994.

10. Phillips, O. M., Spectral and statistical properties of the equilibrium range in the wind-generated gravity waves, *J.Fluid Mech.*, 156, 505-531, 1985.
11. Plant, W.J., Bragg scattering of electromagnetic waves from the air/sea interface, in *Surface Waves and Fluxes, Volume II - Remote Sensing*, 41-108, 1990.
12. Romeiser R., and W.Alpers, An improved composite surface model for the radar backscattering cross section of the ocean surface. 2. Model response to surface roughness variations and the radar imaging of uderwater bottom topography, *J. Geophys. Res.*, 102, C11, 25,251-25,267, 1997.
13. Thomson, D.R., Calculation of radar backscatter modulations from internal waves, *J. Geophys. Res.*, 93, C10, 12,371-12,380, 1988.
14. Valenzuela, G.R., M.B.Laing, and J.C.Daley, Ocean spectra for the high frequency waves as determined from airborne radar measurements, *J. Marine Res.*, 29, №.2, 69-84, 1971.

ICE SESSION

Chairs: R. Shuchman & S. Sandven

**This page intentionally
left blank (pagination)**

SAR Measurement of Sea Ice Parameters: Sea Ice Session Overview Paper

Robert A. Shuchman⁽¹⁾, Dean G. Flett⁽²⁾

⁽¹⁾*Altarum Institute (formerly ERIM), P.O. Box 134001, Ann Arbor, Michigan 48113-4001 USA,
robert.shuchman@altarum.org*

⁽²⁾*Canadian Ice Service, 373 Sussex Drive, E-3, Ottawa, Ontario K1A 0H3 Canada, dean.flett@ec.gc.ca*

ABSTRACT

The SAR sea ice community consists of operational users, radar and computer engineers who perform sensor verification and algorithm development, and climate scientists who want to use changes in sea ice characteristics to quantify climate change. The SAR sensors on board the RADARSAT and Envisat satellite systems are providing the sea ice community with several gigabytes/day in data. Algorithms have been created and validated to automatically locate the ice edge. The RADARSAT geophysical processor system has produced a multiyear record of arctic sea ice motion, sea ice deformation, and new ice formation. Uncertainties still exist in totally automated sea ice classification particularly for the new ice, young ice, and first year ice categories. The multi-frequency and multi-polarization SAR data obtainable from a combination of Envisat, RADARSAT 2, and ALOS (and other SAR sensors) can potentially be used to aid in differentiating the thin ice types.

1. INTRODUCTION

Sea ice mapping has been significantly improved during the last decade by the introduction of high-resolution synthetic aperture radar (SAR). Operational sea ice monitoring as performed by the United States National Ice Center (NIC), Canadian Ice Service (CIS), and various commercial and government ice centers in Finland, Sweden, Denmark, Norway, Germany, and Russia requires daily information about ice edge, ice concentration (fractional area coverage), ice type (new ice, young ice, first year, multi-year), ice thickness, ice deformations (ridges) and ice dynamics (drift). Additionally, the various ice centers require information on lake and river ice as well as iceberg locations. Operational sea ice monitoring has traditionally been based on NOAA AVHRR visual and thermal infrared radiometer and SSM/I passive microwave data. With the advent of all-weather wide-swath SAR data from RADARSAT-1 and Envisat, ice monitoring can be performed with higher resolution and better quality.

In addition to providing sea ice information for operational activities such as ship routing, military operations, offshore oil and gas drilling, and fishing

fleet support, SAR data can also play a significant role in polar and climate change monitoring. High-resolution SAR can potentially provide velocity fields, convergence/divergence fields, ice volume fluxes, vertical heat fluxes, brine rejection from the freezing ice, and onset of the melt season, all parameters that are very important in respect to understanding the response of sea ice to climate change.

In this overview paper we summarize both the operational and climate change research uses of SAR for sea ice parameter detection. The uncertainties and future direction for research in respect to extraction of SAR derived sea ice parameters is also presented.

Five focused technical papers provide additional details to the summary statements provided in this overview paper. Three papers (see Table 1) address operational uses of SAR, one addresses automated detection of the sea ice edge from SAR data, while the remaining paper discusses the use of SAR sea ice data starting with the Seasat SAR for studying climate change in the polar region as well as the algorithms used in those studies. In addition to the listed papers, the reader is referred to a paper entitled "Ocean Observer Study: A Proposed National Asset to Augment the Future U.S. Operational Satellite System." This paper [1] suggests a SAR instrument be added to the present suite of sensors that are being flown on NPOESS.

2. OPERATIONAL USE OF SAR TO MONITOR SEA ICE, ICEBERGS, LAKE AND RIVER ICE

The Canadian Ice Service (CIS), the U.S. National Ice Center (NIC), and various European countries utilize SAR as an integral part of their ice forecast efforts. The first three technical papers listed in Table 1 summarize the operational use including issues pertaining to requirements, SAR data requests, data capture, near-real-time processing, ice parameter extraction from the SAR data, and integration of the information into a focused data product.

The summary of the Canadian Ice Service ("Operational Use of SAR at the Canadian Ice Service: Present Operations and a Look to the Future," by Dean Flett) is a comprehensive paper that captures the

Table 1. Focused papers that address the use of SAR for sea ice detection

Title	Author(s)	Subject
Operational Use of SAR at the Canadian Ice Service: Present Operations and a Look to the Future	Dean G. Flett	Operational sea ice monitoring
Routine Production of SAR-Derived Ice and Ocean Products in the United States	William Pichel Pablo Clemente-Colón Cheryl Bertoia Michael Van Woert Chris Wackerman Frank Monaldo Donald Thompson Karen Friedman Xiaofeng Li	Operational sea ice monitoring
Sea Ice Mapping using Envisat ASAR Wideswath Images	Stein Sandven Kjell Kloster Helge Tayen Tommy S. Andreassen Harvey Goodman Kim Partington	Operational sea ice monitoring (ship routing)
Automated Location of Ice Regions in RADARSAT SAR Imagery	Chris Wackerman William Pichel Pablo Clement-Colón	Automated ice edge algorithm
Sea Ice Investigation from Seasat to Present, with Emphasis on Ice Motion: A Brief Review and A Look Ahead	Ben Holt Ron Kwok	Use of SAR for polar climate change studies (justification and algorithms)

requirements, procedures and methodology used to produce the required ice charts. A discussion on the role the new multi-frequency and polarization SAR satellite sensor in improving the ice products is also presented.

A complementary paper describing NOAA's ("Routine Production of SAR-Derived Ice and Ocean Products in the United States," by Pichel et al.) current use of and development of SAR applications to support its mission, provides a summary of algorithms used to produce wind field, vessel detection, SAR image, and ice/land mask products. Center geophysical requirements and the future vision for NIC are also presented.

The last paper in this group ("Sea Ice Mapping Using Envisat ASAR Wideswath Images," by Sandven et al.) describes a commercial pilot monitoring program referred to as ICEMON which has a program goal to develop and demonstrate an integrated monitoring service for sea ice and related atmospheric and ocean processes in high latitude regions. Examples of ICEMON products collected near Svalbard using Envisat wideswath images are discussed.

A typical standard daily ice product, created in this case by CIS, is shown in Fig. 1. The charts present the total ice concentration and the partial concentration, stage of development (ice type), and floe size for the three thickest ice categories in each polygon area.

Special features such as icebergs and heavily ridged ice are also shown when and where appropriate. A product such as the one shown in the figure is not created solely from the SAR data, but rather is created by integrating analysis of the SAR data with other remote sensing data such as, NOAA AVHRR visible and infrared data as well as SSM/I (passive microwave data), and other data sources. In some cases satellite altimeter and scatterometer data are also used. The merging of the various satellite data is done manually by trained ice image analysts. They utilize computers to register and overlay the data to assist the interpretation. The output is a digital product registered to Earth coordinates.

Figs. 2 and 3 are typical SAR images of sea ice that are analyzed by expert interpreters. Fig. 2 is an Envisat C-band (HH) image collected on 8 February 2004, in the Gulf of St. Lawrence, in the vicinity of Prince Edward Island, while Fig. 3 is a RADARSAT C-band (HH) image from 5 February of Lancaster Sound. The land masses on each image are outlined in red. The ice edge on the Gulf of St. Lawrence image is visible at the top of the figure, while Lancaster Sound is totally ice covered.

The three papers all discuss the positive attributes of SAR (i.e. all weather, day or night, and fine resolution), but at the same time indicate that fully automated algorithms for ice typing are still not reliable enough for operational ice charting in support

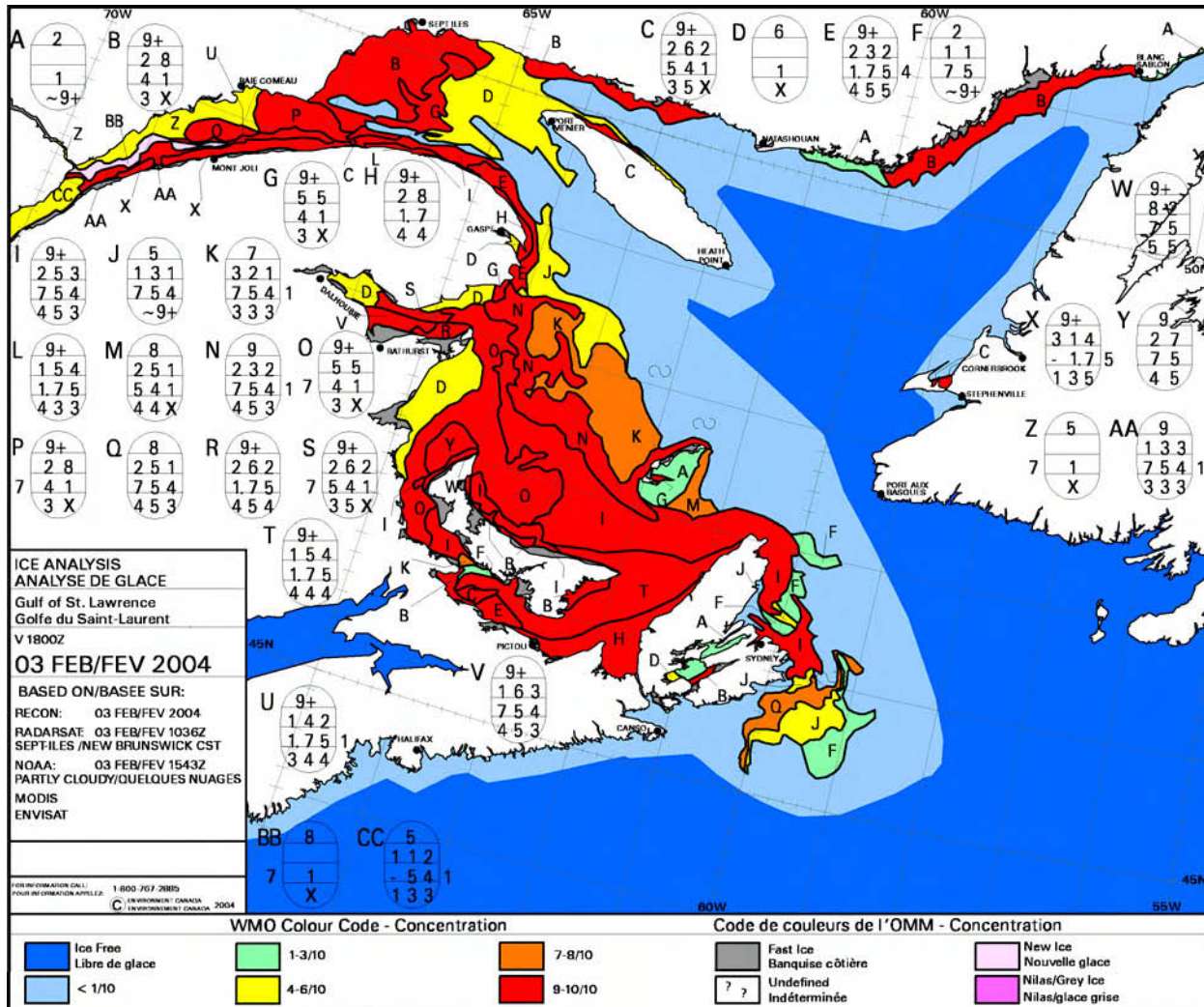


Fig. 1. Standard Daily Ice Analysis Chart

of navigation. Thus data analysis and chart production is done entirely by the expert ice analysts and forecasters using machine assisted manual interpretation techniques.

The first task of the operational sea ice forecasters is the identification of the boundary between ice and water or the ice edge. The ability to discriminate open water from sea ice is a function of the operating frequency and polarization of the SAR, the incidence angle, as well as the surface wind speed over the ocean and the resultant contrast between the ice and water backscatter [2-5]. High winds at the ice edge imaged at steep incidence angle can create ambiguities with respect to differentiating ice from water. Single channel (polarization) SARs, such as ERS-1/2 and RADARSAT-1, have experienced difficulties in these situations [6]. However, with the advent of polarization diverse or multiple-polarization satellite SAR, such as Envisat ASAR, there is great potential to realize improvements in ice versus water

differentiation. Open water backscatter from cross-polarization data (i.e. HV and VH), even under wind-roughened conditions, is much reduced. Selective use of the co-polarization channels (i.e. HH or VV) as a function of incidence angle can also reduce the ice/water ambiguity [3]. Also, the future availability of fully polarimetric as well as additional frequency sensors (e.g. ALOS PalSAR, TerraSAR X and L) offers potential improvements. The multi-frequency and polarization data also offer the potential to discriminate iceberg from the surrounding sea as well as thinner ice types. The disadvantage to the use of polarimetric data for use in operational ice monitoring is the reduced swath [5].

3. POLAR AND ENVIRONMENTAL CLIMATE STUDIES USING SAR

Sea ice plays a key role in the Earth's climate and has long been postulated to be a primary candidate as an indication of global warming [8]. As reported by Holt

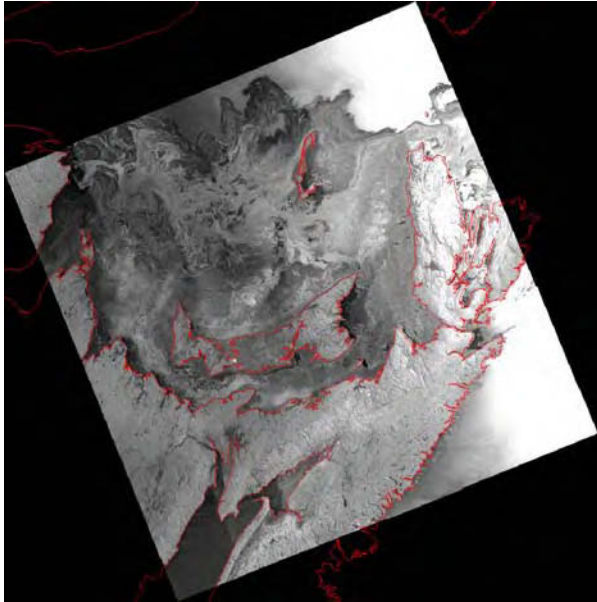


Fig. 2. Envisat SAR image showing sea ice in Gulf of St. Lawrence, collected on 8 February 2004. The ice edge is the dark boundary at the top of the image. (©ESA 2004; Data processed by Canada Centre for Remote Sensing)

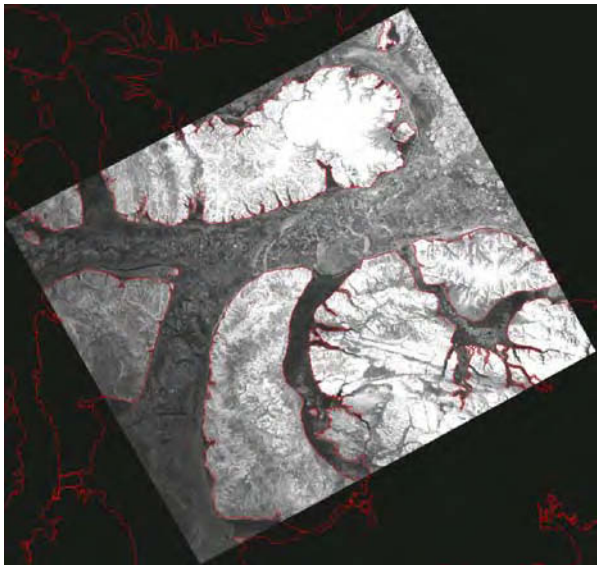


Fig. 3. RADARSAT image of sea ice collected on 5 February 2004 off Lancaster Sound. The Sound is most likely 100% ice covered with the darker areas being newer smooth ice. The brighter returns represent ice that is thicker and more deformed. (© CSA 2004; Data processed by RADARSAT International)

and Kwok ("Sea Ice Investigations from Seasat to Present, with an Emphasis on Ice Motion: A Brief Review and A Look Ahead"), sea ice acts to reduce the flux of heat from the comparatively warm ocean to the

colder atmosphere. When open water appears as the ice cover diverges and deforms, the heat flux increases tenfold, whereas it rapidly decreases again as new ice forms and thickens. As sea ice forms, salt is released from the water crystallization process to form brine, which drains from the ice into the ocean. Rapid ice growth can generate dense upper ocean water that mixes downward into the ocean column, thus being a source for convective overturning and eventually, deep water formation. The relatively salt-free sea ice (3-8 parts for thousand) then advects generally equatorward, thus supplying freshwater to other parts of the ocean for vertical mixing.

Sea ice also contributes significantly to the Earth's albedo. Sea ice has a large albedo and reduces significantly during the summer melt. Albedo is sharply reduced when summer melt takes place with absorption of shortwave radiation increasing with the presence of liquid water, particularly within surface melt ponds on multiyear ice floe. Multiyear ice is sea ice that has survived one summer melt. Most of the brine has drained into the ocean. Multiyear ice in the arctic is typically 3-5 meters thick. The thinning of multiyear ice and percent of multiyear ice to the total ice cover are issues of concern, and climate models do predict a gradual retreat of Arctic sea ice volume and extent leading to ice free summer conditions by 2070 [9].

Recent observations strongly indicate significant climate changes in the Arctic are taking place. The arctic sea ice cover was found to have thinned by over 40% between 1958-1997, as measured by upward looking submarine sonar [10-11]. The Arctic ice cover has decreased in both the maximum and minimum extent and the length of the melt season appears to be increasing.

Recent climate changes, starting with the 1989 shift in the arctic oscillation (AO) have strongly affected the ice cover, circulation, and export of water from the arctic. It appears likely that polynya (open water or leads) activity in the Arctic and their possible role in halocline variability may be directly coupled to atmospheric circulation [12-14]. Synoptic, systematic high resolution SAR observation of the sea ice, and polynya formation would be a valuable tool to better understanding this complex system. To generate the synoptic observation of sea ice coverage in the Arctic, the RADARSAT Geophysical Processor System was established.

The RADARSAT Geophysical Processor System (RGPS) is designed to carry out semi-automatic tracking of the sea ice within single channel SAR images. Only the winter freezing months from

November to April are examined in order to avoid uncertainties induced by episodic melting-freezing events during spring and summer that can mask the sea ice texture/feature recognition. The texture or sea ice feature tracking is therefore effective, and one can observe when changes in area occur and thus keep track of the age of the corresponding newly formed ice areas. In addition, characteristics of the multiyear ice (MY) field can be determined. Currently the SAR image database contains approximately five years of RADARSAT data (approximately 15,000 scenes) of the Arctic Ocean (3-day repeat within US/Canadian Arctic mask; 6-day outside this mask), and systematic and regular RGPS analyses of three years of the data (1996-1999) are available.

The RGPS products include:

- Sea ice motion dataset;
- Records of sea ice deformation, new ice formation areas and their ages covering the Arctic Ocean;
- Conversion of new ice age distribution into estimates of ice thickness distribution, (relevant and important to Cryosat sea ice thickness retrievals);
- Records of backscatter; and
- Multiyear ice fraction and timing of melt onset.

The availability of these regular fields to the scientific community has been welcomed and in particular has led to growing awareness of the complicated dynamic and thermo-dynamic behavior of the Arctic sea ice cover during winter. An offspring of this has, in turn, led to focused development and implementation of new sea ice rheology formulation in sea ice models. The RGPS Science Working Group meets every year to present, discuss, and obtain an overview of progress and development in science and application of the RGPS products [15-18].

Regular access to such sea ice products (see Fig. 4 for an example) should also gradually stimulate new interest in the climate research community, in particular as the data records exceed 10 years. In so doing one needs to define and recommend standard sea ice monitoring products that possibly blend and optimize high-resolution SAR images with coarser resolution active and passive microwave data. With the current rapid development of web mapping technology such information products, building on the RGPS products, should be easy to access and allow for user friendly browsing capabilities in space and time. The RGPS products could also support the IPY in 2007-08, encouraging hemispheric collaborative work. It would therefore be quite timely and desirable to also start discussion on collaboration and implementation of the RGPS at a European SAR receiving station/processing

center to ensure parallel and complementary information production of the European sector of the Arctic. In the context of the near future possible regular flow of wide swath SAR imaging data issues to be considered (not exclusive) are thus:

- Establishment of systematic and continuous monitoring of the Arctic Ocean using SAR data from Envisat, RADARSAT-2, and (in the near future) ALOS;
- Implementation of RGPS in Europe and the division of the task of processing the Arctic Ocean SAR image data between Europe and North America;
- Optimizing the complementarity between RGPS products from imaging radar and sea ice thickness retrievals from Cryosat and ICESat; and
- Generation of Arctic scale sea ice products (synergy between SAR, altimeters and coarser resolution active – passive microwave sensors) for environmental and climate studies.

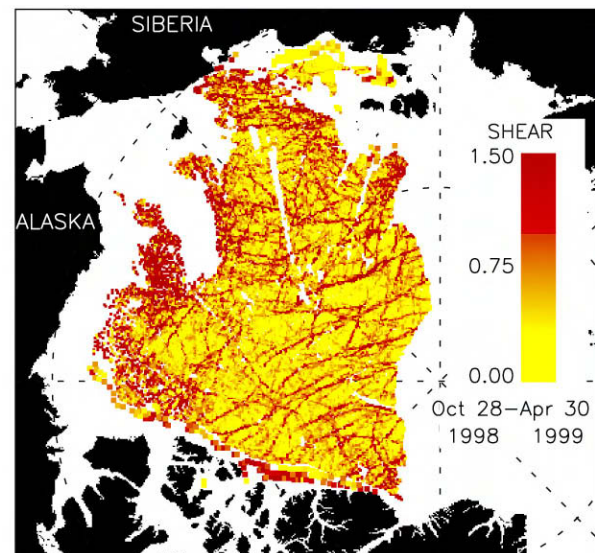


Fig. 4. This shows the net shear at each RGPS element (~10 km on a side) over the winter (end of October through April) as sampled by the small-scale kinematics observed in RADARSAT data.

At the margin of the sea ice cover (the edge), the abrupt transition to open water gives rise to unique processes including water mass formation, oceanic upwelling, wave propagation into the ice, eddy formation and atmospheric boundary layer processes [19]. The ice extent, the latitude of the ice edge as a function of longitude, is both of climatological and practical importance. Annual variation of sea ice extent is carefully observed as an early indication of greenhouse-induced climate change [20]. Monitoring

the ice extent and variability of the ice edge is important for practical reasons such as sea traffic, fisheries, offshore operations and other military marine activities in ice edge regions.

High resolution SAR data is the sensor of choice to study the marginal ice zone (MIZ). The present set of spaceborne scatterometers lack sufficient resolution to resolve subtle MIZ features. A detailed discussion on SAR detection of MIZ feature can be found in Synthetic Aperture Radar Marine User's Manual; Chapter 18. Processes at the Ice Edge – The Arctic [21].

The dynamics of the MIZ as imaged by SAR is illustrated in Fig. 5, an area of the Greenland Sea. Each SAR strip, which is 500-km long and 100-km wide, covers the same geographical area in the ice-edge region between 76°N to 80°N, and 8°W to 4°E. This series of annotated ERS-1 images and corresponding interpretation maps shows how the ice-edge location and features changed during the period from 13 to 16 January 1992. During this period, oceanographical investigations in the area were conducted from the R/V Håkon Mosby showing a number of shallow surface tongues of colder and fresher water associated with the ice tongues in Fig. 5 [22].

SAR images with 25-m resolution were the only data capable of providing accurate ice-edge location in a period of almost no daylight. SAR images transmitted to the ship in near-real-time were used to route the ship to positions near the edge of the ice. Without SAR imagery, the R/V Håkon Mosby would not have been able to operate close to the edge of the ice, as the wind conditions were variable and included storm events with wind speeds exceeding 25 m s^{-1} . During southeasterly winds, the ice edge was pushed towards the west. From 10 to 13 January, the wind began as northerly and then shifted to southerly, resulting in a more eastward location of the edge. On 16 January the effects of a north-northwest wind is made visible by ice streamers in the open ocean oriented parallel to the wind. Three days later, westerly winds produced an ice edge that is very diffuse. The rapid change in edge location and detailed ice features as characteristic of this area could only be observed from a time series of SAR images. The repeat period for the ERS SAR coverage was three days.

4. AUTOMATED SAR SEA ICE ALGORITHMS

As discussed in the operational monitoring section, the most important parameter to extract from the SAR data is the ice water boundary or ice edge. The Wackerman et al. paper on the “Automated Location of Ice Regions in RADARSAT SAR Imagery” summarizes the

NOAA/NESDIS Alaska SAR Demonstration Project. The demonstration project includes ship detection and wind vector determination. The ice edge algorithm (see Fig. 6 for an example) was used to remove ice from the data to improve the ship and wind vector performance. The sea ice classification algorithm is a supervised training algorithm that uses a series of hyperplanes to separate different classes in a n-dimensional feature space. The algorithm employs use of a combination of statistical measures and texture metrics drawn from the co-occurrence matrix to form the feature vector. The algorithm has been tested; less than 7% misclassification from the algorithm with almost no errors after applying spatial rules about the area imaged. This algorithm thus shows promise for creation of an automated procedure that can be used by the operational ice forecasters.

5. SUMMARY AND CONCLUDING REMARKS

The SAR sea ice community consists of operational users, radar and computer engineers who perform sensor validation and algorithm development, and climate scientists who want to use changes in sea ice characteristics to quantify climate change. Since the first SAR workshop held at Johns Hopkins in 1999, single channel SAR algorithms have been developed for first year and multiyear ice determination and ice feature tracking for ice dynamics.

The onset of RADARSAT provided the sea ice community with approximately 1 Gigabyte/day in data. Algorithms have been created and validated to automatically locate the ice edge. The RADARSAT geophysical processor system has produced a five-year record of arctic sea ice motion, records of sea ice deformation, new ice formation areas and their ages covering the Arctic ocean, conversion of new ice distribution into estimates of ice thickness distribution, radar backscatter records, multiyear ice fraction and timing of melt onset. Although these JPL products produced by the Geophysical Processor are exciting, not all of the products have been extensively validated and the algorithms have only been run on RADARSAT data. Calibration will be necessary before Envisat or ALOS data is routinely used.

Uncertainties exist in totally automated sea ice type classification particularly for the new ice, young ice and first year categories. This problem is exacerbated in the late spring and summer, when the snow covering sea ice becomes wet. The multi-frequency and multi-polarization SAR data obtainable from a combination of Envisat, RADARSAT 2, and ALOS (and other SAR sensors) can potentially be used to aid in differentiating the thin ice types. Typically the polarimetric data is narrow swath, versus the single frequency and

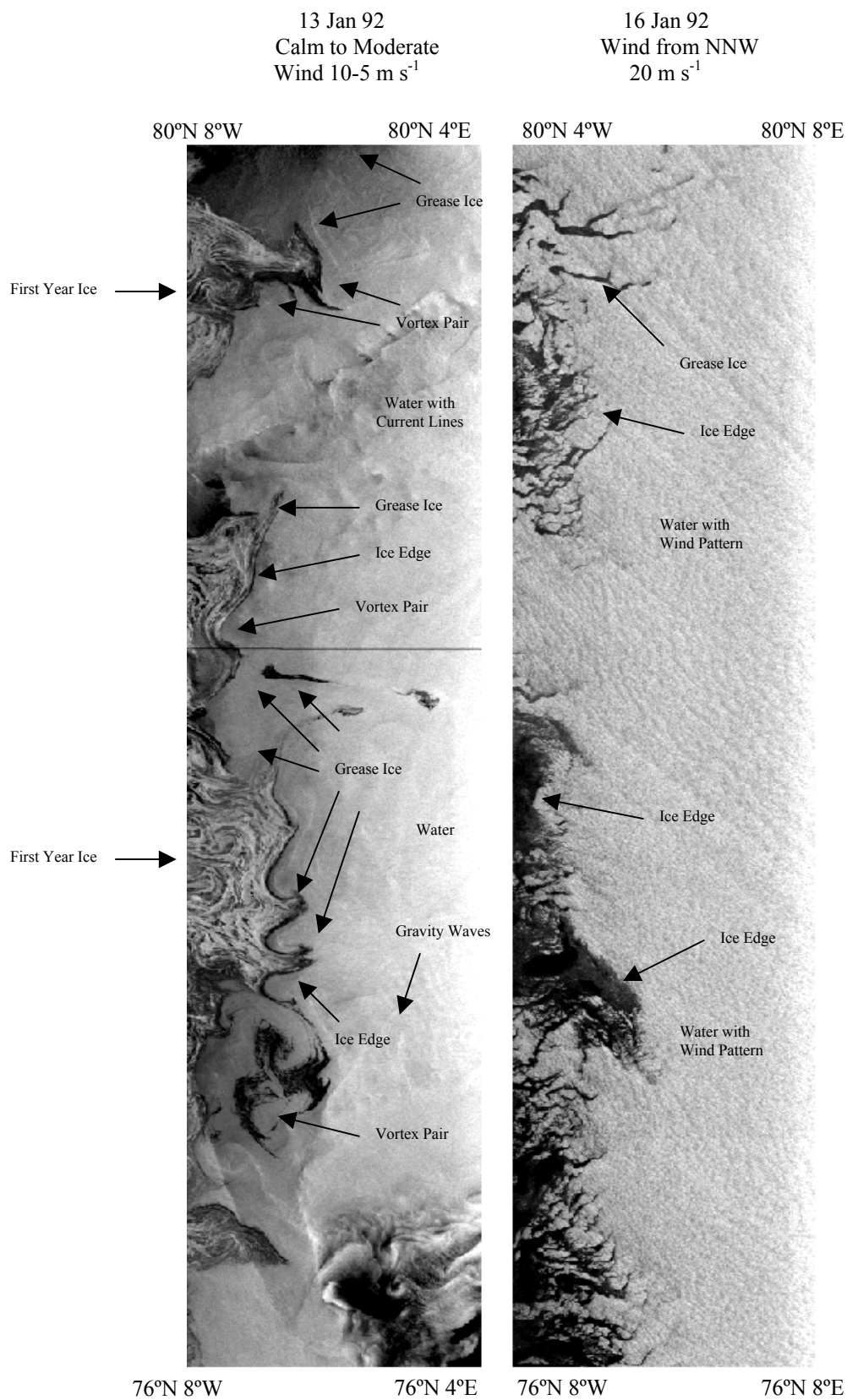


Fig. 5. ERS-1 SAR Example of rapid ice edge variability in the Greenland Sea – Fram Strait area as a result of strong off-ice winds. The ice edge is delineated on the SAR images. (From reference 21)

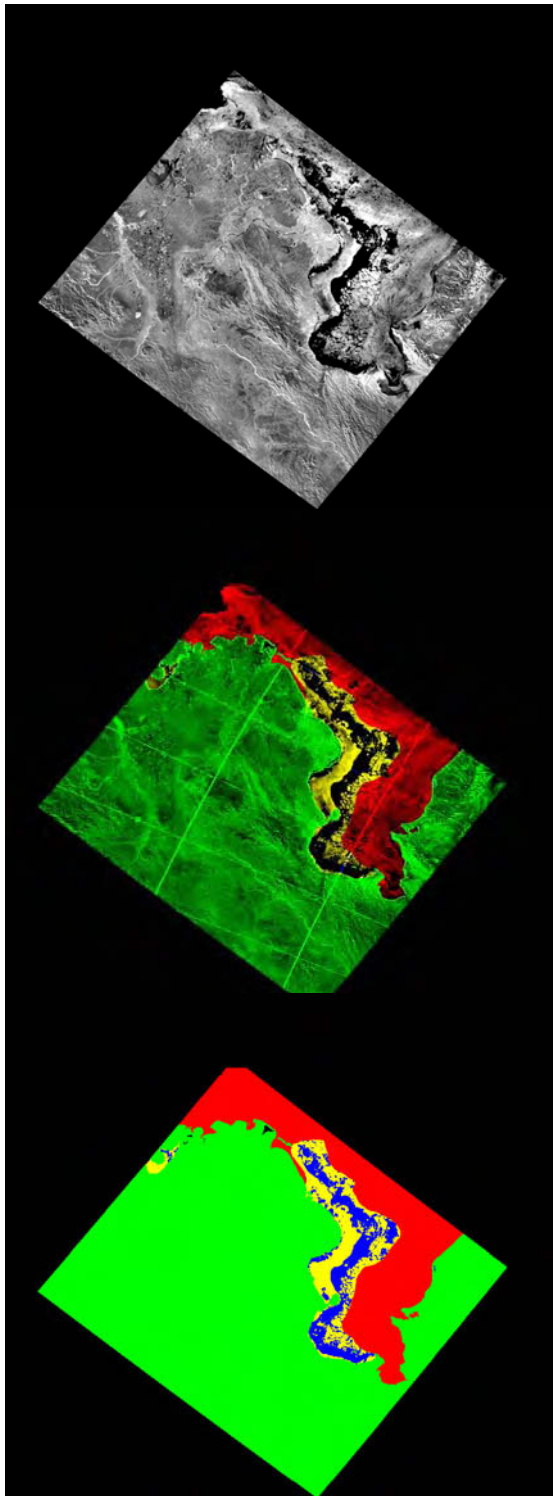


Fig. 6. Example of the ice classification results. Top image is the original SAR image, middle image is the classification map scaled by the SAR image, bottom image is the classification map. Red = solid ice, yellow = finger ice, blue = open water, green = land. (From Wackerman, *et al.*)

polarization wide swath data. Thus a nesting concept where the high-resolution polarimetric data is used to “truth” the wide swath data has been suggested.

Ice thickness is the fundamentally most important sea ice measurement. Sea ice thickness from SAR is presently inferred based on ice type. One approach discussed by Holt and Kwok is to measure freeboard, the portion of the ice cover above sea level (approximately 10% of the entire sea ice thickness). Fusion of SAR satellite data with altimetry holds the most immediate promise for accurate determination of thickness.

In summary, in the field of SAR sea ice mapping, a real user base exists, paying actual dollars to acquire the data. It is a mature operational tool, where manual interpretation techniques are utilized. The ice drift information obtainable from the high-resolution SAR is very useful. When fully validated, the additional use of SAR to obtain ice thickness distribution and ice volume changes (in combination with Cryosat and ICESat) will be very powerful operational, scientific research, and climate monitoring products.

Challenges remain in respect to fully exploiting SAR sea ice data. These challenges include:

- Most operational users largely rely on manual analysis;
- Little use of SAR data in models to date (e.g. ice drift assimilation); and
- Real operational benefits dependent on more reliable, volume access.

Opportunities exist to better integrate SAR in the operational and research communities. For example, the operational use of ice drift data (assuming SAR spatial and temporal sampling is adequate) into regional ice models is expected to emerge. Moreover, opportunities will soon exist to improve the SAR’s ability to discriminate the ice edge and thin ice types. These opportunities include:

- Use of wideswath multi-polarization data – ice/water and type ambiguity resolution. Fully polarimetric data for limited regions;
- Possible use of Envisat Global SAR monitoring mode at 1 km resolution;
- Near simultaneous X and L band data in a few years; and
- Along-track INSAR for regional information.

A key question for operational sea ice monitoring will center on assessing the potential advantages of fully polarimetric data against the disadvantage of reduced coverage. In addition, the impact of commercialization

of new SAR satellite missions and future data policies on the scientific and operational communities will need to be addressed

Envisat, RADARSAT-2, and several other SAR missions planned for launch in the next 1-5 years encompassing swath, multi-frequency, polarization diverse, and polarimetric technology will be capable of providing both the operational and scientific communities with a wealth of data to meet their respective needs. Operational applications in support of ship routing and navigation, oil and gas offshore development, fishing fleet support, iceberg tracking, and support to submarine operations should be well served with a variety of robust data sources and options. So too should studies examining changes of sea ice extent and dynamics as a result of climate change. Although the Envisat, RADARSAT, and ALOS satellites provide a large amount of SAR data (RADARSAT early-morning and evening; Envisat late-morning and evening; ALOS similar to Envisat, but at L-band), a truly international program where the U.S. under NPOESS would fly a SAR at a time to complement these satellites is highly desirable.

6. REFERENCES

1. Cunningham J. D., Chambers D., Davis C. O., Gerber A., Helz R., McGuire J. P., and Pichel W., *Ocean Observer Study: A Proposed National Asset to Augment the Future U.S. Operational Satellite System*, NPOESS Integrated Program Office, Washington, DC, August 2003.
2. Johnston M. and Flett D., First Year Ridges in RADARSAT ScanSAR Imagery: Influence of Incidence Angle and Feature Orientation, *Proceedings, International Symposium on Remote Sensing in Glaciology*, College Park, Maryland, 4-8 June, 2001.
3. Nghiem S. V. and Bertoia C., Study of Multi-Polarization C-Band Backscatter Signatures for Arctic Sea Ice Mapping with Future Satellite SAR, *Canadian Journal of Remote Sensing*, vol. 27, no. 5, October 2001.
4. Scheuchl B., Hajnsek I., and Cumming I., Sea Ice Classification Using Multi-Frequency Polarimetric SAR Data, *Proceedings, IGARSS 2002*, Toronto, Ontario, Canada, 2002.
5. Scheuchl B., *Utilization of Multi-Polarization and Polarimetric Data for Sea Ice Monitoring in an Operational Environment – Final Report*, MDA report RX-RP-51-4919 1/0 for Canadian Space Agency, November 2003.
6. Livingstone C. E., Chapter 11 – Synthetic Aperture Radar Images of Sea Ice, in Haykin, et al., eds., *Remote Sensing of Sea Ice and Icebergs*, John Wiley and Sons, Inc., 540-569, 1994.
7. Drinkwater M. R., Kwok R., Winebrenner D. P., and Rignot E., Multifrequency polarimetric synthetic aperture radar observations of sea ice, *Journal of Geophysical Research*, 96(C11), 20,679-20,698, 1991.
8. Kattenberg A., Giorgi F., Grassl H., Meehl G. A., Mitchell J. F. B., Stouffer R. J., Tokioka T., Weaver A. J., and Wigley T. M. L., Climate models: Projections of Future Climate, in Hough, J. T., Miera Filho L. G., Callender B. A., Harris, N., Kattenberg A., and Maskell K., eds., *Climate Change 1995*, Cambridge, 285-357, 1996.
9. *Climate Change 2001: The Scientific Basis*, contribution of working group to the Third Assessment Report of the Intergovernmental Panel on Climate Change, Cambridge University Press, Cambridge, UK, 2001.
10. Rothrock D. A., Yu Y., and Maykut G. A., Thinning of the Arctic sea-ice cover, *Geophys. Res. Lett.*, 26(23), 3469-3472, 1999.
11. Rothrock D. A., Zhang J., and Yu Y., The arctic ice thickness anomaly of the 1990s; A consistent view from observations and models, *Journal of Geophysical Research*, 108(C3), art. no. 3083, 2003.
12. Steele M. and Boyd T., Retreat of the cold halocline layer in the Arctic Ocean, *Journal of Geophysical Research*, 103(C5), 10,419-10,435, 1998.
13. Bjork G., Soderkvist J., Winsor P., Nikolopoulos A., and Steele M., Return of the cold halocline layer to the Amundsen Basin of the Arctic Ocean: Implications for the sea ice mass balance, *Geophys. Res. Lett.*, 29(11), art. no. 1513, 2002.
14. Proshutinsky A. Y. and Johnson M. A., Two circulation regimes of the wind-driven Arctic Ocean, *Journal of Geophysical Research*, 102, 12,493-12,514, 1997.
15. Kwok R., Recent changes in the Arctic Ocean sea ice circulation associated with the NAO, *Geophys. Res. Lett.*, 27(6), 775-778, 2000.
16. Kwok R. and Cunningham G. F., Seasonal ice area and volume production of the Arctic Ocean: November 1996 through April 1997, *Journal of Geophysical Research*, 107(C10), art. no. 8038, 2002.

17. Kwok R., Cunningham G. F., and Yueh S., Area balance of the Arctic Ocean perennial ice zone: October 1996 to April 1997, *Journal of Geophysical Research*, 104(C11), 25,747-25,759, 1999.
18. Kwok R., Schweiger A., Rothrock D. A., Pang S., and Kottmeier C., Sea ice motion from satellite passive microwave imagery assessed with ERS SAR and buoy motions, *Journal of Geophysical Research*, 103(C4), 8191-8214, 1998.
19. Muench R. D., Martin S., and Overland J., Preface: Second marginal ice zone research collection, *Journal of Geophysical Research*, 92, 1987.
20. Stouffer R., Manabe S., and Bryan K., Interhemispheric asymmetry in climate response to a gradual increase of atmospheric CO₂, *Nature*, 342, 660-682, 1989.
21. Jackson C. R. and Apel J. R., *Synthetic Aperture Radar User's Manual*, U.S. Department of Commerce, NOAA/NESDIS, October 2003.
22. Johannessen O. M., Budgell W. P., Johannessen J. A., Sandven S., and Shuchman R. A., Observation and simulation of ice tongues and vortex-pairs in the marginal ice zone, *The Polar Oceans and their Role in Shaping the Global Environment, Geophys. Monogr.*, No. 85, American Geophysical Union, 109-136, 1994.

SEA ICE MAPPING USING ENVISAT ASAR WIDESWATH IMAGES

Stein Sandven⁽¹⁾, Kjell Kloster⁽¹⁾, Helge Tangen⁽²⁾, Tommy S-Andreassen⁽²⁾, Harvey Goodwin⁽³⁾,
and Kim Partington⁽⁴⁾

⁽¹⁾Nansen Center (NERSC), E.Griegsv.3A, N-5059 Bergen, Norway. kjell@nersc.no, Stein@nersc.no

⁽²⁾Norwegian Meteorological Institute, N-9293 Tromsø, Norway. Helge.Tangen@met.no, Tommy@met.no

⁽³⁾Norwegian Polar Institute, N-9296 Tromsø, Norway, Harvey.Goodwin@npolar.no

⁽⁴⁾Vexcel UK Limited, Newbury, Berkshire RG20 0BP, UK, Kim.Partington@vexcel.co.uk

ABSTRACT

Sea ice mapping has been significantly improved during the last decade by introduction of Synthetic Aperture Radar (SAR) images. SAR sea ice mapping started with the ERS programme and continued with RADARSAT providing ScanSAR images with operational monitoring capability. From 2003 ENVISAT Advanced SAR (ASAR) images have started to be produced over sea ice areas in the European Arctic and the Baltic Sea. This paper shows preliminary results of case studies with ASAR Wideswath Mode images in the Svalbard area. The case studies include the Svalbard area in winter and spring time where different stages of ice formation were studied by use of ASAR images and validated by aerial photographs. The Fram Strait ice drift and area flux has been investigated using consecutive wideswath SAR images. The case studies were performed as preparation for new operational ice monitoring products in the ICEMON project which is one of the European Space Agency's service consolidation actions in Global Monitoring for Environment and Security (GMES).

1. INTRODUCTION

Operational sea ice monitoring is traditionally based on National Oceanic and Atmospheric Administration (NOAA) Advanced Very High Resolution Radiometer (AVHRR) visual and thermal infrared radiometer and Special Sensor Microwave Imager (SSM/I) passive microwave radiometer data. With wideswath SAR data from RADARSAT and ENVISAT, ice monitoring can be performed with higher resolution and better quality. The sea ice centres in Finland, Sweden (the Baltic Sea), Greenland, Canada and USA are using RADARSAT ScanSAR in operational services, whereas other countries (i.e. Norway, Russia) plan to use these data in

ice monitoring if financing can be resolved. Several demonstration projects have used RADARSAT ScanSAR images to support ice navigation in the Russian Arctic, as shown by Pettersson et al., (1999), Sandven et al., (2000), Alexandrov et al., (2001). The present study is focused on the implementation of operational SAR ice monitoring in the European sector of the Arctic.

Sea ice monitoring in near real time requires daily data about ice edge, ice concentration (fractional area coverage), ice type (new ice, young ice, firstyear, multiyear), ice thickness and ice drift. For climate and environmental monitoring, additional parameters are required such as velocity fields and derived convergence/divergence fields, ice volume fluxes, vertical heat fluxes and brine rejection from the freezing of ice. For several of these parameters, satellite-derived information, in particular from SAR data, is needed at regular intervals, for example every 3 days. Use of ASAR data in this study is part of the ESA CryoSat CalVal experiment in the Fram Strait and the ESA GMES project ICEMON which both started in February 2003.

2. ENVISAT ASAR

For the ASAR sea ice studies in the Fram Strait area, more than 70 Wideswath scenes (HH-polarisation) have been obtained during 2003, both in near realtime from Kongsberg Satellite Services (KSAT) and offline data from the European Space Agency (ESA). The main advantage of the ASAR Wide Swath mode, covering a 400 km wide swath, is the good spatial and temporal coverage of sea ice areas in polar regions. Every three days the Svalbard study area can be completely covered by descending orbits (morning passes) as well as by the ascending orbits (evening passes), as shown in Fig. 1.

The ASAR Wideswath image pixels, which are originally 150 by 150 m, have been averaged to 300 by 300 m, reducing the noise without losing any sea ice information. In order to estimate sea ice concentration, it is necessary to discriminate between open water and sea ice pixels. However, this is not a straightforward procedure, because open water can attain a range of backscatter values, depending on the wind speed. Sea ice backscatter depends on salinity and surface roughness as the main input parameters. For new and young ice types the backscatter can be similar to open water, resulting in ambiguities in classification if it is based on backscatter only.

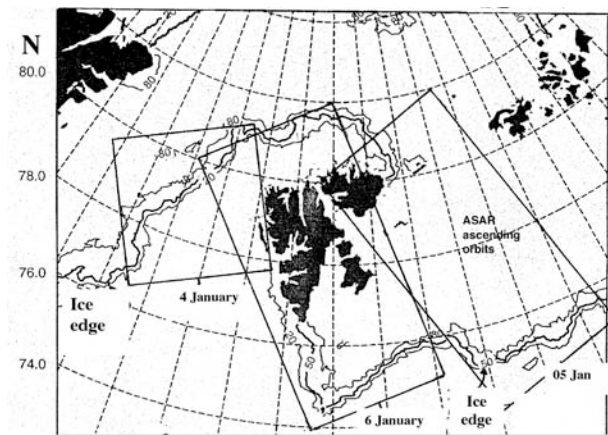


Figure 1. Example of ASAR Wideswath coverage from ascending orbits over three days in the Svalbard area. The ascending orbits cover the area in the afternoon (1800 – 2100 GMT), while the descending orbits are available in the morning (0900 – 1200 GMT).

Furthermore, the range in incidence angle from 17 to 43 degrees of the ASAR Wideswath has a strong impact on the backscatter signal from any given ice or water surface. The effect of incidence angle can be corrected for, but since the variation is much greater for water than for ice, separate correction factors must be applied for the two surface types.

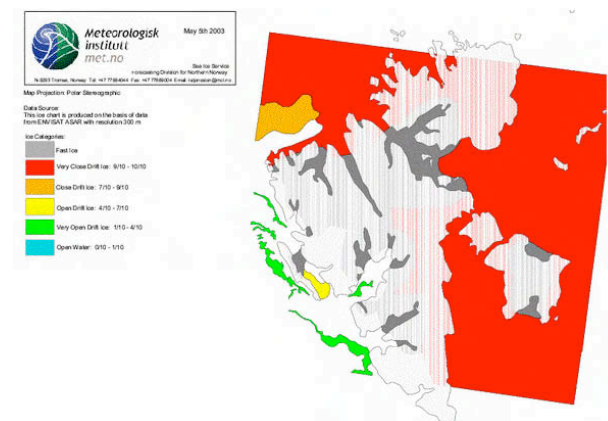
To retrieve ice types and calculate ice concentration based on backscatter is therefore dependent on these correction factors. In practical ice mapping, most of the ice analysis is done by human interpretation, taking advantage of the contrast in backscatter between open water and various ice types. It is envisaged that more use of algorithms, especially semi-automatic algorithms, can help to extract more ice information from the SAR images and streamline the ice analysis.

3. HIGH RESOLUTION ICE MAPS FROM ASAR IMAGES

The first examples of high-resolution ice maps from ASAR Wideswath images have been tested in the Svalbard area during the winter and spring of 2003. One Wideswath scene of 400 by 400 km can cover most of the Svalbard archipelago. An example of an ASAR scene and the corresponding high resolution ice chart produced by met.no is shown in Fig. 2.



a



b

Figure 2. a) ENVISAT ASAR image of the Svalbard archipelago from 5 May 2003, where the small white rectangle indicate the validation area described in Fig. 3. The large rectangle shows the location of the image in Fig. 4. b) Ice map produced by met.no from the ASAR image showing five ice concentration categories and fast ice.

The main advantages of the high-resolution ice map are the following: SSM/I based maps have too coarse a resolution and are not applicable close to land, whereas AVHRR-based maps are only useful occasionally due to the frequent cloud cover. The need for SAR-based ice maps in the Svalbard area is significant due to growing traffic with tourist ships, fishing vessels and scientific expeditions.

Furthermore, SAR ice images can provide more accurate input data as well as validation data for weather and ice forecasting models. Climate research and environmental monitoring also need more accurate data on various sea ice parameters such as ice edge, ice drift, leads, polynyas and fastice areas. The SAR-based ice map as shown in Fig. 2 b only uses a part of the ice information contained in the SAR images. It is possible to classify several stages in ice development from the SAR images such as grease ice, frazil ice, nilas, various stages of young ice and firstyear ice, multiyear ice, level ice versus deformed ice and fastice versus drifting ice. Before these parameters can be implemented in operational ice maps, considerable validation efforts are needed.

An example of validation methodology that is simple to implement is to collect in situ and airborne ice observations whenever there are ship expeditions and aircraft surveillance flights over the ice areas covered by SAR imagery (Fig. 3). Then these observations, which need to be carefully geolocated, are used to determine ice type and ice concentration for validation of the SAR-based ice charts. In Fig. 3 the transition zone between fastice and nilas (area 1), and a stripe of drifting firstyear ice surrounded by nilas and grey-white ice (area 2) are documented by aerial photographs.

More detailed validation can be done by taking vertical video from helicopters flying over the various ice types and ice features that SAR images can identify. An example of such a validation flightline on top of a SAR image is shown in Fig. 4 where a dedicated helicopter survey was performed in the Storfjorden polynya in April. The Storfjorden polynya is characterised by frequent opening and new ice formation during northerly winds in winter time. The polynya therefore contains various types of new and young ice as well as firstyear ice and various levels of deformed ice. These can all be detected in SAR images.

Previous studies have shown that the ERS SAR has a large capability to identify a number of ice types in this region (i.e. Sandven et al., 1999, Haarpaintner, 1999). With Wideswath SAR data covering larger sea ice areas

at regular intervals, it will be possible to systematically identify more ice types and ice features than what is done in the ice charts.

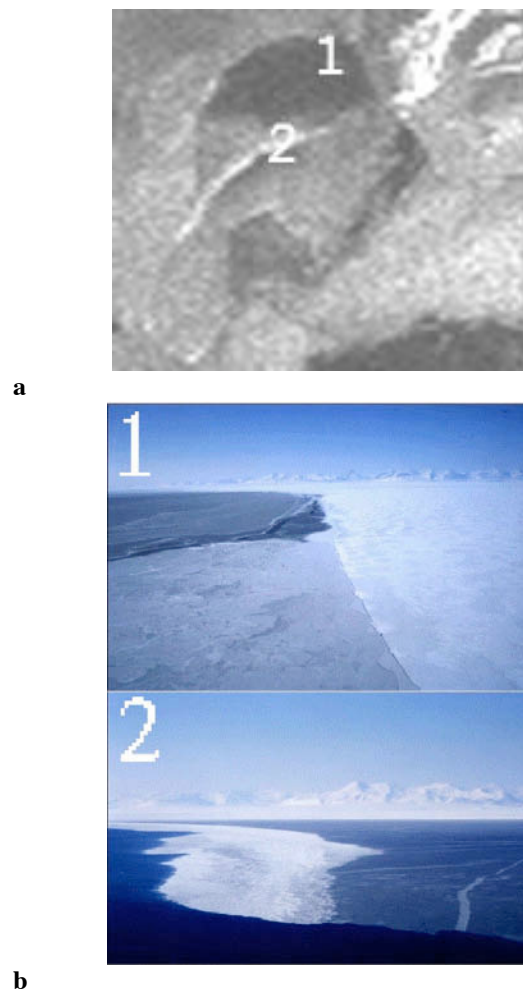


Figure 3. a) Sub-image of the ASAR Wideswath scene from 7 May in Isfjorden, covering about 10 by 10 km. The location is shown by the square in Fig. 2 a. The positions of the aerial photographs (1 and 2) are marked. (b) photographs documenting some of the ice types and features that are identified in the SAR image.

The dominant features in the subset of the ASAR Wideswath image in Fig. 4 are the following: Landfast ice is found along the coasts, mainly in the innermost part of Storfjorden (area 1) as a semi-permanent feature which does not change much from day to day in the freezing season. The inner part of the polynya has open water or thin new ice (area 2), with dark signature in the SAR image.

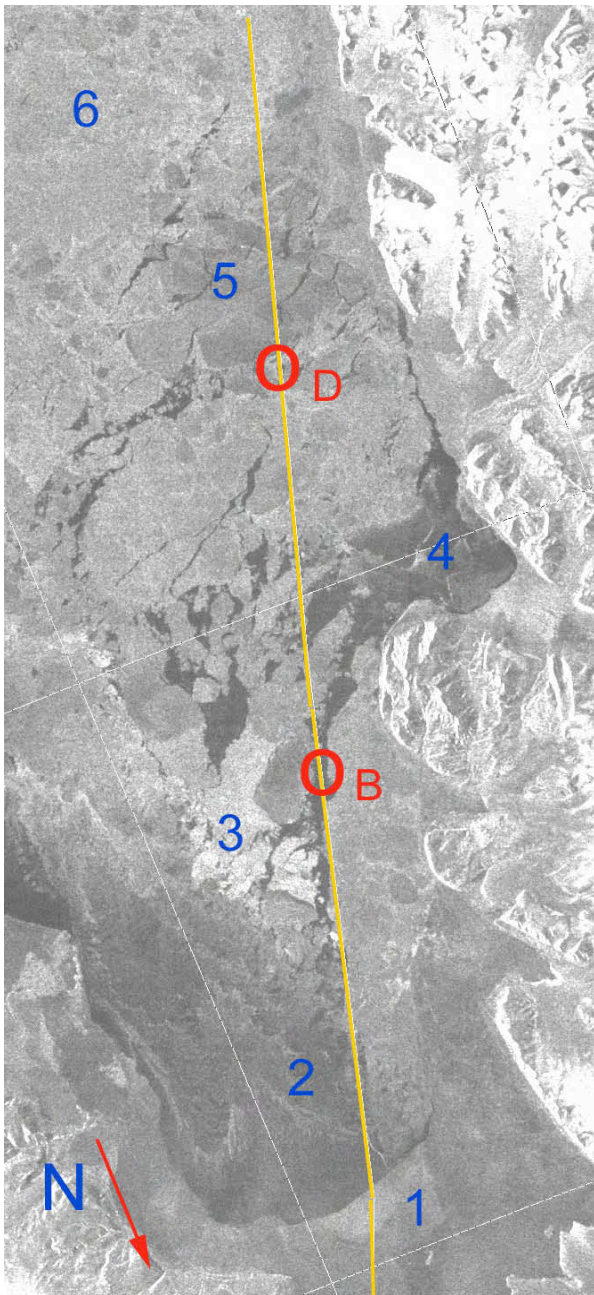


Figure 4. A subimage of 100 km by 40 km from the ASAR Wideswath image (23 April 2003) covering the Storfjorden polynya. The image is oriented upside down (north is down), following the flight line from area 1 to 6, to facilitate comparison between SAR image and video photographs. The image is HH-polarisation with pixel size of 75 m. The yellow line is the validation flight line where continuous vertical video were obtained from helicopter flying at 500 feet altitude at the same time as the satellite overflight. Examples of photographs in area B and D are shown in Fig. 5.

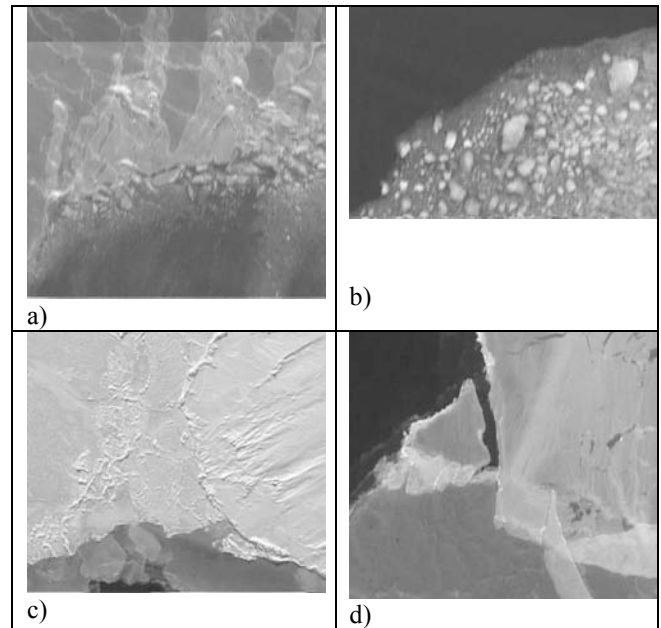


Figure 5. Vertical video photos covering areas of about 150 by 150 m: (a) Nilas and grey ice (10 – 20 cm thick) adjacent to open water in area B where the SAR signature is dark; (b) Open water in area B with the edge of the fastice boundary which has been broken into brash ice in the previous days; (c) Firstyear ice in area D identified by the ridges and level grey-white ice to the right. The grayish signature at the bottom is nilas and open water; (d) Grey-white ice (upper right side), nilas (lower part) and open water (black part) in area D.

Moving southwards, the ice cover is first dominated by grey-white ice, which is 10 – 30 cm thick (area 3), and with patches of nilas (area 4) up to 10 cm thick. Area 5 and 6 is dominated by firstyear ice, defined to be thicker than 30 cm, which has developed during the freezing season. In two areas along the validation line, marked by the circles B and D, there are several pronounced ice types with different SAR signatures. Area B has mainly open water and nilas adjacent to the fastice edge, while D has a mixture of nilas, young ice and firstyear ice. These ice features have been documented by vertical video images as shown in Fig. 5.

The detailed analysis of sea ice types and features in Storfjorden is needed for the study of polar bear habitats carried out by the Norwegian Polar Institute. Fig. 6 shows an example of SAR ice classification and a plot of the migration of a polar bear using Argos and GPS position data. The migration pattern is assumed to be correlated with leads, ridges and other ice parameters that can potentially be observed by SAR data. The SAR ice

type classification and polarbear migration data in Fig. 6 show that one particular polarbear is located mainly in the transition zone between the fastice and the drifting ice where leads and ridges are a predominant feature. By mapping the Storfjorden area with ASAR images every 3 days during the ice season, lasting from December to June, it will be possible to follow the variability of the ice edge position, leads, polynya, the fastice border, and deformation zones with ridges which have impact on the migration of polarbear habitats.

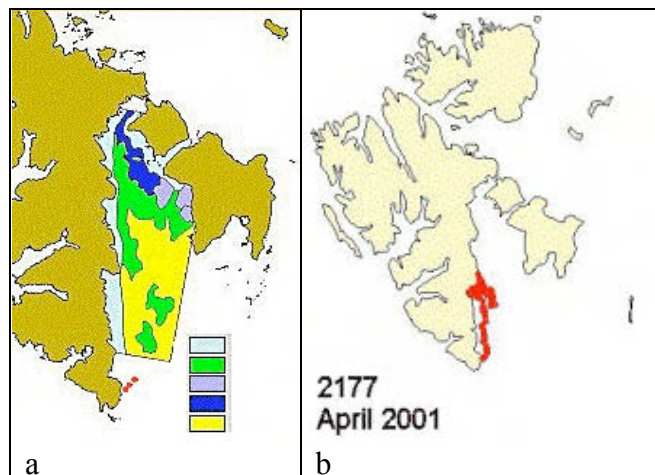


Figure 6. (a) Example of ice classification from ERS SAR in Storfjorden in April 2001: light blue is fastice, medium blue is young ice, dark blue is open water/nilas, green is undeformed firstyear ice, and yellow is rough firstyear ice. (b) The red dots are positions of one polar bear over one month using Argos data transmission.

4. ICE AREA FLUX THROUGH THE FRAM STRAIT

Ice volume fluxes through the Fram Strait is an important component of the Arctic freshwater flux, which is presently observed by an array of moorings with Upward-Looking Sonars (ULS). The ULSs measure ice drift, ice concentration and ice thickness at fixed positions (Vinje et al., 1999). The ice flux in the Fram Strait has been investigated from satellite data by Kwok and Rothrock (1999) who retrieved ice drift from time series of passive microwave data. These data have fairly coarse resolution and it is therefore of interest to investigate the benefit of using time series of SAR images for ice flux studies. With wideswath SAR images, covering the whole ice-covered part of the strait,

obtained at regular intervals (for example every 3 days), the area fluxes can be calculated from ice drift vectors retrieved by recognizing ice features in a sequence of SAR images. An example of ice drift calculation in the Fram Strait from 20 – 24 October 2003 is shown in Fig. 7.

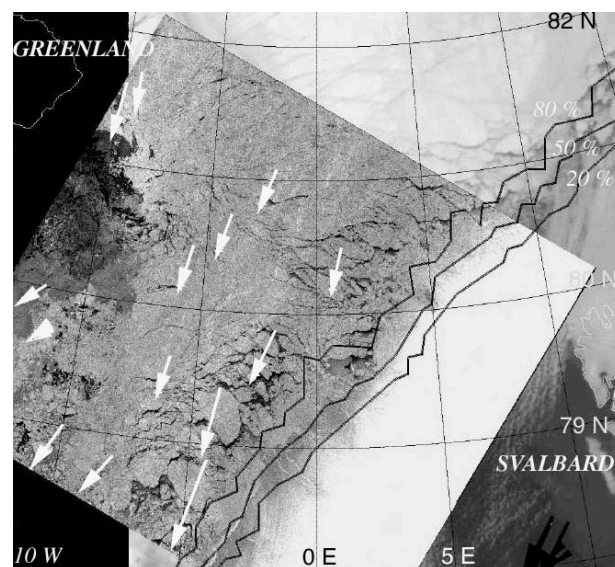


Figure 7. ASAR Wideswath image from 20 October 2003, superimposed on an AVHRR image from the same day and with SSM/I-derived ice concentrations isolines for 20%, 50% and 80%. The drift vectors represent ice displacement in the period 20 – 24 October.

The ice drift vector components across 79 N are used together with ice concentration profile derived from SSM/I data to calculate the area flux for the period 24–27 October, as shown in Fig. 8. The ice drift vectors can be retrieved from AVHRR as well as from SAR and optical images with sufficient resolution to identify the displacement of floes and other features in a sequence of images. It will also be interesting to compare ice drift from coarser resolution data (passive microwave data and scatterometer data) with SAR retrieved ice drift, taking into account the complex structure of the ice motion in this area. Ice area fluxes can be combined with ice thickness measurements, primarily derived from the ULS moorings, to estimate ice volume export through the Fram Strait. This is the interesting parameter to monitor for ice budget calculations as part of sea ice climate research (Vinje et al., 1998, Houssais and Herbaut, 2003). In order to monitor the area fluxes on regular basis, it is required to cover the strait with wideswath

SAR at least every 3 days. This is possible with the present RADARSAT and ENVISAT SAR systems.

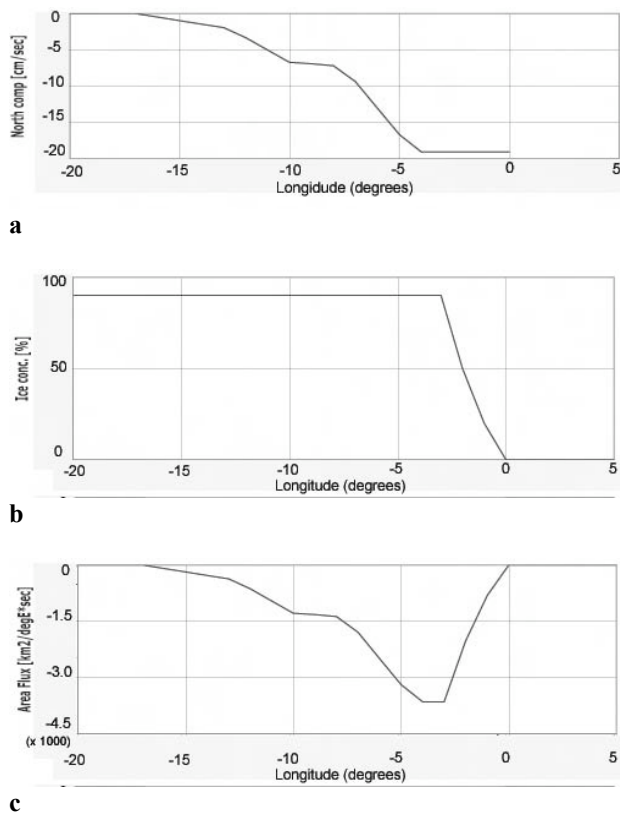


Figure 8. Profiles across the Fram Strait at 79° of (a) ice drift retrieved from interpolated SAR motion vectors; (b) ice concentration retrieved from SSM/I data, and (c) ice area flux retrieved for the period 20 – 24 October 2004 by combining the profiles in (a) and (b).

5. SERVICE IMPLEMENTATION UNDER GMES

This study is performed under the ICEMON project, which is one of the ESA GMES studies preparing for the implementation of monitoring services for the high latitudes, including sea ice, meteorological, oceanographic and other services. ICEMON represents the European component of a circumpolar service system where Canadian, US, Russian and European monitoring and forecasting services are co-ordinated in an integrated service network as shown in Fig. 9 (Seina et al., 2003). The services will focus on the sea ice areas both in the Northern hemisphere and in the Antarctica. Polar orbiting satellites, which are particularly well configured to observe the high latitudes of the earth, will provide the

most important sources of information. The ICEMON products will utilize existing and new satellite sensors such as, passive microwave data, optical and infrared images, wide-swath SAR, scatterometer and radar altimeter data. Non-space data will have a key role as supplement to EO-data to fill gaps and for validation of the EO-based products. Use of coupled ice ocean models and data assimilation methods will be a central element in ICEMON to deliver both monitoring and forecasting products as well as hindcast data. The backbone of the ICEMON service system is the existing institutions that provide remote sensing and other operational oceanography services in high latitudes.

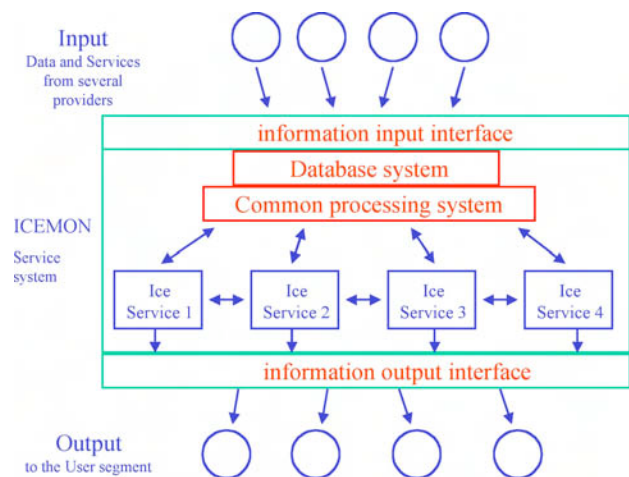


Figure 9. Concept of an integrated service system, proposed in ICEMON, where several independent ice service institutions share common resources related to input data, databases, processing systems and output interface to user groups, as highlighted in red (Seina et al., 2003).

Operational oceanography services in the Arctic Ocean and surrounding seas, including the Baltic Sea, will become more important because of increased human activities and climate change which is expected to have severe impact on the Arctic environment. There are enormous oil and gas fields, minerals, fisheries and other resources in the Arctic regions that will be increasingly important for Europe. The exploration and exploitation of the resources in these regions are severely hampered by harsh climate and in particular by the presence of sea ice. Sea traffic in the Baltic Sea is growing, especially oil transport from Russia via the new oil terminal in the Gulf of Finland. Marine operations including transportation by

ships in the Northern Sea Route between Russia and Western Europe is increasing with associated risk for accidents and damage to the environment. Transit transportation between Europe and the Far East through the Northern Sea Route, which has been demonstrated to be technically feasible, can become economically attractive in the event of reduced sea ice cover due to any climate change in this century. This will add further risk to the vulnerable Arctic environment.

Monitoring and forecasting services will support both operational users who need real time services and climate-related users who need long-term data sets and statistics. This implies that various met-ice-ocean products need to be produced on daily, weekly, monthly and annual scales. Research and development work to support and upgrade the services will be conducted for building capacity to retrieve quantitative information from new satellite data, improving modeling and forecasting skills, and for utilization of state-of-the-art information technologies, communication and end user systems.

6. ACKNOWLEDGEMENT

The study is supported by the ESA GMES programme and the ICEMON partners: Nansen Environmental and Remote Sensing Center, Finnish Institute of Marine Research & Finnish Ice Centre, Technical Research Centre of Finland, Finnish Maritime Administration, Swedish Meteorological and Hydrological Institute, Alfred Wegener Institute for Polar and Marine Research, Vexcel UK Limited, University College London / Centre for Polar Ocean Modelling, Norwegian Meteorological Institute, Kongsberg Spacotec, Kongsberg Satellite Services AS, Norwegian Polar Institute, Det Norske Veritas, Ifremer, Canadian Ice Service and ControlWare. The study has also been supported by the Norwegian Space Centre.

7. REFERENCES

Alexandrov, V. Yu., S. Sandven, O. M. Johannessen, Ø. Dalen and L. H. Pettersson. Winter navigation in the Northern Sea Route. *Polar Record*, Vol. 36 (1999), 333-342, 2000.

Haarpaintner, J. The Storfjorden polynya: ERS-2 SAR observations and overview. *Polar Research* 18 (2), 175 – 182, 1999.

Houssias, M.-N. and C. Herbaut. Variability of the ice export through the Fram Strait in 1993-98: the winter 1994/95 anomaly. *Polar Research* 22(1), 99 – 106, 2003.

Johannessen, O. M. and S. Sandven. Monitoring of the Arctic Ocean. In *Operational Oceanography, Implementation at the European and Regional Scales*. Proceedings from the Second international Conference on EuroGOOS, 11 – 13 March 1999, Rome, Italy, pp. 165 – 177, Elsevier Oceanography Series, 66, 2002.

Kwok, R. and D. A. Rothrock. Variability of Fram Strait flux and North Atlantic Oscillation. *J. Geophys. Res.* 104 (C3), 5177 – 5189, 1999.

Pettersson, L. H., S. Sandven, Ø. Dalen, V. V. Melentyev and N. I. Babich. Satellite radar ice monitoring for ice navigation of the ARCDEV tanker convoy in the Kara Sea. Proceedings of The 15th International Conference on Port and Ocean Engineering under Arctic Conditions, Helsinki, Finland, August 23 – 27, 1999, pp. 141 - 153.

Sandven, S., O. M. Johannessen, Martin Miles, Lasse H. Pettersson and K. Kloster. Barents Sea seasonal ice zone features and processes from ERS-1 SAR. *J. Geophys. Res.* Vol. 104, No. C7, p. 15843 – 15857, July 15, 1999.

Sandven S., Ø. Dalen, M. Lundhaug, K. Kloster, V.Y. Alexandrov, and L. V. Zaitsev, Sea Ice Investigations in the Laptev Sea Area in Late Summer Using SAR Data, *Canadian Journal of Remote Sensing*, Vo.27, 502 –516, 2000.

Seina, A. et al. ICEMON Strategy plan, version 0.7, December 2003, 44 pages (<http://www.icemon.org>).

Vinje, T., N. Nordlund and Å. Kvambekk. Monitoring ice thickness in Fram Strait. *J. Geophys. Res.* 103(C5), 10437-10449, 1998.

**This page intentionally
left blank (pagination)**

AUTOMATED LOCATION OF ICE REGIONS IN RADARSAT SAR IMAGERY

Christopher Wackerman⁽¹⁾, William G. Pichel⁽²⁾, Pablo Clement-Colón⁽²⁾

⁽¹⁾General Dynamics Advanced Information Systems, P.O. Box 134008 Ann Arbor Michigan 48113-4008 USA
chris.wackerman@gd-ais.com

⁽²⁾NOAA/NESDIS, WWB E/RA3, Room 102 5200 Auth Rd. Camp Springs MD 20746-4304 USA
William.G.Pichel@noaa.gov

ABSTRACT

A supervised classification algorithm has been developed to automatically remove regions of ice from consideration by ship detection and wind vector estimation algorithms. The output from the classifier is then put through a series of rule-based modifications to eliminate erroneous classifications that do not have the correct spatial relationships. Performance analysis on RADARSAT ScanSAR Wide imagery shows a 7% mis-classification rate with the classification algorithm, all of which are corrected by the subsequent set of spatial rules.

1. INTRODUCTION

As part of the NOAA/NESDIS Alaska SAR Demonstration Project [1], a multi-year demonstration of the production and use of SAR imagery to generate products in a pre-operational environment, a ship detection product is generated that automatically locates larger ships within the SAR image [2] and a wind product is generated that automatically generates wind vectors over the ocean [3]. It was found that regions of ice generated huge numbers of false ship detections, which made images with ice regions unusable without a manual interpretation of the results. In addition, the wind product relies on models for the radar cross section of the water which are inappropriate for ice regions, and thus generate erroneous wind vectors over ice. For both of these products, an automated way to locate ice regions and exclude them from the processing of the algorithms could significantly improve the quality of the products. Therefore a study was launched to develop an algorithm that could automatically locate ice regions in RADARSAT SAR imagery.

2. CLASSIFICATION ALGORITHM

The algorithm approach was based on previous work done for ice classification in the marginal ice zone [4] and for terrain classification using dual-antenna airborne SAR systems [5]. It is a supervised classifier that first gets trained on examples of the types of classes to be generated in order to create a series of classification vectors, then applies these classification vectors to separate the image regions into classes.

Assume that there are N classes desired, and the user has specified a window size, $M_1 \times M_2$, that will be used to classify the image. The window must be big enough to contain the tone and texture information that can differentiate between the classes, yet small enough to generate sufficient spatial resolution for the resulting classification. The user has also specified a series of algorithms that are applied to the image samples within the $M_1 \times M_2$ window and that generate measures of the tonal or texture information within the window. That is, each algorithm inputs the image values within the window and outputs a scalar quantity that measures, for example, the statistics, texture, or correlation properties of the image within the window. The scalar outputs from all of the algorithms are assembled into a feature vector, \vec{f} , that will be used to classify the samples within the window. From the training of the algorithm, we will generate the mean feature vector for each class: \vec{m}_k where k goes from 1 to N. Also from the training we will generate a classification vector for each pair of classes, \vec{c}_{kj} , and a scalar threshold value, T_{kj} , where k goes from 1 to N and j goes from 1 to N. The classification process is then as follows. For each pair of classes, the scalar p_{kj} is formed via

$$p_{kj} = (\vec{f} - \vec{m}_k) \bullet \vec{c}_{kj} \quad \text{for } k \neq j \quad (1)$$

where \bullet represents the vector dot product. If $p_{kj} < T_{kj}$ for all $j = 1$ to N, $j \neq k$, then the image samples within the window are assign to class k. In essence, the algorithm assumes that in the space of the image features represented by the feature vector \vec{f} , each class occupies a unique convex region. The classification vectors, \vec{c}_{kj} , define hyperplanes that separate pairs of classes, where the hyperplane is orthogonal to the classification vector and located at a distance T_{kj} from the location of the mean feature vector from class k along the classification vector. A feature vector is assigned to class k if it is on the "correct" side of each hyperplane between class k and each other class, which implies that p_{kj} from Eq. 1 is $< T_{kj}$ for all $j = 1$ to N, $j \neq k$. Note that we can always normalize the length of \vec{c}_{kj} such that

$$(\bar{\mathbf{m}}_j - \bar{\mathbf{m}}_k) \bullet \bar{\mathbf{c}}_{kj} = 1 \quad (2)$$

so that the threshold values, T_{kj} , are always between 0 and 1.

The classification vectors are generated in the training session by finding the vector direction that maximizes the distance between the two classes in the feature space. Specifically, if we let s_k represent the scalar values generated from the dot product of the feature vectors from class k and the classification vector $\bar{\mathbf{c}}_{kj}$, and likewise let s_j represent the dot product values between the class j feature vectors and $\bar{\mathbf{c}}_{kj}$, then we want to define $\bar{\mathbf{c}}_{kj}$ such that we maximize the distance metric, d , defined as

$$d = \frac{(E[s_j] - E[s_k])^2}{(\text{var}[s_k] + \text{var}[s_j])} \quad (3)$$

where $E[]$ and $\text{var}[]$ represent the mean and variance, respectively of the values within the brackets. Note that we can re-write Eq. (3) as

$$d = \frac{\bar{\mathbf{c}}_{kj}^T \mathbf{M} \bar{\mathbf{c}}_{kj}}{\bar{\mathbf{c}}_{kj}^T (\mathbf{C}_k + \mathbf{C}_j) \bar{\mathbf{c}}_{kj}} \quad (4)$$

where \mathbf{M} is a matrix defined as

$$\mathbf{M} = (\bar{\mathbf{m}}_j - \bar{\mathbf{m}}_k)(\bar{\mathbf{m}}_j - \bar{\mathbf{m}}_k)^T, \quad (5)$$

\mathbf{C}_j is the covariance matrix for the feature vectors from class j and \mathbf{C}_k is the covariance matrix for the feature vectors from class k . We can re-write Eq. (4) as an eigenvalue problem

$$(\mathbf{C}_k + \mathbf{C}_j)^{-1} \mathbf{M} \bar{\mathbf{c}}_{kj} = d \bar{\mathbf{c}}_{kj} \quad (6)$$

where the -1 superscript indicates matrix inversion. The classification vector we want is the eigenvector that generates the maximal eigenvalue and thus maximizes the distance metric d . Since the matrix \mathbf{M} has unit rank, Eq. (6) has only a single eigenvector solution which can be written as

$$\bar{\mathbf{c}}_{kj} = (\mathbf{C}_j + \mathbf{C}_k)^{-1} (\bar{\mathbf{m}}_j - \bar{\mathbf{m}}_k) \quad (7)$$

which generates a distance metric value of

$$d = (\bar{\mathbf{m}}_j - \bar{\mathbf{m}}_k)^T (\mathbf{C}_j + \mathbf{C}_k)^{-1} (\bar{\mathbf{m}}_j - \bar{\mathbf{m}}_k). \quad (8)$$

Since the feature vector values are usually not independent, the matrix inverses in Eqs. (6) through (8) need to be performed using the standard pseudo-inversion process. Note that this classification approach is based on standard discrimination theory [6].

The training of the algorithms proceeds as follows. The user generates a database of example image subsets from the various classes, from which are generated example feature vectors. The mean feature vector and covariance matrix of the feature vectors are generated for each class from the database of example feature vectors. For each pair of classes, the classification vectors are generated using Eq. (7). Finally, the threshold values, T_{kj} , are generated by calculating the statistics $E[s_k]$, $\text{var}[s_k]$, $E[s_j]$, $\text{var}[s_j]$ as defined above, assuming the density functions of these variables are Gaussian, and finding the location where the two density functions intersect. This generates all of the parameters we need for the classification: the mean feature vectors for each class, the classification vectors for each pair of classes, and the thresholds for each pair of classes.

Since we are using a $M_1 \times M_2$ window to perform the classification of the image, for each placement of the window we assign the resulting class to every image sample in the window. If we move the window by one sample each time and re-classify, we actually classify each image sample $M_1 M_2$ times. In the algorithm we keep track of these individual classifications for each image sample, and when we have finally left the image sample, we assign it the class that occurred most often. This helps to significantly clean up the classification results near edges within the image.

The classification process as defined is not guaranteed to classify every image sample. It may be that a feature vector resulting from some placement of the window does not fall on the "right" side of all the hyperplanes for any single class. If this happens, the algorithm puts the sample into a special "No Class" category. Note that the final classification will only be "No Class" if this occurs most often for a given image sample over every placement of the window.

Because the classification vectors are eigenvectors, they can be very sensitive to the image values in the training set. Thus this approach will only work well if the training set is sufficiently large to be an adequate representation of the statistical properties of each class; that is, there must be enough samples from each class to generate statistically accurate entries in the covariance matrices.

Finally, note that if $C_k = C_j$ for any pair of classes, then this approach is equivalent to a Normal distribution likelihood ratio test.

The accuracy of this approach is determined by what algorithms are used to generate the feature vector. In our experience using this approach on other applications, we have seen that a mixture of statistical measures to estimate tonal properties and values drawn from the co-occurrence matrix [7] to measure texture properties has worked well. Specifically for the statistical measures we use $E[x]$, $(E[x^2])^{1/2}$, $(E[x^3])^{1/3}$, $(E[x^4])^{1/4}$, $(E[(x-E[x])^2])^{1/2}$, $(E[(x-E[x])^3])^{1/3}$ and $(E[(x-E[x])^4])^{1/4}$ where the superscripts are used to normalize the values to the same scale, and x represents the image sample values within the local window. We also use the same statistics divided by the mean, and the same statistics divided by the standard deviation. Thus there are 21 statistical measures in the feature vector. For the texture measures we use the standard definition of the co-occurrence matrix in the literature; we first define a vector offset of some shift in lines, Δl , and some shift in columns, Δc , and then let the co-occurrence matrix, C_o , be defined so that $C_o(i,j)$ equals the probability that an image sample value of i and an image sample value of j are separated in the image by the vector $(\Delta l, \Delta c)$. Normally C_o is $M \times M$ where M is the number of possible different image sample values, but for this algorithm we combine image samples into 20 different bins and then calculate the co-occurrence matrix to maintain the size of the matrix to 20×20 . Note that the co-occurrence matrix is dependent on the vector offset used to create it. We do not know *a priori* what direction or length scale to use for any given image, so instead we generate an average co-occurrence matrix over a series of vector offsets. We use vector lengths of $1/4$, $1/2$, and $3/4$ the window width and for each length generate an average co-occurrence matrix for vector directions of 0, 45, 90, and 135 degrees. This generates three co-occurrence matrices to use.

Typically what is then done is some metric is calculated on the co-occurrence matrix that measures the distributions of probabilities within the matrix. A number of standard metrics have been defined [7]. We use a standard set of six which are referred to as inertia (sometimes called contrast), cluster shade, cluster prominence, local homogeneity (sometimes called inverse difference moment), energy (sometimes called uniformity) and entropy; see Ref. 7 for details. Since these values are extracted from each of the three averaged co-occurrence matrices, this generates 18 texture measures for the feature vector. Putting these together with the statistical measures, the final feature vector has 39 elements.

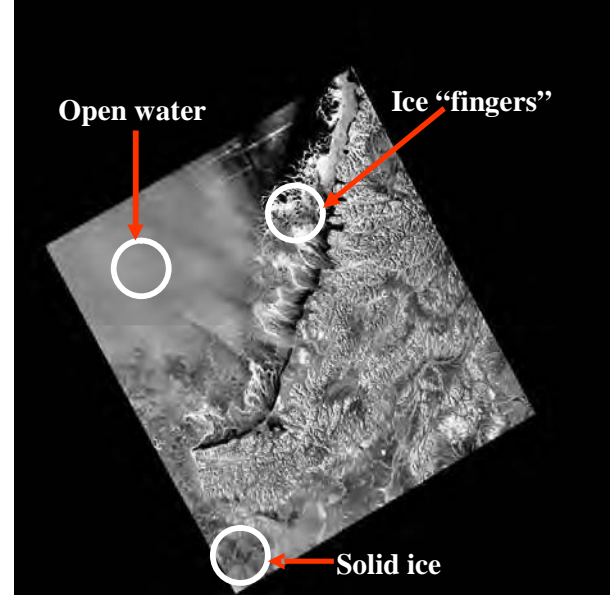


Fig.1. Example of the training regions used for the open water, finger ice, and solid ice classes. Image was collected off the coast of Alaska, 2000. ©CSA 2000

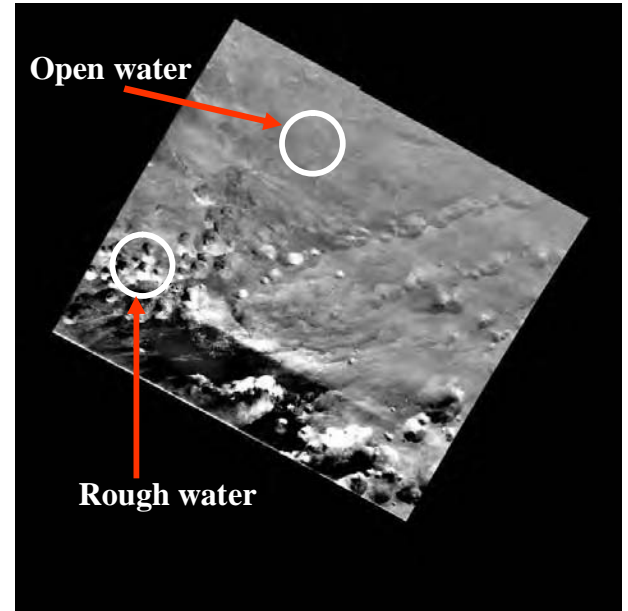


Fig. 2: Examples of the training regions used for open water and rough water classes. Image was collected off the coast of Alaska in 2000. ©CSA 2000.

3. APPLICATION TO ICE REGION LOCATIONS

For the application of this classification approach to the problem of locating ice regions, we wanted to minimize the number of classes as much as possible, since we were not interested in actually classifying kinds of ice, but rather in strictly eliminating ice

regions from the ship detection and wind vector estimation algorithms. We also assumed that map data could be used to isolate land regions so these were not considered.

In looking through the images, we decided to divide the problem into four classes; finger ice, solid ice, open water, and rough water. Figs. 1 and 2 show examples of each kind of class. We divided the ice regions into solid ice and finger ice because visually they had strikingly different tonal and texture qualities. In addition, we needed to treat finger ice regions separately because ships often fished between the fingers, so we had to pay more attention to the detailed spatial shapes of these regions. Solid ice almost always occurred in blocks, so we did not have the same concern with fine spatial details. We divided the water regions into two classes, again due to texture differences, between “very rough” water caused by atmospheric turbulence (such as convective cells or wind fronts) and other open water (which note can also be rough, but which does not have the large contrast features in the “very rough” water class). For the training set we used RADARSAT-1 ScanSAR Wide Mode imagery with 100 meter sample spacing; therefore to date this is the only image data for which the algorithm is applicable. We decided on a 30 x 30 image sample window size (3km x 3km) for the classification in order to be able to capture all of the image texture for each class and manually extracted regions from the training set that were representative of each of the four classes to generate the feature vectors. We had 832 examples from solid ice, 624 from open water, 31 from finger ice, and 36 from rough water. Note that we were a little low on the number of examples from finger ice and rough water for robust statistics.

Table 1 shows the classification results of applying the algorithm to the training set. It performed very well in separating out the 4 classes, indicating that the approach was powerful enough to capture the differences between our training sets. Note that the original goal is to only separate ice and water, thus if we clump the two ice classes together and clump the two water classes together, Table 1 indicates that only 1 % of the ice was mis-classified and only 0.5% of the water.

Of course, performance on the training set is indicative of the ability of the algorithm to separate classes; performance on data outside of the training set is usually poorer. To improve operational performance we added a number of spatial rules after classification that took into account knowledge about how ice and water regions should appear in imagery. To apply these rules, we first identified all of the connected

Table 1: Classification results from the first training set.

True Class	Class It Was Put Into			
	Solid Ice	Finger Ice	Open Water	Rough Water
Solid Ice	88%	8%	1%	1%
Finger Ice	6%	94%	0%	0%
Open Water	1%	0%	98%	1%
Rough Water	0%	0%	3%	97%

“blobs” in the classified image; i.e. sets of image samples that were contiguous to each other and that had been classified into the same class. For each “blob” we identified the number of image samples within the blob and the percentage of perimeter samples (i.e. image samples on the edge of the blob) that fell into each other class. We then applied the following rules.

- If a blob was too small (less than 5000 samples) its class was converted to whatever class the majority of its perimeter samples were next to. This essentially replaces small blobs with what was surrounding them.
- If an ice blob was completely surrounded by water, it was changed to water. This was because we did not care about floating or isolated ice regions, and one difficulty the algorithm had was classifying rough water as ice, which this rule eliminated.
- If a water region was surrounded by ice, it was changed to ice. This was because water within ice regions would never contain ships, and never generate accurate wind vectors.
- Finger ice regions had to have at least 45% of their perimeter samples be either solid ice or water, otherwise they were changed to water. This ensured that finger ice had to be connected to something that they had “grown” from, and not isolated in open water.

Finally, we had to treat finger ice somewhat separately due to the fact that we still wanted to detect ships that were fishing between the fingers. Thus for finger ice regions, we went back and examine the radar cross section of the image samples. If this value was below a threshold, we converted that individual pixel into water. This allowed us to fill in between the finger ice regions with water.

Figs. 3 and 4 show examples of the classification results. In each figure the top image is the original SAR image, the middle image is the classification map scaled by the SAR image, and the bottom figure is just the classification map. We show all three so that the user can see where water regions are indicated next to ice regions.

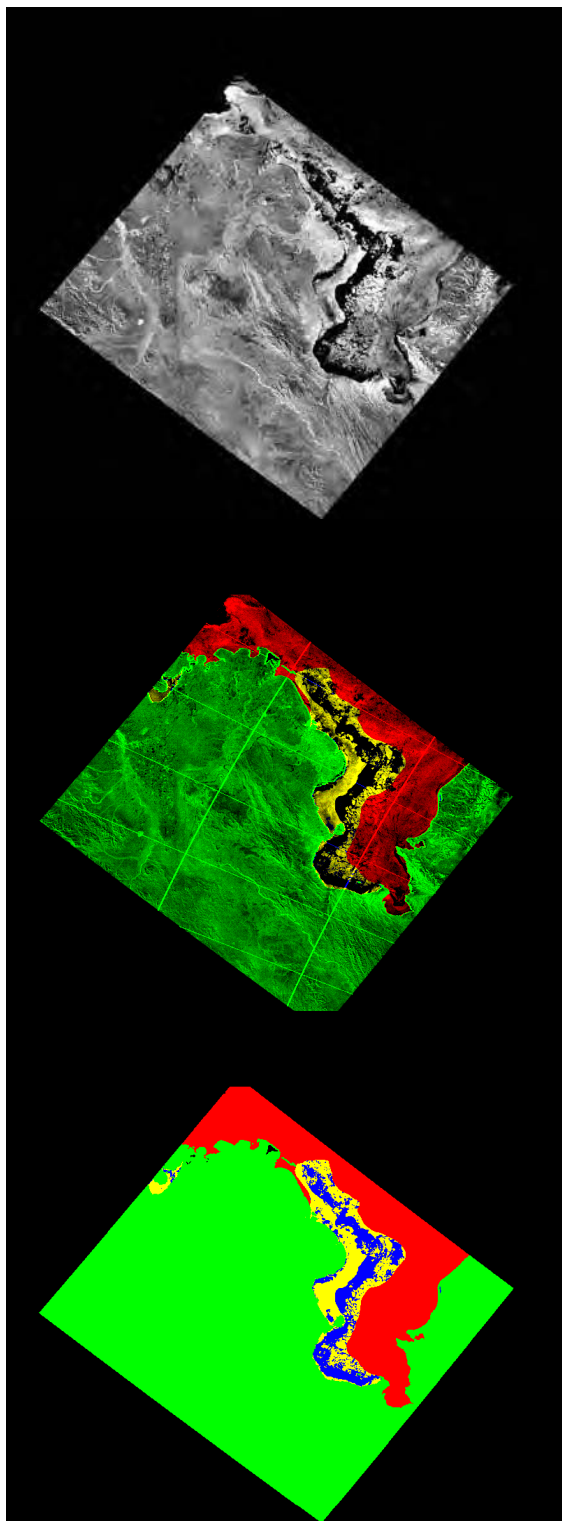


Fig.3. Example of the ice classification results. Top image is the original SAR image, middle image is the classification map scaled by the SAR image, bottom image is the classification map. Red = solid ice, yellow = finger ice, blue = open water, green = land. Image was collected off the coast of Alaska in 2000. ©CSA 2000.

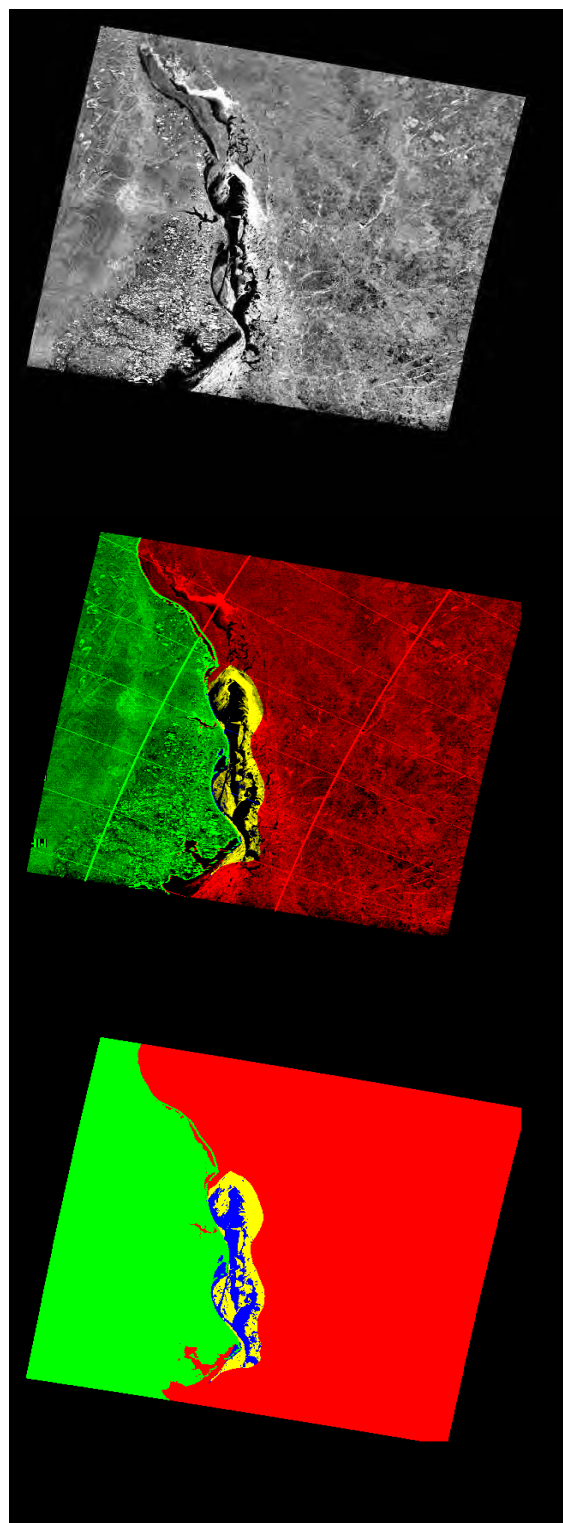


Fig. 4: Example of the ice classification results. Top image is the original SAR image, middle image is the classification map scaled by the SAR image, bottom image is the classification map. Red = solid ice, yellow = finger ice, blue = open water, green = land. Image was collected off the coast of Alaska in 2000. ©CSA 2000.

Table 2: Classification results from the second training set.

True Class	Class It Was Put Into			
	Solid Ice	Finger Ice	Open Water	Rough Water
Solid Ice	85%	7%	1%	7%
Finger Ice	7%	93%	0%	0%
Open Water	0%	0%	95%	5%
Rough Water	7%	0%	9%	84%

In general the algorithm has performed well, however we have found some consistent errors in the classification results as the algorithm was run operationally. To handle these we have re-trained the algorithm periodically, adding the regions where mistakes were made into the training set (also keeping the original examples) and re-generating the algorithm parameters. Table 2 shows the classification results after the first addition to the training set, the purpose of which was to address rough water regions that were being classified as ice. This training set had the original 832 samples of solid ice and 624 samples of open water, but we significantly increased the rough water samples to 647 and slightly increased the finger ice samples to 41. Table 2 shows that in the larger data set the algorithm is having some increased difficulty separating rough water from solid ice using these feature metrics; note that we now have a 7% misclassification rate versus the 1% in Table 1. As the sample sizes are much larger here for rough water, we believe that this is probably a better estimate of the algorithm capability than the original training set. Note though that almost all of these misclassifications get corrected when the spatial rules are applied by eliminating the regions of solid ice that are surrounded by water. Manual analysis of the final products for a subset of images not in the training set have shown that all of the mis-classifications have been eliminated. The algorithm is still being tested before it goes operational to determine if other errors are being generated.

4. SUMMARY

To improve the performance of automated ship detections and wind vector estimations in the NOAA/NESDIS Alaska SAR Demonstration Project, we are developing an automated algorithm for locating ice regions so that they can be removed from consideration in the ship and wind algorithms. The classification algorithm is a supervised training algorithm that uses a series of hyperplanes to separate different classes in an n-dimensional feature space. We use a combination of statistical measures and texture metrics drawn from the co-occurrence matrix to form the feature vector. The results have been encouraging to date; less than 7% mis-classification from the algorithm with almost no errors after applying a series

of spatial rules that incorporate what we know about ice and water regions in the imagery. Testing of the algorithm is ongoing before it can become operational.

5. ACKNOWLEDGMENTS

This study was supported and monitored by the Office of Research and Applications of the National Oceanic and Atmospheric Administration (NOAA) under ONR Contract N00014-00-D-0114.

The views, opinions, and findings contained in this report are those of the authors and should not be construed as an official National Oceanic and Atmospheric Administration or U.S. Government position, policy or decision.

6. REFERENCES

1. Pichel, W., Clemente-Colón, P. NOAA Coastwatch SAR Applications and Demonstration, *John Hopkins APL Tech. Dig.*, vol. 21(1), 49-57, 2000.
2. Wackerman, C.C., Friedman, K.S., Pichel, W.G., Clemente-Colón, P. Automatic Detection of Ships in RADARSAT-1 SAR Imagery, *Canadian J. Remote Sens.*, vol. 27, 568-577, 2001.
3. Monaldo, F.M., Thompson, D.R., Beal, R.C., Pichel, W.G., Clemente-Colón, P. Comparison of SAR-Derived Wind Speed With Model Predictions and Buoy Measurements, *IEEE Trans. Geosc. Remote Sens.*, vol. 39, 2587-2599, 2001.
4. Wackerman, C., Miller, D. An Automated Algorithm For Sea Ice Classification In The Marginal Ice Zone Using ERS-1 Synthetic Aperture Radar, *Erim Technical Report 252000-25-T*, May 1996.
5. Wackerman, C. Use of An Interferometric SAR For Terrain Classification, *Proc. 26th AIPR Workshop*, SPIE vol. 3240, 75-86, 1997.
6. Lachenbruch, P.A., *Discriminant Analysis*, Hafner Press, 1975
7. Haralick, R.M., K. Shanmugam, I. Dinstein, Textural Features for Image Categorization, *IEEE Trans. Systems, Man Cyber.*, vol. SMC-3, 610-621, 1973.

ROUTINE PRODUCTION OF SAR-DERIVED ICE AND OCEAN PRODUCTS IN THE UNITED STATES

William G. Pichel⁽¹⁾, Pablo Clemente-Colón⁽¹⁾, Cheryl Bertoia^(3,2), Michael Van Woert^(1,2), Christopher C. Wackerman⁽⁴⁾, Frank Monaldo⁽⁵⁾, Donald R. Thompson⁽⁵⁾, Karen S. Friedman⁽¹⁾, and Xiaofeng Li⁽¹⁾

⁽¹⁾NOAA/NESDIS/ORA, 5200 Auth Road, Camp Springs, MD 20746, USA, William.G.Pichel@noaa.gov, Pablo.Clemente-Colon@noaa.gov, Karen.Friedman@noaa.gov, Xiaofeng.Li@noaa.gov

⁽²⁾Cospas-Sarsat Secretariat, 99 City Road, London EC1Y 1AX, United Kingdom, Cheryl_Bertoia@imso.org

⁽³⁾National Ice Center, 4251 Suitland Road, Suitland, MD 20395, USA, Michael.Vanwoert@noaa.gov

⁽⁴⁾General Dynamics Advanced Information Systems, P.O. Box 134008, Ann Arbor, MI 48113-4008, USA, chris.wackerman@gd-ais.com

⁽⁵⁾The Johns Hopkins University Applied Physics Laboratory, 11100 Johns Hopkins Road, Laurel, MD 20723-6099, USA, f.monaldo@jhuapl.edu, donald.r.thompson@jhuapl.edu

ABSTRACT

In the United States, satellite Synthetic Aperture Radar (SAR) imagery from the Canadian RADARSAT-1 satellite are being used routinely by the National Ice Center (NIC) in the production of sea ice analysis charts. The routine production of other SAR ocean products is also being demonstrated by the National Oceanic and Atmospheric Administration (NOAA) National Environmental Satellite, Data, and Information Service (NESDIS). Since 1998, NOAA/NESDIS has supported the development and demonstration of SAR oceanographic and hydrologic applications. In particular, automated algorithms to determine ocean surface wind speed and direction, to detect vessel location, and to map sea ice have been developed and are being evaluated by U.S. operational agencies. In addition, SAR images are being analyzed routinely for the detection of polar mesoscale cyclones, oil spills, and river ice breakup and associated ice jams and flooding in the spring. Efforts are underway to develop an international consensus on the best tools for operational use of present and future SAR data streams. The approach includes the selection and/or merging of the most suitable algorithms for efficient operational processing leading to a robust products system that can be incorporated into national environmental monitoring programs. SAR data streams under consideration include the ENVISAT Advanced SAR (ASAR) as well as the upcoming Advanced Land Observing Satellite (ALOS) Phased Array L-band SAR (PALSAR) and the RADARSAT-2 SAR.

1. INTRODUCTION

The planning, development, demonstration, and production of operational environmental products in the

United States is now determined to a great degree by formal requirements for environmental data and products. These requirements have been gathered in many ways, including formal requests from government agencies, reports from workshops and publications of working groups. Two recent requirements documents have been generated for the National Polar-orbiting Operational Environmental Satellite System (NPOESS) which will be the next generation of polar operational environmental satellites. These are the Integrated Operational Requirements Document II (IORD-II) and the Ocean Observer User Requirements Document (OOURD). Both of these documents contain specifications of environmental parameters required primarily by various U.S. Government agencies. Some of these environmental parameters can only be or can best be measured with Synthetic Aperture Radar (SAR) instruments. Table 1 lists the SAR-derivable parameters included within the NPOESS requirements documents. It is the goal of the NPOESS Integrated Program Office (IPO) and the National Oceanic and Atmospheric Administration (NOAA), National Environmental Satellite, Data, and Information Service (NESDIS) to develop, demonstrate, and eventually produce at a minimum the IORD II parameters operationally. The Oceanic Research and Applications Division (ORAD) of the Office of Research and Applications (ORA) in NESDIS is interested in the research and development of the products indicated under the column "ORAD Interest." This paper describes the current status of progress toward this goal. In particular, the routine use of SAR imagery in the National Ice Center (NIC) and the Alaska SAR Demonstration (AKDEMO) will be described. The paper concludes with a vision for the development and eventual production of all the products specified.

Table 1 - Environmental Parameters Derivable from SAR

#	<u>EDR TITLE</u>	<u>IORD II Requirement</u>	<u>OOURD Requirement</u>	<u>ORAD Interest</u>
	<u>OCEANIC</u>			
1	Coastal Sea Surface Winds & Wind Stress	4.1.6.8.8.5	2.1b, 2.2b	X
2	Wave Characteristics - Significant Wave Height	4.1.6.6.8	2.4a	X
3	Wave Characteristics. - Wave Direction/Wavelength	4.1.6.8.8.8	2.4b	X
4	All Weather Day/Night Imagery	4.1.6.8.6	2.5c	X
5	Oil Spill Location	4.1.6.8.8.12	2.6	X
6	Vessel Positions		2.7	X
7	Bathymetry (Near Shore)	4.1.6.8.8.10	2.8	X
8	Littoral Currents	4.1.6.8.8.1	2.16c	X
9	Surf Conditions	4.1.6.8.8.9	2.18	X
10	Ocean Mesoscale Features (Fronts/Eddies)		2.19	X
11	Mixed Layer Depth (Internal Waves)			X
	<u>CRYOSPHERIC</u>			
12	Sea & Lake Ice Concentration/Age/Motion/Edge Location	4.1.6.8.7	3.1	X
13	Ice of Land Origin (Icebergs)		3.2	X
14	River Ice Location/Condition		3.5	X
15	Glacier Volumetric Change		3.6	
16	Continental Ice Sheet Melt Zone		3.7	
17	Ice-Sheet Motion		3.8	
18	Ice-Sheet Grounding Line Position		3.9	
	<u>HYDROLOGIC</u>			
19	Flood Mapping		4.1	X
20	Snow Water Equivalent Mapping		4.2	
21	Regional Soil Moisture		4.3b	
22	Coastal Wetland Mapping		4.4	X
	<u>LAND</u>			
23	Land Surface Topography		5.1	
24	Land Surface Deformation		5.2	
25	Land Surface Freeze/Thaw State		5.3	
26	Vegetation Classification/Biomass		5.4	
27	Coastal Change		5.5	X
28	Wetland Mapping			X
	<u>ATMOSPHERIC</u>			
29	Mesoscale Atmospheric Features		6.1	X
30	Microscale Atmospheric Features		6.2	X

2. SAR DATA SYSTEM IN THE U.S.

Production of SAR environmental products in the U.S. relies exclusively on the availability of foreign SAR data, currently from the SAR on the Canadian Space Agency's RADARSAT-1 satellite. In exchange for the National Aeronautics and Space Administration (NASA) providing the launch for RADARSAT-1, the U.S. has access to 15.82% of the SAR on-time for use by NASA, NOAA, and researchers with accepted proposals in response to one of the RADARSAT-1 research announcements. In the mid 1990's, NASA and NOAA developed a near-real-time data system that has worked quite well to support routine production of products at the NIC and within the AKDEMO. Data are received and processed into SAR images at four acquisition stations: the Alaska Satellite Facility (ASF)

located at the University of Alaska (UAF) Fairbanks, the Gatineau Satellite Station near Ottawa in Canada, the Tromsø Satellite Station in Norway, and the West Freugh Ground Station in Scotland. Imagery received by these stations are processed in near-real time and sent via dedicated communication lines or via the Internet to the NESDIS Satellite Active Archive (SAA) or directly to the NIC and then forwarded to the SAA. At the SAA, they are stored for retrospective access and automatically forwarded to the NIC, to the National Weather Service (NWS) Alaska Region, and to NESDIS for data analysis and product production. Approximately 15-20 images are received every day. Within the NIC, SAR data are analyzed together with other satellite, *in-situ* and observer reports to produce ice analyses interactively for all the ice-covered regions of the globe. In addition, NESDIS produces a number of ocean products in near-real time and provides them to users in Alaska.

3. ROUTINE USE OF SAR AT THE NATIONAL ICE CENTER

SAR satellite data are used at the NIC, a joint agency sponsored by the U.S. Navy, NOAA, and the U.S. Coast Guard (USCG), to classify ice type and monitor ice condition. Ice charts are provided in support of safety of maritime traffic in all ice covered regions of the world, including the Great Lakes, the Arctic, the Antarctic, and the Arctic marginal seas (Bering Sea, Sea of Okhotsk, and Sea of Japan). The use of SAR by NIC is the closest to a true operational application of these data in the U.S. Most of the spaceborne SAR data obtained by NIC are acquired from the Canadian RADARSAT-1 satellite and are received at ASF. The station mask at ASF allows for near-real-time access to SAR data for the Beaufort Sea, Chukchi Sea, most of the Bering Sea, and the Northern Gulf of Alaska. Additional Arctic SAR data are received from the Gatineau, Tromsø, and West Freugh acquisition stations. These stations provide near-complete coverage of the Arctic using mostly the RADARSAT-1 ScanSAR Wide mode (450-510 km swath and 100-200 m resolution). RADARSAT-1 can in fact image every point on the earth's surface north of 65° N at least once per day. Near-real-time RADARSAT-1 data acquired at the Gatineau station are also available for the Great Lakes region during the winter season as part of an arrangement between the Canadian Ice Service (CIS) and the NIC (see Fig. 1 for an example of these data). Limited collection of data over regions outside these station masks (e.g. the Sea of Okhotsk and Antarctica) may also be requested using the RADARSAT-1 on-board recorder.

Many types of data are utilized in the production of ice analyses including airborne reconnaissance, ship and buoy meteorological and ice reports, satellite visible and infrared imagery, and satellite passive and active microwave imagery and measurements. Each type of data has its own strengths and weaknesses. Some have good temporal resolution and spatial coverage but poor spatial resolution or are limited by the Polar region's pervasive cloud cover. Clouds or fog typically obscure the edge of the ice pack in the Arctic about 70% of the time. SAR imagery, however, is the data source preferred by NIC analysts because of its high-resolution, day/night and all-weather viewing capabilities, as well as its sensitivity to surface roughness and salinity (useful in ice type discrimination). Customers of the NIC demand detailed and reliable information for critical operations and satellite SAR imagery provides the most reliable means to accomplish this. Thus, SAR is the primary data source used when available. It is the only data source with resolution sufficient for providing the highly

detailed ice information required for tactical support. At the NIC, about 23% of the analysis lines in Northern Hemisphere ice charts and 50% of those for the Alaska and Great Lakes ice charts come directly from SAR data analysis [1]. If more data were available, these percentages would be much higher. Use of SAR is limited primarily by available coverage, cost, and access restrictions. In addition to sea ice mapping and characterization, SAR data are used to monitor break-up of ice shelves and iceberg shedding in both the Arctic and Antarctic and for validation and tuning of scatterometer and passive microwave ice products.

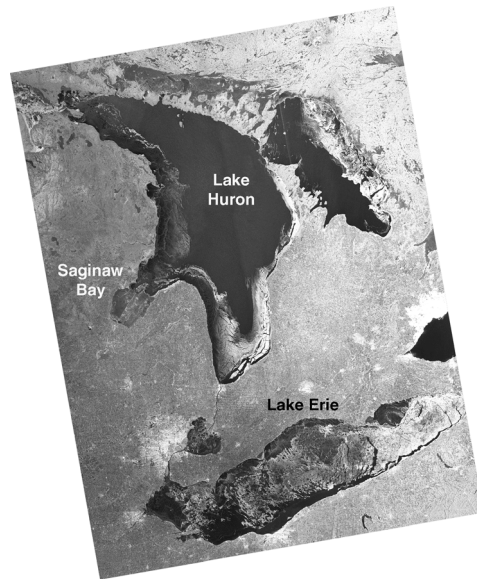


Fig.1. Example of SAR data used for Great Lakes Ice Analysis. This image is a RADARSAT-1 ScanSAR Wide A image from February 22, 2001, at 23:33 UTC. © Canadian Space Agency, 2001.

The NIC produces an extensive suite of operational global sea-ice products year round as well as charts of Great Lakes Ice (produced in partnership with the CIS) in the winter. In Alaskan waters, twice-weekly charts are produced with the aid of approximately 5000 RADARSAT-1 ScanSAR Wide B images per year. These data are received and processed into imagery at the ASF and transmitted to the NIC via the NESDIS SAA within 3 hours of acquisition [1]. Products are generated primarily by interactive analysis rather than via automated algorithms. Automated algorithms for data fusion, expert-system ice classification, ice-motion, and ice thickness [2,3,4,5,6,7] still do not meet timeliness and accuracy requirements for operational ice analysis. A wide variety of products including analyses, 30 day forecasts, and seasonal outlooks are prepared by the NIC and disseminated over the Internet as images or files formatted for Geographic Information System (GIS) display. Fig. 2 is a sample product.

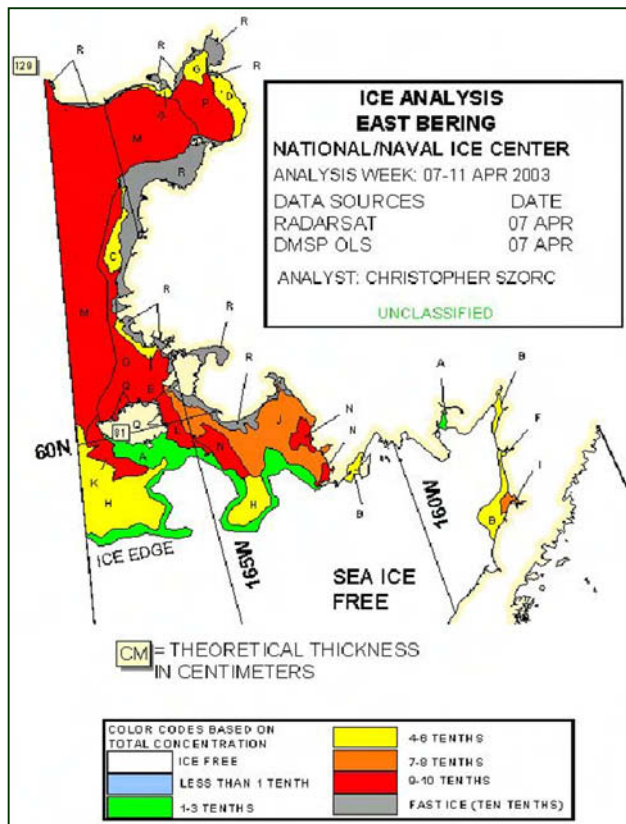


Fig. 2. This is an example of an operational sea ice analysis chart produced at the NIC. The data for this analysis came from the Defense Meteorological Satellite Program (DMSP) Operational Linescan System (OLS) visible/infrared instrument and the RADARSAT-1 SAR. Total ice concentration in tenths is shown in a color code.

The enhanced capabilities of the new generation of satellite SAR instruments should lead to improvements in automated sea ice algorithms. Dual polarization SAR data are just now becoming available from the Alternating Polarization mode of the Advanced SAR (ASAR) instrument on ENVISAT. The RADARSAT-2 SAR and the Advanced Land Observing Satellite (ALOS) Phased Array L-band SAR (PALSAR) will also have dual and quad polarization modes. The ALOS PALSAR is an L-band SAR and Germany and Italy are planning on launching X-band SAR instruments. By utilizing multi-polarization and multiple frequencies, improvements are expected in automated ice type discrimination, iceberg detection, summer ice analysis, and detection of ice at low concentrations [8]. Access to multiple satellites will also improve temporal and spatial coverage to support operations.

4. PRE-OPERATIONAL SAR DEMONSTRATION AT NOAA/NESDIS

NESDIS is the line office within U.S. Department of Commerce NOAA responsible for managing the U.S. civil operational environmental remote-sensing satellite systems, as well as global databases for meteorology, oceanography, solid-earth geophysics, and solar-terrestrial sciences. In addition to the operation of NOAA geostationary and polar satellites, NESDIS acquires, archives, and distributes data and geophysical products from non-NOAA domestic and foreign satellite systems, including RADARSAT-1. The focal point for SAR research support and product development within NESDIS is ORA/ORAD.

A pre-operational demonstration of SAR cryospheric and oceanic high-resolution products is now being conducted by NESDIS/ORA/ORAD in Alaska to evaluate the use of SAR by operational agencies. This demonstration, known as the AKDEMO, uses RADARSAT-1 ScanSAR Wide B (450 km swath, and 100-200 meter resolution) and Standard Mode (100 km swath and 25 meter resolution) imagery of coastal Alaska, the Bering Sea, Chukchi Sea, Beaufort Sea, and Northern Gulf of Alaska to produce and provide a number of derived products to a select group of operational users in the region [9]. The region chosen contains 54% of the U.S. coastline, as well as an extensive region of ocean within the U.S. Exclusive Economic Zone requiring fisheries management and enforcement. There is a severe lack of conventional ship and buoy meteorological and ocean observations in these waters. In addition, the region is characterized by long periods of cloudiness and darkness, severe winter weather, extensive sea ice cover, and large rivers which freeze in winter and may flood during spring ice break-up. These characteristics make Alaska and its adjacent seas an attractive candidate for experimentation with using SAR as a remote sensing tool to assist operational agencies in carrying out their missions of providing forecasts and warnings for safety of life and property, protecting endangered species, managing fisheries, and enforcing U.S. fishing regulations.

The AKDEMO system has four main products: (1) the SAR imagery itself, (2) ocean vessel positions from SAR, (3) ocean surface winds from SAR, and (4) ice/land masks. Near-real-time availability of SAR imagery can provide users with a unique indication of the location of the ice edge, which is critical for some Alaskan fisheries. SAR imagery is also being used to routinely monitor river ice breakup, ice jams, and the development of associated flooding conditions. Automatic detection of SAR hard targets can be useful

for fisheries management (ship detection) or iceberg monitoring. High resolution wind imagery pinpoints areas of locally dangerous winds such as downslope or gap winds (i.e. williwaws), barrier jets, and mesoscale cyclones. Besides wind speed, the ability of SAR to capture mesoscale and microscale atmospheric circulation patterns associated with boundary layer dynamics is being used as an important new tool by meteorological scientists and weather forecasters. Ice and land masks assist in filtering out incorrect wind vectors or vessel positions over ice or land.

4.1 SAR-Derived Winds

The most mature non-ice SAR oceanographic application is the routine production of SAR-derived wind maps [10]. A modified scatterometer geophysical model function that takes into account the horizontal polarization of RADARSAT-1 SAR is used in conjunction with forecast or calculated wind directions to derive SAR ocean surface wind speeds. The large amount of SAR data available under the U.S. allocation agreement has allowed for the accuracy of these winds to be well validated against NOAA buoy winds and NASA's QuikSCAT scatterometer wind vectors collected within a time window of a few hours. Statistics generated in comparisons against both data types indicate a robust retrieval of SAR ocean surface winds with Root-Mean-Square (RMS) errors of around 1.3 m/s [11]. Since SAR wind speed inversion needs *a-priori* knowledge of wind direction, wind direction information from forecast models or from near-coincident ancillary observations such as those from scatterometers or buoys is required. An additional algorithm to automatically obtain wind direction from linear features associated with wind-aligned phenomena such as wind rows or wind shadows observed in a SAR scene is also being used. Development of a strategy is underway to incorporate into the wind speed algorithm the best wind direction information obtainable for a particular SAR scene; i.e., from atmospheric models, scatterometer observations, or features in the SAR image itself. In addition, an investigation of polarization effects on the SAR wind algorithm is underway using ENVISAT ASAR Alternating Polarization data. SAR high-resolution wind patterns can provide important information on physical processes typically not captured by models, *in-situ* observations, or other spaceborne sensors. Fig. 3 is an example of the AKDEMO wind image product. See the winds review paper in these proceedings [12] for other examples of SAR-derived wind images.

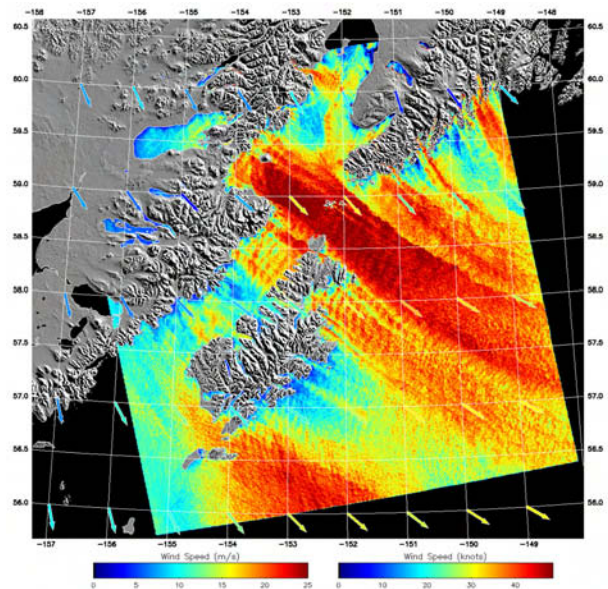


Fig. 3. AKDEMO wind image of the Gulf of Alaska. Kodiak Island is in the center of the image. Arrows are model winds from the Fleet Numerical Meteorological and Oceanographic Center (FNO) forecast model. This product was produced from a RADARSAT-1 image taken on November 26, 2002 at 03:46 UTC.

4.2 Vessel Detection

The positions of offshore and coastal fishing vessels are determined by locating bright targets in the SAR imagery. The core of the detection algorithm is a process that identifies regions of bright image samples that are statistically different from the surrounding ocean clutter. This procedure is often referred to as a constant false alarm rate (CFAR) process since it is a relative measure based on the local statistics of the background clutter and thus keeps the number of false alarms constant as the mean of the clutter varies [13]. Images such as that shown in Fig. 4 have been used to: (1) monitor fisheries to see if observers on fishery vessels are well distributed throughout the fleet, (2) detect vessels on the wrong side of the U.S./Russia Maritime Boundary, and (3) check for vessel traffic in areas restricted for the protection of endangered species. In a test of the ship detection algorithm used in the AKDEMO, it was found that between 45% (for 200 m resolution data) and 60% (for 100 m resolution data) of the vessels participating in the Bristol Bay Alaska red king crab fishery were detected in RADARSAT-1 ScanSAR Wide imagery. It is estimated that the detected ships were all longer than 33.5 m [14]. Another study [15] obtained a detection rate (for ships averaging 120 m) of 84% overall and 97% using the higher resolution modes of RADARSAT-1 that are

recommended for ship detection. Ship detection performance improved as wind decreased, angle of incidence increased, and resolution increased.

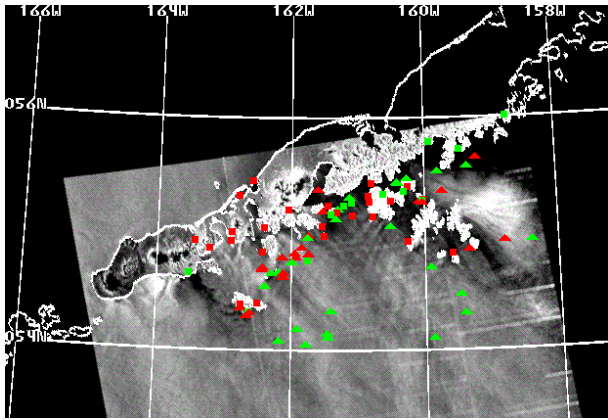


Fig. 4. An example of the vessel detection product for an image of the western tip of the Alaska Peninsula, June 13, 2003 04:27:28 UTC. Strong targets are shown in green, weaker targets in red. Triangles are off-shore targets, squares are targets within 2 km of land. Background image is © Canadian Space Agency, 2003.

4.3 Ice Mask

Since erroneous ship detections and wind vectors are generated when ice is present in an image, it is necessary to mask out ice-covered regions. A product has been developed to do this automatically by using a supervised classification scheme to develop a set of optimal classification vectors. Both statistics and texture are used. The image is partitioned at a 1 km resolution into land (determined by a geographic land/sea database), water, ice, “ice fingers” (i.e., loose rubble regions at the ice edge), and water with atmospheric convective patterns [16]. Fig. 5 is an example of the resulting product.

4.4 Imagery Applications

Studies of mesoscale atmospheric circulation systems such as polar mesoscale cyclones and hurricanes have also been conducted using SAR imagery. In particular, SAR offers an effective way of pinpointing the location of these systems at the ocean's surface. SAR imaging of storm systems may also include patterns of convective cell activity, precipitation, cloud ice, and even storm-induced ocean swell. Other ocean features readily imaged by SAR and under active research include ocean fronts and mesoscale ocean circulation, river plume outflow and coastal interaction, oceanic internal gravity waves, upwelling, biological activity, and near-shore bathymetric features. SAR data are also being Used routinely to detect and monitor accidental oil

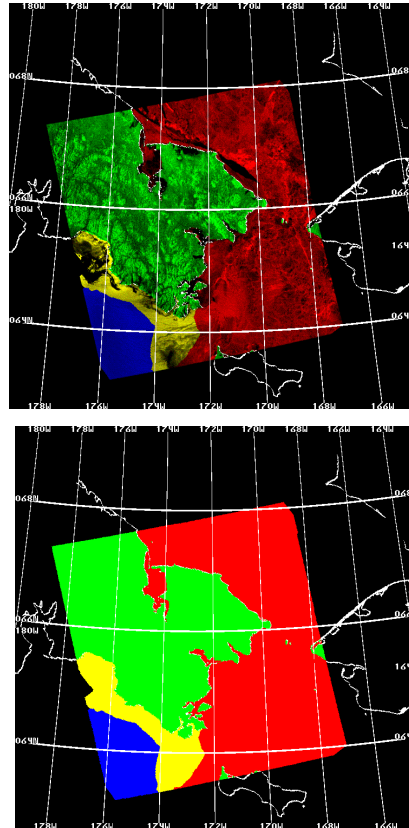


Fig. 5. An example of the AKDEMO ice mask product. Top image is a RADARSAT-1 SAR image of the Bering Sea with the Bering Strait in the middle of the image. The SAR image is colored with the ice mask. The lower image is just the ice mask. Green is land, red is consolidated ice, yellow is ice fingers (broken ice at the ice edge), and blue is open water. Image is from 17 December 2003 at 03:42 UTC (image © Canadian Space Agency, 2003).

spills, seepage from natural sources or submerged structures, and illegal ocean dumping activities.

4.5 User Access to Products and Data

The AKDEMO makes data and products available to users in two basic forms. All products are posted as images in commonly available formats on a web site (<http://www.orbit.nesdis.noaa.gov/sod/mecb/sar/>) and are also available for interactive access via the World Wide Web Interactive Processing Environment (WIPE). This latter system allows users to display, overlay, and analyze SAR and ancillary data via a web browser. WIPE's animation capabilities and ability to overlay satellite image, meteorological model data and point/vector information allow sophisticated analysis, validation, and interpretation of the AKDEMO products.

5. VISION FOR DEVELOPMENT AND IMPLEMENTATION OF AN OPERATIONAL SAR OCEAN PRODUCTS SYSTEM

The goal of the NOAA SAR research and development effort is the development of an integrated end-to-end SAR ocean products system for operational generation of the SAR-derived products specified in the NPOESS requirements documents (Table 1). To accomplish this requires planning, research, software development, applications demonstrations, user training, data access agreements, and the operational implementation of products. The results of the 2nd Workshop on Coastal and Marine Applications of SAR held in Svalbard in September 2003 should help identify the most mature algorithms and approaches for generating these products. Additional collaboration with domestic and international partners is envisioned to refine automated versions of these algorithms. NESDIS will continue wind product development in partnership with The Johns Hopkins University Applied Physics Laboratory and General Dynamics Advanced Information Systems to merge SAR winds with scatterometer and passive microwave polarimeter winds for validation and improvement of direction information. Extending existing algorithms to ENVISAT ASAR and ALOS PALSAR is also planned. Development has already begun on a prototype portable automated operational SAR wind system for deployment at the University of Miami Rosenstiel School of Marine and Atmospheric Science (RSMAS) Center for Southeastern Tropical Advanced Remote Sensing (CSTARS) satellite acquisition station. Based on the CSTARS wind system and Alaska SAR Demonstration experience, we propose to work closely with several domestic and international partners in the development and implementation of a

fully automated operational SAR ocean product generation system to be deployed at selected acquisition stations providing routine access to SAR (Fig. 6). We envision efficient, automated, and routine near-real-time generation of ocean products from each acquired pass, with products made readily available to a broad user community in helpful formats (including common GIS formats). It is hoped that innovative data policy agreements and data purchase/use arrangements will allow large amounts of SAR data to be processed into useful ocean products at reasonable cost. An agreement among the Japanese Aerospace Exploration Agency (JAXA), NOAA, and ASF on the establishment of an ALOS America's Data Node at ASF may provide some of the required coverage.

6. CONCLUSIONS

In the U.S., the unique information provided by SAR imagery is being employed routinely by the NIC for the production of operational ice analyses, predominately via the use of RADARSAT-1 SAR data. In addition, NOAA/NESDIS is conducting an applications demonstration, the AKDEMO, for oceanographic and hydrologic applications of SAR, including the production of high-resolution wind, vessel detection, SAR image, and ice/land mask products. Requirements analyses and research activities have identified a number of other SAR-derived products of great utility. It is the goal of NOAA/NESDIS, working with domestic and international partners, to develop an operational system using data from all of the available SAR satellites scheduled for operation during the next few years for the routine production of a wide range of SAR products. This software system could be ported to acquisition stations for the creation of products in near-real time, using as much of the available SAR imagery

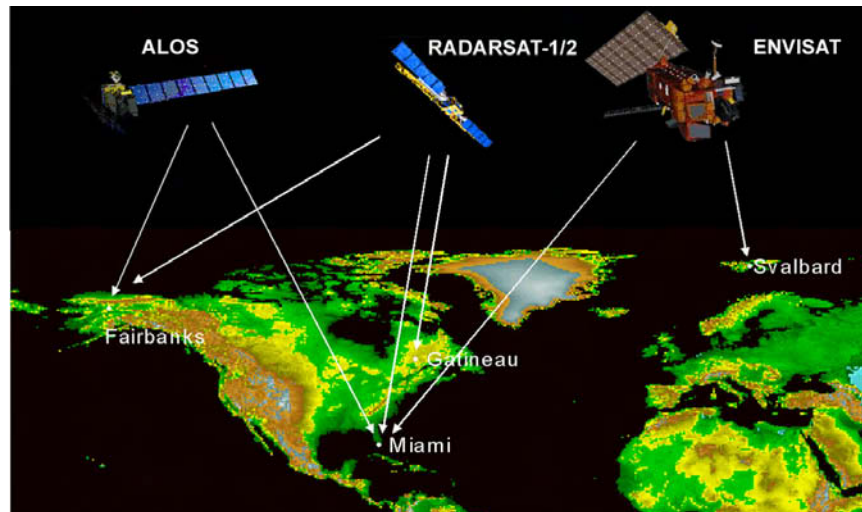


Fig. 6 Concept for International SAR Ocean Products System

as budgets and data policies permit. Multiple satellites and access to large amounts of data would result in revisit times of one day or less, which is the requirement for operational production of many products.

7. ACKNOWLEDGMENTS

The views, opinions, and findings contained in this report are those of the authors and should not be construed as an official National Oceanic and Atmospheric Administration or U.S. Government position, policy, or decision.

8. REFERENCES

1. Bertoia, C., M. Manore, H. S. Andersen, C. O'Connors, K.Q. Hansen, C. Evanego, Synthetic aperture radar for operational ice observation and analysis at the U.S., Canadian, and Danish National Ice Centers, *Synthetic Aperture Radar Marine User's Manual*, C. Jackson and J.R. Apel, eds., *in press*, 26 pp., 2003
2. Bertoia, C., J. Falkingham, and F. Fetterer, Polar SAR data for operational sea ice mapping, in R. Kwok and C. Tsatsoulis (Eds.), *Recent Advances in the Analysis of SAR Data of the Polar Oceans*, Springer Verlag: Berlin, 201-234, 1998.
3. Bertoia C., D. Generis, K. Partington, L.-K. Soh and C. Tsatsoulis, Transition from research to operations: ARKTOS: A knowledge-based sea ice classification system, *Proceedings International Geosciences and Remote Sensing Symposium 1999, Hamburg, Germany*, 1573-1574, 1999.
4. Soh, L.-K. and C. Tsatsoulis, Unsupervised segmentation of ERS and Radarsat sea ice images using multiresolution peak detection and aggregated population equalization. *Int. J. Remote Sensing*, Vol. 20, No. 15&16, 3087-3109, 1999.
5. Clausi, D.A., Comparison and fusion of co-occurrence, Gabor, and MRF texture features for classification of SAR sea ice imagery, *Atmosphere-Ocean, NOW Special Issue*, Vol. 39, No. 4, 183-194, 2001.
6. Clausi, D.A., An analysis of co-occurrence texture statistics as a function of grey level quantization. *Canadian J. of Remote Sensing*, Vol. 28, 45-62, 2002.
7. Kwok, R. and T. Balzer, The Geophysical Processor System at the Alaska SAR Facility, *Photogrammetry Engineering and Remote Sensing*, Vol. 61, No. 12, 1445-1453, 1995.
8. Nghiem, S. and C. Bertoia, Study of multi-polarization C-band backscatter signatures for Arctic sea ice mapping with future satellite SAR, *Canadian J. of Remote Sensing*, Vol. 61, No. 12, 1445-1453, 2001.
9. Pichel, W.G. and P. Clemente-Colón, NOAA CoastWatch SAR applications and demonstration, *The Johns Hopkins Univ. Tech. Dig.*, Vol. 21, No. 1, 49-57, 2000.
10. Thompson, D.R. and R.C. Beal, Mapping high-resolution wind fields using synthetic aperture radar, *The Johns Hopkins Univ. Tech. Dig.*, Vol. 21, No. 1, 58-67, 2000.
11. Monaldo, F.M., D.R. Thompson, W.G. Pichel, and P. Clemente-Colón, A systematic comparison of QuikSCAT and SAR measured wind speeds, in print in *IEEE Trans. Geosci. and Remote Sensing*, TGRS-00347-2002.R1, 2003.
12. Monaldo, F. and V. Kerbaol, The SAR measurement of ocean surface winds: an overview for the 2nd Workshop on Coastal and Marine Applications of SAR, *Proc. Second Workshop on Coastal and Marine Applications of SAR*, this issue, 2004.
13. Wackerman, C.C., K.S. Friedman, W.G. Pichel, P. Clemente-Colón, X. Li, Automatic detection of ships in RADARSAT-1 SAR imagery, *Canadian J. of Remote Sensing*, Vol. 27, No. 5, 568-577, 2001.
14. Friedman, K. S., C. C. Wackerman, F. Funk, K. Rowell, W. G. Pichel, P. Clemente-Colón, and X. Li, Validation of an automatic vessel detection algorithm using *in-situ* positions, *Proceedings International Geosciences and Remote Sensing Symposium, 2000, The Role of Remote Sensing in Managing the Global Environment, 24-28 July 2000, Honolulu, Hawaii*, 3 pp, 2000.
15. Vachon, P.W., S.J. Thomas, J. Cranton, H.R. Edel, M.D. Henschel, Validation of ship detection by the RADARSAT synthetic aperture radar and the ocean monitoring workstation, *Canadian J. of Remote Sensing*, Vol. 26, No. 3, 200-212, 2000.
16. Wackerman, C. C., W.G. Pichel, and P. Clemente-Colón, Automated location of ice regions in RADARSAT SAR imagery, *Proc. Second Workshop on Coastal and Marine Applications of SAR*, this issue, 2004.

OPERATIONAL USE OF SAR AT THE CANADIAN ICE SERVICE: PRESENT OPERATIONS AND A LOOK TO THE FUTURE

Dean G. Flett⁽¹⁾

⁽¹⁾Canadian Ice Service, 373 Sussex Drive, Ottawa, Ontario, CANADA K1A 0H3, Email: dean.flett@ec.gc.ca

ABSTRACT

This paper describes the current state of operations at the Canadian Ice Service (CIS) with a focus on the use of satellite SAR data. The end-to-end processing chain from data acquisition to product distribution is described. Current operational issues with SAR are noted and a discussion of the anticipated impact of some of the new and future SAR sensors and missions is presented. Emphasis is on expected improvements in analysis and interpretation areas where the CIS currently has difficulty and in the operational potential for the future.

1. INTRODUCTION

The Canadian Ice Service (CIS), a branch of the Meteorological Service of Canada (MSC), is the leading authority for information about ice in Canada's navigable waters. Ice in its many forms - sea ice, lake ice, river ice and icebergs - are encountered in all of Canada's waters, except along the west coast. As a result, ice affects Canadian life in many ways including: marine transportation in Canada's southern and eastern waters as well as in the North; commercial fishing; offshore resource development; hunting and fishing patterns of aboriginal peoples; tourism and recreation; and local weather patterns and long-term climate.

At the Canadian Ice Service (CIS), our mandate is to provide the most timely and accurate information about ice in Canada's navigable waters. In support of this, our two main objectives are:

- To ensure the safety of Canadians, their property and their environment by warning them of hazardous ice conditions in Canadian territorial waters; and
- To provide present and future generations of Canadians with sufficient knowledge about their ice environment to support sound environmental policies.

To meet our mission and objectives, we collect and analyze vast amounts of data on ice conditions in all Canadian regions affected by the annual cycle of pack ice and iceberg growth and disintegration. In Summer, we focus on the Arctic and the Hudson Bay regions,

while in Winter and Spring, attention shifts to the Labrador Coast and East Newfoundland waters, the Gulf of St. Lawrence, the Great Lakes and the St. Lawrence River (Fig. 1).

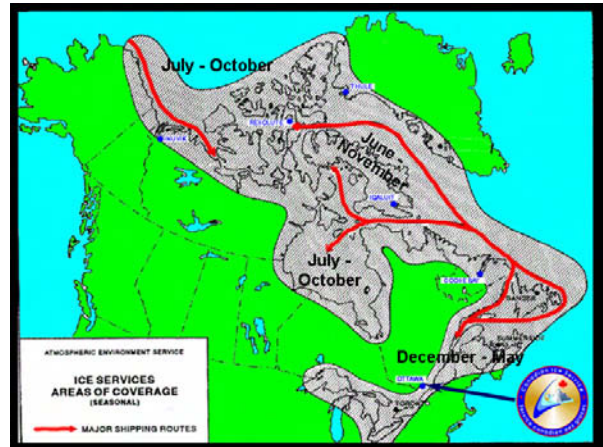


Fig. 1. CIS Operational Areas of Interest

This paper describes the current operations that the Canadian Ice Service undertakes, using both SAR and non-SAR data sources, to carry out its sea ice monitoring operations activities. In addition, this document briefly describes how the CIS anticipates its operations to evolve with the availability of new and future SAR missions.

2. DATA ACQUISITION

The Canadian Ice Service annually collects vast amounts of ice and iceberg data - mostly from remote sources (satellites, reconnaissance aircraft, and ships). Drawing on years of experience, CIS experts analyse these data to prepare and issue charts, bulletins and special warnings for safe and efficient marine operations in Canada's ice-encumbered waters. In the field, our Ice Service Specialists (ISS) conduct visual observations from shore, ship, and aircraft to prepare accurate and timely ice and iceberg information.

While remote sensing data forms the core of the data used in generating our daily ice information products, there are several other sources of data and information, including: meteorological data (temperature, wind, etc.); oceanographic information (currents, bathymetry, etc.); fields from numerical ice models (e.g.

drift/trajectories, ice concentration, ocean currents and temps, etc.); climatological data; and previous ice charts.

RADARSAT-1 SAR data is the primary remote sensing data source used in the analysis and preparation of our ice chart and other information products. RADARSAT-1 has proven to be a great success at addressing ice information requirements and Canada is recognized as a world leader in operational use of spaceborne SAR for sea ice monitoring. RADARSAT-1 has been the preferred data source because of its wide geographic coverage (500km swath) and because the HH polarization provides generally superior ice-water discrimination at intermediate incidence angles (e.g. 25° - 35°) over VV polarization.

The CIS also began using Envisat ASAR Wide Swath Mode data operationally in the late summer of 2003. Several other remote sensing data sets, including data from other sensors (optical - GOES, NOAA AVHRR, DMSP OLS, Terra MODIS; passive microwave - DMSP SSM/I; active microwave - airborne SLAR, QuikScat) are also used.

For SAR data, and in particular RADARSAT-1 and Envisat ASAR, this involves customized ordering, rapid delivery of data, in-house pre-processing (geocoding, enhancement), interpretation and, finally, dissemination of products. RADARSAT-1 and Envisat data are typically ordered 2-3 weeks in advance based on past knowledge of ice conditions in the regions of active commercial shipping. For the other satellite remote sensing data sources, we typically either have standing orders and regional geographical "cookies" for data acquisition (e.g. NOAA AVHRR).

Because of the large volume of RADARSAT-1 data used by the CIS, we are equipped with one of only five RADARSAT-1 Order Desks which permits direct entry of requests to the Mission Control System located at Canadian Space Agency Headquarters in St. Hubert, Quebec. The CIS primarily makes use of the ScanSAR modes of RADARSAT-1 which provide nominal swaths of 500km (at 100m resolution - ScanSAR Wide) or 300km (at 50m resolution - ScanSAR Narrow). These modes are preferred because of the excellent geographic coverage and revisit capabilities at sufficient resolution for the interpretation of significant ice features.

Canada has two receiving stations for SAR data - at Gatineau, Quebec and at Prince Albert, Saskatchewan. The CIS orders RADARSAT-1 data from these stations through the Mission Control Order Desk System (ODSys). All data is processed into image

products at the Canadian Data Processing Facility (CDPF) at Gatineau, Quebec. An Anik satellite link is used to move signal data from the Prince Albert site to Gatineau prior to processing. A high-speed Wide Area Network (WAN) is also being tested to transfer the data to the CDPF (2003). The processed data is received at the Ice Service in Ottawa by means of a dedicated T1 digital link - the Image Transfer Network (ITN). Turn-around is guaranteed under contract with RADARSAT-1 International (RSI) to be less than 2.5 hours from data acquisition. Delivery times for a nominal data take of 2 to 3 scenes is generally around 2 hours for all frames.

ASAR data are ordered through the Canada Centre for Remote Sensing (CCRS) which has a "Niche" agreement with ESA to acquire data in support of operational applications for five Canadian government organizations. Data are processed at both Canadian stations by CCRS and Level 1 image products are delivered via a WAN ftp server to the CIS. Delivery time from acquisition to product availability is nominally 2 hours for the first scene and then 1 hour (or less) for each subsequent scene of the same contiguous pass segment thereafter.

3. DATA PRE-PROCESSING

The Ice Services Integrated System (ISIS) - consisting of a series of fast servers and dual-screened client workstations - is used to process, display, and analyze all data received at the CIS, remote sensing or other. At the highest level, ISIS servers process and catalogue the incoming data, which is then made available to analysts and forecasters at the ISIS workstations (Fig. 2). All incoming data are handled automatically - ISIS detects new data and determines the type, invokes the appropriate processing programs for the particular data type, and forwards data to other systems as required. Once processed, ISIS client workstations are able to use the Catalogue Browser to visually browse the catalogue database based on themes and retrieve any data for analysis.



Fig. 2 Ice Forecaster analysing imagery on ISIS workstation.

For RADARSAT-1 data, each image segment is 2x2 block-averaged and geocoded into a custom Lambert Conic Conformal map projection (to which all products are warped) prior to cataloguing. Block averaging is done to reduce the file size for faster processing. While the resolution of the image is coarsened, the effective loss of detail for the analysis function is minimal. During this processing, the file format is converted from the original CEOS to ERDAS Imagine (.img) format (the native image format of ISIS) for internal system manipulation. Envisat Wide Mode data are not block-averaged as the data volumes are already manageable and the resolution and pixel spacing is already slightly coarser than RADARSAT-1 ScanSAR Wide.

In addition, all SAR data image frames (scenes) are geocoded and compressed into MrSID™ format and made available to authorized clients, such as Canadian Coast Guard (CCG) ships, for direct transmission of the image frames. The COTS MrSID software from LizardTech is able to compress the files from approximately 40 MB per frame (ISIS native format) to around 2-3 MB per frame with minimal degradation in image detail.

4. DATA ANALYSIS, PRODUCT GENERATION AND DISTRIBUTION

As automated algorithms for ice typing are still not robust and reliable enough for operational ice charting in support of navigation, data analysis and chart production is done entirely by expert ice analysts and forecasters visually analysing imagery in the ISIS GIS-Image Analysis System environment. ISIS is a distributed system which leverages the capabilities of several commercial packages with custom interfaces. The ISIS Client component includes the analysis and product (“chart”) preparation tools and provides all the analysis, data integration, and product preparation tools required by the CIS analysts and forecasters. The ISIS Client is designed as an integrated application uniting via a custom interface the functionality of COTS packages such as ERDAS Imagine, ESRI ArcInfo, ESRI ArcView and Oracle RDBMS.

The ISIS client Viewer Module (Fig. 3) allows simultaneous viewing of image, graphical, and textual data in order to prepare a product, such as an ice chart. Imagery can be viewed with supporting features like continuous pan, virtual roam, scroll and zoom. A variety of data is loaded into the viewer to be arranged and enhanced such that rough vectors (i.e. not topologically complete) of ice edges and polygons can be digitized.

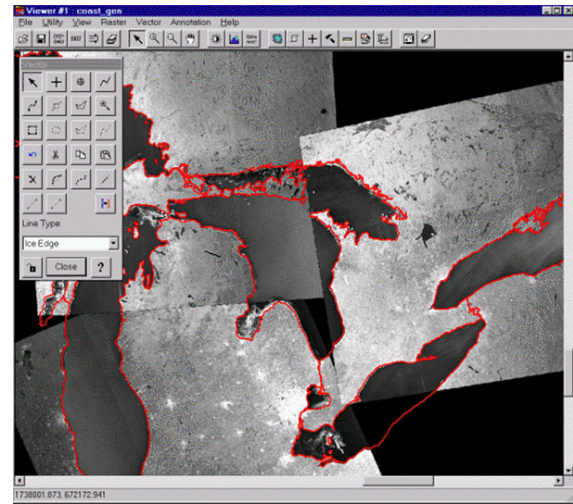


Fig. 3 ISIS Viewer Module screen

The client Product Generation (PGN; Fig. 4) Module is the “final stage” in the preparation of a chart. The rough ice edges and polygons digitized in the viewer are completed and are described formally (i.e. with ice code attributes). Polygon topology errors (e.g. overshoots and undershoots) and egg description errors are automatically identified in PGN. Once all errors are resolved, complete polygon topology is created and ice products such as PostScript ice charts and grid point data extractions (for model use) are created.

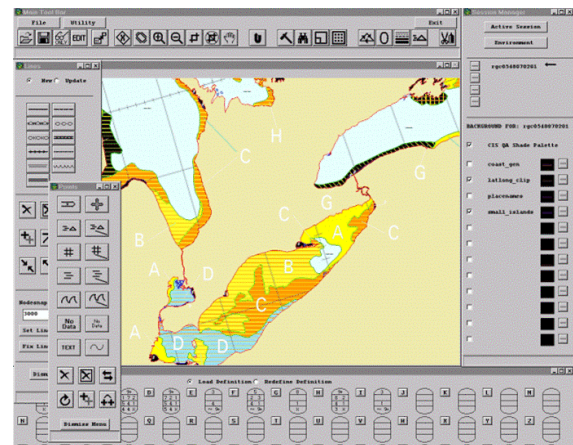


Fig. 4 ISIS Product Generation Module screen

All available image data including RADARSAT-1, Envisat ASAR, NOAA AVHRR, QuikScat, DMSP SSM/I and OLS, and aircraft SLAR is visually interpreted by experienced analysts and forecasters in ISIS and integrated with visual airborne reconnaissance, ship/shore reports, meteorological, and other available data. CIS Operations typically takes a single-image approach to image analysis, (i.e. each image type is examined separately for ice information) and then information from multiple sources is

qualitatively synthesized by the analysts and incorporated into the ice analysis and output products.

As noted earlier, RADARSAT-1 is the primary remote sensing data source used in preparation of our primary product, the daily analysis chart. On a daily basis, if RADARSAT-1 data are available from either the previous nights pass or the current morning pass for the operations area of interest, it is the first data set analysed.

Products resulting from the daily production flow (e.g. Fig. 5.) are automatically made available or distributed electronically via the Product Distribution System (PDS). All products are made available by mandate to the CIS's primary client, the Canadian Coast Guard. All products generated are assigned unique product names to enable automatic distribution of selected products to clients. Irrespective of the means by which clients receive their products, using a standard product naming system, the suite of products they need can be easily configured for automatic delivery.

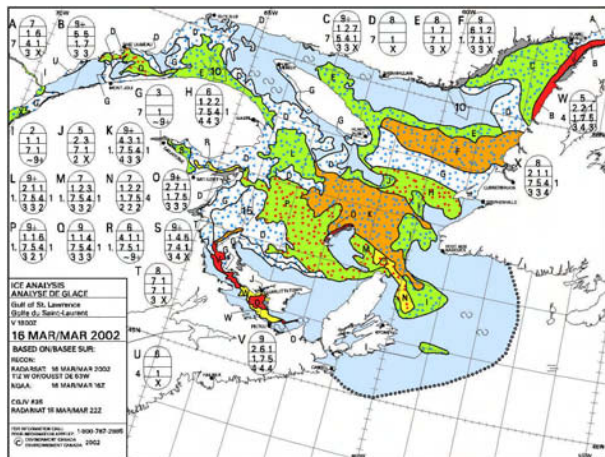


Fig. 5 Standard daily Ice Analysis chart

The Coast Guard Icebreakers and Ice Offices access the charts and images using a Windows-based workstation called ICE-VU. Shipboard ICE-VU systems are connected to the ship GPS such that when the georeferenced images and charts are loaded into a viewer, the ship's position is automatically displayed as a layer on top of these products (Fig. 6). As the ship traverses the waterway, the GPS updates the ship position on the viewer allowing the ships navigation officers to view the ship position relative to the surrounding ice. ICE-VU has its own data acquisition, processing and cataloguing functions, as well as unique browsing, image analysis and display functions. The ICE-VU system has a suite of image analysis and enhancement tools plus navigational aid tools to facilitate route planning based on ice conditions, to

track the ship's location, to generate navigational reports and even playback the ship's tracks. Analyses done in ICE-VU may also be transmitted back to the CIS for use in the daily production of the standard chart and bulletin products.



Fig. 6 Ice Services Specialist operating IceVu system on the bridge of Canadian Coast Guard icebreaker

With respect to present CIS operations with RADARSAT-1, its strength lies in its repeat frequency and swath coverage. RADARSAT-1 imagery is used as an important strategic-level vessel management tool for the deployment of icebreakers. The data is received within hours of capture allowing Ice Operations Officers to more effectively deploy their ships to areas where ice poses a hazard. Imagery products are typically available to clients within 3 hours from data capture, and analyses are normally available within 6 hours. The frequency of coverage has lead to a reduction of airborne surveillance and the flight hours saved has been directed towards tactical support to the icebreakers.

5. INFORMATION REQUIREMENTS AND CURRENT OPERATIONAL ISSUES

Table 1 (end of paper) summarizes the spatial and temporal ice information requirements as defined by the CIS, separated into Strategic and Tactical scales. For the purposes of the table, Strategic refers to the level of detail and information required for the preparation of a Canadian Ice Service Daily Ice Analysis Chart (e.g. Fig. 5). Tactical refers to the level of detail and information required to support daily operations and ship navigation in ice. As an example of the use of Strategic and Tactical levels of information, the CIS Ice Service Specialist (ISS) field personnel onboard the Canadian Coast Guard icebreakers may use the Daily Ice Analysis Chart to assist the Captain in preliminary route planning. In contrast, tactical information of finer detail is collected in the vicinity of the vessel, e.g. by visual reconnaissance from helicopters, to support immediate operations.

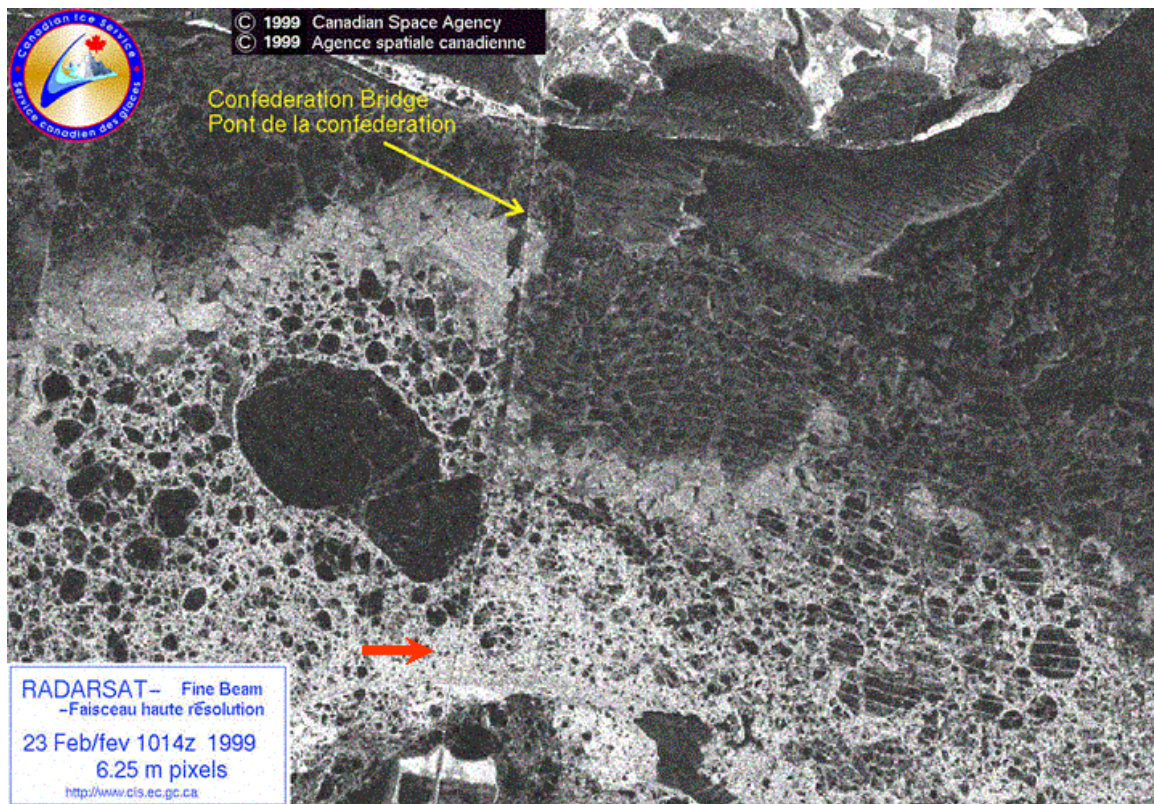


Fig. 7 RADARSAT-1 Fine beam image of ice moving through Northumberland Strait under the Confederation bridge. Note how the ice illustrates how the floes are “sliced” by the bridge piers. © CSA 1999.

The regional coverage of ScanSAR provides the CCG with the ice information they require to design shipping routes and to balance their deployment of icebreakers, for example, between operations in the Gulf of St. Lawrence and the St. Lawrence River. However, the revisit capability is currently a limitation, particularly at southern latitudes. While ScanSAR is the default operational mode, the CIS will acquire higher resolution non-ScanSAR modes where more detailed surveillance over smaller areas is required. For instance, RADARSAT-1 Standard and Fine beam images have been acquired over the Confederation Bridge (between Prince Edward Island and New Brunswick – Fig. 7) and the new mine site at Voisey’s Bay, Labrador. However, this can be in conflict with standard wide-area monitoring operational requirements for ScanSAR coverage and need to be balanced.

Although generous in geographic coverage, RADARSAT-1 ScanSAR imagery can have trade-offs in image signature stability. Generally speaking, the signatures of ice types and capability of detecting topography improve incrementally away from nadir. This is a result of changes in incidence angle (20-49 degrees for ScanSAR Wide). To partially compensate

for this across-swath variability, the Canadian processor uses an Ice Look-Up Table (LUT) to apply a nominal correction to scenes ordered by the CIS to balance the ice appearance with range.

The first and primary task for sea ice mapping is to be able to identify the boundary between ice and open water, or the ice edge. Presently with RADARSAT-1 its HH polarization is an improvement over the VV polarization available from earlier ERS satellites. However, clear definition of the ice edge can still be difficult with RADARSAT-1, particularly in the near range when varying sea surface signatures can often “contaminate” a scene to such an extent that reliable analysis of ice features is difficult.

The problem of a steep incidence angle in the near range can be counteracted to some degree in the swath selection process. During the ordering routine at CIS, consideration is given to whether the ascending or descending pass will image an operationally sensitive location in the preferable mid- to far-range of the swath, and the data are ordered accordingly. However, this still may result in difficulties as the data are typically ordered 2-3 weeks in advance.

Because of the dynamic nature of the ice environment and the nature of ship operations, satellite orbit restrictions can be limiting. We cannot acquire data "on-demand" for a particular geographic location with satellite systems. To some degree, this is the reason why ScanSAR is chosen over narrower, higher resolution modes, as we need to cover as much area as possible. This reality combined with the tradeoff one must make between ScanSAR and higher resolution modes limits the current capability to support ships on a tactical basis. Thus, dedicated aircraft support with real-time downlink is still an important element of the service.

Ice topography and structure and ice deformation features, such as ridging, are important parameters as these features pose a significant hazard and impediment to navigation. While ScanSAR data can be used successfully to identify areas of deformed ice and ridging, identification and measurement of specific ridges is not feasible [1]. Higher resolution modes (e.g. Fine, Standard) may be more successful at ridge identification. In addition, modes with higher incidence angles approaching those of airborne SARs would be preferable for achieving improved results. Again, the trade-off between coverage and resolution comes into play. However, at coarser resolutions (i.e. km's) for climatological and modelling purposes, the RADARSAT Geophysical Processor System (RGPS) [2] has demonstrated a capability to characterize sea ice ridging and other fields.

One of the main operational issues for the CIS has been the fact that RADARSAT-1 has been the only wide-swath capable SAR system for several years. The availability of Wide Swath Mode data from Envisat ASAR, and others planned for the near-future (e.g. RADARSAT-2, ALOS PALSAR, TerraSAR, etc.) will provide us with greater flexibility in our operations. Redundancy and flexibility are key components of an operational service and multiple SAR satellite platforms will provide this. In addition to providing redundancy, the CIS would be able to mix ScanSAR modes of data collection with higher resolution modes for more detailed mapping of specific channels and waterways without sacrificing revisit and coverage needed to meet strategic level wide area monitoring requirements.

6. ANTICIPATED CHANGES WITH NEW SAR SENSORS

6.1 Envisat ASAR

Envisat ASAR is providing the first opportunity for routine acquisition and availability of multiple polarization SAR data from satellite. Envisat ASAR

has dual-polarization capabilities and the Alternating Polarisation Mode allows acquisition of three dual-polarization combinations - HH and HV, VV and VH, or HH and VV. The latter mode is unique to Envisat ASAR and is presently not planned for RADARSAT-2. ASAR is capable of wide area coverage achieved by switching between different swaths using the ScanSAR technique. This allows 405 km coverage at resolutions of either 150 m (Wide Mode) or 1 km (Global Monitoring Mode). In contrast to the ERS SARs, which had a fixed swath position (23° mid-swath incidence angle), ASAR Image (and Alternating Polarization) Modes will allow data acquisition in seven different swath positions (i.e., IS1 to IS7), over incidence angles ranging from 15° to 45°. Nominal resolutions of these so-called Narrow Swath modes are 30m with swath widths from approximately 50 to 100 km.

As with RADARSAT, the mode of highest interest for operational use at the CIS is the Wide (ScanSAR) mode. Its 400+ km swath width is between RADARSAT-1 (and RADARSAT-2's) ScanSAR Narrow (300 km) and ScanSAR Wide (500 km). Availability of Wide Swath data in tandem with presently available RADARSAT-1 ScanSAR data provides complementary wide area coverage (Fig. 8).

Polarization selection for ASAR Wide mode is either HH or VV. Based on operational experience at the CIS, HH will likely be the operational polarization of choice. However, as noted earlier, attempting to distinguish ice from water in certain sea state and ice conditions with HH polarization can be problematic. There may be instances where VV could be the preferred choice, particularly in marginal ice zones under rough open water and new and thin ice conditions where contrast between ice and water signatures are reversed (i.e. water bright and ice dark) [3]. Alternating Polarization mode data from ASAR provides the opportunity to explore some of these issues of HH versus VV across the wide range of incidence angles covered by the seven sub swaths.

The availability of multiple polarization data now available from Envisat ASAR, gives the CIS the opportunity to explore the potential of multi-channel SAR satellite data operationally for the first time. While the Alt-Pol data are only available in narrow swaths (< 100 km), making it less than ideal for strategic operational ice monitoring, it gives us the possibility to prepare for dual-channel ScanSAR planned for RADARSAT-2 (limited to HH/HV or VV/VH at present). Notwithstanding the limited swath widths, Alt-Pol data could play a role at the more detailed, close to tactical level of ice monitoring, as RADARSAT-1 is still available for wide area

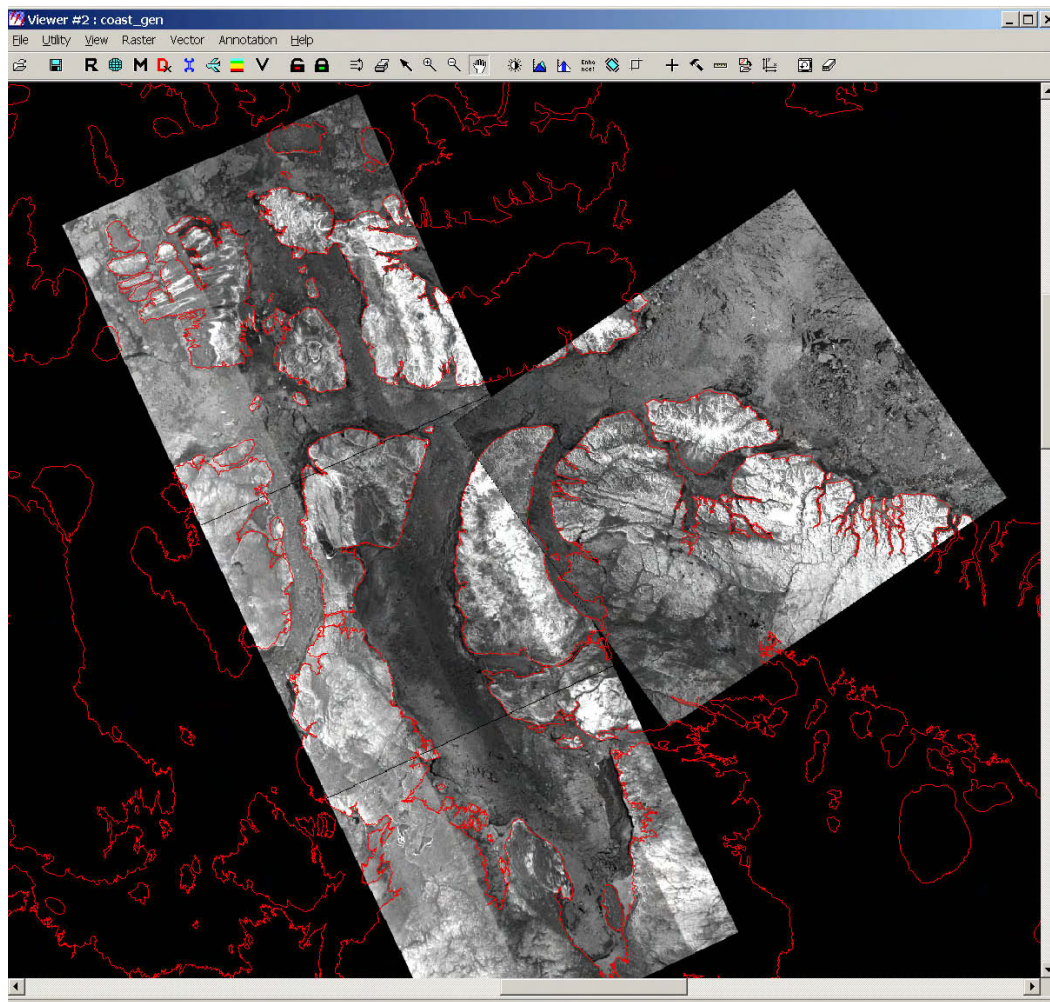


Fig. 8 Envisat Wide Swath pass (left side of figure) and RADARSAT-1 ScanSAR Wide scene of entrance to Lancaster Sound and Barrow Strait in Canadian Arctic acquired the same day. Images © ESA and CSA, 2003.

monitoring, as noted above. Initial results from ASAR Alt-Pol data suggest that cross-polarization will improve the potential for distinguishing ice from open water under challenging analysis conditions [4] (Fig. 9).

Of some concern with the cross-polarization channel is the issue of the sensor noise floor limiting its utility for sea ice applications, particularly for discrimination of thin, new ice and open water areas. Indeed, early results from Cal/Val cross-polarization data of sea ice from Envisat ASAR Alternating Polarization data confirm this, and suggest that proper adjustment of the gain settings of the sensor to ensure good signal to noise ratio (SNR) are critical for situations where the signals of interest are close to the noise floor. Fig. 10 shows HH (left) and HV (right) polarization images from an Alternating Polarization acquisition of the Resolute Bay area in the Canadian Arctic Archipelago.

The cross-pol image is significantly enhanced to improve contrast. It is clear from the images that the response from the sea ice in the cross-polarization channel is significantly lower than in the co-polarization image. Measurements indicate that, while the backscatter difference between the land areas in the image is on the order of 6 dB, the differences over the ice are 10 dB or greater [5]. Also, measurements over ice areas of lowest response in the image are around -23 dB or lower, the noise floor of this mode.

If the noise floor issue for the cross-polarization mode proves to be a problem upon examination of further data, then selecting the co-polarization option (HH and VV) of the Alternating Polarization mode may be preferable as research has shown that the co-polarization ratio may also be useful for discriminating ice from open water areas [6]. The limitation from the operational perspective would be the narrow swaths.

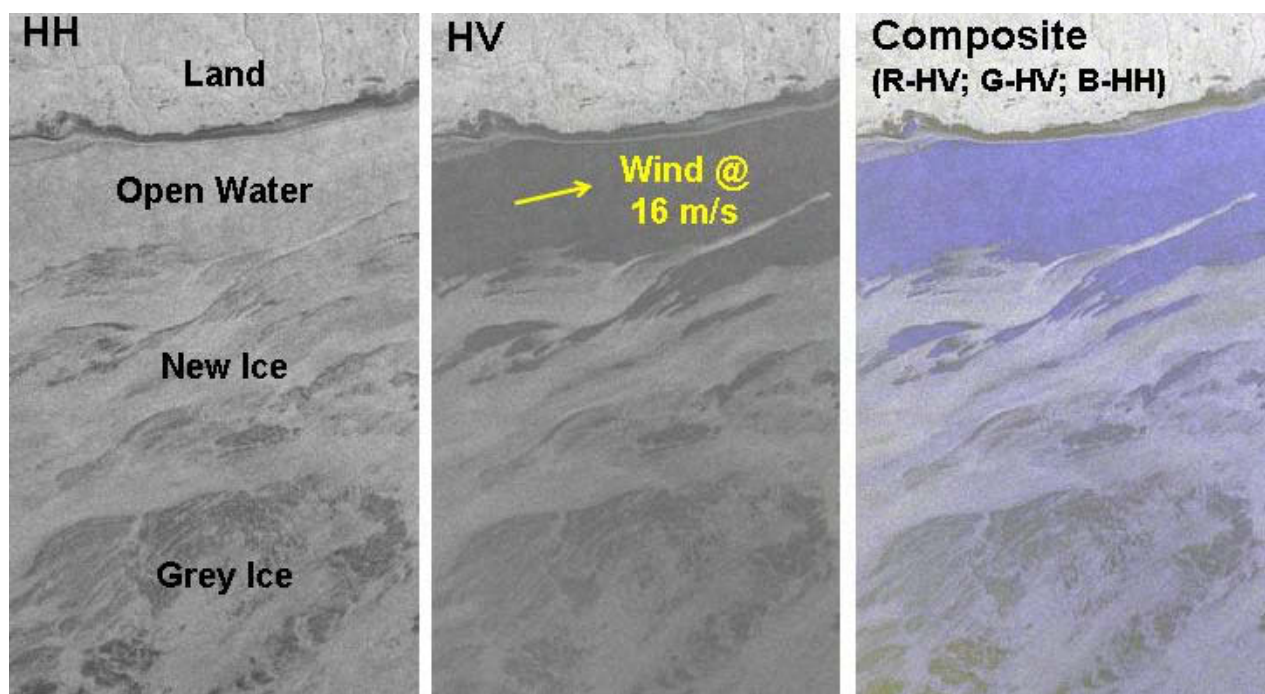


Fig. 9 Marginal ice zone subset of Feb. 7, 2003 Envisat Alt-Pol image acquired in beam IS4 (31-36°): Modelled wind speed and direction shown in yellow lettering. © ESA 2003.

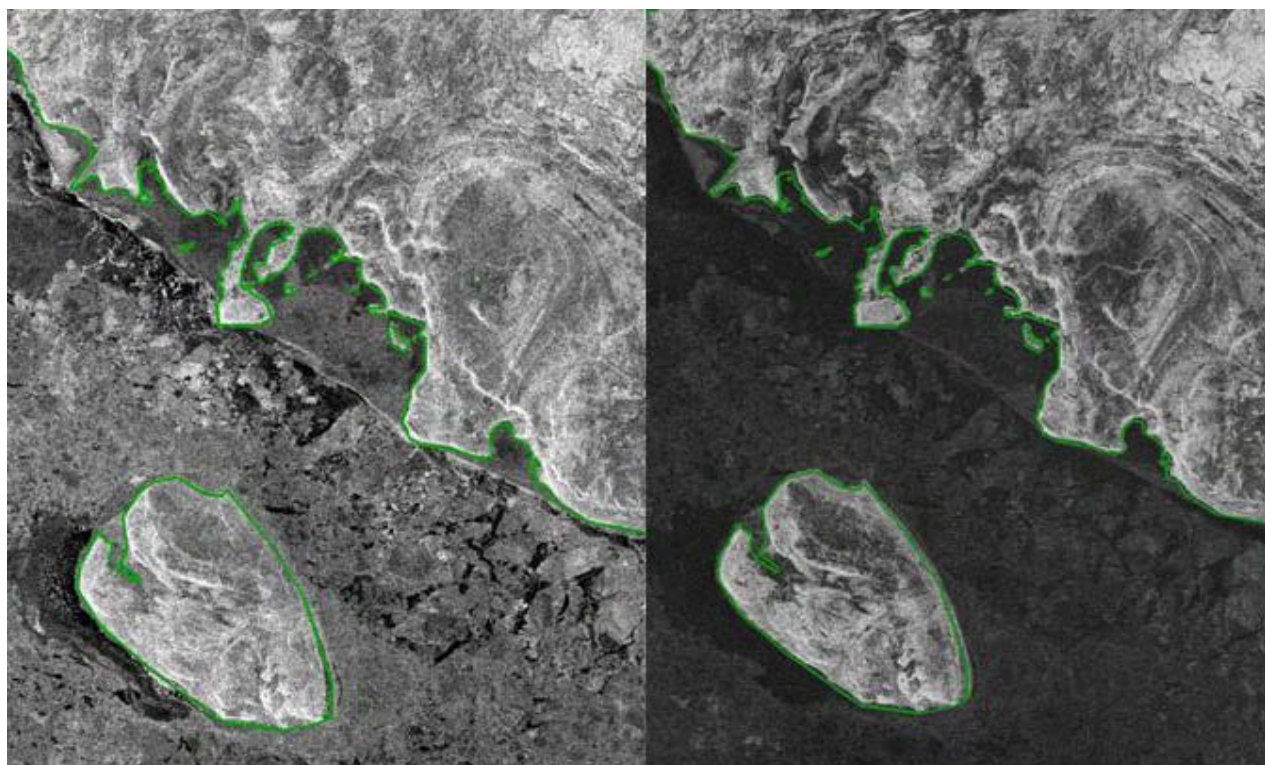


Fig. 10. Envisat ASAR Alternating Polarization Mode image of Resolute Bay, Canadian Arctic. This is an IS2 swath image acquired on November 6, 2002. HH polarization is on the left and HV polarization is on the right. Note the significant difference in backscatter brightness (even with the contrast enhancement) between the sea ice covered areas between the two polarizations. © ESA 2002.

In order to select from the available multi-polarization choices and optimally use the resulting data, we will need to understand under what conditions one would want to choose a particular single or dual-polarization combination over another. Multi-channel data also necessitates new visualization schema to be developed as the Analysts and Forecasters are accustomed to interpreting single channel, like-polarization SAR. Methods such as false colour compositing, IHS transformations, channel ratioing, and others are being investigated to determine the optimal presentation for analysis and interpretation [7]. Fortunately, operational personnel are already familiar with false colour representations with optical data such as NOAA AVHRR and MODIS from the Terra and Aqua satellites and the transition should not be too onerous. Training will be a key element in this period.

6.2 RADARSAT-2

RADARSAT-2 will provide all imaging modes of the current RADARSAT-1 satellite, as well as some new modes that incorporate significant innovations and improvements. RADARSAT-2 will be able to image at spatial resolutions ranging from 3 to 100 metres with nominal swath widths ranging from 20 to 500 kilometres. Depending on the beam, RADARSAT-2 will have the capability to operate in Selective Single Polarization (SSP), Selective Dual Polarization (SDP) or Quad Polarization (QP) mode. The SSP mode will provide images that comprise a single channel the polarization of which is HH or HV or VV or VH. In the SDP mode the satellite will acquire images that comprise both a like- and cross-polarized radar channel, i.e. either an HH and HV channel or a VV and VH channel. Finally, in the QP (fully polarimetric) mode, the RADARSAT-2 SAR will measure the amplitude and phase of the backscattered wave for the four available transmit and receive linear antenna polarization combinations (HH, HV, VV, VH). Additionally, all imaging modes will be available to either the left or right sides of the satellite track.

Much of our evaluation of the potential of future SARs for ice monitoring applications has focused on looking ahead to RADARSAT-2, primarily due to its heritage in the RADARSAT-1 system upon which the CIS relies. Based on evaluation of SIR-C (Fig. 11) and other airborne data sets, and more recently with Alt-Pol ASAR (previous section), the ice-ocean contrast in cross-polarization RADARSAT-2 modes should be greater than for either of the like-polarization channels and should improve the potential for clear ice edge definition. The Selective Polarization mode of RADARSAT-2 will allow the acquisition of cross-polarization data in all currently available RADARSAT-1 modes, including ScanSAR.

The potential of exploiting the co-polarization ratio will be operationally limited as, other than for the narrow swath Quad-Pol modes, the two like-polarization channels will not be acquired simultaneously. A corollary to accurate ice/water separation is the ability to more accurately estimate ice concentration and thus cross-polarization data should be useful in this regard as well.

With additional polarization channels for a single image comes added overhead in terms of data volume, processing and delivery time, time available for analysis, and cost. It may be necessary to stage the processing and delivery of multi-channel products, particularly when we are considering RADARSAT-2 ScanSAR. Evaluation and analysis with Envisat Alt-Pol ASAR data should help us answer some of these questions.

Analysis of airborne polarimetric data in the Central Canadian Arctic suggest that only small differences can be expected between the co-polarization channels for discriminating between the multi-year and first-year sea ice for data acquired under cold and dry winter-like conditions, and there appears to be little additional information for ice typing into the operational age and thickness classes [8]. However, the cross-polarization data may offer additional information of value. Fig. 12 illustrates C-HH and C-HV imagery of a multi-year (MY) ice floe surrounded by a mixture of undeformed first-year (FY) ice and a rubble field of deformed FY ice. Multi-year versus first-year ice contrast is as high as 9 dB in the cross-polarization data, compared to less than 3 dB in the like-polarization channels [8]. Thus, cross-polarization data could be advantageous if maximum discrimination between these two primary ice types is needed, particularly in highly deformed ice where ridging can cause confusing bright signatures.

Ice topography, structure, and deformation features, such as ridges, are also important parameters as these features pose a significant hazard and impediment to navigation. Airborne cross-polarization data has illustrated enhancement of structural information and has demonstrated utility for enhancing discrimination between smooth and deformed ice. This is a function of the combined volume scattering and multiple-reflection surface scattering in the ice ridges enhancing the cross-polarization radar returns [9]. Observations of C-band scatterometer measurements of Baltic sea ice [10] quantitatively illustrated that the backscatter contrast between level ice and ice ridges is larger at cross-polarization than co-polarization. Figure 12 visually illustrates this enhancement with C-band HH and HV data for cold winter ice conditions [8].

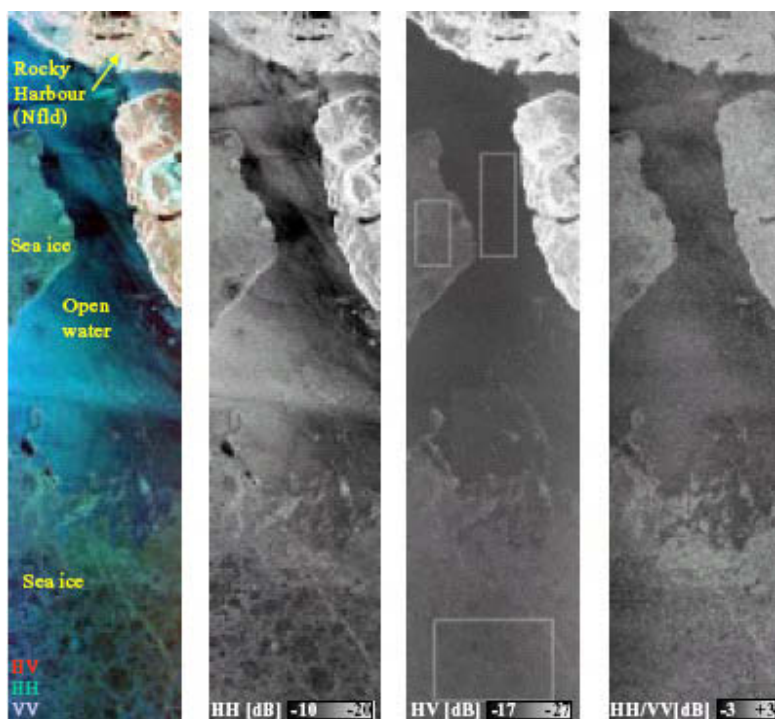


Fig. 11. C-band SIR-C data of the Gulf of St. Lawrence, April 18, 1994. This late season imagery was acquired under wet ice/snow conditions. Local wind speed variable between 4m/s to 10 m/s. Resolution is 25m (4 looks) with an incidence angle range in this figure of 26°-29°.

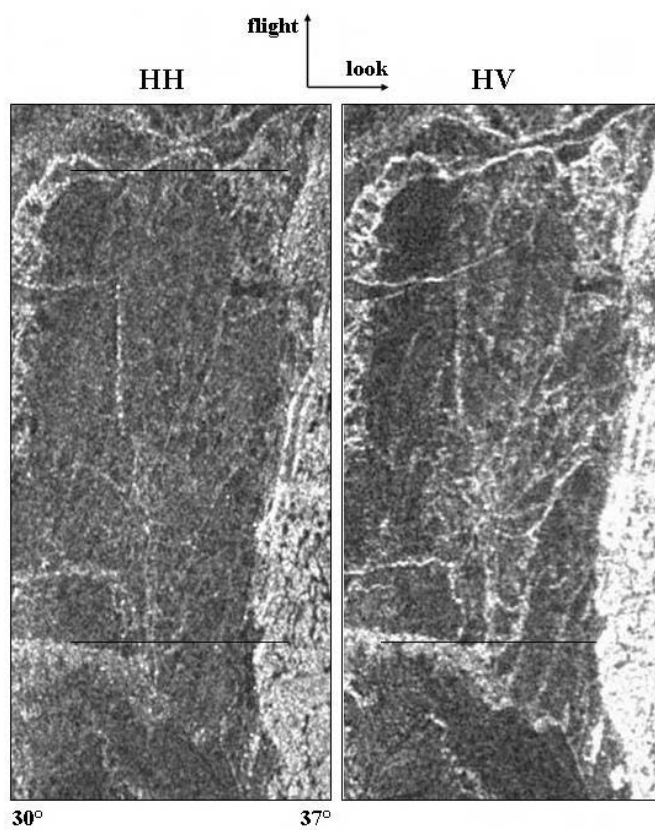


Fig. 12 Airborne C-band CV-580-SAR of multi-year (right edge of each frame) and first-year ice (left side) near Resolute Bay, May 3, 1993. Contrast between MY and FY ice, and discrimination of ridge features is clearer on the C-HV image. Resolution of the original data is 6m (7 looks).

It is hoped that cross-polarization ScanSAR data from RADARSAT-2 will be an improvement over the current like-polarization case for detection of ice topography and structure. Operationally, these effects may improve the detection of hazards to navigation in ice, specifically traces of MY in a matrix of FY ice and the detection of pressure ridges. However, both of these features are relatively small compared to the resolution of the wide-swath radar modes used operationally, so their detectability will likely remain resolution limited. Additionally, the afore-mentioned signal-to-noise ratio and noise floor limitations of satellite systems (e.g. 23 to 26 dB) will reduce the contrast of undeformed FY ice with ridge features. In fact, early assessment of Envisat Alt-Pol data suggests that this may be the case for the satellite situation (Fig. 13).

The separation of thin and new ice types from open water is one of the major problems with current single-channel SARs. Although as noted previously, the expectation is that ice-water separation should be enhanced with cross-polarization data, the expected noise-floor of the satellite systems may limit the utility for discrimination of new ice types. This is being investigated with Alt-Pol ASAR data.

6.3 ALOS PALSAR

The Japanese ALOS satellite is scheduled for launch in summer of 2004 and will have an L-band (1.27 GHz) SAR, called PALSAR (Phased Array L-Band SAR). PALSAR [11]. PALSAR will have fully polarimetric capabilities, operating with either single polarisation (HH or VV), dual polarisation (HH+HV or VV+VH), or in full polarimetric mode (HH+HV+VH+VV). The look angle is variable between 7° and 51° (8-60° incidence angle). PALSAR can also operate in coarse resolution ScanSAR mode, with single polarisation (HH or VV) and 250-350 km swath width..

While a relatively limited amount of spaceborne L-band SAR data has been acquired in the past (e.g. Seasat, JERS-1, Shuttle Imaging Radar), the planned launch of ALOS and the availability of data from the PALSAR sensor will be the first L-band system to provide routinely available data from space. From previous research it is known that, due to the longer wavelength and thus greater penetration of the microwave energy, the L-band backscatter of first-year and multi-year ice are very similar [12]. Thus, it may be marginal for primary ice typing as compared to higher frequencies (such as C and X-band). However, while C-band backscatter is dominated mostly by surface scattering from the ice and volume scatterers in the upper ice and snow layers, L-band is less sensitive

to the small-scale surface roughness and penetrates much further to provide information on the mechanical deformation features of the ice. Thus, we expect PALSAR data, particularly for cold conditions, to preferentially map fractures and deformation zones compared to C-band which details the ice surface. This includes large-scale topographic features such as pressure ridges, ridgelines, fractures, and rubble zones. Deformation features such as these are another significant navigation hazard. This information will be very useful and complementary to the current C-band data sources from which these features are very difficult to characterize and quantify (Fig. 14).

This sensitivity to structural deformation may also have some advantage over C-band during the melt period. It is suspected that PALSAR data may be able to better separate between ice types during these periods than higher frequencies which are very sensitive to the presence of moisture at or near the ice (and snow) surfaces, which masks the underlying ice. Indeed, it has been shown that L-band has some potential to discriminate between thick and thin ice at this time in the seasonal cycle due to reduced absorption loss as compared to C or X-band [12].

C-band wavelengths are very sensitive to surface roughness and during the freeze-up period the presence of frost flower formations on thin ice causes high backscatter which can cause confusion with other thicker ice types. The longer wavelengths of L-band are not sensitive to this roughness and thus should result in the ability to resolve this condition when compared and integrated with C-band imagery. It has been suggested that L-band may also improve the contrast between areas with thin and thick snow cover during the summer melt period. This would be an excellent result as during this time when the snow cover is wet and sticky, the thickness of the snow cover can exert as much influence on the ability to navigate through ice as the ice thickness.

The operating modes of PALSAR are somewhat limited for operational sea ice monitoring. While the high resolution modes offer cross-polarization capabilities, the swath width is just 70 km and thus is limited for operational utility. The ScanSAR mode is more attractive with its 250-350 km coverage, similar to RADARSAT's ScanSAR Narrow. However, only single co-pol channel (i.e. HH or VV) selection is possible. Overall, we expect that L-band PALSAR data will prove to be complementary to the currently available SAR data sources. Proper access to tasking the satellite and receiving and processing the data in near-real time will be the key for assessing its potential for sea ice monitoring.

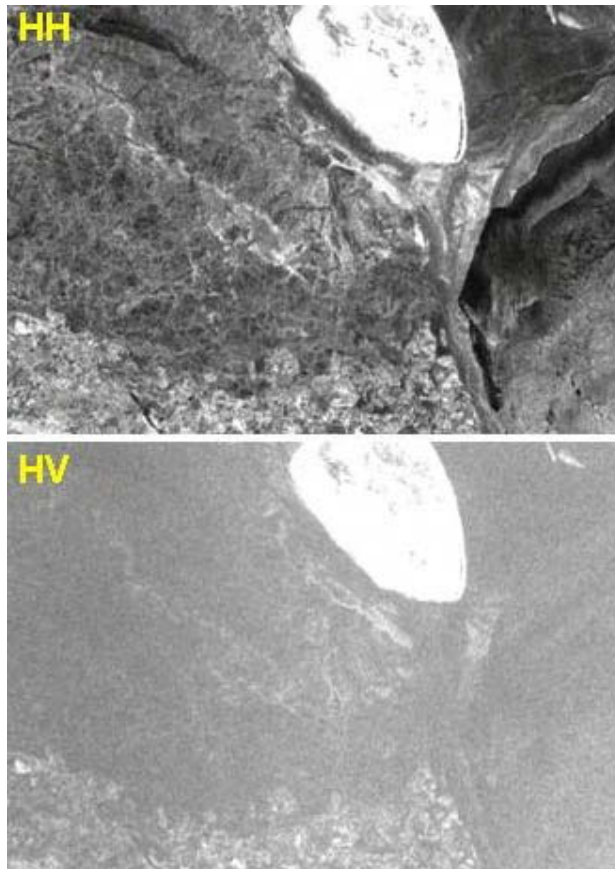


Fig. 13 Envisat ASAR Alternating-Polarization IS6 ($\sim 39\text{--}43^\circ$) image near Resolute Bay, Canadian Arctic. Acquired April 3, 2003. Even when enhanced, the structural detail in the ice pack apparent in the HH channel is not evident in the HV channel. © ESA 2003.

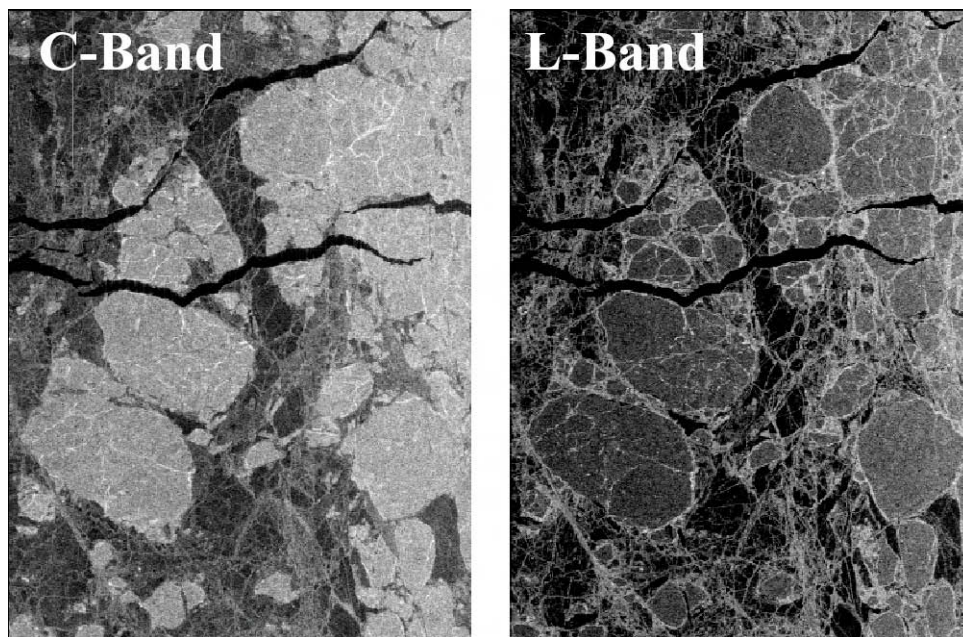


Fig. 14 JPL AIRSAR image of multi-year floes in a first-year ice pack in acquired in the Beaufort Sea, March 1988. Total Power images for C- and L-band illustrating the enhancement of mechanical deformation features in the L-band data.

6.4 TerraSAR

The TerraSAR mission is to make near-simultaneous observations of the Earth in high spatial resolution up to 1 m in X-band and with full polarimetry [13] and high radiometric resolution in L-band [14]. The system will operate using two spacecraft, one with each wavelength/frequency, traveling in the same orbit spaced approximately 12 minutes apart - hence the near-simultaneous observations. TerraSAR will have Spotlight, Stripmap, and ScanSAR modes. The Stripmap modes will provide 30 km swaths at 3-6 m resolution while the ScanSAR mode will have a 100 km swath at 16 m resolution.

The multi-frequency and polarimetric/multi-pol capability of the TerraSAR systems and their complementarity to the existing and planned C-band missions promises to be of great interest to explore the potential for sea ice information extraction. Operationally in a stand-alone mode, their utility may be limited as the ScanSAR mode is restricted to swaths around 200 km or greater (L-band).

6.5 On Sea Ice Polarimetry

The promise of polarimetric data from the future proposed satellite SARs is intriguing in terms of how this could be exploited operationally. At present, the specifications for planned polarimetric modes are swath-limited for use in operational ice monitoring (i.e. < 50 km). Additionally, the data volumes will be quite large and processing and delivery times will likely increase as well. Thus, while research has shown that fully polarimetric data shows potential for providing increased ice information, its use will depend on the trade-off between the limited coverage and the actual utility of the increased information, plus the ability to extract it effectively and consistently. At present, it is likely that, at least initially, the use of polarimetric data for ice monitoring operations will be limited to R&D activities.

It is suggested that multi-frequency data is perhaps more attractive than polarimetry for ice applications, particularly when combined with multi-polarization. The information from different frequencies (e.g. X, C, and L) could be most complementary (Fig. 15). Again, the availability of such data sets would necessitate careful implementation in an operational environment to ensure timely and efficient integration and use of the data. Data fusion, data integration, and automation would be key elements in this regard as data overload could hinder, not help, effective operations.

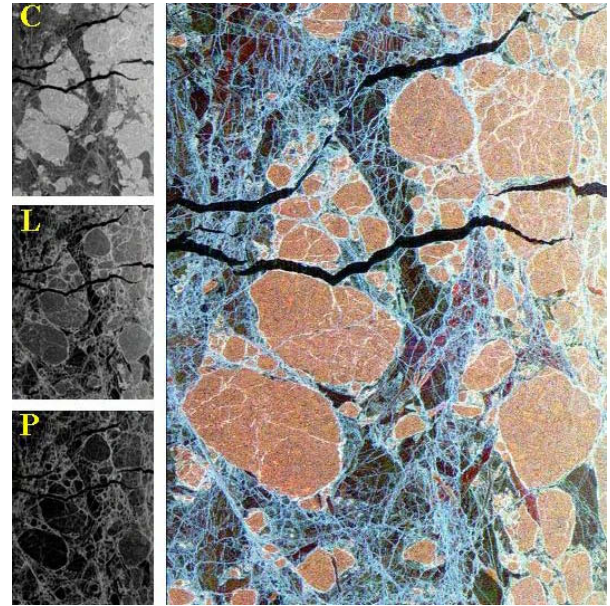


Fig. 15. Multi-frequency JPL AirSAR data of sea ice from the Beaufort Sea acquired in 1988. Total Power images for C, L, and P bands and false colour composite (Red: C-band; Green: L-band; Blue: P-band) illustrating the visual synergy of the three frequencies when combined.

6.6 On Automated Information Extraction

While the CIS does run an automated algorithm to extract ice motion from SAR imagery and has done so for several years, it is not used operationally to provide information for ice forecasting. However, it is being used for model verification and case studies on ice dynamics. Additionally, the CIS is planning on experimenting with assimilating this information with model output to improve forecast model drift.

The CIS has been working with C-CORE over the last several years on developing automated tools for detecting icebergs in SAR imagery. The capabilities of RADARSAT-1 for iceberg detection have been well documented [15] and are well understood. Tradeoffs must be made between coverage (swath) and detection capability (resolution). Also, incidence angle and sea state greatly affect detection performance. Modes with incidence angles greater than 35-40 degrees afford the best detection results and minimize false alarms. C-CORE began delivering iceberg detection information services derived from SAR to the U.S. International Ice Patrol (IIP) during the iceberg season of 2003 under their ESA-sponsored GMES (Global Monitoring for Environment and Security) project. While developed based on RADARSAT-1 data, the capability has been expanded to use Envisat data, and early results suggest that the Alt-Pol mode (HH and HV) provides additional information which can be used to improve ship versus iceberg discrimination. C-CORE will be

providing both the IIP and the CIS with iceberg detections from Envisat during the 2004 season. Additionally, the CIS will be running the Iceberg Detection Software (IDS) developed by C-CORE and operationally evaluating the integration of SAR-derived detections with traditional data sources (e.g. ship/shore reports and visual airborne reconnaissance).

Robust automated ice classification from SAR has been an elusive goal in the operational sea ice community for years, and is still in the research domain. Results using single channel SAR have generally been less than impressive, particularly for wide-swath modes which span large incidence angle ranges thus resulting in widely varying and overlapping ice (and water) signatures. Recent results with polarimetric data suggest that there is potential for improved classification performance by exploiting the full scattering matrix to extract additional parameters other than the co- and cross-pol channels to be used in the classification process [16]. However, as noted before, the near-future planned polarimetric modes will be swath-limited. Of more recent interest are initially promising results achieved with Envisat Alt-Pol data combining both channels to segment ice and water automatically [7]. Currently, the output classes must still be assigned either ice or water by the analyst, but if this method should prove robust, we envision the potential for development of an automated ice/water product using just the SAR image data, and perhaps other ancillary information.

7. SUMMARY

In summary, it is expected that the main near-term operational benefit of the future SAR sensor capabilities for ice monitoring beyond redundancy and greater flexibility will be the availability of multi-polarization data for improved information retrieval and feature discrimination, primarily ice versus water. However, the noise floor of the satellite systems and the reduced signal response in the cross-polarization channels may limit the separation of water and new ice types and distinction of ice topography and ridging. As an additional benefit, it also appears that the availability of cross-polarized data is expected to improve the detectability of icebergs and discrimination from ships.

Of highest interest in the new satellite systems are imaging modes which combine wide-swath and polarization diversity. RADARSAT-2 will offer selective-polarization in the 500km ScanSAR mode and will provide large area like- and cross-polarization observations well suited to operations. Envisat-ASAR and ALOS-PALSAR will offer selective- or alternating-polarization but only in their 100km

imaging modes, so operational use of the multi-channel capability will be targeted to specific ship routes and harbours. Work is also underway to assess the robustness of multiple polarization ice/water segmentation with ASAR.

While polarimetric data, particularly multi-frequency polarimetric data, shows promise for ice typing and classification [10;17], wide-swath systems are not currently available or planned. Also, it is still not clear at present whether polarimetry is of any practical benefit and added value to existing operational services. It is still relatively unknown what additional ice information will be retrievable from polarimetric data that could be of utility for operational ice monitoring. Based on data which has been around for over a decade, multi-frequency data may be more attractive for sea ice. In reality there has been a relatively limited body of work on analysis of both polarimetric and multi-frequency sea ice data sets, particularly over a variety of surface and environmental conditions, and at different frequencies. In this respect, the availability of these modes of data from future SARs will be useful to more fully explore their dimensionality and potential for ice applications.

8. REFERENCES

1. Johnston, M. and Flett, D., "First Year Ridges in RADARSAT ScanSAR Imagery: Influence of Incidence Angle and Feature Orientation", *Proceedings International Symposium on Remote Sensing in Glaciology*, College Park, Maryland, USA, 4-8 June, 2001.
2. Holt, B. and Kwok, R., "Sea Ice Geophysical Measurements From SEASAT To The Present With An Emphasis On Ice Motion: A Brief Review And A Look Ahead", *Proc. Second Workshop on Coastal and Marine Applications of SAR*, this issue, 2004.
3. Nghiem, S.V. and Bertoia C., "Study of Multi-Polarization C-Band Backscatter Signatures for Arctic Sea Ice Mapping with Future Satellite SAR," *Canadian Journal of Remote Sensing*, vol. 27, no.5, October, 2001.
4. De Abreu R., Flett D., Scheuchl B., and Ramsay B., "Operational Sea Ice Monitoring with RADARSAT-2 – A Glimpse into the Future," *Proceedings, IGARSS 2003*, Toulouse, France, July 21-25, 2003.
5. Hawkins, R.K. and Flett, D.G., "Applications of AP Products", *ASAR Session Presentation, Envisat Validation Workshop*, ESA, Frascati, Italy, Dec 10-13, 2002.

6. Scheuchl, B., Caves R., Cumming I., and Staples G., "Automated Sea Ice Classification Using Spaceborne Polarimetric SAR Data," *Proceedings, IGARSS 2001*, Sydney, Australia, July 9-13, 2001.

7. Scheuchl, B., *Utilization of Multi-Polarization and Polarimetric Data for Sea-Ice Monitoring in an Operational Environment – Final Report*, MDA report RX-RP-51-4919 1/0 for Canadian Space Agency, November, 2003.

8. Flett, D.G., "C-Band Polarimetric Synthetic Aperture Radar Signatures of Winter Sea Ice Conditions" Masters Thesis, University of Waterloo, Waterloo, Ontario, April 1997.

9. Livingstone, C.E., Chapter 11 – Synthetic Aperture Radar Images of Sea Ice, In: Haykin et al., (Eds.), *Remote Sensing of Sea Ice and Icebergs*, John Wiley and Sons, Inc.: 540-569, 1994.

10. Makynen, M, and Hallikainen M., "C-Band Backscattering Signatures of Baltic Sea Ice", *Proceedings IGARSS'98*, Seattle, Washington, July 6-10, 1998.

11. Rosenqvist, A., Ichitsubo, D., Osawa, Y., Matsumoto, A., Ito, N., and Hamazaki, T., "A brief overview of the Advanced Land Observing Satellite (ALOS) and its potential for marine applications", *Proc. Second Workshop on Coastal and Marine Applications of SAR*, this issue, 2004.

12. Drinkwater, M.R., Kwok R., Winebrenner D.P., and Rignot E., "Multifrequency polarimetric synthetic aperture radar observations of sea ice", *Journal of Geophysical Research*, 96(C11): 20,679-20,698, 1991.

13. Lehner, S., Horstmann, J., Schulz-Stellenfleth, J., Roth, A., and Eineder, M., "TerraSAR-X for Oceanography – Mission Overview", *Proc. Second Workshop on Coastal and Marine Applications of SAR*, this issue, 2004.

14. Zink, M., "The TerraSAR-L System and Mission Objectives", *Proc. Second Workshop on Coastal and Marine Applications of SAR*, this issue, 2004.

15. C-CORE, "The capabilities for iceberg detection using RADARSAT-1", C-CORE Contract P-03-037 report for the Canadian Ice Service, January, 2004.

16. Scheuchl, B., Caves R., Cumming I., and Staples G., "H/A/ α -based classification of sea ice using SAR polarimetry," *Proceedings 23rd Canadian Symposium on Remote Sensing*, Quebec, Canada, August 21-24, 2001.

17. Scheuchl, B., Hajnsek, I., and Cumming, I., "Sea Ice Classification Using Multi-Frequency Polarimetric SAR Data", *Proceedings, IGARSS 2002*, Toronto, Ontario, Canada, 2002.

Table 1. Canadian Ice Service Ice Information Requirements

Ice information requirement		Primary			Secondary					Iceberg
		Ice/water boundary or Ice edge	Ice concentration	Stage of development (e.g. new, thin, first-year, and multi-year ice)	Presence and location of leads (open water)	Ice thickness	Ice topography and roughness	Ice decay state (or, more specifically, Ice strength)	Snow properties (e.g. thickness; also wetness, density)	Iceberg detection
Spatial resolution	strategic	5 km	+/- 10% requires resolution < 100 m	50-100 m	50-100 m similar to ice concentration	5 km for average thickness over an area to +/- 20 % of total thickness	< 50 m to determine extent of ridging; need average ridge heights to within +/- 20 %	20 km for average strength over an area to +/- 20% of total strength	5 km for average snow depth to +/- 20 %	< 50 m
	tactical	<1 km	+/- 5 % requires resolution < 25 m	<20 m	<20 m	< 100 m to determine average and maximum thickness (including rafting) over an area to +/- 10% of total thickness	< 10 m to determine mean and maximum ridge heights to within +/- 10 %	5 km for average strength over an area to +/- 10% of total strength	1 km for average snow depth to +/- 10 %	<5 m
Temporal resolution	strategic	daily	daily	daily	daily	2x/week	daily	weekly	weekly	daily
	tactical	6 hours	6 hours	6 hours	6 hours	daily	6 hours	daily	daily	hourly
Description		In case of a diffuse ice edge, the CIS defines the ice/water boundary as 10% ice concentration	Percentage of ice covered area. Ice concentration is a key parameter in the WMO egg code	Ice classes are defined by WMO	Leads and polynyas	Important for navigation and/or loads on structures (Remark: Rafts show double or more the average floe thickness)	Presence, location and height of ridges Roughness indicated by concentration of ridges (in % or in number per unit area) – ridge density plus average height (or total thickness) of ridges	Identification of melt onset and ponding	To determine hull friction for ship resistance – also important for ice strength	Detection and tracking, possibly classification of type

SEA ICE GEOPHYSICAL MEASUREMENTS FROM SEASAT TO THE PRESENT, WITH AN EMPHASIS ON ICE MOTION: A BRIEF REVIEW AND A LOOK AHEAD

Benjamin Holt ⁽¹⁾ and Ron Kwok ⁽²⁾

⁽¹⁾*Jet Propulsion Laboratory, California Institute of Technology, Pasadena CA, 91109, USA, Email: Ben.Holt@jpl.nasa.gov*

⁽²⁾*Jet Propulsion Laboratory, California Institute of Technology, Pasadena CA, 91109, USA, Email: Ron.Kwok@jpl.nasa.gov*

ABSTRACT

NASA launched Seasat in June 1978 carrying a remarkable array of microwave instruments designed to observe the global oceans, including an active microwave altimeter, scatterometer, and SAR along with a passive microwave radiometer. While the satellite mission ended abruptly in mid-October 1978 after only about 100 days of operation, unique and comprehensive views of the oceans were obtained that clearly showed the extraordinary scientific value of the instruments by improving the knowledge of the oceans circulation, wind and wave field, and characterization of key aspects of the cryosphere. Aside from optical and thermal sensor data, this data set from 25 years ago essentially set the stage, providing a legacy if you will, for most of the major dedicated ocean satellite missions that have taken place since and are planned for the near future.

In this paper, we provide a short review of sea ice measurements starting from Seasat, including sea ice motion, the seasonal melt cycle, ice extent and concentration, and estimates of thickness from the proxy measurements of ice type and age and more directly from freeboard. We end with a brief discussion on how these measurements might be improved in the future.

1. SEA ICE AND CLIMATE

Sea ice plays a key role in Earth's climate and has long been thought to be a primary candidate as an indicator of global warming, of particular value since the polar regions are projected by global climate models to undergo the largest greenhouse warming (e.g. Kattenberg et al., 1996). Sea ice acts to reduce the flux of heat from the comparatively warm ocean to the colder atmosphere. When open water appears as the ice cover moves and deforms, the heat flux increases tenfold, which then gradually decreases as new ice forms and thickens. During ice formation, salt is released from the ice crystallization process to form brine, which is entrained within the ice and eventually drains out of the ice into the upper ocean. Rapid ice growth and subsequent salt rejection may result in locally dense water that mixes downward into the ocean column until it reaches its equilibrium depth. In fact, the dense water formed within areas of intense ice growth contributes significantly to formation and maintenance of the deepest waters of the world's oceans. The nearly salt-free sea ice is gradually transported equatorward by ocean currents and winds to eventually melt, putting freshwater back into the ocean at another location from initial formation which may impact ocean vertical mixing. The final key interaction is that sea ice has a high albedo during winter that effectively reflects incoming heat back to the atmosphere. Albedo is sharply reduced when summer melt takes place, with absorption of short-wave radiation increasing

Recent observations strongly indicate significant climatic changes in sea ice are taking place, particularly within the Arctic. The Arctic sea ice cover was found to have thinned by over 40% between 1958-1976 and 1993-1997 as measured by submarine-mounted upward-looking sonar (Rothrock et al., 1999; 2003). The Arctic ice cover has decreased in both maximum (Johannessen et al., 1999; Parkinson and Cavalieri, 2002) and minimum (Comiso, 2002) areal extent since the late 1970s. The length of the Arctic melt season appears to be increasing (Smith, 1998), which combined with the decrease in minimum extent, suggests lengthening periods of low albedo and increased heating of the extended areas of open ocean, which most likely will delay and thus reduce sea ice growth during the following winter. Hydrographic data from recent submarine and icebreaker cruises reveal large-scale changes in the structure of the Arctic upper ocean (Steele and Boyd, 1998; Bjork et al., 2002). Some of the above changes appear to be highly correlated with the North Atlantic Oscillation (NAO) and related Arctic Oscillation (AO), which are indexes of sea level pressure anomalies in the Northern Hemisphere (Proshutinsky and Johnson, 1997; Steele and Boyd, 1998). These patterns strongly affect the dominant pressure fields in the Arctic and thus both the upper ocean and ice circulation. During the late 1980's through the late 1990's, the NAO/AO index remained positive, which resulted in a weakening of the Beaufort Sea cyclonic gyre and an increase in ice transport across the Arctic and out through the Fram Strait into the North Atlantic (Kwok and Rothrock, 1999; Kwok, 2000). This pattern is thought to have reduced the overall longevity of sea ice within the Arctic and thus the thinning in mean thickness and related volume as measured by submarine sonar data.

From this simplistic view of the key sea ice interactions and the recent changes taking place, the primary geophysical measurements needed to monitor the state of the sea ice cover include thickness distribution, extent, amount of open water, albedo, and motion. The broad, synoptic view is best done with satellites and microwave sensors to provide the all-weather year round vantage point. The Seasat instrument suite was the first demonstration of four complementary microwave sensors to provide these measurements. Most of the above measurements are made directly while thickness measurements have proven to be more elusive and thus have been largely measured indirectly.

2. SEASAT INSTRUMENTS

The Seasat instruments were designed to return the maximum information from the ocean surface, including sea ice in the polar oceans. The Radar Altimeter (ALT) carefully measured the spacecraft altitude above the ocean surface, which provided wave

to ± 2 m/s and 20 deg. in direction. The Scanning Multichannel Microwave Radiometer (SMMR) was used to measure surface wind speed (± 2 m/s), ocean surface temperature (± 2 deg C), atmospheric water vapor content, rain rate, and ice coverage. The SMMR operated at 6.6, 10.7, 18, 21, and 37 GHz with a 600 km swath width. The first passive microwave radiometer (Electronically Scanning Microwave Radiometer or ESMR) was flown in 1973 and an identical SMMR to Seasat's was launched on Nimbus 7 in November 1978, just after the Seasat mission. The Synthetic Aperture Radar (SAR) was designed to image the ocean surface (wave patterns), polar ice, and coastal regions. The SAR operated at L-band (1.275 GHz), with a single polarization of horizontal transmit-horizontal receive (HH), a fixed 100 km swath over an incidence angle range of 20-26°, and a resolution of 25 m. The National Oceanic and Atmospheric Administration (NOAA) provided a fifth instrument to the Seasat mission, a visible and infrared radiometer (VIRR), from their weather satellite program to provide surface mapping that could be compared to the data from the radar sensors.

Seasat was launched on June 26, 1978, from Vandenberg Air Force Base, California, into a near-circular polar orbit at an altitude of about 800 km and an inclination of 108°. The mission ended suddenly on October 10, 1978 due to a failure of the vehicle's electric power system. Although Seasat was operational for only about 100 days, the mission not only demonstrated the feasibility of using microwave sensors to monitor ocean and sea ice conditions, but also laid the groundwork for many future missions. Evans et al. (2003) has recently summarized the legacy instrumentation and geophysical measurements accomplished since Seasat.

3. SEA ICE MEASUREMENTS

We discuss four primary sea ice geophysical measurements from microwave spaceborne sensors: ice motion, ice extent and concentration, the seasonal melt cycle, and ice thickness.

3.1 Ice Motion

In this section, we discuss fine resolution ice motion first from the SARs on Seasat and ERS-1 and then RADARSAT, followed by motion fields derived from coarse resolution sensors.

3.1.A SAR Ice Motion

The motion of sea ice provides critical information on the ice cover over several scales. On scales larger than several hundred kilometers, the general circulation of the ice cover provides the advective component of the ice mass balance as well as a velocity boundary condition on the ocean surface. On smaller scales of kilometers, motion fields show the detailed motion of individual floes, how ice floes move as aggregates, the opening of leads, and the ridging processes. Ice motion controls the abundance of thin ice and therefore the intensive heat flux from the ocean to the atmosphere, ice production, and salinity flux. Accurate measurements of ice motion on a continuous basis over a broad region can be used in other key geophysical derivations.

Seasat SAR provided the first extensive fine resolution SAR images of the western Arctic sea ice, enhanced by the 'collapse' of orbits in the polar regions which improves temporal sampling. The imagery was used to make the most detailed sea ice motion maps ever produced at the time, from which openings and closing

of the ice cover clearly revealed where the largest heat exchange from the ocean to the air takes place. The identification of individual floes between images separated by a few days in time enabled the unambiguous tracking of the ice field within the central pack ((Hall and Rothrock, 1981; Curlander et al., 1985), where a deformation grid showed areas of motion and no motion (Fig. 1) (Fily and Rothrock, 1987), and at the ice margins, where free drift is prevalent and the motion field can be significantly impacted by wind and upper ocean forcing (Fig. 2) (Carsey and Holt, 1987).

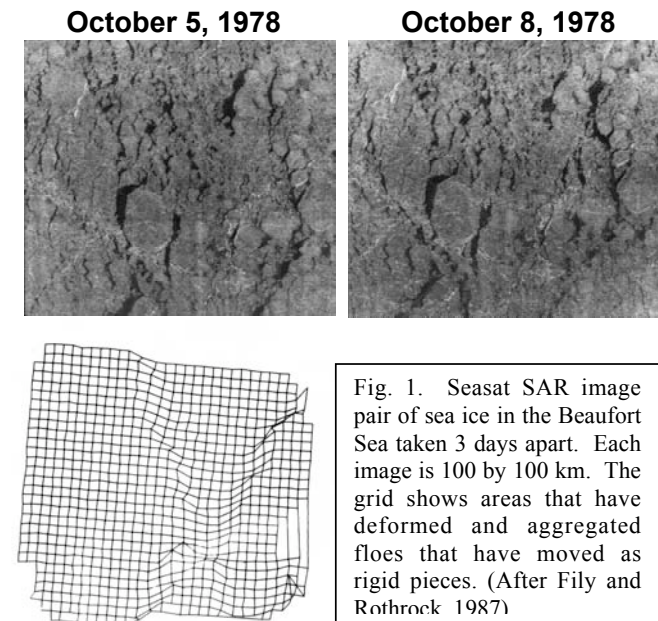


Fig. 1. Seasat SAR image pair of sea ice in the Beaufort Sea taken 3 days apart. Each image is 100 by 100 km. The grid shows areas that have deformed and aggregated floes that have moved as rigid pieces. (After Fily and Rothrock 1987)

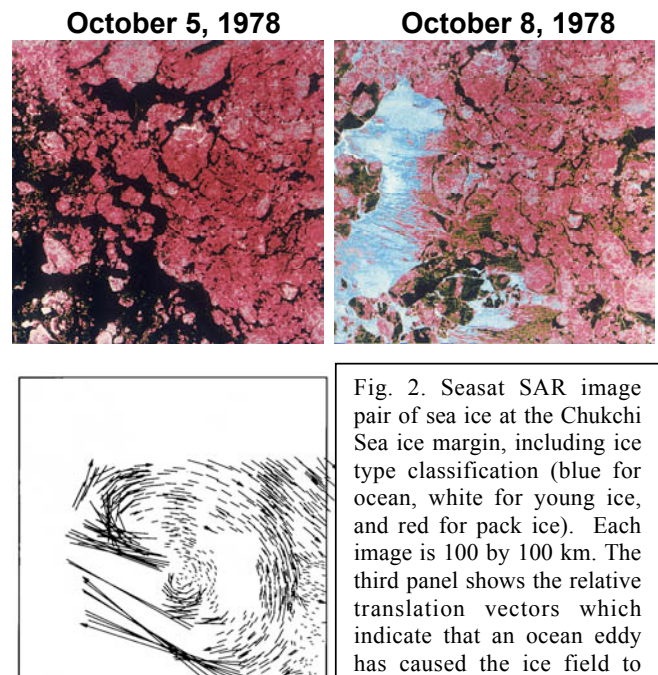


Fig. 2. Seasat SAR image pair of sea ice at the Chukchi Sea ice margin, including ice type classification (blue for ocean, white for young ice, and red for pack ice). Each image is 100 by 100 km. The third panel shows the relative translation vectors which indicate that an ocean eddy has caused the ice field to rotate and form an open water area. (After Carsey and Holt, 1987).

The Seasat SAR ice motion maps generated considerable interest, sufficient to form the scientific rationale for NASA to support the development of the Alaska SAR Facility in Fairbanks, Alaska, to receive ERS-1 SAR imagery of the Arctic. There was a related flurry of activity to develop satisfactory image processing algorithms, which could efficiently capture the dynamic ice motion fields under varying ice conditions and radar signatures. This led to the development of the first geophysical SAR product generation system, designed to automatically produce ice motion maps from ERS-1 SAR imagery (Kwok et al., 1990). Also included in this system was an algorithm for identification of sea ice types (see 3.4).

3.1.B. RADARSAT Geophysical Processor System.

The experience gained from the initial ice motion algorithm development led to the next generation of motion observations capitalizing on the wide swath capability of the Canada's RADARSAT-1, called the RADARSAT Geophysical Processor System (RGPS) (Kwok, 1998). This satellite has provided complete coverage maps of the entire Arctic Ocean every 3-6 days continuously since October 1996. Included in this second-generation product system was the addition of a very significant tracking enhancement. The first algorithm utilized Eulerian tracking, which tracks floes from image A to image B and then resets the grid to track floes from image B to image C (Kwok et al., 1990). The RGPS was implemented using Lagrangian tracking, which tracked a grid element (cell) continuously over time without reinitializing between image pairs (Kwok et al., 1995). With Lagrangian tracking, not only could the trajectory and detailed deformation of that element be observed, but the age of any newly formed ice as well as loss of ice area to ridging could be derived as well (see 3.1.4). The semi-automated RGPS allows the analysis of the relatively large volume of high-resolution of SAR data of over 1 GB per day.

The following provides a brief description of the RGPS approach used in estimating ice age and thickness from the time-varying cell deformations derived from ice motion. An age histogram of sea ice specifies the fractional area covered by ice of different chronological ages. The construction of such a histogram involves the steps below. At each time step, positive area changes are interpreted as the creation of areas of open water. New ice is assumed to grow over these areas immediately after opening. For this ice, a new age category in the histogram is introduced. At the same time, pre-existing age categories in the histogram are 'aged' by the length of the time step. A decrease in cell area is assumed to have ridged the youngest ice in the cell, reducing its area. The assumption here is that once ridging starts, the deformation tends to be localized in the recently formed thinner and weaker ice in leads. This area of ridged ice is tracked as a separate category in the age histogram. In Fig. 3, this procedure created five age categories from the sequence of positive area changes since Day 335. Ice age is converted to ice thickness using an empirical ice growth formula. The growth rate is approximated using Lebedev's parameterization, which depends on the number of freezing-degree days. Volume is conserved and ridged ice is assumed to be five times its original thickness and occupies a quarter of the area [Parmerter and Coon, 1972]. The dataset provides fine age/thickness resolution of only the young/thin end of the age/thickness distributions, but this is the crucial range that produces the most ice growth, the most turbulent heat flux to the atmosphere and the most salt flux to the ocean.

For a given winter, typically 30,000 grid cells with initial dimensions of 10 km on a side are used to sample the motion and deformation of the ice cover. Effectively, this is identical to deploying the same number of drifting buoys. Fig. 4 shows a basin-scale view of the divergence, vorticity, and shear of the ice cover sampled by the RGPS cells. The deformation fields show linear kinematic features (LKFs) that characterize the opening, closing, and shear of the ice cover. These high-resolution ice motion vectors derived from the RGPS, with data quality comparable to that from buoy drifts (~ 0.1 cm/s) [Lindsay and Stern, 2003], have provided an unprecedented level of spatial and temporal detail of deformational features. For the first time, we can map on a routine basis the location, coverage, and seasonal development of leads and ridges. The RGPS data have shown that narrow fracture zones (up to kilometers wide) are long linear features that can extend for thousands of kilometers and these fracture patterns appear as oriented rather than random patterns from the kilometer scale to the scale of the Arctic basin (Fig. 4). With the advent of high-resolution coupled ice-ocean models (10 km) that approaches the widths of leads, there is an increased need for high-resolution measurements for validation of model results [e.g. Zhang et al., 2003]. Simulation and model performance can now be examined in detail using the small-scale RGPS observations now available [Hibler, 2001; Richter-Menge et al., 2002].

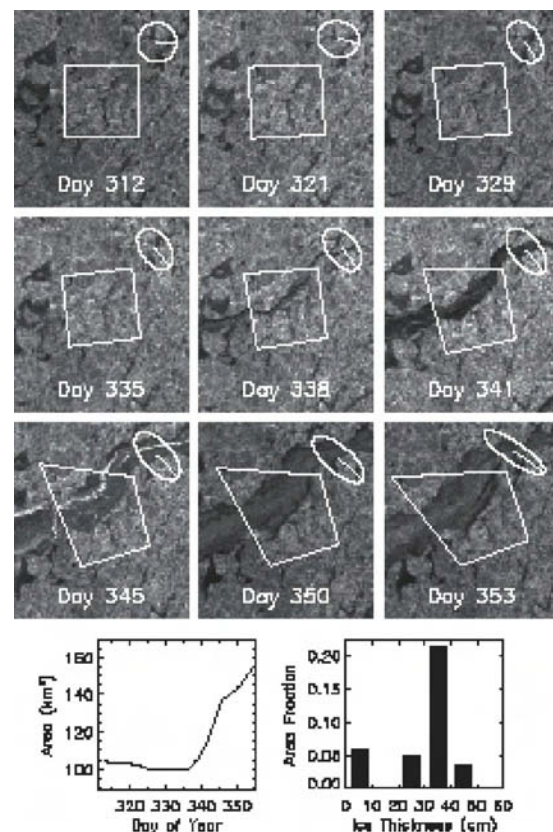


Fig. 3. The deformation of a 10 km by 10 km cell over a 41-day period is shown from RADARSAT. The record of area change reflects the opening of the lead running through the cell. The strain ellipses are computed from strain rates.

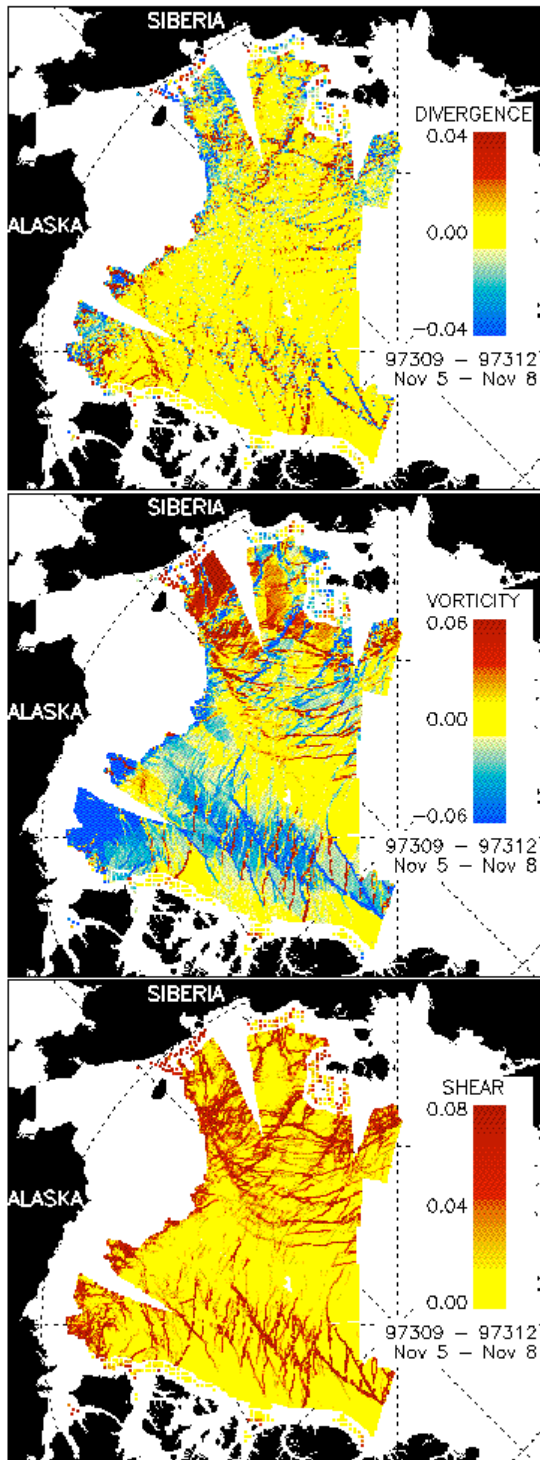


Fig. 4. The deformation of the ice cover over three days between Day 309 and 312 in 1997 derived from RADARSAT data by the RGPS. (a) Divergence. (b) Vorticity. (c) Shear.

As of this writing, the RGPS has produced ~4 years of sea ice observations of the Arctic Ocean. Extensive measurements of the ice motion can be used in concert with a variety of ice models for verification studies, for driving the models as forcing fields, and in data assimilation procedures. The ice production rates estimated with RGPS can be compared to those computed by models driven

by the geostrophic wind and a force balance approach. The ice motion measured with RGPS can be used directly as a forcing field for an ice model and the uncertainty in the ice motion can thus be reduced. Finally, the RGPS ice displacement measurements can be assimilated directly into an ice/ocean model so that ice trajectories in the model can be made to match the observed trajectories. The value of these uses for the RGPS products will increase as the observational record becomes longer and a greater variety of seasons are recorded. The preliminary results for four winter seasons have seen that the ice cover evolved in markedly different manners. Ultimately, a long record of the ice deformation and ice production rates can be developed that will contribute to the assessment of the evolution of the Arctic Ocean.

3.1.C Lower Resolution Ice Motion Fields

Ice motion fields also have been produced from a variety of lower resolution sensors. It has been demonstrated [Agnew et al., 1997; Emery et al., 1997; Liu and Cavalieri, 1998; Kwok et al., 1998] that despite antenna footprints of ten or more kilometers, data from low-resolution passive microwave radiometers and scatterometers can provide rather coarse measurements of ice motion. The combination of daily ice motion from the 85 GHz channel of SSM/I and 2-day ice motion from the 37 GHz channel of SMMR, has provided an ice motion data record dating back to 1978. The quality of the scatterometer motion fields (~5 km uncertainty in displacement) obtained from NSCAT and SeaWinds on QuikSCAT (Liu et al., 1999) are comparable to that derived from the 85 GHz SSM/I data. The daily ice motion measurements from QuikSCAT seem complementary to the passive microwave observations. The relative merits of the scatterometer versus the passive microwave ice motion remain to be examined. Summer ice motion from scatterometers and radiometers are unreliable due to surface melt and, in the case of passive microwave data, the added contamination by increased atmospheric water content with increasing temperature. With the level of uncertainty from these low resolution data, these measurements are more suited to the study of large-scale circulation patterns [Emery et al., 1997; Kwok, 2000] and ice export [Kwok and Rothrock, 1999; Martin and Augstein, 2000], rather than the small-scale processes associated with openings and closings of the ice cover.

Sequential AVHRR imagery provides moderate resolution ice motion from its visible, near-infrared, and thermal infrared bands with uncertainties of 1 km and 5 km, depending on the data products. The thermal bands can be used in winter darkness. The only drawback is that clouds obscure the surface, moderately during the winter and quite substantially during the summer. An ice motion data set dating back to 1982 is available at the National Snow and Ice Data Center in Boulder, Colorado.

3.2 Ice Extent and Concentration

The extent of the sea ice cover is highly correlated with air temperature, since ice will only form when the upper ocean temperatures have been sufficiently cooled to the freezing point by overlying air temperatures. Ice concentration provides an estimate of the percent of open water and ice within the ice cover, which can provide an indication of the heat fluxes and ice production. The multi-channel combinations of the spaceborne passive microwave radiometers are sensitive to open water and ice, which combined with the all-weather, broad daily coverage of the polar regions, results in these sensors being a primary observational sensor for ice extent and concentration.

The ice extent measurements from these sensors provide the longest continuous time series of sea ice observations available, dating back to 1978, and have been extensively used to examine climatic trends. As mentioned before, the Arctic has undergone considerable recent retreat in ice extent (e.g. Johannessen et al., 1999; Parkinson and Cavalieri, 2002; Comiso, 2002) while the Antarctic sea ice cover has shown a slight increase in extent (Zwally et al., 2002A). Recent studies have examined possible improvements to ice edge detection with higher resolution data, including from the recently launched AMSR sensors, and also from other sensors including the scatterometers on NSCAT and QuikSCAT, and the wide swath SAR on RADARSAT (Yueh et al., 1997; Remund et al., 2000).

3.3 Seasonal Melt Cycle

With the onset of sea ice melt, surface albedo is reduced allowing more absorption of short-wave radiation. The open ocean adjacent to the sea ice also is warmed, enhancing lateral ice melt. When the air temperatures cool below freezing in fall, the switch is reversed, signalling the increase in albedo and the end of significant freshwater flux from sea ice to the ocean. Soon after the end of melt, the surrounding water will eventually cool to freezing when ice formation is initiated. The duration of the melt season and the resulting open water play important roles in the overall sea ice mass balance (e.g. Zhang et al., 2000). Albedo is a difficult measurement to obtain, as it is impacted by ice type, snow cover, temperature, ice concentration and cloud cover, which by themselves are difficult to measure in summer. The seasonal melt cycle is detectable by both active and passive microwave sensors, which provide a method of capturing melt duration or the effective period of reduced albedo.

Both the SASS and SMMR were found to be sensitive to the presence of liquid water (Carsey, 1985). Melt onset is commonly a rather sharp transition when the snow and ice surfaces become wet, which results in a sharp reduction in backscatter and an increase in brightness temperature (Fig. 5). During mid-summer, the surface conditions can vary rapidly as melt ponds form and then drain and as air temperatures cycle rapidly above and below freezing. Freeze-up is usually considered as the end of surface melt, where the above trends in brightness temperatures and backscatter reverse. Freeze-up tends to be more gradual, however, and the responses can rapidly vary until settling into characteristic winter-like sea ice signatures.

Most time-series studies of sea ice seasonal transitions in the Arctic focus on melt onset using passive microwave radiometers (Drobot and Anderson, 2001). A correlation between varying melt onset dates has been found with the AO index, indicating the sensitivity of this signal to air temperature (Drobot and Anderson, 2001). A combined sensor analysis using SMMR and NSCAT has shown substantial differences in the date of melt onset (Forster et al., 2001). Combining RADARSAT and SSM/I, substantial variation during the seasonal cycle was related to the extent of melt ponding and new ice formation after freeze-up (Comiso and Kwok, 1996). Scatterometer seasonal cycles have also been examined in the Antarctic using scatterometer data from ERS and NSCAT (Drinkwater and Liu, 2000). The single time series study using both SMMR and SSM/I, where both seasonal transitions were detected, showed an apparent increase in the duration of the melt season had occurred between 1978-1996 (Smith, 1998). SAR algorithms for both melt onset (Winebrenner et al., 1994; De Abreu et al., 2001) and freeze-up (Winebrenner et al., 1996) were

developed and demonstrated for limited regions. Recently, melt onset maps of the entire Arctic were developed using RADARSAT data (Kwok et al., 2003).

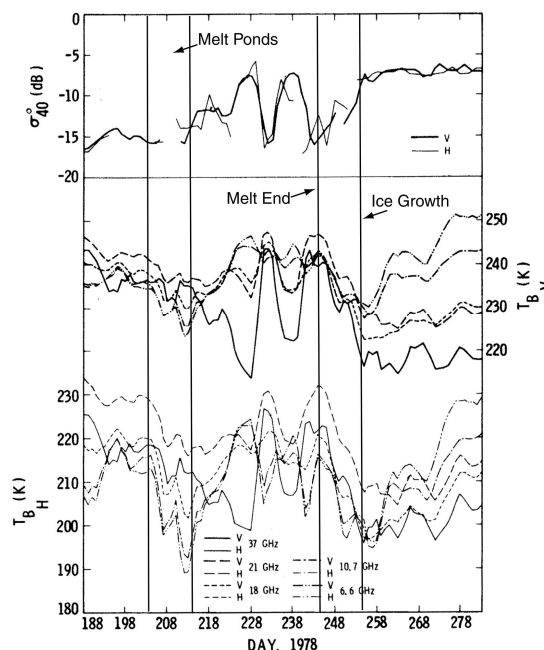


Fig. 5. The seasonal cycle of sea ice melt in the Beaufort Sea detected by the Seasat SASS (top panel) and SMMR (bottom panel) in 1978. Melt onset and freeze-up occur on about day 204 and day 245, respectively. Also indicated are the formation of melt ponds and the beginning of ice growth. (After Carsey, 1985).

3.4 Ice Thickness and Its Proxy Measurements

Ice thickness is the single most important sea ice measurement, having been discussed as the 'great integrator' of polar climate, because thickness responds to fluxes and forcings in both the atmosphere and ocean. Thickness is thought to be the primary indicator of global greenhouse warming, yet it has proven to be one of the most difficult variables to measure particularly on meaningful synoptic and climatic scales including from satellites (U. S. National Research Council, 2001). The most comprehensive thickness measurements have been obtained from upward-looking sonar data mounted on submarines or moorings. The submarine-based results provide synoptic but highly irregular ice draft measurements over the central pack ice dating back to the 1950s, but until recently these data were classified and difficult to access. Fortunately, in the early 1990's the US Navy made submarine cruises available for scientific exploitation, which also helped make data from earlier cruises more accessible for analysis and publication. From these data, Rothrock et al. (1999) found a decrease in mean sea ice draft—portion of ice below the ocean surface—from 3.1 m in 1958-1976 to 1.8 m in 1993-1997.

From a remote sensor, there are several approaches that may be taken to measure thickness. One approach is to measure freeboard, the portion of the ice cover above sea level. This requires highly accurate measurement of the absolute height since freeboard is approximately 10% of the entire sea ice thickness volume, the identification of open water to correct for freeboard, and some knowledge of the overlying snow cover. Both laser and radar altimeters provide important approaches for freeboard

measurements. Another possible approach is the direct detection of both the ice surface- and bottom-sides. This requires lower than normal spaceborne radar frequencies (less than 1 GHz) to overcome the lossy nature of sea ice and to penetrate to many meters of thickness. However, as the frequencies less than 1 GHz allocated for scientific research are quite limited, innovative techniques are required to make use of the limited bandwidth to obtain satisfactory vertical resolution. The use of electromagnetic induction (frequencies of tens of Hz) has become a standard in situ device but these measurements have reduced accuracy with increasing height off the ice surface and over thick ice. Low frequency impulse radars were tested with mixed results (Kovacs and Morey, 1986).

More commonly, proxy indicators of thickness have been used, specifically ice type and recently ice age via the RGPS (3.1.B). There is sensitivity to ice types in microwave brightness temperature, surface temperature obtained with near infrared and thermal imagers, and radar backscatter derived with synthetic aperture radars and scatterometers. Various combinations of channels are sensitive to the primary ice types – thin and thick first-year, multiyear ice, and the rapidly varying new and young ice.

All the Seasat instruments were evaluated for ice type to some degree (Carsey, 1985; Carsey and Pihos, 1989) including the use of altimeter waveforms (Ulander, 1987). With ERS-1, it was found that C-band (both SAR and scatterometer) provided much better discrimination between multiyear and first-year ice than Seasat's L-band SAR. While there was still some confusion between young ice and multiyear ice the value of the ice type products was considerable (Kwok et al., 1992; Fetterer et al., 1994; Stern et al., 1995). The wide swath of the C-band RADARSAT data led to significant improvements in ice typing for ice charts developed by the US and foreign ice centers (Bertoia et al., 1998). As first indicated by the Seasat SASS results (Carsey, 1985), the 13-14 GHz frequencies of NSCAT and QuikSCAT enable the clear separation of the perennial and seasonal ice zones, which are currently being developed as a climatically valuable dataset over the Arctic (Kwok and Cunningham, 2002). Lastly, as mentioned previously in 3.1.B, the use of Lagrangian tracking in the RGPS led to the ability to measure ice age (based on initial date of ice formation) (Fig. 4). This key step jumped over the confusion in ice type measurement accuracy by deriving the even more valuable measurement of ice age. This age tracking has been used to derive first year ice thickness over entire winter seasons, thereby accounting for a major component of the mass balance of sea ice, which has been found to vary annually and in relation to the overall transport of ice within and out of the Arctic (Kwok and Cunningham, 2002).

In addition to sea ice typing, the Seasat altimeter was used to measure the elevation of polar ice sheets of Greenland and Antarctic, specifically to estimate mass balance and slope changes in ice shelves (Zwally et al., 2002B). Improvements in the waveform tracking over land were made on the ERS-1/2 altimeters, leading to time series studies of elevation change (Wingham et al., 1998; Zwally et al., 2002B). It was pointed out by Laxon [1994] that height deflections associated with diffuse echoes over ice-covered seas could be used to estimate ice freeboard. The first example of ice freeboard measurements was given in Peacock et al. [1998]. Since only 10% of the floating ice is above the ocean surface, freeboard measurement errors are magnified when applied to estimating ice thickness. Comparisons of altimetric ice thickness estimates with observations of ice draft

from moored and submarine give an estimate of the uncertainty in the retrieved ice thickness of approximately 0.5 m. Fig. 6 shows an example of a gridded field of altimeter ice thickness derived from the ERS-2 radar altimeter. The radar altimeter measurements address the mean ice thickness over length scales of perhaps 100 km.

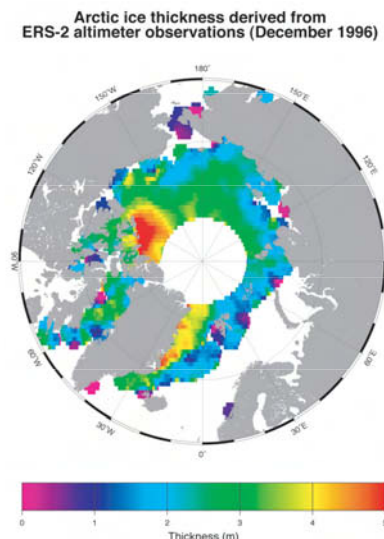


Fig. 6. Gridded (100 km) estimates of ice thickness derived from altimeter measurements of freeboard from the ERS-2 radar altimeter. (Figure courtesy of S. Laxon).

There are still a number of difficulties associated with understanding the achievable accuracy of the freeboard measurement. Some examples include the possible height biases introduced by the snow layer and the dependence of the height measurement on the location of the scattering center (snow-ice boundary or within the snow layer). Another issue is the variability in the estimates due to ice advection and deformation since height estimates within a grid cell are taken from measurements obtained over a month. Nevertheless, this technique represents a significant advancement in the measurement of sea ice thickness. The impact of this method for climate and sea ice studies would be enormous if continual long-term direct observations of ice freeboard and thence ice thickness can be realized.

Just recently, sea ice freeboard measurements from ERS-1 and ERS-2 have shown a high-frequency interannual variability in mean ice thickness that the authors suggest is related to summer melt rather than circulation (Laxon et al., 2003). Such freeboard studies are expected to continue with NASA's laser altimeter on the ICESat mission launched in early 2003, the ENVISAT altimeter launched in 2002, and ESA's upcoming CryoSat radar altimeter mission to be launched in 2004 (Wingham, 1999).

4. DISCUSSION AND FUTURE ASSESSMENTS

We have attempted to briefly illustrate the value of the initial suite of Seasat microwave instruments for sea ice studies and how following missions and sensors have led to the development of critical time series to assess the climatically changing polar regions. Now we provide considerations on how these measurements might be improved in the future.

The RGPS basin-scale products of sea ice age and thickness are truly unique and we anticipate that these data products will have

important utility for use in comparisons with climate models and other sensors and data sets. The RGPS observations points to the importance of understanding the consequence of the ice pack as an anisotropic material with large-scale oriented fracture patterns. For climate studies, the impact of an anisotropic ice cover is not well understood in terms of the modelled surface heat and mass balance. The RGPS data set is a crucial component in the testing of new models that accounts for the spatial and temporal characteristics of the linear kinematic features observed here (Kwok, 2001). Also, the Arctic is undergoing measurable change this decade in several key indicators of climate warming. The to-date 4-year time record from RADARSAT is fortuitously timed to also potentially provide indicators of climate change through ice motion and age/thickness derivations, which are used to determine the surface heat and mass balance of the Arctic Ocean. It therefore seems both desirable and justifiable to continue the unique RGPS derivations over an extended time period. In the future, the synergistic availability of RGPS-type observations of ice kinematics and the ice freeboard observations from ICESat and CryoSat will provide a powerful dataset for characterizing the time-varying changes of the ice volume of the Arctic Ocean.

In terms of general SAR requirements for the RGPS, repeat wide-swath SAR surveys of the entire Arctic at preferably 3-day near repeat sub-cycles are needed to determine the motion field of the ice cover. Resolution on the order of 100-200 m will resolve moderate deformation and opening/closing of important size-scale of leads. From these, ice age and thickness can be derived over comparatively short time periods. Relative radiometric accuracy of 1 dB or less across the swath provides adequate stability needed for maintaining high areal correlation of ice features between successive images. Geometric location of 300 m or better is needed to reduce feature-tracking errors. For frequency, C-band SAR is preferred due to the high radar contrast between first-year, multiyear, and wind-roughened open water, which improves feature tracking. One caveat is that the Lagrangian tracking approach used to obtain ice age places high demand on successful and regular repeating mappings. If an 'ice particle' is not imaged every 3 or 6 days, a time step uncertainty is imparted that particularly affects new ice and ridged ice production. In fact, a time gap of more than 15 days requires that a grid cell be stopped and not propagated or reinitialized with a new grid cell at a later time.

The ENVISAT ASAR wide swath mode presents an excellent opportunity for continued acquisition of high-resolution SAR mapping of the Arctic Ocean. The characteristics of the ENVISAT ASAR wide swath image mode provide excellent compatibility with the RGPS input image requirements, including frequency and resolution. The 400 km swath enables nearly 100% mapping of the Arctic basin every 3-days or 12 mappings every 35-day orbit repeat cycle. Several key calibration parameters will be improvements over the RADARSAT data quality and should likewise improve the RGPS output quality. These parameters include absolute location accuracy down to 2 pixels (150 m) and radiometric error of 0.2 dB. Also, the availability of strip map data will reduce data manipulation requirements within the RGPS. The RGPS would ingest ASAR Level 1 image data and make the output products globally available. With dedicated and long-term mappings, this Arctic data would continue the monitoring of the climatic changes of the Arctic sea ice cover. Lastly, another key consideration is for development of similar products for the Antarctic sea ice cover, which at minimum would require an increase in SAR data acquisitions over key selected regions. The upcoming ALOS PALSA, RADARSAT-2, and TERRASAR

missions should be valuable for sea ice investigations but it is not clear whether the continuous mapping required for ice motion and ice age via the RGPS is feasible with any one of these satellites.

Recently, the ADEOS-2 spacecraft was lost which carried onboard two critical polar instruments, AMSR and SeaWinds, the follow-on sensors to SSM/I and SeaWinds on QuikSCAT, respectively. While currently there are no gaps in these equivalent sensors, as the long-running SSM/I on the DMSP and AMSR-E on NASA's Terra mission, and NASA's QuikSCAT are all fully operational, the increased temporal coverage for both the PM and scatterometers was likely to be of exceptional scientific value. QuikSCAT is already operating beyond its designed lifetime, and as a replacement will take a few years to launch, there could exist in the future a gap in scatterometer measurements should QuikSCAT fail. Both types of sensors are needed so that the time series of ice extent, seasonal melt, and the more recently developed identification of the perennial and seasonal ice zones continues. Also it is clear that the synergistic use of both types of sensors will lead to improvements in each of these measurements.

The measurement of ice thickness from space has proven elusive until the recent publication of time series results using ERS-1/-2 altimeters (Laxon et al., 2003). These measurements will be improved in the future, as the ENVISAT altimeter has increased accuracy in vertical resolution and waveform tracking compared to ERS and CryoSat, scheduled for launch in late 2004, will measure topography within a 10+ km wide nadir swath which enables the acquisition of a complete map of the sea ice cover over a shorter time interval than previous altimeters and has a higher polar orbital inclination. ICESat has finer horizontal resolution than any of the radar altimeter missions, but snow thickness and cloud cover impact the laser altimeter measurement accuracy. Of key value for observing sea ice thickness as a climate indicator would be increased knowledge of the synoptic-scale perennial ice thickness distribution, needed to understand mass volume as well as which portion of the thickness regime might be changing. This knowledge would require even further improvements in height accuracy for freeboard measurements than are currently planned and novel concepts that would enable the direct measurement of the ice thickness volume. The legacy of sea ice measurements initiated with Seasat is extensive, but the most critical sea ice measurement, ice thickness, awaits continued improvement and instrument capabilities.

5. REFERENCES

- Agnew, L., H. Le, and T. Hirose, Estimation of large-scale sea ice motion from SSM/I 85.5 GHz imagery, *Ann. Glaciol.*, 25, 305-311, 1997.
- Bertoia, C., J. Falkingham, and F. Fetterer, Polar SAR data for operational sea ice mapping, in R. Kwok and C. Tsatsoulis (Eds.), *Recent Advances in the Analysis of SAR Data of the Polar Oceans*, Springer Verlag, 201-234, 1998.
- Bjork, G., J. Soderkvist, P. Winsor, A. Nikolopoulos A., and M. Steele, Return of the cold halocline layer to the Amundsen Basin of the Arctic Ocean: Implications for the sea ice mass balance, *Geophys. Res. Lett.*, 29(11): art. no. 1513, 2002.
- Carsey, F. D., Summer Arctic sea ice character from satellite microwave data, *J. Geophys. Res.*, 90(C3), 5015-5034, 1985.

- Carsey, F., and B. Holt, Beaufort-Chukchi ice margin data from Seasat - Ice motion, *J. Geophys. Res.*, 92(C7), 7163-7172, 1987.
- Carsey, F. and G. Pihos, Beaufort-Chukchi ice margin data from Seasat for ice conditions analogous to those of the Labrador Sea, *IEEE Trans. Geosci. Remote Sens.*, 27, 41-551, 1989.
- Comiso, J., and R. Kwok, Surface and radiative characteristics of the summer Arctic sea ice cover from multisensor satellite observations, *J. Geophys. Res.*, 101(C12), 28,397-28,416, 1996.
- Comiso, J., A rapidly declining perennial sea ice cover in the Arctic, *Geophys. Res. Lett.*, 29(20), 1956, 2002GL015650, 2002.
- Curlander, J. C., B. Holt, and K. J. Hussey, Determination of sea ice motion using digital SAR imagery, *IEEE J. Oceanic Eng.*, OE-10(4), 358-367, 1985.
- De Abreu, R., J. Yackel, D. Barber, and M. Arnett, Operational satellite sensing of Arctic first-year sea ice melt, *Canadian J. Remote Sens.*, 27(5), 487-501, 2001.
- Drinkwater, M. R., and X. Liu, Seasonal to interannual variability in Antarctic sea-ice surface melt, *IEEE Trans. Geosci. Remote Sens.*, 38(4), 1827-1842, 2000.
- Drobot, S., and M. A. Anderson, An improved method for determining snowmelt onset dates over Arctic sea ice using scanning multichannel microwave radiometer and Special Sensor Microwave/Imager data, *J. Geophys. Res.*, 106(D20), 24,033-24,049, 2001.
- Emery, W. J., C. W. Fowler, and J. A. Maslanik, Satellite-derived maps of Arctic and Antarctic sea ice motion, 1988-1994, *Geophys. Res. Lett.*, 24(8), 897-900, 1997.
- Evans, D., W. Alpers, A. Cazenave, C. Elachi, T. Farr, D. Glackin, B. Holt, L. Jones, W. T. Liu, W. McCandless, Y. Menard, R. Moore, and E. Njoku, Seasat-A 25 year legacy of success, *IEEE Trans. Geosci. Remote Sens.*, submitted 2003.
- Fetterer, F. M., D. Gineris, and R. Kwok, Sea ice type maps from Alaska Synthetic Aperture Radar Facility imagery: An assessment, *J. Geophys. Res.*, 99(C11), 22,443-22,458, 1994.
- Fily, M., and D. A. Rothrock, Sea ice tracking by nested correlations, *IEEE Trans. Geosci. Remote Sens.*, GE-25(5), 570-580, 1987.
- Forster, R. R., D. G. Long, K. C. Jezek, S. D. Drobot, and M. R. Anderson, The onset of Arctic sea-ice snowmelt as detected with passive- and active-microwave remote sensing, *Ann. Glaciol.*, 33, 85-93, 2001.
- Hall, R. T., and D. A. Rothrock, Sea ice displacement from Seasat synthetic aperture radar, *J. Geophys. Res.*, 86(C11), 11,078-11,082, 1981.
- Hibler, W. D., Modelling the formation and evolution of oriented fractures in sea ice, *Annal. Glaciology*, 33: 157-164, 2001.
- Johannessen, O. M., E. V. Shalina, and M. W. Miles, Satellite evidence for an Arctic sea ice cover in transformation, *Science*, 286, 1937-1939, 1999.
- Kattenberg, A., F. Giorgi, H. Grassl, G. A. Meehl, J. F. B. Mitchell, R. J. Stouffer, T. Tokioka, A. J. Weaver, and T. M. L. Wigley, Climate models: Projections of Future Climate, in J. T. Houghton, L. G. Miera Filho, B. A. Callander, N. Harris, A. Kattenberg, and K. Maskell, eds., *Climate Change 1995*, Cambridge, 285-357, 1996.
- Kovacs, A., and R. M. Morey, Electromagnetic measurements of multi-year sea ice using impulse radar, *Cold Regions Sci. Tech.*, 12, 67-93, 1986.
- Kwok, R. The RADARSAT Geophysical Processor System, in *Analysis of SAR data of the Polar Oceans: Recent Advances*, Tsatsoulis, C. and R. Kwok, Eds., Springer-Verlag, 235-258, 1998.
- Kwok, R., Recent changes in the Arctic Ocean sea ice circulation associated with the NAO, *Geophys. Res. Lett.*, 27(6), 775-778, 2000.
- Kwok, R., Deformation of the Arctic Ocean sea ice cover: November 1996 through April 1997, in *Scaling Laws in Ice Mechanics and Dynamics*, edited by J. Dempsey and H. H. Shen, Kluwer Academic, 315-323, 2001.
- Kwok, R., and G. F. Cunningham, Seasonal ice area and volume production of the Arctic Ocean: November 1996 through April 1997, *J. Geophys. Res.*, 107(C10): art. no. 8038, 2002.
- Kwok, R., G. F. Cunningham, and S. V. Nghiem, A study of the onset of melt over the Arctic Ocean in RADARSAT synthetic aperture radar, *J. Geophys. Res.*, 108(C11), 3363, doi:10.1029/2002JC001363, 2003.
- Kwok, R., G. F. Cunningham, and S. Yueh, Area balance of the Arctic Ocean perennial ice zone: October 1996 to April 1997, *J. Geophys. Res.*, 104(C11), 25747-25759, 1999.
- Kwok, R., J. C. Curlander, R. McConnell, and S. S. Pang, An ice-motion tracking system at the Alaska SAR Facility, *IEEE J. Oceanic Eng.*, 15(1), 44-54, 1990.
- Kwok, R., E. Rignot, B. Holt, and R. Onstott, Identification of sea ice types in spaceborne synthetic aperture radar data, *J. Geophys. Res.*, 97(C2), 2391-2402, 1992.
- Kwok, R. and D. A. Rothrock, Variability of Fram Strait Flux and North Atlantic Oscillation, *J. Geophys. Res.*, 104(C3), 5177-5189, 1999.
- Kwok, R., D. A. Rothrock, H. L. Stern, and G. F. Cunningham, Determination of ice age using lagrangian observations of ice motion, *IEEE Trans. Geosci. Remote Sens.*, 33(2), 392-400, 1995.
- Kwok, R., A. Schweiger, D. A. Rothrock, S. Pang, and C. Kottmeier, Sea ice motion from satellite passive microwave imagery assessed with ERS SAR and buoy motions, *J. Geophys. Res.*, 103(C4), 8191-8214, 1998.
- Laxon, S. W., Sea ice altimeter processing scheme at the EODC, *Int. J. Remote Sens.*, 15(4), 915-924, 1994.
- Laxon S., Peacock N., and Smith D., High interannual variability of sea ice thickness in the Arctic region, *Nature*, 425 (6961), 947-950, 2003.

- Lindsay, R. W., and H. L. Stern, The RADARSAT geophysical processor system: Quality of sea ice trajectory and deformation estimates, *J. Atmos. Oceanic Tech.*, 20(9), 1333-1347, 2003.
- Liu, A. and D. J. Cavalieri, On sea ice drift from the wavelet analysis of DMSP SSM/I data, *Int. J. Remote Sens.*, 19(7), 1415-1423, 1998.
- Liu, A., Y. Zhao, and S. Y. Wu, Arctic sea ice drift from wavelet analysis of NSCAT and SSM/I data, *J. Geophys. Res.*, 104(C5), 11529-11538, 1999.
- Martin, T. and E. Augstein, Large-scale drift of Arctic sea ice retrieved from passive microwave satellite data, *J. Geophys. Res.*, 105(C4), 8775-8788, 2000.
- Parkinson, C. L., and D. J. Cavalieri, A 21 year record of Arctic sea-ice extents and their regional, seasonal and monthly variability and trends, *Ann. Glaciol.*, 34, 441-446, 2002.
- Parmerter, R. R., and M. Coon, Model of pressure ridge formation in sea ice, *J. Geophys. Res.*, 77, 6565-6575, 1972.
- Peacock, N.R., S.W. Laxon, W. Maslowski, D.P. Winebrenner, and R.J. Arthern, Geophysical signatures from precise altimetric height measurements in the Arctic Ocean, paper presented at IGARSS '98, Seattle, WA, USA, edited T.I. Stein, 1964-1966, IEEE, 1998.
- Proshutinsky, A. Y., and M. A. Johnson, Two circulation regimes of the wind-driven Arctic Ocean, *J. Geophys. Res.*, 102, 12,493-12,514, 1997.
- Remund, Q. P., D. G. Long, and M. R. Drinkwater, An iterative approach to multisensor sea ice classification, *IEEE Trans. Geosci. Remote Sens.*, 38(4): 1843-1856 Part 2, 2000.
- Richter-Menge, J. A., S. L. McNutt, J. E. Overland, and R. Kwok, Relating arctic pack ice stress and deformation under winter conditions, *J. Geophys. Res.*, 107(C10), 8040, doi:10.1029/2000JC000477, 2002.
- Rothrock, D. A., Y. Yu, and G. A. Maykut, Thinning of the Arctic sea-ice cover, *Geophys. Res. Lett.*, 26(23), 3469-3472, 1999.
- Rothrock, D. A., J. Zhang, and Y. Yu, The arctic ice thickness anomaly of the 1990s: A consistent view from observations and models, *J. Geophys. Res.*, 108(C3), art. no. 3083, 2003.
- Smith, D. A., Recent increase in the length of the melt season of perennial Arctic sea ice, *Geophys. Res. Lett.*, 25(5), 655-658, 1998.
- Steele, M., and T. Boyd, Retreat of the cold halocline layer in the Arctic Ocean, *J. Geophys. Res.*, 103(C5), 10,419-10,435, 1998.
- Stern, H. L., D. A. Rothrock, and R. Kwok, Open water production in Arctic sea-ice – Satellite measurements and model parameterizations, *J. Geophys. Res.*, 100(C10), 20601-20612, 1995.
- Ulander, L. M. H., Interpretation of Seasat radar-altimeter data over sea ice using near-simultaneous SAR imagery, *Inter. J. Remote Sens.*, 8(11), 1679-1686, 1987.
- U. S. National Research Council, *Enhancing NASA's contributions to polar science*, National Academy Press, Washington DC, 124 pp., 2001.
- Winebrenner, D. P., E. D. Nelson, R. Colony, and R. D. West, Observation of melt onset on multiyear Arctic sea ice using the ERS-1 synthetic aperture radar, *J. Geophys. Res.*, 99(C11), 22425-22441, 1994.
- Winebrenner, D. P., B. Holt, and E. D. Nelson, Observation of autumn freeze-up in the Beaufort and Chukchi Seas using the ERS-1 synthetic aperture radar, *J. Geophys. Res.*, 101(C7), 16401-16419, 1996.
- Wingham, D.J., A.J. Ridout, R. Scharroo, R.J. Arthern and C.K. Shum, Antarctic elevation change 1992 to 1996, *Science*, 282, 456-458, 1998.
- Wingham, D., The first of the European Space Agency's opportunity missions: CryoSat, *Earth Observation Quarterly*, 63, ESA, 1999.
- Yueh S.H., R. Kwok, S-H. Lou, and W.-Y. Tsai, Sea ice identification using dual-polarized Ku-band scatterometer data, *IEEE Trans. Geosci. Remote Sens.*, 35(3), 560-569, 1997.
- Zhang, J., D. Rothrock, and M. Steele, Recent changes in Arctic sea ice: The interplay between ice dynamics and thermodynamics, *J. Climate*, 13, 3099-3114, 2000.
- Zhang, J. L., D. R. Thomas, D. A. Rothrock, R. W. Lindsay, Y. Yu, and R. Kwok, Assimilation of ice motion observations and comparisons with submarine ice thickness data, *J. Geophys. Res.*, 108(C6): art. no. 3170, 2003.
- Zwally, H. J., M. A. Beckley, A. C. Brenner, and M. B. Giovinetto, Motion of major ice-shelf fronts in Antarctica from slant-range analysis of radar altimeter data, 1978-98, *Annal. Glaciol.*, 34, 255-262, 2002B.
- Zwally, H. J., J. C. Comiso, C. L. Parkinson, D. J. Cavalieri, and P. Gloersen, Variability of Antarctic sea ice 1979-1998, *J. Geophys. Res.*, 107(C5), art. no. 3041, 2002A.

**This page intentionally
left blank (pagination)**

VALIDATION

**This page intentionally
left blank (pagination)**

VALIDATION OF SAR OCEAN DATA PRODUCTS AND VERIFICATION OF PROCESS MODELS USED FOR SAR INTERPRETATION

Ian Robinson and Susanne Ufermann

Laboratory for Satellite Oceanography, Southampton Oceanography Centre, European Way, Southampton, SO14 3ZH, United Kingdom, Email: Ian.S.Robinson@soc.soton.ac.uk, ufermann@soc.soton.ac.uk

ABSTRACT

This paper examines the issue of the quality analysis of ocean data products derived from SAR. It is based on work in the EU MARSAIS Project. The principles of quality assessment are addressed, distinguishing between the tasks of calibration, process verification and validation. These principles are applied to four classes of SAR ocean data product; wind, waves, features measured by their surface current signatures, and oil slick monitoring. Wind and wave products are shown to be quite well validated, but the retrieval of information about current-based features or about oil slicks are poorly validated, even though the process models used have been verified. The reason is the scarcity, or absence, of any independent measurements of the ocean variables retrieved from SAR. This shortcoming must be addressed if SAR is to be widely accepted as a tool for measuring ocean phenomena.

1. INTRODUCTION

If SAR ocean data products are to become widely accepted for operational use in ocean and coastal management contexts, it is essential that the quality of the data products is properly assessed. Users need to know how much confidence can be placed in the accuracy, applicability and reliability of the methods used to derive oceanographic information from SAR image data. For this reason the European Union's Framework 5 research project to create a Marine SAR Analysis and Information System (MARSAIS) included a study to address the issue of data quality. The results of that study [1] highlighted shortcomings as well as strengths in the present status of validating SAR ocean data products. Because they are highly relevant to the breadth of issues reported and discussed at the Svalbard SAR Workshop, the general findings of the study are summarised here.

The generic issues concerning data product quality are discussed first, distinguishing between the separate procedures of sensor calibration, model verification and product validation. Then it is possible to consider to what extent these procedures are being effectively applied to the retrieval of various types of ocean data products. The objective is to determine whether

existing quality tests of SAR-derived ocean products are adequate, and where additional effort is needed to enhance confidence in such data.

2. PRINCIPLES OF QUALITY ASSESSMENT FOR SAR ANALYSIS

The term "quality assessment" encompasses a broad range of activities that enable us to determine the accuracy of all the data processing stages between the acquisition of a SAR image and the delivery of a marine environmental product to the user. Fig. 1 is a schematic summary of the stages of processing by which ocean information is obtained from SAR data. It identifies the ways in which external information is required to calibrate or validate each of the procedures.

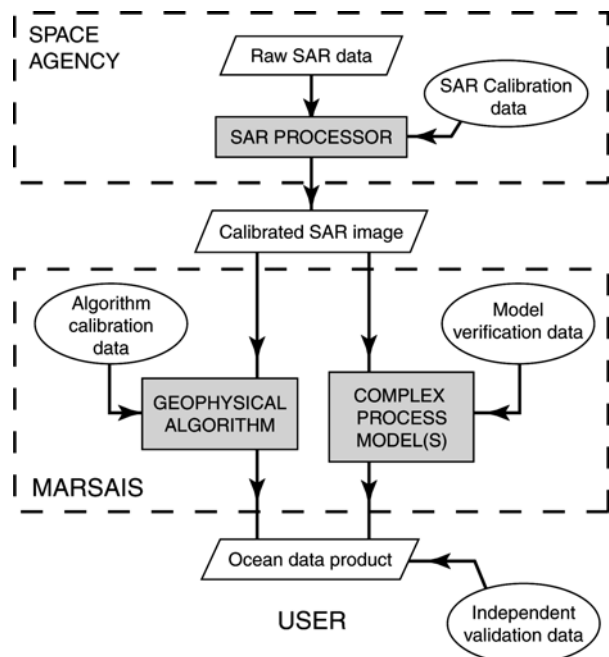


Fig. 1. Stages in the processing of SAR data into ocean products.

The first procedure is the generation of SAR precision images. The raw signal received from the sensor provides the input to the SAR Processor which produces an image representing σ_0 , the normalised radar cross-section of the sea surface. The calibration of the σ_0 field depends on a variety of careful

procedures, ranging from pre-launch calibration of radar components to post-launch field campaigns and the use of calibrated ground targets. The accuracy and stability of this calibration is fundamental to the retrieval of most of the SAR-based ocean products. Users of such products must ensure that the accuracy of the input σ_0 field is adequate for the method being used. It is assumed here that the Agency operating the SAR is responsible for monitoring and maintaining its quality.

The second procedure, deriving a useful ocean product from the given SAR image, is what primarily concerns us here. Broadly there are two ways in which this is done. For retrieving measurements of waves or wind from SAR data, fairly straightforward methods are applied using algorithms to derive the desired products from the input SAR data as represented by the left branch in Fig. 1. The quality of the algorithms can be assessed by evaluating how well they perform with the training set from which they were derived. This consists of matched values of the SAR σ_0 field and the corresponding *in situ* measurements of the ocean variable to be retrieved from the algorithm. The wider the range of conditions for which the training set is obtained, the wider should be the applicability of the algorithm.

More complex procedures are needed to interpret other features, as represented by the right branch in fig. 1. This often uses a chain of models which describe different stages in the process by which the ocean phenomenon of interest influences the σ_0 recorded on the SAR image. Quality assessment requires model verification. This evaluates how closely the forward model or chain of models is able to predict the SAR-observed σ_0 field when provided with *in situ* measurements of the derived ocean parameter, obtained at the same time as the SAR acquisition. Ideally the model should be tested using a number of matched sets of *in situ* and SAR data, corresponding to different locations and diverse environmental circumstances. If the forward model is shown to perform well for a wide variety of conditions it can be used with more confidence than when it has been compared with only one or two test sets. The analysis of further SAR image data then consists of inverting such models, analytically, numerically or by using an iterative procedure, with the σ_0 field as input and deriving the ocean parameter as the data product. Such a procedure typically attempts to minimise the difference between the model predicted σ_0 field and that measured by the SAR.

Whether the SAR analysis is based on a simple algorithm or uses the more complex model-inversion approach, confidence in the resulting ocean data

product can not be based solely on how well the model or algorithm has been verified. Additional matched pairs of *in situ* and SAR data are needed to test how closely the retrieved data product corresponds to the actual conditions. This is the process of validation. If this is to provide an objective evaluation of the data product quality, the validation datasets need to be completely independent of the training datasets used for algorithm development or model tuning and verification. They also need to span a wide range of the values of the retrieved product, so that reliable error bars can be assigned across a wide output range.

It is here that the greatest weakness is found in the quality assessment of SAR data products, largely because such independent validation measurements do not exist or are difficult to obtain.

3. HOW EFFECTIVELY CAN QUALITY ASSESSMENT PRINCIPLES BE APPLIED TO SAR OCEAN PRODUCTS ?

A complete assessment of the quality of SAR products needs sensor calibration, process or model verification, and product validation. Assuming that the sensor calibration is given, the quality assessment of SAR data products therefore depends firstly on how well verified the process model is, and secondly on how extensively the end products have been independently validated. In relation to this, we now consider four different types of SAR-derived ocean products.

3.1 Winds over the sea

The measurement of wind speed from a SAR image has been based mostly on the standard scatterometer function in which σ_0 is determined empirically as a function of wind speed, direction relative to the radar azimuth, and the frequency, inclination to the vertical, and polarisation of the radar beam. For a particular radar this relationship can be well established and verified. For example, the CMOD-4 scatterometer equation [2, 3] used for ERS SAR data, and revised versions of it [4] have been well verified, providing a sound basis for quality data products.

However, an estimate of wind speed retrieved from a SAR image using the scatterometer function requires *a priori* knowledge of the wind direction, and so depends on what method was used to estimate the wind direction, for example using meteorological forecasts, the orientation of streaks on the image, or the orientation of low frequency spectral peaks in a 2-D image FFT. Thus assessment of the wind retrieval accuracy requires additional verification of the method used to obtain direction. This also can be achieved with little difficulty [5] in the majority of cases.

Finally, independent validation data are required to confirm the quality of SAR wind vector products over a wide variety of conditions. Validation of this type is possible when *in situ* measurements of wind vectors are available. There are several operational examples, such as [6], where such validation has been performed effectively. Moreover, more widespread validation can be achieved by comparing SAR wind vectors with the products of alternative remote sensing methods.

Thus it can be concluded that the measurement of locally detailed wind fields using SAR is not only a well verified process but also one whose products are capable of adequate validation. It remains important to acquire independent wind data to validate the SAR-derived products for every new operational context in which radar images are to be applied.

3.2 Ocean Waves

There are various ways of obtaining ocean surface wave measurements such as significant wave height and dominant wave period from satellite sensors, but only from SAR data can estimates of the directional wave spectrum be retrieved. This, and the ability to map the spatial variability of the wave field properties over short length scales, are the data products uniquely provided by SAR. Is the quality of such products capable of being objectively determined?

The imaging processes by which swell and long wind waves present a signature in the simple (real) σ_0 field imaged by a SAR are fairly well, but not completely, understood and forward models of the process [7, 8] are generally well verified. These models are the basis for inversion schemes which retrieve estimates of wave spectra from image spectra.

However, a thorough validation of the wave products derived from applying the SAR image spectrum inversion methods has proved difficult because of the lack of independent directional wave spectra. Some validation work has matched SAR products against wave model predictions [9]. The most systematic attempt to validate ERS SAR-derived wave measurements against *in situ* data [10] was based on comparisons with (non-directional) wave frequency spectra. In that study the data from directional wave buoys could not be used as they were located in coastal shallow water sites where the wave parameters are spatially inhomogeneous and could therefore not be matched properly to SAR wave mode data. Further validation studies can be expected in future as directional data become available from open sea, deep water sites.

The ready availability of complex SAR image data from Envisat has changed the approach to retrieving ocean wave spectra. Given complex images additional information in the phase data can be used to eliminate the directional ambiguity. The analytical techniques [11] used to do this are still being developed and benefit from the improved cross spectral and multi-polarisation data available from Envisat's ASAR. The range of wave products being derived from ASAR includes the significant wave height H_s , the mean wave period T_p and the mean spectral wave direction Φ . There are also products H_s^{12} and T_p^{12} representing the significant wave height and mean wave period for the low frequency part of the spectrum up to a frequency of 1/12 Hz.

It should now be easier to validate these since, apart from the direction Φ , they are properties that can be obtained from non-directional wave buoys. During the first year of Envisat's mission, much of the validation of ASAR has been accomplished by comparing against the wave data predicted by the wave model (WAM) operated by ECMWF, which assimilates *in situ* data and represents the best available measure of the true *in situ* wave properties.

Overall, the prospects for being able to perform satisfactory quality analysis of SAR wave products is good, given the number of different measurements of wave parameters available either *in situ* or from independent remote sensing methods. The weakest aspect of validation remains the directionality, and it is important that all available directional ocean wave buoy data are harnessed for validation experiments.

3.3 Features identified by surface current signatures

Another class of potential ocean products from SAR is those which describe a phenomenon which has a SAR signature by virtue of its surface current field modulating the surface roughness. Examples are internal waves, shear and convergent fronts, ocean eddies, and tidal flow over shallow bathymetry. The methodology for retrieving ocean information from such SAR signatures is based on a sequence of "forward" models representing the current modulating effect of the phenomenon, the hydrodynamic modulation of the surface roughness by the modulated current, and the effect on the radar backscatter of the roughness patterns.

If a comprehensive set of reference data is available, verification of the SAR imaging model suite can be achieved quite precisely, and parameter modifications or an addition of new or improved model components can be performed in an efficient and physically adequate way. This has been demonstrated, for

example, with the development of an optimized parameterization of the input wave spectrum for best reproduction of measured σ_0 values [12]. Although there are few suitable reference datasets combining measurements of σ_0 and surface current modulation fields, these are sufficient to give confidence in the verification of the SAR imaging model suite.

However, the status of the validation of the ocean products derived from inverting such models is very much weaker. The main problem here is that the types of information which the SAR yields, such as the shear across a front, or the amplitude of an internal wave, are very difficult to measure by independent means, coincident with a SAR acquisition. Indeed the SAR may be the only sensible way to measure a particular phenomenon and the variables which define it. Moreover, because the wind conditions are often critical to such results, a satisfactory validation programme for SAR “current-derived” products must obtain data that are representative of a wide range of wind conditions.

Apart from specific information about internal wave crest kinematic properties, where systematic analysis has been performed [13, 1], it must be admitted that the objective independent validation of SAR products related to ocean current features is almost non-existent. If SARs are to be used for operational monitoring of such features, or for scientific investigations of them, it will be important to make every effort to acquire at least some independent validation data which can test the applicability of the method for a range of wind speeds and directions and for different sea states.

3.4 Oil slick monitoring by analysis of SAR surface slicks

A number of different systems have been developed to analyse SAR images in order to identify surface oil slicks. Although developed by experts and used in operational contexts, there have so far been few reports of objective tests being used to establish how well the different oil slick detection methods perform, irrespective of whether they are automatic or depend on operator intervention. The reason for this is the lack of independent information available. If an oil spill detection method is to be properly validated for a particular region there must be reliable knowledge about the occurrence of all confirmed oil slicks in the region. There needs to be as much confidence about when and where there are no spills as when and where slicks do occur. Only then can comparison be made with the incidents detected as oil slicks from SAR data, in order to compile statistics not only on the number of correct detections but also the number of false positives

(when oil slicks are erroneously flagged) and false negatives (when a genuine oil slick is missed).

Of course, even when comprehensive independent data about oil spills are available, the results of validation would strictly apply to only the region covered by the validation data. An ideal validation dataset needs to include regions containing those other phenomena, such as natural organic films, wind shadow areas, sea ice formation which can generate oil spill-like signatures on SAR images. Such validation data sets were not available to permit full validation of the oil slick detection methods presented in MARS AIS, although there are now programmes underway within Europe to assemble reliable data on oil spills matched to SAR data. Until they become available, the best quality assessment that can be applied to SAR oil spill monitoring is to compare the results of analyses by different methods and operators in an attempt to determine at least the natural variability arising from the subjective element in most oil spill detection methods.

4. CONCLUSION

The results of this brief survey of the validation of different types of ocean measurements that can be derived from SAR data are summarised in Table 1. This indicates that the quality of the products is somewhat variable.

Table 1: Summary of the validation status of SAR ocean data products

Application	Status of validation
Wind speed	Well validated. Many matchup datasets available.
Waves	Fairly well validated. Matchup data available, although in situ wave instruments and SAR measure slightly different properties of the waves.
Current gradients	Insufficient datasets matching the in situ surface current field to their SAR signature exist for reliable validation.
Internal waves	No other techniques can measure the spatial detail of I.W. Methods to detect I.W. occurrence by SAR are verified, but there is insufficient coincident data to validate retrieval of wave amplitudes.
Oil spill detection	Comparisons can be performed between different methods and operators, but objective validation awaits the accumulation of sufficient independent records of oil slick occurrence.

For some of the key applications of SAR data, such as measuring wind and waves, there exist well documented quality assessment references for the methods and reliable sources of independent validation

data for the products. The same cannot be said for some of the other methods, such as those based on deriving the current gradients that modulate the surface roughness. While in these cases the analytical process models have been calibrated and verified, there have been insufficient independent trials of the methods to generate more than a few isolated independent data sets which validate the end products.

It is important to recognise that the main reason why some SAR applications are more difficult to validate independently than others is that the alternative means for measuring the ocean parameter either do not exist or are very difficult. Whereas there are established alternative methods for measuring wind and waves, and these allow the SAR measurements to be validated, there is no other way of easily measuring the propagation characteristics of internal waves, determining the current shear across ocean fronts, or for routinely monitoring surface slicks and films.

In these cases the difficulty of providing independent validation represents the classic problem for any new remote sensing system that has unique capabilities. Such a problem is a consequence of a measuring technique's success rather than the reverse. The reality is that SAR provides a more effective, or in some cases the only, way to measure certain ocean properties. In that situation validation in its purest form may not be possible, but users should not be deterred from making use of SAR products.

Users of data products that are, as yet, poorly validated should do so with caution. Nonetheless it is only by using these products and testing their consistency within the circumstances where they are being applied, that confidence in them can gradually be established. Whenever possible, users should be encouraged to assemble their own validation data sets appropriate for their particular task and location. Meanwhile the SAR research community should promote every opportunity to perform independent validation of the data products being discussed in this volume, and should facilitate the dissemination of validation datasets when they do exist.

5. REFERENCES

1. Robinson, I. S. and Ufermann, S. (2003) *Data Validation and Model Verification within MARSAIS*. D16/2003/1, MARSAIS Project Office, Nansen Environmental and Remote Sensing Centre, Bergen, Norway, Dec 2003, 30 pp.
2. Stoffelen, A. C. M. and Anderson, D. L. T. Wind retrieval and ERS-1 radar backscatter measurements. *Adv. Space Res.*, **13** (5), 53-60, 1993.
3. Stoffelen, A. C. M. and Anderson, D. L. T. Scatterometer data interpretation: Estimation and validation of the transfer function CMOD4. *J. Geophys. Res.*, Vol. 102 (C3), 5767 - 5780, 1997.
4. Quilfen, Y., Chapron, B., Elfouhaily, T., Katsaros, K. and Tournadre, J. Observation of tropical cyclones by high resolution scatterometry. *J. Geophys. Res.*, Vol. 103 (C4), 7767 - 7786, 1998.
5. Horstmann, J., Lehner, S., Koch, W. and Tonboe, R. Computation of wind vectors over the ocean using spaceborne synthetic aperture radar. *Johns Hopkins APL Technical Digest*, Vol. 21 (1), 100 - 107, 2000.
6. Furevik, B. R. and Espedal, H. Wind energy mapping using synthetic aperture radar. *Can. J. Remote Sensing*, Vol. 28 (2), 196 - 204, 2002.
7. Hasselmann, S., Brüning, C., Hasselmann, K. and Heimbach, P. An improved algorithm for the retrieval of ocean wave spectra from SAR image spectra. *J. Geophys. Res.*, Vol. 101, 16615 - 16629, 1996.
8. Mastenbroek, C. and De Valk, C. F. A semi-parametric algorithm to retrieve ocean wave spectra from SAR. *J. Geophys. Res.*, Vol. 105 (C2), 3497 - 3516, 2000.
9. Heimbach, P., Hasselmann, S. and Hasselmann, K. Statistical analysis and intercomparison with WAM model data of three years of global ERS-1 SAR wave mode spectral retrievals. *J. Geophys. Res.*, Vol. 103, 7931 - 7977, 1998.
10. Voorrips, A. C., Mastenbroek, C. and Hansen, B. Validation of two algorithms to retrieve ocean wave spectra from ERS Synthetic Aperture Radar. *J. Geophys. Res.*, Vol. 106 (C8), 16825 - 16840, 2001.
11. Chapron, B., Johnsen, H. and Garello, R. Wave and wind retrieval from SAR images of the ocean. *Ann. Télécommun.*, Vol. 56 (11-12), 682 - 699, 2001.
12. Romeiser, R., Alpers, W. and Wismann, V. An improved composite surface model for the radar backscattering cross section of the ocean surface, 1. Theory of the model and optimization / validation by scatterometer data. *J. Geophys. Res.*, Vol. 102, 25237 - 25250, 1997.
13. Brandt, P., Romeiser, R. and Rubino, A. On the determination of characteristics of the interior ocean dynamics from radar signatures of internal solitary waves. *J. Geophys. Res.*, Vol. 104, 30039-30047, 1999.

**This page intentionally
left blank (pagination)**

USER SURVEY

**This page intentionally
left blank (pagination)**

USER REQUIREMENTS FOR SAR DATA IN THE COASTAL AND MARINE ENVIRONMENT

C. O'Mahony⁽¹⁾, V. Cummins⁽¹⁾, N. Dwyer⁽¹⁾ and J. A. Johannessen⁽²⁾

⁽¹⁾*Coastal and Marine Resources Centre, Environmental Research Institute, University College Cork, Naval Base, Haulbowline, Cobh, Co. Cork, Ireland. c.omahony@ucc.ie*

⁽²⁾*Nansen Environmental and Remote Sensing Center, Edv. Griegsvei 3a, 5059 Bergen, Norway, johnny.johannessen@nersc.no*

ABSTRACT

Several efforts have already been undertaken to analyse user requirements for Earth observation (EO) data in the marine and coastal environment. However, little has been done to identify the specific requirements for Synthetic Aperture Radar (SAR) data. A fundamental component of the current EU 5th Framework project Marine SAR Analysis and Interpretation System (MARSAIS), deals specifically with user requirements explicit to SAR data and SAR application capabilities. The project aims to identify and involve potential end users of SAR data and to generate end user feedback, which in turn will be fed into the development of an operational MARSAIS prototype focussing on sea state, winds, slicks and surface currents near fronts and internal waves.

The collation of end user feedback was achieved using a range of interview techniques, end user workshops, and a Context of Use (CoU) survey. The latter included a questionnaire survey in 2002 to assess SAR data needs, capability and capacity constraints, benefits of SAR data use and perceived obstacles to SAR data use.

Analysis of the 96 CoU survey questionnaires returned shows potential for greater exploitation of SAR data and SAR derived products within the coastal and marine environment. End users showed a preference for processed products and more frequent temporal coverage. Cost emerged as a primary obstacle to the use of SAR data within the coastal and marine community.

1. INTRODUCTION

Earth observation (EO) data provides a valuable contribution to the monitoring and management of the marine and coastal environment. Over the last decade Synthetic Aperture Radar (SAR) data has increasingly been employed for a number of applications of specific relevance to the coastal and marine environment e.g. detection and monitoring of oil slicks, sea state, high resolution wind field, shallow water bathymetry, ship detection and fisheries management [1, 2, 3]. In order to exploit the maximum potential of SAR data in the marine and coastal environment it is essential to understand the needs and requirements of coastal and marine end users and to incorporate this into the development of SAR products [4].

Having reviewed the available literature, it has become clear that a number of efforts have been undertaken to analyse user requirements for Earth observation (EO) data in general [5, 6]. However, little has been done to identify the specific requirements for SAR data in the marine and coastal environment. Thus, a key objective of the EU 5th Framework Project MARSAIS, is to ensure that user driven SAR derived products are developed and effectively exploited [7, 8, 9, 10].

End user involvement is pivotal in the development and refinement of the MARSAIS prototype. By incorporating end user opinion in the research, their information needs are recognised and a tangible transfer of requirements into applied technology can be achieved. MARSAIS looks to determine state of the art analysis and interpretation capabilities for SAR image data and to allow for a more user-friendly exploitation of the large volume of existing SAR and other remote sensing data in Europe in the context of the coastal and marine environment. End user feedback was attained using a series of interview techniques. However, this paper focuses specifically on one aspect, namely the Context of Use (CoU) survey.

2. METHODOLOGY

As one of the components of MARSAIS, a multi-faceted end user requirements work package was designed to assess end user requirements. A number of mechanisms were utilised: literature review; consultation with MARSAIS User Group (MUG)¹ and MARSAIS Advisory Group (MAG)²; end user workshops (Germany [Hamburg, 2001], Ireland [Cork, 2002]), Greece [Athens – EuroGOOS, 2002], Norway

¹ The MARSAIS Users Group (MUG) refers to potential end users who provided input to the end user requirement work package, contact with these key end users was maintained throughout the duration of the project.

² The MARSAIS Advisory Group (MAG) is composed of a group of SAR experts who act as external consultants throughout the lifespan of the MARSAIS project providing feedback and recommendations where appropriate.

[Svalbard – Workshop on Coastal and Marine Applications of SAR, 2003]); Context of Use (CoU) survey; product and project reviews; dissemination and promotion of project information. The aforementioned mechanisms enabled the project team to collate significant information on current and potential end users of SAR data within the coastal and marine environment.

This paper focuses on one feature of the end user requirements study, namely the CoU survey. The CoU survey involved the analysis of the data obtained from respondents to a questionnaire. The CoU questionnaire survey was undertaken between April and November 2002 to identify the requirements of current and potential end users of SAR data within the coastal and marine environment. The style and format of the MARS AIS questionnaire was developed in close consultation with the project partners. Previous studies involving end user questionnaires, e.g. EuroGOOS Data Requirements Survey [5] and MAG recommendations were taken into consideration and influenced the final development of the questionnaire.

The CoU survey focused on eight potential applications of SAR data use (pollution incidents, current features, waves, wind, ice, natural films, internal waves and shallow water bathymetry) and the nature of use associated with these applications (examining the following eight variables: geographic coverage; SAR product type; delivery medium; latency of delivery [time from the request for data to the delivery of data]; spatial resolution; temporal resolution; forecast period and synergy). In addition, respondents were asked to provide their opinion on limiting factors in their use of SAR data. The choices focused on cost, capability and capacity.

The Coastal and Marine Resources Centre (CMRC) built up a database of contacts relating to potential end users of SAR data. The Potential User Database (PUD) was generated to house the contact details of individuals and organisations considered to be potential end users of SAR data. The value of this resource is pertinent to MARS AIS but also to end user research currently underway in initiatives such as Global Monitoring for Environment and Security (GMES) [11].

Using the PUD the MARS AIS questionnaire was distributed to almost 500 remote sensing/SAR experts, coastal managers and individuals in other marine application domains (such as harbour authorities and offshore operators). In order to obtain feedback individuals were contacted by phone, by e-mail and in person (via workshop and conference attendance). All returned questionnaires were examined for

completeness and quality. Ambiguities were clarified by direct communication with the respondent.

3. RESULTS

Questionnaire respondents were grouped into the following sectors of activity: transport, energy production, environmental protection/preservation, mineral extraction, defence, engineering, services, basic and strategic research and other. For the purpose of analysis, respondents were also categorised into the three broad user categories of commercial, academic and government sectors. A variety of methods were used to obtain feedback (which reduced bias in the selection of respondents), resulting in a wide geographical distribution of respondents.

Individuals from the aforementioned sectors of activity returned completed questionnaires from 19 countries. A total of 96 completed questionnaires formed the basis of the CoU survey results, 65 were from the MARS AIS partner countries (Ireland, Norway, Germany, Greece, France, UK) seven were from other European countries and 24 were from outside Europe. This rate of response is considered good [12] and forms an adequate sample base for the purpose of the research. The number of responses varied according to the sector of activity.

The highest number of respondents came from within the environmental protection and preservation sector, followed by those in the basic and strategic research, service and engineering sectors. The defence, transport, mineral extraction and energy production sectors all featured in the response to a lesser extent. The number of respondents who do not use SAR data at the moment exceeded the number of SAR data users by a ratio of 3:1.

Respondents indicated a strong preference for the use of SAR imagery in the examination of current features, shallow water bathymetry and pollution incidents. Lower levels of interest were demonstrated for the use of SAR data in relation to features such as internal waves, wind and waves.

In a choice between cost, capability and capacity, cost was cited as the most significant limiting factor in the use of SAR imagery in the marine and coastal end user community. The issue of cost was found to relate to both the price of the data and the associated pricing scheme. The former is significant due to the actual expenditure involved and the latter is a complex system that can appear perplexing even to experienced SAR users [13].

Capability (training and skills) and capacity (infrastructure) also influence the use of SAR data [13,

14] in the coastal and marine environment. The CoU survey showed that the effects of capability and capacity on the use of SAR data among end users are intrinsically linked.

The results of the CoU survey highlighted a number of issues relating to the following variables: SAR product type; geographic coverage; delivery medium; synergy; and temporal resolution within the coastal and marine end user community.

The responses indicated a clear requirement for processed imagery, as opposed to raw data and statistics. In addition, the demand is highest for SAR data acquired closer to the coast rather than in the open ocean.

At present, SAR data users largely employ disc as a delivery medium, with a strong demand for networked data also apparent. SAR data users frequently use optical data and infrared data in synergy with SAR data. Examples of such synergy are demonstrated in the MARS AIS project e.g. use of AVHRR and SAR to examine current fronts. Respondents also expressed a strong desire for synergy with hyperspectral data should the opportunity be made available in the future.

There is a demand from the coastal and marine end user community for more frequent temporal coverage, particularly in the case of pollution incidents where the immediate post incident period is critical in the monitoring and containment of the spill.

4. DISCUSSION

The level of response to the questionnaire varied between sectors. Despite efforts to obtain a balanced view from a wide audience of end users, the feedback was predominantly from the environmental protection, research and engineering sectors. Where prudent, gaps identified within the response were followed up by conducting informal interviews. This additional material and other elements of ongoing work will be included in the final user requirements document.

The low level of response from the defence, marine transport, mineral extraction and energy production sectors could also suggest that some effort should be directed towards increasing awareness of the potential of SAR data for these marine and coastal activities in particular.

The comparatively low response for the use of SAR data for studying wind and waves is surprising and potentially misleading as we know that SAR derived ocean wave spectra are assimilated into the WAM model at several weather centres (i.e. European Centre

for Medium-Range Weather Forecasts [ECMWF]). Trends in demand are also likely to be influenced by the availability of sophisticated products. For example, relatively sophisticated SAR data products currently exist for oil spill detection and shallow water bathymetry [15, 16, 17, 18]. A gap exists in the availability of mature end user orientated SAR products for other application areas such as for ocean surface current applications.

In relation to product availability it is important to note that SAR algorithms relevant to the monitoring of marine parameters are currently at different levels of maturity. As a result, certain applications are at a more advanced stage than others. Thus, further basic research is needed to improve SAR data analysis as described in the expert papers presented in this document.

The level of expertise of an end user will greatly influence their capability to access and utilise SAR imagery. Users need to consider the cost of improving capacity and capability (investment in hardware and employing or training individuals to interpret SAR data) against the increased cost of purchasing processed data.

SAR data providers, including the European Space Agency (ESA), should take steps towards the simplification of pricing schemes to ensure maximum uptake of SAR products by potential end users, in particular by first time and non-expert end users. Initiatives such as Open Distributed Information and Services for Earth Observation (ODISEO) are a positive step in this regard. Similarly, ESA's implementation of the category 1 and 2 pricing schemes is to be welcomed and certainly supports a wider use of SAR data. Data cost effectiveness, accessibility and distribution have also been identified as key issues to be addressed by the GMES initiative [19].

The survey results indicate that many organisations lack the capacity and capability to access and interpret SAR imagery for themselves. This coincides with a gap in the marketplace for interpretive, value adding services; particularly in relation to less mature and emerging application areas, such as those related to wind fields and sea state. Value adders are a crucial link between raw data providers, who distribute SAR data, and the end users who need valuable information relevant to their activities. The challenge is to provide well developed products and/or services to suit end user needs at an attractive cost.

Support should be provided for SMEs willing to maximise new opportunities to exploit SAR data in the marine and coastal environment. As an example, some end users are not interested in SAR data itself, but rather in the information that can be derived via thematic maps

to aid decision making. SAR data products should be developed with the level of expertise of the end user in mind. Tools should be adapted for use by non-specialists.

The promotion of SAR data products for the marine and coastal environment should be focused on concrete examples where efficiency, availability and affordability can be demonstrated. This is a key factor for consideration by the MARS AIS consortium and other EU FP5 research projects of a similar nature.

Careful attention should be paid to the strong trends that emerged in the results for particular variables in the development of future SAR products and technologies (e.g. demand from the coastal and marine end user community for more frequent temporal coverage, particularly in the case of pollution incidents).

Solving current environmental problems often requires more than one algorithm or model. The potential of combining multiple tools to produce more generic products should be examined. In some instances, SAR products of this category may be more marketable than single application products. Combining slick detection and wind retrieval algorithms for improved wind estimates is one example.

The CoU questionnaire survey was designed to reduce or eliminate sources of potential bias or ambiguity and to be as representative of the user community as possible. Despite this, certain limitations were identified during the analysis of the data, in particular, the low number of responses to the questionnaire from certain sectors (e.g. marine transport and mineral extraction as already mentioned). Rather than being a failing of the sampling regime this may simply be due to the different levels of maturity and advancement of SAR use within certain sectors.

5. CONCLUSION

The conclusions on end user requirements derived from the CoU survey will be used as guidelines by the MARS AIS consortium in the future development of generic coastal and marine applications for SAR, both within and beyond the scope of the MARS AIS project. Although MARS AIS is a three year funded FP5 project, due to end in December 2003, the post project options for utilisation of the tools and products are outlined under the Technical Implementation Plan (TIP) to be delivered before the end of the project.

The findings of the CoU survey, with the overall results of the end user work package, will be useful to scientists involved in developing tools and algorithms for SAR data (including the MARS AIS project consortium),

policy makers and stakeholders concerned with the distribution of SAR data, value adding commercial entities, and coastal and marine area managers interested in learning more about applications of SAR in their working environment.

The results of this survey should not be considered in isolation. It is important to bear in mind that the future of coastal area management involves the use of EO based technologies in integrated management systems, where EO products will be integrated into intelligent systems capable of assimilating different types of data to produce what is requested by resource managers.

The above recommendations are of relevance to the GMES Services Element programme which focuses upon the delivery of policy-relevant services to end users, primarily (but not exclusively), from EO services. The results of the CoU survey were disseminated to appropriate audiences in ESA and the EU.

In summary, this survey shows that there is potential for the further development of SAR data, targeted towards the desires of end users in the marine and coastal environment. This potential can be realised through continued basic and applied research into the application of SAR data for use in coastal and marine environmental monitoring.

REFERENCES

1. Johannessen J. A., Coastal Observing Systems: The Role of Synthetic Aperture Radar. *John Hopkins APL Technical Digest*, Vol. 21, No. 1, 41-48, 2000.
2. Vachon P. W., et al. Canadian Progress Toward Marine and Coastal Applications of Synthetic Aperture Radar, *John Hopkins APL Technical Digest*, Vol. 21, No. 1, 33-40, 2000.
3. Vachon P. W., et al. Monitoring the Coastal Zone with the RADARSAT Satellite, *Proceedings of Oceanology International*, Brighton, 1998.
4. European Space Agency, *Coastal Zones: A survey of data requirements of the operational community*, ESA, 1995.
5. Fischer J. and Flemming N. C., *Operational Oceanography: Data Requirements Survey*, EuroGOOS Publication No. 12, Southampton Oceanography Centre, Southampton, 1999.
6. Centre for Earth Observation, *Pathfinder Study on the Coastal Zone: Final Report*. ACRI, under contract to CEO. ACR-CEO-FR, 1995.

7. Johannessen J. A., et al. Marine SAR analysis and interpretation system – MARS AIS, *Special Issue of Annals of Telecommunications*, Vol. 56, No. 11-12, pp 655-660, 2001.
8. Johannessen J. A., et al. *Marine SAR Analyses and Interpretation System – MARS AIS*, Proceedings of the 3rd EuroGOOS Conference, 2002.
9. O'Mahony C. and Cummins V., *End user perspective towards the development of a Marine Synthetic Aperture Radar (SAR) Analysis and Interpretation System – MARS AIS*, Proceedings of the 13th Irish Environmental Researchers Colloquium, NUI Galway, 2003.
10. Johannessen J. A., et al. A Marine SAR analysis and interpretation system (MARS AIS), *The EGGS*, Issue 3, 19-24, 2003.
11. European Commission and European Space Agency, *A European approach to global monitoring for environment and security (GMES): Towards meeting users' needs – SEC (2001) 993*, European Commission, 2001.
12. Denscombe M., *The Good Research Guide for small scale social research projects*, Open University Press, Buckingham, UK 1998.
13. Briggs D. J., et al. *Matching Demand and Supply for Earth Observation Data and Information*. A report of a study undertaken as part of the EUFOREO Thematic Network, 2001.
14. Raney R. K. and Nielsen C. S., International Policy on Wide Swath SAR Ocean Weather Data, *John Hopkins APL Technical Digest*, Vol. 21, No. 1, 170-176, 2000.
15. Samad R. and Mansor, S., *Detection of oil spill pollution using RADARSAT SAR imagery*, Proceedings of the 23th Asian Conference on Remote Sensing, 2002.
16. Fiscella B., et al. Oil spill detection using marine SAR images, *International Journal of Remote Sensing*, Vol. 21, No. 18, 3561-3566, 2000.
17. Hesselmanns G., et al. *Mapping of Seabed Topography to and from SAR*. In: Proceedings of the 3rd ERS Symposium, 1997.
18. Hesselmanns G. H. F. M., et al. Bathymetry Assessment Demonstration off the Belgian Coast – BABEL, *The Hydrographic Journal*, Vol. 96, 2000.
19. Liljelund L. E. *Global Monitoring for Environment and Security (GMES) Workshop 'The Users Perspective' - The Chairman's Report*, Stockholm, 2001.

**This page intentionally
left blank (pagination)**

FUTURE SPACEBORNE SAR SYSTEM

**This page intentionally
left blank (pagination)**

The TerraSAR-L System and Mission Objectives

Manfred Zink

TerraSAR Project, ESA-ESTEC

Keplerlaan 1, 2200 AG, Noordwijk, The Netherlands

Tel: +31 71565 3038, Fax: +31 71565 3191, Email: Manfred.Zink@esa.int

ABSTRACT

TerraSAR-L is the new imaging radar mission of the European Space Agency. The platform, based on the novel Snapdragon concept, is built around the active phase array antenna of the L-band Synthetic Aperture Radar (SAR). Specification of the L-SAR has been guided by careful analysis of the product requirements resulting in a robust baseline design with considerable margins.

Besides having a commercial role for the provision of geo-information products, TerraSAR-L will contribute to the Global Monitoring for Environment and Security (GMES) initiative and serve the scientific user community. Major application areas are: Kyoto inventory and wetland monitoring, solid earth science including seismic and volcanic activity as well as land slides and subsidence, land cover classification in different levels of detail and marine applications like shallow water bathymetry, retrieval of wave spectra, monitoring of surface current fronts and internal waves.

The TerraSAR-L operations strategy is based on a long-term systematic and repetitive acquisition scenario to ensure consistent data archives and to maximise the exploitation of this very powerful SAR system.

1. INTRODUCTION

ESA's new imaging radar mission, TerraSAR-L, is currently being studied in a Phase B and the preliminary design review is planned for December 2004. The TerraSAR-L system will provide Europe with its most powerful SAR programme to date. Key features of the 5-year mission are a short (14-day) repeat cycle in a Sun-synchronous dawn-dusk orbit, global imaging coverage, tight orbit control and high precision orbit determination. The L-SAR is built around an active phased array antenna and provides full polarimetric capabilities, maximum bandwidth (more than 80Mhz) within the 85MHz allocation in L-band for Earth observation and repeat-pass ScanSAR interferometry.

Such a system can serve a number of applications and will be an important complement to current and future

X- and C-band SAR sensors. Because of its penetration into vegetation canopies L-band SAR has strong capabilities in land cover classification. This feature is important for applications related to Climate Change like the Kyoto inventory and wetland monitoring and in combination with X-band data for commercial services in the area of agriculture, forestry and cartography. The capability to penetrate vegetation and to interact with the mechanically more stable lower parts of the canopy is also the main reason for increased coherence levels in L-band over vegetated surfaces and facilitates applications based on differential interferometry, which up to now have been limited to urban areas and bare surface, on global scale. Besides standard stripmap and ScanSAR modes the system also features a Wave mode similar to the one on ENVISAT and ERS.

The following chapters provide an overview of the TerraSAR-L system and its mission objectives. Important considerations for the operations strategy and a summary of the main mission features conclude this paper.

2. THE TERRASAR-L SYSTEM

The TerraSAR-L system comprises a spacecraft carrying a large, fully polarimetric L-Band SAR, and a complementary ground segment architecture.

2.1 Snapdragon Configuration

The TerraSAR-L spacecraft (Fig. 1), based on the novel snapdragon configuration, is optimised for and built around the large L-SAR antenna. One single deployment of the whole spacecraft deploys the 11m by 2.86m SAR antenna. The snapdragon architecture retains the modularity of conventional platforms, offers ample space for equipment accommodation and simplifies the payload design and AIT of a large spacecraft. It furthermore permits verification by testing at high levels of integration and overall reduces the risk, costs and schedule. The spacecraft has a high agility due to low roll inertia and a low aerodynamic coefficient (lower than GOCE). A simple solar array and a simplified thermal design are further advantages of the snapdragon concept.

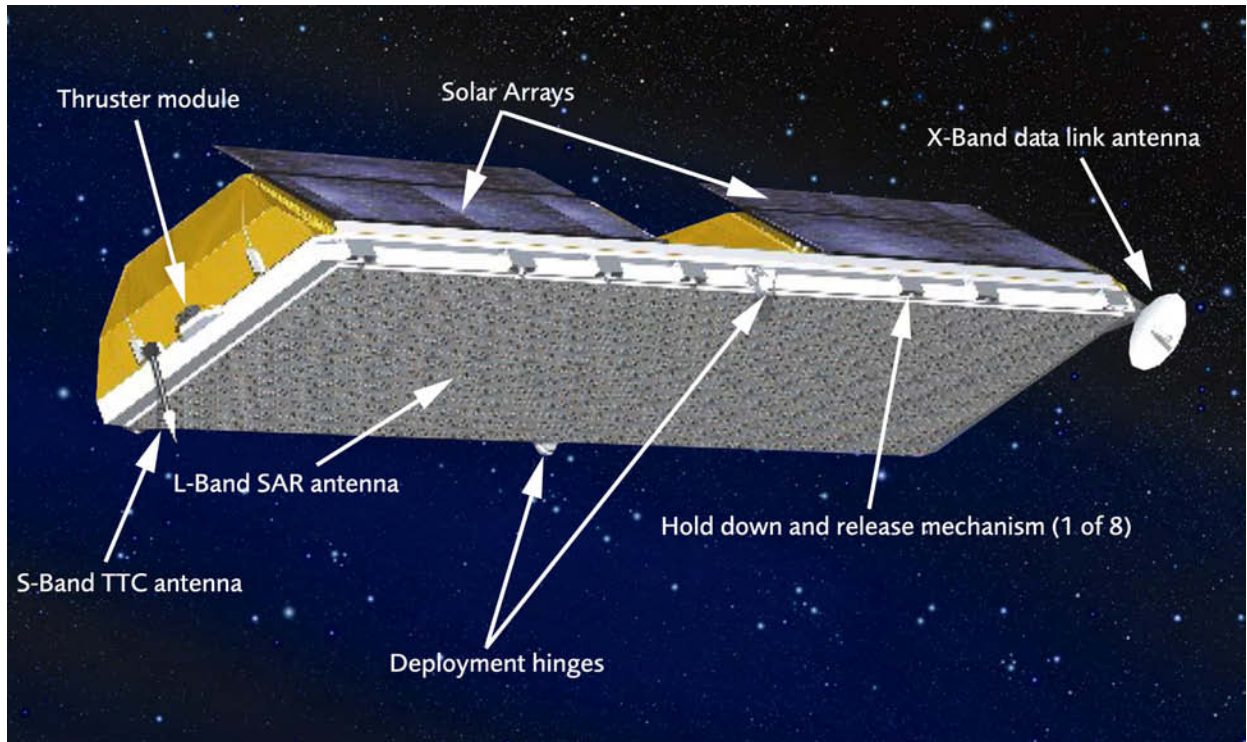


Fig. 1. Annotated View of the TerraSAR-L Spacecraft

With a total launch mass of 2.8 tons (including contingencies and system margin), the Soyuz Fregat launcher has ample margins in volume to accommodate the stowed snapdragon and in mass to place TerraSAR-L into its ~630km orbit. The solar array provides more than 5kW power for an average L-SAR consumption of ~2kW during data acquisition. Consequently, the TerraSAR-L spacecraft has margins in all aspects of its design.

2.2 The TerraSAR-L Orbit

TerraSAR-L will operate from a ~630km Sun-synchronous dawn-dusk orbit with a mean local solar time of 18:00 hours on the ascending and 06:00 on the descending orbits respectively. The short revisit time of only 14 days is optimised with respect to ensuring global coverage, effort and performance of the orbit maintenance manoeuvres and is a key feature of this mission, especially for INSAR applications.

Tight orbit control (required to be within 100m tube) will be achieved by ground-generated manoeuvres, pointing accuracy is required to within 50mdeg (3σ) in all axes.

A dual-frequency GNSS receiver allows for precise orbit determination to within 5cm, and a star tracker provides highly accurate spacecraft attitude (2mdeg).

2.3 L-SAR Characteristics

The L-SAR operates at a centre frequency of 1257.5MHz. Observing the ITU regulations a maximum bandwidth beyond 80MHz is feasible in the allocated frequency band between 1215 and 1300MHz. Nominal modes are:

- Stripmap mode in single, dual and quad polarization
- ScanSAR mode in single and dual polarization
- Wave mode (sampled stripmap, vignettes of 20x20km acquired every 100km)

Table 1 summarizes the main performance requirements on the L-SAR modes including the incidence angle range, swath width, azimuth and ground range resolution, Distributed Target Ambiguity Ratio (DTAR), radiometric accuracy and Noise Equivalent Sigma Zero (NESZ). The nominal look direction is right-looking, but for limited periods data can be acquired in left-looking geometry. In the high rate modes the maximum operations time per orbit is limited to 20 minutes, Wave mode data can be acquired over full orbits. The 20 minutes limit is driven by the data volume and downlink capacity, instrument thermal and power constraints allow more than 30 minutes of operation per orbit.

Mode	Inc. Angle	Swath Width	Resolution azi x rg	DTAR	Rad. Accuracy (3 σ)	NESZ
Quad Pol	20-36 deg	40 km	5 x 9 m	-20 dB	1 dB	-30 dB
Dual Pol	20-45 deg	70 km	5 x 9 m	-20 dB	1 dB	-30 dB
Single Pol	20-45 deg	70 km	5 x 5 m	-20 dB	1 dB	-27 dB
ScanSAR Dual Pol	20-45 deg	>200 km	50 x 50 m	-20 dB	1.5 dB	-30 dB
ScanSAR Single Pol	20-45 deg	>200 km	20 x 5 m	-20 dB	2 dB	-27 dB
Wave	20-45 deg	20 km	5 x 9 m	-20 dB	1 dB	-30 dB

Tab. 1. Summary of L-SAR mode characteristics

The above performance requirements have to meet under the end-of-life assumption of 6% random module failure. Primary design driver for the L-SAR instrument and the size of the antenna aperture is not sensitivity but ambiguity performance at high incidence angles. With dimensions of 11m x 2.86m the L-SAR active phase array antenna is more than twice as big as the ASAR antenna and radiates more than twice the power of ASAR at a similar weight of ~900 kg. It consists of 160 sub-arrays fed by 160 transmit/receive modules (TRMs) arranged in 16 rows and 10 columns (panels). The antenna front-end and the snapdragon deployment mechanism are the only critical new developments of the TerraSAR-L system. Both are covered under ongoing pre-development (risk retirement) activities, where in case of the antenna front-end a complete antenna panel is being designed and built.

In L-band propagation disturbances and especially ionospheric effects like Faraday rotation and phase delay have to be considered and if possible corrected. Quad-pol data allow estimating and compensating the Faraday rotation from the data itself. Dual-frequency (split-band) SAR operation permits Total Electron Content (TEC) estimation and is foreseen to support the ionospheric phase screening for interferometric applications.

The principal constraint on the TerraSAR-L system is transferring data to the ground. Optimised sampling schemes and advanced encoding techniques are required to reduce overheads on the instrument data rate as much as possible. The data management subsystem provides SAR data formatting, a mass memory of more than 600 Gbit and downlink encryption. Via a single channel 300 Mbit/s X-band downlink the data are transferred to a network of 3 ground stations.

2.4 Ground Segment

The ground segment is composed of three subsystems: the flight operations segment, the payload data segment and the instrument calibration segment. A modular architecture and re-use of existing facilities wherever beneficial is required. The ground segment must be compatible with the needs for interoperability with other missions, in particular TerraSAR-X, which is being developed as a German national programme. There is provision to accommodate direct access stations that could download data from the TerraSAR-L spacecraft directly using their own receiving station.

Encryption of the X-band downlink and the S-band uplink is required, in order to prevent unauthorized access to the TerraSAR system. A data-driven approach is the baseline for the payload ground segment, removing the need for detailed scheduling of the ground segment facilities/elements beyond the contact plan for the X-band receiving stations.

3. OVERVIEW OF MISSION OBJECTIVES

An L-band SAR system provides unique contributions in several application areas and will be an important complement to future X- and C-band mission. The TerraSAR-L system has the capabilities to serve a number of highly relevant applications, which can be categorised under the following areas.

3.1 Climate Change

Monitoring of the compliance to the Kyoto Protocol requires quantification of areas subject to land use change with respect to Afforestation, Reforestation and Deforestation (ARD). L-band SAR has strong capabilities in land cover classification in general, but especially in forest/non-forest area delineation. In addition, because of increased interaction depth in forest canopies, the L-band is also more sensitive to biomass changes than shorter wavelengths and reaches saturation at biomass levels of 50 t/ha, which enables the identification of afforestation and reforestation [1]. Beyond the detection of changes, biomass estimates as such are required for global carbon cycle science.

Another important and unique application of L-band SAR is wetland monitoring [2]. Reversing the global trend of wetland degradation and destruction is the objective of the UN's Ramsar Convention. Natural and anthropogenic wetlands (rice cultivation) are also sources of methane, one of the most effective greenhouse gases.

3.2 Interferometry

Penetration of the L-band signals into the vegetation volume and interaction with mechanically more stable parts underneath is the reason for higher coherence. These increased levels of coherence over vegetation are a key advantage of L-band allowing to extend the successful C-band applications to global scales [3].

With a short 14-day repeat-cycle combined with repeat-pass ScanSAR interferometry enabled by precise burst synchronisation TerraSAR-L is well suited to serve Solid Earth applications like monitoring of seismic and volcanic activities. The system will also provide important contributions to subsidence and landslides, especially for vegetated surfaces and fast motions.

Another important application is the monitoring of ice sheet and glacier dynamics, which are direct indicators of global warming and climate change. Up to now only case studies from the ERS ice phase and tandem mission are available and the urgent need for systematic monitoring of the major ice sheets and mountain glaciers is obvious.

3.3 Land Cover Classification

Highly accurate land cover classification into a number of individual classes requires a full-polarimetric L-band sensor. Due to the complementary properties of the L-

and X-band backscattering joint products from TerraSAR-L and TerraSAR-X enable even higher levels of classification performance necessary for crop monitoring and forest inventory. Dual frequency combinations are also required for cartographic maps of different thematic content and scale.

A full-polarimetric L-band SAR is the ideal sensor for soil moisture retrieval including surfaces with vegetation cover. Monitoring flood extent and supporting flood forecast in providing information on vegetation cover are further applications benefiting from TerraSAR-L products.

3.4 Marine Applications

TerraSAR-L features a Wave mode like the one on ENVISAT or ERS for retrieving ocean wave spectra. SAR observations represent the only global source of directional wave information enabling short-term forecasts for navigation and maritime operational applications and as input to meteorological models. Compared to numerical models, Wave mode derived climatologies of swell exhibit valuable differences related to local and seasonal environmental conditions and therefore allow investigating improved sea state warning related to extreme sea state conditions.

Knowledge of the sea bottom topography is essential for activities such as shipping, fishing, dredging, offshore construction and pipeline laying. Bathymetry can be derived from L-SAR images acquired over shallow water (typically 30-40 m) in the presence of strong tidal currents.

L-band radar may be more attractive for imaging of surface current fronts, eddies and internal waves at lower wind speed. The longer L-band (compared to C-band) wave is less sensitive to rapid variations in the boundary layer wind speed and will therefore be more modulated by varying surface currents.

Sea ice influences a number of important processes within the climate system. Among these processes are the radiation balance, the energy exchange between the ocean and the atmosphere, and deep ocean water formation. In order to gain a more detailed understanding of the various interactions and feedback mechanisms between sea ice and its environment, parameters such as extent, concentration, thickness, drift, type distribution, and deformation need to be monitored. TerraSAR-L will provide data complementary to the currently available C-band missions and will help to minimize sea ice classification ambiguities and to improve the detection of ice deformation features.

4. SYSTEMATIC OPERATIONS STRATEGY

Providing long-term systematic and repetitive observations over large areas is one of the major strengths of remote sensing technology, in particular for microwave sensors, which are not limited by low sun angle or persistent cloud cover. Our best example is the archive of data collected by ERS-1/-2 missions. For a system with basically one mode of operation a consistent and useful archive can be achieved without major planning efforts. For a more powerful system like TerraSAR-L, which can serve a number of quite different user needs, new strategies have to be implemented to optimise the mission exploitation.

We plan to identify key driving applications early in the preparation phase and to establish a systematic observation plan. Key elements of such a systematic acquisition scenario are: adequate and consistent sensor modes, adequate repeat cycle, and adequate timing of the acquisition to account for seasonal changes. Long-term continuity is another important factor to guarantee consistent data archives. Pre-launch, this planning can be performed and potential conflicts identified and resolved, resulting in an optimised use of the system resources.

5. CONCLUSIONS

TerraSAR-L is a very powerful SAR system based on a robust design with considerable margins. The spacecraft is based on the snapdragon architecture, which is optimised for large SAR antennas. Repeat-pass ScanSAR interferometry, more than 80MHz bandwidth

and full polarimetric capabilities are the key characteristics of the L-SAR. The 14-day repeat cycle provides global coverage and enhanced performance for INSAR applications.

Besides major contribution to applications in areas of climate change and interferometry, TerraSAR-L will also serve marine applications. Joint products from TerraSAR-L and TerraSAR-X are important for commercial services relying on detailed land cover classification products.

A systematic operations strategy will ensure optimum use of the system resources, consistent data archives and maximised exploitation of the TerraSAR-L mission.

6. REFERENCES

1. A. Rosenqvist, et.al., *Support to Multi-national Environmental Conventions and Terrestrial Carbon Cycle Science by ALOS and ADEOS-II – the Kyoto & Carbon Initiative*, Proceedings IGARSS 2003, Toulouse, France, 21-25 July 2003.
2. A. Rosenqvist, et.al., *The Use of Spaceborne Radar Data to Model Inundation Patterns and Trace Gas Emission in the Central Amazon Floodplain*, International Journal of Remote Sensing, Vol. 23, No. 7, pp. 1283-1302, 2002.
3. K. Daito, et.al., *L-band PS Analysis: JERS-1 Results and TerraSAR-L Predictions*, Proceedings of Fringe 2003, ESRIN, Frascati, 01-05 Dec 2003.

**This page intentionally
left blank (pagination)**

TerraSAR-X for Oceanography – Mission Overview

S. Lehner¹, J. Horstmann², J. Schulz-Stellenfleth¹, A. Roth¹, and M. Eineder¹

¹German Aerospace Center
Remote Sensing Technology Institute
D-82230 Wessling, Germany
Susanne.Lehner@dlr.de

²GKSS Research Center
Institute for Coastal Research
D-22087 Geesthacht, Germany
Horstmann@gkss.de

1. INTRODUCTION

TerraSAR-X is a new generation, high resolution radar satellite to be launched at the end of 2005. The objective of the mission is the setup of an operational spaceborne X-Band synthetic aperture radar (SAR) system in order to produce remote sensing products for commercial and scientific use. TerraSAR-X is the scientific and technological continuation of the highly successful Space Shuttle missions Spaceborne Imaging Radar-C/X-band Synthetic Aperture Radar (SIR-C/X-SAR) in 1994 (Evans and Plaut, 1996) and Shuttle Radar Topography Mission (SRTM) in 2000 (Werner, 2000). After an in-orbit commissioning period of approximately 5 month, in which the instrument will be calibrated and the system performance will be verified, TerraSAR-X will be fully operational for an active lifetime of 5 years.

The German Aerospace Center (DLR) and the ASTRIUM GmbH have agreed on an innovative co-operation scheme for the implementation of Earth observation satellites by realizing Germany's first Earth observation space project based on public-private partnership with considerable contributions from industry.

The TerraSAR-X mission will serve two main objectives:

- to provide the scientific community with high-quality, multi-mode X-band SAR-data for scientific research and applications
- to support the establishment of a commercial EO-market; and
- to develop a sustainable EO-service business in Europe, based on TerraSAR-X derived information products.

The broad spectrum of scientific applications, include: Hydrology, Geology, Climatology, Oceanography, Environmental- and Disaster Monitoring as well as Cartography. The scientific potential of TerraSAR-X is based on a combination of unprecedented features of the SAR instrument, which have never before been operational in space (Roth et al., 2002, Suess et al., 2002, Mittermayer et al., 2003).



Fig. 1: Artist view of the TerraSAR-X satellite.

- High geometric and radiometric resolution with an experimental very high resolution (~ 1 m) in 300 MHz mode
- Single-, Dual- and Full- Polarization modes
- Long term observation with the opportunity for multi-temporal imaging
- Precise attitude and orbit control and determination as well as phase stability e.g. for Repeat-Pass interferometry
- High synergy potential with other frequency bands (L-band: ALOS, TerraSAR-L, C-band: ENVISAT ASAR, RADARSAT-1 and 2 SAR)
- New imaging modes like ScanSAR, sliding/staring Spotlight and Dual Receive Antenna Mode
- the possibility of Repeat-pass as well as Along Track Interferometry (ATI) for moving target indication, and
- Full operator access to the highly flexible active phased array antenna for the realization of new imaging modes (like Along-track interferometry, Moving Target Identification, etc.) and the acquisition of custom designed image products

These technical features of TerraSAR are of strong interest for oceanography. In this paper several promising applications concerning wind, wave and current measurements as well as monitoring of morphodynamic changes are discussed.

2. SPACECRAFT

The TerraSAR-X satellite constitutes a mission-tailored *FlexBus* design with a total wet mass of

Product	Coverage [az x rg]	Resolution [az x rg]	Polarization	Full Performance Range
HR SpotLight	5 x 10 km ²	1.0 m x (1.5 – 3.5 m)	single, dual, quad	20 – 55 °
Spotlight	10 x 10 km ²	2.0 m x (1.5 – 3.5 m)	single, dual, quad	20 – 55 °
StripMap	≤1650 km x 30 km	3.0 m x (1.7 – 3.5 m)	single	20 – 45 °
StripMap (polarimetric)	≤1650 km x 15 km	6.0 m x (1.7 – 3.5 m)	dual, quad	20 – 45 °
ScanSAR	≤1650 km x 100 km	16.0 m x (1.7 – 3.5 m)	single, dual, quad	20 – 45 °
300 MHz Exp.-Mode Spotlight	5 x 10 km ²	1.0 m x (0.6 – 1.5 m)	single, dual, quad	20 – 55 °
Dual Receive StripMap	≤1650 km x 30 km	1.5 m x (1.7 – 3.5 m)	single, dual, quad	20 – 45 °
ATI		Acc. 15-60 km/h		

Table 1: Parameters of TerraSAR-X imaging modes. The blue color indicates experimental modes.

approximately 1025 kg related to 1350 kg total lift capability of the Dnepr-1 launch vehicle for the intended mission orbit. The body-mounted solar array delivers an orbit average power of ~800 W under EOL and worst case solar illumination conditions. A standard S-band TT&C System with 360° coverage in uplink and downlink is used for satellite command reception and telemetry transmission.

The attitude control system is based on reaction wheels for fine-pointing with magnet torquers for wheel desaturation. A mono propellant propulsion system is implemented to facilitate attitude control maneuvers necessary to achieve rapid rate damping during initial acquisition. Attitude measurement is performed with a GPS/Star Tracker system during nominal operation and a Coarse Earth and Sun Sensor in safe mode situations and during the initial acquisition.

3. SAR INSTRUMENT

The spacecraft will be equipped with a X-band SAR instrument with the following characteristics: The instrument is an active phased array X-band system with 384 transmit/receive (T/R) modules capable of operation in two polarizations, H and V. Beam steering is possible in azimuth (0.75°) and elevation (20°). Acquired SAR data are stored in a Mass Memory Unit of 256 Gbit capacity before they are down linked via a 300 Mbit/s X-band link. The antenna is body fixed and its approximate dimensions are 4.8 m in length, 0.7 m in width and 0.15 m in depth.

The instrument is designed for multiple imaging modes like Spotlight, Stripmap and ScanSAR operating with either single-, dual- or full polarization (Fig. 2). In addition it will enable an experimental high-resolution

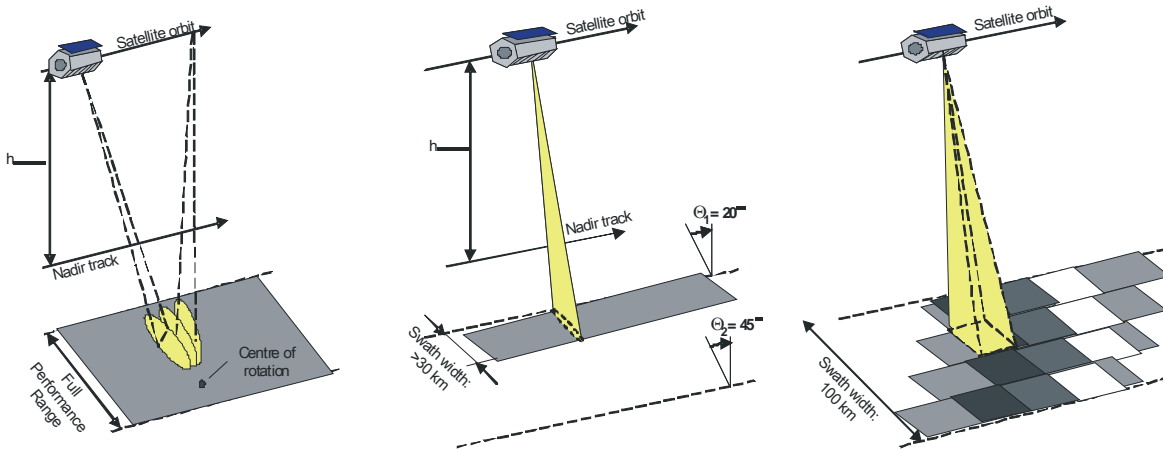


Fig. 2: Schematic sketch of the different imaging modes, which will be available for TerraSAR-X: Spotlight, Stripmap, and ScanSAR (from left to right).

300 MHz mode as well as the so-called Dual Receive Antenna Mode, which is based on the usage of the antenna in two azimuth halves and utilizes the redundant electronics set as a second Receiver channel. Main applications of the Dual Receive Antenna Mode will be

- Along-track interferometry, e.g. for ocean surface current measurements, and
- a full polarimetric mode, by simultaneously receiving H and V with the two subapertures.

In addition, it also allows an improvement of azimuth resolution as well as new calibration strategies.

An overview of the different TerraSAR imaging modes with the key parameters is given in Table 1, where the modes highlighted in blue are experimental modes.

4. OCEANOGRAPHIC APPLICATIONS

Due to its polarimetric and interferometric capabilities as well as the high spatial resolution TerraSAR-X is an interesting measurement tool for various oceanographic applications. In the following a short overview is given of some applications, which are of both scientific and commercial interest.

4.1 High resolution wind fields

In particular for applications like offshore wind farming a high spatial resolution of the SAR system is important (Lehner and Horstmann, 2001). SAR is the only system, which provides a synoptic view of wind fields over the ocean covering large areas (Lehner et al., 1998, Horstmann et al., 2002, Horstmann and Koch, this issue). An example wind field of the southern North Sea, acquired with the SAR aboard the European remote sensing satellite ERS-2, is given in Fig. 3. To analyze detailed wind field structures like e.g. wind blocking by a wind farm or wind shadowing within the grid of turbines, it is essential to look at finer spatial scales. A more detailed description of this application is given in Schneiderhan et al. (this issue). It is also expected that the polarimetric capabilities of TerraSAR-X will help to discriminate between atmospheric and oceanic features, which is e.g. important for the retrieval of wind direction from wind induced streaks.

Near grazing incidence it has been demonstrated that X-band radars are capable of measuring high resolution wind fields with an accuracy of up to 0.85 m/s in wind speed and 15° in wind direction (Dankert et al., 2003). For a future TerraSAR-X wind algorithm it is necessary to translate existing C-band wind speed algorithms to X-band. This can to some extent be done with existing X-band data from both airborne and spaceborne systems.

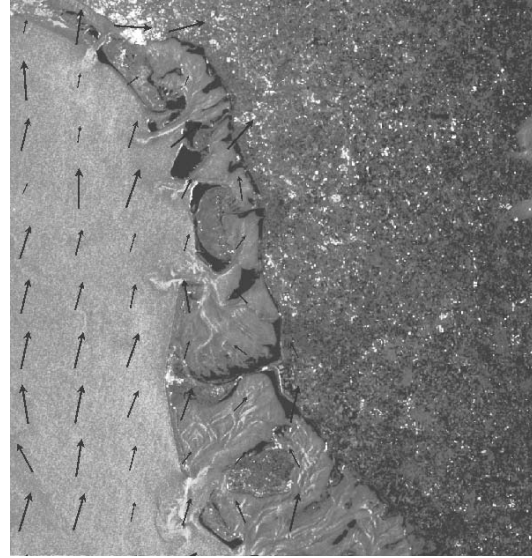


Fig. 3: ERS-2 SAR image mode scene (100 by 100 km) with imprinted derived wind field acquired on July 11, 2002, at 10:24 UTC.

Airborne X-band data suitable for such studies were e.g. acquired in the SINEWAVE (SAR Interferometry Experiment for validation of ocean wave imaging models) experiment (Schulz-Stellenfleth et al. 2001, Schulz-Stellenfleth and Lehner, 2001) and the Gijon experiment (Lehner et al., 2002).

In the Gijon experiment, which was carried out in the framework of the EUROROSE project, a three antenna airborne X-band InSAR system with about 1 m spatial resolution acquired data near the harbour of Gijon with simultaneous wind, wave and current measurements taken by HF radar and nautical radar.

4.2 High resolution ocean wave fields

Another interesting application of TerraSAR-X is the measurement of high resolution ocean wave fields in particular in coastal areas (compare Fig. 4). These measurements are especially important for applications dealing with harbour protection, offshore wind parks as well as wave farming.

Apart from the high spatial resolution the relatively low flight altitude of the satellite is beneficial for ocean wave measurements, especially because nonlinear effects (Hasselmann and Hasselmann, 1991) are less important than they are for the ERS or ENVISAT case. This improves the retrieval of ocean wave information as for example the measurement of the two-dimensional ocean wave spectrum (Schulz-Stellenfleth et al., this issue) or of the two-dimensional sea surface elevation fields (Schulz-Stellenfleth and Lehner, 2004) easier.

Furthermore, it is known that the availability of polarimetric information will improve the ocean wave measurements, as it gives some independent estimation of the ocean to SAR transfer functions (Engen et al., 2000). It is also expected that a statistical analysis of polarimetric TerraSAR-X data will give some new insight into the SAR ocean wave imaging process, e.g. the relative role of Bragg scattering and specular reflection.

A summary of the state of the art of wave measurements with SAR systems is given in Lehner and Ocampo-Torres (this issue).

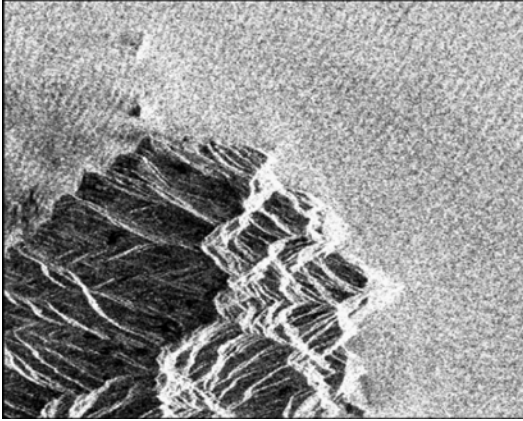


Fig. 4: ERS-2 SAR image of the north tip of the island Tenerife showing ocean surface waves.

4.3 Current measurements

High resolution current information is needed for many coastal applications like offshore operations or ship navigation. Another application, the high relevance of which has become evident in the recent Prestige disaster, is the estimation of oil slick drift in the case of ship accidents.

It has been shown in many studies that along track InSAR systems are capable of providing high resolution information on current fields (Goldstein and Zebker, 1987, Siegmund et al., 2004, Romeiser and Thompson, 2000).

The split antenna mode of TerraSAR-X enables along track interferometry and thus the estimation of current fields (Goldstein and Zebker, 1987). A first analysis of this application has shown that the retrieved current fields have to be smoothed over quite large areas in order to get reasonable signal to noise ratios (Romeiser et al., 2003). However, the achievable spatial resolution is still in the order of the promising results obtained with the SRTM system. Figure 5 shows a current field in the river Elbe estimated from SRTM data.

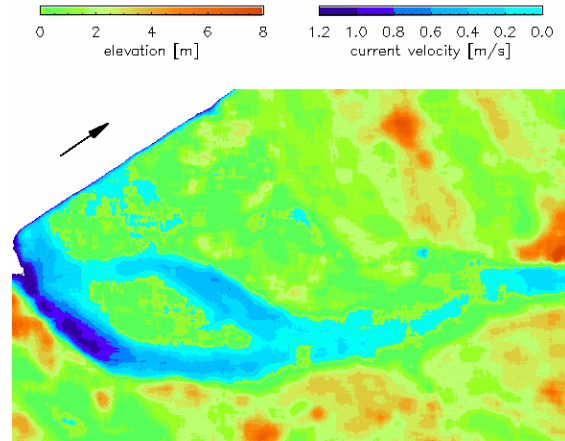


Fig. 5: Surface current field in the river Elbe derived from SRTM data

To measure jointly wave and current fields by the SAR gives a new opportunity to analyze ocean wave current interaction. This interaction is known to play an important role in the generation of extreme waves, causing many ship accidents, which was investigated in the European MaxWave project (Rosenthal et al., 2003).

4.4 Monitoring of Morphodynamic processes

Due to its high spatial resolution and polarimetric capabilities TerraSAR-X data are also ideally suited to observe morphodynamic processes, e.g. in river estuaries (Sigmund et al., 2004). These processes play a big economical role and are difficult to measure with traditional *in situ* instruments.

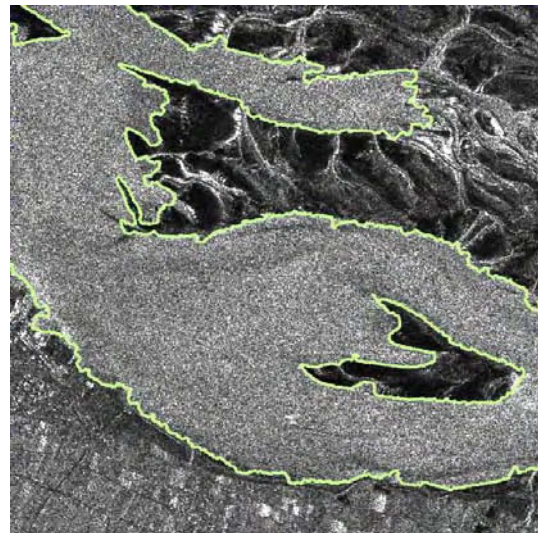


Fig. 6: Coastline in the river Elbe derived from an ERS-2 SAR image using a wavelet technique.

Techniques to measure morphodynamic changes from SAR data have been developed (Niedermeier et al., 2000), but were so far limited by the system resolution of the common systems like the ERS SAR. Furthermore, it is expected that the polarimetric information will improve the land water discrimination. It has also been shown that it is possible to use some information about scene coherence taken from the along track data to improve the land-water classification (Schwäbisch et al., 1997). In Fig. 6 an example is given, which shows an ERS-2 image acquired over the river Elbe to which the land-water boundary is superimposed, which was extracted by a wavelet based technique.

Furthermore, methods to derive information on topography from along-track data have been proposed in (Romeiser et al., 2000).

4.5 Polarimetry

An additional feature of the TerraSAR-X instrument is its polarimetric capability (see table 1). It is well known that polarimetric data contain information, which can help to

- discriminate between oceanic and atmospheric features
- improve wave measurements by providing estimates of the SAR transfer functions
- provide additional ocean wave information, e.g. on wave breaking

A polarimetric image acquired by the shuttle SIR-C/X mission over the western pacific ocean in 1994 is shown in Fig. 7. The white, curved area at the top of the image is a part of the Ontong Java Atoll, which belongs to the Solomon Islands group. The yellowish green area near the bottom of the image is an intense rain cell. This image is centered near 5.5° S and 159.5° E. The area shown is 50 km by 21 km. The colors in the image are assigned to different frequencies and polarizations as follows: Red is C-band horizontally transmitted and received; green is L-band horizontally transmitted and vertically received and blue is L-band horizontally transmitted and received.

5. OUTLOOK AND CONCLUSION

A first overview of the potential of the new TerraSAR-X system for oceanographic applications has been given. The new system has polarimetric and interferometric capabilities as well as very high spatial resolution, which makes it a valuable tool for wind, wave and current measurements as well as the monitoring of morphodynamic changes. Its relatively short revisit time of 11 days (4.5 days if look direction is changed) also makes TerraSAR an interesting instrument for monitoring accidents like oil disasters.

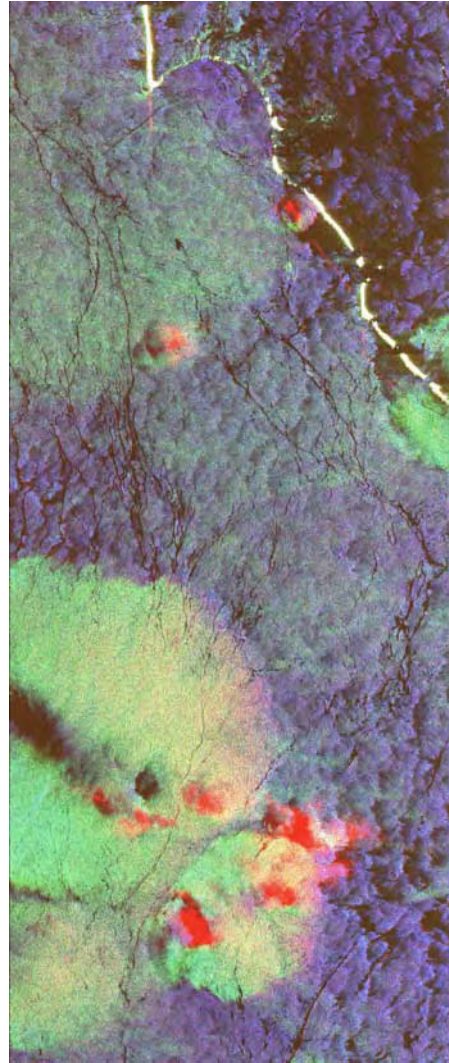


Fig. 7: Polarimetric image acquired by the shuttle SIR-C/X mission in 1994 (©NASA).

TerraSAR-X will ensure the operational acquisition of SAR data beyond the ERS and ENVISAT era. To make it more consistent with the data products currently used at weather centres it is desirable to define additional oceanographic modes similar to the ERS and ENVISAT wave mode. Furthermore, it will be necessary to translate the existing C-Band wind and wave retrieval algorithms to X-Band. Airborne and spaceborne proxy data to start this translation, like e.g. taken during the SIR-C/X-SAR and SRTM missions, exist.

REFERENCES

Dankert H., J. Horstmann, and W. Rosenthal, *Ocean Wind Fields Retrieved from Radar-Image*

- Sequences*, J. Geophys. Res., Vol. 108/C11, 3352, doi: 10.1029/2003JC002056, 2003.
- Engen, G., Vachon, P.W., Johnson, H., Dobson, F.W., *Retrieval of ocean wave spectra and RAR MTF's from dual-polarization data*, IEEE Trans. Geosc. Rem. Sens., Vol 38, pp- 391-403, 2000.
- Evans, D.L. and J. Plaut, *Science Results from the Spaceborne Imaging Radar-C/X-Band Synthetic Aperture Radar (SIR-C/X-SAR)*, Progress Report: Su Doc# NAS 1.26:206707, 271 p., 1996.
- Goldstein, R.M., Zebker, H.A., Interferometric radar measurements of ocean surface currents, *Nature*, Vol 328, pp 707-709, 1987.
- Hasselmann, K., and Hasselmann, S., *On the nonlinear mapping of an ocean wave spectrum into a synthetic aperture radar image spectrum*, J. Geophys. Res., pp. 10713-10729, 1991.
- Horstmann J., W. Koch, S. Lehner, and R. Tonboe, *Ocean winds from RADARSAT-1 ScanSAR*, Can. J. Remote Sensing, Vol. 28, No. 3, pp. 534-533, 2002.
- Horstmann J., and W. Koch, *High Resolution Ocean Surface Wind Fields Retrieved from Spaceborne Synthetic Aperture Radars Operating at C-Band*, ESA SP-Series, this issue.
- Lehner, S., Horstmann, J., Koch, W., Rosenthal, W., Mesoscale wind measurements using recalibrated ERS SAR images, J. Geophys. Res., Vol 103, pp 7847-7856, 1998.
- Lehner S. and J. Horstmann, *High resolution wind fields retrieved from spaceborne synthetic aperture radar images and numerical models*, in Proc. of Offshore Wind Energy Conference, Brussels, Belgium, 2001.
- Lehner, S., H. Günther, J. Horstmann, M. Bao, J. Schulz-Stellenfleth, Joint along-across track interferometry of ocean waves, Proceedings of the IGARSS 2002 conference in Sidney, Australia, 2002.
- Lehner, S., and F.J. Ocampo-Torre, *The SAR Measurements of Ocean Waves: Wave Session White Paper*, ESA-SP Series, this issue.
- Mittermayer, J. Lord, R., Boerner, E., *Sliding Spotlight SAR Processing for TerraSAR-X Using a new formulation of the extended chirp scaling algorithm*, Proc. IGARSS 2003, Toulouse, 2003.
- Niedermeier, A., Romaneessen, E. Lehner, S., *Coastlines In SAR Images Using Edge Detection By Wavelet Methods*, IEEE GRS, Vol. 38, No. 5, pp. 2270-2281, 2000.
- Romeiser, R., D.R. Thompson, Numerical study on the along track interferometric radar imaging mechanism of oceanic surface currents, IEEE TGARS, 38, pp 446-458, 2000.
- Romeiser, R., O. Hirsch, M. Gade, Remote Sensing of surface currents and bathymetric features in the German bight by along track SAR interferometry, In Proc. of the IGARSS 200 conference, pp 1081-1083, Piscataway, 2000.
- Romeiser, R., Breit, H., Eineder, M., Runge, H., Flament, P., De Jong, K., Vogelzang, J., *On the suitability of TerraSAR-X split antenna mode for current measurements by along track interferometry*, Proc. of the IGRASS 2003 conference, Toulouse, 2003
- Rosenthal W., S. Lehner, A. Niedermeier, J.C. Nieto Borge, J. Schulz-Stellenfleth, H. Dankert, and J. Horstmann, *Analysis of two dimensional sea surface elevation fields using spaceborne and ground based remote sensing techniques*. In: 13th International Offshore and Polar Engineering Conference & Exhibition, ISOPE 2003. Honolulu, HI (USA), 25.-30.05.2003, 2003.
- Roth, A., M. Eineder, B. Schättler, *TerraSAR-X: A New Perspective for Applications Requiring High Resolution Spaceborne SAR Data*, in Proc. of the International Geoscience and Remote Sensing Symposium, in Toronto, Canada, 2002.
- Schneiderhan T., J. Schulz-Stellenfleth, S. Lehner, and J. Horstmann, *SAR Wind Fields for Offshore Windfarming*, ESA-SP Series, this issue.
- Schulz-Stellenfleth, J., S. Lehner, Ocean wave imaging using an airborne single pass cross track interferometric SAR, IEEE TGARS, Vol 39, pp 38 – 44, 2001.
- Schulz-Stellenfleth, J., J. Horstmann, S. Lehner, W. Rosenthal, Sea surface imaging with an across-track interferometric synthetic aperture radar: The SINEWAVE Experiment, IEEE TGARS, Vol 39, pp 2017-2028, 2001.
- Schulz-Stellenfleth, J., and S. Lehner, *Estimation of Two-dimensional Sea Surface Elevation Fields from Complex Synthetic Aperture Radar Data*, IEEE Trans. Geosci. Remote Sens., accepted, 2004.
- Schulz-Stellenfleth, J., S. Lehner, and D. Hoja, *Ocean Wave Measurements from ENVISAT ASAR Data using a Parametric Inversion Scheme*, ESA-SP Series, this issue.
- Schwäbisch, M., S. Lehner, N. Winkel, Coastline extraction using ERS SAR interferometry, Proceedings of the third ERS Symposium Space at the Service of our Environment in Florence, pp 1049-1053, 1997.
- Siegmund, R., M. Bao, S. Lehner, R. Mayerle, First Demonstration of surface currents imaged by hybrid along and cross track interferometric synthetic aperture radar, Accepted for publication in IEEE TGARS, 2004.
- Suess, M., Riegger, S., Pitz, W. Werninghaus, R. *TerraSAR-X – design and Performance*, Proc. of EUSAR 2002, Köln, Germany
- Werner, M., *Shuttle Radar Topography Mission (SRTM) - Mission Overview*, in Proc. of EUSAR 2000, Munich, Germany, 2000.

A brief overview of the Advanced Land Observing Satellite (ALOS) and its potential for marine applications

Ake Rosenqvist⁽¹⁾, Daisuke Ichitsubo⁽²⁾, Yuji Osawa⁽²⁾
Akihiro Matsumoto⁽²⁾, Norimasa Ito⁽²⁾ and Takashi Hamazaki⁽³⁾,

⁽¹⁾Earth Observation Research & Applications Center, JAXA, Harumi 1-8-10-X23, Chuo-ku, Tokyo 104-6023, JAPAN

Email: ake.rosenqvist@jaxa.jp

⁽²⁾ALOS Project Team, Japan Aerospace Exploration Agency, 2-1-1 Sengen, Tsukuba-city, Ibaraki 305-8505, JAPAN

Email: ichitsubo.daisuke@jaxa.jp, osawa.yuji@jaxa.jp, matsumoto.akihiro@jaxa.jp, ito.norimasa@jaxa.jp

⁽³⁾GOSAT Project Team, Japan Aerospace Exploration Agency, 2-1-1 Sengen, Tsukuba-city, Ibaraki 305-8505, JAPAN

Email: hamazaki.takahi@nasda.go.jp

ABSTRACT

The Advanced Land Observing Satellite (ALOS) is scheduled for launch by the Japan Aerospace Exploration Agency (JAXA) in JFY 2004. ALOS will carry three remote sensing instruments: an L-band polarimetric Synthetic Aperture Radar (PALSAR), an along-track 2.5 metre resolution stereo mapper (PRISM) and a 10-metre multi-spectral scanner (AVNIR-2). The successor of the JERS-1 satellite (1992-1998), ALOS will not only provide enhanced sensor performance, but also novel technologies for high accuracy positioning and attitude determination. This paper, its technical part based largely on [1] and [2], provides a summary of ALOS characteristics, and brief discussion on its potential for marine applications

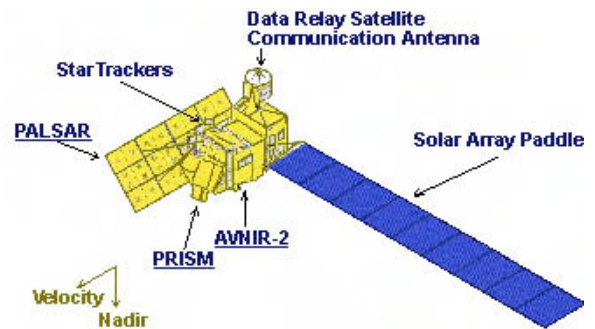


Fig. 1. ALOS in-orbit configuration

Table 1. ALOS characteristics.

Item	Characteristics
Orbit	Sun synchronous, Sub recurrent
Altitude	691.65 km
Recurrent period	46 days, sub-cycle: 2 days
Inclination	98.16 degree
Generated power	~ 7 kW (end of life)
Weight	Approx. 4,000 kg
Data recorder	96 G bytes, solid-state
Data link	240 Mbps (via DRTS) 120 Mbps (direct down link)

1. ALOS SATELLITE OVERVIEW

With a mass of about 4,000 kg, ALOS is the largest satellite built in Japan (Fig.1), planned for launch by an H-IIA rocket from Tanegashima Space Center in southern Japan in the fiscal year (JFY) of 2004. It will be placed in a sun-synchronous orbit at 691 km, with a descending local Equator pass time at about 10:30 (22:30 in ascending mode). The orbital revisit period is 46 days, with a potential 2-day revisit capability for the side-looking instruments. ALOS will carry three remote sensing instruments: PALSAR, PRISM and AVNIR-2 [3].

To accommodate the large data amounts generated by the three instruments, ALOS is equipped with an on-board 96 Gbyte solid-state data recorder. Down-linking of all global data will primarily be performed directly to Hatoyama Earth Observation Center (EOC), north of Tokyo, via JAXA's Data Relay Test Satellite (DRTS). The DRTS was launched into a geostationary orbit (E90°) in September 2002, and it operates with a data rate of 240 Mbps (K_a-band). Direct transmission from ALOS to local ground stations can be performed at a reduced data rate of 120 Mbps (X-band).

2. REMOTE SENSING INSTRUMENTS

2.1. PALSAR

The **Phased Array type L-band Synthetic Aperture Radar (PALSAR)** is an active microwave sensor developed jointly by JAXA and the Japan Resources Observation Systems Organization (JAROS). It is an enhanced version of the Synthetic Aperture Radar on JERS-1 (HH-polarisation; 35°off-nadir angle), also operating at L-band. The antenna consists of 4 segments, with a total size of 3.1 by 8.9 metres when deployed.

Table 2. PALSAR characteristics [4]

Polarization	Off-nadir angle (swath, resolution)
Center frequency	1270 MHz / 23.6 cm
Chirp band width	28 MHz (single pol.) 14 MHz (dual, quad-pol.)
Polarization modes	Single, dual, quad-pol.
Off-nadir angle	Variable: 7.2 - 51.4 deg.
Swath width	70 km (single/dual) 30 km (quad-pol) 350 km (ScanSAR 5-beam)
Noise Equivalent Sigma-0	< -24 dB (single pol) < -27 dB (dual pol) < -30 dB (quad-pol) < -25 dB (ScanSAR 5-beam)
S/A (Range)	~ 23 dB (single/dual) ~ 21 dB (quad-pol) ~ 25 dB (ScanSAR 5-beam)
Radiometric accuracy	< 1 dB relative (within scene) < 1.5 dB absolute (between orbits)
Data rate	240 Mbps (ScanSAR 120 Mbps)

PALSAR is a fully polarimetric instrument, operating with either single polarisation (HH or VV), dual polarisation (HH+HV or VV+VH), or full polarimetric mode. The look angle is variable between 7° and 51° (8-60° incidence angle). PALSAR can also operate in coarse resolution ScanSAR mode, with single polarisation (HH or VV) and 250-350 km swath width.

PALSAR can be technically operated in as many as 132 different modes. From an applications point of view however, such a large number of potential mode combinations rather becomes contra-productive, as the risk for programming conflicts between users becomes a real issue. In order to minimise such mode conflicts, seven modes of operation have been identified as the default modes to be used (Table 3). The default mode selection was made as a compromise taking scientific criteria, programmatic aspects and satellite operational constraints into consideration.

The data recording rate is 240 Mbps in single-, dual- and full-polarimetric modes, which thus requires down-linking via the DRTS. The ScanSAR however operates at 120 Mbps, which allows direct down-link of data to local ground stations (within the ALOS ground network).

Table 3. PALSAR default observation modes

Polarization	Off-nadir angle (swath, resolution)
HH	34.3 deg. (70 km, 10 m)
HH	43.4 deg. (70 km, 10 m)
HH+HV	34.3 deg. (70 km, 20 m)
HH+HV	43.4 deg. (70 km, 20 m)
HH+HV+VH+VV	21.5 deg. (30 km, ~30 m)
ScanSAR (HH)	5-beam mode (350 km, 100 m)

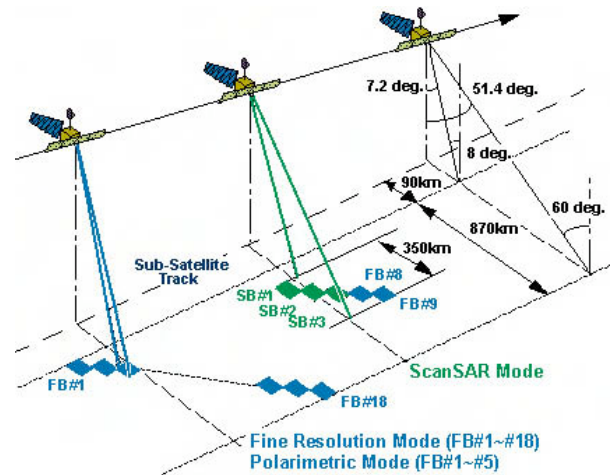


Fig. 2. PALSAR observation characteristics

2.2 PRISM

The **Panchromatic Remote-sensing Instrument for Stereo Mapping (PRISM)** is a panchromatic (520-770 nm) radiometer with 2.5-metre spatial resolution [5]. It has three independent optical systems for nadir, forward and backward looking to achieve along-track stereoscopy. Each telescope consists of three mirrors and a CCD array for push-broom scanning. The swath width is 70 km in nadir-only mode, and 35 km during triplet mode operations (Fig. 3)

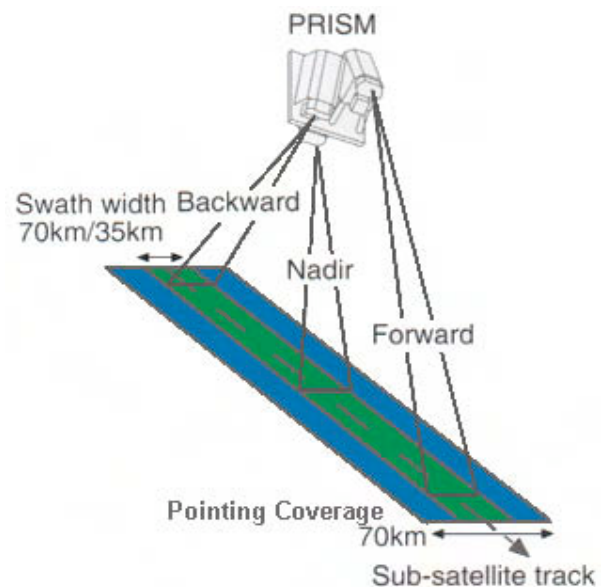


Fig. 3. PRISM observation characteristics

Table 4. PRISM characteristics.

	Characteristics
Spectral range	520-770 nm
Number of optics	3 (forward, nadir, backward)
Base-to-height ratio	1.0
Spatial resolution	10 m (nadir)
Swath width	70 km (nadir only) 35 km (triplet mode)
Pointing angle	+/- 1.5 deg. (across-track)
Data rate	240 Mbps

The PRISM telescopes are installed on both side of an optical bench with precise temperature control. The forward and backward telescopes are inclined + and – 24 degrees from nadir to realise a 1.0 base-to-height ratio. The wide field of view (FOV) provides fully overlapped three-stereo (triplet) images (35 km width) without mechanical scanning or yaw steering of the satellite (Fig. 3). To achieve full ground coverage with a 35 km swath, two 46-day cycles are required, during which the three telescopes are tilted (+/- 1.5°) in across-track direction.

The prime mission of PRISM is global topographic mapping at a scale corresponding to 1:25,000 and generation of fine resolution digital elevation models.

2.3 AVNIR-2

The successor to the VNIR and AVNIR instruments on JERS-1 and ADEOS, the **Advanced Visible and Near Infrared Radiometer type-2 (AVNIR-2)** on ALOS is a multispectral radiometer with 10 metres ground resolution.

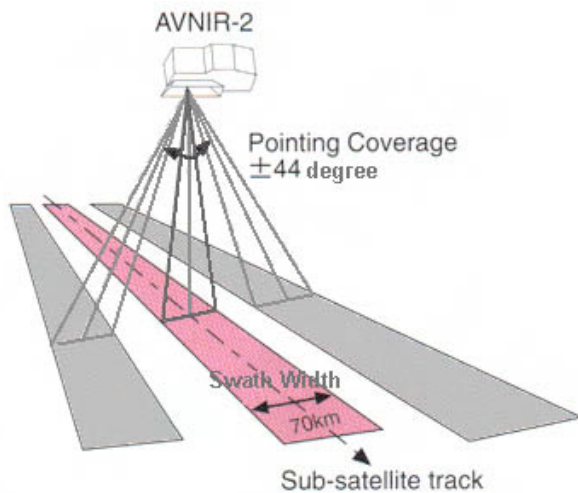


Fig. 4. AVNIR-2 observation characteristics

Table 5. AVNIR-2 characteristics.

	Characteristics
Blue	420-500 nm
Green	520-600 nm
Red	610-690 nm
Near-Infrared	760-890 nm
Spatial resolution	10 m (nadir)
Swath width	70 km
Pointing angle	+/- 44 deg. (across-track)
Data rate	120 Mbps

The primary objectives of AVNIR-2 are disaster monitoring and land cover mapping and with its across-track viewing capabilities (+/- 44°), observation of disaster areas within 2 days' repeat can be foreseen. The side-looking capacity also allows simultaneous observations with the PALSAR – a unique property which can be expected to contribute to microwave-optical data fusion applications.

3. ALOS OBSERVATION STRATEGY

Retrieval of bio- and geophysical parameters from remote sensing data in an operational manner is a strong driver of current scientific work, requiring not only the availability of appropriate sensors and inversion algorithms, but also that the data that are to be utilised are acquired in a planned and systematic manner. Regional extrapolation of locally developed retrieval algorithms is in this context imperative if the applications are to be more than of mere academic interest, and spatially consistent data over large areas – ranging from national to continental scales - thus become a requirement.

JAXA has acknowledged the critical need for regionally consistent data by setting aside a significant share of the ALOS acquisition capacity for this purpose, to establish dedicated a Global Data Observation Strategy in support to climate change research and environmental conventions [6]. The strategy is designed to provide spatially and temporally consistent, multi-seasonal coverage of all land areas on a repetitive basis, with all three sensors, during the lifetime of the ALOS satellite. It also comprises consistent, repetitive coverage of all major coastal areas, lakes and inland seas.

The observation strategy, based on a number of basic acquisition concepts [7], is described in detail in [8].

4. ALOS TECHNICAL DEVELOPMENT

Very high accuracy mapping capacity is a major mission driver for ALOS, and the following accuracy requirements have been taken into account in the satellite design [9, 1, 2]:

- Satellite positioning information within 2.5 m;
- Satellite attitude information within 0.0002 deg.
- Long term attitude stability within 0.0002 degrees per 5 seconds
- Absolute time information for each pixel within 370 μ s accuracy.
- Minimizing thermal distortion of sensor's optical axes and between the optical axis and attitude sensors (Star Tracker and Inertial Reference Unit) during the entire orbital period (~100 minutes).

4.1 Precise Position and Attitude determination

To accommodate high accuracy mapping without the use of ground control points (GCP's), new systems for position and attitude determination have been developed. A dual frequency carrier phase tracking type GPS receiver provides 1 metre position accuracy and a high accuracy star tracker (STT) provides 0.0002 degrees accuracy in attitude, corresponding to a 2.5 metre nadir pointing uncertainty on ground). The STT is equipped with three optics (STO), two are used simultaneously and one is redundant. In order to achieve the best star position accuracy possible, the optics use a low-thermal distortion structure, implementing tight temperature regulations.

Table 6. Star Tracker specifications

Item	Characteristics
Number of trackers	3 (2 in operation, 1 redundant)
FOV	8 * 8 deg
Magnitude	4 ~ 6.5 mag
No. of stars	10*2 sets (acquisition) 5*2 sets (track)
Star Position	9 arc sec (random)
Error (3 sigma)	0.74 arc sec (bias)
Output Rate	1 Hz

4.2. Absolute Time Clock

Rather than utilizing a traditional on-board crystal oscillator as internal clock, which require periodical calibration, the internal clock on ALOS is completely synchronized within the accuracy of 404 ns (3 sigma) to the GPS absolute time, yielding 1 μ s order absolute time accuracy.

4.3. High Stability attitude control system

When observing the land surface from a high altitude orbit, attitude stability is critical. In order to minimize geometric distortion in the imagery, the attitude movement (angular velocity) of the ALOS platform is stabilized within 0.0002 degree per 5 seconds, corresponding to 2.5 m, or one pixel, distortion within a 35 km square scene. Disturbances from major vibration sources, such as the data relay communication antenna pointing mechanics, the AVNIR-2 pointing mirror drive mechanics, the solar array paddle drive mechanics and the PALSAR antenna structure, are carefully controlled with a feed forward technique and on-board parameter tuning.

4.4. Thermal Distortion

During an orbital revolution, variations in the solar input along the orbit causes thermal distortion of various components of the instruments and satellite structure, subsequently resulting in instrument performance degradation.

In order to minimize the effects of thermal distortion, ALOS features an integrated optical bench concept, with the PRISM optics, star trackers (STT), inertial reference unit (IRU), and jitter sensors (ADS), are all integrated on one rigid optical bench (Fig. 5). The bench is covered by a Multi Layer Insulator (MLI) allowing temperature control within +/-3 degrees (K).

The satellite primary structure and truss members are also insulated with MLI and thermal expansion is cancelled by a negative expansion, so called CFRP, truss mechanism.

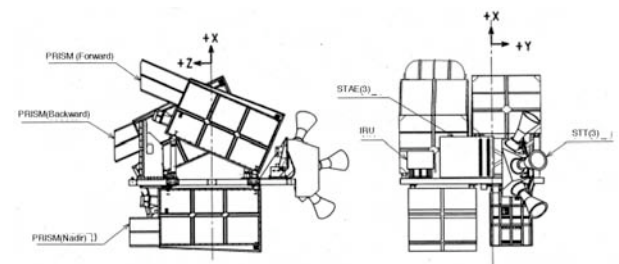


Fig. 5. PRISM, STT, IRU and ADS on the optical bench

5. L-BAND MARINE APPLICATIONS

PALSAR utilisation is primarily focused on terrestrial applications, in particular global monitoring of forest and wetlands [6] and crustal deformation measurements, as well as DEM generation, disaster monitoring and geological resources surveys. These are established L-band applications which have been amply demonstrated by JERS-1 SAR.

PALSAR can however also be expected to contribute to marine and ice applications, to complement Envisat and Radarsat C-band observations with less common L-band data.

JERS-1 SAR has not been utilised widely for marine and ice applications, primarily due its comparably poor noise floor (~ -18 dB), which was caused by reduced power supply to the SAR antenna (325 W) following initial technical problems with the antenna deployment. Despite this shortcoming however, JERS-1 can be used to demonstrate the potential value of L-band SAR for certain marine applications, thus indicating a role for ALOS PALSAR.

Fig. 6 shows internal waves in the Andaman Sea, off the west coast of Thailand, that are clearly visible in the JERS-1 L-band SAR data. Notable is the temporal stability of the wave patterns, which extend over two adjacent JERS-1 swaths, acquired 24 hours apart on Jan. 24 (centre) and Jan. 25, 1997 (far left).

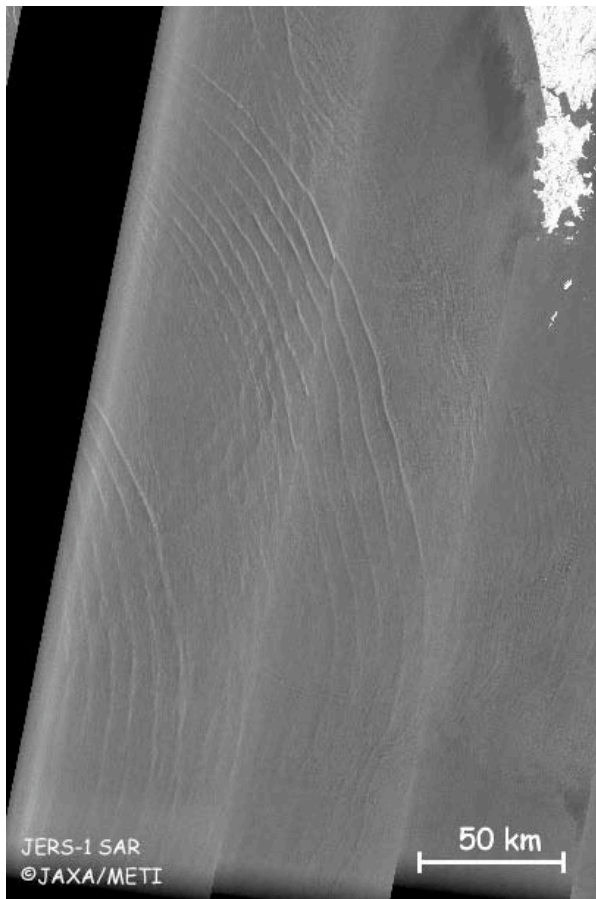


Fig. 6. Extract from the JERS-1 SAR Global Rain Forest Mapping (GRFM) mosaic of South-East Asia, providing an L-band SAR view of internal waves in the Andaman Sea (Jan. 23-25, 1997),

L-band SAR sensitivity to sea surface waves and wind patterns is illustrated in Fig. 7, which indicates varying surface roughness, and presumably winds from the south-east, off the islands of Samui and Phangan in the Gulf of Thailand. The relatively shallow off-nadir angle, fixed at 35° for JERS-1, does not seemingly affect the backscatter response, which also allows detection of ships and suspected oil slicks (Fig. 8).

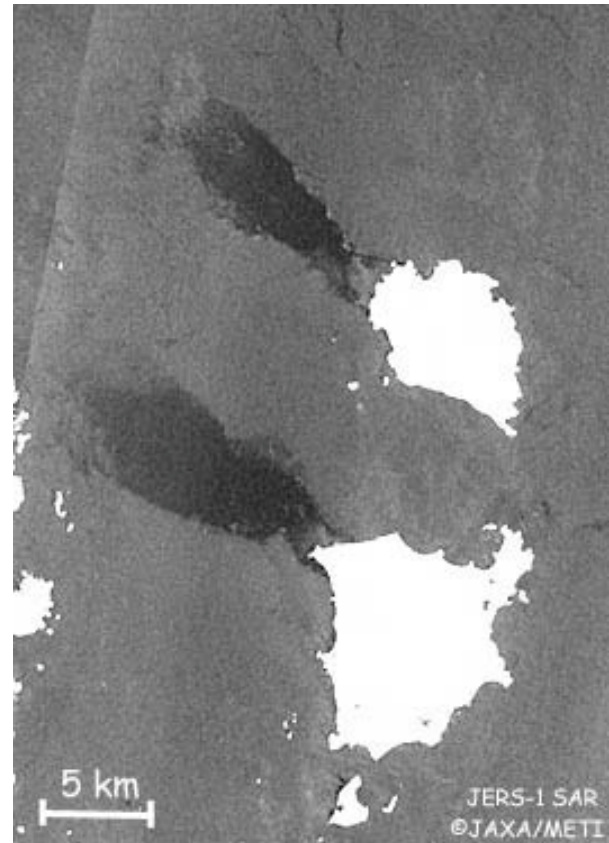


Fig. 7. Surface wind patterns observed by JERS-1 SAR on Nov. 25, 1997.

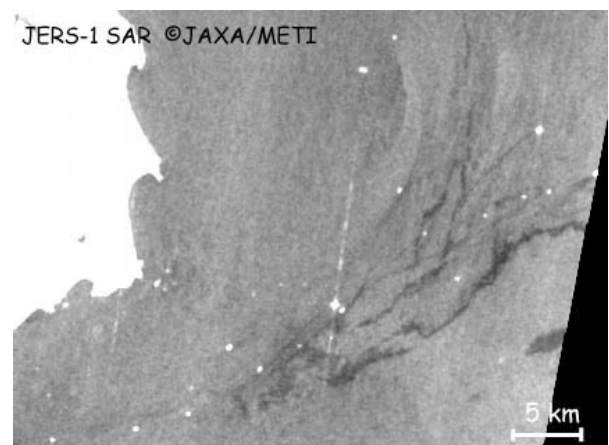


Fig. 8. Ships in the Singapore Strait (JERS-1 SAR, Nov. 14, 1997)

The limited radiometric sensitivity has however restricted JERS-1 SAR applications to ice, and the utility of L-band SAR for retrieval of ice physical parameters has instead been demonstrated using Pi-SAR, a Japanese airborne SAR system [10, 11].

To support such applications, as well as that of terrestrial ice sheets, fine resolution PALSAR acquisitions over Antarctica and its surrounding oceans are planned several times per year. PALSAR is expected to contribute to ship routing and monitoring of sea ice movements in the Sea of Okhotsk, where the Japan Coast Guard plan frequent observations during the winter season in the low resolution ScanSAR mode.

6. SATELLITE DEVELOPMENT STATUS

The integration and testing of the ALOS Proto-Flight Model (PFM) is currently in progress at JAXA Tsukuba Space Center (Fig. 9), following successful system development tests using the Mechanical Test Model (MTM), the Thermal Test Model (TTM), and the Engineering Model (EM).



Fig. 9. ALOS PFM at JAXA Tsukuba Space Center

Following integration of all subsystems on the PFM, proto-flight tests are being conducted, including both electrical and environmental tests (vibration, acoustic, separation shock and thermal vacuum tests). Transportation of the satellite hardware to the launch site in Tanegashima, in southern Japan, will take place during the summer of 2004. The launch is currently scheduled for the Japanese Fiscal Year 2004 (April 2004 – March 2005), possibly in December 2004.

7. REFERENCES

1. Ichitsubo. A., Hamazaki T., Osawa Y. and Matsumoto A. *Development Status for the Advanced Earth Observing Satellite*, Proc. ISPRS Commission VII WG6, Kyoto, October 2003.
2. Matsumoto A., Hamazaki T., Osawa Y. and Ichitsubo. A. *Development Status of ALOS's Sensors*, Proc. ISPRS Commission VII WG6, Kyoto, October 2003.
3. Hamazaki, T., *Overview of the Advanced Land Observing Satellite (ALOS): Its Mission Requirements, Sensors, and Satellite System*, ISPRS Joint Workshop "Sensors and Mapping from Space 1999", Hanover, Germany, 1999.
4. Hamazaki, T., *PALSAR Performance*, NASDA doc. NBF99019, National Space Development Agency of Japan, Oct. 1999.
5. Osawa, Y., *PRISM: a panchromatic three-line sensor for mapping onboard ALOS*, pp. 173 – 180, Proc. of SPIE, vol. 3498, EUROPT, Barcelona, Sept. 1998.
6. Rosenqvist A., M. Shimada, T. Igarashi, M. Watanabe, T. Tadono and H. Yamamoto, *Support to Multi-national Environmental Conventions and Terrestrial Carbon Cycle Science by ALOS and ADEOS-II – the Kyoto & Carbon Initiative*. International Geoscience and Remote Sensing Symposium (IGARSS'03), Toulouse, France. July 21-25, 2003.
7. Rosenqvist, A., Milne T. and Zimmermann, R., 2003. *Systematic Data Acquisitions—A Pre-requisite for Meaningful Biophysical Parameter Retrieval?* IEEE Transactions on Geoscience and Remote Sensing, Communications, Vol. 41, No. 7, pp.1709-1711.
8. Rosenqvist A., M. Shimada, M. Watanabe and T. Tadono, *Systematic Data Observation Strategies for ALOS PALSAR, PRISM and AVNIR-2*. JAXA EORC proc. 2nd ALOS PI Workshop, Awajishima, Japan, Jan. 19-23, 2004.
9. Iwata, T. et al, *Precision Attitude and Orbit Control System for The Advanced Land Observing Satellite (ALOS)*, AIAA Guidance, Navigation & Control Conference, Austin, August 2003.
10. Matsuoka T., S. Uratsuka, M. Satake, A. Nadai, T. Umehara, H. Maeno, H. Wakabayashi, F. Nishio and Y. Fukamachi. *Deriving sea-ice thickness and ice types in the Sea of Okhotsk using dual-frequency airborne SAR (Pi-SAR) data*, Annals of Glaciology, vol.34, pp. 429-434 (2002).
11. Wakabayashi H., T. Matsuoka, K. Nakamura and F. Nishio, "Estimation of sea ice physical parameters using polarimetric SAR : Results from Okhotsk and Lake Saroma campaign", Annals of Glaciology, vol.33, pp. 120-124 (2001).

SAOCOM – 1 ARGENTINA L BAND SAR MISSION OVERVIEW

Alberto E. Giraldez

CONAE, Av. Paseo Colon 751, (1063) Buenos Aires, ARGENTINA, Email:agiral@conae.gov.ar

ABSTRACT/RESUME

The Argentinian Space Agency (CONAE) decided to build and operate a SAR Mission in 1996, as indicated in the National Space Plan 1996-2007, and subsequent revisions.

During the period 1996-1999, several meetings with potential users from different areas (emergencies, agriculture, ecology, forestry, glaciology, geology, oceanography, etc.) have been organized by CONAE, and the users requirements were processed and refined in an iterative process with them.

The driving concept is to build up a SAR Mission mainly devoted to be used in operational applications, with technical specifications useful also for the development of new scientific developments.

The next section will be devoted to explain briefly the main reasons of a SAR Mission, and of the Band selection, based on envisioned applications and environment constraints.

In Section 2 the specific requirements to the instrument will be explained.

Section 3 will describe the requirements on the satellite to be fulfilled in order to get the necessary information.

Section 4 describes the ground segment architecture being developed to be in line with the Mission requirements, and Section 5 describes the present status of the construction of satellite and associated activities in the ground segment.

1. GENERAL SPECIFICATIONS

The basic concept of this satellite Mission is that it must provide information for natural and anthropogenic disasters prevention, assessment and mitigation, and be also useful for economic activities as agriculture, mining, ocean monitoring etc..

There is a third set of activities as important as the ones described, related with Antarctic monitoring, continental glaciers evolution and global change related indicators monitoring, which must also be satisfied.

Based on the above constraints and requirements, it must be a day/night observation mission, with a high revisit frequency, and almost immune to meteorological conditions. Therefore, the best solution to those simultaneous demands is a SAR mission.

As one of the most common emergencies is the flooding of extense areas, in most cases heavily

forested ones, the most appropriate band for this purpose is the L Band.

As it also must satisfy the agricultural and oceanic demands, as well as science ones, it has been decided to implement polarimetric capability as one operation mode.

To cover extense areas and provide a high revisit frequency, for emergencies as well as for oceanic observations, two ScanSAR modes are available, and the possibility of left (default) and right looking capability.

The list of application areas identified in agreement with the users is detailed in the Mission Requirement Document [1].

In order to enhance the area coverage, two regions were defined in the illuminated zone, the first one, is formed by the standard beams, with a high noise equivalent Sigma0 and high values of ambiguity rejection, useful for studies and applications requiring a good absolute calibration, and a second region of extended beams, with less sensitivity, useful for applications not requiring absolute calibration and with high thematic contrasts.

This double approach has been very useful at the time of the detailed analysis of requirements and needs of different users.

At present we still continue working with the users in refining some aspects, and trying to maximize the applications of the mission.

The Table 1 summarizes the instrument specifications for standard beams (Single Pol. or Double Pol.)

Table 1

Frequency (MHz)	1275
Max. Bandwidth (MHz)	50
Transmit Power (Kw)	4.1
Operation modes	Stripmap & ScanSAR
Antenna looking angle	Leftside (default)
$NE\sigma_0$	<-25 dB
Cross Pol. Isolation	> 25 dB
Operation time per orbit	15 minutes
Digitization	8 bits
Stripmap resolution	10 meters x 10 meters
ScanSAR resolution	100 meters x 100 meters
Swath width in stripmap	>65 km (each beam)
Swath in ScanSAR wide	>320 km
Transmission	HH or VV

Reception (Single Pol)	HH or VV
Reception (Double Pol.)	HH & HV or VV&VH

Both in Single and Dual polarization modes, the transmitter is set to one polarization (Horizontal or Vertical), and remains so during the acquisition time of a frame (minimum 30 seconds), while the two reception channels are activated in different polarizations (Double), or only one receiver is active in copolar reception (Single mode).

The looking direction can be shifted to right-looking for acquisition of data during a maximum of 5 minutes in one orbit. The manoeuvre takes several minutes, so it cannot be made more than once per orbit. As in that condition the solar power collection is diminished, and probably there is no ground station in visibility of the satellite data downloading antenna, the acquisition in that position will be stored onboard to be downloaded in a future pass over a ground station.

The Table 2 summarizes the instrument specifications for standard beams (Quadpol.)

Table 2

Frequency (MHz)	1275
Max. Bandwidth (MHz)	50
Transmit Power (Kw)	4.1
Operation modes	Stripmap
Antenna looking angle	Leftside (default)
NE σ_0	<-25 dB
Cross Pol. Isolation	> 25 dB
Operation time per orbit	5 minutes
Digitization	8 bits
Strimap resolution	10 meters x 10 meters
Swath width in stripmap	>30 km (each beam)
Available illumination range	> 170 km
Transmission (QuadPol)	Alternating HH and VV
Reception (QuadPol)	HH&HV and VV&VH
Mission lifetime	5 years

In Quadrupole mode (Quadpol), the transmitter power is directed to the Vertical antenna in one pulse, and to the horizontal antenna in the following pulse, continuing this alternate polarization transmission during all the acquisition time.

Simultaneously, both receiver channels are activated, receiving co and cross-pol signal simultaneously. As each polarization must transmit at an adequate PRF, dictated by the antenna size and nadir echo blocking, the effective PRF of the instrument becomes duplicate, with a duplication of power consumption and halved reception times. This impacts in the time available for echo reception, reducing the available swath width to

less than half as compared with single or double pol. Operation.

Even resulting in a very narrow swath for many applications, is of great value for many other applications involving the analysis of polarization rotation depending on the type and topology of the scattering region.

2. SPECIFIC INSTUMENT REQUIREMENTS

As mentioned in the previous section, there are two viewpoints in the instrument specifications, depending on the users needs.

One of them requires high quality radiometric and geometric accuracy (eg. natural resources identification, interferometry, glaciology) and the other needs high revisit frequency for monitoring of a specific operational requirement (eg. Floods , fires, ocean characteristics, ice on sea), perhaps without the extremely high accuracy in the radiometric information needed in the other set of applications.

The satisfaction of both sets of requirements simultaneously, and with the highest set of information quality and resolution specifications implies a dense constellation of instruments, far beyond our possibilities. The adopted decision has been twofold. First to use two identical satellites, looking left or right, depending on requirement, and with a scanning in range high enough to reduce the revisit time to nearly two days at the equator in Single and Double modes. The wide area coverage conspires against the high data quality requirement, then that area is divided in two subareas, with different requirements in ambiguities and NES σ_0 specifications. This approach gives us an expanded capability in revisit frequency, but not enough for a daily monitoring capability of emergencies. The second one is an agreement with the Italian Space Agency (ASI), which is planning the COSMO SkyMED constellation of four X Band SAR satellites, to share information in an operational agreement.

The agreement has been signed in 2000, and since then we are working together to get the maximum from such mixed system. This way, the revisit time reduces to 12 hours, and the monitoring of emergencies is fully covered, and simultaneously both agencies will have two band SAR information, to generate merged X and L band products. In the last four years, we have been working with ASI as a Joint Team, to assess the

feasibility of such system, and the set of instruments, satellites and ground segment common requirements for this to be successful [2] and [3].

In our last revisions, which are taking place now, a considerable improvement of the joint system has emerged, with the definition of common observation areas, with similar geometry, for polarimetric, bi-band products[4].

The system so defined is named SIASGE (Sistema Italo Argentino para la Gestion de Emergencias), and is in its final stage of detailed definition.

Under this last configuration, both SAOCOM satellites will cover incidence angles from 20 to 57 degrees, corresponding to an access width of 600 km for the single and double polarization, and a reduced width of 170 km in quadpol modes. In all cases looking left as default, with the option of right looking whenever necessary.

Table 3 shows the set of possible sensing capabilities for Single polarization and Double polarization modes.

Table 3

Stripmap High Resolution	Pixel size < 10m x 10m
Stripmap Mid Resolution	Pixel size > 25m x 25m
ScanSAR Narrow	Pixel size 50m x 50m
ScanSAR Wide	Pixel size 100m x 100m
Stripmap High Resolution	Range swath > 60 km
Stripmap Mid Resolution	Range swath > 60 km
ScanSAR Narrow	Range swath > 170 km
ScanSAR Wide	Range swath > 320 km

Table 4 shows the set of possible sensing capabilities for Quadpol polarization modes.

Table 4

Stripmap High Resolution	Pixel size < 10m x 10m
Stripmap High Resolution	Range swath > 30 km
Number of possible beams	6 Beams

3. SATELLITE REQUIREMENTS

As indicated in the previous section, the types and interests of users is broad and diverse. In some cases users are not interested in high absolute calibrated products, but fast availability of the information and

useful for the evaluation of a specific type of information as roughness and specific pattern in highly variable environment surface (ocean applications) , in the widest available area and as frequently as possible. In the other end, the interferometric applications require a very precise orbit control and stability with the lowest possible ambiguity figure.

As this pair of cases, there are several pairs of competing requirements.

The decision has been to adopt the most demanding requirement as baseline for the system design.

Table 5 describes the orbital and satellite control requirements adopted.

Table 5

Orbit type	Polar, Sun-synchronous
Local time Desc. Node	06:00 PM
Repeat cycle	16 days
Coverage	Global in all modes
Orbit Control	Within 25% of baseline
Orbit error determination	< 1 m (GPS) position
Orbit error determination	<1m/s in velocity
Attitude determination	InSAR requirements
Yaw steering capability	+/- 3.5 deg /orbit
Geolocation error	On line: < 7 pixels
Pointing accuracy (3 axes)	< 0.01 degree

Table 5 indicates the satellite control in real time.

Off line, by orbit restitution and telemetry data processing the position and attitude information precision is increased in one order of magnitude.

The data downlink will be channel of 320 Mhz, (two adjacent subcarriers 110 Mhz bandwidth each), in X band, in the frequency slot assigned by ITU for this purpose.

The telemetry, Tele-command and Control (TT&C) channel will be at S Band, as also assigned by international regulations.

4. GROUND SEGMENT

The ground segment, includes all the activities from spacecraft control to product generation and distribution.

The spacecraft control will be done in the Cordoba ground station, as it is being done for SAC-C, and also the Mission Operation Centre will be at the ground station.

The engineering model of the spacecraft and instruments will be on line to perform all tests and commands tests, previous to sending them to spacecraft.

The Data Acquisition Centre, will download the data, pre-process and process the SAR data locally, archive it and distribute to users.

The cataloguing is connected on line with the processing and archiving facility, in order to transfer to the web the information on available information and images almost in real time.

The Mission Operation Centre will have a system and instrument simulator, to perform the following tasks:

Satellite operation planning

Instruments operation planning

Satellite troubleshooting capability

Instrument troubleshooting capability

Generate simulated raw data for satellite and instrument specific conditions.

Process the simulated raw data to detect and fix contingencies.

Instrument and products calibration will be performed at the Mission Operation Centre by means of onboard calibration information as well as sensing over specific calibration areas (deployed corner reflectors, transponders and extended uniform backscatter areas).

2. ASI / CONAE , *ASI-CONAE EO Joint Applications and Products Identification* , June 2003.

3. ASI / CONAE , *SIASGE Mission Requirements*, Doc. RQS /SIA/ 008 /ASI-CONAE

4. ASI / CONAE , *SIASGE System Requirements*, Doc. RQS /SIA/ 0009 /ASI-CONAE.

5. MISSION STATUS

The present status of the Mission is as follows.

The satellite and the services are all defined and under construction.

The SAR antenna is in its engineering model construction stage, checking the quality and repeatability of antenna units (eight antennas in a single block), and the qualification of tiling process of antenna units.

SAR electronics is in its prototype stage, and engineering units are being tested.

SAR simulation operation and SAR processing software is already built and being tested with a set of prototype operation modes, and will be finished once the final flight configuration be accepted. This task is being done in cooperation with the Centre Spatial de Liege (Belgium), cooperation which includes a SAR Processor and Polarimetric and Interferometric tools.

All the details on applications and project status can be found in the CONAE web page (www.conae.gov.ar) .

6. REFERENCES

1. Giraldez, A. E. *SAOCOM Mission Requirements* CONAE Doc. SOG-SRM-RQ-00100-A. Rev 2003.

List of Participants

**This page intentionally
left blank (pagination)**

name	Institution	Country	E-post
Don Atwood	Alaska Satellite Facility	ALASKA	datwood@asf.alaska.edu
Alberto Giraldez	Conae	ARGENTINA	agiral@conae.gov.ar
João Antonio Lorenzetti	Brazilian Space Research Institute	BRASIL	loren@ltid.inpe.br
Paris W. Vachon	Canada Centre for Remote Sensing, Natural resources Canada	CANADA	paris.vachon@ccrs.nrcan.gc.ca
Dean Flett	Canadian Ice Service	CANADA	dean.flett@ec.gc.ca
Mohamed Farhat	Canadian Space Agency	CANADA	mo.farhat@space.gc.ca
Gordon Staples	RADARSAT International	CANADA	gstaples@rsi.ca
Ian Robinson/Diane Robinson	Southampton Oceanography Centre	ENGLAND	ian.robinson@soc.soton.ac.uk
Susanne Ufermann	Southampton Oceanography Centre	ENGLAND	ufermann@soton.ac.uk
Kim C. Partington	VEXCEL UK	ENGLAND	kim.partington@vexcel.co.uk
Fabrice Collard	BOOST Technologies	FRANCE	fabrice.collard@boost-technologies.com
Vincent Kerbaol	BOOST Technologies	FRANCE	vincent.kerbaol@boost-technologies.com
Alexis Mouche	CETP/CNRS	FRANCE	amo@cetp.ispl.fr
Niamh Connolly	ESF Marine Board	FRANCE	nconnolly@esf.org
Bertrand Chapron	IFREMER	FRANCE	Bertrand.chapron@ifremer.fr
Susanne Lehner	DLR	GERMANY	susanne.lehner@dlr.de
Johannes Stolz-Stellenfleth	Germany Aerospace center	GERMANY	johannes.stolz-stellenfleth@dlr.de
Jochen Horstmann	GKSS Research Center	GERMANY	horstmann@gkss.de
Werner Alpers	Institute of oceanography, University of Hamburg	GERMANY	alpers@ifm.uni-hamburg.de
Roland Romeiser	University of Hamburg	GERMANY	rmeiser@ifm.uni-hamburg.de
Ned Dwyer	Coastal and Marine Resources Centre-UCC	IRELAND	n.dwyer@ucc.ie
Valerie Cummins	Coastal and Marine Resources Centre-UCC	IRELAND	v.cummins@ucc.ie
Stephen Briggs	ESA/ESRIN	ITALY	stephen.briggs@esa.int
Yves-Louis Desnos	European Space Agency-ESRIN	ITALY	yves.loius.denos@esa.int
Harm Greidanus	JRC	ITALY	harm.greidanus@jrc.it
Francisco J. Ocampo-Torres	Oceanograffa Fisica CICFSF	MEXICO	ocampo@cicese.mx
Einar ARNE Herland	European Space Agency	NETHERLANDS	einar-arne.herland@esa.int
Mark R. Drinkwater	European Space Agency	NETHERLANDS	mark.drinkwater@esa.int
Camilla Brekke	FFI	NORWAY	camilla.brekke@ffi.no
Richard B. Olsen	FFI	NORWAY	richard.olsen@ffi.no
Jan Petter Pedersen	Kongsberg Satellite Services	NORWAY	janp@ksat.no
Marte Indregard	Kongsberg Satellite Services	NORWAY	marte@ksat.no
Lars-Petter Gjølvik	Kongsberg Spacetec	NORWAY	larspg@spacetec.no
Tove Tennvassås	Kongsberg Spacetec	NORWAY	tove@spacetec.no
Tommy Andreassen	Meteorologisk Institutt, Værvarslinga for Nord-Norge	NORWAY	tommy.andreassen@met.no
Birgitte R. Furevik	Nansen Environmental and remote sensing Center	NORWAY	birgitte.furevik@nersc.no
Heidi A. Espedal	Nansen Environmental and remote sensing Center	NORWAY	heidi.espedal@nersc.no
Johnny A. Johannessen	Nansen Environmental and remote sensing Center	NORWAY	johnny.johannessen@nersc.no
Stein Sandven	Nansen Environmental and remote sensing Center	NORWAY	stein.sandven@nersc.no
Bo Andersen	Norsk Romsenter	NORWAY	bo@spacecentre.no
Guro Dahle Strøm	Norsk Romsenter	NORWAY	guro.dahle.strom@spacecentre.no
Geir Engen	NORUT IT AS	NORWAY	geir.engen@itek.norut.no
Harald Johnsen	NORUT IT AS	NORWAY	harald.johnsen@itek.norut.no
Ann Lisbeth Ruud	Norwegian Space Centre	NORWAY	ann.lisbeth.ruud@spacecentre.no

Per Erik Skrøvseth	Norwegian Space Centre	NORWAY	per.erik.skrøvseth@spacecentre.no
Alexei Stuliy	UNIS	NORWAY	alexei.stuliy@unis.no
Josê da Silva	Institute of oceanography, University of Lisbon	PORTUGAL	jdasilva@fc.ul.pt
Vladimir Kudryavtsev	Nansen Environmental and remote sensing Center	RUSSIA	Vladimir.kudryavtsev@niersc.spb.ru
Dmitry B. Akimov	Nansen International Enviromental and Remote Sensing Center	RUSSIA	Dmitry.akimov@niersc.spb.ru
Alexey A. Romanov	VNIERKH	RUSSIA	romanov@vnierkh.ru
Konstantin Ts. Litovchenko	VNIERKH	RUSSIA	litov@vnierkh.ru
Giulio Ruffino	Starlab	SPAIN	giulio.ruffini@starlab.es
Robert A. Shuchman	Altarum Institute	USA	lisa.phillips@altarum.org
Ralph Foster	APL/University of Washington	USA	ralph@apl.washington.edu
Jamos P. Mc. Guire	Integrated Program Office/NASA	USA	jamos.mcguire@noaa.gov
Donald R. Thompson	Johns Hopkins University Applied Physics Laboratory	USA	donald.r.thompson@jhuapl.edu
Frank Monaldo	Johns Hopkins University Applied Physics Laboratory	USA	f.monaldo@jhuapl.es
John Overton	NAONESS IPO	USA	john.overton@noaa.gov
Melody Bledsoe	Naval Oceanographic Office, N 211	USA	bledsoe@navo.navy.mil
Pablo Clemente-Colón	NOAA/NESDIS	USA	pablo.clemente-colon@noaa.gov
William G. Pichel	NOAA/NESDIS/ORA	USA	william.g.pichel@noaa.gov
Xiaofeng Li	STG Inc.	USA	xiaofeng.li@noaa.gov
Todd D. Sikora	United States Naval Academy	USA	sikora@usna.edu
Christopher c. Wackerman	Veridian Systems	USA	chris.wackerman@veridian.com
David Lyzenga	Veridian Systems	USA	david.lyzenga@veridian.com